# MECHANICAL BEHAVIOUR OF UNSATURATED AGGREGATED SOILS

THÈSE N$^{O}$ 4011 (2008)

PRÉSENTÉE LE 25 JANVIER 2008

À LA FACULTÉ DE L'ENVIRONNEMENT NATUREL, ARCHITECTURAL ET CONSTRUIT

LABORATOIRE DE MÉCANIQUE DES SOLS

PROGRAMME DOCTORAL EN MÉCANIQUE

ÉCOLE POLYTECHNIQUE FÉDÉRALE DE LAUSANNE

POUR L'OBTENTION DU GRADE DE DOCTEUR ÈS SCIENCES

PAR

Azad KOLIJI

M.Sc. in civil engineering, Iran University of science and technology, Tehran, Iran
et de nationalité iranienne

acceptée sur proposition du jury:

Prof. L. Laloui, président du jury
Prof. L. Vulliet, directeur de thèse
Prof. R. Charlier, rapporteur
Prof. P. Delage, rapporteur
Prof. H. Flühler, rapporteur

ÉCOLE POLYTECHNIQUE
FÉDÉRALE DE LAUSANNE

Suisse
2008

*To my grandmother Daya & my aunt Mina*

# Contents

# Acknowledgments

This thesis is the result of four years of work whereby I have been accompanied and supported by many people. I would like to thank the diverse group of individuals who supported my work, influenced my thoughts and participated in this study. Without each one of them, this project simply would not have been possible.

Foremost, I would like to express my sincere gratitude to my thesis supervisor, Prof. Laurent Vulliet, for his support and mentorship through this study, and for his constant confidence in my abilities. I admire his affirmative professional attitude, and his efficient mindful approach to simplify complexities.

I would like to acknowledge my debt to Prof. Lyesse Laloui for his highly responsive supports over the duration of this work. His contribution is apparent all over my dissertation. Beyond all his contribution to my work, I would like to thank Prof. Laloui for his limitless facility to initiate exploration in the world of scholarship and for opening my eyes to the elegance of "scholarly life".

I would like to thank Peter Vontobel, Eberhard Lehmann and, René Hassanein of the Neutron Imaging group of PSI, for providing me with the opportunity of running long experiments at NEUTRA, and for their strong support during and after all the measurements.

Special thanks to Andrea Carminati for his help during the experiments at PSI - no beam, beam back - and during the further evaluation of the results. I enjoyed our collaboration and the good time we had together.

I am deeply thankful to Prof. Hannes Flühler for his fruitful comments and discussions during this work, and for his participation to the Jury. I also extend my sincere thanks to the other members of my PhD committee, Prof. Pierre Delage and Prof. Robert Charlier, for accepting to review and evaluate this thesis, and again to Prof. Laloui for accepting to chair my PhD thesis jury on behalf of the doctoral school.

Doing an experimental project is not possible without a strong technical support; my thanks, therefore, go to Jean-Marc Terraz for the brilliant construction of the experimental equipments, and to Gilbert Gruaz, Patrick Dubey and, Lionel Pittet for their help in carrying out the laboratory experiments. I appreciate the precious help of David Ubals Picanyol for installation and calibration of the experimental equipments during his trainee stay at LMS.

I am grateful to Massoud Dadras for his real help in carrying out the microscopy observations, and to Gwenn Le Saoût for the MIP tests. I would like to express my deep appreciation to Peter Lehmann and Anders Kaestner for helping me with image analysis of tomography data.

My friends at LMS and LMR made these years at Lausanne very special. I have to say a big 'thank-you' to all of them, wherever they are: Hérvé Péron with whom I shared the office and who helped me a lot to learn French language, Mathieu Nuth (good-hearted man), Bertrand François (candid fellow), Irene Manzella and Stefano Nepa (lovely couple), Laurent Gastaldo, Patrick Dubey, Matteo Moreni, Cane Cekerevac, Véronique Triguero, Suzanne Chalindar (thanks Suzanne also for the résumé), Federica Sandrone, Rafal Obrzud (who helped me a lot with LaTeX), Emilie Rascol, Nina Mattsson, Claire Sauthier, Tohid Kazerani, Alessio Ferrari, Laurent Jäggi and, Thierry Schepmans.

Also special thanks to Rosa Ana Menendez, Antonella Simone, Karine Barone, Anh Le, Gilbert Steinmann and, Christophe Bonnard who helped me at several occasions.

I cannot express how I am, deeply and forever, indebted to my beloved parents, Sabah and Ebrahim, for the encouragement, affection, and the spirit they continuously bring to my life. I wish to express my warmest thanks to my brothers Hooman and Alan, as well as to Azin's parents and sisters for having made this effort easier.

A journey is easier when we travel together. At last, but not certainly least, I would like to give my most heartfelt thanks to Azin, for her unconditional support, her continual love and, for being my endless source of peace.

# Abstract

Particle aggregation is a commonly observed phenomenon in many types of soils, such as natural clays and agricultural soils. These soils contain porous aggregates, often separated by large, interaggregate pores. Two levels of intra- and interaggregate porosity are, therefore, present in these soils. Depending on the size and strength of the aggregates, aggregation may alter the water retention and mechanical behavior of the soil and make it different from that of a reconstituted soil of the same mineralogy.

The present work is aimed at studying the mechanical behavior of unsaturated, aggregated soils with respect to soil structure effects. It involves theoretical developments, a multi-scale experimental study, and constitutive modeling.

As a first step, the theory of multiphase mixtures was used to evaluate effective stress and to derive the coupled hydro-mechanical governing equations for a double porous soil. In this way, from the outset, the field variables and the required constitutive equations were identified.

In the first experimental part, a new suction-controlled oedometer was developed for investigating the stress-strain response and water retention properties of the soil. The tests were carried out on reconstituted and aggregated samples of silty clays with an average aggregate size of about 2 $mm$. The results were interpreted in terms of a Bishop's type effective stress, suction, void ratio, and degree of saturation.

From the tests carried out on the aggregated samples, an apparent preconsolidation stress was seen which depends not only on stress state and stress history, but also on the soil structure.

The results of unsaturated tests revealed that the apparent effective preconsolidation stress increases with suction for both reconstituted and aggregated soils; however, the rate of increase is higher for aggregated soils. The results showed that the virgin compression curve of aggregated soils is on the right side of the normal consolidation line of the corresponding reconstituted soil. The two curves, however, tend to converge at higher values of stress when the aggregated structure is progressively removed by straining. It was observed that the degree of saturation in aggregated samples can increase during mechanical loading under constant suction because of the empty inter-aggregate pores being closed during the compression.

In the following experimental part, soil structure and its evolution were tested using a combination of three methods: mercury intrusion porosimetry (MIP), environmental scanning electron microscopy (ESEM), and neutron tomography.

Results of the MIP and ESEM tests revealed a homogeneous fabric with a uni-modal pore size distribution for the reconstituted soil, and a bi- or multi-modal pore size distribution for the aggregated soil. Comparison of different observations revealed that the larger pores in the aggregated soil disappear as a result of mechanical loading or wetting. The non-destructive method of neutron tomography was used to assess the evolution of the aggregated soil structure during oedometric loading. An important observation was that the change in the volume fraction of macropores is mainly associated with irreversible deformations. Tomography results also suggest similarity of the water retention behavior for single aggregates and the reconstituted soil matrix.

Based on the experimental results, a new constitutive framework was proposed for the extension of the elasto-plastic models of reconstituted soils to aggregated soils. Using this framework, a new mechanical constitutive model, called ACMEG-2S, was formulated within the critical state concept and the theory of hardening elasto-plasticity.

A parameter called "degree of soil structure" was introduced to quantify the soil structure physically in terms of macroporosity. Evolution of this parameter, as a state parameter, was then linked to the plastic strains. The apparent effective preconsoliodatoin pressure in aggregated soils was introduced as an extension of the effective preconsolidation pressure of the reconstituted soil. The extension is controlled by two multiplicative functions in terms of suction and the degree of soil structure. These functions describe the gain in the apparent preconsolidation pressure due to the current fabric of the soil at the current suction.

The model adopts the effective stress and suction as stress variables. It uses non-linear elasticity and two mechanisms of plasticity.

In addition to the mechanical model, an improved water retention model was proposed which incorporates the combined effects of suction, volume change, and the evolving double porous fabric.

The proposed mechanical model, coupled with the water retention model, unifies the combined effects of partial saturation, inter-particle bonding, and soil fabric.

The model was then used to simulate the experiments carried out during the course of this study. Simulations showed that the model could successfully address the main features of the behavior of aggregated soils. Typically, it can reproduce the non-linearity of stress-stress response under virgin compression and the increase of degree of saturation during compression at constant suction.

Finally, the model was examined for its capability in reproducing the behavior of structured bonded soils. With for the appropriate set of parameters, the model can reasonably reproduce the mechanical behavior of saturated bonded soils reported in the literature.

***Keywords:*** Aggregated soil, soil structure, structured soil, partial saturation, suction, water retention, oedometer, multiphase mixture theory, neutron tomography, constitutive modeling

# Résumé

L'agrégation de particules est un phénomène couramment observé dans une grande variété de sols tels que les argiles naturelles et les sols agricoles. Ces sols contiennent des agrégats poreux, souvent séparés par d'importants pores inter-agrégat. Deux niveaux d'intra- et inter-porosité d'agrégats sont donc présents dans ces sols. L'agrégation peut altérer le comportement de rétention d'eau ainsi que le comportement mécanique du sol. Elle peut modifier ces comportements selon la taille et la résistance des agrégats, par rapport à un sol reconstitué de même minéralogie. Le présent travail a ainsi pour but d'étudier le comportement mécanique des sols agrégés non saturés face aux effets de structure. Ceci se fera au travers de développements théoriques, d'études expérimentales multi-échelles et de modélisation constitutive.

La première étape a été d'utiliser la théorie des mélanges multiphasiques dans le but d'évaluer la contrainte effective et de dériver les équations hydro-mécaniques couplées pour un sol à double porosité. De cette façon, les variables de champ et les équations requises ont pu être identifiées.

Dans la première partie de l'approche expérimentale, un nouvel oedomètre à succion contrôlée a été développé pour étudier les propriétés de réponse en contrainte-déformation et de rétention d'eau du sol. Les tests ont été effectués sur des échantillons d'argile limoneuse reconstitués et agrégés, avec une taille d'agrégats moyenne de 2 mm. Les résultats ont été interprétés en termes de contrainte effective de Bishop, succion, indice des vides et degré de saturation.

D'après les tests effectués sur les échantillons agrégés, une pression de pre-consolidation apparente, ne dépendant pas seulement de l'état de contrainte et de l'histoire des contraintes, mais aussi de la structure du sol, a été identifiée. Les résultats d'essais non saturés ont révélés que la pression de preconsolidation effective apparente augmente avec la succion pour les sols reconstitués et agrégés. Cependant, elle augmente plus rapidement pour les sols agrégés. Les résultats ont également montrés que la courbe de compression vierge d'un sol agrégé se situe à la droite de la courbe de consolidation normale du sol reconstitué correspondant. En revanche, pour des valeurs de contrainte plus élevées, les deux courbes ont tendance à converger du fait que la structure agrégée est progressivement effacée par la déformation du sol. Il a également été observé que le degré de saturation dans les échantillons agrégés peut augmenter durant le chargement mécanique à succion constante à cause de la fermeture du vide inter-agrégat durant la compression.

Dans la partie expérimentale suivante, la structure du sol et son évolution ont été testées en utilisant trois méthodes combinées: porosimétrie par intrusion de

mercure (MIP), microscopie à balayage de type environnemental (ESEM) et tomographie par neutrons. Les résultats des essais MIP et ESEM ont montré une organisation porale homogène avec un mode de distribution de taille de pores unique pour le sol reconstitué et double ou multiple pour le sol agrégé. Par comparaison entre diverses observations, il a été observé que les pores les plus importants dans le sol agrégé disparaissent suite au chargement mécanique ou à l'humidification. La méthode non-destructive de tomographie par neutrons a été utilisée pour évaluer l'évolution de la structure de sols agrégés durant le chargement oedométrique. Une découverte importante fut celle de voir que le changement de fraction volumique de macropores est principalement associé à des déformations irréversibles. Par ailleurs, les résultats tomographiques suggèrent une similarité entre le comportement de rétention d'eau d'un agrégat seul et celui d'une matrice de sol reconstitué. Sur la base des résultats expérimentaux, un nouveau cadre constitutif a été proposé pour l'extension de modèles elasto-plastiques de sols reconstitués aux sols agrégés. Un nouveau modèle constitutif mécanique nommé ACMEG-2S a ainsi été formulé dans la cadre du concept de l'état critique et de la théorie d'elasto-plasticité avec écrouissage. Un paramètre appelé degré de structure de sol a été introduit pour quantifier physiquement la structure du sol en termes de macroporosité. L'évolution de ce paramètre, qui est un paramètre d'état, a été liée aux déformations plastiques. La pression de preconsolidation effective apparente des sols agrégés a été introduite par extension de la pression de preconsolidation effective des sols reconstitués. Cette extension est contrôlée par deux fonctions multiplicatives en termes de succion et de degré de structure du sol. Ces fonctions décrivent le gain de pression de preconsolidation effective apparente du à l'organisation porale actuelle du sol et à la succion actuelle. Le modèle adopte la contrainte effective et la succion comme variables de contrainte. Il utilise l'élasticité non-linéaire ainsi que deux mécanismes de plasticité. En plus du modèle mécanique, un modèle de rétention d'eau amélioré incorporant les effets combinés de succion, changement de volume et d'organisation porale évolutive, a été proposé. Le modèle mécanique proposé couplé avec le modèle de rétention d'eau, unifie les effets combinés de saturation partielle, de liens inter-particules et d'organisation porale de sols.

Le modèle a ensuite été utilisé pour simuler les essais réalisés au courant de cette étude. Les simulations ont montré que le modèle saisit les principales caractéristiques du comportement de sols structurés avec succès. Typiquement, il est capable de reproduire la non-linéarité de la réponse en contrainte-déformation durant la compression vierge, ainsi que l'augmentation du degré de saturation durant la compression à succion constante.

Pour terminer, le modèle a été évalué quant à sa capacité à reproduire le comportement de sols structurés cimentés. En choisissant un ensemble de paramètres approprié, le modèle peut raisonnablement reproduire le comportement mécanique de sols saturés cimentés répertoriés dans la littérature.

***Mots clés:*** Sol agrégé, structure de sols, sols structurés, saturation partielle, succion, rétention d'eau, oedometer, théorie des mélanges multiphasiques, tomographie par neutrons, modélisation constitutive.

# List of Symbols

## Roman Symbols

| | |
|---|---|
| $A$ | relative proportion of deviatoric and volumetric de-structuring |
| $a$ | growth rate parameter for deviatoric elastic radius |
| $b$ | shape parameter for deviatoric yield surface |
| $Bx$ | Brix degree |
| $\mathbf{b}$ | body force density for the mixture |
| $\mathbf{b}_\alpha$ | body force density for constituent $\alpha$ |
| $C$ | mass concentration of PEG solution |
| $c$ | growth rate parameter for isotropic elastic radius |
| $C_2$, $C_3$ | variables of PSD evolution model for Zone 2 and 3 |
| $c_\alpha$ | mass interaction supply of constituent $\alpha$ |
| $C_c$ | compressibility index |
| $C_s$ | swelling index |
| $C_{ts}$ | tangential compressibility index for structured soil |
| $\boldsymbol{C}^e$ | elastic compliance tensor of rank four ($9 \times 9$ matrix) |
| $d$ | spacing ratio |
| $\boldsymbol{D}^e$ | elastic constitutive tensor of rank four ($9 \times 9$ matrix) |
| $\boldsymbol{D}^{ep}$ | elasto-plastic constitutive tensor of rank four ($9 \times 9$ matrix) |
| $\mathbf{D}^e$ | elastic constitutive matrix ($6 \times 6$) |
| $\mathbf{D}^{ep}$ | elasto-plastic constitutive matrix ($6 \times 6$) |
| $e$ | total void ratio |

| | |
|---|---|
| $f$ | yield function |
| $f(\log r_i)$ | Pore size density function, in Eq. (5.2) |
| $f_{iso}$, $f_{dev}$ | isotropic and deviatoric yield function |
| $\mathbf{F}$ | vector of yield functions |
| $G$ | shear elastic modulus |
| $g$ | gravity acceleration |
| $g$ | plastic potential |
| $g_{iso}$, $g_{dev}$ | isotropic and deviatoric plastic potential |
| $\mathbf{G}$ | vector of plastic potential functions |
| $\mathbf{g}$ | gravity density |
| $H$ | hardening modulus |
| $H^{st}$ | hardening modulus linked to structure degradation (or formation) |
| $\mathbf{H}$ | matrix of hardening moduli |
| $i$ | the van't Hoff factor, in Eq. (4.3) |
| $I_1, I_2, I_3$ | first, second and third invariants of stress tensor |
| $\mathbf{I}$ | second order identity tensor |
| $J$ | second invariant of deviatoric stress tensor |
| $K$ | bulk elastic modulus |
| $k_{\alpha r}^{\mathrm{m}}$ | relative permeability of mixture $m$ for fluid constituent $\alpha$ |
| $K_0$ | coefficient of earth pressure at rest |
| $K_{\alpha}^{\mathrm{m}}$ | bulk modulus of fluid constituent $\alpha$ in mixture $m$ |
| $\mathbf{K}_{\alpha}^{\mathrm{m}}$ | permeability tensor of mixture $m$ for fluid constituent $\alpha$ |
| $\mathbf{k}^{\mathrm{m}}$ | intrinsic permeability tensor of mixture $m$ |
| $M$ | Molecular mass of water, in Eq. (4.1) |
| $M$ | molarity, in Eq. (4.3) |
| $M$ | slope of the critical state line in the effective stress plane $q - p'$ |
| $\overset{e}{\mathbf{m}}_{\alpha}$ | extra part of linear momentum supply of constituent $\alpha$ |
| $\overset{\circ}{\mathbf{m}}_{\alpha}$ | equilibrium part of linear momentum supply of constituent $\alpha$ |

| | |
|---|---|
| $\overset{\circ}{\mathbf{m}}{}^{\mathrm{m}}_{\alpha(i)}$ | equilibrium part of linear momentum supply for fluid constituent $\alpha$ in mixture $m$ arising from constituents of the complement mixture |
| $\overset{\alpha\beta}{m}_D$ | drag coefficient between the two constituents $\alpha$ and $\beta$ |
| $\mathbf{m}_\alpha$ | linear momentum interaction supply of constituent $\alpha$ |
| $n$ | total porosity |
| $N$ | van Genuchten parameter |
| $N^V_{agg}$ | number of aggregate voxels in a section of tomography volume |
| $N^V_{total}$ | total number of voxels in a section of tomography volume |
| $n_e$ | exponent of non-linear elasticity |
| $n_\alpha$ | volume fraction of constituent $\alpha$ within the mixture |
| $n_{st}$ | parameter of suction-induced hardening for soil structure |
| $\mathbf{n}_F$ | derivative matrix of yield functions with respect to effective stress |
| $\mathbf{n}_G$ | matrix of flow rule directions |
| $p'$ | mean effective stress |
| $p'_{c0}$ | saturated preconsolidation pressure |
| $p_\alpha$ | pressure of fluid constituent $\alpha$ |
| $p_{at}$ | atmospheric pressure |
| $q$ | deviatoric stress |
| $R$ | constant of perfect gases, in Eq. (4.1) |
| $R$ | degree of soil structure |
| $r^e_{iso}$, $r^e_{dev}$ | initial radius of elastic domain for isotropic and deviatoric mechanism |
| $r_c$ | the radius of curvature of liquid meniscus |
| $r_p$ | entrance pore radius |
| $r_{iso}$, $r_{dev}$ | isotropic and deviatoric elastic radius |
| $RH$ | relative humidity |
| $s$ | matric suction |
| $s^{\mathrm{m}}$ | matric suction in mixture $m$ |
| $s_e$ | air entry value suction |

| | |
|---|---|
| $s_L^{\mathrm{m}}$ | local degree of liquid saturation in mixture $m$ |
| $s_t$ | total suction |
| $s_\pi$ | osmotic suction |
| $S_r$ | degree of liquid saturation |
| $S_{res}$ | residual degree of liquid saturation |
| $\mathbf{S}$ | deviatoric stress tensor |
| $T$ | absolute temperature |
| $\mathbf{u}_\alpha$ | displacement of particles in constituent $\alpha$ |
| $v$ | specific volume |
| $V$ | volume of the whole mixture |
| $V_\alpha$ | volume of constituent $\alpha$ within the mixture |
| $\mathbf{v}$ | velocity of the mixture |
| $\mathbf{v}_\alpha$ | velocity of $\alpha$ constituent |
| $\mathbf{w}_\alpha^{\mathrm{m}}$ | seepage velocity of constituent $\alpha$ in mixture $m$ |
| $\mathbf{x}$ | spatial position at current configuration |
| $\mathbf{X}_\alpha$ | spatial position of constituent $\alpha$ particles at reference configuration |

## Greek Symbols

| | |
|---|---|
| $\alpha$ | parameter of non-associative flow rule |
| $\alpha_\alpha$ | effective stress parameter for fluid phase $\alpha$ |
| $\alpha_s$ | modified van Genuchten parameter |
| $\alpha_w$ | original van Genuchten parameter |
| $\alpha_{st}$ | parameter of suction effects on soil fabric , in Eq. (6.36) |
| $\varpi_\alpha$ | intrinsic thermodynamic equilibrium pressure of constituent $\alpha$ |
| $\beta$ | $v_i/(\lambda^* - \kappa)$ |
| $\beta_\alpha$ | configuration pressure of constituent $\alpha$ |
| $\Gamma$ | specific volume on the critical state line for $p' = 1$ unit |
| $\Gamma_\alpha$ | leakage term for fluid constituent $\alpha$ |

| | |
|---|---|
| $\gamma_w$ | unit weight of water |
| $\boldsymbol{\gamma}_s$ | parameters of the intrinsic suction-induced hardening |
| $\Delta m_0$ | initial mass drop in the osmotic oedometer system |
| $\boldsymbol{\epsilon}$ | vector of the strain tensor components ($1 \times 6$) |
| $\boldsymbol{\varepsilon}$ | strain tensor ($3 \times 3$ matrix) |
| $\varepsilon_1$ | vertical (principal) strain in triaxial condition |
| $\varepsilon_3$ | lateral (principal) strain in triaxial condition |
| $\varepsilon_d$ | deviatoric strain |
| $\varepsilon_d^{p,dev}$ | deviatoric plastic strain induced by deviatoric mechanism |
| $\varepsilon_d^{p,iso}$ | deviatoric plastic strain induced by isotropic mechanism |
| $\varepsilon_v$ | volumetric strain |
| $\varepsilon_v^{p,dev}$ | volumetric plastic strain induced by deviatoric mechanism |
| $\varepsilon_v^{p,iso}$ | volumetric plastic strain induced by isotropic mechanism |
| $\varepsilon^D$ | de-structuring plastic strain |
| $\boldsymbol{\zeta}$ | vector of internal variables |
| $\theta$ | the contact angle of fluid interface to solid |
| $\Theta_2$ | cumulative difference between the volume fraction of pores of Zone 2 at saturated and driest state in the PSD evolution model |
| $\Theta_3$ | cumulative difference between the volume fraction of pores of Zone 3 at saturated and driest state in the PSD evolution model |
| $\Theta_{2e}$ | total moving volume fraction of PSD from macropores to micropores |
| $\Theta_s$ | total volume fraction of pores influenced by suction $s$ |
| $\Theta_{se}$ | effective volume fraction of pores influenced by suction $s$ |
| $\vartheta$ | volume fraction of pores per unit weight of soil |
| $\kappa$ | slope of isotropic unloading-reloading curve in the space $v - \ln p'$ |
| $\boldsymbol{\lambda^p}$ | vector of plastic multipliers |
| $\lambda^p$ | plastic multiplier |
| $\mu_\alpha^{\mathrm{m}}$ | dynamic viscosity of constituent $\alpha$ in mixture $m$ |
| $\nu$ | Poisson's ratio |

| | |
|---|---|
| $\overline{\xi}_{\alpha}$ | mass fraction of constituent $\alpha$ within the mixture |
| $\Pi$ | osmotic pressure |
| $\varpi$ | static pressure acting on the physically saturated mixture $m$ixture |
| $\overline{\rho}_{\alpha}$ | partial (bulk) mass density of constituent $\alpha$ within the mixture |
| $\rho$ | mass density of the mixture |
| $\rho_{\alpha}$ | intrinsic (real) mass density of constituent $\alpha$ |
| $\boldsymbol{\sigma}$ | vector of the stress tensor components ($1 \times 6$) |
| $\boldsymbol{\sigma'}$ | effective stress tensor ($3 \times 3$ matrix) |
| $\boldsymbol{\sigma}$ | total stress tensor ($3 \times 3$ matrix) |
| $\boldsymbol{\sigma}_{\alpha}$ | Cauchy stress tensor of constituent $\alpha$ |
| $\overset{e}{\boldsymbol{\sigma}}_{\alpha}$ | non-equilibrium (extra) part of stress of constituent $\alpha$ |
| $\sigma_1$, $\sigma'_1$ | total and effective vertical (principal) stress in triaxial condition |
| $\sigma_3$, $\sigma'_3$ | total and effective lateral (principal) stress in triaxial condition |
| $\sigma_{\mathrm{v}}$, $\sigma'_{\mathrm{v}}$ | total and effective vertical stress |
| $\sigma_{\mathrm{v}net}$ | vertical net stress |
| $\phi^{\mathbf{m}}$ | relative contribution of mixture $m$ to the total fluid pressure; relative volume fraction of pores of mixture $m$ within the whole system of double mixture |
| $\phi^{\mathrm{m}}_{\alpha}$ | relative volume fraction of fluid constituent $\alpha$ within the whole system of double mixture which belongs to mixture $m$ |
| $\varphi'$ | Mohr-Coloumb friction angle |
| $\chi$ | Bishop's parameter |
| $\chi^{\mathbf{m}}$ | relative contribution of liquid to the fluid pressure in mixture $m$ |
| $\chi_{\alpha}$ | function of motion for constituent $\alpha$ |
| $\psi^{st}$ | function of yield limit extension due to the soil structure effects |
| $\psi^{t}$ | function of yield limit extension due to intrinsic suction-hardening |
| $\Psi$ | water retention parameter for void ratio effects |
| $\Psi^{\mathrm{m}}_{\alpha}$ | thermodynamic deriving variables involved in mass exchange of fluid constituent $\alpha$ between two mixtures |

| | |
|---|---|
| $\Omega_{st}$ | rate of variation of $\omega$ with suction |
| $\Omega_s$ | rate of variation of $\lambda^*$ with suction |
| $\omega$ | rate of structural degradation with plastic strains |
| $\Omega_{st}$ | parameter of suction effects on soil fabric , in Eq. (6.36) |

## Superscripts

| | |
|---|---|
| $'$ | the generalized effective stress quantity |
| $*$ | intrinsic property of the corresponding reconstituted soil |
| 1 | property of mixture 1 (micropores) |
| 2 | property of mixture 2 (macropores) |
| $e$ | elastic component |
| $p$ | plastic component |

## Subscripts

| | |
|---|---|
| 0 | value at saturated state |
| $c$ | preconsolidation value |
| $cr$ | value at critical state |
| $dev$ | values related to deviatoric mechanism |
| $g$ | property of gas phase constituent |
| $iso$ | values related to isotropic mechanism |
| $l$ | property of liquid phase constituent |
| $s$ | property of solid phase constituent |
| ref | reference value of a parameter |

## Operators

| | |
|---|---|
| $\cdot$ | inner product of tensors with single contraction |
| : | inner product of tensors with double contraction |
| $\otimes$ | dyadic (tensorial) product of two tensors |

| | |
|---|---|
| $\nabla(.)$ | gradient |
| $\nabla \cdot (.)$ | divergence |
| $\mathrm{d}(.)$ | increment |
| $\partial(.)/\partial x$ | partial derivative with respect to a variable $x$ |
| $D(.)/D_t$ | material time derivative |
| $\delta_{ab}$ | Kronecker delta type function, $\delta_{ab} = 1$ if $a = b$, but 0 if $a \neq b$ |
| $\langle . \rangle$ | McCauley brackets, $\langle a \rangle = 1$ if $a > b$, but 0 if $a \leq 0$ |
| $\sum_a$ | summation over all possible values of $a$ |
| $\sum_{a \neq b}$ | summation over all possible values of $a$ except $b$ |

**Nota Bene:** Throughout this dissertation, except for Chapter 3, the sign convention is the usual convention of soil mechanics which is that compression is positive. In Chapter 3, however, the consistent sign convention of tension positive is adopted from continuum mechanics.

# Chapter 1

# Introduction

## 1.1 From saturated homogeneous to unsaturated structured soil

Since the foundation of the engineering discipline of soil mechanics by Terzaghi, exploration of the various aspects of soil behavior has continued ceaselessly. In classical saturated soil mechanics, soil has often been treated as a homogeneous continuum, the pore-scale heterogeneities being smoothed out within a representative volume.

In reality, however, many soils are structured, i.e., they are characterized by a particular structure which makes them different from the same soil from which the structure has been removed by remolding. Natural soils, for instance, often contain bonded particles, and possibly have large voids or fissures within their structure which are usually filled with more than one fluid.

Over the last two decades, major efforts have been made to incorporate the additional effects linked to soil structure and the presence of different pore fluids into the description of soil behavior. Despite major achievements, the effect of soil structure on the mechanical behavior, especially under unsaturated conditions, is still far from being well understood.

An issue of great complexity for researchers in various fields, such as agronomy, soil physics and soil mechanics, is the mechanical and hydraulic behavior of unsaturated soils subjected to aggregation. Particle aggregation is a commonly observed phenomenon in many types of soils, such as natural clays and agricultural soils. These soils contain porous aggregates, often separated by large inter-aggregate pores. Hence, in the general sense, aggregated soils are structured soils with double porosity due to the intra- and inter-aggregate pores.

Aggregation may alter different aspects of the soil behavior and make it different from that of a reconstituted soil of the same mineralogy. The permeability and water retention properties of the soil, under unsaturated conditions, are influenced by the geometry of the pores and aggregates, their arrangement and the physical state of the fluids occupying the pores. The mechanical behavior and the stress-strain response of the soil can be also affected by the strength and stiffness of the aggregates.

The main motivation to launch the present research project was to achieve an improved understanding of the behavior of unsaturated aggregated soil in relation to its structure. The present work has been inspired by the idea that *there's plenty of room at the bottom*[1]; i.e., the causes for the macroscopic complexities in soil behavior might be found at the smaller scales deep in the soil structure.

Acquiring a better understanding of soil behavior requires proper tools, among them appropriate theoretical approaches and new testing methods with the capability of inspecting new aspects of soil behavior. '*If we only perform routine tests and explore the response of our constitutive and theoretical models only within the context of these tests, not only is there the danger that we fail to discover irregularities in our theoretical models, but also we are neglecting potentially wide and fascinating tracks of geotechnical knowledge which are waiting exploration.*'[2] This project has been envisaged to combine new experimental studies with modeling aspects in aggregated soils.

## 1.2 Objectives

The present work is a part of a comprehensive joint research project whose ultimate goal is to understand and model the mechanical and hydraulic behavior of unsaturated aggregated soils.

The joint project combines different specialties and brings together three research teams,

- Institute of Terrestrial Ecology (ITÖ) at ETHZ (for soil physics),
- Soil mechanics Laboratory (LMS) at EPFL, (for soil mechanics),
- The Paul Scherrer Institute, PSI-NEUTRA, (for neutron radiography and tomography experiments).

The research project has been conducted in two companion PhD theses: the PhD dissertation of Carminati (2006) at ITÖ-ETHZ, and the present dissertation at LMS-EPFL. In both of these works, the advanced method of neutron tomography has been used for the experimental evaluation of soil structure features.

The work carried out at ITÖ-ETHZ focused on hydraulic aspects, including experimental evaluation of water storage, exchange, and transport among and within the aggregates. It proposed improved hydraulic models for soils, taking into account additional features linked to the double porosity effects and the contact area among the aggregates.

The present study focuses on the mechanical aspects in the behavior of unsaturated aggregated soils. It is aimed at studying the stress-strain response of the soil and to propose an improved formulation of constitutive models coupled with water retention effects. The work involves theoretical developments, a multi-scale experimental study, and constitutive modeling. The main explicit scopes of the present study are:

[1] Richard Feynman's classic 1959 talk: *There's plenty of room at the bottom.*

[2] David Muir Wood, 2004, in the envoi of the textbook *Geotechnical modeling.*

(i) to identify the field variables and the required constitutive relations involved in the coupled hydro-mechanical processes in double porous soils,
(ii) to evaluate the macroscopic stress-strain and water retention behavior of unsaturated aggregated soils,
(iii) to evaluate the soil structure and its evolution at the pore-scale and to assess the relationship between the macro- and the pore-scale behavior of the soil,
(vi) and finally, to propose an improved mechanical constitutive model, coupled with the water retention properties, for unsaturated aggregated soils.

The research project finds its applications in civil engineering and environmental geomechanics. For instance, the proposed constitutive model can be potentially used in landslide hazard assessments and the prediction of seasonal wetting-drying induced deformation of natural slopes where the soil possesses complex in-situ structure. The research is beneficial to agricultural engineering as well. It addresses a key issue related to the marked impact of machinery loading and suction variations induced by soil tillage on soil structural properties.

## 1.3 Outline of the thesis

The present study has been conducted in different steps comprising theoretical developments for a double porous soil, an experimental study at both macro and pore scales, and constitutive modeling. The material in this thesis is presented as follows.

**Chapter 2** reviews the current state of knowledge concerning the experimental study and constitutive modeling of soil behavior with respect to soil structure and partial saturation effects. This chapter presents the required principal concepts and provides the background to the study. Also in this chapter, the existing gaps in knowledge and the anticipated contribution of the present study to fill these gaps are outlined.

**Chapter 3** is devoted to the development of coupled hydro-mechanical governing equations for structured soils with double porosity within the multi-phase mixture theory. The formulations are developed in a general thermodynamically consistent framework into which different mechanical constitutive models can be incorporated. This sketches the theoretical framework and highlights, from the outset, the field variables under study.

**Chapter 4** aims at the macroscopic characterization of the mechanical behavior of the structured soil with respect to the combined effects of suction and structure by means of oedometric testing methods. The suction control method and the development and calibration of the new suction-controlled oedometer are described first. Then, the experimental program and results are presented in detail. The results provide a list of special features which should be addressed by the new constitutive model.

**Chapter 5** presents the experimental study of soil structure at small scales carried out using a combination of three testing methods: mercury intrusion

porosimetry (MIP), environmental scanning electron microscopy (ESEM), and neutron tomography. The experimental results of this part, together with the results presented in the preceding chapter, provide a multi-scale experimental base for the description of the mechanical behavior of the material.

**Chapter 6** presents the explicit formulation of a constitutive model for unsaturated structured soils with double porosity incorporating the structural degradation. The model parameters and the typical numerical response of the model is then evaluated. Finally, the validity of the model is assessed by simulating the experimental results of this study. At the end, the model is tested for its capability in reproducing the behavior of saturated bonded soils.

**Chapter 7**, finally, summarizes the concluding remarks and proposes outlooks for further studies.

# Chapter 2

# Background and problem addressing

This chapter is aimed to analyze the current state of knowledge about the behavior and constitutive modeling of soils with respect to the soil structure and partial saturation effects. First, the main required concepts are presented. In the three subsequent sections, the influence of partial saturation, soil fabric and inter-particle bonding on the mechanical response and water retention behavior of soils are evaluated based on the experimental evidences. Next, a review of the soil structure studies and in particular, evolution of soil structure during mechanical loading and wetting-drying process is presented. The literature review is then closed by analyzing the constitutive modeling of soils incorporating the partial saturation and soil structure effects. On the basis of the extensive literature review, the gaps in the current knowledge as well as the anticipated contribution of the present study to fill them are outlined at the end.

## 2.1 Essential concepts

### 2.1.1 Soil structure

Soil is a mixture of various natural substances including solid constituents, e.g. mineral particles, and fluid constituents like water and air. Combination of solid particles forms the soil skeleton. Depending on the nature of constituents, the soil might exhibit different *textures* referring to the degree of fineness and uniformity of a soil (Terzaghi et al., 1996).

In general, a soil with a given mineralogy might be found with different internal structures arising from different physico-chemical causes (Yong and Warkentin, 1975). These differences are usually addressed by the concept of soil structure. Following Mitchell (1993), the term *soil structure* here corresponds to the combination of *soil fabric* which is the arrangement of particles and *inter-particle bonding*.

Soil structure, regardless of its formation causes, should be described based on the geometrical and physical properties of structural units. For the purpose of description, Collins and McGown (1974) divided the structural features

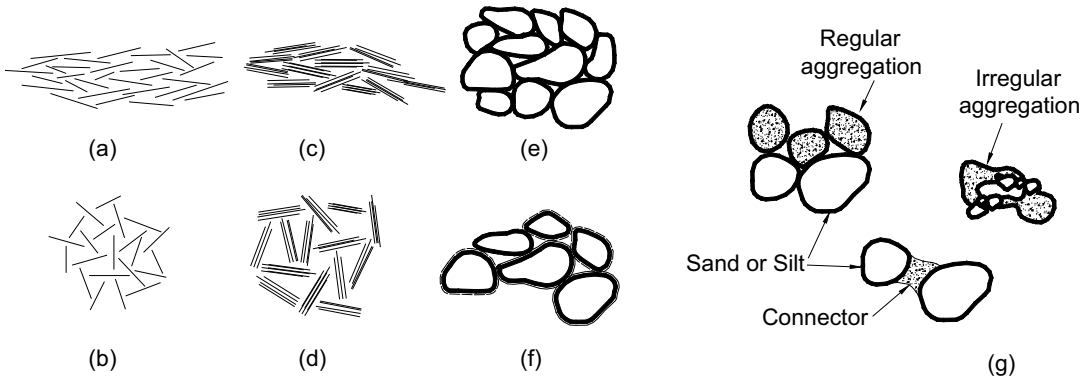


*Figure 2.1:* Elementary particle arrangements and particle assemblages (after Collins and McGown, 1974): (a) individual clay platelet interaction , dispersed structure, (b) individual clay platelet interaction, flocculated structure, (c) clay platelet group interaction, turbostatic structure, (d) clay platelet group interaction, bookhouse structure, (e) individual silt or sand interaction, (f) clothed silt or sand particle interaction (g) particle assemblage

observed in variety of soils in three different types: (i) elementary particle arrangements (ii) particle assemblages, and (iii) pore spaces.

Elementary particle arrangement consists of single forms of particle at the level of individual clay, silt or sand particles or small groups of clay platelets or clothed silt and sand particles. Occurrence of a single individual particle is rare and usually platelets of clays tend to form a group of particles. Combination of these arrangements forms different patterns of structure at the elementary particle arrangement such as bookhouse and honeycomb as shown in Figure 2.1.

Elementary particles tend to group together rather than existence as individual particles. These groups of elementary particles may regroup in larger order and form what is termed here as particle assemblages. Depending on the type, environmental conditions and origin of the *structuring phenomenon* (formation of structures), different types of assemblages may exist. *Connectors*, for example, are bridge-like assemblages that connect two (or more) other assemblages which are usually of larger size.

*Aggregates* are other types of particle assemblages acting as individual units in the structure. The cause for *aggregation* of particles and also size and shape of aggregates may vary. According to Collins and McGown (1974), aggregation might be found to be regular or irregular. In regular aggregation, unlike irregular aggregation, aggregates have a definite physical boundary and therefore particular hydro-mechanical properties can be attributed to aggregates themselves. *Particle matrices* are also another type of particle assemblages which form the background of the structure and depending on the extensiveness, in some cases, act as a binder in overall soil structure. It is plausible to assume that when special particle assemblages such as connectors, aggregates or interweaving punches are destroyed and removed by any environmental cause, the remaining structure of the soil contains mainly particle matrice assemblages.

*Pore space* is defined to be the space within and between the elementary

particles and assemblages of particles. Volume of voids in soil is usually represented by one of the following parameters: *porosity*, $n$, defined as the ratio of void volume over the total volume of the soil, *void ratio*, $e$, defined as the ratio of void volume over the volume of solid particles, or *specific volume*, $v$, which is the total volume of soil which contains unit volume of solid particles. From these definitions, it yields:

$$e = \frac{n}{1-n} \tag{2.1a}$$

$$v = 1 + e \tag{2.1b}$$

With respect to the classification of soil fabric, Collins and McGown (1974) defined different pore classes as follow: (i) intra-elemental pores: pores within the elementary particle arrangements, (ii) intra-assemblage pore: pores within particle assemblages which may occur between sets of elementary particle arrangements or between smaller particle assemblages within a larger assemblage, (iii) inter-assemblage pore, pores between the particle assemblages, and (iv) trans-assemblage pores, defined as being pores traversing the soil fabric without any relationship to the individual micro fabric features.

This classification does not account for size; however, the nature of the classifications adopted implies the absolute size to increase from intra-elemental to trans-assemblage pore space. In certain types of soil fabric this classification becomes simplified in single, double or multi-modal distributions for the pore size.

### 2.1.2 Pore fluid

The pore space can be filled with a combination of fluids. The pore fluid in soils is often comprised of water as the liquid and air as the gas phase. Dry and fully saturated soils correspond to the two extreme cases when the pores are only filled with air or water respectively. In soil mechanics, the intermediate states of the soil in which the pores are filled with two (or more) fluids are termed as *unsaturated* or *partially saturated*. In partially saturated soils, both the relative proportion of liquid and gas occupying the pore space and the energy state of the liquid phase has important influences on the mechanical response of the material. The relative proportion of liquid and gas is represented by the well known parameter of *degree of saturation* $S_r$ defined as the ratio of pore liquid volume over the total volume of the pores. The energy state, however, should be evaluated in terms of water or liquid potential.

#### 2.1.2.1 Pore water potential

Water potential is the potential energy of water relative to pure water in a reference state. It quantifies the tendency of water to move from one area to another due to osmosis, gravity, mechanical pressure, or capillary action. An element of unsaturated soil, when in contact with a reference hypotethical reservoir of free water, is capable of drawing water through the liquid and gas

phase. In simple words, the term *suction* could be used to describe this property (Tarantino and Jommi, 2005). More rigorously, the *total suction* in the soil refers to the potential of soil water and it can be measured in terms of the partial vapor pressure of the soil water (Richards, 1965; Fredlund and Rahardjo, 1993). This is equivalent with the definition of total suction as the stress required to extract a water molecule from liquid phase of soil matrix into the vapor phase (Ridley, 1993, in Monroy (2005)). Many different potentials affect the total water potential, and these effects are additive. In a simple system, two components are the pressure potential and the solute potential.

**(i) Pressure potential:** The pressure potential corresponds to the intrinsic pressure of the water which could be evaluated with respect to the atmospheric reference pressure. In saturated soils, e.g. a soil element lying below the water table, the water pressure is positive and the liquid is in compression. While, in unsaturated soil, e.g. a soil element above the water table, the hydrostatic water pressure is negative and therefore the liquid is in tension. This tension, generated through the interaction of soil water and the soil matrix, is called *matric suction* and it represents the pressure difference between the soil water and the surrounding gas:

$$s = p_a - p_w \tag{2.2}$$

In the above relation, $s$ denotes the matric suction, and $p_w$ and $p_a$ are water and air pressure respectively. In most cases, the air pressure is the atmospheric pressure and hence, the suction is equal to the negative water pressure.

The matric suction is a result of adsorption effects between soil and water molecules and capillary action within the soil matrix. In the vicinity of soil particles in unsaturated soil, the soil water is divided into capillary water and adsorbed water. In soils with an aggregated structure, this could occur in the vicinity of the aggregates or in the vicinity of primary particles within the aggregates. The adsorbed water is tightly bonded to the soil particles and could be considered as a part of solid skeleton (see e.g., Ma and Hueckel, 1993). Contrary to capillary and adsorbed water, free or bulk water could move through the pore space. At the condition of equilibrium, it is plausible to assume that the water has the same pressure everywhere within the soil matrix.

Capillary action is a result of the liquid surface tension. Surface tension is defined as the force along a line of unit length where the force is parallel to the surface but perpendicular to the line.

The capillary effect can be demonstrated using the familiar example of capillary tube. When the lower end of a vertical glass tube is placed in a liquid such as water, a concave meniscus forms. Surface tension pulls the liquid column up until there is a sufficient weight of liquid for gravitational forces to overcome the intermolecular forces. The pressure difference at two sides of the water interface with air are retained by the surface tension:

$$p_a - p_w = \frac{2T_s}{r_c} \tag{2.3}$$

where $r_c$ is the radius of meniscus curvature and $T_s$ is the surface tension.

**(ii) Solute potential:** Solute or osmotic potential of water is linked to the dissolved solutes in soil water. Pure water is usually defined as having a solute potential of zero, and in this case, solute potential of soil water containing dissolved solutes can never be positive. The suction corresponding to this negative water potential is called *osmotic suction*, $s_\pi$. The osmotic suction represents the difference between the measured values of total water potential with respect to two similar reference systems with free pure water and water identical in composition with the soil water.

#### 2.1.2.2 Suction in unsaturated soils

Following the description given above, the total suction, $s_t$, could be written as

$$s_t = s + s_\pi \tag{2.4}$$

in which $s$ and $s_\pi$ represent matric and osmotic suction in soil respectively. The osmotic suction could be observed only if the soil water is in contact with pure water through a perfect semi-permeable membrane which allows only the water molecules to pass and not the solutes. Providing such a membrane is rather complex and the osmotic suction is not usually measured in soils. However, the concept of osmotic pressure, per se, has been used to design new testing equipments for unsaturated clayey soils (Kassif and BenShalom, 1971; Delage et al., 1998, among others).

The matric suction is widely accepted to be the governing component of suction in description of the mechanical behavior of unsaturated soils, and it has been used to formulate the mechanical constitutive models for these materials (Alonso et al., 1990; Cui and Delage, 1996; Geiser, 1999). Accordingly, from now later on in this study, the term suction refers to matric suction unless otherwise stated.

### 2.1.3 Multi-scale heterogeneity

If the soil is idealized to be bundle of capillary tubes, the matric suction and the meniscus formed at the particle contact point at the pore entrance is controlled by Equation (2.3). However in reality, attention should be given to the soil fabric and the heterogeneity of the soil matrix.

Most soils show different kinds of heterogeneity depending on the considered scale. In classical soil mechanics problems, the level of heterogeneity is usually limited to the differences among the characteristics of the soil layers. Inside a specific soil layer at the scale of geotechnical testing samples, termed here *macro-scale*, the soil is usually assumed to be homogeneous as soon as enough grains or aggregates are considered. While at smaller scales corresponding to that of the pores, here termed *pore scale*, heterogeneity can be defined by means of smaller structural units, such as different pores, fissures or aggregates.

Postulation of a homogeneous soil at the macro-scale implies the consideration of a representative elementary volume (REV) of a given material. A REV is required to include a significant amount of small-scale heterogeneity to

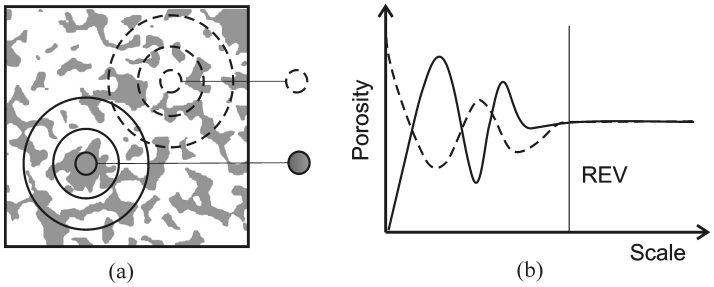


*Figure 2.2:* Effect of sample size on the porosity: (a) sample sizes (gray: solid, white: void) (b) porosity vs. sample scale.

respect a meaningful statistical average (Vogel and Roth, 1998). As an example, the dependence of the sample porosity on its scale is schematically shown in Figure 2.2. It can be seen that the REV may be representative of a homogeneous medium, while smaller samples are completely heterogeneous. For volumes below the REV, as may be seen in Figure 2.2(a), the whole sample can be located completely within the pores or within the particles, leading to quite different values of porosity. However, when the sample sizes increase, the difference between the two values of porosity decreases and they tend to a single one obtained at the REV level. It is noteworthy that depending on the heterogeneity of the medium at larger scales, the different measured values of a parameter like porosity might again diverge at larger scales.

### 2.1.4 Structured soil

There is a strong relationship between the soil structure and soil heterogeneity. In the classical soil mechanics, soil is considered to be a homogeneous continuum in which heterogeneity at the pore and particle scale is usually smoothed out (Laloui et al., 2003). It means that the effects of soil structure on its macroscopic behavior is assumed to be insignificant. However in some soils, the response to environmental loading is strongly influenced by the soil structure. These soils, in general sense, are here referred to as *structured soils*. The behavior of these materials are usually associated with special complexities in different aspects that cannot be explained by classical soil mechanics theories without taking the soil structure into account.

In the literature, soil structure effects on the material behavior have been evaluated for two groups of soils: natural bonded soils where the inter-particle bonding governs the material behavior, and aggregated soils including compacted and expansive clays and, natural and agricultural aggregated soils in which the soil fabric receives the main focus.

#### 2.1.4.1 Natural bonded soils

Natural soils show various structures, characterized by structural units, such as aggregates, porous block, fissures, earth worm holes and root channels. They

differ from *reconstituted soils*, namely the soil with the same mineralogy from which the structures are removed by remolding, in a number of important aspects. The differences arise from their particular in-situ structure (Burland, 1990). The mechanical behavior of these materials is predominantly influenced by inter-particle bonding. These materials are often referred to as *natural structured soils* (Wood, 1995; Baudet and Stallebrass, 2004; Liu and Carter, 2000b; Cuccovillo and Coop, 1999) or *bonded soils* (Gens and Nova, 1993; Nova et al., 2003).

In these materials, different causes for development of bondings could be considered; among them are solution and deposition of silica at particles contacts in sands, cold welding at inter-particle contacts at high pressure, deposition of carbonates, hydroxides and organic matter from solution, and the modification of the adsorbed water layer and inter-particle attractive forces in clayey soils (Leroueil and Vaughan, 1990). Although the cause of special structures in these materials might be different and rather complex, according to Leroueil and Vaughan (1990) the structural effects on the behavior could be described in the same way.

In these materials, the bonds could be subjected to degradation and the initial soil structure might change during different environmental loadings (see e.g Callisto and Rampello, 2004). This phenomenon is referred to as *structure degradation* or *de-structuring*. Reconstituted soil of the same mineralogy is considered as the fully de-structured material and it is considered as reference state to interpret the characteristics of structured soil (Burland, 1990).

#### 2.1.4.2 Aggregated soils

Structured soils exhibit, in contrast to reconstituted soils, a wide and often bi- or multi-modal pore size distribution. There are two extremes in conceptualizing the fabric of these materials: aggregation of particles and macro void formation, e.g., fissures, cracks or cavities.

Aggregation of particles results in an open structure for soil. The size of aggregates ranges from tenths of microns to centimeters or even larger units (clumps, clods). Soil aggregates in general may differ in properties such a texture, resistance, porosity or relative density (Terzaghi et al., 1996). The morphological characteristics of the pore space between the aggregates depends on the size, distribution and shape of the aggregates and on their history of formation and compaction.

The other extreme corresponds to the voids that form a continuous pore space within a matrix. The openings (apertures) of such macropores are in the order of some ten microns and larger. Fissures in swelling/shrinking soils, root channels in forestry and arable soils and even bio-pores dug by the soil fauna (e.g. earth worms) are main examples of macro void formation.

Aggregation of particles is a commonly observed phenomenon in natural and agricultural soils (Horn, 2003) as well as in compacted clays at dry side of optimum water (Barden and Sides, 1970; Sridharan et al., 1971; Collins and McGown, 1974) and compacted expansive clays (Lloret et al., 2003). However,

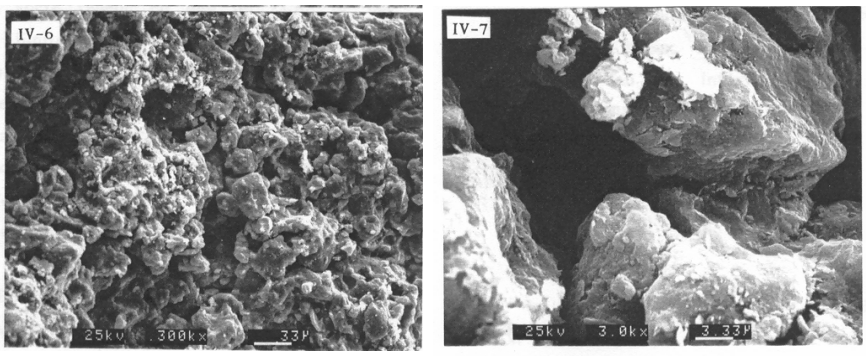


(a) (b)

*Figure 2.3:* Scanning electron microscopy of compacted clay at dry side of optimum (Delage et al., 1996): (a) 300×, (b) 3000×

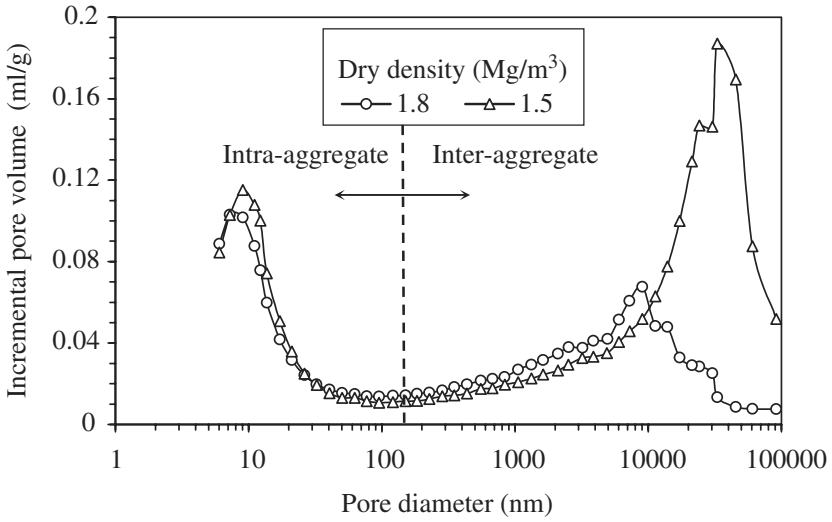


*Figure 2.4:* Distribution of incremental pore volume for two compacted bentonite samples at different dry densities. Mercury Intrusion Porosimeter test (Lloret et al., 2003)

size of aggregates in expansive and compacted clays are some orders of magnitude smaller than aggregates in natural or agricultural soils. Figure 2.3 shows the Scanning Electron Microscopy of clays compacted at dry side of optimum in which aggregation of particles could be observed (Delage et al., 1996).

It has been observed that soils with an aggregated structure including compacted clays (Al-Mukhtar, 1995; Delage et al., 1996; Griffiths and Joshi, 1990), expansive clays (Gens et al., 1995) and natural aggregated soils (Cuisinier and Laloui, 2004), are all characterized by a fabric with two dominant pore sizes corresponding to micro- (intra-aggregate) and macropores (inter-aggregate). Figure 2.4 shows the bi-modal pore size distribution of an expansive clay obtained by Mercury Intrusion Porosimetry. Hence, in the general sense, aggregated soils are structured soils with double porosity.

The hydro-mechanical properties of aggregates, as particle assemblages with a definite physical boundary, could be to some extend treated separately from the whole assembly of soil. These soils are termed *double structure soil* (Alonso et al., 1999), as two levels of structure could be identified for these materials: macro- and microstructure. The soil microstructure is defined as the elementary particle associations within the soil aggregates, whereas the arrangement of these soil aggregates and the relation among the structural units at the aggregate level is referred to as the macrostructure (Al-Mukhtar et al., 1996). The *micropores* or *intra-aggregate pores* are considered to be the smaller capillaries and pores within the aggregates and their vicinity; whereas, *macropores* or *inter-aggregate pores* are the much larger intercluster voids between the aggregates. However, the boundary between micropores and macropores is arbitrarily chosen in the literature with vague criteria (Kodikara et al., 1999).

### 2.1.5 Concept of double porosity

Such a division of pores into macro and micro levels leads to the concept of double porosity for soils. This concept has been extensively used in different fields and it can address the both features depicted in Figure 2.5.

The concept of double porosity was first introduced by Barrenblatt et al. (1960) as a flow model for non-deformable fissured porous media. This model was simplified by Barrenblatt (1963) and Warren and Root (1963). Then Aifantis (1977) extended this concept by sketching the basis of a multi-porosity model to include mass exchange of solutes through diffusion between the mobile and stagnant water phases. The general theory of Aifantis unified the earlier proposed models of Barenblatt for fluid flow through non-deformable porous media with double porosity and Biot's theory for consolidation of deformable porous media with single porosity (Biot, 1941). This theory was widely applied to model the consolidation phenomena in fissured clays and deformable fractured media (Wilson and Aifantis, 1982; Musso et al., 1990; Khalili and Valliappan, 1991; Ghafouri and Lewis, 1996; Khalili et al., 1999; Callari and Federico, 2000). A new coupling link between the elastic volumetric deformations of the two pore systems was added by Khalili and Valliappan (1996).

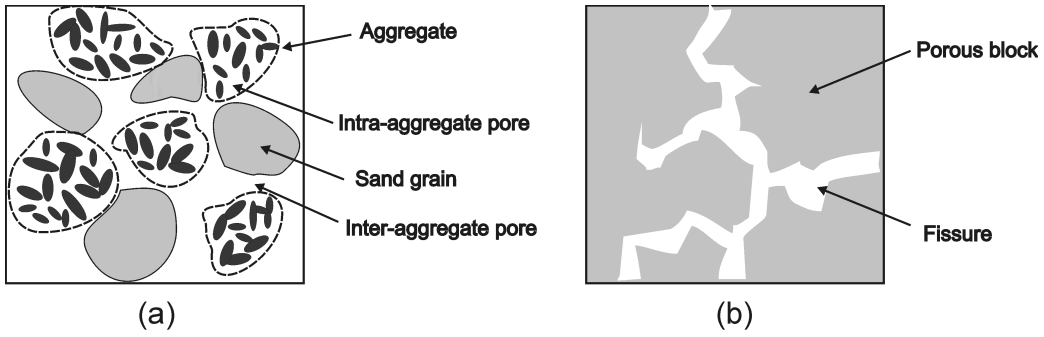


*Figure 2.5:* Concept of double porosity: (a) Aggregated soil; (b) Fissured porous medium

The concept of double porosity has been also used in analysis of multiphase flow related to petroleum reservoirs in fractured media (Lewis and Ghafouri, 1997). It has been also widely used in description of the behavior of swelling materials (Alonso et al., 1991; Gens and Alonso, 1992; Alonso, 1998; Sanchez et al., 2005).

Parallel to the problems of deformation, double porosity models are also widely used in solving problems of water and solute transport in soil. In such media, water flows preferentially through the macropores (Gwo et al., 1995; Simunek et al., 2003) and this results in more complex water flow in the media. In the existing models for flow in double porosity media, the porous medium is assumed to be a system of two overlapping interacting regions associated with macro- and micropores (Simunek et al., 2001; Huang et al., 2003). Although most of the fluid mass is stored in the micropores, the permeability of the macropores is much higher than that of the micropores (Tuncay and Corapcioglu, 1995). This concept leads to models in which two distinct pore pressures are present in two system of pores (Wang and Berryman, 1996).

Two different approaches exist for water flow in a double porosity medium: dual permeability and dual-porosity approach (e.g. Gerke and Van Genuchten, 1993). The first one allows for the water to flow in both macropores and the matrix. Darcy's law is postulated for both systems of pores with different values of permeability providing additional terms for water transfer between macro- and micropores. This approach has been used for the study of consolidation in double porosity media (Wilson and Aifantis, 1982; Musso et al., 1990; Lewallen and Wang, 1998; Khalili et al., 1999; Callari and Federico, 2000) and water flow in deformable double porosity soils (Khalili and Valliappan, 1996; Lewis and Ghafouri, 1997; Lewandowska et al., 2004). The second approach assumes that water flow happens only through the macropores. Micropores are assumed to be only involved in the local water exchange between two system of pores and to act as feeding sources for macropores that can exchange, retain and store water but do not permit convective flow (Huyakorn et al., 1983; Simunek et al., 2003). As a result, water in aggregated soil is either mobile water, namely free bulk water in macropores, or immobile water in micropores within the aggregates (Gwo et al., 1995; Pini and Putti, 1997; Simunek et al., 2001; Huang et al., 2003; Simunek et al., 2003). The immobile water in intra-aggregate pores is considered by some authors as the water adsorbed by solid particles that should be treated as a part of solid phase (Loret et al., 2002; Ma and Hueckel, 1993; Murad and Cushman, 2000). Each approach requires its own set of appropriate hydraulic constitutive equations that should be introduced to derive the field equations.

Recently, Sanchez et al. (2005) developed the formulation of double porosity media applied to an aggregated expansive soil consists of clay pellets. They used the conceptual model of Ghafouri and Lewis (1996) in which the medium with double porosity is divided into two overlapping but distinct continuum corresponding to two different structures of pores. The first one is related to the solid particles and the voids inside the pellets, and the second medium is associated with the pellets and the pores between them. Although, this concept offers

different possibilities to better describe problems of double porosity media, it suffers from the fact that degradation of structures and structure modifications are not integrated in it.

## 2.2 Partial saturation effects

### 2.2.1 Water retention characteristics

The relation between the the liquid potential and the relative proportion of liquid and gas occupying the pore space in unsaturated soils is evaluated by the soil water retention characteristics. For a soil with given void ratio and fabric, the degree of saturation, $S_r$, in the isothermal condition depends on suction $s$. In general, the relation between degree of saturation ($S_r$), suction ($s$), and void ratio ($e$) identifies the water retention characteristics of a soil and the plots representing this relations are called *water retention curves*.

Water retention curve of unsaturated soils has been studied both in soil physics (Van Genuchten, 1980; Green et al., 1996) and soil mechanics (Sivakumar, 1993; Geiser, 1999; Cunningham et al., 2003; Tarantino and Tombolato, 2005, among others). Figure 2.6 presents the experimentally determined relation between degree of saturation, suction, and void ratio for London Clay during drying and wetting under constant external stress (Cunningham et al., 2003).

In general, and as it can be seen in this figure, the degree of saturation decreases with suction. However, experimental observations have shown that the degree of saturation for a given suction is not identical in drying and wetting path. This phenomenon corresponds to the *hydraulic hysteresis* (Croney, 1952). The hydraulic hysteresis should be ascribed to the fabric of soil and the different effects of pore entrapments in drying and wetting paths.

When a sample of saturated soil is subjected to suction increase at constant

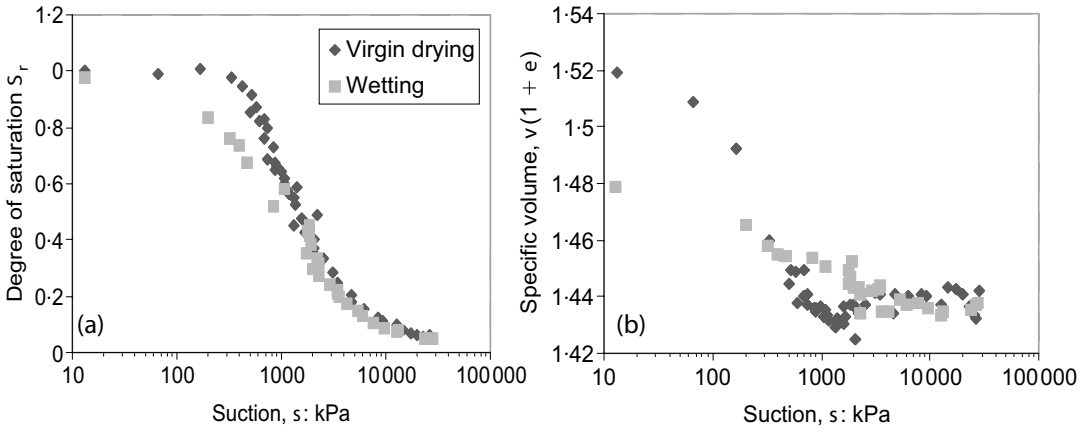


*Figure 2.6:* Water retention curve for a clay-silt mixed soil (Cunningham et al., 2003): (a) degree of saturation-suction, (b) specific volume-suction

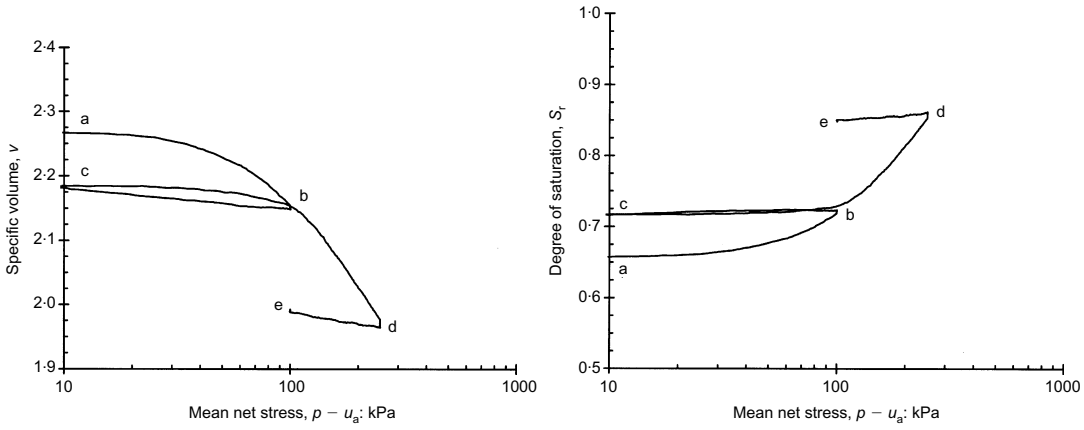


(a) (b)

*Figure 2.7:* Behavior of bentonite-kaolin during isotropic loading at constant suction (Sharma, 1998, in Wheeler et al. (2003)): (a) specific volume, (b) degree of saturation

external loading, the pores remain *saturated* until a given suction (Blight, 1967; Geiser, 1999, among others). This suction is called *air entry value suction* and it is usually denoted by $s_e$. When this limit is surpassed, the soil enters a *quasi-saturated* state in which occluded air bubbles exist in the soil with the water menisci being formed at the boundary of bubble with the bulk water (Tarantino and Jommi, 2005). After this state, the degree of saturation of the sample continues to decrease in a *partially saturated* state until a residual value $S_{res}$ termed as *residual degree of saturation*. At the residual state, only small water menisci with high values of negative water potential exist within the soil.

The explicit dependence of degree of saturation on void ratio has been usually ignored. When dealing with the assumption of incompressible material, the consequences are limited. However, experimental results on real deformable soil show that an increase in void ratio (even at constant suction) could increase the degree of saturation in soil (Sivakumar, 1993; Sharma, 1998; Monroy, 2005).

An example of such behavior is presented in Figure 2.7 for unsaturated bentonite-¨kaolin during isotropic compression under constant suction. The mean net pressure in these figures is the total pressure from which the air pressure has been subtracting and it represents the mechanical loading applied to the soil.

Equivalent increase of degree of saturation was observed by Cuisinier and Laloui (2004) during the oedometric compression of aggregated silt at constant suction. In natural aggregated soils, macropores are usually drained even at low values of suction. When these empty pores are closed as a result of mechanical loading, the total volume of voids are modified while the mass and volume of water in the aggregates remains almost constant. Hence even at constant suction, the degree of saturation could be subjected to significant increase depending on the state of compression.

A direct consequence of suction increase, in general, is shrinkage of the soil. Different interpretations have been given for the volume change of soils with

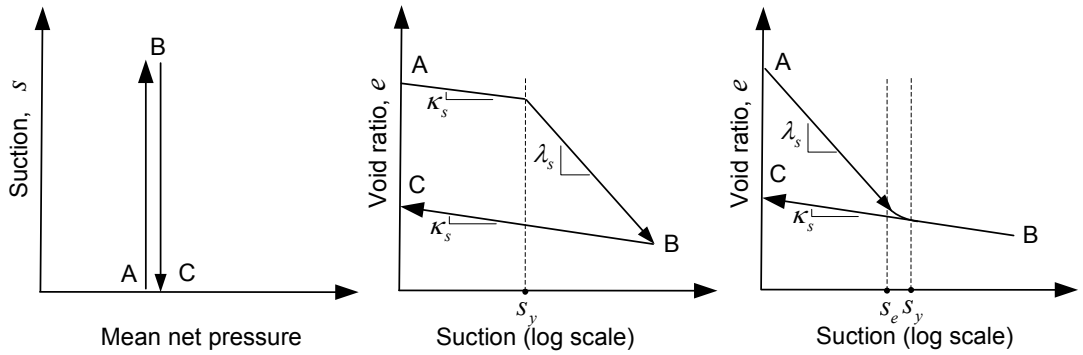


*Figure 2.8:* Typical interpretations for suction-induced volume change: (a) drying path, (b) interpretation of Alonso et al. (1990), (c) interpretation of Geiser (1999)

suction increase (Fig. 2.8). Alonso et al. (1990) suggested for a soil in a drying path, an elastic deformation until reaching a yield suction beyond which plastic volume change occurs in the same way as in an isotropic mechanical loading path (Fig. 2.8(b)). If the soil is then subjected to wetting, it again follows an elastic path like mechanical unloading. In line with definition of preconsolidation stress, the yield suction ($s_y$) in this interpretation is considered to be the maximum previously experienced suction.

Another interpretation, given by Geiser (1999) who evaluated the experimental results of Zehrouni (1991) and Taibi (1994), appears to be more realistic. In this interpretation, depicted in Figure 2.8(c), the suction-induced deformations are mainly irreversible in the domain of saturated pores and reversible in the domain of unsaturated pores. The yield limit suction, $s_y$, is allowed to be equal to or slightly different from the air entry value suction, $s_e$. In this latter case, the yield suction has been linked to the shrinkage limit of the soil.

The slopes of reversible and irreversible parts, in both interpretations, are considered to be material properties.

### 2.2.2 Capillary effects

The capillary effects could be evaluated through the concept of water meniscus. According to Gens and Alonso (1992), the water menisci could be present at the particle contact between individual sand and silt grains or between the soil aggregates. The effects of the water meniscus on the mechanical behavior of the soil at the macro-scale have been discussed by several authors (Tarantino and Tombolato, 2005; Jennings and Burland, 1962, among others). It is commonly accepted that the water meniscus could act as bonding between soil particles, retains the soil particles together, and therefore, enhances the overall stability of the soil skeleton.

One of the major consequences of the presence of inter-particle menisci in partially saturated soils is dependency of yield limit, during loading at constant suction, on the suction level (Wheeler and Sivakumar, 1995; Alonso et al., 1987,

among others). In general, the higher the tensile pressure of water meniscus, the higher the yield limit in unsaturated soil. This implies the yield limit to be a function of not only stress state and stress history, but also of suction.

Another important effect of water menisci is collapse upon wetting of unsaturated soils (see e.g. Wheeler and Sivakumar, 1995). This phenomenon is linked to the removal of water menisci and capillary effects at saturated state.

Logically, it is plausible for the soil rigidity to be affected by the presence of water menisci in the unsaturated soils. The influence of suction on soil rigidity will be reflected in the elastic modulus and the mechanical compressibility.

It has been repeatedly suggested for the elastic properties to be independent of or insignificantly dependent on suction (Geiser, 1999; Rifa'i, 2002). Accordingly, a constant slope of unloading-reloading is usually considered in the compression space of $v - \ln p_{net}$ ($p_{net}$ is the mean net pressure). However, some authors argued that this slope increases with suction (Al-Mukhtar et al., 1993).

The mechanical compressibility in unsaturated soils has been often evaluated by studying the influence of suction on the slope of normal consolidation line in $v - \ln p_{net}$ space. Most authors agree in the fact that this slope decreases due to the suction increase (Matyas and Radhakrishna, 1968; Alonso et al., 1987; Charlier et al., 1997; Sivakumar, 1993; Geiser, 1999). However, some authors argued that the evolution of this slope with suction depends on the suction level and stress state of the soil (Wheeler and Sivakumar, 1995). Hence, the understanding of the evolution of soil compressibility with suction still demands more rigorous investigations.

## 2.3 Fabric effects in unsaturated soils

### 2.3.1 Influence on water retention characteristics

The influence of fabric on the water retention characteristics has been evaluated for natural aggregated soils (Coppola, 2000; Burger and Shackelford, 2001) as well as for compacted clays at dry side of optimum and compacted expansive soils (Romero et al., 1999, among others). As previously mentioned, these materials exhibit double porosity fabric; therefore, some understanding of fabric effects in these materials is helpful in the current study.

Figure 2.9 shows the evolution of volumetric water content with suction for a specimen containing pellets of about 1 $mm$ diameter from processed diatomaceous earth reported by Burger and Shackelford (2001). The results are presented in terms of volumetric water content (the fraction of the total volume of soil that is occupied by the water contained in the soil). The measured soil-water characteristic curve data are bimodal, reflecting both the microporosity region within the individual pellets, or intra-pellet porosity, and the macroporosity region between the pellets, or inter-pellet porosity. These authors introduced the inflection point in the bimodal water retention curve (Fig. 2.9(b)) as the point where the macroporosity appears to have completely desaturated and the microporosity begins to desaturate. They suggested that the water retention data for soil suctions greater than, and less than the suction corresponding to

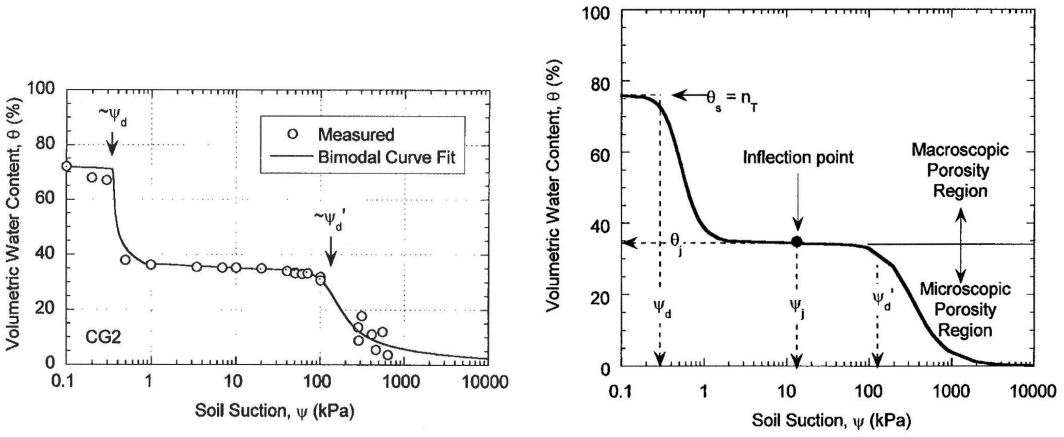


*Figure 2.9:* Bimodal soil-water characteristic curve (Burger and Shackelford, 2001): (a) measurements and fits for specimens containing pellet processed diatomaceous earth, (b) schematic of a conceptual representation

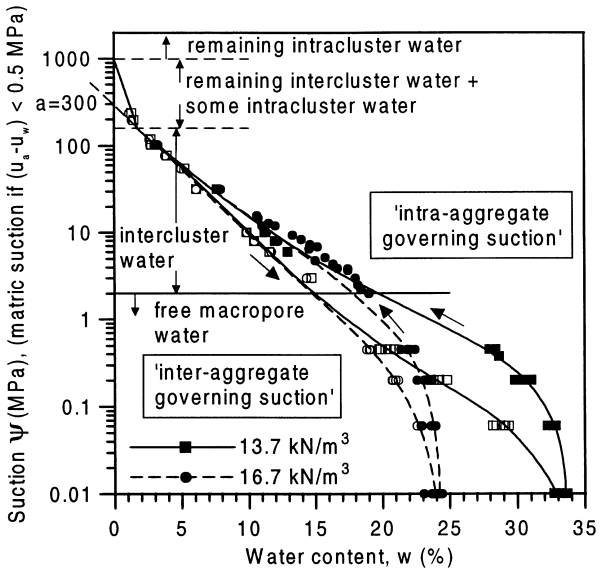


*Figure 2.10:* Main wetting and drying retention curves for the different packings of compacted Boom clay (Romero et al., 1999)

this point could be evaluated separately according to the physical properties of macro- and micropores. In the joint study of the present research work, Carminati (2006) studied the water retention properties of aggregates and micropores within them. Results of that work showed that the water retention behavior of aggregates are influenced by different factors such as the geometry of pores and aggregate contacts.

Figure 2.10 illustrates the relation between degree of saturation and suction for different packings of a compacted Boom clay, a material with initial double porosity fabric (Romero et al., 1999).

The water retention curve of the aggregated clay in Figure 2.10 shows two regions with different responses to change in void ratio. At lower values of suction, dependence of retained water on soil void ratio (dry density) is observed; however, at higher suctions, the retained water is independent of soil void ratio. Romero et al. (1999) associated these two regions with intra- and inter-aggregate governing suction zones. They discussed that in the inter-aggregate governing suction zone, the water content is high enough to partly fill the inter-aggregate voids. This zone is sensitive to mechanical actions, since the mechanical loading reduces the macroporosity and affects the bulk water contained in the inter-aggregate pores. While, the intra-aggregate porosity is not significantly affected by this effect.

Equivalent observations of two regions were made by Lloret et al. (2003) for the water retention curve of compacted bentonite. They reported that the region of high suctions in the water retention curve corresponds to the intra-aggregate pores, where total porosity plays no relevant role and the water uptake is mainly governed by electro-chemical forces. Bernier et al. (1997) and Cuisinier and Masrouri (2004) expressed similar explanations for their experimental evidence in which retained water at high suctions appeared to be independent of dry density for compacted clay.

Theoretically, the macropores require lower suction, in comparison with micropores, to be drained (Eq. 2.3). Accordingly, there is a possible suction state at which the macropores are drained while the micropores are still saturated. With respect to this point, Gens and Alonso (1992) postulated the assumption that clay aggregates in compacted expansive soils remain saturated, whatever the state of the soil would be, and therefore their behavior could be described using saturated soil concepts.

### 2.3.2 Collapsible behavior

A possible scenario during the wetting of aggregated soils is the removal of inter-particle bondings and disintegration of soil aggregates.

It is noteworthy that in the case of compacted material, the bonding could be either strong inter-particle water menisci or electro-chemical forces. Removal of these bonds yields the collapse of the aggregated structure and consequently results in dramatic deformations of the whole soil.

Observations made by Alonso et al. (1995) during the soaking of expansive clay pellet samples under constant vertical stress showed that the applied confining stress plays an important role on the response of aggregated structure upon wetting. In these tests, carried out in conventional oedometer cells, specimens were soaked under vertical loads in the range of 10 $kPa$ to 2.4 $MPa$ and the real time deformations were recorded, as presented in Figure 2.11.

For the samples wetted at low confining stress, clay pellets were found to expand because of their expansive nature. In these samples, an increase in void ratio could be observed up to a certain point where aggregates and subsequently the soil at the macro-scale collapse. However, the final deformation was reported to be a swelling strain.

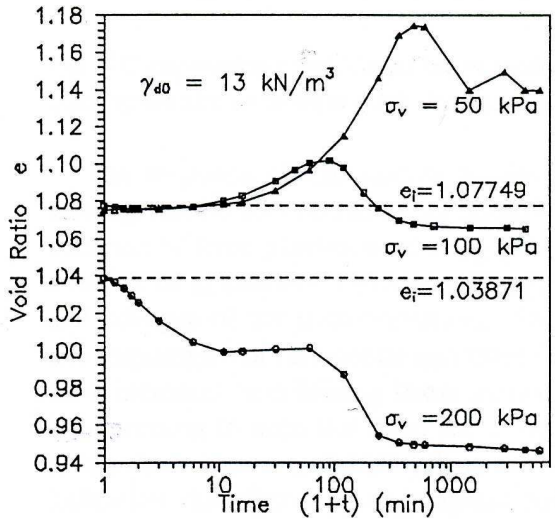


*Figure 2.11:* Soaking of compacted Boom clay samples under different vertical loads for dry unit weight of 13 $kN/m^3$ (Alonso et al., 1995)

When confining stress increases, swelling tendency of aggregates is masked by their distortion and collapse of aggregates; therefore, void ratio of soil starts to decrease from the beginning of wetting. It was observed that reduction in void ratio happens in two main steps. This behavior was attributed to the wetted aggregates occupying the empty macropores at the first step and then to the overall collapse of the soil structure at the second step. It is also observed that the time or average suction for the outset of collapse decreases as confining stress increases.

Hoffmann et al. (2006) showed that the required time for collapse of a compacted clay specimen during wetting is controlled by the rate of application of moisture at the specimen boundaries. They reported an immediate collapse of specimens wetted by liquid water, while the collapse of specimens wetted by vapor happened later.

Interpreting their experimental observations, Hoffmann et al. (2006) stated that in the case of slow application of suction variations, water potential at micro- and macropores have the opportunity to remain equal through the wetting process and this prevents a sudden collapse before the condition close to saturation.

These observations could be compared with those made by Or (1996) who stated that major deformation of agricultural aggregated soil during wetting, in presence or absence of external load, is due to wetting-induced disintegration of aggregates at the top layer of the soil.

## 2.4 Inter-particle bonding effects

Experimental evidence of the bonded soil structure effects on the mechanical response have been reported for a wide variety of natural soils, including soft rocks (Tavenas and Leroueil, 1990; Smith et al., 1992), stiff clays and clay shales (Calabresi and Scarpelli, 1985; Anagnostopoulos et al., 1991; Burland et al., 1996), granular soils (Mitchell and Solymar, 1984; Coop and Atkinson, 1993) and residual soils (Vaughan and Kwan, 1984; Vaughan et al., 1988; Wesley, 1990). In almost all of these works, the influence of soil structure has been evaluated with respect to inter-particle bonding effects and explicit investigation of soil fabric has been rarely done (Cuccovillo and Coop, 1999). Furthermore, study of this works has been mainly limited to the saturated states. To identify the extra features in the mechanical behavior of natural soils arising from soil structure, it is widely accepted to compare it with reconstituted soil of the same mineralogy as a reference state. Burland (1990) should be cited as the first one who suggested the term *intrinsic* for properties of the reconstituted soils, a terminology which has been widely used by others in further works in this field.

### 2.4.1 Pre-yield behavior

The pre-yield behavior of soils is commonly characterized by the elastic (recoverable) deformations. Influence of soil structure on the elastic properties has been evaluated by Callisto and Calabresi (1998) who compared the behavior of structured Pisa clay with the corresponding reconstituted samples. They reported a fair agreement between the elastic stiffness of the reconstituted and structured clay for small stress increments. This implies for elastic properties to be independent of the soil structure. The assumption of independence of elastic behavior from the soil structure has been a common postulation in development of constitutive models for structured soils (Gens and Nova, 1993; Rouainia and Wood, 2000).

However, Leroueil and Vaughan (1990) argued that although behavior before the primary yield is stiff, it is not necessarily elastic. These authors, based on the experimental observation of Bressani and Vaughan (1989), reported that structure may be destroyed and yield stress reduced while a sample is following a stress path within the primary yield limit.

### 2.4.2 Yield limit

In an intact state, the inter-particle bonding could enhance the overall stability of the soil skeleton, hence, it is logical for the strength and the yield limit of the soil to increase due to presence of these bondings.

The yield limit in isotropic compression condition is represented by the normal consolidation line. For a reconstituted saturated soil, all possible states lie to the left side of this curve in a $v - p'$ space where $p'$ is the mean effective pressure. However, experimental observations proved that the virgin compression curve for most of sedimentary natural soils lie well above the normal consolida-

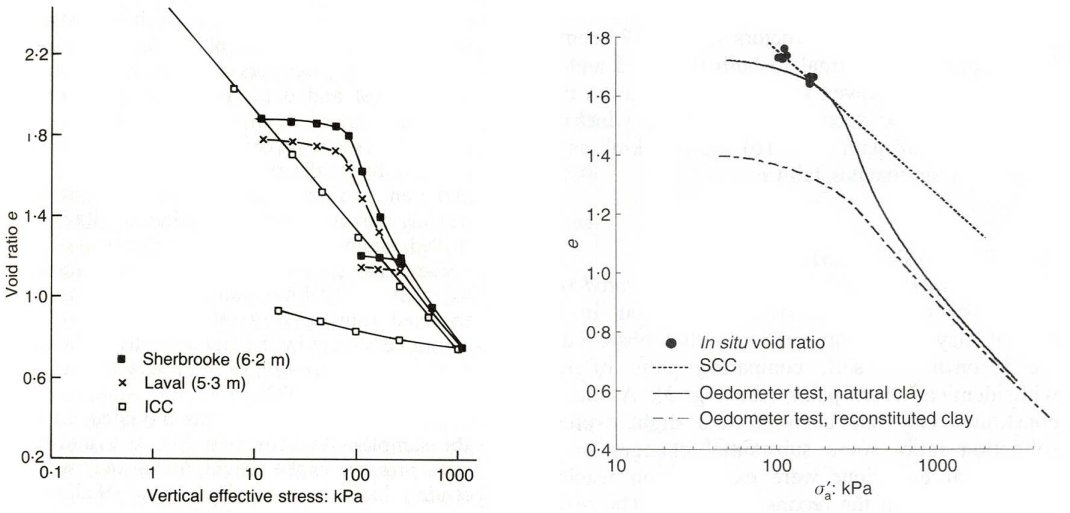


(a) (b)

*Figure 2.12:* One-dimensional compression of natural structured and reconstituted clays: (a) Bothkennar Clay, natural clay taken with two different different samplers (Smith et al., 1992), (b) Pisa clay (Callisto and Calabresi, 1998)

tion line of reconstituted soil (Burland, 1990).

Effects of bonded structure with respect to this fact have been examined by Leroueil and Vaughan (1990) for different natural soils. They reported that many of the naturally occurring sedimentary and residual soils have components of strength which cannot be accounted for by porosity and stress history alone. Leroueil and Vaughan (1990) showed that the void ratio for both residual and sedimentary structured soils is greater than can be sustained by the same soil from which structure has been removed by remolding. Similar observations were made by Smith et al. (1992) who studied the yielding behavior of Bothkenar natural clay. They compared the oedometric compression curve of undisturbed Bothkenar clay with the compression curve of reconstituted soil termed as intrinsic compression curve (ICC), as presented in Figure 2.12(a). These authors reported a higher oedometric yield stress for the structured clay. For a given stress, this allows the structured clay to sustain higher void ratio in comparison with reconstituted soil. Equivalent observations were made by Callisto and Calabresi (1998) for the oedometric compression of both natural and reconstituted Pisa clays, as presented in Figure 2.12(b).

The observed behavior of structured natural clays can be often reasonably approximated by straight pre-yield and post-yield segments (Graham et al., 1988). Leroueil and Vaughan (1990) stated that while bonded structure in these materials might arise from different causes, its consequences on the material behavior is similar and corresponds to a stiff behavior followed by yield. Accordingly, they described this yield in a similar way to that occurring due to overconsolidation, although it is a different phenomenon.

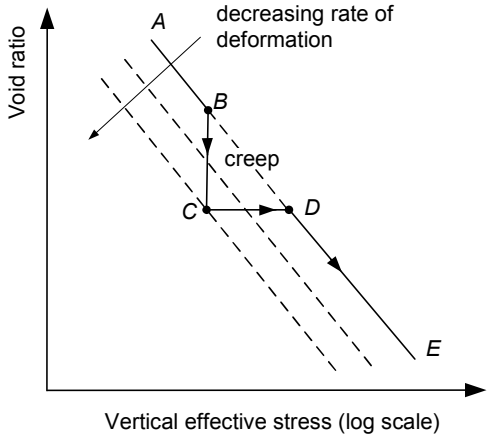


*Figure 2.13:* Effect of creep on one-dimensional compression of clay (after Wood, 1990)

The apparent overconsolidation behavior of bonded soils could be compared to the effects of creep and aging in soils (Bjerrum, 1972). The term *creep* is usually used to describe deformation continuing with time at constant effective stress. The description given by Wood (1990) is adapted here for the relation between creep and the apparent overconsolidation behavior. If an oedometer test ($AB$ in Fig. 2.13) is stopped in the middle of the test, creep occurs ($BC$). As the rate of creep deformation gradually falls with time, the state of the soil moves to lower compression curve appropriate to the falling rate of deformation.When the loading is restarted, state of the soil returns back to the compression curve following which it had been loading from the beginning of the test ($CDE$). Therefore, sample appears to have become apparently overconsolidated and an apparent preconsolidation pressure would be assigned to $D$ (in Fig. 2.13) even though the soil had never previously experienced effective stresses higher than those at $B$ (in Fig. 2.13) and $C$. This description could explain the behavior of marine deposits and aged soil in which creep have been occurring in large scales of time.

The relation between creep and the soil structure has been studied by some authors (Leroueil, 2006; Sorensen et al., 2007). However, further evaluation of this relation is beyond the scopes of this study and will not be treated here.

### 2.4.3 Yielding behavior

The inter-particle bonding has been found to have a major effect not only on the yield limit but also on the post-yield and the material response during the occurrence of yielding.

Burland (1990) showed that natural sedimentary clays are more sensitive and they exhibit a more brittle behavior than reconstituted material and the post-yield compression index is usually much greater in natural soils. It has been reported that the compressibility index for structured soft clay correlates with initial void ratio and the sensitivity of the clay rather than with plasticity in

conventional manner (Leroueil et al., 1983). Brittle behavior was also observed in the compression behavior of natural Bothkennar clay by Smith et al. (1992). They identified a sharp yielding corresponding to the transition from recoverable to irrecoverable domain of material behavior in various stress-path triaxial tests.

In the case of natural Pisa clay, however, triaxial and oedometer results of Callisto and Calabresi (1998) showed that the yielding in this material is a gradual phenomenon. While, the post-yield compression curve of natural clay was still characterized by greater compressibility value in comparison with reconstituted soil. They ascribed the increase in the compressibility to a progressive change in the microstructure of the clay. They showed that when the stress path involves greater changes in the deviatoric stress than mean pressure, the behavior of reconstituted and natural material is qualitatively similar. While, the behavior of the two soils are different for stress paths where the reverse change of stress applies.

It has been commonly reported that the compression curve of structured clay tends to converge to that of reconstituted clay, as the applied stress increases (Burland, 1990; Callisto and Calabresi, 1998). As expressed by Graham et al. (1988), after Bjerrum (1967), in the region between the pre-yielding and post-yielding the microstructure of natural clays experiences major disturbance or de-structuring. Consequently, the influence of soil structure becomes less important and the response of the materials becomes closer to that of the reconstituted soil without inter-particle bonding.

Leroueil and Vaughan (1990) argued that the complete removal of structure does not necessarily imply coincidence of the compression curves of structured and reconstituted soil and further strains might be required to achieve similar fabric and particle packing. Rouainia and Wood (2000) also discussed that the occurrence of localization in these materials will prevent any further homogeneous de-structuring and only within the zone of concentrated shearing, loss of structure will be completed. Therefore, it will not be possible to deduce the asymptotic behavior of reconstituted materials.

Microstructural study of natural clays has shown that some elements of structure remain in the clay even at very large strains or after reconstituting (Cotecchia and Chandler, 1998). This can be better described using the concept of *metastable fabric* for sedimentary soils (Mitchell and Soga, 2005). In these materials, the initial fabric after deposition is quite open with large pores. During consolidation this fabric can carry effective stress at a void ratio higher than would be possible if the particles and particle groups were arranged in an efficient parallel arrangement (Mitchell and Soga, 2005). When the soil is remolded, the fabric is progressively disrupted and the strength is decreased. Compression of the initial metastable state corresponds to the virgin compression of the soil, as depicted in Figure 2.14(a). States to the right side of this curve would be possible only in the presence of bondings which enables the soil to resist additional compressive stress ($ab$) or to exhibit additional void ratio ($bc$). While, the difference between the virgin compression of metastable state and the compression of fully de-structured soil, namely $cd$, is ascribed to the soil fabric.

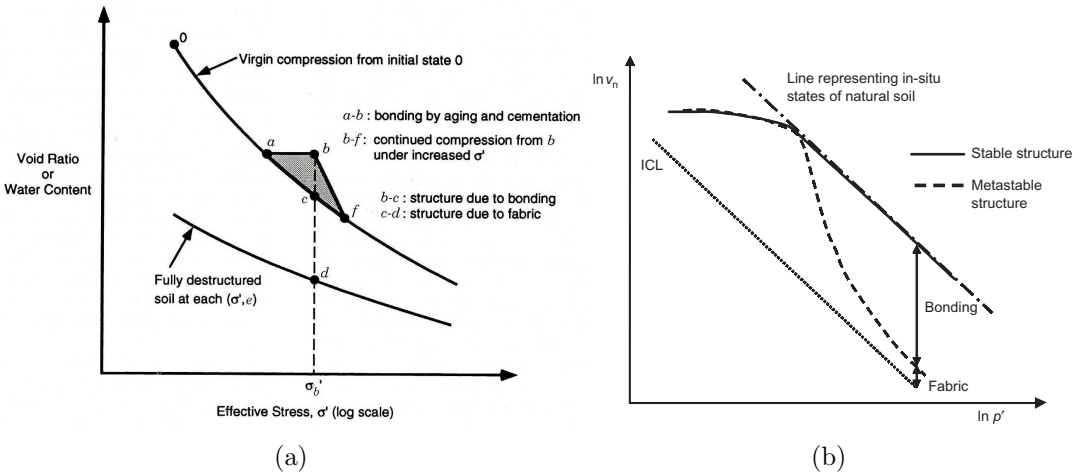


*Figure 2.14:* Effects of bonding and metastable fabric on the compression of clays (a) possible states in void ratio-effective stress plane (Mitchell and Soga, 2005), (b) the difference in behavior of clays with stable and metastable structure in compression (Baudet and Stallebrass, 2004)

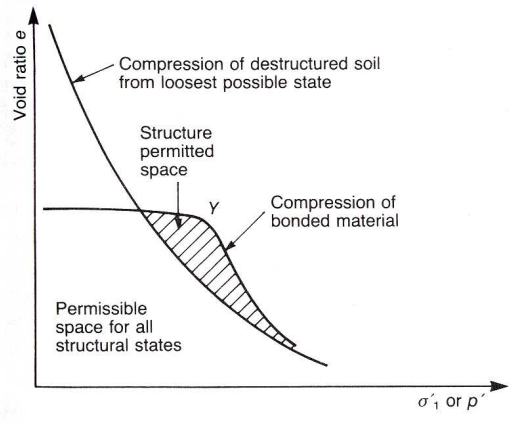


*Figure 2.15:* Compression behavior of structured and reconstituted soil (Leroueil and Vaughan, 1990)

Using this concept, Baudet and Stallebrass (2004) divided the soil structure into stable structures that do not degrade; and metastable structures which undergo de-structuring (Fig. 2.14(b)). They reported that the convergence toward intrinsic states is characteristic of natural clays with metastable structure. For clays with stable elements of structure, it is hypothesized that no strain path could ever achieve a level of de-structuration that would bring it to the intrinsic state. In such case, they considered that the soil could reach a stable state that is not the intrinsic state due to existence of stable elements in the soil fabric.

In general, as proposed by Leroueil and Vaughan (1990), compression curve of structured soil and reconstituted soil from loosest possible state could be simplified as depicted in Figure 2.15. They introduced a *structure permitted space* for structured soils, in which soil can exist only due to structure.

### 2.4.4 Combined effects of bonding and partial saturation

Although many natural structured soils are unsaturated, only few studies have considered the combined effect of unsaturation and bonded soil structure on soil behavior. These effects were discussed by Alonso and Gens (1994) for the purpose of constitutive modeling. To our knowledge, the only representative experimental research in this field is the work done by Leroueil and Barbosa (2000). These authors examined the combined effects of bonding and partial saturation on yielding of artificially cemented soils and non-cemented soil by means of triaxial and oedometer tests. Despite the difference between the nature of tested material and the structured soil concerned in this study, the results of that work provide a background about the suction effects in bonded material. They examined the oedometric yield stress of cemented and non-cemented soil at different suctions. The yield stresses deduced from their tests are plotted in Figure 2.16 in the space of suction versus the vertical net stress. The increase due to suction of yield stress in reconstituted soil ($\Delta\sigma_{y,suc}$) is determined by curve $LC_a$, named Loading-Collapse curve after Alonso et al. (1990). At saturated condition, cementation induces an additional increase in the yield stress ($\Delta\sigma_{y,st}$). If this value is added to the curve $LC_a$, the dashed line is obtained. However, yield stress given by the obtained curve appeared to be less than the real yield stress for unsaturated cemented soils. The difference ($\Delta\sigma_{y,suc}$) has been attributed to the hardening effect of suction on bondings. Therefore, they showed that the yield stress resulting from the combined effect of partial saturation and bonding is larger than the sum of the contribution of the two factors. As observed in these results and proposed by Alonso and Gens (1994), suction in bonded soils has two effects corresponding to capillary effects on soil matrix and strengthening of inter-particle bonds which should be taken into account when dealing with these materials at unsaturated states.

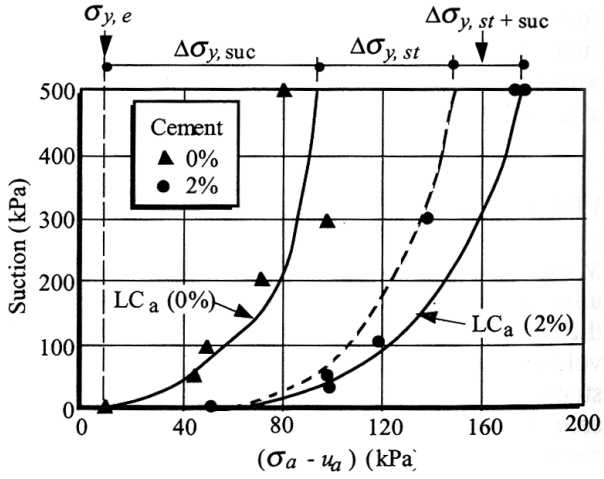


*Figure 2.16:* Loading-Collapse curves for cemented and non-cemented Viçosa residual soil Leroueil and Barbosa (2000)

## 2.5 Study of soil structure

### 2.5.1 Experimental methods for soil fabric study

Over the few recent years, experimental study of soil structure has received an increasing interest with the purpose of relating the soil structure at the pore scale to the macroscopic behavior.

There are several ways to study the structure of geomaterials, among them being scanning electron microscopy, nitrogen adsorption, mercury intrusion porosimetry (MIP) and new methods based on computed tomography.

In general, these techniques are aimed at evaluating and characterizing the soil fabric and they provide information about the geometry of pores and particles in soil. These techniques can be classified according to several criteria. These criteria include the direct or indirect and the destructive or non-destructive nature of the method and also the type of obtained information and the measured porosity. They might provide information on total porosity or on connected porosity with only the mere knowledge of the global porosity or with additional three-dimensional information about the connected porosity pathways (Pleinert and Degueldre, 1995).

Technically, experimental methods involved in the study of soil fabric can be divided into two main categories: direct and indirect methods. In the first group, as the name indicates, the evaluation of soil fabric is based on direct observation of the geometry of the pores using images. This includes for example optic or electron microscopy. For the indirect methods, usually a second material is injected into the pores and the geometrical information of pores is related to a physical measurable variable of the material in contact with soil. The methods usually give quantitative information about the soil fabric. The most popular technique of the latter type is the mercury intrusion porosimetry (Sridharan et al., 1971). Using mercury intrusion porosimetry combined with scanning electron microscopy as a supplement has been the most popular approach to study the soil fabric (Monroy, 2005; Delage and Lefebvre, 1984; Romero, 1999).

Recently, new advanced experimental methods based on radiography and computed tomography (CT) have been used to evaluate the structure and the physical and mechanical properties of geomaterials in different fields. Radiography allows evaluating the soil texture and disturbance; while, CT allows reconstruction of a three-dimensional volume of the sample by assembling two-dimensional radiographic images taken at different angles.

The most commonly used method of this kind is X-ray CT and radiography (see e.g. Otani, 2006). X-ray radiography has been used to evaluate the physical properties of geomaterials in different fields. Peyton et al. (1992) and Zeng et al. (1996) used the X-ray radiography to evaluate the macro pore size and bulk density in undisturbed samples of soil. The method has been also used to assess the distribution of pores in samples of sand and cemented clays (Anderson and Hopmans, 1994). X-ray tomography has been used to evaluate the evolution of density and pore structure in soils and the crack propagation in rocks (Desrues et al., 1996; Alshibli et al., 2000; Wong, 2000; Otani et al., 2000). A discussion

of using X-ray CT for geotechnical engineering is given in Otani (2006).

Neutron radiography and tomography is another method of this type which has been recently used for geomaterials. The main advantage of neutron radiography to X-ray is its high sensitivity to hydrogen-containing materials and its ability to track the water in soil. Neutron radiography has been used to image both fluid infiltration into dry sand and steady state flow fields with the purpose of measuring wetting front velocity and hydraulic conductivity of the medium (Deinert et al., 2002). Combination of neutron radiography and tomography has been also used for some experiments in order to evaluate the influence of initial moisture content and type of infiltrating fluid on the formation of preferential flow paths (Tullis et al., 1992). Neutron tomography has been also used to study the variation of fluid saturation in sandstone samples and relate it to the pore geometry (Solymar et al., 2003). In the joint study of the present work, Carminati (2006) used neutron radiography and tomography in order to study the water retention behavior and water flow in series of aggregates. As it will be presented later, this technique is as well used in the present work for non-destructive study of soil structure. Detailed description of the employed method and the testing procedure are given in Chapter 5.

Each method of soil structure study has its own requirements and testing condition. For example, MIP or SEM are destructive methods and their application is limited to small samples. CT methods could provide morphological information of larger samples with the price of higher costs and usually lower resolution. As proposed by Mitchell and Soga (2005), the use of several methods of fabric analysis may be appropriate in some cases in order to obtain information of more than one type or level of detail.

### 2.5.2 Fabric evolution

In the case of structured double porosity soils, a few studies have been undertaken to characterize the fabric evolution during the mechanical loading or suction variations. One point of interest has been the fabric modifications provoked by mechanical loading under saturated condition. Delage and Lefebvre (1984) studied non-compacted Champlain clay fabric with mercury intrusion porosimetry (MIP) and scanning electron microscopy. This material shows an initial double porosity fabric. The results showed that during consolidation only the largest pores collapse at a given stress increment. Small pores are compressed only when all of the macropores have been completely closed by loading. These results were confirmed by similar evidences in other experimental studies (Lapierre et al., 1990; Griffiths and Joshi, 1990).

Soil fabric is sensitive to suction increase, as evidenced by Simms and Yanful (2001, 2002) who investigated the fabric of a compacted glacial till under different suctions, from saturation up to a matric suction of 2500 $kPa$. They showed that increase of suction brought about a progressive rise in the microporosity associated with macroporosity reduction. They modified the measured pore size distribution for pore trapping effects and proposed a model for shrinkage of pores and evolution of pore size distribution due to drying.

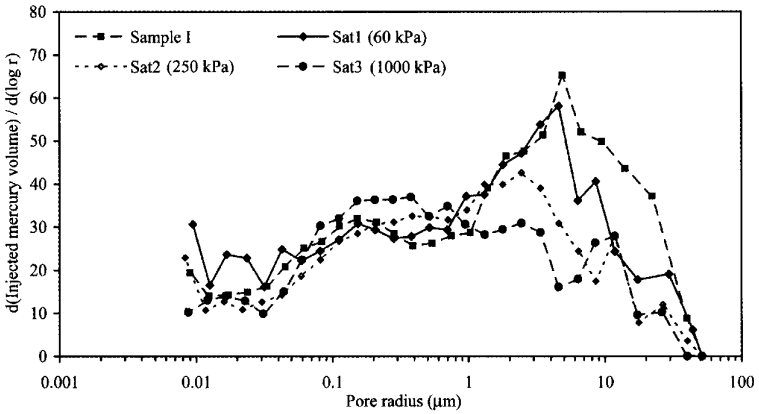


(a)

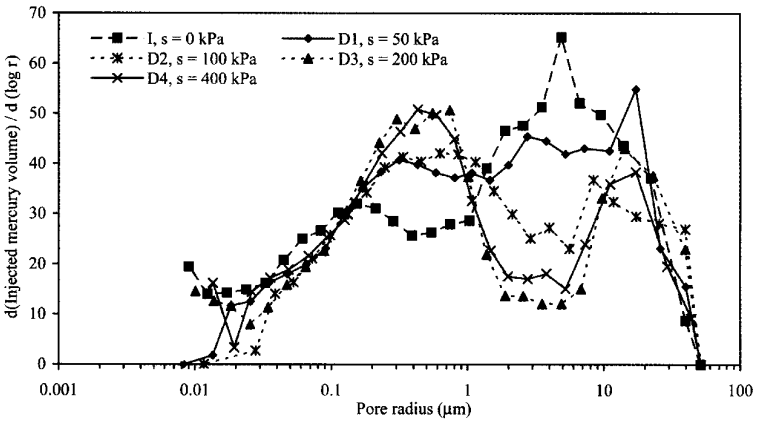


(b)

*Figure 2.17:* Fabric modification due to mechanical loading and suction variations: (a) suction increase at constant net vertical stress 10 $kPa$, (b) mechanical loading under saturated condition (Cuisinier and Laloui, 2004)

Cuisinier and Laloui (2004) studied the combined effects of suction and mechanical loading on the fabric of unsaturated aggregated silt. Figure 2.17 shows the pore size distribution of the tested samples at different levels of applied net stress and suction. The results confirmed that mechanical loading affects mainly the macropores. They also showed that suction increase is associated with decrease in the volume of macropores and a slight increase in the volume of micropores.

However, only a few other authors (Al-Mukhtar et al., 1996; Qi et al., 1996), have studied fabric modification during the mechanical loading of an unsaturated soil. These authors evaluated the influence of suction on deformation process for remoulded Boom clay, which is a swelling material, and a synthetic model clay named Na-Laponite. Their interest was essentially focused at the clay particle level and the initial fabric of these materials was very different from the double porosity encountered in natural or compacted soils, as the materials they used were initially remoulded. Hence, it is difficult to extrapolate their conclusions to natural or compacted soils with a double porosity fabric.

An interesting issue in the mechanical behavior of soils with double porosity, is the relation between the deformation at the pore scale and macroscopic response of the soil. In soils with double porosity, the deformation should be considered as a combined phenomenon at macro- and pore scale. Deformation of aggregates could induce total deformation of the soil. Experimental evidence on the pore scale deformation of soils is scares in the literature; therefore, description of deformations at pore scale has remained mainly based on the assumptions rather than experimental evidences. In the development of constitutive models for unsaturated expansive soil, the microstructural deformation has been assumed to be totally reversible (see e.g. Gens and Alonso, 1992; Lloret et al., 2003; Alonso et al., 1994; Sanchez et al., 2005). However this assumption would appear to be far from reality for soils in which soil structure could be subjected to degradation during a hydro-mechanical process. Understanding of the relationship between fabric evolution and the macroscopic response of the soil is, however, limited and requires further studies combining fabric investigations and a hydro-mechanical evaluation of the soil behavior.

## 2.6 Constitutive modeling

The mechanical constitutive equations provide the relation between the stresses and strains of the material. They are of great importance in completing the general formulation for solution of mechanical problems. The mechanical behavior of reconstituted saturated soils could be successfully described with constitutive models within the framework of elasto-plasticity. Following the pioneer developments of Original Cam-Clay, OCC (Roscoe and Schofield, 1963) and Modified Cam-Clay, MCC (Roscoe and Burland, 1968), elasto-plastic constitutive models of saturated reconstituted soils has been widely evaluated.

However, these models are classically developed for two extreme cases of fully saturated or dry condition. Therefore, they cannot be applied, without modification, to the wide intermediate range of partially unsaturated soils. Moreover, in the classical constitutive models, soil is considered as a homogeneous media, and usually no specific consideration is made for the influence of soil structure on its behavior.

An appropriate constitutive model for unsaturated structured soil therefore requires new developments or improvements of the existing models, through which, the combined effects of partially saturation and soil structure on the mechanical behavior are included.

### 2.6.1 Effective stress

The mechanical constitutive study of multi-phase porous media requires, in the first step, the determination of the effective stress in solid skeleton. Expressed as a function of the externally applied stresses and the internal fluid pressures, the effective stress converts a multi-phase, multi-porous media into a mechanically equivalent, single-phase, single-stress state continuum. It enters the elastic as well as elasto-plastic constitutive equations of the solid phase, linking a change

in stress to straining or any other relevant quantity of the soil skeleton (e.g. see Biot, 1941; Rice and Cleary, 1976; Loret and Khalili, 2000; Laloui et al., 2003; Khalili et al., 2004).

Over the years, significant contributions have been made to the understanding and evaluation of the effective stress in porous media. Notable examples include the work of Terzaghi (1936), Biot (1941), Skempton (1961), and Nur and Byerlee (1971) for saturated single porosity media, and the contributions of Bishop (1959), Hutter et al. (1999), Loret and Khalili (2000), Laloui et al. (2003), and Khalili et al. (2004) for single porosity media with two immiscible fluids.

Significant differences of opinion exist in the literature for the definition of the effective stress in porous media with two or more saturating fluids. Houlsby (1997) defines effective stress as that capturing the energy dissipation/accumulation within the system. Wheeler and Sivakumar (1995) required effective stress to solely control the elastic as well as the elasto-plastic responses of the system. Fredlund and Morgenstern (1977) define effective stress as that controlling the state of the sample.

As a general definition and as proposed by Khalili et al. (2005), the effective stress could be simply defined as that emanating from the elastic (mechanical) straining of the solid skeleton:

$$\boldsymbol{\varepsilon}^e = \mathbf{C}^e : \boldsymbol{\sigma'} \tag{2.5}$$

in which $\boldsymbol{\varepsilon}^e$ is the elastic strain tensor of the solid skeleton, $\mathbf{C}^e$ is the drained compliance matrix, $\boldsymbol{\sigma'}$ is the effective stress tensor and the symbol ':' denotes the inner product of tensors with double contraction. Within this concept, no further restriction is placed on the definition of the effective stress. In terms of externally applied stresses and the pressure of the fluid constituents, the effective stress (in the total sense) is expressed as:

$$\boldsymbol{\sigma'} = \boldsymbol{\sigma} - \sum_{\alpha} \alpha_\alpha p_\alpha \mathbf{I} \tag{2.6}$$

where $\boldsymbol{\sigma}$ is the total stress tensor, $\alpha_\alpha$ is the effective stress parameter, $p_\alpha$ is the phase pressure, subscript $\boldsymbol{\alpha} = 1, ...n$ represents the number of fluid phases within the system, and $\mathbf{I}$ is the second order identity tensor.

The effective stress parameters can be evaluated based on an elastic strain equivalency analysis satisfying Equation (2.5) (e.g., see Nur and Byerlee, 1971; Khalili and Valliappan, 1996), or from a thermodynamic analysis (e.g., see Hutter et al., 1999; Hassanizadeh and Gray, 1990; Gray and Schrefler, 2007).

The well know principle of Terzaghi's effective stress for saturated soils (Terzaghi, 1936) reads:

$$\boldsymbol{\sigma'} = \boldsymbol{\sigma} - p_w \mathbf{I} \tag{2.7}$$

As an extension of the principle of Terzaghi's effective stress for saturated soils, a general expression of effective stress for unsaturated soils was proposed by Bishop (1959):

$$\boldsymbol{\sigma'} = (\boldsymbol{\sigma} - p_a \mathbf{I}) + \chi(p_a - p_w)\mathbf{I} \tag{2.8}$$

with $p_w$ and $p_a$ being the water and air pressure respectively. Parameter $\chi$ in this relation is called Bishop's parameter and it is linked to the degree of saturation which varies between 0 and 1. Jennings and Burland (1962) experimentally evaluated the relation between $\chi$ and degree of saturation, $S_r$, and reported that this relation might significantly change in different materials.

The physical interpretation of the Bishop's parameter has been discussed by several authors. Khalili and Khabbaz (1998) and Loret and Khalili (2002) argued that this parameter is a physical variable that should be described using the current suction and the air entry value of the material. However, on the basis of thermodynamic analysis, this parameter is found to represent the volumetric ratio of liquid to fluid phase and therefore it is equal to degree of saturation (Hutter et al., 1999; Gray and Schrefler, 2001). Adapting this approach, the *generalized effective stress* for unsaturated soils reads:

$$\boldsymbol{\sigma'} = (\boldsymbol{\sigma} - p_a\mathbf{I}) + S_r(p_a - p_w)\mathbf{I} \tag{2.9}$$

where $S_r$ is the degree of (liquid) saturation.

The proposed expressions of effective stress in Equations (2.8) and (2.9) are appropriate for soils with single porosity, namely having a single pressure field for each fluid. As presented in this study, many natural geomaterials exhibit two scales of porosity, with micropores surrounded by macropores. In addition to showing two scales of porosity, the void space in these materials is frequently filled with more than one fluid and requires multi-phase constitutive modelling.

A substantial amount of work has been undertaken in the area of double porous media since the pioneering work of Barrenblatt et al. (1960) and Barrenblatt (1963). Effective stress parameters have been proposed for saturated double porous media by Khalili and Valliappan (1996) and Callari and Federico (2000). However, the use of the effective stress in unsaturated double porous media has rarely been investigated (Pao and Lewis, 2002; Khalili et al., 2005).

Due to its relevance with the current study, the work of Khalili et al. (2005) is briefly described here. To derive the effective stress parameters for an unsaturated double porous medium, like fissured clay, an elementary volume of the medium is considered to be subjected to an isotropic external mean stress, $\overline{\sigma}$, and four internal fluid pressures, $p_1$, $p_2$, $p_3$, and $p_4$ representing the pore-water, pore-air, fissure-water and fissure-air pressures, respectively. To obtain the volumetric strain of the element, the stresses acting on the element are decomposed into five loading cases, as shown in Figure 2.18.

Case I corresponds to an external isotropic stress of $\pi_I = \overline{\sigma} - p_4$ with internal fluid pressures maintained at a reference value of zero. Case II corresponds to an equal pore-water, pore-air, fissure-water, fissure-air and external isotropic pressure of pressures of $\pi_{II} = p_1$. Case III corresponds to an equal fissure-water, fissure-air and external isotropic pressure of $\pi_{III} = p_4 - p_2$ and zero pore-water and pore-air pressures. Case IV corresponds to an equal fissure-water, fissure-air, pore air and external isotropic pressure of $\pi_{IV} = p_2 + p_3 - p_1 - p_4$ and zero pore-water pressure. Finally, case V corresponds to an equal fissure-air, pore-air and external isotropic pressure of $\pi_V = p_4 - p_3$ and zero pore water and fissure-water pressures.

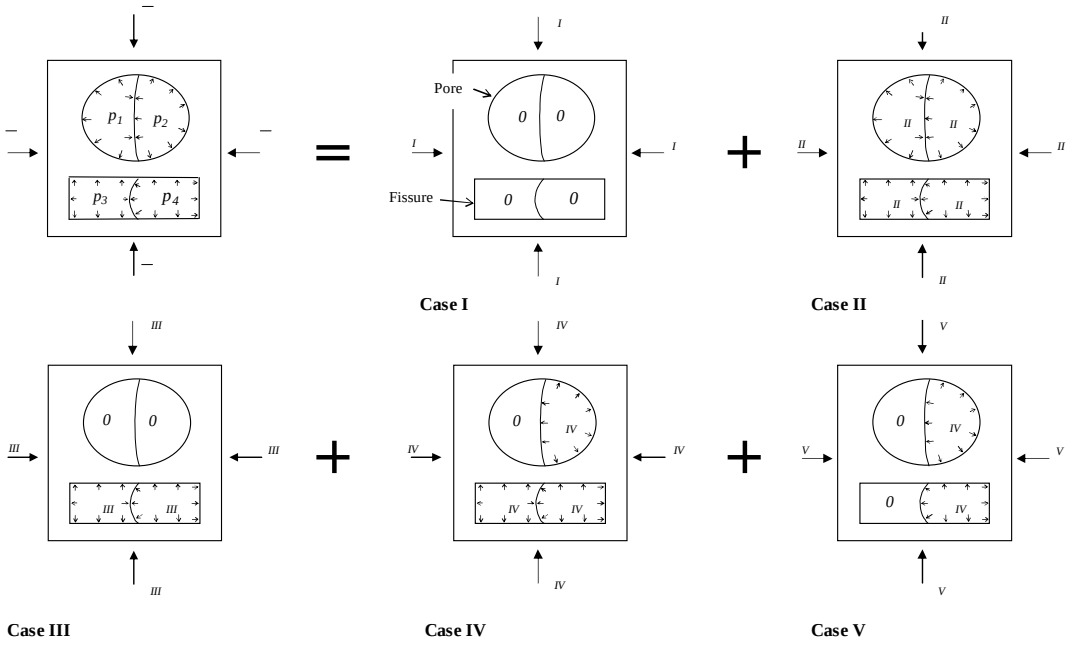


*Figure 2.18:* Stress decomposition of unsaturated double porous media (Khalili et al., 2005)

Following and extending Nur and Byerlee (1971) and Khalili and Valliappan (1996) analysis to unsaturated double porous media, Khalili et al. (2005) wrote the volumetric elastic strain of the elementary volume $\varepsilon_v^e$ as:

$$\varepsilon_v^e = \varepsilon_{v(I)}^e + \varepsilon_{v(II)}^e + \varepsilon_{v(III)}^e + \varepsilon_{v(IV)}^e + \varepsilon_{v(V)}^e \tag{2.10}$$

in which

$$\varepsilon_{v(I)}^e = c(\overline{\sigma} - p_4) \tag{2.11a}$$
$$\varepsilon_{v(II)}^e = c_s(p_1) \tag{2.11b}$$
$$\varepsilon_{v(III)}^e = c_p(p_4 - p_2) \tag{2.11c}$$
$$\varepsilon_{v(IV)}^e = c_{mp}(p_2 + p_3 - p_1 - p_4) \tag{2.11d}$$
$$\varepsilon_{v(V)}^e = c_{mfp}(p_4 - p_3) \tag{2.11e}$$

where $c$ is the underlying drained compressibility of the double porous medium, $c_s$ is the compressibility of the solid, $c_p$ is the underlying drained compressibility of the porous blocks, $c_{mp}$ is the secant compressibility coefficient of the porous blocks with respect to a change in the pore-matric suction, $s_p = p_2 - p_1$, and $c_{mfp}$ is the secant compressibility coefficient of the double porous medium with respect to a simultaneous change in matric suction in pores and fissures, $s_f = s_p$, with $s_f = p_4 - p_3$.

On the other hand, according to the effective stress principle, the volumetric strain, $\varepsilon_v^e$, can be calculated as (Eqs. 2.5 and 2.6):

$$\varepsilon_v^e = c(\overline{\sigma} - \alpha_1 p_1 - \alpha_2 p_2 - \alpha_3 p_3 - \alpha_4 p_4) \tag{2.12}$$

Comparing Equations (2.10) and (2.12) and imposing the incompressibility of solid grains ($c_s = 0$), the effective stress equation is written as,

$$\boldsymbol{\sigma'} = \boldsymbol{\sigma} - (\alpha_p p_2 + \alpha_f p_4)\mathbf{I} + \alpha_p \chi_p s_p \mathbf{I} + \alpha_f \chi_f s_f \mathbf{I} \tag{2.13}$$

in which, $\alpha_p$ and $\alpha_f$ are the conventional effective stress parameters for saturated double porous media (Khalili and Valliappan, 1996); and, $\chi_p$ and $\chi_f$ are the unsaturated effective stress parameters of the pores and fissures, respectively:

$$\alpha_p = \frac{c_p}{c}, \quad \alpha_f = 1 - \frac{c_p}{c} \tag{2.14a}$$

$$\chi_p = \frac{c_{mp}}{c_p}, \ \chi_f = 1 - \frac{c_{mf}}{c_f} \tag{2.14b}$$

$c_f = c - c_p$ represents the contribution of fissures to the overall compressibility of the double porous medium, and $c_{mf} = c_{mfp} - c_{mp}$ is the compressibility coefficient representing volume change in the fissures due to a change in fissure matric suction, $s_f = p_4 - p_3$.

The physical interpretation of parameters of Equation (2.13) is that $\chi_p$ and $\chi_f$ scale/average air and water pressures in the pores and fissures to equivalent pore-fluid and fissure fluid pressures; and, $\alpha_p$ and $\alpha_f$ quantify the contribution of these equivalent pressures to the effective stress of the double porous medium.

## 2.6.2 Constitutive modeling of unsaturated soils

### 2.6.2.1 Modeling approaches

The validity of the Bishop's effective stress and single effective stress framework for constitutive modeling of unsaturated soils was soon questioned by Jennings and Burland (1962). They reported that the phenomenon of wetting collapse observed in unsaturated soils cannot be explained in this framework. During the wetting, suction and subsequently the effective stress in unsaturated soil decreases. In the single effective stress description, this reduction should be followed by swelling of the material. However, experimental observations shows the inverse phenomenon which is the plastic compression (Jennings and Burland, 1962; Matyas and Radhakrishna, 1968).

Following the considered limitations of the single effective stress framework, other approaches involving multiple stress variables were proposed as a new constitutive framework (Cleman, 1962). Matyas and Radhakrishna (1968) adopted two independent stress variables and state surfaces to describe the volume change in unsaturated soil. Fredlund and Morgenstern (1977) proposed that any two of the three possible state variables, namely total stress ($\boldsymbol{\sigma}$), air pressure ($p_a$), and water pressure ($p_w$) can be used to define the stress state. Therefore the following combinations would be possible:

$$[\boldsymbol{\sigma}_{net}, s] \qquad [(\boldsymbol{\sigma} - p_w\mathbf{I}), s] \qquad [(\boldsymbol{\sigma} - p_w\mathbf{I}), \boldsymbol{\sigma}_{net}]$$

where $s$ is suction given by Equation (2.2) and $\boldsymbol{\sigma}_{net}$ is *net stress* defined as

$$\boldsymbol{\sigma}_{net} = \boldsymbol{\sigma} - p_a\mathbf{I} \tag{2.15}$$

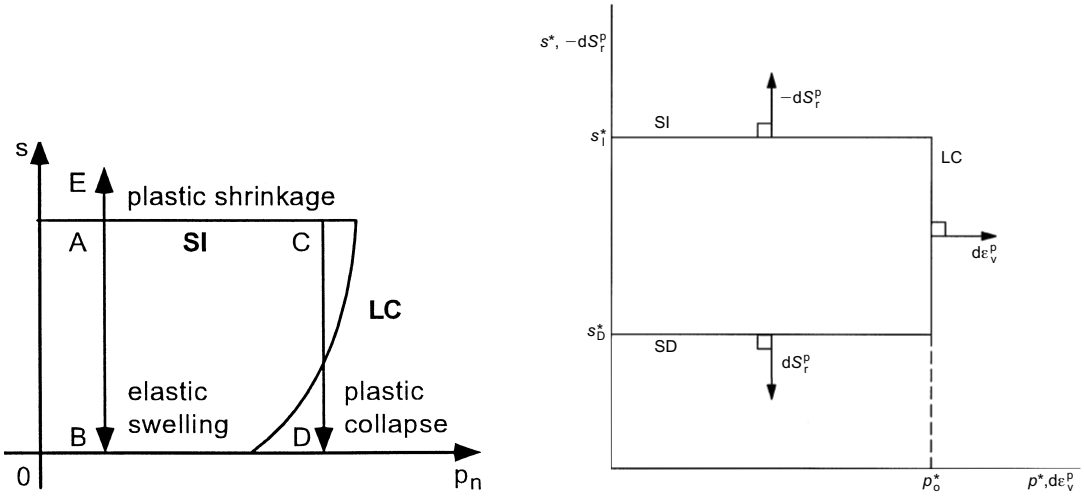


(a) (b)

*Figure 2.19:* Loading-Collapse curve (a) BBM (Alonso et al., 1990) in suction vs. net mean pressure plane (in Vaunat et al., 2000), (b) model of Wheeler et al. (2003) in modified suction vs. generalized effective stress plane

This proposition is based on the null tests in which each variable of the combined stress pair is increased by the same amount. Results of these experiments show that, under such a condition, there is neither tendency for volume change of the sample nor change in degree of saturation (see e.g. Tarantino and Mongiovi, 2000).

Increasing interest in understanding and modeling the mechanical behavior of unsaturated soils led to development of a new generation of constitutive models within the framework of elasto-plasticity. One of the first models of this kind was proposed by Alonso et al. (1990), known as Barcelona Basic Model (BBM). The model was formulated using net stress and suction. The yield surface corresponds to the MCC model which increases in size when extended to the unsaturated domains. An explicit relation was proposed to incorporate this rate of increase. In the space of suction versus mean net pressure, the proposed relation corresponds to a curve, called Loading-Collapse (LC) curve as depicted in Figure 2.19(a), which represents the increase of apparent net mean preconsolidation pressure with suction. The elastic domain is also limited by yield limit related to suction increase (SI). This limit is determined by the maximum previously experienced suction.

The BBM model appeared to be capable of addressing the main features in the mechanical behavior of unsaturated soils such as wetting-induced swelling or collapse depending on the magnitude of applied stresses or the increase of shear strength with suction.

During the recent years, several constitutive models have been developed for unsaturated soils. In general, these models could be evaluated with respect to the adopted stress framework. As proposed by Gens et al. (2006), three main classes of models could be identified depending on the choice of stress used in the constitutive equations. These are the models that have adopted, as stress

variable, a general function of suction and a constitutive stress which is: (i) net stress, (ii) net stress plus a function of suction and not of degree of saturation, and (iii) net stress plus a combined function of suction and degree of saturation.

In the first class, e.g. the BBM and the model proposed by Wu et al. (2004), the stress path could be easily represented. This is convenient in evaluating the model with respect to experimental results. These models require an explicit variation of apparent cohesion and critical state line with suction. More important, the use of these models is associated with difficulties in the transition between saturated and unsaturated states.

In the second class, the expression of constitutive model includes suction but not degree of saturation. Examples of such constitutive models are the models developed by Geiser (1999), Loret and Khalili (2002), Modaressi and Abou-Bekr (1994) and Russell and Khalili (2006). Although this approach provide a more flexible transition between saturated and unsaturated states, this transition again involves some difficulties associated with the physical justification of constitutive equations.

The constitutive stresses in the third class of models include both suction and degree of saturation (Bolzon et al., 1996; Wheeler et al., 2003). Representation of stress path in these models is rather complex and it requires data of water content. However, transition from saturated to unsaturated state is smooth and straightforward. The strength increase is often a natural consequence of the adopted constitutive stress with no need for further explicit considerations.

When dealing with unsaturated soils in a hydro-mechanical process, the degree of saturation could vary due to a combination of effects such as suction variation or mechanically-induced volume change. However, this variation is usually ignored in early constitutive models, e.g. the BBM, and this appears to be a limitation of the model in reproducing the coupling between the mechanical and water retention behavior of unsaturated soils. This coupling is of significant importance if the constitutive stress depends on the degree of saturation.

Recent developments have been done to include in the constitutive models of unsaturated soil, the coupling effects of mechanical and water retention behavior (Vaunat et al., 2000; Wheeler et al., 2003).

The model proposed by Wheeler et al. (2003) adopts, as stress variables, the generalized effective stress and modified suction defined as suction multiplied by porosity ($ns$). The LC curve is simplified to a vertical straight line in the space of modified suction versus the generalized effective mean pressure, as shown in Figure 2.19(b). In addition to LC, two yield limits are introduced to incorporate the hydraulic hysteresis and plastic deformations occurring during drying (SI for suction increase) and during wetting (SD for suction decrease). The model was found to be capable of addressing the main features in the mechanical behavior of unsaturated soils.

#### 2.6.2.2 Double structure model for unsaturated soils

As previously mentioned, double porosity fabric is a common feature in expansive clays. It has been shown that these materials show significant swelling

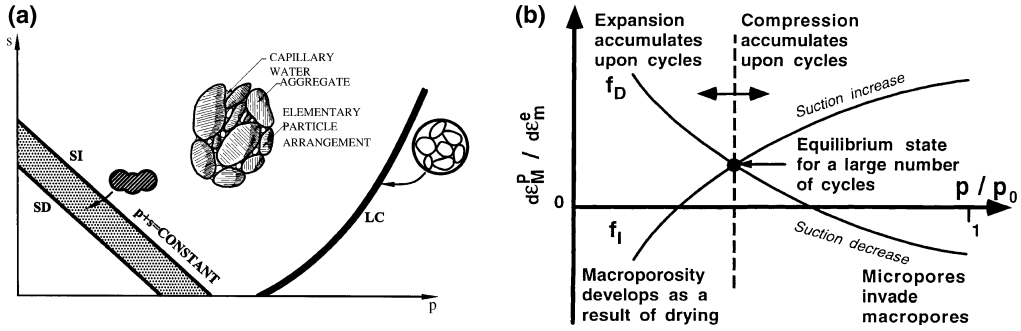


*Figure 2.20:* Double strutcure model for expansive soils (a) Schematic representation of the double structure model in the isotropic plane. (b) Interaction function linking microstructural and macrostructural strains (Sanchez et al., 2005)

strains that are strongly stress-path dependent and cannot be easily accommodated by conventional elasto-plastic unsaturated soil models. Gens and Alonso (1992) related this behavior to the double porosity fabric, a feature to be considered to achieve an appropriate constitutive model for these materials.

Alonso et al. (1999) proposed a conceptual model for double structure expansive clays in which two levels of formulation had been presented: microstructure model where the interactions at particle level occur, and macrostructure model that accounts for the overall fabric arrangement of the material including aggregates and macropores.

In the model proposed by Alonso et al. (1999), clay aggregates are assumed to be saturated and, therefore, their behaviour is governed by saturated soil mechanics concepts. Moreover, deformations at microstructural level are assumed to be reversible.

The macrostructure is governed by the BBM model in which the yield limit increases with suction following LC curve. It is assumed that the macrostructure does not influence the behavior of the microstructure; while, microstructural deformation may cause irrecoverable strains in the macrostructure. Accordingly, in addition to LC curve, two yield surfaces, namely SI and SD, are introduced which represent the loci of the points from which irreversible strains on the macrostructure due to microstructure start to occur (Fig. 2.20(a)).

The relation between the magnitude of increments of micro- and macrostructural irrecoverable strains are determined by interaction function given for suction increase and suction decrease as depicted in Figure 2.20(b). These functions depend on the normalized distance to the macrostructural yield locus (LC) which is considered to represent a measure of the density of the macrostructure. Closer a soil state lies to the LC, denser and less collapsible the macrostructure.

Recently, Sanchez et al. (2005) formulated the model in the framework of generalized plasticity (Zienkiewicz and Mroz, 1984; Lubliner, 1991) using the concept of multi-dissipative materials.

### 2.6.3 Constitutive modeling of natural bonded soils

#### 2.6.3.1 Modelling approaches

In line with the experimental observations revealing the importance of soil structure effects on the mechanical behavior of natural bonded soils, improvements of constitutive models for these materials have been proposed by making explicit consideration of soil structure and its degradation. The common idea in the development of constitutive models for structured soils is to include soil structure effects in a model which is already capable of describing the behavior of reconstituted soil as a reference state.

Inclusion of structural effects in constitutive models of structured soils is done by introducing a yield limit depending on soil structure. However, the way it is implemented in the models seems to be different. The existing constitutive models for saturated natural structured soils can be classified based on three main approaches that will be birefley described below.

**(i) Kinematic hardening and boundary surface plasticity:** In this approach, the model is formulated within the framework of kinematic hardening (Mroz, 1967) with elements of boundary surface plasticity concept (Dafalias, 1986). The material behavior is described at least with two yield surfaces: a bounding surface and a bubble-type surface that moves with the current state inside the bounding surface according to a kinematic hardening rule. This surface separates regions of elastic and plastic response.

Recently some constitutive models for structured soils have been developed in this framework (Rouainia and Wood, 2000; Kavvadas and Amorosi, 2000; Baudet and Stallebrass, 2004). In structured soils, a third surface is usually defined inside the bounding surface that corresponds to the behavior of reconstituted soil. The effects of structure in this models are usually simulated in part by an increase in the size of the bounding surface defined in the model which then decreases to that of the reconstituted soil at very large strains.

These models, in general, are advantageous in the way that they allow the retention of some information concerning the recent stress history of the material by introducing an extra yield surface or bubble. However, the main drawback of these models is the complexity of the formulations and the geometrical assumptions which are usually needed to derive the kinematic hardening rule.

**(ii) Single yield surface with isotropic hardening.** This approach is based on the explicit introduction of soil structure effects within a single yield locus. This is usually done by allowing the current size and location of the yield surface to depend on the soil structure. Structure degradation are accounted for by damage-type function which appear explicitly in the model formulation. Accordingly, the hardening modulus in these models has two components: one stemming from the original model of reconstituted soil and the other from the added terms of structure. Examples of constitutive models for bonded soils developed following this approach are provided by Gens and Nova (1993); Oka et al. (1989).

The main advantage of this approach is the simple transition of the original model to the structured model. This transition, in general, is not associated with important added complexity in model formulation; therefore, it allows focusing more on the rigorous consideration of structural effects with less concern about the model complexity.

**(iii) Damage-type approach.** This approach is associated mainly with the work of Liu and Carter (1999, 2000a) which has been further formulated using the disturbed state concept (Desai, 1974, 1995, 2001). In this approach the structured soil is compared with reconstituted soil of the same mineralogy. Structural effects are directly introduced through a mathematical relation between additional void ratio of structured soil over the reconstituted soil and the current state of stress with respect to a reference value in oedometric or isotropic compression curve. This relation is then used to describe the virgin compression of the structured soil.

#### 2.6.3.2 Representative models for saturated bonded soil

In this section, a review of the most representative models for bonded soils will be presented. The following models have all been developed for natural structured soil at the saturated state. These models and the equations through which they incorporate the degradation of structures are summarized at the end of this section in Table 2.1. Parameters of the equations given in this table are defined in line with description of the models in the text.

**Bubble model by Rouainia and Wood (2000).** This model is based on an existing extension of the Modified Cam-Clay (MCC) model (Roscoe and Burland, 1968) for reconstituted soils to the framework of kinematic hardening and bounding surface plasticity.

The model introduces three surfaces with the same shape and function as the MCC yield surface (Fig. 2.21(a)). The structure surface acts as a bounding surface and contains information about the current magnitude and anisotropy of the structure. As plastic straining occurs, the structure surface tends to collapse toward a third reference surface which passes through the stress origin and represents the behavior of the reconstituted or completely remolded soil.

The elastic properties are assumed to be constant. The size and location of the structure surface with respect to the reference surface are controlled by the process of de-structuring. A scalar variable, $r$, which is the ratio of the sizes of the structure surface and reference surface, represents strength components of soil structure. The evolution rule for this variable is proposed to be a monotonically decreasing function of both volumetric and deviatoric plastic strain rates which are combined through a non-dimensionless scaling parameter ($A$ in Table 2.1).

The original model requires eight parameters and the de-structuration model then introduces two further parameters: $k$, rate of loss of structure with damage strain; and $A$, relative proportion of distortional and volumetric de-structuration.

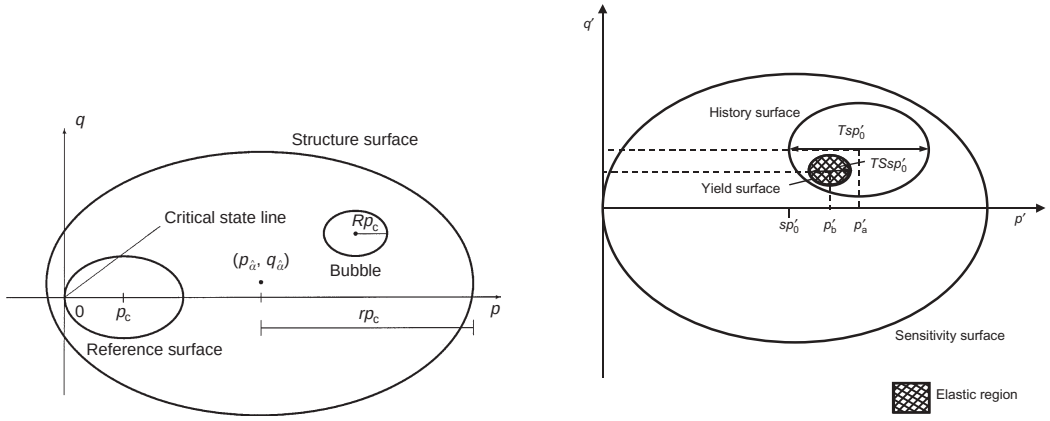


(a) (b)

*Figure 2.21:* Kinematic hardening models for saturated structured soils: (a) Bubble model for de-structuration of clays (Rouainia and Wood, 2000), (b)S3-SKH model (Baudet and Stallebrass, 2004)

As an additional initial conditions, the center of the structure surface, describing the initial degree of structure and anisotropy of structure of the soil should be specified in the new model.

**S3-SKH model by Baudet and Stallebrass (2004).** The S3-SKH model (Sensitivity Three-Surface Kinematic Hardening) was developed based an existing constitutive model for reconstituted soils. The model uses the sensitivity, defined as the ratio of the undrained shear strength of the natural clay to that of the corresponding reconstituted soil (Terzaghi, 1944), in order to quantify the structure.

The model introduces three surfaces: the history and yield surfaces lying within a sensitivity (natural state) boundary surface (Fig. 2.21(b)). Following Cotecchia and Chandler (2000), the sensitivity boundary surface is considered to be larger than, but the same shape as the intrinsic surface assumed to be the same as in the MCC model. The ratio between the size of sensitivity and equivalent intrinsic bounding surfaces is measured by current sensitivity, indicated by $s$ (not to be confused with suction in the present study).

For the sake of simplicity, the model ignores material anisotropy as well as any additional effects of soil structure on elastic stiffness. Plastic deformations are assumed to follow the normality rule. De-structuring is described by change in sensitivity through a decreasing exponential function of plastic strain where volumetric and shear strains are of equal importance (see Table 2.1). The proposed equation can be adjusted so that sensitivity reaches asymptotically the value of unity or a stable value greater than unity for natural clays with stable elements of structures.

The new parameters in the model are (see Fig. 2.21(b)): $s_f$ , the ultimate sensitivity, which accounts for the stable elements of structure and $k$, a parameter that controls the rate of de-structuration with plastic strain. The other

eight parameters remain the same as in the 3-SKH model, and are derived from test data of reconstituted clay. The additional initial condition to be specified is $s_0$ the initial sensitivity which represents the initial degree of structure.

**MSS model by Kavvadas and Amorosi (2000).** The MSS model is a kinematic hardening model with two characteristic surfaces of similar shapes: an internal plastic yield envelope (PYE) and an external bond strength envelope (BSE) corresponding to material states associated with appreciable rates of structure degradation. The preconsolidation pressure is considered as a parameters unifying the stress history and the bond strength effects which controls the size of the BSE

The model can account for anisotropic bond development. Structure degradation is assumed to occur with plastic strains. Both volumetric and deviatoric structure degradations are directly and separately introduced in the hardening rule through an exponential damage-type form equation with a different set of rate controlling parameters for each component (see Table 2.1). The model follows an associated flow rule.

The MSS model requires eleven parameters, four of which control the volumetric and deviatoric structure degradation and 3 are parameters control anisotropic characteristics of the proposed model. The remaining parameters correspond to the reconstituted properties. There is also an optional structure parameter that controls the steady-state deviatoric structure degradation/hardening. The determination of the initial state of the material involves two additional variables compared to MCC: position of the center of the BSE controlling the primary structure anisotropy and position of the center of the PYE controlling the secondary anisotropy.

**Conceptual model for bonded soils by Gens and Nova (1993).** Gens and Nova (1993) presented a conceptual base for constitutive modeling of saturated bonded soils and weak rocks. They discussed that the existence of a certain degree of bonding can manifest itself by the fact that the point representing the state of the material in the compression plane ($e - \ln p'$) in Figure (2.22(a)) is located to the right of virgin isotropic consolidation line $AA'$, at a point such as $B$. At a given value of $p'$, this materials exhibits a higher void ratio in comparison with unbonded soil ($\Delta e$). The model uses, as the starting point, a constitutive law for unbonded material which will be modified according to the magnitude of bonding. The modification is made by allowing the current size of the yield surface to depend on the amount of de-structuring. The ratio of the sizes of the current yield surface (surface C in Fig. 2.22(b)) and the yield surface corresponding to unbonded material (surface A) is defined to be a general function of structural variable $b$ ($p_{co}/p_c = 1 + b$, see Fig. 2.22(b)). The soil structure variable, $b$, changes through the volumetric and deviatoric effects following a general evolution rule. Similar expressions could be proposed to link $p_t$ to $p_c$ in Figure 2.22(b). The structure degradation is assumed to be associated with both plastic and volumetric strains (see Table 2.1 for the equations).

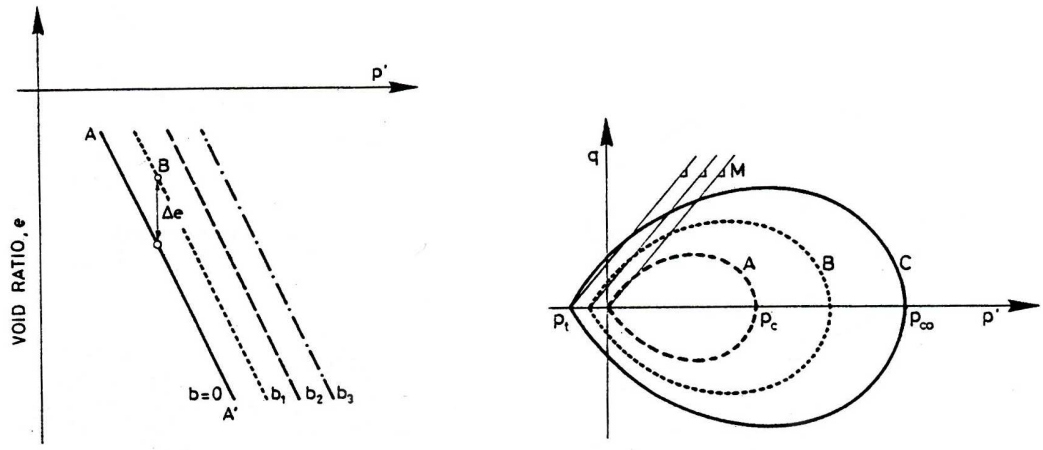


(a) (b)

*Figure 2.22:* Conceptual model proposed by Gens and Nova (1993): (a) virgin isotropic consolidation lines for materials with different degrees of bonding, (b) successive yield surfaces for increasing degrees of bonding

Once the modification of yield surface is done, the model could be considered as an elasto-plastic hardening model with a new yield surface for which the model elements such as hardening law or plastic multipliers can be obtained in the usual manner. However, these elements are in general controlled by two effects corresponding to unbonded material on one hand and the soil structure on the other hand. For instance, the hardening modulus is a combination of two terms: one of them being related to the original model and representing the unbonded material hardening (or softening) and the other arising from the softening of material due to structure degradation.

**Model for bonded geomaterials by Nova et al. (2003).** Nova et al. (2003) presented a general constitutive framework for describing the mechanical behavior of a bonded geomaterial subjected to mechanical and/or chemical degradation. The basis of the model is similar to the conceptual model of Gens and Nova (1993). For the sake of simplicity, they assumed that degradation, whatever its cause may be, affects internal variables only and not other material properties, e.g. elastic moduli or friction angle. They assumed that the material behavior can be considered as isotropic and they formulated the model in the framework of isotropic hardening plasticity.

The yield surface in this models is obtained by simple modification of the yield surface of reconstituted soil. The modification is introduced by allowing the yield surface to increase in size and to acquire some tensile strength due to bonded structure. The size of the yield surface is controlled by the internal (hardening) variables describing the effects of loading the previous (mechanical and non-mechanical) loading history which includes the structure effects.

The degradation of inter-particle bonds is considered to occur for both mechanical and non-mechanical effects, like grain rearrangements or chemical dis-

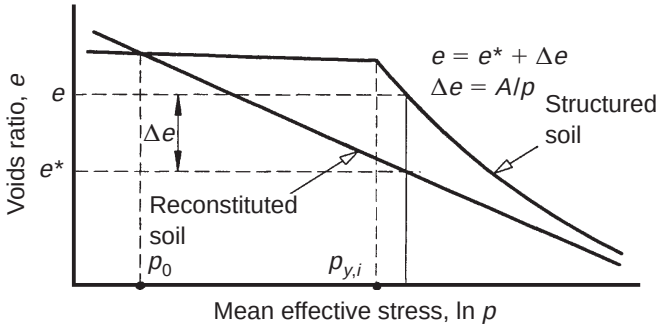


*Figure 2.23:* Idealization of the compression behavior of reconstituted and structured soils (Liu and Carter, 1999)

solution. The bonding degradation in this model is linked to the occurrence of plastic strains. Hence for the internal parameter, $p_m$, defined as $p_m = p_{co} - p_c$ in Figure 2.22(b), an evolution equation as a function of both volumetric and deviatoric plastic strains is proposed for mechanical degradation (see the equation in Table 2.1. In this equation, two material parameters $\rho_m$ and $\xi_m$ control the rate of mechanical degradation of bonding.

**Model of structured soils by Liu and Carter (1999).** This approach, associated mainly with the work of Liu and Carter (1999, 2000a), uses a direct introduction of structural effects into the model formulation by means of an explicit mathematical relation. In this approach, the development of the model begins in the oedometric (or isotropic) compression plane (Fig. 2.23). The initial yield limit of structured soil and the excess void ratio of structured soil over reconstituted soil at this yield limit are considered as parameters of structured soil. As a starting point, an equation for the virgin compression curve of structured soil dependent on these parameters is proposed. This equation is a mathematical relation expressing the value of decreasing excess void ratio of structured soil non-linearly proportional to the ratio of current pressure over the initial yield limit. The parameter of non-linearity, so-called *de-structuring index*, represents the rate of structure degradation.

Liu et al. (2000) used an equation of this kind to model the compression of structured soils in a mathematical framework using the disturbed state concept (Desai, 1974, 1995, 2001) with $\overline{D}_{\varepsilon v}$ in Table 2.1 being the disturbance function. In a later work, Liu and Carter (2002) used the proposed equation to develop formulation of an elasto-plastic model for structured soil. They used the incremental form of this mathematical relation to define the volumetric strains. The obtained relations for volumetric strains are then subjected to a direct modification in order to include the effects of structure degradation due to deviatoric effects. Deviatoric strains are then deduced according to the flow rule. The model uses a strain hardening rule as in modified Cam-Clay model.

The model provides a simple mathematical way of reproducing the behavior of structured soils. The main limitation of this method, when used in an elasto-plastic model, is the fact that it uses an interpolation function between

structured and reconstituted soil which directly links the void ratio to the mean effective stress without considerations of elasto-plastic mechanisms.

#### 2.6.3.3 Extension of models for unsaturated bonded soil

The constitutive modeling of the unsaturated natural (cemented) soils has been discussed by Alonso and Gens (1994). They reported that in cemented soils, suction influences both the soil matrix and the strength of the bonds. They adapted the conceptual model of Gens and Nova (1993) incorporating the suction effects in unsaturated soils. They used the BBM model (Alonso et al., 1990) as the reference model for unsaturated reconstituted soil. The suction-induced hardening due to capillary effects in reconstituted soil ($\Delta p^s$) is represented by $LC_u$ (loading-collapse) curve in Figure 2.24 where $p$ is net mean pressure.

The yield limit given by $LC_u$ is then extended due to bonding effects according to the model of Gens and Nova (1993). This yields the curve $LC_{bs}$ where $\Delta p^s_{co}$ corresponds to capillary effects as in reconstituted soil and bonding effects. They proposed to model the additional effects of suction on the strengthening of the bonds by introducing the soil structure parameter, $b$ in the model of Gens and Nova (1993), to be dependent on suction as presented in Table 2.1. The proposed modification corresponds to the LC curve $LC_b$, the difference of which with $LC_{bs}$ ($\Delta p^s_{co}$, i.e. hatched area in Fig. 2.24), represents the additional effects of suction of bondings.

Leroueil and Barbosa (2000) investigated the combined effects of fabric, bonding and partial saturation on yielding of soils and proposed a general model of yielding (GFY for Given Fabric Yielding) which would apply to saturated or unsaturated, and structured or non-structured soils. The yield curve corresponds to a given soil fabric and bonding. Consequently, any change in the soil fabric or the bonding effects could alter the properties of the yield curve such as size, anisotropy effects and the induced-cohesion.

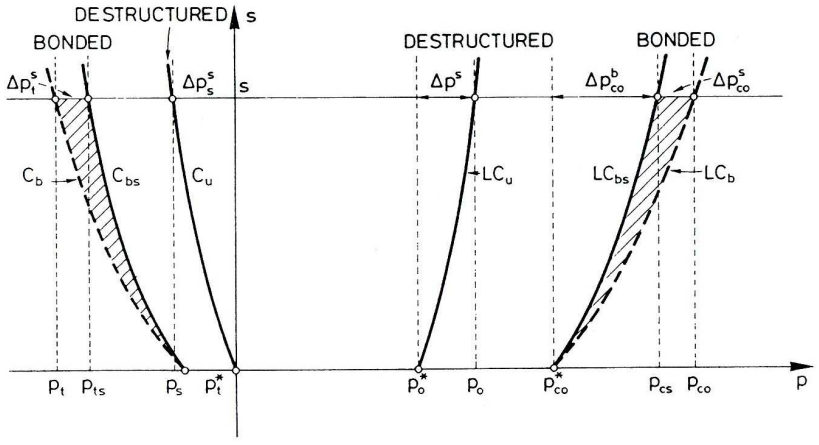


*Figure 2.24:* Yield limits under isotropic condition for unsaturated cemented soils (Alonso and Gens, 1994)

*Table 2.1:* Constitutive models for bonded soils

| **Model** | **Type*** | **De-structuring rule** | **Damage parameter** |
|---|---|---|---|
| **Saturated bonded soils** | | | |
| Bubble Model<br>Rouainia and Wood (2000) | (i) | $r = 1 + (r_0 - 1)\exp\left[\frac{-k\varepsilon^d}{\lambda^* - \kappa^*}\right]$ | $\mathrm{d}\varepsilon^d = \sqrt{(1-A)\mathrm{d}\varepsilon_v^{p2} + A\mathrm{d}\varepsilon_d^{p2}}$ |
| S3-SKH<br>Baudet and Stallebrass (2004) | (i) | $\mathrm{d}s = -\frac{k}{\lambda - \kappa}(s - s_f)\mathrm{d}\varepsilon^d$ | $\mathrm{d}\varepsilon^d = \sqrt{\mathrm{d}\varepsilon_v^{p2} + \mathrm{d}\varepsilon_d^{p2}}$ |
| MSS<br>Kavvadas and Amorosi (2000) | (i) | Volumetric $\zeta_v \exp(\eta_v \varepsilon_v^p)\mathrm{d}\varepsilon_v^p$<br>Deviatoric $(\theta_d - \zeta_d \exp(\eta_d \varepsilon_d^p))\,\mathrm{d}\varepsilon_d^p$ | $\varepsilon_v^p$ and $\varepsilon_d^p$ |
| Model for Bonded soils<br>Gens and Nova (1993) | (ii) | $b = b_0 e^{-(h-h_0)}$ | $h = h_1 \int \lvert\mathrm{d}\varepsilon_d^p\rvert + h_2 \int \lvert\mathrm{d}\varepsilon_v^p\rvert$ |
| Model for Bonded soils<br>Nova et al. (2003) | (ii) | $\mathrm{d}p_m = -\rho_m p_m \left(\lvert\mathrm{d}\varepsilon_v^p\rvert + \xi_m \lvert\mathrm{d}\varepsilon_v^p\rvert\right)$ | $\varepsilon_v^p$ and $\varepsilon_d^p$ |
| DSC Compression model<br>Liu et al. (2000) | (iii) | $\overline{D}_{\varepsilon v} = 1 + b\left(\frac{p'_{yi}}{p'}\right)$ | $p'$ |
| Structured Cam Clay<br>Liu and Carter (2002) | (iii) | $\Delta e_i \left(\frac{p'_{yi}}{p'}\right)^b$ | $p'$ |
| **Unsaturated bonded soils** | | | |
| Model of Bonded soils extended for unsaturation effects<br>Alonso and Gens (1994) | (ii) | $b = b_u e^{-(h-h_0)}$<br>$b_u = b_0 + \Delta b(1 - e^{-as})$ | $h = h_1 \int \lvert\mathrm{d}\varepsilon_d^p\rvert + h_2 \int \lvert\mathrm{d}\varepsilon_v^p\rvert$ |

## 2.7 Summary and anticipated contribution

From the above-presented synthesis, it is understood that the influence of soil structure on the soil behavior has been studied in four parallel fields dealing with: (i) fissured clays and fractured rocks, (ii) agricultural and arable soils, (iii) natural structured soils, and (vi) expansive or compacted clays. These are summarized in Table 2.2.

In the first group, i.e. fissured clays and fractured rocks, the focus has been placed on deriving the governing equations of flow and deformation in double porous media mainly to solve the problems of consolidation with respect to the fabric.

In the second group, i.e. agricultural and arable soils, the concept of double porosity has been used to evaluate the influence of soil fabric on the water transport and water retention properties of the soil. The joint research study of the present work, realized by Carminati (2006), mainly addresses this field of study.

In the last two groups, namely natural soils and expansive and compacted soils, the influence of soil structure on the mechanical behavior has been evaluated. Therefore, they are in closer relation with the present work.

Previous works done on the natural structured soils are mainly focusing on the added strength of the soil due to inter-particle bonding effects. The stress-strain response of these soils has been experimentally evaluated mainly under the saturated condition. Change in the soil response during the loading has been described with respect to the evolution of the soil structure and degradation of the inter-particle bondings. However, the soil fabric and its evolution has been rarely taken into account. Mechanical constitutive models proposed for natural bonded soils are similar in most aspects. In general, these models quantify the soil structure effects with respect to the added strength due to bonding. In these models, structure evolution is usually linked to the occurrence of plastic strains. However, to introduce the evolution rule, these models use ad hoc and usually hypothetical equations. Apart from the mathematical developments, the main difference between these models lies in the way they introduce soil structure parameter and the corresponding evolution rules.

*Table 2.2:* Different fields involving the study of soil structure and/or its evolution

| **Material** | **Field of study / Focus / Structure evolution** |
|---|---|
| (i) Fissured clays & fractured rocks | Flow & consolidation / Soil fabric / No consideration |
| (ii) Agricultural & arable soil | Flow & water retention / Soil fabric / No consideration |
| (iii) Saturated bonded soils | Mechanical response / Bonding / Explicit consideration |
| (iv) Unsaturated expansive or compacted clays | Mechanical response / & water retention Soil fabric / No consideration |

In the case of expansive or compacted clays, mechanical behavior has been evaluated with respect to aggregated microstructure for both saturated and unsaturated states. Study of stress-strain response under unsaturated states has been often accompanied by the study of water retention properties. In these works, no evidence of inter-bonding effects has been reported, and instead, the emphasis has been placed on the influence of double porous fabric on soil response. The constitutive models proposed for unsaturated expansive soils use the concept of double porous fabric to address the extra features of behavior linked to the soil structure. These models, however, do not explicitly consider the evolution of soil fabric during a loading process. Moreover, the mechanical response and the water retention properties are teated separately and the coupling link is usually missing.

From this summary, it is realized that concurrent study of inter-particle bonding and soil fabric effects on the mechanical response, specially under unsaturated conditions, is still far from being well understood. Hence, there is room for further investigation of the combined effects in material where both effects are present. Examples of such materials are aggregated soils. In the aggregated soils, the aggregates are often separated by large inter-aggregate pores. The existence of large pores and open fabric depends on the size and strength of aggregated particle assemblages; and, the aggregates themselves are formed as a result of inter-particle bonding.

The present study deals with unsaturated aggregated soil as a structured soil with a double porosity. For sake of simplicity, from now later on, *structured soils* refers to *aggregated soils* unless otherwise stated. The present study looks to the stress-strain response and water retention properties of unsaturated aggregated soils with respect to the soil structure effects.

The main contribution of this work is to address the inter-particle bonding, fabric and partial saturation effects in a single framework. It uses a multi-scale experimental approach to characterize the material behavior with respect to soil structure and its evolution during mechanical loading or drying-wetting process. The experimental results are then used to propose a mechanical constitutive model coupled with water retention properties for unsaturated structured soils with explicit consideration of soil structure evolution.

# Chapter 3

# Hydro-mechanical formulation for double porous soil

The hydro-mechanical study of porous media requires, in the first step, the development of field equations governing flow and deformation in the material. Hydro-mechanical models of unsaturated soils and the related governing equations are well established by different authors (see e.g. Laloui et al., 2003; Collin et al., 2002). However, when soils with double porosity are concerned, the model formulation should be adapted to the double porous media. This chapter presents the formulation of a model for double porous media in a general thermodynamically consistent framework to which different mechanical constitutive models can be incorporated. The presented formulation is aimed to sketch the theoretical framework and to highlight, from onset, the field variables concerned in the experimental part of the study as well as the needed constitutive equations. First, the theoretical framework is defined and then the physical properties and phase relations in double porous media are presented. Subsequently, the balance equations are introduced and the required constitutive equations are presented in their general form. Finally, the general field equations are derived from the combination of balance equations and constitutive equations.

## 3.1 Theoretical framework

### 3.1.1 Thermodynamic approaches

In the study of the mechanics of continuum multiphase porous media, three general approaches can be distinguished. The first one, named here as *Biot's approach*, is a phenomenological approach associated with the early work of Biot where the phases are not treated separately (definition of phases and constituents will come at the end of this section). While, the two other approaches, namely *averaging* and *theory of multiphase mixtures*, both use the concept of volume fraction in order to consider each single phase of the multiphase system. The choice of an approach to obtain the appropriate formulation requires the knowledge of the characteristics of each approach. Therefore, these approaches are briefly discussed next.

**Biot's approach:** The so called Biot's approach is mainly based on the theoretical description of porous materials by Biot who studied different problems of porous elastic bodies (Biot, 1941, 1956, 1972).

In this family of approaches, the description starts at the macro scale and from the beginning it is assumed that the stress and other related concepts are all macro scale concepts. They are formulated in a Lagrangian description with respect to the kinematics of the solid skeleton. This means that in these theories, special attention is paid to solid skeleton constituent. However, the balance laws as well as constitutive equations are introduced without any distinction between the constituents. The mass balance and momentum balance equations are given for the whole porous medium. Recently, the Biot's theory has been extended by Coussy (1995) to a modern thermodynamic consistent framework.

**Averaging approach:** The averaging approaches are named also as hybrid mixture theories or more often continuum theory of materials with micro structures (Bedford and Drumheller, 1983; De Boer and Ehlers, 1988).

In these approaches, two geometrical scales are defined: microscopic scale corresponding to the pore level and macroscopic scale corresponding to the whole domain of porous media. At the macroscopic scale, it is assumed that each phase is a continuum that fills up the entire domain and to which the averaged variables are assigned. A representative elementary volume (REV) which always, regardless of its position in the domain, contains both solid and pores is considered to obtain the average values of variables. The size of REV should be such that the parameters representing the distribution of solids and pores within it are statistically meaningful (Bachmat and Bear, 1986).

The development of macroscopic field equations starts from a microscopic description and it is done by use of averaging procedures. Conservation laws are introduced at microscopic scale. In most of these approaches, assumptions are made about the microscopic behavior and constitutive equations are introduced at this scale (see e.g. Whitaker, 1986). The resulting field equations describe the considered phenomenon at the microscopic scale. Using different averaging rules (Bachmat and Bear, 1986), these equations are then averaged over suitable time and space segments to derive an averaged or macroscopic set of field equations. For this purpose different averaging methods are used that a discussion of which is given in Kalaydjian (1987) and Nigmatulin (1979).

The main advantage of this method is that the information available at microscopic scale are taken into account. However, these approaches suffer from the fact that usually many assumptions are made before, during and after averaging that can impose restrictions to the method. Most often, ad hoc assumptions are made to obtain the desired final form of equations. The latter fact sometimes results in loss of generality that does not allow having a systematic development of formulations. Moreover in this approach, a REV must be defined for each physical property, therefore a common REV for all properties of the porous medium is unsure (Kalaydjian, 1987).

Improvements of these approaches have been proposed with the purpose of minimizing the assumptions at microscopic scale and obtaining more systematic

development procedures (Hassanizadeh and Gray, 1979b,a; Nigmatulin, 1979; Marle, 1982; Kalaydjian, 1987). The improvements are mainly targeting the averaging methods and the shift from microscopic to macroscopic scale. In the improved approaches, fundamental principles, such as conservation laws are introduced at microscopic scale, while constitutive equations are introduced at macroscopic scale in the form of phenomenological equations. This procedure allows the introduction of physical assumptions at the macroscopic level; meanwhile, maintains the connection between the two scales.

**Theory of multiphase mixtures:** In these approaches, named also as the continuum theory of mixtures (Bedford and Drumheller, 1983; De Boer and Ehlers, 1988), the multiphase porous media is considered as a mixture of overlapping phases all being able to occupy the same region of space simultaneously.

The developments of balance equations in theory of multiphase mixture starts by writing the local form of equations in their usual form for a single continuum, except that some supply terms are also added to take into account the interaction between the constituents. In this approach, the field equations are obtained using the thermodynamics of immiscible mixtures. The development starts at the macroscopic scale. The concept of volume fraction is used to obtain the balance laws for single phase bodies at macroscopic scale. The interaction between phases is taken into account by means of additional terms for property exchange between the phases. Assumptions are made about the macroscopic behavior of phases; and accordingly, constitutive laws are introduced at macroscopic scale. In these approaches volume fractions are treated as internal state variables and they appear in the constitutive equations (Bowen, 1980, 1982).

The advantage of this method is that the assumptions are kept minimum and limited to the macroscopic scale. However, in the macroscopic description there is no more direct connection with microscopic scale which can be considered as a drawback of this method. The scalar definition of volume fraction restricts the approaches to the case of isotropic pore structure (De Boer and Ehlers, 1988); while, the pore structures might be taken into account by introducing some additional definitions in the tensorial forms (Kubik, 1986).

The choice of an appropriate approach to derive the governing equations depends on the requirements of the problem in relation with features provided by the approach. The main difference between the above mentioned approaches is in the assumptions made during the developments. Opting for any of these approaches, however, one might obtain more or less the same final formulation.

Coussy et al. (1998) showed that the macroscopic field equations derived by averaging approaches can be reformulated in terms of measurable quantities involved in the Biot's approach. From a comparative study of Biot's approach and continuum theory of mixtures, Schanz and Diebels (2003) concluded that the two approaches have the same structure and they differ mainly in the coefficients of differential equations and their physical interpretation. A comprehensive review of these approaches are given in Bedford and Drumheller (1983).

In the present study, the approach of theory of multiphase mixtures is used to develop the model formulation. This choice is made due to the fact that this approach offers, in a relatively simple framework, possibilities to better understand the interaction between the phases.

The soil is considered here as a multiphase porous material consisting of solid particles and pores which vary in shape and size. *Phase* here denotes a portion of matter with smoothly varying physical properties and chemical composition which are separated from one another by well-defined boundaries. This refers to *solid*, *liquid*, and *gas* phases in porous media. In general, each phase might be a mixture of different identifiable *constituents* (or species); e.g., solid phase in soil might consist of different minerals and the gas phase might include dry air as well as water vapor.

In soil mechanics, the soil mixture is called *saturated*, implying that the liquid fills the entire pore space, or *unsaturated*, provided the pore space is partly filled by liquid and partly by gas. However, in earth science and multiphase literature, a mixture is called saturated only if the entire pore space is filled by fluid (gas or liquid). According to this latter definition, an unsaturated mixture possesses a fraction of volume whose space is massless (Ehlers, 1993; Wilmanski, 1995; De Boer, 1996; Wilmanski, 1996). Throughout this work, saturation and the related terms refer, in general, to its first definition by soil mechanicians unless explicitly stated otherwise. The terms *physically saturated* and *physically unsaturated*, however, are used to make the distinction when addressing the definition of saturation as it is given in the literature of multiphase mixtures.

Using the multiphase mixture theory, Hutter et al. (1999) developed the thermodynamically-based mathematical formulation for saturated/unsaturated, compressible/incompressible soils. Based on the results of the latter work, Laloui et al. (2003) presented the coupled hydro-mechanical formulation of three-phase porous media and the corresponding numerical validations. The formulation was presented for porous media with single continuous porosity. However, in the case of unsaturated soils with double porosity, where the assumption of single continues pores is no more valid, the appropriate form of formulation should be adopted. In the next section, the general thermodynamic formulations of the theory of multiphase mixtures are first presented. In the rest of this chapter, the emphasis is placed on the case of porous media with double porosity and the governing equations are derived for unsaturated soils with double porosity.

*Notations and conventions:* throughout this dissertation, tensor quantities are identified by boldface letters. Symbols '$\cdot$' and ':' between tensors of various orders denote their inner product with single and double contraction respectively. The dyadic (tensorial) product of two tensors is indicated by $\otimes$. $\mathbf{I}$ denotes the second-order identity tensor. d(.) indicates the increment and $\partial(.)/\partial x$ is partial derivative with respect to a variable $x$. $\nabla(.)$ denotes spatial gradient and $\nabla \cdot (.)$ the divergence operator. The summation sign $\sum_a$ denotes the summation over all possible values of $a$; while when summation is considered only over certain values of $a$, these values are specified in the subscript of summation sign, for instance, $\sum_{\alpha=1,2}$ denotes summation over $\alpha = 1$ and 2 only.

Throughout the entire dissertation, except for this chapter, the sign convention is the usual convention of soil mechanics which is that compressions is positive. In this chapter, however, the consistent sign convention of tension positive is adopted from continuum mechanics.

### 3.1.2 General formulation

Consider a mixture of $N \geq 2$ constituents, each constituent of the mixture being denoted with the subscript $\alpha$. This mixture is considered as a sequence of bodies $\mathscr{B}_\alpha$, all being able to occupy the same region of space simultaneously. Any material particle of $\mathscr{B}_\alpha$ is identified by its position in some reference configuration, $\mathbf{X}_\alpha$. The motion of $\mathscr{B}_\alpha$ is a mapping,

$$\mathbf{x} = \chi_\alpha \left( \mathbf{X}_\alpha, t \right) \tag{3.1}$$

that gives the spatial position, $\mathbf{x}$, of a particle $\mathbf{X}_\alpha$ in the current configuration, at any time, $t$. Each constituent has its own kinematics and to each is assigned its own function of motion $\chi_\alpha$. The velocity of constituent $\alpha$ is then defined as:

$$\mathbf{v}_\alpha = \frac{\partial \chi_\alpha \left( \mathbf{X}_\alpha, t \right)}{\partial t} \tag{3.2}$$

The displacement of particles in each constituent is also defined as:

$$\mathbf{u}_\alpha = \chi_\alpha \left( \mathbf{X}_\alpha, t \right) - \mathbf{X}_\alpha \tag{3.3}$$

Any time-dependent field may be regarded either as a function of particle and time or as a function of the position and time. If one regards time, $t$, and $\mathbf{X}_\alpha$ as the independent variables, the material or Lagrangean description is adopted; while one adopts the spatial or Eulerian description if time, $t$, and position, $\mathbf{x}$, are regarded as independent variables. Accordingly, material time derivative is defined and related to the spatial time derivative as follows:

$$\dot{(.)} = \frac{D(.)}{D_t} = \frac{\partial (.)}{\partial t} + \mathbf{v}_\alpha \nabla (.) \tag{3.4}$$

where $\mathbf{v}_\alpha$ is the spatial velocity of constituent. It will be seen later that material time derivative is of great importance in obtaining simplified forms of balance and field equations.

In the context of multiphase mixtures, where each constituent occupies a volume, two different density functions can be defined, namely the intrinsic or real density, $\rho_\alpha$, relating the mass of constituent to its own volume and partial or bulk density, $\overline{\rho}_\alpha$, relating the same mass to the volume of whole mixture. Constituent $\alpha$ is called *incompressible* or *density preserving* when $\rho_\alpha$ is constant. Partial and intrinsic densities are related using the constituent volume fraction, $n_\alpha$:

$$\overline{\rho}_\alpha = n_\alpha \rho_\alpha \tag{3.5}$$

where

$$n_\alpha = \frac{V_\alpha}{V} \tag{3.6}$$

with $V_\alpha$ and $V$ being the volume of constituent in the mixture and total volume of the mixture respectively. It follows from its definition that volume fraction reflects a certain local structure of the mixture. In a miscible mixture, no distinction is made between mixture volumes; therefore, the local structure has no effect on the response of the mixture. While in an immiscible mixture, constituent volumes can be locally distinguished. This would necessarily allow the volume fractions to affect the response of the mixture (Bowen, 1980). According to definition of saturation in the literature of multiphase mixtures, the volume fractions of the various constituents add up to unity if the mixture is physically saturated, but sum up to less than unity if it is physically unsaturated:

$$\sum_\alpha n_\alpha = 1 \qquad \text{; physically saturated mixture} \tag{3.7}$$

$$\sum_\alpha n_\alpha \leq 1 \qquad \text{; physically unsaturated mixture} \tag{3.8}$$

The general form of balance equations for each constituent is similar to the balance equations for a single phase continuum with the exception that there are some additional interaction terms. In a spatial description, the local balance relations for the mass and linear momentum of a single constituent are:

$$\mathscr{R}_\alpha := \frac{\partial}{\partial t}\left(\overline{\rho}_\alpha\right) + \nabla \cdot \left(\overline{\rho}_\alpha \mathbf{v}_\alpha\right) - c_\alpha = 0 \tag{3.9}$$

$$\mathscr{M}_\alpha := \frac{\partial}{\partial t}\left(\overline{\rho}_\alpha \mathbf{v}_\alpha\right) - \nabla \cdot \left(\overline{\rho}_\alpha \mathbf{v}_\alpha \otimes \mathbf{v}_\alpha + \boldsymbol{\sigma}_\alpha\right) - \overline{\rho}_\alpha \mathbf{b}_\alpha - \mathbf{m}_\alpha = 0 \tag{3.10}$$

where $\overline{\rho}_\alpha$ is the partial mass density of the constituent, $\mathbf{v}_\alpha$ the spatial velocity of constituent, $c_\alpha$ the constituent mass interaction supply, $\mathbf{b}_\alpha$ the constituent body force density, $\mathbf{m}_\alpha$ the constituent linear momentum interaction supply, and $\boldsymbol{\sigma}_\alpha$ the constituent Cauchy stress tensor.

An alternative form of balance equations can be obtained by adopting the material description in which particle and time are regarded as independent variables. Using constituent material derivative, blanace equations (3.9) and (3.10) read:

$$\mathscr{R}_\alpha := \frac{D}{D_t}\overline{\rho}_\alpha + \overline{\rho}_\alpha \nabla \cdot \mathbf{v}_\alpha - c_\alpha = 0 \tag{3.11}$$

$$\mathscr{M}_\alpha := \overline{\rho}_\alpha \frac{D}{D_t}\mathbf{v}_\alpha - \nabla \cdot \boldsymbol{\sigma}_\alpha - \overline{\rho}_\alpha \mathbf{b}_\alpha + c_\alpha \mathbf{v}_\alpha - \mathbf{m}_\alpha = 0 \tag{3.12}$$

From the axioms of balance for the mixture, it is required that the interaction supply terms represent only the exchange among constituents (Passman et al., 1984). Therefore they are constrained by the relations:

$$\sum_\alpha c_\alpha = 0 \tag{3.13}$$

$$\sum_\alpha \mathbf{m}_\alpha = 0 \tag{3.14}$$

Balance equations for the mixture are obtained from the local balance equations of the constituents. In the above balance equations, it is postulated that each constituent is subjected to two kinds of actions: the prescribed actions at a distance, represented by density of body force, $\mathbf{b}_\alpha$, and the contact actions, represented by stress tensor, $\boldsymbol{\sigma}_\alpha$. The inner parts of the resultant actions on the whole mixture are simply the sum of partial actions on constituents. However, the mixture itself is considered as a moving body; therefore, total contact actions on the mixture should account for the motion of constituents with respect to the mixture (see chap. 5 of Truesdell, 1984). The partial constituent and total mixture balance equations are related through the following relations:

$$\rho = \sum_\alpha \overline{\rho}_\alpha \tag{3.15}$$

$$\rho \mathbf{v} = \sum_\alpha \overline{\rho}_\alpha \mathbf{v}_\alpha \tag{3.16}$$

$$\boldsymbol{\sigma} - \rho \mathbf{v} \otimes \mathbf{v} = \sum_\alpha \left( \boldsymbol{\sigma}_\alpha - \overline{\rho}_\alpha \mathbf{v}_\alpha \otimes \mathbf{v}_\alpha \right) \tag{3.17}$$

$$\rho \mathbf{b} = \sum_\alpha \overline{\rho}_\alpha \mathbf{b}_\alpha \tag{3.18}$$

where $\rho$, $\boldsymbol{\sigma}$, $\mathbf{v}$, and $\mathbf{b}$ are respectively density, stress tensor, velocity, and body force density for the mixture.

It can be shown, from exploitation of entropy inequality, that the constituent stress tensor is divided into two parts (see Bowen, 1989; Truesdell and Noll, 1992, among others):

$$\boldsymbol{\sigma}_\alpha = -n_\alpha \varpi_\alpha \mathbf{I} + \overset{e}{\boldsymbol{\sigma}}_\alpha \tag{3.19}$$

where the first term in r.h.s represents the partial constituent thermodynamic equilibrium stress and $\overset{e}{\boldsymbol{\sigma}}_\alpha$ is the non-equilibrium part of stress or extra stress (normal stresses positive in tension). The first term is governed by constituent pressure and the second one results from the constituent motion. In a physically saturated mixture, $\varpi_\alpha$ is the constituent thermodynamic pressure. Svendsen and Hutter (1995) presented the general form of $\varpi_\alpha$ for both physically saturated and unsaturated mixtures as follows:

$$\varpi_\alpha = \begin{cases} \beta_\alpha & ; \text{physically unsaturated mixture} \\ \beta_\alpha + \varpi & ; \text{physically saturated mixture} \end{cases} \tag{3.20}$$

where $\beta_\alpha$ is the constituent configuration pressure and $\varpi$ is a static pressure acting on the mixture and common to all constituents.

Passman et al. (1984) interpreted the configuration pressure, in a saturated mixture of particles suspended in viscous fluid, as a pressure representing the forces acting at the interfaces between the particles and between the particles and fluid. Therefore, Equation (3.20) means that in such a mixture the particles experience both a hydrostatic pressure (that can be the fluid pressure) and the forces acting at their interfaces. The specific interpretation of $\beta_\alpha$ will be different for different mixtures and depends on the system of forces acting on the mixture.

The difference between physically saturated and unsaturated cases in Equation (3.20) arises from the constraint of volume fractions. In a physically unsaturated mixtures, constituent volume fractions are all independent variables satisfying Equation (3.8). While when the mixture is physically saturated, variable $\varpi$ replaces one of the volume fractions which is lost as an independent variable through the constraint of Equation (3.7).

The extra stress, $\overset{e}{\boldsymbol{\sigma}}_\alpha$, referred sometimes also to as dissipative part of stress (Bowen, 1989), is the dynamic contribution of stress and arises from the motion of constituent. In the mixture of solid and fluids, the solid extra stress is also referred as effective solid stress (De Boer and Didwania, 2002; Ehlers et al., 2003). Hutter et al. (1999) showed that for a saturated binary mixture of solid and perfect fluid (water in that case) under condition of pressure equilibrium (configuration pressures equal zero), the solid extra stress becomes the well known Terzaghi's effective stress. This point will be discussed later in this chapter.

Similar to stress, the constituent linear momentum interaction supply, $\mathbf{m}_\alpha$, consists of an equilibrium part, $\overset{\circ}{\mathbf{m}}_\alpha$, corresponding to the thermodynamic equilibrium condition and another part, named extra term, $\overset{e}{\mathbf{m}}_\alpha$, corresponds to departure from equilibrium condition:

$$\mathbf{m}_\alpha = \overset{\circ}{\mathbf{m}}_\alpha + \overset{e}{\mathbf{m}}_\alpha \tag{3.21}$$

The equilibrium part of linear momentum supply represents the body forces acting on constituent $\alpha$ due to all other constituents and arises from internal constraints (see Passman et al., 1984). It follows from Equation (3.14) that:

$$\sum_\alpha \overset{\circ}{\mathbf{m}}_\alpha = 0 \tag{3.22a}$$

$$\sum_\alpha \overset{e}{\mathbf{m}}_\alpha = 0 \tag{3.22b}$$

Svendsen and Hutter (1995) showed that in an isothermal mixture of $M$ compressible and $N - M$ incompressible constituents, where only evolution of constituent density and volume fraction is concerned, this term reads:

$$\overset{\circ}{\mathbf{m}}_\alpha = \sum_\beta^M \left( \overset{\alpha\beta}{m}_\rho \nabla \rho_\beta \right) + \sum_\beta^N \left( \overset{\alpha\beta}{m}_n \nabla n_\beta \right) \tag{3.23}$$

where

$$\overset{\alpha\beta}{m}_\rho = \left( \delta_{\alpha\beta} - \overline{\xi}_\alpha \right) \frac{p_\beta}{\rho_\beta} \tag{3.24a}$$

$$\overset{\alpha\beta}{m}_n = \left( \delta_{\alpha\beta} - \overline{\xi}_\alpha \right) \varpi_\beta \tag{3.24b}$$

and

$$\overline{\xi}_\alpha = \frac{\overline{\rho}_\alpha}{\rho} \tag{3.25}$$

whre $\overline{\xi}_\alpha$ is the mass fraction of the constituent. In these equations, $p_\beta$ is the constituent thermodynamic pressure, $\varpi_\beta$ is given by Equation (3.20) for physically saturated and unsaturated mixtures, and $\delta_{\alpha\beta}$ denotes a Kronecker delta-type function:

$$\delta_{\alpha\beta} = \begin{cases} 1 & ; \text{if } \alpha = \beta \\ 0 & ; \text{if } \alpha \neq \beta \end{cases} \tag{3.26}$$

It is noteworthy that the equilibrium supply terms given by Equation (3.23) satisfies relation Equation (3.22a) because of Equation (3.15).

The extra part of linear momentum supply, $\overset{e}{\mathbf{m}}_\alpha$, represents the non-equilibrium condition. In an isothermal mixture, the extra term accounts for the motion of constituents with respect to each other and it takes the form (Hutter et al., 1999):

$$\overset{e}{\mathbf{m}}_\alpha = \sum_{\beta \neq \alpha} \overset{\alpha\beta}{m}_D (\mathbf{v}_\beta - \mathbf{v}_\alpha) \tag{3.27}$$

where

$$\overset{\alpha\beta}{m}_D = \overset{\beta\alpha}{m}_D \tag{3.28}$$

is the drag coefficient between the two constituents $\alpha$ and $\beta$.

The formulation presented in this section provides the balance equations and thermodynamic requirements for a general multiphase mixture. These equations together with an appropriate set of constitutive relations allow deriving the general field equations for the phenomena under study.

## 3.2 Mixture model of soil with double porosity

### 3.2.1 Double mixture approach

Unsaturated soil is a multiphase porous medium. It is a ternary mixture of solid and fluids in which the pores are filled partly by gas and partly by liquid. In this study, as well as most of geomechanical problems, the solid phase consists of soil particles; and, the liquid and gas phases correspond to water and air constituents respectively. The mineralogical variations in soil are not considered. Moreover, mixture of different miscible species in the gas phase is represented by single air constituent. Likewise, any compositional variation in liquid phase such as dissolved air in water is ignored. It follows a one-to-one correspondence between the phases and the constituents in the mixture. Therefore, the terms phase and constituent are interchanged in the present study, e.g., solid constituent represents the equivalent constituent within the solid phase. In the notation, $\alpha = s, l$, and $g$ are used to refer to solid, liquid and gas constituent respectively.

In unsaturated soils with double porosity, the pores are divided into two main classes of macropores and micropores. Associated with these two classes, the fluid phases (gas and liquid) are each one divided into two levels. Particular distinctions should be made between the fluids in macropores and micropores. In aggregated soils where the liquid phase is water, aggregate boundaries enclose the micropore water and separate it from free water in macropores. Although there are some differences in the physical properties of fluids at two levels, the

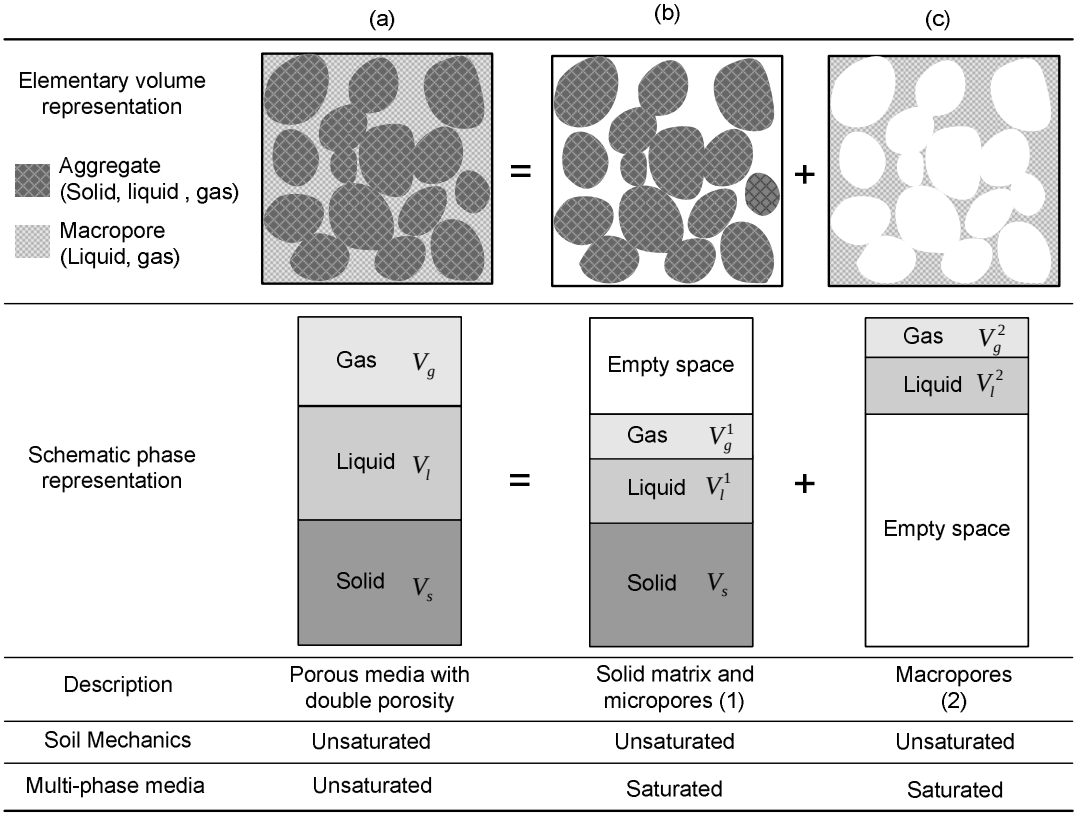


| Description | Porous media with double porosity | Solid matrix and micropores (1) | Macropores (2) |
|---|---|---|---|
| Soil Mechanics | Unsaturated | Unsaturated | Unsaturated |
| Multi-phase media | Unsaturated | Saturated | Saturated |

*Figure 3.1:* Schematic representation of the mixture of soil with double porosity

chemical composition remains more or less the same. Therefore, it is not entirely consistent with theory of multiphase mixture to consider them as different phases in a single mixture. It is therefore concluded that a model of single multiphase mixture fails to precisely describe such a material.

In order to avoid this conflict and to keep the consistency with thermodynamics of multiphase mixtures, an alternative approach is adopted here. The soil mixture of double porosity is divided into two distinct but overlapping mixtures with interactions between them (Fig. 3.1). Mixture 1 (Fig. 3.1(b)), represents the aggregates and pores within them and therefore it is a mixture of solid and fluids corresponding to the solid matrix and fluid in the micropores; while mixture 2, is a mixture of only fluid constituents representing the fluids in macropores (Fig. 3.1(c)).

It can therefore be stated that the physically saturated mixture of aggregates and fluids is considered to be the superimposed continuum of two physically unsaturated mixtures with empty spaces. Interaction between phases can be taken into account by means of different supply terms of thermodynamic variables.

These two mixtures are considered as the sequence of bodies denoted by $\mathscr{B}_\alpha^1$ with $\alpha$ =s, l, g and $\mathscr{B}_\alpha^2$ with $\alpha$ =l, g. As a general notation rule, later on we refer any related variable to these mixtures by superscript m=1 and 2 respectively; e.g., $\mathbf{v}_\mathrm{g}^1$ denotes the velocity of gas constituent of mixture 1 . Since solid constituent exists only in mixture 1, for any variable, a simplified notation

is introduced as follows:

$$(.)_{\mathrm{s}} = (.)^1_{\mathrm{s}} \tag{3.29}$$

The two mixtures are selected based on some postulates. These postulates are presented here.

**Postulate (i):** Two mixtures share the same reference configuration in which any material particle is labelled by its position ($\mathbf{X}_{\mathrm{s}}$ for solid and $\mathbf{X}^{\mathrm{m}}_{\alpha}$ for fluids).

Each body of $\mathscr{B}^1_\alpha$ and $\mathscr{B}^2_\alpha$ follows its own motion through an equation similar to Equation (3.1). From Equation (3.2) velocity of each constituent is defined as:

$$\mathbf{v}_{\mathrm{s}} = \frac{\partial \chi_{\mathrm{s}}\left(\mathbf{X}_{\mathrm{s}}, t\right)}{\partial t} \tag{3.30a}$$

$$\mathbf{v}^{\mathrm{m}}_{\alpha} = \frac{\partial \chi^{\mathrm{m}}_{\alpha}\left(\mathbf{X}^{\mathrm{m}}_{\alpha}, t\right)}{\partial t} \qquad \alpha = \mathrm{l},\ \mathrm{g} \quad \mathrm{m} = 1, 2 \tag{3.30b}$$

**Postulate (ii):** The mixtures have an equal total volume. This volume is denoted by $V$:

$$V^1 = V^2 = V \tag{3.31}$$

Therefore, volume fraction of constituents (Eq. 3.6) are given by:

$$n_{\mathrm{s}} = \frac{V_{\mathrm{s}}}{V} \tag{3.32a}$$

$$n^{\mathrm{m}}_{\alpha} = \frac{V^{\mathrm{m}}_{\alpha}}{V} \qquad ; \alpha = \mathrm{l},\ \mathrm{g} \quad \mathrm{m} = 1, 2 \tag{3.32b}$$

**Postulate (iii):** Mixtures are subjected to the constraint:

$$n_{\mathrm{s}} + \sum_{\mathrm{m}} \sum_{\alpha=\mathrm{l},\ \mathrm{g}} n^{\mathrm{m}}_{\alpha} = 1 \tag{3.33}$$

This means that the volume of empty pores in mixture 1 is equal to the sum of the volume of constituents in mixture 2.

**Postulate (iv):** There is no mass production of constituents (no phase change), but, mass transfer of constituents of the same type is possible between the mixtures. Therefore, Equation (3.13) is replaced by:

$$c_{\mathrm{s}} = 0 \tag{3.34a}$$

$$\sum_{m} c^{\mathrm{m}}_{\alpha} = 0 \qquad \alpha = \mathrm{l},\ \mathrm{g} \tag{3.34b}$$

**Postulate (v):** Each constituent in one of the mixtures might have a linear momentum supply due to all other constituents, either in the same mixture or in the other mixture. This means that the linear momentum interaction between mixtures is possible. The interaction still represents only the exchange among the constituents. Therefore, Equation (3.14) reads:

$$\mathbf{m}_{\mathrm{s}} + \sum_{\mathrm{m}} \sum_{\alpha=\mathrm{l},\ \mathrm{g}} \mathbf{m}^{\mathrm{m}}_{\alpha} = 0 \tag{3.35}$$

**Postulate (vi):** It is assumed that the solid constituent is incompressible; while fluid constituents (liquid and gas) are not. We recall the fact that the true density of constituent is an intrinsic property of the material that may change with state of the constituent. It means that the true density of fluids, $\rho_{\alpha}^{\mathrm{m}}$, and their variation should not be necessarily the same in two mixtures. Bulk density of each mixture, $\rho^{\mathrm{m}}$, is obtained through an equation similar to Equation (3.15). The total bulk density for the the total system of two mixtures is then defined as:

$$\rho = \rho^1 + \rho^2 \tag{3.36}$$

**Postulate (vii):** All constituents in the system of two mixtures are continuous.

**Postulate (viii):** Both mixtures are isothermal and there is thermal equilibrium between constituents and mixtures.

We introduce the global porosity corresponding to each mixture as

$$n^{\mathrm{m}} = \frac{V_{\mathrm{l}}^{\mathrm{m}} + V_{\mathrm{g}}^{\mathrm{m}}}{V} = n_{\mathrm{l}}^{\mathrm{m}} + n_{\mathrm{g}}^{\mathrm{m}} \qquad \mathrm{m} = 1, 2 \tag{3.37}$$

and the total porosity as:

$$n = n^1 + n^2 \tag{3.38}$$

It follows from Equation (3.33):

$$n_{\mathrm{s}} = 1 - n \tag{3.39}$$

In order to maintain the relation with traditional definition of degree of liquid saturation in soil mechanics, we introduce a local degree of liquid saturation which is defined with respect to the local volume of constituents in each mixture:

$$s_L^{\mathrm{m}} = \frac{V_{\mathrm{l}}^{\mathrm{m}}}{V_{\mathrm{l}}^{\mathrm{m}} + V_{\mathrm{g}}^{\mathrm{m}}} = \frac{n_{\mathrm{l}}^{\mathrm{m}}}{n^{\mathrm{m}}} \qquad \mathrm{m} = 1, 2 \tag{3.40}$$

It yields:

$$n_{\mathrm{g}}^{\mathrm{m}} = n^{\mathrm{m}} \left(1 - s_L^{\mathrm{m}}\right) \qquad \mathrm{m} = 1, 2 \tag{3.41}$$

On the other hand, the global degree of liquid saturation represents the volume of liquid with respect to the total volume of fluids in the whole system of two mixtures. The global degree of liquid saturation can be defined for each mixture; however, the interest is here mainly in the global degree of liquid saturation for the whole system of two mixture, which is termed as the total degree of saturation:

$$S_r = \frac{\sum_{\mathrm{m}} V_{\mathrm{l}}^{\mathrm{m}}}{\sum_{\mathrm{m}} \sum_{\alpha=\mathrm{l},\,\mathrm{g}} V_{\alpha}^{\mathrm{m}}} \tag{3.42}$$

The relationship between total and local degree of saturation is:

$$n S_r = n^1 s_L^1 + n^2 s_L^2 \tag{3.43}$$

It should be noted that the denominator in equations (3.40) and (3.42) represents the volume of fluids (liquid and gas) in the mixtures which is not equal to the volume of pores in a physically unsaturated mixture.

### 3.2.2 Mass balance

#### 3.2.2.1 Solid mass balance

With the assumption of solid incompressibility and use of Equations (3.34a) and (3.39), the mass balance Equation (3.9) reduces to the volume fraction balance equation in the following form:

$$-\frac{\partial n}{\partial t} + \nabla \cdot ((1-n)\,\mathbf{v}_{\mathrm{s}}) = 0 \tag{3.44}$$

#### 3.2.2.2 Fluid mass balance

The mass balance equations for liquid and gas constituents should be written for each mixture with the interaction supply terms provided in the equations. The supply terms represents the mass exchange of liquid constituents as well as gas constituents in two mixtures. From Equation (3.9), the liquid and gas balance in each mixture can be expressed as:

$$\frac{\partial}{\partial t}\left(n_{\mathrm{l}}^{\mathrm{m}}\rho_{\mathrm{l}}^{\mathrm{m}}\right) + \nabla \cdot \left(n_{\mathrm{l}}^{\mathrm{m}}\rho_{\mathrm{l}}^{\mathrm{m}}\mathbf{v}_{\mathrm{l}}^{\mathrm{m}}\right) - (-1)^{\mathrm{m}+1}\Gamma_{\mathrm{l}} = 0 \qquad \mathrm{m} = 1, 2 \tag{3.45}$$

$$\frac{\partial}{\partial t}\left(n_{\mathrm{g}}^{\mathrm{m}}\rho_{\mathrm{g}}^{\mathrm{m}}\right) + \nabla \cdot \left(n_{\mathrm{g}}^{\mathrm{m}}\rho_{\mathrm{g}}^{\mathrm{m}}\mathbf{v}_{\mathrm{g}}^{\mathrm{m}}\right) - (-1)^{\mathrm{m}+1}\Gamma_{\mathrm{g}} = 0 \qquad \mathrm{m} = 1, 2 \tag{3.46}$$

or in terms of degree of saturation:

$$\frac{\partial}{\partial t}\left(n^{\mathrm{m}}s_L^{\mathrm{m}}\rho_{\mathrm{l}}^{\mathrm{m}}\right) + \nabla \cdot \left(n^{\mathrm{m}}s_L^{\mathrm{m}}\rho_{\mathrm{l}}^{\mathrm{m}}\mathbf{v}_{\mathrm{l}}^{\mathrm{m}}\right) - (-1)^{\mathrm{m}+1}\Gamma_{\mathrm{l}} = 0 \qquad \mathrm{m} = 1, 2 \tag{3.47}$$

$$\frac{\partial}{\partial t}\left(n^{\mathrm{m}}(1-s_L^{\mathrm{m}})\rho_{\mathrm{g}}^{\mathrm{m}}\right) + \nabla \cdot \left(n^{\mathrm{m}}(1-s_L^{\mathrm{m}})\rho_{\mathrm{g}}^{\mathrm{m}}\mathbf{v}_{\mathrm{g}}^{\mathrm{m}}\right) - (-1)^{\mathrm{m}+1}\Gamma_{\mathrm{g}} = 0 \qquad \mathrm{m} = 1, 2 \tag{3.48}$$

In these equations $\Gamma_{\mathrm{l}}$ and $\Gamma_{\mathrm{g}}$ are the so-called fluid leakage terms that represent respectively the mass exchange of liquid and gas between two mixtures. It means:

$$c_{\alpha}^{\mathrm{m}} = (-1)^{\mathrm{m}+1}\Gamma_{\alpha} \qquad \alpha = \mathrm{l},\, \mathrm{g} \tag{3.49}$$

It can be seen that the supply terms given by the above relation satisfy the requirement of Equation (3.34b).

### 3.2.3 Linear momentum balance

The linear momentum balance equation for each mixture is obtained from the local balance equations of its constituents with some additional terms provided to take into account its interaction with the other mixtures.

The linear momentum supply for each constituent in one of the mixtures might have two sources. The first one is due to other constituents in the same mixture given by Equations (3.23), (3.24) and (3.27). The other part arises from the interaction with the constituents of the other mixture which is shown by a

supply term with an additional subscript $(i)$; e.g., $\overset{\circ}{\mathbf{m}}{}^{1}_{\mathrm{g}(i)}$ denotes the equilibrium part of linear momentum supply for gas constituent in mixture 1 that arises from constituents of mixture 2. Using Equations (3.23) and (3.24), the equilibrium parts of linear momentum supply for solid constituent in mixture 1 as well as liquid and gas constituents in both mixtures (m=1, 2) are expressed as:

$$\begin{aligned}\overset{\circ}{\mathbf{m}}_{\mathrm{s}} = \quad & -\overline{\xi}_{\mathrm{s}}\beta^{1}_{\mathrm{l}}\nabla n^{1}_{\mathrm{l}} && -\overline{\xi}_{\mathrm{s}}\beta^{1}_{\mathrm{g}}\nabla n^{1}_{\mathrm{g}} + \left(1-\overline{\xi}_{\mathrm{s}}\right)\beta_{\mathrm{s}}\nabla n_{\mathrm{s}} \\ & -\overline{\xi}_{\mathrm{s}}\frac{p^{1}_{\mathrm{l}}}{\rho^{1}_{\mathrm{l}}}\nabla\rho^{1}_{\mathrm{l}} && -\overline{\xi}_{\mathrm{s}}\frac{p^{1}_{\mathrm{g}}}{\rho^{1}_{\mathrm{g}}}\nabla\rho^{1}_{\mathrm{g}} + \overset{\circ}{\mathbf{m}}_{\mathrm{s}(i)} \end{aligned} \tag{3.50a}$$

$$\begin{aligned}\overset{\circ}{\mathbf{m}}{}^{m}_{\mathrm{l}} = \quad & \left(1-\overline{\xi}^{\mathrm{m}}_{\mathrm{l}}\right)\beta^{\mathrm{m}}_{\mathrm{l}}\nabla n^{\mathrm{m}}_{\mathrm{l}} && -\overline{\xi}^{\mathrm{m}}_{\mathrm{l}}\beta^{\mathrm{m}}_{\mathrm{g}}\nabla n^{\mathrm{m}}_{\mathrm{g}} - \left\langle(-1)^{\mathrm{m}+1}\right\rangle\overline{\xi}^{m}_{\mathrm{l}}\beta_{\mathrm{s}}\nabla n_{\mathrm{s}} \\ & + \left(1-\overline{\xi}^{\mathrm{m}}_{\mathrm{l}}\right)\frac{p^{\mathrm{m}}_{\mathrm{l}}}{\rho^{\mathrm{m}}_{\mathrm{l}}}\nabla\rho^{\mathrm{m}}_{\mathrm{l}} && -\overline{\xi}^{\mathrm{m}}_{\mathrm{l}}\frac{p^{\mathrm{m}}_{\mathrm{g}}}{\rho^{\mathrm{m}}_{\mathrm{g}}}\nabla\rho^{\mathrm{m}}_{\mathrm{g}} + \overset{\circ}{\mathbf{m}}{}^{\mathrm{m}}_{\mathrm{l}(i)} \qquad \mathrm{m}=1,2 \end{aligned} \tag{3.50b}$$

$$\begin{aligned}\overset{\circ}{\mathbf{m}}{}^{\mathrm{m}}_{\mathrm{g}} = \quad & -\overline{\xi}^{\mathrm{m}}_{\mathrm{g}}\beta^{\mathrm{m}}_{\mathrm{l}}\nabla n^{\mathrm{m}}_{\mathrm{l}} + \left(1-\overline{\xi}^{\mathrm{m}}_{\mathrm{g}}\right)\beta^{\mathrm{m}}_{\mathrm{g}}\nabla n^{\mathrm{m}}_{\mathrm{g}} - \left\langle(-1)^{\mathrm{m}+1}\right\rangle\overline{\xi}^{\mathrm{m}}_{\mathrm{g}}\beta_{\mathrm{s}}\nabla n_{\mathrm{s}} \\ & -\overline{\xi}^{\mathrm{m}}_{\mathrm{g}}\frac{p^{\mathrm{m}}_{\mathrm{l}}}{\rho^{\mathrm{m}}_{\mathrm{l}}}\nabla\rho^{\mathrm{m}}_{\mathrm{l}} + \left(1-\overline{\xi}^{\mathrm{m}}_{\mathrm{g}}\right)\frac{p^{\mathrm{m}}_{\mathrm{g}}}{\rho^{\mathrm{m}}_{\mathrm{g}}}\nabla\rho^{\mathrm{m}}_{\mathrm{g}} + \overset{\circ}{\mathbf{m}}{}^{\mathrm{m}}_{\mathrm{g}(i)} \qquad \mathrm{m}=1,2 \end{aligned} \tag{3.50c}$$

Likewise, the extra part of linear momentum supply reads:

$$\overset{e}{\mathbf{m}}_{\mathrm{s}} = \quad \overset{\mathrm{sl}}{m}{}^{1}_{D}\left(\mathbf{v}^{1}_{\mathrm{l}} - \mathbf{v}_{\mathrm{s}}\right) + \quad \overset{\mathrm{sg}}{m}{}^{1}_{D}\left(\mathbf{v}^{1}_{\mathrm{g}} - \mathbf{v}_{\mathrm{s}}\right) + \overset{e}{\mathbf{m}}_{\mathrm{s}(i)} \tag{3.51a}$$

$$\overset{e}{\mathbf{m}}{}^{\mathrm{m}}_{\mathrm{l}} = \left\langle(-1)^{\mathrm{m}+1}\right\rangle \overset{\mathrm{ls}}{m}{}^{\mathrm{m}}_{D}\left(\mathbf{v}_{\mathrm{s}} - \mathbf{v}^{\mathrm{m}}_{\mathrm{l}}\right) + \overset{\mathrm{lg}}{m}{}^{\mathrm{m}}_{D}\left(\mathbf{v}^{\mathrm{m}}_{\mathrm{g}} - \mathbf{v}^{\mathrm{m}}_{\mathrm{l}}\right) + \quad \overset{e}{\mathbf{m}}{}^{\mathrm{m}}_{\mathrm{l}(i)} \qquad \mathrm{m}=1,2 \tag{3.51b}$$

$$\overset{e}{\mathbf{m}}{}^{\mathrm{m}}_{\mathrm{g}} = \left\langle(-1)^{\mathrm{m}+1}\right\rangle \overset{\mathrm{gs}}{m}{}^{\mathrm{m}}_{D}\left(\mathbf{v}_{\mathrm{s}} - \mathbf{v}^{\mathrm{m}}_{\mathrm{g}}\right) + \overset{\mathrm{gl}}{m}{}^{\mathrm{m}}_{D}\left(\mathbf{v}^{\mathrm{m}}_{\mathrm{l}} - \mathbf{v}^{\mathrm{m}}_{\mathrm{g}}\right) + \quad \overset{e}{\mathbf{m}}{}^{\mathrm{m}}_{\mathrm{g}(i)} \qquad \mathrm{m}=1,2 \tag{3.51c}$$

In these equations $\langle\rangle$ is the McCauley brackets:

$$\langle a\rangle = \begin{cases} a & a > 0 \\ 0 & a \leq 0 \end{cases} \tag{3.52}$$

It is noteworthy that the above supply terms in one mixture do not sum up to zero because of the additional terms corresponding to interaction with the other mixture. However, the supply terms of two mixtures all together satisfy Equation (3.35). This means that linear momentum supply terms sum up to zero only if they are summed over both mixtures. It can be therefore concluded that:

$$\overset{\circ}{\mathbf{m}}_{\mathrm{s}(i)} + \sum_{\mathrm{m}}\sum_{\alpha=\mathrm{l},\,\mathrm{g}} \overset{\circ}{\mathbf{m}}{}^{\mathrm{m}}_{\alpha(i)} = 0 \tag{3.53a}$$

$$\overset{e}{\mathbf{m}}_{\mathrm{s}(i)} + \sum_{\mathrm{m}}\sum_{\alpha=\mathrm{l},\,\mathrm{g}} \overset{e}{\mathbf{m}}{}^{\mathrm{m}}_{\alpha(i)} = 0 \tag{3.53b}$$

It is assumed that the field evolutions are quasi-static and no acceleration is considered. Moreover, the only body force acting on the constituents is assumed to be through the gravity density, $\mathbf{g}$.

The acceleration free balance equation of linear momentum for constituents in each mixture is obtained from Equations (3.12), (3.19), (3.34a) and (3.49):

$$\nabla \cdot \overset{e}{\boldsymbol{\sigma}}_{\mathrm{s}} - \nabla\left(n_{\mathrm{s}}\beta_{\mathrm{s}}\right) + n_{\mathrm{s}}\rho_{\mathrm{s}}\mathbf{g} + \overset{e}{\mathbf{m}}_{\mathrm{s}} + \overset{\circ}{\mathbf{m}}_{\mathrm{s}} = 0 \tag{3.54}$$

$$\nabla \cdot \overset{e}{\boldsymbol{\sigma}}^{\mathrm{m}}_{\alpha} - \nabla\left(n_{\alpha}\beta^{\mathrm{m}}_{\alpha}\right) + n^{\mathrm{m}}_{\alpha}\rho^{\mathrm{m}}_{\alpha}\mathbf{g} - (-1)^{\mathrm{m}+1}\mathbf{v}^{\mathrm{m}}_{\alpha}\Gamma_{\alpha} + \overset{e}{\mathbf{m}}^{\mathrm{m}}_{\alpha} + \overset{\circ}{\mathbf{m}}^{\mathrm{m}}_{\alpha} = 0 \quad ;\alpha = \mathrm{l},\ \mathrm{g} \tag{3.55}$$

The supply terms in the above equations are given by set of Equations (3.24) and (3.51).

The balance of linear momentum for the mixture is now obtained by summing up the balance equations of its constituents. Adding Equations (3.54) and (3.55) for mixture 1 (m=1) and recalling the definition of bulk density for the mixture yields the linear momentum balance for mixture 1:

$$\begin{aligned}\nabla \cdot \left(\overset{e}{\boldsymbol{\sigma}}_{\mathrm{s}} + \overset{e}{\boldsymbol{\sigma}}^{1}_{\mathrm{l}} + \overset{e}{\boldsymbol{\sigma}}^{1}_{\mathrm{g}}\right) - \nabla\left(n_{\mathrm{s}}\beta_{\mathrm{s}} + n^{1}_{\mathrm{l}}\beta^{1}_{\mathrm{l}} + n^{1}_{\mathrm{g}}\beta^{1}_{\mathrm{g}}\right) + \rho^{1}\mathbf{g} = \\ \sum_{\alpha=\mathrm{l},\ \mathrm{g}}\left(\mathbf{v}^{1}_{\alpha}\Gamma_{\alpha}\right) - \left(\overset{e}{\mathbf{m}}_{\mathrm{s}i} - \overset{\circ}{\mathbf{m}}_{\mathrm{s}(i)}\right) - \sum_{\alpha=\mathrm{l},\ \mathrm{g}}\left(\overset{e}{\mathbf{m}}^{1}_{\alpha(i)} - \overset{\circ}{\mathbf{m}}^{1}_{\alpha(i)}\right)\end{aligned} \tag{3.56}$$

Similarly, the linear momentum balance for mixture 2 is obtained by adding Equation (3.55) for liquid and gas constituents in mixture 2 (m=2):

$$\begin{aligned}\nabla \cdot \left(\overset{e}{\boldsymbol{\sigma}}^{2}_{\mathrm{l}} + \overset{e}{\boldsymbol{\sigma}}^{2}_{\mathrm{g}}\right) - \nabla\left(n^{2}_{\mathrm{l}}\beta^{2}_{\mathrm{l}} + n^{2}_{\mathrm{g}}\beta^{2}_{\mathrm{g}}\right) + \rho^{2}\mathbf{g} = \\ -\sum_{\alpha=\mathrm{l},\ \mathrm{g}}\left(\mathbf{v}^{2}_{\alpha}\Gamma_{\alpha}\right) - \sum_{\alpha=\mathrm{l},\ \mathrm{g}}\left(\overset{e}{\mathbf{m}}^{2}_{\alpha(i)} - \overset{\circ}{\mathbf{m}}^{2}_{\alpha(i)}\right)\end{aligned} \tag{3.57}$$

Equation (3.56) and (3.57), each one represents the balance of linear momentum in a single mixture in which the r.h.s is non-zero due to interaction with the other mixture.

The total balance equation of linear momentum in the whole system of two mixtures is the sum of these two equations. Adding Equations (3.56) and (3.57), using Equation (3.36) for total density, and considering Equation (3.53), the total linear momentum balance equation takes the form:

$$\begin{aligned}\nabla \cdot \left(\overset{e}{\boldsymbol{\sigma}}_{\mathrm{s}} + \sum_{\mathrm{m}}\sum_{\alpha=1,2}\overset{e}{\boldsymbol{\sigma}}^{\mathrm{m}}_{\alpha}\right) - \nabla\left(n_{\mathrm{s}}\beta_{\mathrm{s}} + \sum_{\mathrm{m}}\sum_{\alpha=1,2}n^{\mathrm{m}}_{\alpha}\beta^{\mathrm{m}}_{\alpha}\right) + \rho\mathbf{g} = \\ \sum_{\alpha=\mathrm{l},\ \mathrm{g}}\left(\left(\mathbf{v}^{1}_{\alpha} - \mathbf{v}^{2}_{\alpha}\right)\Gamma_{\alpha}\right)\end{aligned} \tag{3.58}$$

The terms on the r.h.s of this equation account for the variation of linear momentum in the system related to mass exchange between the two mixtures.

## 3.3 Constitutive equations

The balance equations that are introduced so far are independent of material properties. To complete the description of material behavior, we now need to specify the constitutive equations for dependent variables.

Constitutive equations, in fact, establish the link between dependent variables and unknowns. According to Passman et al. (1984), dependent variables or the values of constitutive functions are divided into two classes: those describing only the constituent itself, so-called material specific variables, and the other ones named as growth variables that describe the interaction of exchange among constituents. These variables should be appropriately related, through the constitutive equations, to the independent variables.

Here, we postulate the principle of phase separation of Passman et al. (1984) that states that the dependent variables of any constituent that are material-specific depend only on the independent variables of that constituent; while, the growth dependent variables depend on all of the independent variables. This, as a guideline, allows opting for constitutive laws that involve the proper quantities as independent variables. An appropriate set of constitutive equations should be based on measurable quantities. Here, a set of mechanical and hydraulic constitutive equations as well as constitutive relations for interaction terms are presented in their general form. As an essential requirement, identification of stress tensors in constituents and the general stress fields in the mixtures are presented first.

### 3.3.1 Stress tensor

#### 3.3.1.1 Stress tensor in fluids

As given by Equation (3.19), stress in each constituent consists of an equilibrium and an extra part. In hydraulics and geomechanical problems, the extra part of fluid stress is usually ignored (Hutter et al., 1999; Diebels, 2000; Ehlers et al., 2003). Therefore, partial stress tensors of fluid constituents reads:

$$\boldsymbol{\sigma}_{\alpha}^{\mathrm{m}} = -n_{\alpha}^{\mathrm{m}} \beta_{\alpha}^{\mathrm{m}} \mathbf{I} \qquad ;\alpha = \mathrm{l},\, \mathrm{g} \quad \mathrm{m} = 1, 2 \tag{3.59}$$

Equation (3.59) identifies the configuration pressure in fluid as the intrinsic pressure. Therefore, by recalling definition of degree of saturation (Eq. 3.40), partial stress tensor in fluid constituents reads:

$$\boldsymbol{\sigma}_{\mathrm{l}}^{\mathrm{m}} = -n^{\mathrm{m}} s_{L}^{\mathrm{m}} p_{\mathrm{l}}^{\mathrm{m}} \mathbf{I} \qquad ;\mathrm{m} = 1, 2 \tag{3.60}$$

$$\boldsymbol{\sigma}_{\mathrm{g}}^{\mathrm{m}} = -n^{\mathrm{m}} (1 - s_{\mathrm{L}}^{\mathrm{m}}) p_{\mathrm{g}}^{\mathrm{m}} \mathbf{I} \qquad ;\mathrm{m} = 1, 2 \tag{3.61}$$

#### 3.3.1.2 Stress tensor in solid

According to Equation (3.19), stress in solid constituent is given by:

$$\boldsymbol{\sigma}_{\mathrm{s}} = -n_{\mathrm{s}} \beta_{\mathrm{s}} \mathbf{I} + \overset{e}{\boldsymbol{\sigma}}_{\mathrm{s}} \tag{3.62}$$

The configuration pressure of solid constituent $\beta_{\mathrm{s}}$ represents the forces exerted at the interface of solid particles with fluid. This force is exerted by the fluid constituents, namely liquid and gas in both mixtures and it should be therefore equal to a fluid pressure averaged over the two mixtures. Therefore, using Equation (3.39) for solid volume fraction, partial stress tensor in solid constituent reads:

$$\boldsymbol{\sigma}_{\mathrm{s}} = -(1-n)p_{\mathrm{f}}\mathbf{I} + \overset{e}{\boldsymbol{\sigma}}_{\mathrm{s}} \tag{3.63}$$

where $p_{\mathrm{f}}$ is the total fluid pressure.

It should be noted that the contribution of fluid constituents to this pressure is not necessarily the same. Not only liquid and gas may play different roles, but also contribution of the two mixtures to this pressure is by no means equal. In other words, a distinction should be made firstly between liquid and gas constituents, and secondly between fluids of mixture 1 and 2. With no loss in generality, the total fluid pressure can be expressed as:

$$p_{\mathrm{f}} = \phi^1 p_{\mathrm{f}}^1 + \phi^2 p_{\mathrm{f}}^2 \tag{3.64}$$

where $p_{\mathrm{f}}^{\mathrm{m}}$ represents the equivalent fluid pressure in mixtures $m$; and $\phi^1$ and $\phi^2$ are positive scaling parameters representing the contribution of each mixture to total fluid pressure, which satisfy the constraint:

$$\phi^1 + \phi^2 = 1 \tag{3.65}$$

Considering that the equivalent fluid pressure in each mixture arises from a scaled contribution of liquid and gas pressure in the same mixture, Equation (3.64) can be written as:

$$p_{\mathrm{f}} = \phi^1 \left[\chi^1 p_{\mathrm{l}}^1 + (1-\chi^1)p_{\mathrm{g}}^1\right] + \phi^2 \left[\chi^2 p_{\mathrm{l}}^2 + (1-\chi^2)p_{\mathrm{g}}^2\right] \tag{3.66}$$

where, each bracket on the r.h.s represents the equivalent fluid pressure in one mixture to which the contribution of liquid constituent is scaled by $\chi^{\mathrm{m}}$ varying between 0 and 1. It should be noted that $\chi^1$ and $\chi^2$ might be different in value.

Equation (3.66) is a generic form of fluid pressure in which parameters $\chi^{\mathrm{m}}$ and $\phi^{\mathrm{m}}$ (m=1,2) are to be determined mainly from theoretical analysis. Herein, as proposed by Ehlers et al. (2003), we write total fluid pressure in analogy to the Dalton's law of partial pressures:

$$p_{\mathrm{f}} = \frac{1}{n} \sum_{\mathrm{m}} \sum_{\alpha=\mathrm{l},\,\mathrm{g}} n_{\alpha}^{\mathrm{m}} p_{\alpha}^{\mathrm{m}} \tag{3.67}$$

From the comparison between Equation (3.66) and Equation (3.67) for the total fluid pressure, scaling parameters of Equation (3.66) are determined to be:

$$\chi^{\mathrm{m}} = s_L^{\mathrm{m}} \qquad ;\mathrm{m} = 1,2 \tag{3.68}$$

and

$$\phi^{\mathrm{m}} = \frac{n^{\mathrm{m}}}{n} \qquad ;\mathrm{m} = 1,2 \tag{3.69}$$

The stress tensor in solid constituent is hence given by Equation (3.63) in which Equation (3.66) and the above scaling parameters are introduced for fluid pressure.

#### 3.3.1.3 Total stress tensors

Finally, the total stress tensor is obtained by adding Equations (3.60), (3.61) and (3.62) for partial stress tensors in liquid, gas and solid constituents:

$$\boldsymbol{\sigma} = -\phi^1 \left[p_{\mathrm{g}}^1 - \chi^1 \left(p_{\mathrm{g}}^1 - p_{\mathrm{l}}^1\right)\right] \mathbf{I} - \phi^2 \left[p_{\mathrm{g}}^2 - \chi^2 \left(p_{\mathrm{g}}^2 - p_{\mathrm{l}}^2\right)\right] \mathbf{I} + \overset{e}{\boldsymbol{\sigma}}_{\mathrm{s}} \tag{3.70}$$

in which the scaling parameters are given by Equation (3.69) and (3.68).

The stress tensor can be expressed in a more convenient form using the definition of matric suction. In line with definition of matric suction in Chapter 2 (Eq. 2.2), the matric suction in each mixture is here introduced as being the difference between the pressure of liquid as wetting fluid and gas as non wetting fluid in that mixture:

$$s^{\mathrm{m}} = p_{\mathrm{l}}^{\mathrm{m}} - p_{\mathrm{g}}^{\mathrm{m}} \qquad ;\mathrm{m} = 1, 2 \tag{3.71}$$

Therefore, an alternative expression for total stress tensor is derived as:

$$\boldsymbol{\sigma} = \overset{e}{\boldsymbol{\sigma}}_{\mathrm{s}} - \left(\phi^1 p_{\mathrm{g}}^1 + \phi^2 p_{\mathrm{g}}^2\right) \mathbf{I} + \phi^1 \chi^1 s^1 \mathbf{I} + \phi^2 \chi^2 s^2 \mathbf{I} \tag{3.72}$$

where $s^1$ and $s^2$ represent the matric suction in micropores and macropores respectively.

#### 3.3.1.4 Total fluid pressure and total suction

Similar to fluid pressure and by use of Equations (3.40) and (3.42), the expression of total liquid and gas pressure reads:

$$nS_r p_{\mathrm{l}} = n^1 s_L^1 p_{\mathrm{l}}^1 + n^2 s_L^2 p_{\mathrm{l}}^2 \tag{3.73}$$

$$n(1 - S_r) p_{\mathrm{g}} = n^1 (1 - s_L^1) p_{\mathrm{g}}^1 + n^2 (1 - s_L^2) p_{\mathrm{g}}^2 \tag{3.74}$$

or

$$p_{\mathrm{l}} = \phi_{\mathrm{l}}^1 p_{\mathrm{l}}^1 + \phi_{\mathrm{l}}^2 p_{\mathrm{l}}^2 \tag{3.75}$$

$$p_{\mathrm{g}} = \phi_{\mathrm{g}}^1 p_{\mathrm{g}}^1 + \phi_{\mathrm{g}}^2 p_{\mathrm{g}}^2 \tag{3.76}$$

where $p_{\mathrm{l}}$ and $p_{\mathrm{g}}$ are total liquid and gas pressure respectively; and, $\phi_{\mathrm{l}}^{\mathrm{m}}$ and $\phi_{\mathrm{g}}^{\mathrm{m}}$ are scaling parameters for liquid and gas which by recalling Equation (3.43) are given as:

$$\phi_{\mathrm{l}}^{\mathrm{m}} = \frac{n^{\mathrm{m}} s_L^{\mathrm{m}}}{nS_r} = \phi^{\mathrm{m}} \frac{s_L^{\mathrm{m}}}{S_r} \qquad ;\mathrm{m} = 1, 2 \tag{3.77}$$

$$\phi_{\mathrm{g}}^{\mathrm{m}} = \frac{n^{\mathrm{m}} (1 - s_L^{\mathrm{m}})}{n(1 - S_r)} = \phi^{\mathrm{m}} \frac{(1 - s_L^{\mathrm{m}})}{(1 - S_r)} \qquad ;\mathrm{m} = 1, 2 \tag{3.78}$$

Indeed, $\phi_\alpha^{\mathrm{m}}$ represents the portion of the whole volume of constituent $\alpha$ that belongs to mixture $m$. It can be easily deduced from Equations (3.33) and (3.43) that these parameters satisfy the constraint:

$$\phi_\alpha^1 + \phi_\alpha^2 = 1 \qquad \alpha = \mathrm{l},\, \mathrm{g} \tag{3.79}$$

Following the definition of total liquid and gas pressure, the total suction can now be expressed as:

$$s = p_{\mathrm{g}} - p_{\mathrm{l}} \tag{3.80}$$

To obtain an expression for suction, it is mathematically convenient to start with the following equation:

$$s = \frac{1}{S_r}(p_{\mathrm{g}} - S_r p_{\mathrm{l}} - (1 - S_r)p_{\mathrm{g}})$$

in which, Equations (3.75) and (3.76) are introduced for liquid and gas pressure. Mathematical manipulations and use of Equation (3.71) yields an expression of total suction in terms of local degree of saturation, suction and gas pressures in two mixtures:

$$s = \left[\phi^1 \frac{s_L^1}{S_r} s^1 + \phi^2 \frac{s_L^2}{S_r} s^2\right] + \frac{1}{S_r}\left[\phi^1 \left(\frac{S_r - s_L^1}{1 - S_r}\right) p_{\mathrm{g}}^1 + \phi^2 \left(\frac{S_r - s_L^2}{1 - S_r}\right) p_{\mathrm{g}}^2\right] \tag{3.81}$$

or, in a more convenient from as:

$$s = \left[\phi_{\mathrm{l}}^1 s^1 + \phi_{\mathrm{l}}^2 s^2\right] + \frac{\phi^1 - \phi_{\mathrm{l}}^1}{1 - S_r}\left(p_{\mathrm{g}}^1 - p_{\mathrm{g}}^2\right) \tag{3.82}$$

Notice that when gas pressures in two mixtures are equal, i.e. same gas pressure in two system of pores, the second bracket on the r.h.s of Equation (3.82) becomes null.

#### 3.3.1.5 Effective stress

The extra part of solid stress tensor, $\overset{e}{\boldsymbol{\sigma}}_{\mathrm{s}}$, results from the motion of the soil skeleton and, indeed, it is identified as the effective stress, $\boldsymbol{\sigma}'$, in soil mechanics. Accordingly, the expression of effective stress for unsaturated soil with double porosity reads:

$$\boldsymbol{\sigma}' = \boldsymbol{\sigma} + \left(\phi^1 p_{\mathrm{g}}^1 + \phi^2 p_{\mathrm{g}}^2\right)\mathbf{I} - \phi^1 \chi^1 s^1 \mathbf{I} - \phi^2 \chi^2 s^2 \mathbf{I} \tag{3.83}$$

with $s^1$ and $s^2$ being the matric suction in micropores and macropores respectively.

Notice that in the absence of macro pores, we have $\phi^2 = 0$, $\phi^1 = 1$ which yields $\phi^1 \chi^1 = S_r$, $\phi_{\mathrm{l}}^1 \chi^1 = p_{\mathrm{l}}$ and $s = s^1$; therefore, Equation (3.83) is simplified to the generalized effective stress for unsaturated single porosity soils as given by Equation (2.9) (care to be taken to the reversal of sign convention):

$$\boldsymbol{\sigma}' = \boldsymbol{\sigma} + p_{\mathrm{g}}\mathbf{I} - S_r s \mathbf{I} \tag{3.84}$$

When both the macro- and micropores are filled only with liquid, i.e when the medium is liquid saturated, then $\chi^1 = \chi^2 = 1$ and the effective stress for saturated double porous soil is obtained as:

$$\boldsymbol{\sigma}' = \boldsymbol{\sigma} + \phi^1 p_{\mathrm{l}}^1 \mathbf{I} + \phi^2 p_{\mathrm{l}}^2 \mathbf{I} \tag{3.85}$$

Under the saturated condition, if volume of macropores reduces to zero, i.e. $\phi^2 = 0$, $\phi^1 = 1$, the wellknown expression of Terzaghi's stress is recovered:

$$\boldsymbol{\sigma}' = \boldsymbol{\sigma} + p_{\mathrm{l}}\mathbf{I} \tag{3.86}$$

Usually the macro pores are drained in the early steps of suction application ($\chi^2 = 0$). As it will be presented later, this is the case in the experiments carried out in the course of the present study. In such condition, with the assumption of equal gas pressure in two system of pores, Equation (3.83) again reduces to the equation of the generalized effective stress. Moreover, the second term in the expression of total suction (Eq. 3.82) which accounts for the gas pressure difference in macro- and micropores reduces to zero and, therefore, total suction becomes equal to the suction in the micropores. This is an issue of great importance in this work and in many other applications, where the experimental methods and equipments allow only the measurement or control of a single average value for liquid and gas pressure.

Equation (3.83) can be compared with the expression of effective stress in double porous media in Equation (2.13) derived by Khalili et al. (2005). The comparison shows that the thermodynamic approach presented here and the phenomenological approach used by Khalili et al. (2005) and described in Section 2.6.1 result in a similar expression of effective stress in unsaturated double porous media. Parameters of effective stress, however, are physically different in the two approaches. Comparison of these parameters suggests a possible correlation between the compressibility of a double porous medium with the actual porosity of the material at two levels, and the local degree of liquid saturation in two systems of pores.

### 3.3.2 Mechanical constitutive equation

A mechanical constitutive law relates the stress in soil skeleton to its deformation. It is therefore a constitutive law for stress-strain relation in solid constituent. As a result of the principle of phase separation of Passman et al. (1984), $\boldsymbol{\sigma}'$ depends only on quantities associated with solid constituent. With the assumption of infinitesimal strains, the general incremental form of an elasto-plastic mechanical constitutive equations can be expressed as:

$$\mathrm{d}\boldsymbol{\sigma}' = \boldsymbol{D}^{ep} : \mathrm{d}\boldsymbol{\varepsilon} \tag{3.87}$$

where $\boldsymbol{D}^{ep}$ is the elasto-plastic constitutive tensor of rank four, possibly, a non-linear function of stress level and internal variables, and $\boldsymbol{\varepsilon}$ is the solid strain tensor given by the symmetric part of the solid displacement gradient tensor:

$$\boldsymbol{\varepsilon} = \frac{1}{2}\left(\nabla\mathbf{u}_{\mathrm{s}} + \nabla\mathbf{u}_{\mathrm{s}}^{T}\right) \tag{3.88}$$

In soil mechanics, soil strain is equivalent to the strain of solid constituent; therefore, there is no need for allocating subscript $s$ to the strain tensor $\boldsymbol{\varepsilon}$.

It is noteworthy that the incremental form of the constitutive equation given in Equation (3.87) is indispensable in elasto-plasticity; while, it is not essential in linear elasticity.

Different mechanical constitutive laws can be incorporated into Equation (3.87) to describe the mechanical behaviour of the material. In Chapter 6, an elasto-plastic constitutive model for aggregated soil will be presented in detail.

### 3.3.3 Equation of state for fluid

Because of the compressibility of fluid constituents, an equation of state is needed for fluids. Fluids are here assumed to be barotropic. We recall that a barotropic fluid is one whose pressure and density are related by an equation of state that does not contain the temperature as a dependent variable. Therefore the equation of state for fluid constituents can be expressed as:

$$\rho_\alpha^{\mathrm{m}} = \rho_\alpha^{\mathrm{m}}(p_\alpha^{\mathrm{m}}) \qquad ;\alpha = \mathrm{l},\ \mathrm{g} \quad \mathrm{m} = 1,2 \tag{3.89}$$

with

$$K_\alpha^{\mathrm{m}} = \rho_\alpha^{\mathrm{m}} \frac{\mathrm{d}p_\alpha^{\mathrm{m}}}{\mathrm{d}\rho_\alpha^{\mathrm{m}}} = \rho_\alpha^{\mathrm{m}} \frac{\partial p_\alpha^{\mathrm{m}}}{\partial \rho_\alpha^{\mathrm{m}}} \qquad ;\alpha = \mathrm{l},\ \mathrm{g} \quad \mathrm{m} = 1,2 \tag{3.90}$$

where $K_\alpha^{\mathrm{m}}$ is the bulk modulus of fluid $\alpha$ in mixture $m$.

### 3.3.4 Fluid flow

The system of two mixtures provides two overlapping domains for fluid flow. These domains represent flow through the volume of fluids in mixture 1 and 2, namely inter-aggregate and intra-aggregate pores in an aggregated soil.

It is assumed that fluid flow can independently happen in both domains. This approach is similar to the approach of dual-permeability (see 2.1.5). As a simple approach, the generalized Darcy's law is assumed here to be valid both for liquid and gas flow in slow phenomena and it is assumed to govern the fluid flow in both domains. Therefore equation of fluid flow can be expressed as:

$$n_\alpha^{\mathrm{m}} \mathbf{w}_\alpha^{\mathrm{m}} = -\mathbf{K}_\alpha^{\mathrm{m}} . (\nabla p_\alpha^{\mathrm{m}} - \rho_\alpha^{\mathrm{m}} \mathbf{g}) \qquad ;\alpha = \mathrm{l},\ \mathrm{g} \quad \mathrm{m} = 1,2 \tag{3.91}$$

where $\mathbf{w}_\alpha^{\mathrm{m}}$ is the seepage velocity of constituent $\alpha$ in mixture $m$ defined as the relative velocity of fluid constituent with respect to the deforming solid skeleton:

$$\mathbf{w}_\alpha^{\mathrm{m}} = \mathbf{v}_\alpha^{\mathrm{m}} - \mathbf{v}_{\mathrm{s}} \qquad ;\alpha = \mathrm{l},\ \mathrm{g} \quad \mathrm{m} = 1,2 \tag{3.92}$$

and $\mathbf{K}_\alpha^{\mathrm{m}}$ is the permeability tensor of mixture $m$ for fluid constituent $\alpha$, expressed as:

$$\mathbf{K}_\alpha^{\mathrm{m}} = \mathbf{k}^{\mathrm{m}} \frac{k_{\alpha r}^{\mathrm{m}}}{\mu_\alpha^{\mathrm{m}}} \qquad ;\alpha = \mathrm{l},\ \mathrm{g} \quad \mathrm{m} = 1,2 \tag{3.93}$$

in which $\mathbf{k}^{\mathrm{m}}$ is the intrinsic permeability tensor of mixture $m$ that depends on pore structure, $\mu_\alpha^{\mathrm{m}}$ is the dynamic viscosity of constituent $\alpha$ in mixture $m$, and $k_{\alpha r}^{\mathrm{m}}$ is the relative permeability of mixture $m$ for fluid constituent $\alpha$.

Conceptually, the introduction of flow fields and Darcy's law in the above way might be considered as an approach of weak consistency in relation with thermodynamics of multiphase mixtures. Equation (3.92) defines the seepage

velocity of fluids in both mixtures with respect to the solid constituent in mixture 1. This means that flow fields do not coincide with mixtures and they are not symmetric with respect to constituents and mixtures. This might be considered as an inconsistency with the approach of multiphase mixture theory in which flow fields are usually defined with respect to the constituents of the same mixture.

However, from a physical point of view, this can be reasonably justified due to the fact that solid constituent in mixture 1 is responsible for the pore structure of both mixtures as well as for drag forces in fluid flows. In other words, as a result of the constraint of volume fractions of two mixtures (Eq. 3.33) on one hand, and the interaction forces between all fluid constituents and solid constituent on the other hand, the two flow domains should be both evaluated with respect to solid constituent in mixture 1. This yields writing the Darcy's law for each flow field in relation with solid constituent.

Hutter et al. (1999) showed that in a saturated binary mixture of solid and fluid, Darcy's law is a rigorous deduction from the linear momentum balance of fluid. However, Darcy's law is introduced here as a phenomenological equation that relates the seepage velocity to fluid pressure.

Postulating the validity of Darcy's equation in both systems of unsaturated pores is a simple approach which allows identifying the main field variable. The rigorous study of flow in such media, however, demands deepened study of flow field in two system of pores. This issue is beyond the scopes of this study and it had been addressed in the joint study of the current research project by Carminati (2006).

In the framework of the joint study, Carminati et al. (2007c) evaluated the problem of flow between the aggregates and showed that the hydraulic properties of aggregates depend on the aggregate fabric and the way the aggregates are assembled. In a packing of aggregates with different sizes, the water flow was found to be controlled by contacts between aggregates, bottle-necks that slow down the flow. It has been also shown that under unsaturated conditions when the macropores are drained, water is mostly stored in the aggregates and water flow depends on the properties of the aggregates as well as those of the contacts between aggregates. During drainage, the air-water interface recedes and as shown in Figure 3.2, the liquid contact area and subsequently the water transfer between aggregates decreases (Carminati et al., 2007b). It has been concluded that the contacts control the flow, in the way that they are highly conductive when wet, but act as bottle necks under drained conditions. Accordingly, further works were carried out (Carminati et al., 2007a) to investigate the water distribution in the contact region and its impact on the hydraulic conductivity of aggregate packings.

The results of the joint study carried out by Carminati (2006) provide improvements in the hydraulic constitutive equations and could be potentially integrated with the formulation presented herein.

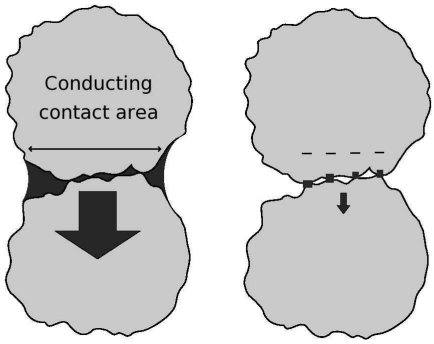


*Figure 3.2:* Contacts between aggregates at different saturation conditions, Carminati et al. (2007b), left: close to saturation the aggregates are connected by a wide capillary bridge and the water-filled contact area is large, right: the contact region is drained and the liquid contact area is reduced by air intruding larger pores in the contact region

### 3.3.5 Liquid retention

The relation between suction and degree of saturation is given by the retention curve. Although such a relation can be considered in each mixture relating its suction to its local degree of saturation, here we are more interested in establishing the link between total degree of saturation and total (matric) suction in the system. However in a compressible material, this relation in general cannot be independent of volume fraction of constituents. Therefore, a general form of this dependency reads:

$$S_r = S_r(s, n) \tag{3.94}$$

Since the total degree of saturation, $S_r$, is related to local degrees of saturation $s_L^{\mathrm{m}}$ through Equation (3.43), the relation of degree of saturation with total suction can be deduced from the relations of local degrees of saturation and total suction. Therefore, the liquid retention constitutive equation for such a system can be expressed as:

$$s_L^{\mathrm{m}} = s_L^{\mathrm{m}}(s, n^{\mathrm{m}}) \qquad ;\mathrm{m} = 1, 2 \tag{3.95}$$

In the framework of the joint project, an equation of this kind has been evaluated by for incompressible aggregates Carminati et al. (2007c). Introducing the suction-degree of saturation in the above form allows the possibility of better description of retention properties with respect to different saturation condition of pores. The explicit form of this equation in soils with double porosity will be evaluated in Chapter 6.

### 3.3.6 Fluid mass transfer between mixtures

The fluid mass transfer between two mixtures is controlled by the leakage term $\Gamma_\alpha$ ($\alpha = \mathrm{l}, \mathrm{g}$) introduced in Equations (3.47) and (3.48). A general form of the equation describing the leakage term can be expressed as:

$$\Gamma_\alpha = \gamma \left(\Psi_\alpha^1 - \Psi_\alpha^2\right) \qquad ;\alpha = \mathrm{l}, \mathrm{g} \tag{3.96}$$

where $\gamma$ is a generic mass exchange parameter, and $\Psi^1_\alpha$ and $\Psi^2_\alpha$ represent the thermodynamic deriving variables involved in the process of mass exchange between two mixtures.

The driving variable is to be defined depending on the characteristics of the problem and the involved thermodynamic variables. For example, in a general process involving chemical and thermal effects, the total chemical potential can be considered as driving variable. In the case of isothermal condition with no chemical interaction between constituents, it is widely accepted to consider the fluid pressure as deriving variable for mass exchange (Barrenblatt et al., 1960; Warren and Root, 1963; Wilson and Aifantis, 1982; Huyakorn et al., 1983; Elsworth and Bai, 1990; Musso et al., 1990; Sanchez, 2004). In this case, the leakage term is expressed as:

$$\Gamma_\alpha = \gamma \left(p^1_\alpha - p^2_\alpha\right) \qquad ;\alpha = \mathrm{l},\, \mathrm{g} \tag{3.97}$$

The mathematical quantification of fluid exchange term can be obtained through two different approaches: the quasi-steady and the unsteady state flow models (Huyakorn et al., 1983; Callari and Federico, 2000). They differ mainly in the way that the mass exchange parameter is treated. In order to maintain generality in the governing equations, the leakage term in formulation is kept in its generic form.

## 3.4 General field equations

Balance equations and constitutive equations should be now combined to obtain the governing equations. This is done by combining the mass balance equation of solid with each fluid constituents and introducing the related constitutive equations. Linear momentum balance equation together with the expressions for stress tensors and mechanical constitutive equation gives the governing equation of equilibrium.

For this purpose, the solid mass balance (Eq. 3.44) is written as:

$$-\frac{\partial n^1}{\partial t} - \frac{\partial n^2}{\partial t} - \nabla \cdot \left((1-n^2)\mathbf{v}_\mathrm{s}\right) - \nabla \cdot \left(n^1 \mathbf{v}_\mathrm{s}\right) = 0 \tag{3.98}$$

Using the vector identity equation for scalar $a$ and vector $\mathbf{b}$,

$$\nabla \cdot (a\mathbf{b}) = a\nabla \cdot \mathbf{b} + \mathbf{b}.\nabla a$$

the mass balance equation for liquid constituent in mixture $m$ (Eq. 3.47) reads:

$$\begin{aligned}&\left(s^\mathrm{m}_L \rho^\mathrm{m}_\mathrm{l}\right) \frac{\partial n^\mathrm{m}}{\partial t} + \left(n^\mathrm{m} \rho^\mathrm{m}_\mathrm{l}\right) \frac{\partial s^\mathrm{m}_L}{\partial t} + \left(n^\mathrm{m} s^\mathrm{m}_L\right) \frac{\partial \rho^\mathrm{m}_\mathrm{l}}{\partial t} \\ &+ \left(s^\mathrm{m}_L \rho^\mathrm{m}_\mathrm{l}\right) \nabla \cdot \left(n^\mathrm{m} \mathbf{v}^\mathrm{m}_\mathrm{l}\right) + \left(n^\mathrm{m} \mathbf{v}^\mathrm{m}_\mathrm{l}\right) \nabla \left(s^\mathrm{m}_L \rho^\mathrm{m}_\mathrm{l}\right) = (-1)^{\mathrm{m}+1} \Gamma_\mathrm{l} \qquad \mathrm{m} = 1, 2\end{aligned} \tag{3.99}$$

Replacing $(\partial n^\mathrm{m}/\partial t)$ in this equation by its equal terms from (3.98), and neglecting the spatial variation of porosity and density ($\nabla \rho^\mathrm{m}_\mathrm{l} = 0$ and $\nabla n^\mathrm{m} = 0$)

yields:

$$s_L^{\mathrm{m}}(1-n^{\mathrm{m}'})\nabla\cdot\mathbf{v}_{\mathrm{s}} - s_L^{\mathrm{m}}\frac{\partial n^{\mathrm{m}'}}{\partial t} + n^{\mathrm{m}}\frac{\partial s_L^{\mathrm{m}}}{\partial t} + n^{\mathrm{m}}s_L^{\mathrm{m}}\frac{1}{\rho_{\mathrm{l}}^{\mathrm{m}}}\frac{\partial \rho_{\mathrm{l}}^{\mathrm{m}}}{\partial t} + \nabla\cdot(n^{\mathrm{m}}s_L^{\mathrm{m}}\mathbf{w}_{\mathrm{l}}^{\mathrm{m}}) + n^{\mathrm{m}}\mathbf{v}_{\mathrm{s}}.\nabla s_L^{\mathrm{m}} = (-1)^{\mathrm{m}+1}\frac{\Gamma_{\mathrm{l}}}{\rho_{\mathrm{l}}^{\mathrm{m}}} \qquad \mathrm{m}=1,2 \tag{3.100}$$

where $\mathbf{w}_{\mathrm{l}}^{\mathrm{m}}$ is the seepage velocity defined by (3.92), and, $m'$ is the superscript denoting the complement mixture to mixture $m$:

$$\mathrm{m}' = \mathrm{m} - (-1)^{\mathrm{m}} \qquad \mathrm{m}=1,2 \tag{3.101}$$

In order to have a better consistency in system of equations, we avoid introducing $n^{\mathrm{m}}$ and $s_L^{\mathrm{m}}$ as primary variables, and instead we write their partial derivatives in terms of variables for which we have the constitutive equation. Using Equation (3.43) for degree of saturation and Equation (3.82) for suction, we can write:

$$\frac{\partial s_L^{\mathrm{m}}}{\partial t} = \frac{\partial s_L^{\mathrm{m}}}{\partial s}\frac{\partial s}{\partial s^{\mathrm{m}}}\frac{\partial s^{\mathrm{m}}}{\partial t} = \frac{\partial s_L^{\mathrm{m}}}{\partial s}\left(\frac{n^{\mathrm{m}}s_L^{\mathrm{m}}}{nS_r}\right)\frac{\partial s^{\mathrm{m}}}{\partial t} \qquad \mathrm{m}=1,2 \tag{3.102}$$

and

$$\frac{\partial n^{\mathrm{m}'}}{\partial t} = \frac{\partial n^{\mathrm{m}'}}{\partial s_L^{\mathrm{m}}}\frac{\partial s_L^{\mathrm{m}}}{\partial s^{\mathrm{m}}}\frac{\partial s^{\mathrm{m}}}{\partial t} = \left(-\frac{n^{\mathrm{m}}}{s_L^{\mathrm{m}'}}\right)\frac{\partial s_L^{\mathrm{m}}}{\partial s}\frac{\partial s^{\mathrm{m}}}{\partial t} \qquad \mathrm{m}=1,2 \tag{3.103}$$

Finally, introducing constitutive equations, i.e. Darcy's equation (Eq. 3.91), equation of state for fluid (Eq. 3.90) and the above two equations into Equation (3.100), a set of two field equations are obtained as:

$$s_L^{\mathrm{m}}(1-n^{\mathrm{m}'})\nabla\cdot\mathbf{v}_{\mathrm{s}} + n^{\mathrm{m}}\left[\left(\frac{n^{\mathrm{m}}s_L^{\mathrm{m}}}{nS_r} + \frac{s_L^{\mathrm{m}}}{s_L^{\mathrm{m}'}}\right)\frac{\partial s_L^{\mathrm{m}}}{\partial s}\frac{\partial s^{\mathrm{m}}}{\partial t} + \mathbf{v}_{\mathrm{s}}.\nabla s_L^{\mathrm{m}}\right] + n^{\mathrm{m}}s_L^{\mathrm{m}}\frac{1}{K_{\mathrm{l}}^{\mathrm{m}}}\frac{\partial p_{\mathrm{l}}^{\mathrm{m}}}{\partial t} + \nabla\cdot[-\mathbf{K}_{\mathrm{l}}^{\mathrm{m}}.(\nabla p_{\mathrm{l}}^{\mathrm{m}} + \rho_{\mathrm{l}}^{\mathrm{m}}\mathbf{g})] = (-1)^{\mathrm{m}+1}\frac{\Gamma_{\mathrm{l}}}{\rho_{\mathrm{l}}^{\mathrm{m}}} \qquad \mathrm{m}=1,2 \tag{3.104}$$

Following a similar procedure for gas constituents, the combined equation of mass balance for solid and gas constituents reads:

$$(1-s_L^{\mathrm{m}})(1-n^{\mathrm{m}'})\nabla\cdot\mathbf{v}_{\mathrm{s}} - (1-s_L^{\mathrm{m}})\frac{\partial n^{\mathrm{m}'}}{\partial t} + n^{\mathrm{m}}\frac{\partial(1-s_L^{\mathrm{m}})}{\partial t} + n^{\mathrm{m}}(1-s_L^{\mathrm{m}})\frac{1}{\rho_{\mathrm{g}}^{\mathrm{m}}}\frac{\partial \rho_{\mathrm{g}}^{\mathrm{m}}}{\partial t} + \nabla\cdot(n^{\mathrm{m}}(1-s_L^{\mathrm{m}})\mathbf{w}_{\mathrm{ls}}^{\mathrm{m}}) + n^{\mathrm{m}}\mathbf{v}_{\mathrm{s}}.\nabla(1-s_L^{\mathrm{m}}) = (-1)^{\mathrm{m}+1}\frac{\Gamma_{\mathrm{g}}}{\rho_{\mathrm{g}}^{\mathrm{m}}} \qquad \mathrm{m}=1,2 \tag{3.105}$$

Introducing the constitutive equations in Equation (3.105), in the same way as for Equation (3.104), another set of two field equations are obtained:

$$(1-s_L^{\mathrm{m}})(1-n^{\mathrm{m}'})\nabla\cdot\mathbf{v}_{\mathrm{s}} - n^{\mathrm{m}}\left[\left(\frac{n^{\mathrm{m}}s_L^{\mathrm{m}}}{nS_r} - \frac{(1-s_L^{\mathrm{m}})}{s_L^{\mathrm{m}'}}\right)\frac{\partial s_L^{\mathrm{m}}}{\partial s}\frac{\partial s^{\mathrm{m}}}{\partial t} + \mathbf{v}_{\mathrm{s}}.\nabla s_L^{\mathrm{m}}\right] + n^{\mathrm{m}}(1-s_L^{\mathrm{m}})\frac{1}{K_{\mathrm{g}}^{\mathrm{m}}}\frac{\partial p_{\mathrm{g}}^{\mathrm{m}}}{\partial t} + \nabla\cdot\left[-\mathbf{K}_{\mathrm{g}}^{\mathrm{m}}.\left(\nabla p_{\mathrm{g}}^{\mathrm{m}} + \rho_{\mathrm{g}}^{\mathrm{m}}\mathbf{g}\right)\right] = (-1)^{\mathrm{m}+1}\frac{\Gamma_{\mathrm{g}}}{\rho_{\mathrm{g}}^{\mathrm{m}}} \qquad \mathrm{m}=1,2 \tag{3.106}$$

The last field equation corresponds to the equilibrium restriction which is obtained from balance of linear momentum (Eq. 3.58). Using Equations (3.59) to (3.69) for stress tensors in constituents and Equation (3.92) for seepage velocity, Equation (3.58) reads:

$$\nabla\cdot\boldsymbol{\sigma}' - \nabla\left[\frac{1}{n}\left(n^1 p_{\mathrm{g}}^1 + n^2 p_{\mathrm{g}}^1\right)\right] - \nabla\left[\frac{1}{n}\left(n^1 s_L^1(p_{\mathrm{g}}^1 - p_{\mathrm{l}}^1) + n^2 s_L^2(p_{\mathrm{g}}^2 - p_{\mathrm{g}}^2)\right)\right] + \rho\mathbf{g} = \sum_{\alpha=\mathrm{l},\,\mathrm{g}}\left(\left(\mathbf{w}_\alpha^1 - \mathbf{w}_\alpha^2\right)\Gamma_\alpha\right) \tag{3.107}$$

where $\rho$ is the total density of two mixtures obtained from Equations (3.15) and (3.36):

$$\rho = (1-n)\rho_{\mathrm{s}} + \sum_{\mathrm{m}}(s_L^{\mathrm{m}}\rho_{\mathrm{l}}^{\mathrm{m}}) + \sum_{\mathrm{m}}((1-s_L^{\mathrm{m}})\rho_{\mathrm{l}}^{\mathrm{m}}) \tag{3.108}$$

## 3.5 Summary of field equations

Using Equation (3.71) for matric suction of each mixture and Darcy's law (3.91) for seepage velocity the field equations for the system of two mixtures may be summarized as follows:

$$s_L^{\mathrm{m}}(1-n^{\mathrm{m}'})\nabla\cdot\mathbf{v}_{\mathrm{s}} + n^{\mathrm{m}}\left[\left(\frac{n^{\mathrm{m}}s_L^{\mathrm{m}}}{nS_r} + \frac{s_L^{\mathrm{m}}}{s_L^{\mathrm{m}'}}\right)\left(\frac{\partial s_L^{\mathrm{m}}}{\partial s}\frac{\partial p_{\mathrm{g}}^{\mathrm{m}}}{\partial t} - \frac{\partial s_L^{\mathrm{m}}}{\partial s}\frac{\partial p_{\mathrm{l}}^{\mathrm{m}}}{\partial t}\right) + \mathbf{v}_{\mathrm{s}}.\nabla s_L^{\mathrm{m}}\right] + n^{\mathrm{m}}s_L^{\mathrm{m}}\frac{1}{K_{\mathrm{l}}^{\mathrm{m}}}\frac{\partial p_{\mathrm{l}}^{\mathrm{m}}}{\partial t} + \nabla\cdot\left[-\mathbf{K}_{\mathrm{l}}^{\mathrm{m}}.\left(\nabla p_{\mathrm{l}}^{\mathrm{m}} + \rho_{\mathrm{l}}^{\mathrm{m}}\mathbf{g}\right)\right] = (-1)^{\mathrm{m}+1}\frac{\Gamma_{\mathrm{l}}}{\rho_{\mathrm{l}}^{\mathrm{m}}} \qquad \mathrm{m}=1,2 \tag{3.109a}$$

$$(1-s_L^{\mathrm{m}})(1-n^{\mathrm{m}'})\nabla\cdot\mathbf{v}_{\mathrm{s}} - n^{\mathrm{m}}\left[\left(\frac{n^{\mathrm{m}}s_L^{\mathrm{m}}}{nS_r} - \frac{(1-s_L^{\mathrm{m}})}{s_L^{\mathrm{m}'}}\right)\left(\frac{\partial s_L^{\mathrm{m}}}{\partial s}\frac{\partial p_{\mathrm{g}}^{\mathrm{m}}}{\partial t} - \frac{\partial s_L^{\mathrm{m}}}{\partial s}\frac{\partial p_{\mathrm{l}}^{\mathrm{m}}}{\partial t}\right) + \mathbf{v}_{\mathrm{s}}.\nabla s_L^{\mathrm{m}}\right] + n^{\mathrm{m}}(1-s_L^{\mathrm{m}})\frac{1}{K_{\mathrm{g}}^{\mathrm{m}}}\frac{\partial p_{\mathrm{g}}^{\mathrm{m}}}{\partial t} + \nabla\cdot\left[-\mathbf{K}_{\mathrm{g}}^{\mathrm{m}}.\left(\nabla p_{\mathrm{g}}^{\mathrm{m}} + \rho_{\mathrm{g}}^{\mathrm{m}}\mathbf{g}\right)\right] = (-1)^{\mathrm{m}+1}\frac{\Gamma_{\mathrm{g}}}{\rho_{\mathrm{g}}^{\mathrm{m}}} \qquad \mathrm{m}=1,2 \tag{3.109b}$$

$$\nabla \cdot \boldsymbol{\sigma}' - \nabla \left[ \frac{1}{n} \left( n^1 p_{\mathrm{g}}^1 + n^2 p_{\mathrm{g}}^1 \right) \right] - \nabla \left[ \frac{1}{n} \left( n^1 s_L^1 (p_{\mathrm{g}}^1 - p_{\mathrm{l}}^1) + n^2 s_L^2 (p_{\mathrm{g}}^2 - p_{\mathrm{g}}^2) \right) \right] + \rho \mathbf{g}$$
$$= \sum_{\mathrm{m}} \left[ \frac{(-1)^{\mathrm{m}+1}}{n^{\mathrm{m}} s_L^{\mathrm{m}}} \left[ -\mathbf{K}_{\mathrm{l}}^{\mathrm{m}} . \left( \nabla p_{\mathrm{l}}^{\mathrm{m}} - \rho_{\mathrm{l}}^{\mathrm{m}} \mathbf{g} \right) \right] \right] \Gamma_{\mathrm{l}}$$
$$+ \sum_{\mathrm{m}} \left[ \frac{(-1)^{\mathrm{m}+1}}{n^{\mathrm{m}} (1 - s_L^{\mathrm{m}})} \left[ -\mathbf{K}_{\mathrm{g}}^{\mathrm{m}} . \left( \nabla p_{\mathrm{g}}^{\mathrm{m}} - \rho_{\mathrm{g}}^{\mathrm{m}} \mathbf{g} \right) \right] \right] \Gamma_{\mathrm{g}} \tag{3.109c}$$

The above equations present the coupled hydro-mechanical formulation of a three phase model for unsaturated porous media with double porosity, and indeed, define the general theoretical framework of this study. Equations (3.109a), (3.109b) and (3.109c) represent a set of five equations for five main unknowns: solid velocity $\mathbf{v}_{\mathrm{s}}$ and four fluid pressures $p_\alpha^{\mathrm{m}}$ ($\alpha$ =l, g and m=1,2). It should be noted that the effective stress ($\boldsymbol{\sigma}'$) or the solid extra stress is linked to displacement through the mechanical constitutive equation; and also, displacement is related to solid velocity by derivation in time.

The field equations derived here together with the explicit form of appropriate hydro-mechanical constitutive equations could be solved for the boundary value problems using numerical methods like finite element or discrete element method.

In this study, however, solution of the boundary value problems are not treated. Instead, the emphasis is placed on proposing the appropriate constitutive equations for double porous soil based on multi-scale experimental evidences.

In the above set of field equations, the mechanical constitutive equation (Eq. 3.87) and liquid retention law (Eq. 3.94) are presented in their general form. The remaining chapters of this dissertation are aimed to evaluate these relations in terms of the identified field variables (effective stress and fluid pressures or suction).

In Chapter 4, the stress-strain relationship ($\boldsymbol{\sigma}' - \boldsymbol{\varepsilon}$) and the water retention behavior ($S_r - s - n$) are experimentally evaluated for a simplified case of drained macropores. Then in Chapter 5, the relation between the macroscopic behavior and the soil structure properties at the pore scale, e.g. the relation between macroscopic strain and evolution of macro- and microporosity, are evaluated using pore scale experimental methods. The multi-scale experimental evidences are compared; and finally in Chapter 6, the explicit form of the mechanical constitutive relation and the liquid retention law, coupled through the expression of the effective stress, are proposed for unsaturated soils with double porosity.

# Chapter 4

# Experimental characterization of macroscopic behavior

This chapter is devoted to the experimental characterization of the mechanical behavior of the aggregated soil. The idea is to figure out the combined effects of suction and soil structure on the material behavior by means of macroscopic experimental testing methods. The outline of this chapter is as follows. First, the objectives and experimental methods are presented. This includes an evaluation of the existing suction control methods and the choice of the method used in the present study. Then development and calibration of the new suction-controlled oedometer used during this study is described. The chapter is then followed by the description of the testing material and the experimental program. Finally, the experimental results of different tests, their interpretation and their comparison are presented. Summary of experimental evidences are presented at the end in order to outline the special features which should be later considered for modeling purposes.

## 4.1 Objectives and methods

### 4.1.1 Objectives and experimental approaches

The experimental program of this study is aimed (i) to characterize the compression and swelling behavior of aggregated soil at different states of water saturation, and (ii) to compare this behavior with the behavior of the corresponding reconstituted soil in order to figure out the special features stemming from soil structure.

The approach used for this purpose is based on oedometer test, also referred to as confined compression or consolidation test, which allows characterizing the soil stress-strain behavior during one-dimensional compression or swelling. The oedometer tests were carried out on dry, saturated and partially saturated soils. Dry and saturated soil samples could be tested in conventional oedometer apparatus for saturated soils. The experimental procedure for saturated oedometer tests has been standardized in BS 1377 (1990). The use of the oedometer tests to study the consolidation process and the stress-strain behavior of soils is de-

scribed in many textbooks of soil mechanics (e.g. Atkinson and Bransby, 1978); so, it will not be repeated here. Testing under unsaturated condition requires, in addition to conventional measures of oedometer testing, a suction-controlled condition during the test. Hence, an oedometer apparatus with an appropriate suction control method was needed to complete the experimental program of this study.

Despite the availability of unsaturated testing equipments at LMS, these equipments had to be modified with respect to the experimental program and testing material of the present work, or new equipment had to be developed. In order to make an appropriate choice of testing method and equipment, the existing methods of suction control in oedometer cells have been reviewed, the description and comparison of which are presented in the following section.

### 4.1.2 Existing suction control methods

There are three techniques to apply and to control suction in the unsaturated oedometer apparatus: (i) axis translation technique, (ii) relative humidity or vapour equilibrium technique, and (iii) osmotic technique. These techniques have been previously used in various experimental researches on unsaturated soils. The principle and the main characteristics of these methods are briefly described below.

#### 4.1.2.1 Axis translation technique

In the axis translation technique, as presented by Hilf (1956), suction is applied by providing an air pressure over a positive water pressure. This technique is mainly developed in order to prevent the cavitation at sufficiently low negative water pressures. To overcome the problem of cavitation, the water pressure is maintained constant at a positive value and air pressure is increased to reach the desired matric suction (the difference between air and water pressure). Therefore, this technique simply translates the origin of reference for the pore water pressure from atmospheric pressure to a higher value equal to the air pressure applied to the sample.

In suction-controlled oedometers using the axis translation technique, a high air entry value (HAEV) ceramic disc is usually placed beneath the sample which allows the passage of water but prevents the passage of free air below a given pressure. Figure 4.1 schematically shows the suction-controlled oedometer apparatus using axis translation technique developed at LMS (Cuisinier and Laloui, 2004). In this apparatus, an air pressure/volume controller regulates the air pressure inside the sample. The water pressure at the base of the sample was maintained constant with a water pressure/volume controller. The ceramic disc at the base of the sample had an air entry value of 500 $kPa$. The vertical mechanical stress was transmitted to the soil sample through the upper chamber of the device, which corresponds to a water tank made with a flexible membrane and pressurized with a pressure/volume controller.

The HAEV ceramic disc used in this method resists only the passage of free water but it does not impede the air diffusion. Therefore, air can diffuse through

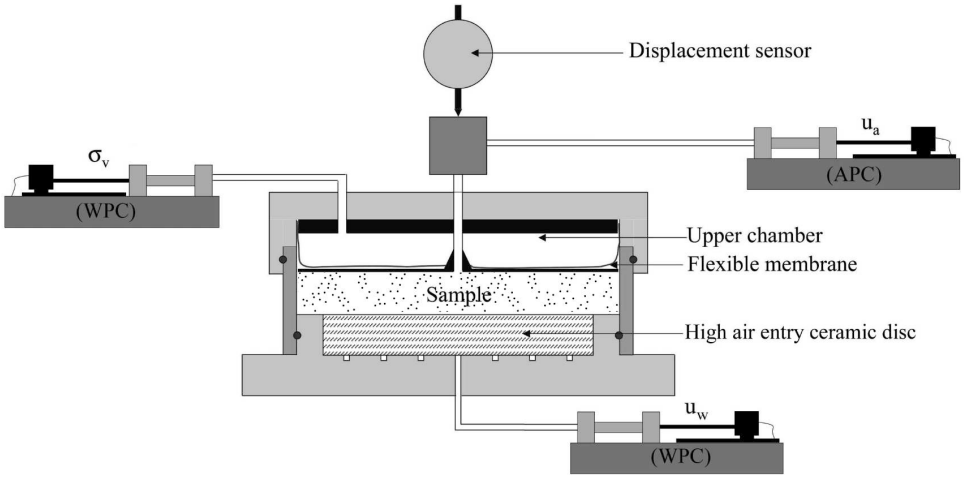


*Figure 4.1:* Suction-controlled oedometer with axis translation technique, APC: air pressure controller, WPC: water pressure controller (Cuisinier and Laloui, 2004)

the ceramic disk and accumulate beneath the disk in the water compartment. The accumulated diffused air causes errors in the measurement of pore water and exchanged water volume. The volume of air diffusing through a HAEV disk over a period of several days can, in some cases, exceed the total volume of water in the soil specimen (Fredlund and Rahardjo, 1993). Hence, it is necessary to measure the volume of diffused air independently and take it into account in order to correct the volume of exchanged water.

Independent measurement of diffused air through the HAEV disk can be done using the diffused air volume indicator (DAVI). It consists of a system allowing a momentarily flushing of the accumulated diffused air beneath the ceramic disc into a graded burette filled with water. The volume of diffused air is measured according to the changes in the elevation of water in the burette. Detailed description of DAVI is given by Fredlund (1975).

The suction range in this technique is controlled by the air pressure supply system and the air entry value of the ceramic disk and is usually between 0.01 $MPa$ up to 1.5 $MPa$. The air pressure supply system should be able to provide high enough air overpressure but not passing the air entry value of the porous ceramic disk. In special cases, nitrogen is used to apply gas overpressure (Villar, 1999) to reach higher values of suction up to 12 $MPa$. In such case, however, the cell should be able to sustain high pressures and its deformation should be taken into account.

Although this methods is an efficient suction control method in oedometer testing of unsaturated soils, it suffers from some limitations. One of the debating issues about this method, but not necessarily a disadvantage, is that whether the condition of high air pressure could really represent the real soil state where the air pressure is often the atmospheric pressure. The main limitation of this technique is linked to its application at high degrees of saturation. At high degrees of saturation, i.e. 0.85 to 0.90 for clays (Romero, 1999), the air phase is discontinuous and the pores contain occluded bubbles of air. In such a condition,

the air pressure of bubble might be different from the applied air pressure; and, axis translation technique may result in over-estimation of the actual suction (Bocking and Fredlund, 1980). Another drawback of this method is related to the required high gas pressure in the system which implies having an air pressure supply system capable of providing high air pressures. Furthermore, special care about the cell, its strength and its deformation is required at high gas pressures. The cell should be able to sustain high internal pressures without undergoing large deformations.

Finally, this method has a disadvantage related to the fact that the HAEV ceramic disc might become desaturated when exposed to air or to large empty pores of soils. Desaturation of the disc results in discontinuity between the water inside and outside the sample; therefore, the water pressure in the sample might differ from the applied water pressure. Moreover, it decreases the efficiency of the disc in impeding the air passage. Therefore, special care is required to saturate the disc prior to each test and to ensure its saturation during the test.

#### 4.1.2.2 Vapor equilibrium method

Vapor equilibrium method was first used in geotechnical testing for unsaturated soils by Esteban (1990). This method is based on the relationship between the relative humidity and suction through Kelvin's equation:

$$s = -\gamma_w \frac{RT}{Mg} \ln(RH) \tag{4.1}$$

where $RH$ is the relative humidity, $s$ suction ($MPa$), $R$ the constant of perfect gases (8.31 $Jmol^{-1}K^{-1}$), $T$ the absolute temperature, $M$ the molecular mass of water ($18.016 \times 10^{-3}$ $gmol^{-1}$), $\gamma_w$ the unit weight of water and $g$ is the gravity acceleration.

The basic principle of this technique is to maintain the relative humidity on soil pores constant in order to control suction. Relative humidity of the air inside a closed chamber, in which the sample is placed, is maintained constant through contact with saline solutions. Under isothermal equilibrium conditions, water vapor in the chamber comes into equilibrium with the saline solution. Therefore at equilibrium condition, the amount of water vapor, and hence, the relative humidity of the chamber is constant.

The relative humidity of the air inside the chamber is measured using a psychrometer. This allows determining the suction at the time of equilibrium. In this method, the gas phase acts as a membrane permeable to water but not to dissolved salts (Romero et al., 2001). In such condition, the immigration of soil salts is impeded and therefore in the total suction is controlled.

The relative humidity at equilibrium depends on the concentration and molality of the solution. Different values of relative humidity might be maintained using volatile solutions (acid solution like sulphuric acid) of a given density (Villar and Martin, 1996), different saturated non-volatile salt solutions (Cuisinier and Masrouri, 2004; Delage et al., 1998; Tang and Cui, 2005), or one unsaturated non-volatile salt solution with different concentrations or one salt solution with different concentrations (Romero et al., 2001).

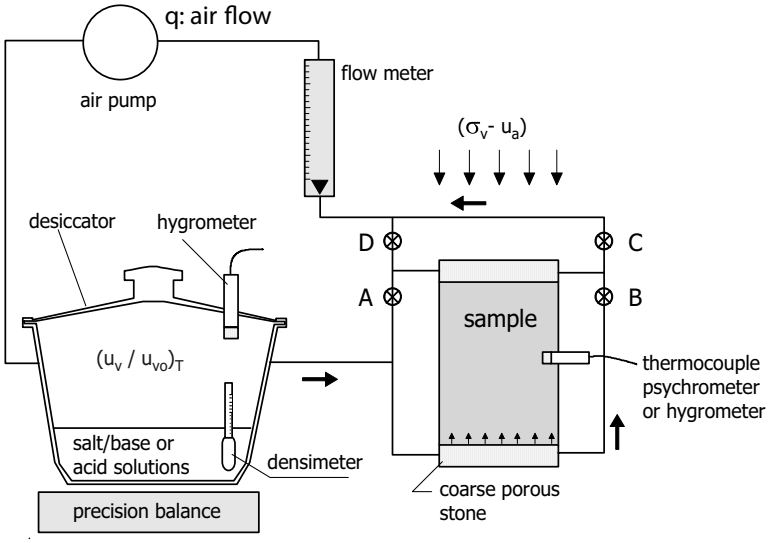


*Figure 4.2:* Suction-controlled oedometer with vapor equilibrium method (Romero, 1999)

In the case of acid solution, the relation between the acid solution activity and the weight percentage of acid, measured through the density of solution, is used to control the imposed relative humidity.

Tang and Cui (2005) reported that using a saturated salt solution, compared with unsaturated solution, allows to impose a constant suction during the test. On the other hand, unsaturated solution has the advantage of giving a continuous range of suction that cannot be obtained by using saturated solutions.

Water exchange in these oedometers are measured by measuring the changes in the mass of the salt solution. Since the humidity exchange happens through vapor transfer, the time required for equilibrium is usually very long. With the purpose of reducing the equilibrium time, some authors (Romero et al., 2001; Bernier et al., 1997) proposed to circulate the air (forced convection) in a closed circulating system passing through the sample and over the solution.

In the oedometer proposed by Romero et al. (2001), as shown in Figure 4.2, the circulation of the vapor could happen either through the sample (valves A and B closed) or from the boundaries of the sample (valve A and B open). They reported that the first procedure is less time consuming but is limited to the sates of soil where the air phase is continuous. Marcial et al. (2002) reported that by using a circulation pump, it is possible to reduce the equilibrium time for each suction step from 3-6 months to 2-4 weeks. According to Bernier et al. (1997), the equilibrium time could be reduced even to one week.

The suction range that could be applied in this method is evaluated by Delage et al. (1998). These authors expressed the relationship between uncertainties of relative humidity and the corresponding suction by differentiating the Kelvin's equation, and showed that the uncertainty of this methods could be acceptable only for suction values higher than 8 $MPa$. In addition to this

uncertainty, Romero et al. (2001) also expressed the difficulty of controlling the humidity at low values of relative humidity. They suggested 3 $MPa$ as a lower limit in using vapour equilibrium technique. The upper limit of the imposed suction depends on the minimum relative humidity that could be achieved and it is about 400 $MPa$.

The last point about the vapor equilibrium technique is related to the temperature dependency of this method. The imposed $RH$, and therefore imposed suction, is a function of temperature difference between the salt solution and the air above the solution and small temperature variation introduces major changes in imposed suction (Cuisinier and Masrouri, 2004). Furthermore, the relative vapour pressure of a saline solution itself is a function of temperature. It means that the sensitivity of relative humidity is dependent both on the absolute temperature and the physical properties of the chemical components (Delage et al., 1998). Therefore, it is essential to maintain a constant temperature in the system during the imposition of suction.

#### 4.1.2.3 Osmotic method

Suction control using the osmotic method is based on the osmosis principle. Osmosis is the net movement of a solvent across a semi-permeable membrane from a region of high solvent potential to an area of low solvent potential due to a concentration gradient. It is a physical process in which a solvent moves, without input of energy, across a semi-permeable membrane (permeable to the solvent, but not to the solute) separating two solutions of different concentrations. A semi-permeable membrane, also termed as selectively permeable membrane, is a membrane which allows certain molecules or ions to pass through it by diffusion. For instance, it allows small molecules like oxygen and water to pass through and not large solute.

A simple explication of this phenomenon is that different concentrations of solute molecules leads to different concentrations of free water molecules on either sides of the membrane. On the side of the membrane with higher free water concentration, i.e. a lower concentration of solute, more water molecules will strike the membrane in a given interval of time. More strikes equates to more molecules passing through the pores, which in turn, results in net diffusion of water from the compartment with high concentration of free water to that with low concentration of free water. Accordingly, water flows in response to difference in concentration across a membrane. Equilibrium is reached once sufficient water is exchanged to equalize the solute concentration on both sides of the membrane, and at that point, net flow of water ceases. Diffusion of water across a membrane - osmosis - generates a pressure called osmotic pressure at that side of the membrane with more solute concentration (Fig. 4.3). Therefore, if the pressure of the salt solution is maintained constant at atmospheric pressure, as in the osmotic oedometer cell, the liquid pressure on the other side of the membrane falls down to negative values.

If such a system could be established at a soil/salt interface, the total suction would be controlled. However, the molecular weights of common soil salts are

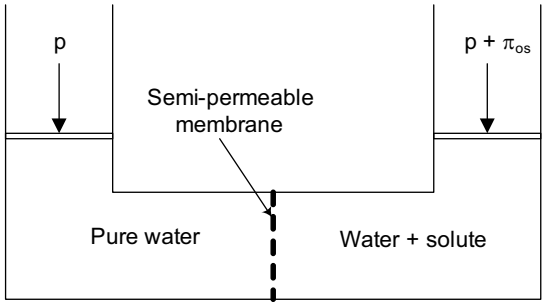


*Figure 4.3:* Schematic representation of osmosis

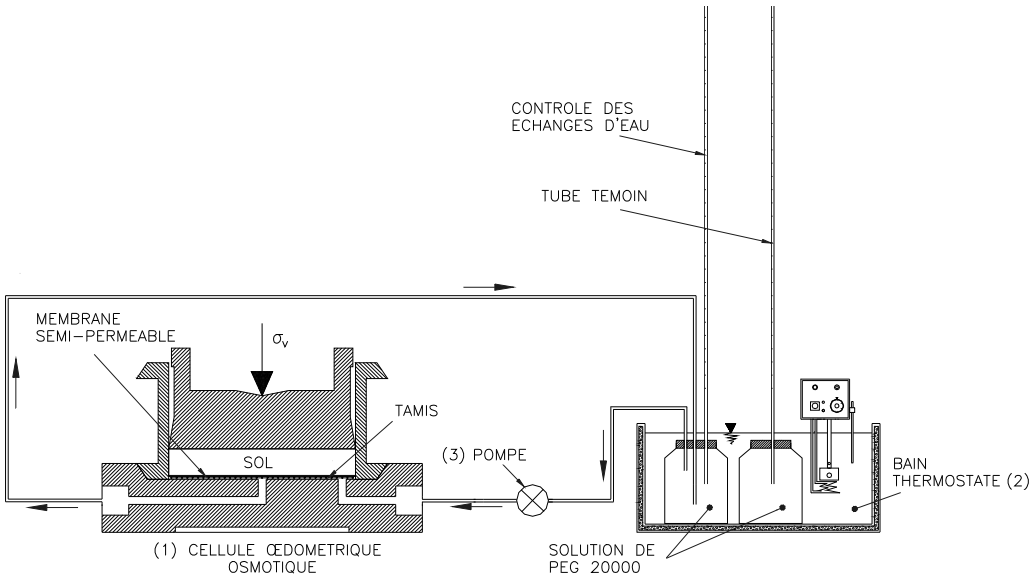


*Figure 4.4:* Suction-controlled oedometer with osmotic method (Delage et al., 1992)

small and providing a semi-permeable membrane acting as a barrier to such molecules is a complex proposition. An alternative to this approach is to use soluble salts with a large molecular weight. In this case, movement of soil salts is not impeded and only the matric suction is controlled by osmotic pressure (Dineen and Burland, 1995).

Historically, Zur (1966) should be cited as the first one who introduced this method in soil science. Later, Kassif and BenShalom (1971) used this method for oedometer tests in geotechnical engineering.

In an osmotic oedometer cell (Fig. 4.4), the soil sample and the salt solution are usually separated by a cellulotic dialysis semi-permeable membrane. These membranes are classified in terms of molecular weight cut off (MWCO), which is the minimum molecular weight that can be retained by the membrane. Solution of aqueous polyethylene glycol ethylene (PEG, $(C_2H_4)_n$) with different molecular weights (6 to 20 KiloDaltons) are often used as salt solution. Matching of a PEG of 20 $kD$ molecular weight to a membrane of MWCO 14 $kD$ or a PEG of 6 $kD$ molecular weight to a membrane of MWCO 4 $kD$ are the most common approaches (Dineen and Burland, 1995; Delage et al., 1998).

Drainage (or wetting) of the sample occurs by means of water exchange between the sample and the solution. This is usually done from bottom of the sample and through a special base which allows well circulation of the salt solution and provides a good contact of the solution with the membrane. However, in some cases, the drainage and contact with the semi-permeable membrane is allowed both at top and bottom of the sample (Delage et al., 1992; Slatter and Allman, 2000).

In the first oedometer of this type, Kassif and BenShalom (1971) connected the cell to a burette containing the fresh solution that they changed daily in order to ensure constant concentration during the test. However, in further developments, the solution is circulated in a closed circulation system containing flexible tubes, a pump, the base (or top cap or both) and a reservoir containing the PEG solution (Fig. 4.4). The reservoir ensures a constant concentration of salt in spite of water exchange happening through the membrane. Usually a peristaltic pump with controllable flow rates is used for this purpose. These pumps operate with continuous tubing which reduces the evaporative losses (Delage et al., 1992; Dineen and Burland, 1995).

The exchanged water is determined by recording the changes in either the volume or the mass of salt solution in the reservoir. In the case of volume measurements, it is necessary to maintain the temperature constant. This could be done by placing the reservoir in a high precision thermo stated water bath (Delage et al., 1992; Cuisinier and Masrouri, 2004).

The imposed suction in this method is determined according to the relationship between the osmotic pressure and the concentration of the salt solution. However in the oedometer developed by Dineen and Burland (1995), an Imperial College tensiometer was placed on the upper face of the sample to measure the matric suction within the soil sample. This allows a continuous measurement of suction. The common range of suction covered by this method is between 0 to 8 $MPa$.

Compared with the two other methods of suction control, the osmotic method is advantageous owning to its simplicity. In this method, there is no need for particular safety measures usually required in axis translation technique for high cell pressure. The required laboratory equipments are less expensive and test can be done easier. In addition, a reasonable range of suction starting from saturated condition could be imposed. The continuity of gas phase is not required; therefore, no limitation is placed concerning the degree of saturation of the sample.

The main drawback of the osmotic method is related to the fragility of the membrane which might cause some problems when it is used in combination with mechanical loading in long time testing. Delage et al. (2001) questioned the efficiency of this method during a wetting path. They reported that sometimes the combination of the PEG and the membrane might yield the molecules of PEG to pass through the membrane in the wetting path, introducing errors in the measurements.

### 4.1.3 Choice of methods and equipments

On the basis of above descriptions, the general features of the three methods in comparison with each other are summarized in Table 4.1.

From the onset, the vapor equilibrium method could be excluded mainly because of its limitation in application of low suctions. The main advantage of this method is its capability of providing high suction values which is not relevant in the present work.

The alternative choice is the suction-controlled oedometer using the axis translation technique. An oedometer apparatus using this method had been previously developed and it was available at LMS (Fig. 4.1). Preliminary tests of the experimental program were carried out using this apparatus. As it will be seen later, these tests gave discrepant results, specially for the exchanged water measurements. This was mainly due to the exposure of the HAEV ceramic disc to the air in the large macropores of the aggregated sample. On the one hand, this could result in higher amount of air diffusion through the disc, and on the other hand, it might increase the probability of desaturation of the ceramic disc. Both of these factors could cause significant errors in the exchanged water and/or suction measurements. The cell was not equipped with the DAVI system and the water exchange volume could not be corrected for the diffused air effects. Moreover, the imposed suction was limited to the AEV of the ceramic disc equal to 500 $kPa$ (possible increase to 1.5 $MPa$). Therefore, development or at least major modification of the testing equipment was required.

The above limitations of vapor equilibrium and axis translation method are overcome in the osmotic method. Moreover, a reasonable range of suction starting from zero could be achieved in this method. This method is believed to be the most appropriate choice with respect to the material and the experimental program of this study. Accordingly, a new suction controlled oedometric apparatus using the osmotic method was especially designed and developed in the present study. The new oedometer cell is presented in the next section.

*Table 4.1:* Suction control methods for oedometer test

| **Method** | **Imposed suction** | **Suction range** | **Features** |
|---|---|---|---|
| Axis Translation | Matric | 0 - 1.5 $MPa$ | $\oplus$ direct mechanical control of matric suction, $\ominus$ narrow suction range, $\ominus$ air diffusion through the disc, $\ominus$ high air pressure, $\ominus$ discontinuity of gas phase, $\ominus$ desaturation of the ceramic disc |
| Vapour Equilibrium | Total | 8 - 400 $MPa$ | $\oplus$ high suction application, $\ominus$ long testing time, $\ominus$ high sensitivity to temperature changes, $\ominus$ need for safety measures for acids |
| Osmotic | Matric | 0 - 8 $MPa$ | $\oplus$ reasonable suction range starting from zero, $\oplus$ no need for special safety measures, $\ominus$ fragility of the membrane, $\ominus$ uncertain efficiency of membrane in wetting |

## 4.2 Development of a new osmotic oedometer

### 4.2.1 Osmotic oedometer components

This section and the following subsections contain the description of the development and the calibration of the osmotic oedometer used during the experimental program of this study. The development of the osmotic oedometer had taken a long time and it involved different subsequent improvements. The main principles of the osmotic method were presented in Section 4.1.2.3. Here, the focus is placed on providing the description of different components as well as the improvements made in the equipment and the testing method.

The general layout of the new osmotic apparatus system is depicted in Figure 4.5 and the specification of different components are listed in Table 4.2. The experimental setup is shown in Figure 4.6. The oedometer system consists of a special oedometer cell placed in a loading frame, a peristaltic pump which operates with continuous flexible tubing, a reservoir for PEG solution, and a balance to monitor the water exchange. Deformation of the sample and the balance values are continuously recorded using data loggers and computers.

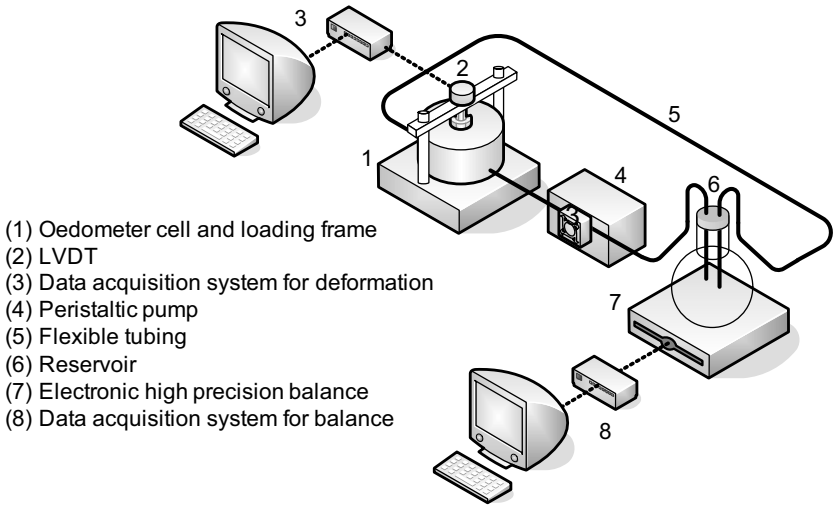


*Figure 4.5:* General layout of the osmotic apparatus system

*Table 4.2:* Components of the osmotic oedometeter system and their specifications

| No. | Description | Specification |
|---|---|---|
| 1 | Semi-permeable membrane | Spectra/Por 3, Dialysis Discs, 3.5 K MWCO, 100 mm Diameter |
| 2 | Pump | Prestaltic pump, MasterFlex L/S Compact, Low-Flow 35-200 RPM |
| 3 | Tubing | MasterFlex Silicon tubing L/S with Peroxyde, Int. Dia. 3.1 mm |
| 4 | Solution reservoir | PEG 6000 |
| 5 | Electronic balance | Mettler Toledo, 0.01 gr |
| 6 | Data Acquisition System | LabView 7.1 |

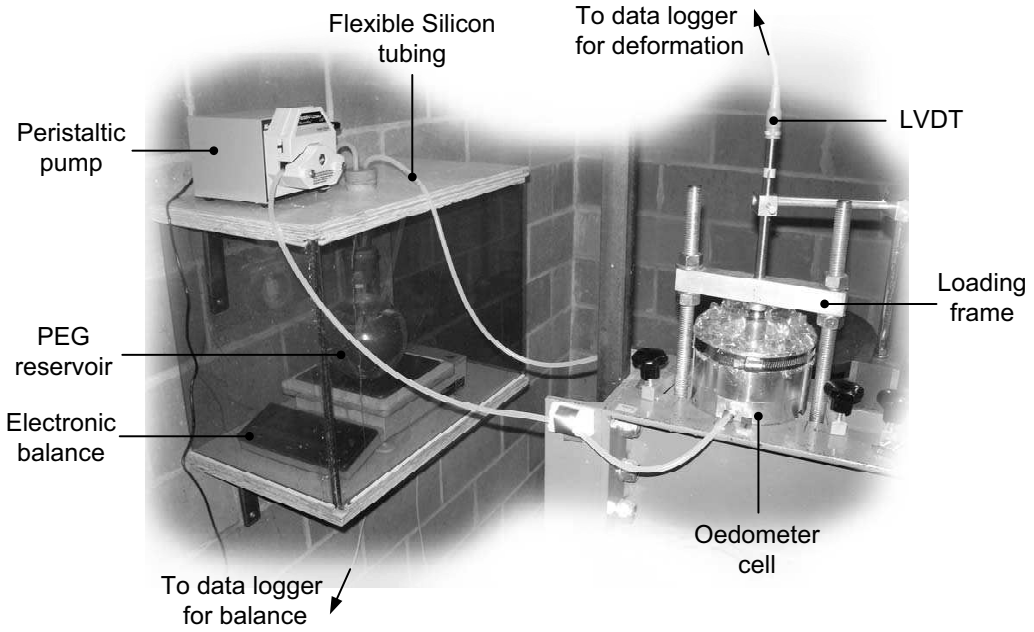


*Figure 4.6:* Experimental setup of the osmotic oedometer

#### 4.2.1.1 Oedometer cell and mechanical loading

The oedometer cell is designed to accommodate a sample of 80 $mm$ in diameter with a maximum height of 35 $mm$. A sample size larger than in conventional oedometers is selected in order to provide a representative volume of aggregated soil samples. Since the oedometer cell was also used to carry out some tomography experiments in the neutron beamline (to be presented in the next chapter), the cell was built in aluminum, a material which is almost transparent to neutron beams (while steel is not).

The oedometer wall is selected to be thick enough in order to prevent large lateral deformation and to satisfy the $K0$ condition. A simple estimation of the lateral strain of the ring is given by (see Fig. 4.7):

$$\frac{\Delta r}{r} = \frac{P}{Et} \tag{4.2}$$

where $P$ is the internal pressure, $r$ and $t$ the radius and the wall thickness of the cell, and $E$ is the Young modulus of the material ($70 \times 10^6\ kPa$ for aluminium). For a thickness of $t = 25\ mm$ and pressure of $P = 1.5\ MPa$ (approximately corresponding to a maximum vertical stress of 3 $MPa$), the lateral strain is 0.085%.

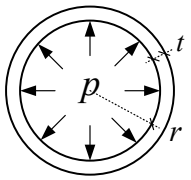


*Figure 4.7:* Radial deformation of the oedometric ring

The layout of the cell is illustrated in Figures 4.8 and 4.9. The special base of the oedometer is provided with inlet and outlets for liquid. The base is carefully machined and a fine mesh is placed on the top of the base in order to allow a uniform diffusion of the solution at the bottom of the sample. The semi-permeable membrane sits directly on this mesh and it is clamped by the oedometer ring which will be screwed to the oedometer base.

After having the oedometer ring mounted, soil sample can be prepared directly in the cell. A guiding ring mounts on the oedometer ring and ensures the vertical motion of the piston without inclination. Three small pins are provided between the guiding and the oedometer ring to ensure the right placement of these pieces; this being important for smooth motion of the piston. A clamping system is used to cover the cell with a plastic film without inferring the movement of the piston and the loading during the test. The plastic cover reduces the evaporation from the sample.

The vertical stress is applied using a conventional loading frame with dead loads. Deformation of the sample is monitored using a Linear Variable Differential Transformer (LVDT), data acquisition system, and a LabView Interface.

#### 4.2.1.2 Semi-permeable membrane and PEG solution

A cellulotic dialysis membrane is used as semi-permeable membrane. Since the dialysis membrane consists of a spongy matrix of cross-linked polymers, the pore rating referred to as Molecular Weight Cut Off (MWCO), is an indirect measure of the retention performance. More precisely, the membrane MWCO is determined as the solute size that is retained by at least 90%. However, the solute's permeability is also dependent upon molecular shape, degree of hydration, ionic charge and polarity. It is therefore recommended to select a MWCO that is half the size of the MW of the species to be retained (Spectrum Laboratories INC., 2006). In this study, a dialysis membrane with a MWCO of 3.500 $kD$ (Spectra/Por 3, Dialysis Discs, 3.5 $kD$ MWCO, 100 $mm$ diameter) is matched with a solution of PEG 6000 (MW 6 $kD$). The membrane is circular in shape with a diameter of 100 $mm$ which fits appropriately to the oedmeter cell.

In the osmotic oedometer, different suctions are applied using solutions with different concentration of PEG. The concentration of the PEG dissolved in pure water can be determined using a refractometer. A refractometer is an optical instrument that is used to determine the refractive index of solution. The measurements are made in the Brix scale which is based on a sucrose (sugar) and water solution. Degrees Brix (symbol $^{\circ}Bx$) is a measurement of the mass ratio of dissolved sucrose to water in a liquid. A 25 $^{\circ}Bx$ solution has 25 grams of sucrose sugar per 100 grams of liquid.

Since most samples contain substances other than sugar (e.g. salts, minerals, and proteins) the Brix percentage represents the total concentration of all soluble solids in the sample. Hence, usually a conversion chart from the Brix percentage to the concentration of a given solute in the solution is needed. In the present work, a hand-held refractometer (ATAGO E Type Series, N-50E, Brix 0-50%) was used to determine the concentration of the PEG in the solution.

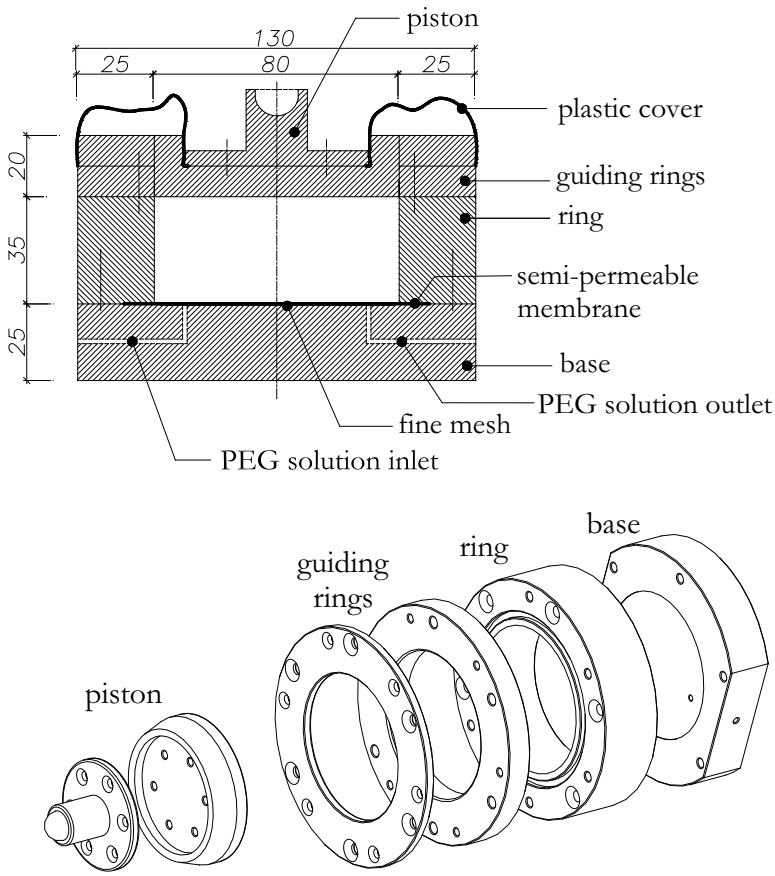


*Figure 4.8:* Schematic representation of the osmotic oedometer cell

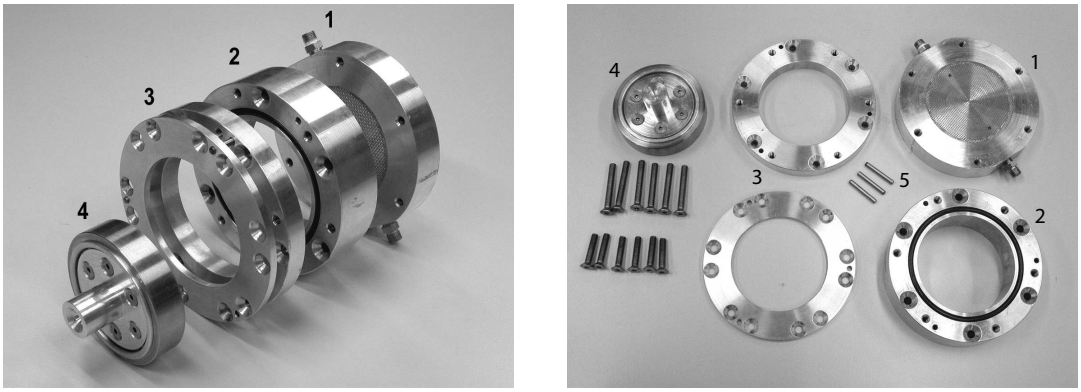


*Figure 4.9:* Osmotic oedometer components: 1. base, 2. oedometer ringe, 3. guiding rings, 4. piston, and 5. pins

#### 4.2.1.3 Tubing, pump and reservoir

To circulate the solution, a peristaltic pump with a variable flow rate was used which operates with continuous flexible silicon tubing (see Table 4.2 for specifications). This combination could provide a flow rate of 28 to 160 $ml/min$. A peristaltic pump prevents any direct contact with the liquid; therefore, the liquid remains in a closed system. Additionally at a given flow rate, it allows a steady flow through the cell, tubes and the reservoir.

The tubes were passed through clamps and they were fixed in a static hanging position before being connected to the reservoir. This prevents the balance measurements from being affected by the hanging weight of the tubes or by the motion of the tube due to the pump rotation.

In order to minimize the evaporation, the reservoir was tightly closed. Furthermore, the reservoir was placed in a closed box at the same elevation as the cell, so that no hydraulic head would be generated between the cell and the reservoir.

#### 4.2.1.4 Electronic Balance

Water exchange was monitored by measurement of the mass variation of the reservoir. Since the solution is in closed circulation, the only input or output of mass in the circulation system happens through the membrane between the sample and the solution.

Extraction of water from the sample increases the amount of water in the circulation system and therefore it gives an increase to the mass of solution in the reservoir. The reservoir was placed on an electronic balance connected to a data acquisition system. Owning to high precision of the balance, even slight air flow might results in fluctuation of measurements. Hence, the whole system of balance and reservoir were placed in a closed box in order to provide stable measurements (see Fig. 4.6). Finally, the temperature of the testing room was always kept constant at 22 degrees of centigrade in order to have stable measurements of the mass.

### 4.2.2 Control and callibration of the cell

In order to verify the efficiency of different components, the new osmotic oedometer has been controlled in different series of tests prior to be used in the experimental testing program. The control tests are listed in Table 4.3. Results of these tests are outlined here; while, the detailed description of the tests and the results are presented in Appendix A.

On the basis of the control tests, the actual configuration of the cell was found to be quite appropriate for testing. It provided a good stability of the membrane without any leakage of circulating solution. The selected mesh allowed homogeneous diffusion of the solution beneath the membrane. Tests showed the importance of providing the same level for the cell and the solution reservoir in order to prevent any hydraulic head in the system. Moreover, the circulation should directed to pull the water from, not to push it into, the

*Table 4.3:* Control tests for the new osmotic oedometer system

| **Test** | **Checking item** |
|---|---|
| C1 | 1. Stability of the balance measurements |
| C2 | 2. Leakage of liquid from the cell base |
| | 3. Efficiency of the mesh to diffuse water beneath the membrane |
| | 4. Deformation and stability of the membrane |
| C3 | 5. Monitoring the exchange of water between reservoir and the cell |
| | 6. Efficiency of the semi-permeable membrane |
| | 7. Leakage of the solution into the cell |
| C4 | 8. Efficiency of the semi-permeable membrane |
| C5 | 9. Efficiency of the system to measure the exchanged water in drying path |
| C6 | 10. Efficiency of the system to measure the exchanged water in wetting path |
| C7 | 11. Influence of pump speed on the equilibrium time |
| C8 | 12. Comparing the oedometric response for a saturated soil |

*Table 4.4:* Calibration of the osmotic cell for total vertical stress

| Nominal stress | Measured force ($kN$) | | Real stress |
|---|---|---|---|
| ($kPa$) | Min | Max | ($kPa$) |
| 15 | 0.069 | 0.073 | 14 |
| 30 | 0.143 | 0.145 | 28 |
| 60 | 0.307 | 0.315 | 61 |
| 90 | 0.486 | 0.493 | 96 |
| 125 | 0.656 | 0.661 | 130 |
| 175 | 0.847 | 0.853 | 168 |
| 250 | 1.185 | 1.19 | 236 |
| 350 | 1.875 | 1.884 | 373 |
| 500 | 2.594 | 2.593 | 516 |
| 750 | 3.848 | 3.849 | 766 |
| 1000 | 5.244 | 5.246 | 1043 |
| 1500 | 7.444 | 7.403 | 1481 |
| 3000 | 13.453 | 13.453 | 2676 |

cell. Providing such a condition, the positive liquid pressure beneath the membrane will be released and hence, the upward deflection of the membrane will be prevented.

Balance measurements showed that the measured exchanged water for a soil sample during a drying path was quite close to the values obtained by direct measurements of water content before and after the test. While, some discrepancies between the corresponding results were observed for a soil sample in wetting path. It was thus concluded that the method might suffer from limited uncertainties for testing in wetting paths. Finally, performance of the new cell for oedometric testing was validated by comparison between the oedometric test results of a saturated samples carried out in both osmotic and conventional oedometer cell.

In the new osmotic cell, a classical loading frame with dead loads was used to apply mechanical stress to the sample. The required dead load was calculated

for each loading step with respect to the cross sectional surface of the sample. The real stress applied to the sample might differ a bit from its theoretical value. This might be first due to small variation in the weights of the lead blocks used as dead loads, and secondly, due to the friction in the loading system. Therefore, the precise stress applied to the sample was obtained by calibration of the cell. A load cell was placed inside the oedometer cell, instead of the sample, and the real values of applied force were measured for different loading steps. Results of the calibration are listed in Table 4.4 for different steps of mechanical loading.

### 4.2.3 Suction control and PEG concentration

In the osmotic method, the imposed suction, in general, is equal to osmotic pressure (the opposite of water potential) of the solution. This is actually the hydrostatic pressure produced by the solution in the space divided by the semipermeable membrane due to a differential in the concentrations of solute. The imposed suction is, accordingly, determined based on the relationship between the osmotic pressure and the concentration of the PEG solution.

In general, the osmotic pressure of a dilute solution, shown as $\Pi$, can be calculated using the van't Hoff's law which expresses the osmotic pressure as a linear function of the molarity (number of moles of a given substance per liter of solution):

$$\Pi = iMRT \tag{4.3}$$

where $i$ is the van't Hoff's factor reprsenting the number of moles of solute actually in solution per mole of solid solute added, $M$ the molarity, $R$ the gas constant, and $T$ is the thermodynamic temperature. At the temperature $21°C$, $RT$ is equal to 2.446 $kg.MPa.mol^{-1}$. This law predicts that the osmotic pressure of a true solutions is directly a function of the number of particles in solution.

However, the relation between the osmotic pressure of aqueous PEGs and their concentration appears to be more complex (Applegate, 1960; Lagerwerff et al., 1961, cited in Steuter et al. (1981)). Figure 4.10 shows the relationship between molarity and the osmotic pressure of $KCl$ and PEGs with different molecular weights reported by Money (1989). It is observed that the relationship between the molarity and the osmotic pressure is not linear. For a given molarity, the larger polymers clearly increases the osmotic pressure more than the smaller ones. Money (1989) concluded that this behavior reflects considerable divergence from ideal behavior ($KCl$ is considered to represent an ideal behavior), and that the PEG media do not observe van't Hoff's law.

Steuter et al. (1981) suggested that the total mass or total number of molecular subunits, rather than total number of particles, may be an important factor controlling the osmotic pressure. This conclusion is in agreement with the data reported earlier by Williams and Shaykewich (1969). Comparing different results on the osmotic pressure of PEG 6000 and PEG 20000, these authors concluded that the osmotic pressure generated by PEG solution is independent of the molecular weight and it is only a function of the PEG concentration

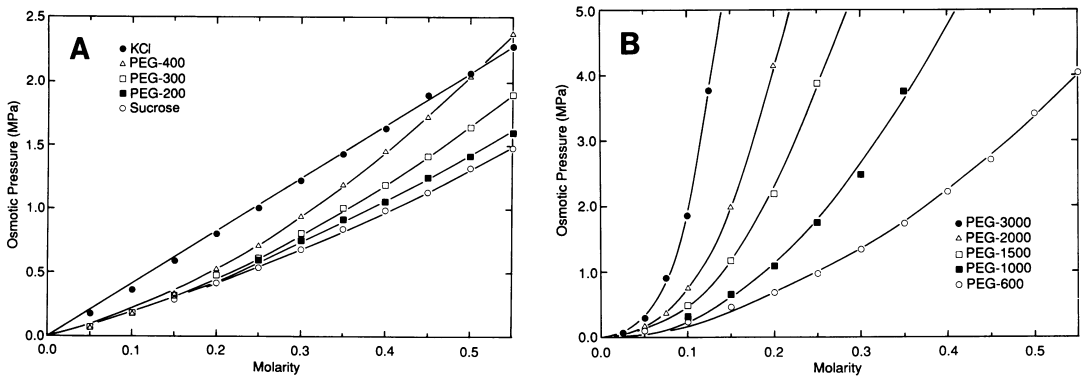


*Figure 4.10:* Relationships between concentration (molarity) and osmotic pressure (Money, 1989), left: for PEG-200 through -400, sucrose, and KCI, right: for PEG-600 through -3000

expressed in terms of weight of PEG per unit weight of water.

A possible explanation of this behavior is given by Steuter et al. (1981). The total water potential in the osmotic system has two additive components: the solute potential obtained by van't Hoff's equation and the matric (pressure) potential which is based on matric forces. Most authors refer to PEG as an osmotic agent which alters the solute potential of a solution. Steuter et al. (1981) described that by using the molal concentration (the number of moles of a given substance per kilogram of solvent) of PEG solution and van't Hoff's formula, the osmotic contribution of PEG particles to the total water potential can be calculated. However, other factors related to matric forces should be considered as well. Steuter et al. (1981) reported (after Schonfeldt, 1969) the formation of micellar structure for certain ethylene oxide adducts in an aqueous medium. This structure is a result of hydrogen bonding between ethylene oxide subunits and $H_2O$ molecules. These authors indicated that the degree of micellation is directly related to the concentration. Hence, PEG solutions of hight $MW$ and high in concentration behave like colloids with high potential of matric forces. Accordingly, matric forces which are not taken into account by van't Hoff's equation, are a major component of the resulting water potential.

The relation between the water potential and the concentration of PEG can be experimentally obtained by different methods, among them freezing-point depression and vapor-pressure deficit methods. Steuter et al. (1981) reported some discrepancies between the results of these methods and attributed them mainly to testing condition such as the difference in the sample temperature at the time of measurements.

Williams and Shaykewich (1969) collected the experimental results reported by different authors for solutions of PEG 6000 and 20000. Results of their work, plotted in Figure 4.11(a), have been widely used in calibration of the imposed suction in osmotic systems. Figure 4.11(a) illustrates as well the results provided by Money (1989) who investigated the osmotic pressure of aqueous PEG solution using the vapor pressure deficit method. Also depicted in this figure are the results obtained by Dineen and Burland (1995). These authors

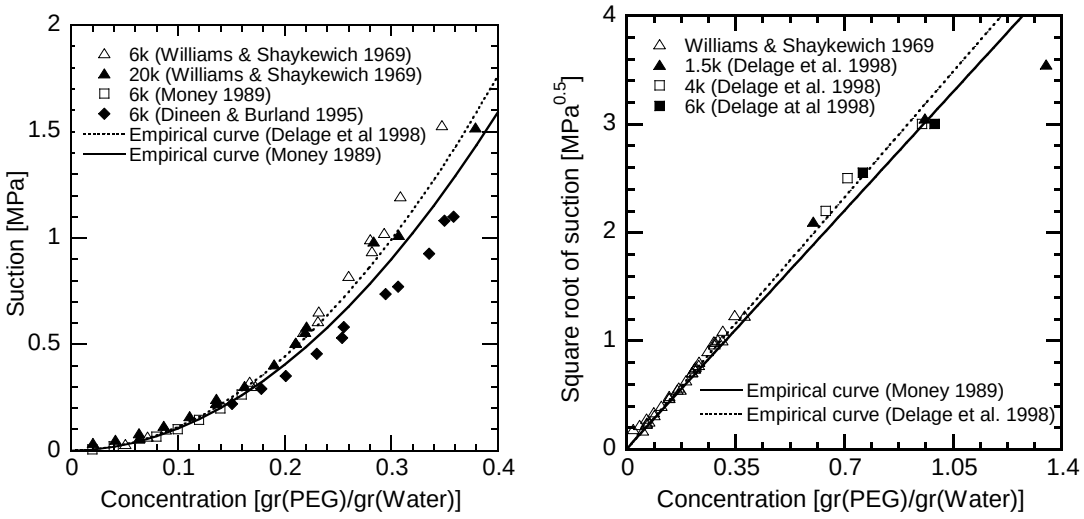


*Figure 4.11:* Calibration of PEG concentration and the generated suction, (a) Low suction values, (b) Extension to high suction values

placed an Imperial College tensiometer on the upper face of the sample in the osmotic oedometer cell to measure the matric suction. This allowed them to have a continuous measurement of suction and to provide a direct calibration of the suction with the PEG concentration (Fig. 4.11(a)). Other authors (Peck and Rabbidge, 1969) also investigated the generated suction by the PEG solution and usually the results are in good accordance with those given by Williams and Shaykewich (1969). The calibration curve provided by Williams and Shaykewich (1969) covers the suction range between 0 and 1.5 $kPa$. This suction range was later extended up to suction of 8.5 $kPa$ by Delage et al. (1998) using PEGs of lower molecular weight which allowed them to have higher concentrations (Fig. 4.11(b)).

Money (1989) suggested the following empirical relation between the suction and the PEG concentration:

$$s = 0.051C + 9.8C^2 \tag{4.4}$$

in which $s$ is the suction expressed in $MPa$ and $C$ is the concentration in terms of the PEG mass per unit mass of water.

A similar relation has been proposed by Delage et al. (1998) on the basis of experimental results collected by Williams and Shaykewich (1969):

$$s = 11C^2 \tag{4.5}$$

The curves corresponding to Equations (4.4) and (4.5) are shown in Figure 4.11. There is a slight difference between the suction values obtained by these equations. However, for suction values above 0.5 $MPa$, Equation (4.4) appears to have predictions closer to experimental results. In the present study, the required concentration of PEG to achieve a desired suction at each step has been calculated according to the relations presented above.

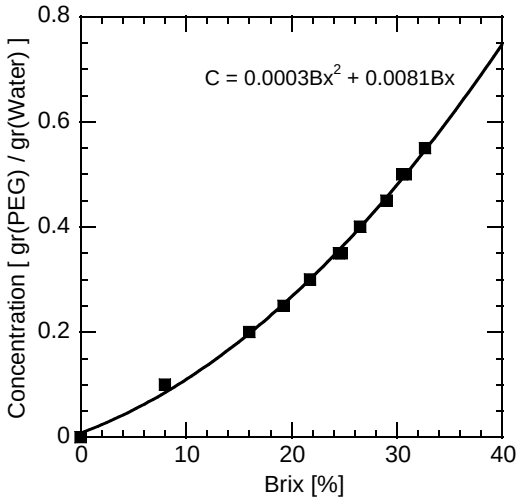


*Figure 4.12:* Relation between Brix index and concentration of aqueous PEG6000

A key factor for suction control in the cell is to prepare the solutions with an exact value of PEG concentration. For each concentration, the PEG was weighed separately and dissolved in distilled de-aired water of the known weight until reaching a homogeneous transparent solution. Theoretically, the PEG concentration of the obtained solution in such condition is supposed to be the desired theoretical one. However, operational errors, very often, might cause the real concentration of the solution to be a bit different from the theoretical one. It was therefore appeared necessary to verify the concentration of the solution. Moreover, it was usually needed to determine and verify the concentration of the solution after the test. For this purpose, the concentration of the solution was determined using the hand-held refractometer (see Sec. 4.2.1.2). Prior to each measurements of Brix number, the scale of the refractometer was first callibrated to indicate zero for distilled de-aired water using a scale adjustment screw provided for this purpose. The reference operational temperature for the refractometer is $20°C$. Measurements at different temperature were corrected according to the correction table provided by the manufacturer.

As mentioned previously, the Brix percentage read by the refractometer have to be converted to the PEG concentration of the solution. To obtain this relation, PEG solutions of different concentration were carefully prepared at the same condition, and the Brix percentage was measured for each solution. The curve relating the Brix index to the concentration, as shown in Figure 4.12, was used as the converting chart in this study. In the tested range of concentration, the proposed relation between the Brix number and concentration of PEG 6000 reads:

$$C = 0.0003(Bx)^2 + 0.0081(Bx) \qquad ; R^2 = 0.99 \tag{4.6}$$

where $Bx$ is the Brix percentage and $C$ is the concentration of PEG solution expressed as grams of PEG per grams of water.

### 4.2.4 Water exchange measurements and calibration

The variations in the water content of the sample during the test corresponds to the water exchange between the sample and the PEG solution in the closed circulation system. Hence, the exchanged water can be calculated based on the variation in the volume or mass of the solution in the reservoir.

In this work, as in the work of Dineen and Burland (1995), the water exchange was determined by the mass measurement. The reservoir was placed on an electronic balance and the mass of the exchanged moisture was measured directly. The advantage of this method in comparison with volume measurements is in the fact that the measurements are not influenced by the volume changes induced by temperature. Moreover, it allows a constant computer monitoring which is helpful in determining the equilibrium.

Parallel to the balance measurements, evaporation from the top of the sample in the cell and/or from the reservoir and tubing system should be taken into account in order to determine the precise water content of the sample.

Evaporation losses from the top of the sample would not interfere in the balance measurements and should be taken into account separately. Though the plastic film on the oedometer cell (see Fig. 4.8) appeared to considerably reduce the evaporation from the top of the sample in the cell, it could not prevent it totally. In order to measure this evaporation, the cell containing the saturated sample and covered with the plastic film (as in the testing set-up) was placed on an electronic balance and the mass readings at different time intervals were made. The results are plotted in Figure 4.13. Evaporation loss was found to be linear function of time with an evaporation rate of 0.0047 $gr/hour$. This evaporation correction is independent of and additive to the balance measurements.

The other source of liquid loss is the evaporation from the reservoir and tubing which can be regrouped with all other possible factors such as precipitation or diffusion of PEG in the tubes. These factors directly affect the balance measurement. Therefore, the raw balance measurements had to be corrected before being used.

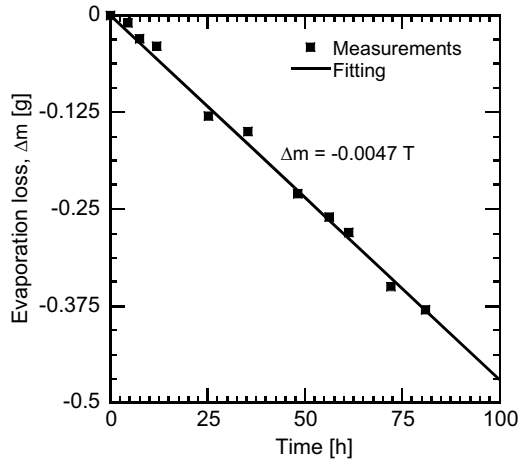


*Figure 4.13:* Evaporation losses from the top of the sample in the cell

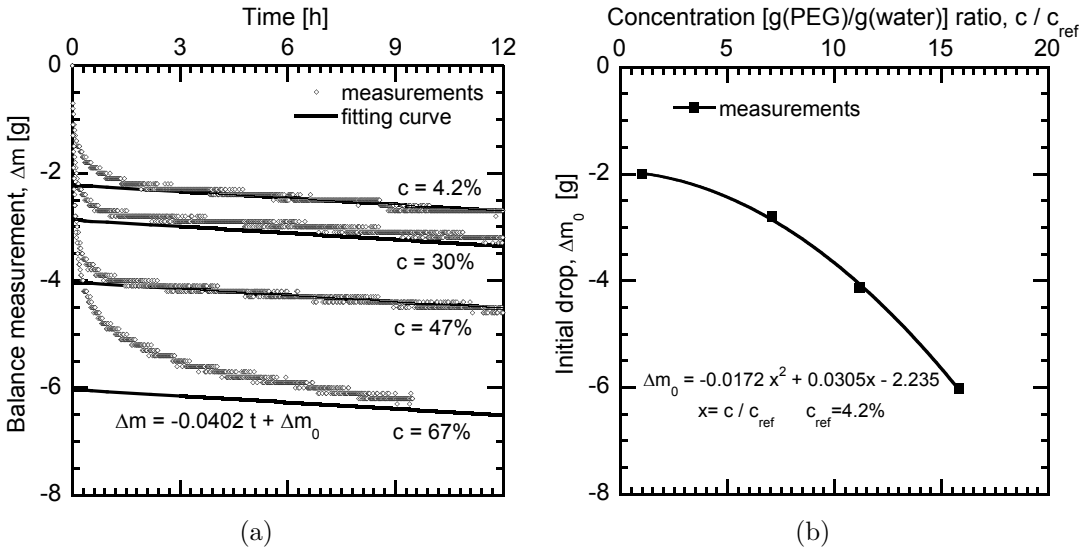


*Figure 4.14:* Calibration of the balance measurements, (a) measurements at different concentrations, (b) initial drop in balance measurements

Accordingly, the balance measurements were calibrated for solutions of different concentration circulating in the system. For each solution, the solution was circulated in the system including the reservoir but excluding the cell. The circulation was continued with a steady flow rate of 45 rpm (with a silicon tube of 3.1 $mm$ internal diameter). Any mass decrease in this condition was considered as unwanted effects that should be extracted from the raw balance measurements.

Figure 4.14(a) shows the results of mass measurements as a function of time for solutions with four different concentration of PEG. The curves are constituted of two parts: an initial drop at the early state of pumping ($\Delta m_0$), and a steady decrease of the measured mass which continues with time at a constant rate. The first effect is believed to be a transitory effect of the pump and the resultant uplift of the liquid in the reservoir. While, the second phenomenon is probably a combined effect of evaporation in the system and deposition and precipitation of PEG in the tubes and connections. As expected, the amount of initial drop is higher for solutions with higher concentration of PEG.

The amounts of initial mass drop are shown in Figure 4.14(b) for different concentrations normalized with respect to a reference concentration, $C_{\text{ref}}$, of 0.42% (PEG mass over water mass). The evolution of initial mass drop in this range of concentration is well reproduced by the proposed polynomial function:

$$\Delta m_0 = -0.0172 \left(\frac{C}{C_{\text{ref}}}\right)^2 + 0.0305 \left(\frac{C}{C_{\text{ref}}}\right) - 2.235 \qquad ; R^2 = 0.99 \qquad (4.7)$$

However, the second effects corresponding to the steady mass decrease was found to be independent of concentration and to occur at a constant rate of 0.042 $gr/hour$. Therefore, the balance measurements for each suction step were

corrected by algebraic subtraction of calibrated values given by:

$$\Delta m = -0.042t + \Delta m_0 \tag{4.8}$$

where $t$ is time with respect to the start of pumping in $hours$ and $\Delta m_0$ is given by Equation 4.7. The initial mass drop correction represents an initial effect which applies only at the time when the pump starts to work, e.g., when the PEG solution is changed and a new suction step is started. Therefore, $t$ in this equation always represents the continuous operating time of the pump.

In addition to the above effects, the electronic balance was found to suffer from electrical drift over time in some cases. This was checked at the all steps where the reservoir was removed and it was accounted for in the correction of balance measurements. However, this effects appeared to be negligible in most of the cases.

### 4.2.5 Hints on testing procedure

Discussion of the new testing equipment will be closed here by presenting some hints about the testing method and the experimental procedure.

Cellulotic membranes are known to be very sensitive to bacteria. This has been reported to be a problem for long tests (e.g. Delage et al., 1992). Furthermore, these membranes are fragile and the contact with soil particles and the mesh might cause them damage at high applied stresses. This would significantly decrease the efficiency of the membrane. In order to overcome this problems, two overlapping membranes were simultaneously used for the tests as proposed by Tarantino and Mongiovi (2000). The PEG solution used in the tests were prepared with distilled de-aired water in order to reduce the possible effects of water minerals on the membrane and to prevent the formation of air bubble in the circulation system in long duration test.

The other point is related to a possible problem of the membrane deflection due to the positive pressure of the solution induced by the pump (see Sec. 4.2.2). This problem was overcome by the reversal in the direction of flow within the circulating system so that the fluid could be pulled, rather than pushed, under the membrane. Doing so, the positive pressure beneath the membrane, and hence the possibility of upward deflection of the membrane were eliminated. It was also found important to keep a constant direction and rate of flow during the test. A low flow rate (45 rpm) was adjusted in order to minimize the risk of air being sucked into the circulating system.

Finally, special care is required when changing the solution at different suction steps. At the end of each step, the solution in the tubes and the cell were emptied before replacement of the new solution. Starting a new step, acquisition of balance measurements has been started only after all air bubbles were driven out of the circulating system. This was done in the same manner for all the tests in order to ensure the consistency of the results.

## 4.3 Material and program

### 4.3.1 Material characteristics

Two soils were used as testing material in this study. The first one was a silty clay from Abist region in the central part of Switzerland; and the second one was Bioley silt coming from the western Switzerland in region of Bioley close to Lausanne. Bioley silt was used as the main testing material and most of the tests were carried out using this soil.

Material properties for both soils are listed in Table 4.5. The particle size distribution of these materials are depicted in Figure 4.15. According to USCS (ASTM D2487, 2000), Abist soil is identified as clay with non-plastic fines (CM), and Bioley soil as clay with low plasticity (CL).

The two soils were tested in both reconstituted and aggregated state. The latter one corresponds to the aggregated form of the soil. Bioley silt had been widely studied at Soil Mechanic Laboratory (LMS) of EPFL, and the material was therefore available at the laboratory. The soil was available in the reconstituted form, from which the soil aggregates had to be obtained. While, Abist soil was collected in the site from a top layer of two meters depth. The soil, at its natural state, was aggregated and had to be remolded for tests on reconstituted samples.

### 4.3.2 Aggregate preparation

Due to the difference in the natural initial state of Abist and Bioley silt, aggregates used in the aggregated samples of these soils were prepared following two different methods.

Abist soil, at its natural state, contained aggregates and clods of different sizes. In order to obtain the desired range of aggregates from this soil, after sampling in the field, the soil was first gently crushed into smaller parts at its natural water content of around 7%. Then the organic parts were carefully removed and aggregates with an average size of 2 to 4 $mm$ and 4 to 8 $mm$ were obtained by sieving. The obtained aggregates were dried by oven-drying for 48 hours.

Unlike the Abist soil, aggregates of Bioley silt were artificially prepared from the reconstituted soil. An identical preparation procedure was respected during the course of the experimental program in order to ensure an identical initial soil structure for all samples. In this method, the aggregates were obtained from the compacted soil at dry side of the optimum. Soil was first wetted up to water content of 13% and then compacted with compaction energy of 0.6 $MJm^{-3}$. As depicted in the the compaction curve of Figure 4.16, this water content is slightly lower than the optimum water content (13.7%) for the given compaction energy. Compacted soil was then removed from the compaction cell and it was gently crushed. The crushed soil was sieved to obtain the aggregates between 2 and 4 $mm$. At the end of this process, aggregates were dried in oven for 48 hours.

*Table 4.5:* Material propertties of Bioley and Abist soil

| Property | **Bioley** | **Abist** |
|---|---|---|
| $w_l$ [%] | 28.9 | 38.4 |
| $w_p$ [%] | 15.5 | 20.7 |
| $I_p$ [%] | 13.4 | 17.7 |
| $G_s$ [t/m3] | 2.703 | 2.595 |
| $< 0.02$mm [%] | 63.8 | 41.9 |
| $< 0.06$mm [%] | 85 | 67 |
| $D_{10}$ [mm] | 0 | 0 |
| | | |
| Classification (USCS) | CL | CM |

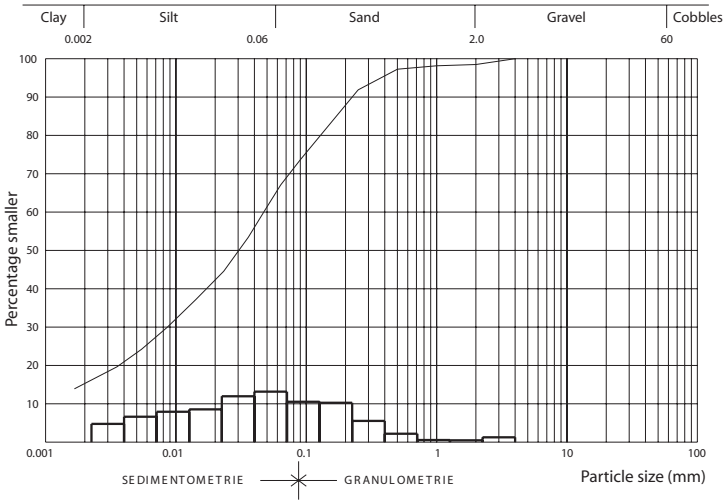


(a)

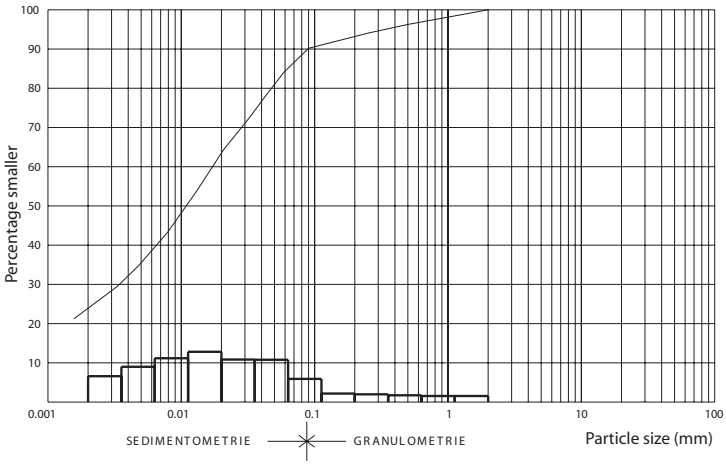


(b)

*Figure 4.15:* Particle size distribution curve of testing material, (a) Abist silt, (b) Bioley silt

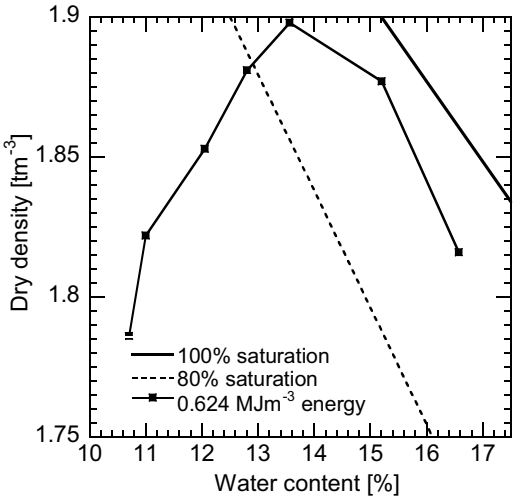


*Figure 4.16:* Dry density-water content relationship for Bioley silt

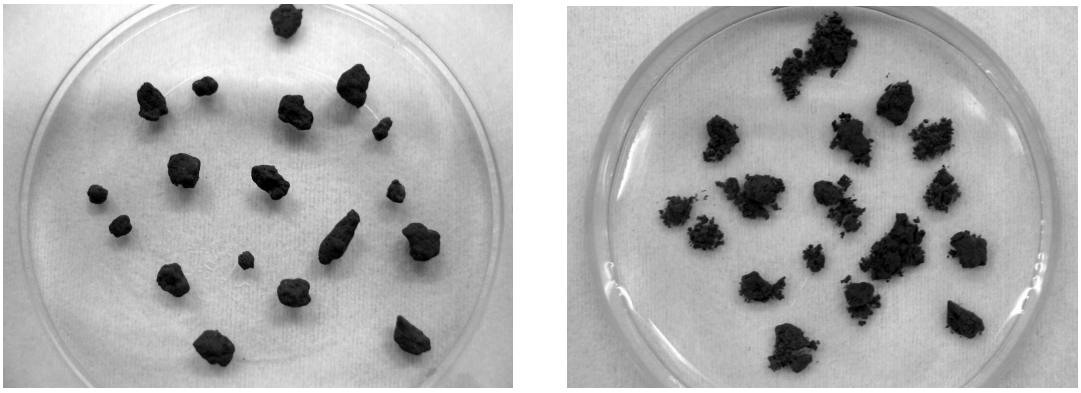

(a) (b)

*Figure 4.17:* Rapid wetting (submerging) of Abist aggregates: (a) before wetting, (b) after wetting

The aggregates obtained in this way were found to be highly sensitive to wetting and they could be easily disaggregated in direct contact with water. Figure 4.17 shows humid Abist aggregates before and after a rapid submerging in water. The aggregates collapsed immediately after the inundation. However, distinction should be made in the response of the aggregates to fast or slow wetting.

Hoffmann et al. (2006) reported that slow wetting using water vapor prevents disaggregation of the aggregates. These authors expressed that the change in the water potential within the aggregate does not occur at the same rate as the variation of the surrounding water potential. In a slow wetting process, there would be enough time for reaching the equilibrium between internal and external water potentials. Accordingly, wherever humid aggregates were needed in these study, the aggregates were wetted following a slow vaporizing wetting procedure, presented below, in order to avoid wetting induced instability and destructuring of aggregates.

*Table 4.6:* Calibration of water loss during water spraying of aggregates

| **Sample** | **Disred** $w$ [%] | **Obtained** $w$ [%] | **Water** loss [%] | **Average water** loss [%] |
|---|---|---|---|---|
| 1 | 10 | 7.61 | 23.90 | |
| 2 | 10 | 7.64 | 23.60 | 22.52 |
| 3 | 15 | 11.99 | 20.07 | |

*Table 4.7:* Wetting steps for aggregates

| **Step** | **Sprayed water [%]*** | **Time interval** $[h]$ |
|---|---|---|
| i | $58.1 = 45 \times 1.29$ | 48 |
| ii | $45.2 = 35 \times 1.29$ | 24 |
| iii | $25.8 = 20 \times 1.29$ | 24 |

* Percentage of theoretical water mass corresponding to desired water content

Aggregate wetting was done by water spraying using a vaporizer. For relatively high water contents, water was added at different steps providing enough time intervals in order to ensure the humidity equilibrium in soil. Using this method, it appeared necessary to estimate the portion of sprayed water that the soil receives.

In order to determine this portion, three samples of aggregated Bioley silt were wetted by a vaporizor from a distance of 25 $cm$ with the weight of vaporized water corresponding to desired water contents of 10% for the first two samples and 20% for the third one. Samples were then kept in an airtight container for 24 hours and then the water content of each sample was measured. The results are shown in Table 4.6. The actual water content of the samples was found to be only about 78% of the desired water content. Or to put it in other way, about 22% of water was lost during the spraying. Therefore, to reach a given value of water content, the mass of water to be sprayed should be increased by a factor of 1.29 ($1/(1 - 0.225) = 1.29$).

On the basis of the above descriptions, wet aggregates in this study were all prepared following an identical wetting procedure described below:

- the theoretical mass of water corresponding to desired water content has been increased by a factor of 1.29 in order to determine the total mass of water to be sprayed;
- using a garden vaporizer at a distance of 25 $cm$ from the soil surface, 45, 35, and 20% of the total mass of water has been sprayed on dry aggregates at three steps;
- in order to reach a homogeneous humidity distribution after each step, aggregates have been kept in an airtight container for a certain time. This time has been 48 hours between steps 1 and 2, 24 hours between steps 2 and 3, and 24 hours after step two and before testing.

Different steps of the wetting procedure for the aggregates are summarized in Table 4.7.

### 4.3.3 Experimental program

Four types of experiments have been carried out during the course of the experimental program: (i) dry oedometer tests, (ii) soaking tests, (iii) saturated oedometer tests, and (iv) unsaturated oedometer tests.

For each type of experiment with the exception of saturated oedometric one, the tests were carried out on samples of aggregated and reconstituted soils. Aggregated structure of the soil could not be maintained in the saturated state because of the phenomenon of particle disaggregation in direct contact with water as described in the preceding section. Therefore, only reconstituted soil samples were under saturated condition. The saturated and unsaturated tests were done only on Bioley silt; while, soaking and dry tests were carried out for both Bioley and Abist soil.

Figure 4.18 and Table 4.8 illustrate the tests carried out at different combinations of saturation and the initial structure of the soil sample. The oedometer tests were performed in the applied range of total vertical stress between 1 and 3000 $kPa$.

For the unsaturated tests, the applied suction varied between zero (at saturation) and about 3000 $kPa$. Preliminary unsaturated oedometer tests (UR and US) were carried out using the axis translation technique, while the main part of the unsaturated tests (USR and USS) was completed using the new osmotic cell. Conventional oedometer cells were used for the rest of the rests oedometer tests (DR, RC, SAT).

*Table 4.8:* Classification of the tests

| **ID** | **Test** | **material** |
|---|---|---|
| DR | Dry oedometer | aggregated |
| RC | Dry oedometer | reconstituted |
| SAT | Saturated oedometer | reconstituted |
| UR | Unsaturated axis translation oedometer | reconstituted |
| US | Unsaturated axis translation oedometer | aggregated |
| USS | Unsaturated osmotic oedometer | aggregated |
| USR | Unsaturated osmotic oedometer | reconstituted |
| SK, SKS | Soaking | aggregated |
| SKR | Soaking | reconstituted |

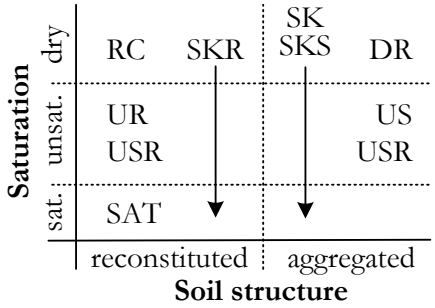


*Figure 4.18:* Classification of the tests

The so-called soaking tests (SK, SKR, SKS) were carried out in the conventional oedometric cell. In these tests, dry samples of aggregated or reconstituted soil were subjected to inundation until reaching the saturated state. These tests are aimed to evaluate and compare the effects of soaking under constant mechanical stress in aggregated and reconstituted soils.

Each experimental class listed in Table 4.8 consists of series of tests varying in testing parameters such as initial void ratio and water content of the sample and the applied range of stress and suction. In this work, different types of experiments are identified by the names given in Table 4.8 as prefix, e.g., DR06 represents the test number 6 of dry oedometer experiments. Detailed description of each test is presented in the corresponding section.

## 4.4 Dry and saturated behavior

### 4.4.1 Description of the tests

Dry and saturated behavior of the material has been evaluated by means of soaking and oedometric tests of dry and saturated samples. These tests, with the exception of two saturated tests performed in osmotic cell, were all carried out using conventional oedometer cell.

A total of 23 successful dry oedometric tests were carried out on aggregated and reconstituted samples of Abist and Bioley silt in the conventional oedometer cell. Samples of dry aggregated soil were prepared by direct placement of dry aggregates in the oedometric cell followed by a slight compaction. Samples prepared in this way exhibited a rough surface and therefore cutting the sample as it is usually done for reconstituted soils was not possible. Accordingly, single aggregates were carefully placed on the top surface of the sample in the remaining empty voids. At the end, the sample was slightly compacted using a blade in order to have a relatively flat surface. This procedure is schematically presented in Figure 4.19. This method of preparation results in relatively large

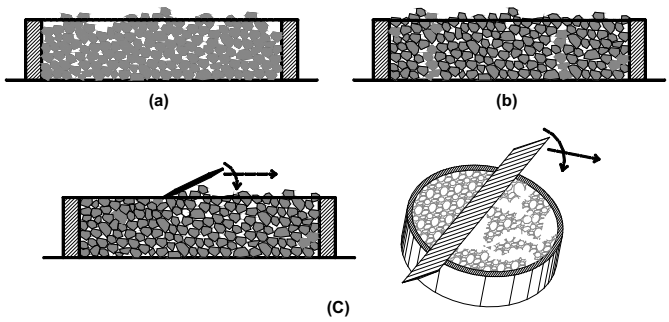


*Figure 4.19:* Preparation of aggregated soil samples

macropores and consequently a high initial void ratio; and, it allows starting the test from a loose normally consolidated state.

Reconstituted samples were directly prepared in the oedometric cell. For initially overconsolidated samples, consolidation phase was imposed prior to the test using the loading frame.

Testing parameters for different dry oedometer tests are given in Table 4.9. Each series of tests represent a group of tests with similar samples and testing condition. The first four series of dry oedometer tests were performed on aggregated sample of Abist soil, of which only the first series were done with large aggregates. Since the material was dry, the required time for equilibrium after each loading step was very short, in the order of minutes for low stresses, and couple of hours for higher values of stress. However, samples of series 2 were subjected to a longer loading duration in order to evaluate the effect of continued loading on the response. Series 3 to 7 of the tests were carried out on aggregated samples and they differ in material, maximum applied stress, and preconsolidation condition. And finally, series 8 to 10 constitute the tests on reconstituted soil with different range of applied vertical stress.

Saturated oedometer tests were carried out on reconstituted samples of Bioley silt using both conventional and osmotic cell. Saturated samples were prepared from a mixture of high water content of 25% which had been kept in an airtight container for 48 hours in order to reach humidity equilibrium. Table 4.10 presents the testing parameters for these tests. In the case of saturated tests in osmotic oedometer, the reservoir was filled with distilled de-aired water and the semi-permeable membrane was replaced by a filter paper to ensure the saturation of the sample during the test. Using conventional and osmotic cell in the same testing condition, the performance of new osmotic cell for oedometric testing could be also evaluated by these tests.

Soaking tests were carried out for both aggregated and reconstituted soil samples using conventional oedometer cells. Dry samples were prepared in the same manner as in the dry oedometric tests. Two types of soaking tests were carried out: simple and oedometric soaking tests. In simple soaking tests, dry aggregated sample was soaked at a given applied vertical stress and deformation versus time was monitored. The oedometric soaking tests were like conventional oedometer test in which the sample was initially dry. At a given stress, the sample was soaked, and then, the test was continued like an oedometric test under saturated condition. In all the tests, the wetting was induced by gradual adding of water around the porous plate at the bottom of the sample until having the water level at the top of the sample. Parameters of these tests, including the vertical stress at which the sample is soaked, are listed in Table 4.11.

Experimental results of these part are presented in terms of void ratio shown as $e$ (Eq. 2.1a), total vertical stress, $\sigma_v$, and Terzaghi's vertical effective stress, $\sigma'_v$, (Eq. 2.7):

$$\sigma'_v = \sigma_v - p_w \tag{4.9}$$

where $p_w$ is the pore water pressure. In the absence of water (dry tests) or in drained condition (conventional oedometer cell), the total and effective stresses are identical.

*Table 4.9:* Dry oedometer tests on Abist and Bioley soil in standard oedometer cell

| **Series** | **ID** | **Material** | **Structure/Agg. size** $[mm]$ | **Initial** $\sigma_{vc}$ $[kPa]$ | **Imposed** $\sigma_v$ $[kPa]$ | $e_i$ |
|---|---|---|---|---|---|---|
| 1 | DR01 | Abist | Agg. / 4 - 8 | - | 1-1500 | 1.38 |
| | DR02 | Abist | Agg. / 4 - 8 | - | 1-1500 | 1.61 |
| | DR03 * | Abist | Agg. / 4 - 8 | - | 1-1500 | 1.68 |
| | DR04 * | Abist | Agg. / 4 - 8 | - | 1-1500 | 1.44 |
| | DR05 | Abist | Agg. / 4 - 8 | - | 1-1500 | 1.35 |
| 2 | DR06 * | Abist | Agg. / 2 - 4 | - | 1-1000 | 1.52 |
| | DR07 | Abist | Agg. / 2 - 4 | - | 1-250 | 1.51 |
| | DR08 | Abist | Agg. / 2 - 4 | - | 1-350 | 1.58 |
| | DR09 | Abist | Agg. / 2 - 4 | - | 1-350 | 1.57 |
| 3 | DR10 | Abist | Agg. / 2 - 4 | - | 1-1000-1 | 1.55 |
| | DR11 | Abist | Agg. / 2 - 4 | - | 1-1000-1 | 1.57 |
| | DR12 * | Abist | Agg. / 2 - 4 | - | 1-1000-1 | 1.54 |
| | DR15 | Abist | Agg. / 2 - 4 | - | 1-1000-1 | 1.46 |
| 4 | DR13 | Abist | Agg. / 2 - 4 | 125 | 1-1000-1 | 1.52 |
| | DR14 | Abist | Agg. / 2 - 4 | 125 | 1-1000-1 | 1.33 |
| 5 | DR16 | Bioley | Agg. / 2 - 4 | - | 1-1000-1 | 1.55 |
| | DR17 * | Bioley | Agg. / 2 - 4 | - | 1-1000-1 | 1.60 |
| | DR18 | Bioley | Agg. / 2 - 4 | - | 1-1000-1 | 1.62 |
| | DR19 | Bioley | Agg. / 2 - 4 | - | 1-1000-1 | 1.56 |
| 6 | DR20 | Bioley | Agg. / 2 - 4 | - | 1-3000-1 | 1.59 |
| 7 | DR21 | Bioley | Agg. / 2 - 4 | 175 | 1-1250-1 | 1.64 |
| | DR22 | Bioley | Agg. / 2 - 4 | 90 | 1-1000-1 | 1.55 |
| 8 | RC01 | Abist | Reconst. | - | 1-1000 | 1.01 |
| 9 | RC02 | Bioley | Reconst. | - | 1-1000-1 | 1.09 |
| | RC03 | Bioley | Reconst. | - | 1-1500-1 | 1.05 |
| | RC04 | Bioley | Reconst. | - | 1-1500-1 | 1.16 |
| | RC05 | Bioley | Reconst. | - | 1-1500-1 | 1.16 |
| 10 | RC06 * | Bioley | Reconst. | - | 1-3000-1 | 1.03 |
| | RC07 | Bioley | Reconst. | - | 1-3000-1 | 1.08 |

* failed tests whose results were not used in the analysis

*Table 4.10:* Saturated oedometer tests on Bioley soil in standard and osmotic cell

| **Series** | **ID** | **Cell** | **Structure** | **Initial** $\sigma_{vc}$ $[kPa]$ | **Imposed** $\sigma_v$ $[kPa]$ | $w_i$ [%] | $e_i$ |
|---|---|---|---|---|---|---|---|
| 1 | SAT01* | Standard | Reconst. | - | - | - | - |
| | SAT03 | Standard | Reconst. | - | 1-1000-1 | 25.2 | 0.70 |
| 2 | SAT02* | Osmotic | Reconst. | - | 1-1000-1 | 25.3 | 0.70 |
| | SAT04 | Osmotic | Reconst. | - | 1-1000-1 | 25.3 | 0.68 |

* failed tests whose results were not used in the analysis

*Table 4.11:* Soaking tests on Abist and Bioley soil

| **Series** | **ID** | **Type** | **Mat.** | **Structure/Agg. size** $[mm]$ | **Soaking** $\sigma_v$ $[kPa]$ | **Imposed** $\sigma_v$ $[kPa]$ | $e_i$ |
|---|---|---|---|---|---|---|---|
| 1 | SK1 | Simple | Abist | Agg. / 4 - 8 | 30 | - | 0.97 |
| | SK2 | Simple | Abist | Agg. / 4 - 8 | 125 | - | 1.07 |
| | SK3 | Simple | Abist | Agg. / 2 - 4 | 125 | - | 1.56 |
| 2 | SKS01 | oedometer | Bioley | Agg. / 2 - 4 | 1.1 | 1-1500 | 1.68 |
| | SKS02 | oedometer | Bioley | Agg. / 2 - 4 | 125 | 1-1500 | 1.44 |
| 3 | SKR01 | oedometer | Bioley | Reconst. | 1.1 | 1-1500 | 1.35 |
| | SKR02 | oedometer | Bioley | Reconst. | 125 | 1-1500 | 1.35 |

### 4.4.2 Results of dry tests

In the first step, the effect of loading time on the dry oedometric response of aggregated samples was evaluated in order to estimate the required time of equilibrium at each loading step. This was done by comparing the test results of series 2, namely DR8 and DR9, where each loading step was continued for about ten days, with those of series 3, namely DR10, DR11 and DR15, where for the same material, the maximum loading time was one day.

Figure 4.20(a) shows the deformation versus the square root of time for single loading step in tests DR8 and DR15B (reloaded sample of DR15 at the end of the test). It is observed that in long loading duration, deformation shows a drop after the initial equilibrium; i.e., the sample experiences secondary deformations (in the general sense). In case of DR15B, also a third major drop in the deformation curve was observed. Similar results were observed for high loading steps in tests of series 2.

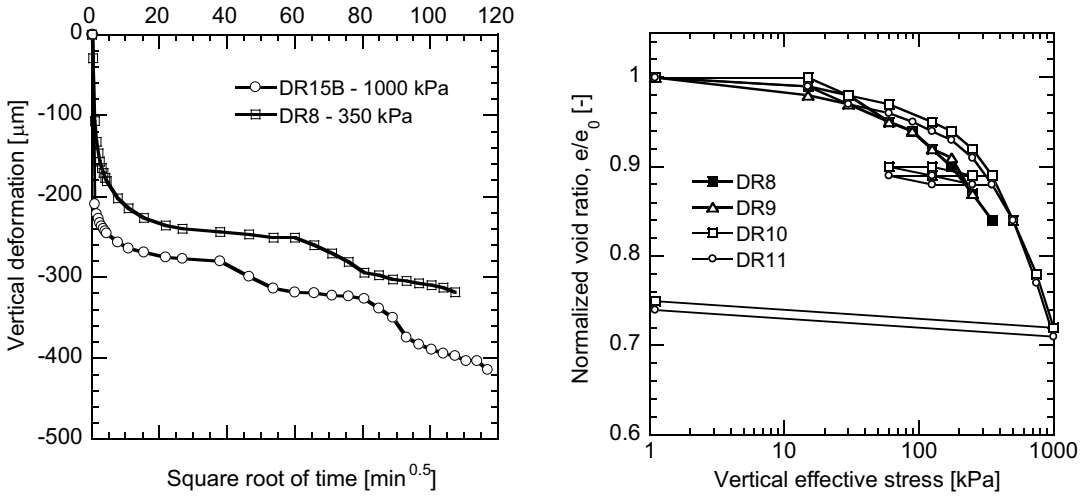


*Figure 4.20:* Creep behavior of dry aggregated samples, (a) Deformation versus time for continued loading, (b) Oedometric response with long (DR8 & DR9) and normal (DR10 & DR11)loading time

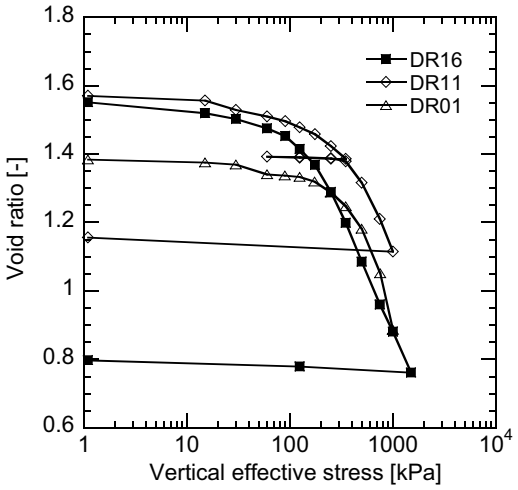


*Figure 4.21:* Dry oedometric curves of aggregated samples with different mineralogy and aggregate sizes (series 1, 3 and 5)

Figure 4.20(b) presents the comparison of the normalized oedometric curves, i.e. normalized void ratio versus the applied vertical stress, for test series 2 and 3. In tests DR10 and DR11 (series 3), each loading step has been continued for maximum one day which corresponds to equilibrium represented by the the first plateau in Figure 4.20(a). As expected, the two series of curves are separated by a difference in void ratio at constant vertical stress. The observed behavior might be due to a combination of different causes like creep or only artifacts. Evaluation of this issue, however, is beyond the scopes of this study and will not be addressed here. Accordingly, loading is the oedometric steps has been stopped when reaching the first plateau in the deformation curve plotted versus square root of time.

Figure 4.21 shows the oedometric curves of tests DR01 and DR11 on aggregated Abist soil with different aggregate size (2-4 and 4-8 $mm$ respectively) and test DR16 on aggregated Bioley silt. According to the preparation method of the samples described in the preceding section, the samples were at a normal consolidated state at the beginning of the test. However, the samples show an initial stiff behavior followed by a yielding in the oedometric compression curve. This behavior is similar to the oedometric response of initially overconsolidated samples.

This behavior can be better understood by comparing the results of tests DR19 and DR22. The two tests were carried out on aggregated Bioley silt with different preconsolidation conditions. Sample in test DR19 was initially normally consolidated, while the one in test DR22 has been subjected to an initial preconsolidation vertical stress of 90 $kPa$. These results are plotted in Figure 4.22. It is observed that the two samples have similar responses and they mainly differ in the yielding limit. The initial stiff behavior of aggregated soils could be compared with the behavior of natural structured soils presented in Chapter 2.

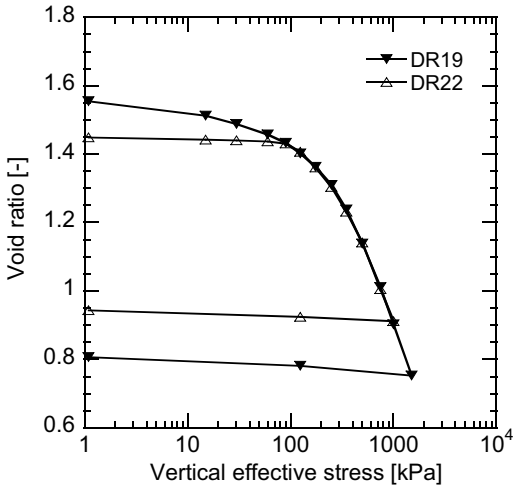


*Figure 4.22:* Oedometric curves of normally consolodated (DR19) and over consolidated (DR22) dry aggregated sample

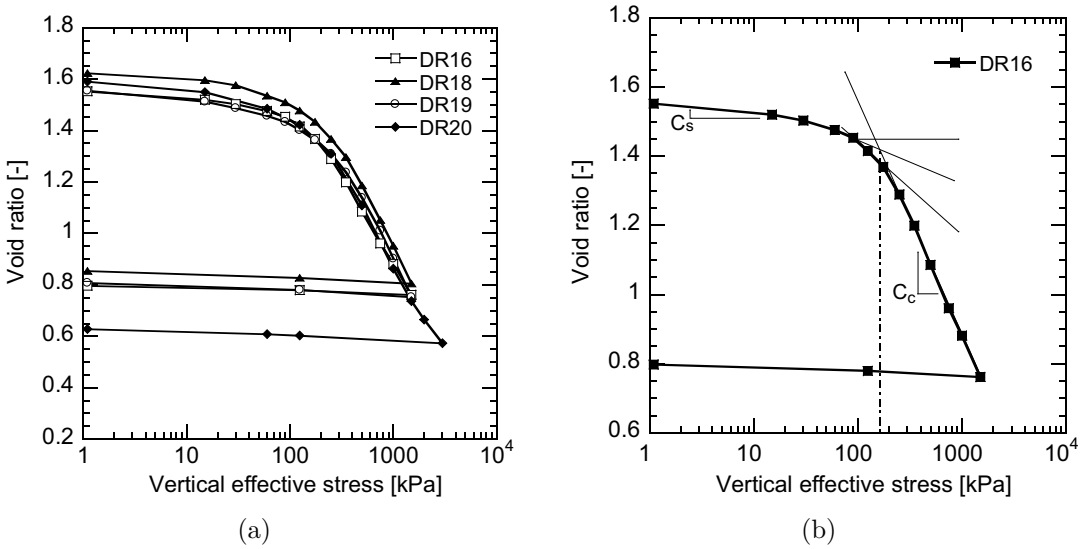


(a) (b)

*Figure 4.23:* Apparent preconsolidation stress for dry aggregated Bioley samples with same structure, (a) oedometric response of samples of series 5 and 6, (b) apparent oedometric preconsolidation stress

Although this stiff behavior in aggregated samples arises from a different phenomenon, it can be described in the same way as induced overconsolidation. Therefore, the limit that seperates the initial stiff behavior from the further yielding is called here initial *apparent preconsolidation stress*.

Figure 4.23(a) shows the oedometric curves of the experiments of series 5 on aggregated Bioley silt with the same structure, namely the same mineralogy, aggregate size and preparation method. It is observed that all samples show analogous behaviors for which the initial apparent preconsolidation stress is almost the same. Similar observation was made for experiments of series 3 (to

be found in Appendix B). It is therefore concluded that the initial apparent preconsolidation stress observed in aggregated soil is identical for soils with same structure.

Similar to initially overconsolidated samples, oedometric curves of the samples in Figure 4.23(a) exhibit an initial linear part corresponding to overconsolidation compression followed by normally consolidation compression part.

In test DR20 where the samples were loaded to a maximum vertical stress of 3000 $kPa$, the normal compression part appears to be non-linear beyond the vertical stress of 1500 $kPa$; while, the slope of unloading remains unchanged. This evidence suggests considering a non-linear part for the compression oedometric curve at high stresses.

The first linear part of the curve can be described using the classical swelling index in soil mechanics, $C_s$, defined as slopes of the unloading-reloading part of the oedometric curves in a semi-logarithmic space of $e - \log \sigma_v$. However for the second part, a tangential value of compressibility index, indicated here by $C_{tc}$ is introduced to represent the slope of the tangent to the oedometric normal compression curve at its early commencement. Oedometric curve of aggregated soil can be characterized by these two parameters together with the initial apparent preconsolidation stress.

These swelling and the tangential compressibility index for dry aggregated Bioley silt are determined as:

$$C_s = (0.0011 \text{ to } 0.016) \ ; \text{average value} = 0.014$$
$$C_{tc} = (0.690 \text{ to } 0.814) \ ; \text{average value} = 0.760$$

According to the proposed method of Casagrande for initially overconsolidated soils, the value of apparent oedometric preconsolidation stress for dry aggregated Bioley silt has been determined to be equal to 140 $kPa$.

Dry oedometer tests were also carried out on reconstituted sample of Abist (RC01, series 8) and Bioley (RC02 to RC07, series 9 and 10). This allowed characterization of the intrinsic behavior of these materials in the absence of aggregated structure. All the tests were performed on normally consolidated samples. Selected experimental results of dry reconstituted oedometric tests are shown in Figure 4.24(a).

Among these tests, test RC07 was loaded to a maximum applied stress of 3000 $kPa$ to be compared with the aggregated samples loaded to the same stress. Result of RC07 is plotted in Figure 4.24(b) where the oedometric normal consolidation line is shown by dotted line.

Based on the experimental results of series 9 on Boiley soil (RC02 to RC05), values of the compressibility index and swelling index for dry reconstituted Bioley silt are determined as:

$$C_s = (0.004 \text{ to } 0.012) \ ; \text{average value} = 0.009$$
$$C_c = (0.251 \text{ to } 0.271) \ ; \text{average value} = 0.267$$

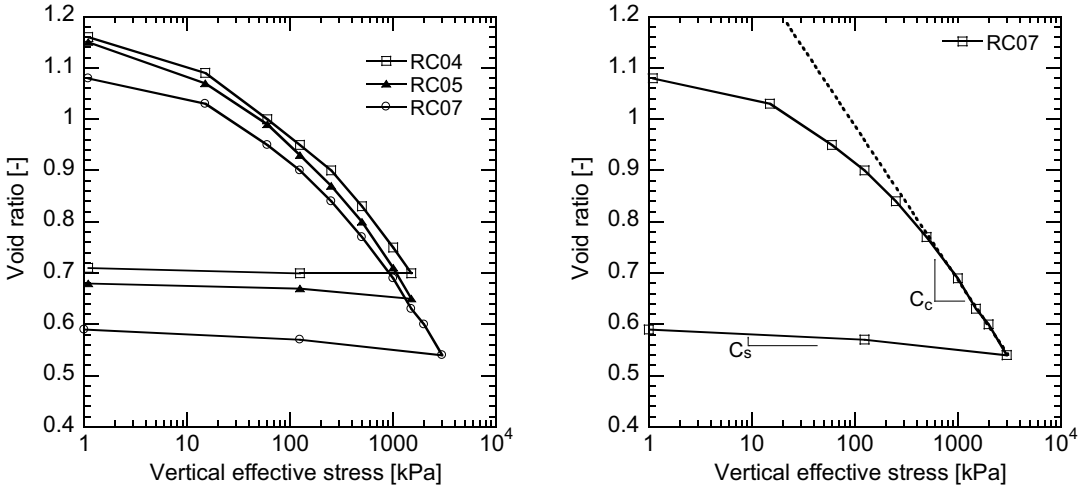


*Figure 4.24:* Oedometric curves for dry reconstituted Bioley samples, (a) oedometric response of samples of series 9 and 10, (b) normal consolidation line

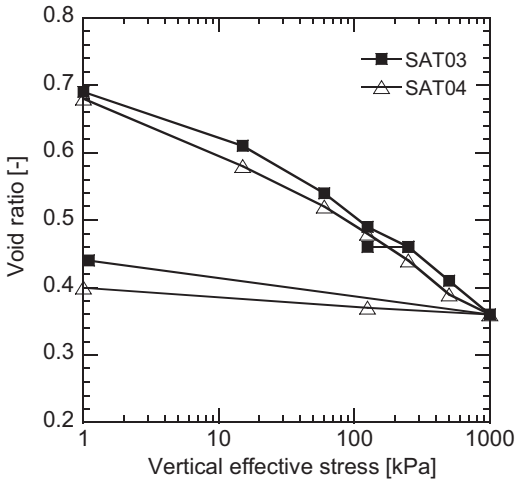


*Figure 4.25:* Saturated oedometeric curves of reconstituted Bioley silt in standard (SAT03) and osmotic cell (SAT04).

### 4.4.3 Results of saturated tests

Saturated oedometer tests were carried out on reconstituted samples of Bioley silt with an initial void ratio of about 0.7 (see Table 4.10) using the osmotic cell (SAT04) and standard conventional oedometer cell (SAT03). The two oedometric curves, presented in Figure 4.25, are quite analogous. Similarity of results validates the performance of the new osmotic cell for oedometric testing (Test C8 in Table 4.3). Based on the results of test SAT04, compressibility and swelling index for saturated reconstituted Bioley silt are:

$$C_s = 0.0276 \quad , C_c = 0.130$$

## 4.4.4 Results of soaking tests

### 4.4.4.1 Simple soaking of aggregated samples

In simple soaking tests, two samples of aggregated Abist soil (SK1 & SK2) were subjected to soaking under a constant vertical stress in a standard oedometer cell. In order to study the effect of applied mechanical stress during wetting, the samples were soaked at two different vertical applied stresses of 30 $kPa$ (SK1) and 125 $kPa$ (SK2).

Figure 4.26(a) and 4.26(b) show the deformation of the samples with time in a linear and semi-logarithmic scale respectively. A dramatic deformation, representing a wetting induced collapse, is observed for both samples at the time of soaking. This deformation is higher in SK2 where the applied vertical stress is higher. The removed sample at the end of the test was found to be like reconstituted soil without any identifiable aggregates, i.e., wetting destroyed the aggregated structure of the soil. Rigorous evaluation of the structure of aggregate samples after soaking will be presented in the next chapter.

This phenomenon is believed to be the reason for the significant deformation induced by soaking. Both in linear and logarithmic scale, the drop in the deformation curves occurs in single step immediately after wetting. No more significant deformation is observed after this step. In other words, the collapse of the aggregated structure during such a rapid wetting occurs in a single phase.

### 4.4.4.2 Oedometric soaking of aggregated samples

Figure 4.27(a) shows results of oedometric soaking tests for two aggregated Bioley samples of SKS01 and SKS02. In the case of SKS01, the sample was

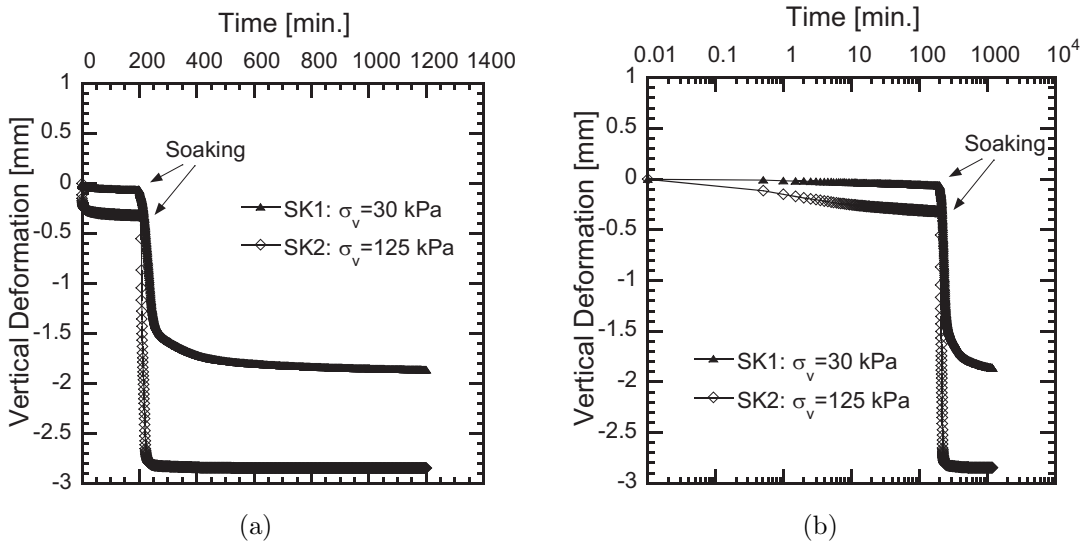


*Figure 4.26:* Simple soaking of aggregated Abist sample at two different vertical stresses 30 $kPa$ (SK1) and 125 $kPa$ (SK2), (a) linear scale, (b) Semi-logarithmic scale

soaked at the beginning of the oedometric test at vertical stress of 1.1 $kPa$; while the sample in Test SKS02 was soaked at vertical stress of 125 $kPa$.

It can be seen for the first sample that soaking induces an initial deformation, after which, the sample undergoes normal consolidation compression during the rest of oedometric compression. Similar behavior was observed for the second sample (SKS02) where soaking was imposed under vertical stress of 125 $kPa$. However in this case, wetting induced deformation is more significant. Comparing these two curves, it is concluded that normal consolidation compression curve of the two samples after wetting coincide. This curve is considered as normal oedometric consolidation curve of aggregated sample in saturated condition. Compression curves of the samples before wetting are well above this curve. When soaking was imposed at the given vertical stress, for instance at 125 $kPa$ for SKS02 in Figure 4.27(a), the induced deformation brings the state of the soil down to saturated normal consolidation curve of the soil.

Similar behavior was observed for reconstituted samples of Bioley silt. These results are depicted in Figure 4.27(b) for samples SKR01 soaked at vertical stress of 1.1 $kPa$ and SKR02 at 125 $kPa$.

The main difference between the response of reconstituted and aggregated samples in soaking tests was the magnitude of the induced deformations. Although the soaking induced-deformation is still considerable in reconstituted samples, it is almost less than the half of the corresponding deformation in aggregated samples. Similar to aggregated soils, the compression curve of the two samples coincide after soaking, which indicates an identical saturated normal oedometric compression. This curve is the well known normal consolidation line (NCL) in classical soil mechanics. As in aggregated samples, the wetting-induced deformation of dry samples results in a new state lying on this line.

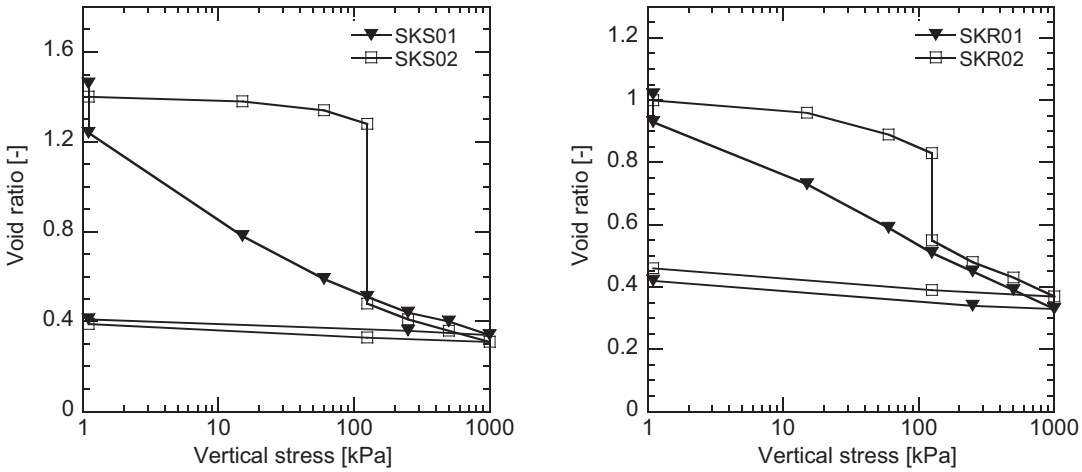


(a) (b)

*Figure 4.27:* Oedometric soaking of Bioley silt samples, (a) aggregated samples at vertical stress of 1.1 $kPa$ (SKS01) and 125 $kPa$ (SKS02), (b) reconstituted samples at vertical stress of 1.1 $kPa$ (SKR01) and 125 $kPa$ (SKR02)

## 4.5 Unsaturated behavior

### 4.5.1 Description of the tests

Suction controlled oedometer tests were carried out on both reconstituted and aggregated soil samples. Samples of aggregated soils were prepared in the same way as dry samples with the exception that dry aggregates were first wetted up to the gravimetric water content of about 13 percent using the method described in Section 4.3.2.

As in the dry samples, all unsaturated samples were prepared by free placement of aggregates directly in the cell followed by a slight compaction. Hence, the initial state of the samples were identical in these tests. The initial suction was unknown and it was estimated to be 50 $kPa$ in the analysis. Uncertainty about this suction is of insignificant importance because the sample has been brought to a known stress state at the onset of the test in the first step. Moreover, as it will be seen later, the suction-induced deformation in aggregated samples is small; and therefore, the influence of initial suction on the induced deformation is negligible.

Unlike the aggregated samples, tests on reconstituted samples started from a saturated state. Similar to saturated tests, reconstituted samples were prepared from a soil mixture of high water content of 25% directly in the cell. Samples USR01, USR02, and USR03 were consolidated to the vertical effective stress of 60, 90, and 200 $kPa$ respectively prior to testing.

Table 4.12 and Figure 4.28 illustrate the parameters of unsaturated tests and the stress path followed in each test. The values of initial water content and void ratio of reconstituted samples listed in Table 4.12 correspond to the state of the material after the primary consolidation phase.

The tests were completed by controlling matric suction and vertical net stress, namely the difference between total stress and air pressure. The suction

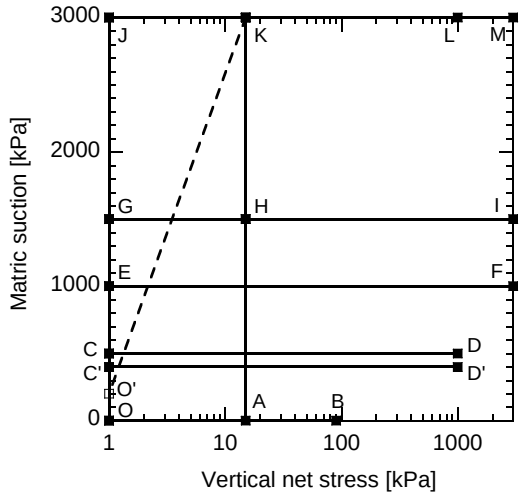


*Figure 4.28:* Followed stress path in unsaturated test (see Table 4.12 for details)

*Table 4.12:* Unsaturated oedometer tests on Bioley soil

| **Series** | **ID** | **Cell** | **Structure** | **Imposed** $\sigma_v[kPa]$ | **Suction** $[kPa]$ | **Stress path** (Fig. 4.28) | $w_i$ [%] | $e_i$ |
|---|---|---|---|---|---|---|---|---|
| 13 | US01 | Hyd. | Agg. | 1-1500 | 400 | O'C'D'C' | 10.8 | 1.55 |
| 14 | UR01 | Hyd. | Reconst. | 1-1500 | 400 | O'C'D'C' | 10.2 | 1.26 |
| 15 | USR01 | Osm. | Reconst. | 1-1000-1 | 500 | OCDC | 22.0 | 0.73 |
| | USR02 | Osm. | Reconst. | 1-3000-1 | 1500 | OAHIG | 22.1 | 0.60 |
| | USR03 | Osm. | Reconst. | 1-3000-1 | 1500 | OBAKMJ | 23.6 | 0.48 |
| 16 | USS01 | Osm. | Agg. | 1-1000 | 3000 | O'KL | 13.6 | 1.57 |
| | USS02 | Osm. | Agg. | 1-350 | 1000 | O'EFE | 15.1 | 1.66 |
| | USS03 | Osm. | Agg. | 1-1000-1 | 500 | O'CDC | 14.3 | 1.63 |
| | USS04 | Osm. | Agg. | 1-1000-1 | 1500 | O'GIG | 13.2 | 1.46 |

was first increased to the desired value and then it was kept constant during the subsequent loading and unloading steps. Accordingly, all the tests were completed in two phases: *phase i* including the suction increase steps prior to the main compression, and *phase ii* correspond to the main oedometric compression (and swelling) performed under constant suction.

The preliminary tests were carried out using the modified hydrocon cell with axis translation technique (see Sec. 4.1.2.1). These tests are two oedometric tests under constant suction of 400 $kPa$ on aggregated (US) and reconstituted (UR) sample of Bioley silt. During the course of these tests, significant discrepancy in the results was observed and the testing equipment appeared not to be suitable for fulfillment of the experimental program. Discussion of these experimental results and the insufficient efficiency of the testing equipment is presented in Appendix B.

Accordingly, the new osmotic oedometer cell previously described in Section 4.2 was used to complete the unsaturated part of the experimental program. Samples of aggregated (USS) and reconstituted (USR) Bioley soil were tested in the osmotic oedometer at suction levels of circa 500, 1000, 1500 and 3000 $kPa$.

Since the tests were carried out at the atmospheric air pressure, the net stress was equal to the total applied stress. Water content of the sample during the test was obtained by measurement and correction of exchanged water at each loading step during the test. Correction of raw balance measurements were made according to the methods described in Section 4.2.4. Having the water content and void ratio known, the degree of saturation at each step has been determined for the sample.

During subsequent analysis of the data, small discrepancies were found between the final water content derived from corrected balance measurements and the one obtained after the soil had been left to dry in the oven at a temperature of $105°C$. This was believed to be related to the effect of the electrical drift of the balance or temperature effects on balance measurements which could not be directly determined for intermediate cases. In these tests, the final water content obtained by drying of the sample has been considered to be accurate and to represent the actual state of the sample. This value has been, therefore, used to linearly adjust the water content in intermediate steps, so that

the corrected cumulative and measured mass of exchanged water agreed. This method is believed to be a simple way to better represent the real condition of the sample.

The experimental results are evaluated in terms of generalized vertical effective stress, $\sigma'_{\mathrm{v}}$, and vertical net stress, $\sigma_{\mathrm{v}net}$ (Eq. 2.9):

$$\sigma'_{\mathrm{v}} = \sigma_{\mathrm{v}net} + S_r s \tag{4.10}$$

$$\sigma_{\mathrm{v}net} = \sigma_{\mathrm{v}} - p_a \tag{4.11}$$

where $S_r$ is degree of saturation (Eq. 3.42), $s$ the matric suction (Eq. 2.2), $\sigma_{\mathrm{v}}$ the total vertical stress and, $p_a$ the air pressure.

### 4.5.2 Osmotic oedometer tests on reconstituted soil

#### (i) Test USR01

Different steps of the stress path followed by sample USR01 is presented in Figure 4.29(a). A PEG solution corresponding to a suction of circa 500 $kPa$ was used to increase the suction at the begining of the test under the constant vertical stress of 1.1 $kPa$. However, further evaluation of results revealed that at the time when the vertical stress of 15 $kPa$ was applied, the water exchange had not reached equilibrium yet. Though, the main water exchange occurred during this last step and the equilibrium is reached only under the vertical stress of 15 $kPa$. This means that the suction of 500 $kPa$ and vertical net stress of 15 $kPa$ have been applied almost simultaneously. The suction at the end of the stress step of 1 $kPa$ has been estimated to be slightly higher than zero (2 $kPa$). The results of this test are presented in Figure 4.29.

The variation of the gravimetric water content during the test is depicted in Figure 4.29(b). The dotted line represents the phase i corresponding to the suction increase and the bold line corresponds to the phase ii during which the net stress varies under constant suction.

It is observed that the sample looses the main part of its humidity in the first phase when the water content decreases from the initial values of 29.7% to 18.7% at the end of the phase i. However, the water content keeps decreasing during the subsequent compression and it undergoes a slight increase in the final unloading step. Meanwhile, the volume and the void ratio of the sample changes. Variation of void ratio with net stress is plotted in Figure 4.29(c). This figure shows an initial shrinkage deformation of the sample at constant net vertical stress of 1.1 $kPa$ where the suction of 500 $kPa$ is applied. It is observed that this deformation continues also at applied net stress of 15 $kPa$. This is due to the fact that equilibrium of water exchange had not yet been reached when the net stress of 15 $kPa$ was applied. This means that suction was still increasing inside the sample at the net vertical stress of 15 $kPa$. Consequently, suction induced deformations also continued occurring at vertical net stress of 15 $kPa$.

Having the water content and the void ratio, degree of saturation can be determined for each step. Using the values of degree of saturation, the generalized vertical effective stress is determined for each loading step. The oedometric

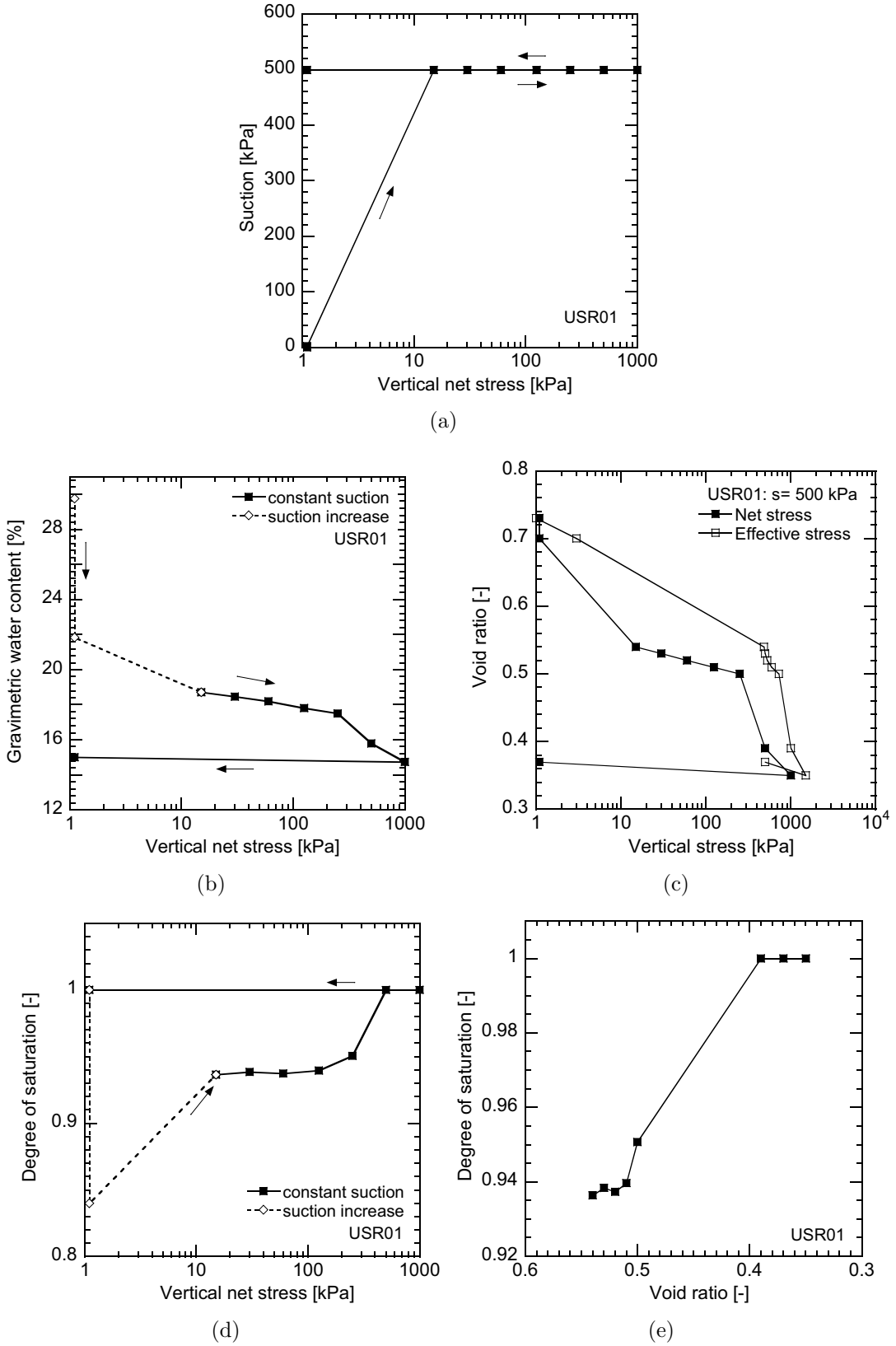


*Figure 4.29:* Results of test USR01: reconstituted Bioley silt, (a) stress path, (b) variation of gravimetric water content, (c) oedometric curve, (d) variation of degree of saturation, (e) variation of degree of saturation at constant suction

response of the sample in terms of effective stress is plotted in Figure 4.29(c). The horizontal separation of net stress and generalized effective stress curves is due to the term $S_r s$ in the expression of effective stress (Eq. 4.10). An effective preconsolidation stress of about 480 $kPa$ has been identified in this figure. The initial suction-induced shrinkage of the sample in the net stress interpretation corresponds to the initial preconsolidation part of the compression curve expressed in terms of effective stress.

Using the effective oedometric curve, the compressibility and swelling parameters of the soil are obtained as follow:

$$C_s = 0.071, \qquad C_c = 0.375, \qquad N = 1.55$$

The variation of degree of saturation as a function of the applied net stress during the test is shown in Figure 4.29(d) for the two phases of the test. It is observed that during the compression phase, the degree of saturation increases despite the decrease of the water content. This is due to the deformation and decrease in the void ratio of the sample. This observation is in line with the evidences reported in the literature (Gallipoli et al., 2003; Wheeler et al., 2003; Cuisinier and Laloui, 2004).

However, the evolution of degree of saturation due to mechanical loading under constant suction could be more representatively evaluated if expressed as a function of the void ratio as illustrated in Figure 4.29(e). In this figure, the abscissa represents the void ratio in the inverse order, as it varies during the test from higher to smaller values. This plot shows that degree of saturation increases with decrease in void ratio from the value of 0.54 at the beginning of compression to the end values of 1. This means that at a given state, all the empty voids are closed and the rest of the voids are filled with water, therefore, the sample maintains a saturated state for the subsequent loading steps. This phenomenon is of great importance in modeling the variation of degree of saturation.

### (ii) Test USR02

The test is similar in nature to the preceding one with difference in the applied level of suction. Figure 4.30(a) shows the stress path followed by sample USR02. Under the constant vertical net stress of 15 $kPa$, suction has been increased in a single step to the final value of circa 1500 $kPa$.

The sample lost a major part of its humidity during the the suction increase phase and the water content decreased from 22.1 to 13.9 percent at the end of this phase (Fig 4.30(b)). The suction increase also results in shrinkage of the sample which is depicted in Figure 4.30 by change of void ratio from 0.55 to 0.47 at the constant vertical net stress of 15 $kPa$. Based on the water content and void ratio, the degree of saturation and subsequently the effective stress are determined for each step. The oedometric response in terms on effective and net stress is shown in Figure 4.30(c). As expected, in the saturated states, the effective and net stress curves coincide. Using the effective stress curve in this figure, the effective preconsolidation stress is estimated as about 1300 $kPa$.

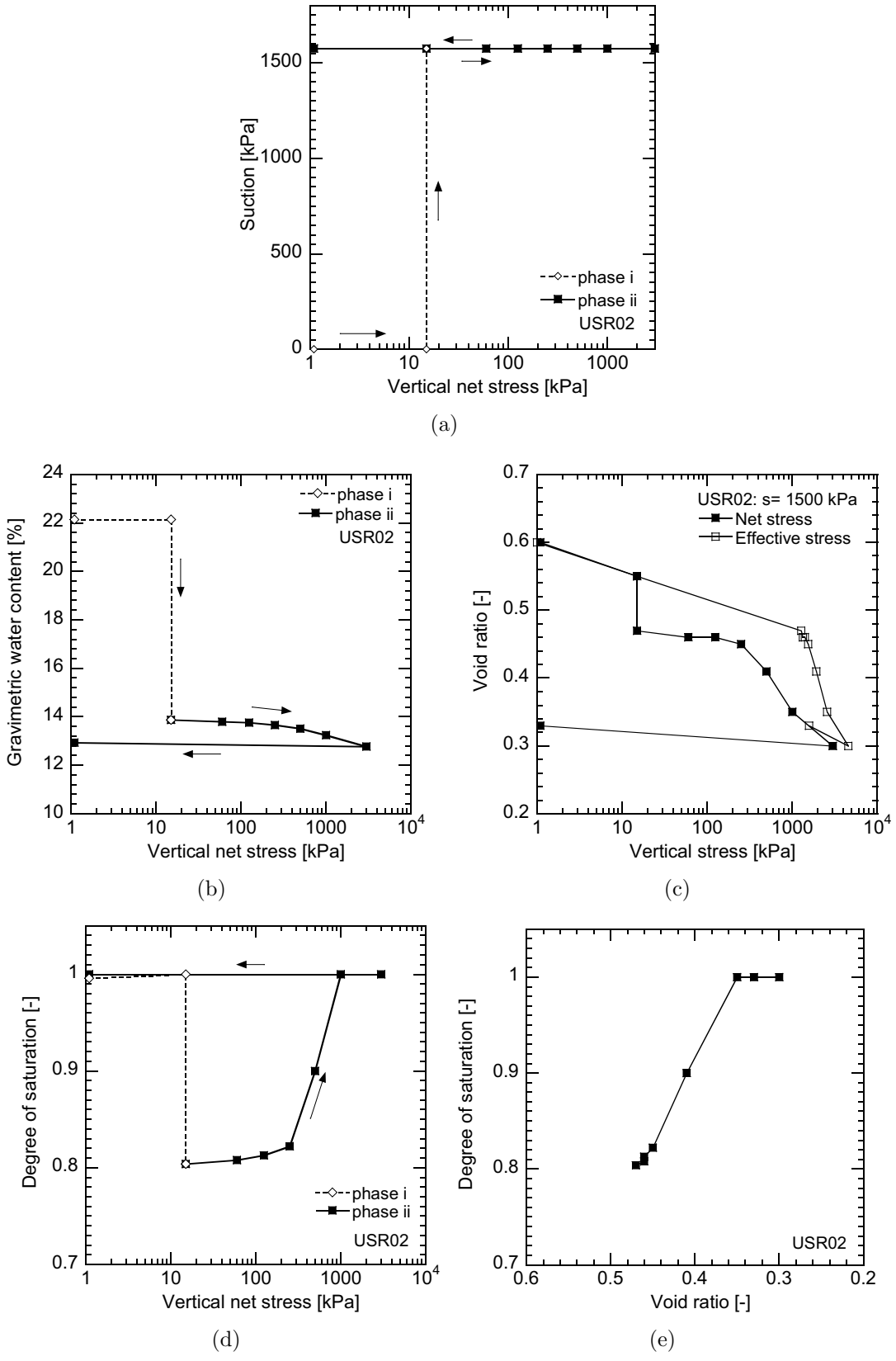


*Figure 4.30:* Results of test USR02: reconstituted Bioley silt, (a) stress path, (b) variation of gravimetric water content, (c) oedometric curve, (d) variation of degree of saturation, (e) variation of degree of saturation at constant suction

The compressibility and swelling parameters of the soil are obtained as follow:

$$C_s = 0.044, \qquad C_c = 0.33, \qquad N = 1.50$$

Figure 4.30(d) shows the variation of degree of saturation as a function of the applied net stress during the test for the two phases of the test. It is observed that during the initial compression from 1 to 15 $kPa$, the sample remained saturated. While after application of suction, the degree of saturation drops down to 0.8 at the end of phase i. Similar to USR01, subsequent compression yields increase of degree of saturation. As observed in Figure 4.30(e), sample becomes saturated ($S_r = 1$) for the void ratio smaller than 0.35. The equivalent observation had been made for test USR01.

**(iii) Test USR03**

Test USR03 is similar to the two previous tests with a different suction and the exception that starting from the saturated state, the maximum suction of circa 3000 $kPa$ is applied in different suction steps. The stress path followed by sample USR03 is depicted in Figure 4.31(a).

The saturated sample was first loaded to a vertical net stress of 15 $kPa$ and then the suction was increased while maintaining the net stress constant. As in previous tests, the suction increase provoked a significant drop of water content from 11.9 to 11.5 percent (Fig 4.31(b)) as well as a shrinkage corresponding to decrease of void ratio from 0.48 to 0.47 under constant vertical net stress (Fig. 4.31(c)).

Using the same principle as in previous test, the effective stress has been determined and used to represent the evolution of void ratio as plotted in Figure 4.31(c). The intermediate states of suction variation lie on the initial stiff part of the curve corresponding to the overconcolidated part in the effective stress interpretation. The effective oedometric preconsolidation stress is estimated to be around 2100 $kPa$. The compressibility and swelling parameters of the soil are obtained as follow:

$$C_s = 0.0067, \qquad C_c = 0.34, \qquad N = 1.59$$

Similar to previous tests, degree of saturation shows a significant drop in the first phase of suction increase followed by a smooth increase during the subsequent compression phase (Fig. 4.31(d)).

The maximum attained degree of saturation at the net stress of 3000 $kPa$ is 0.97. Successive unloading after this step results in a decrease of the degree of saturation. However when expressed as a function of void ratio, as in Figure 4.31(e), the degree of saturation appears to lie on a single curve for all loading and unloading steps.

In additional to the above results, the water retention response of the soil including the evolution of water content and degree of saturation with suction as well as the volume change due to suction increase can be evaluated thanks to the intermediate suction steps.

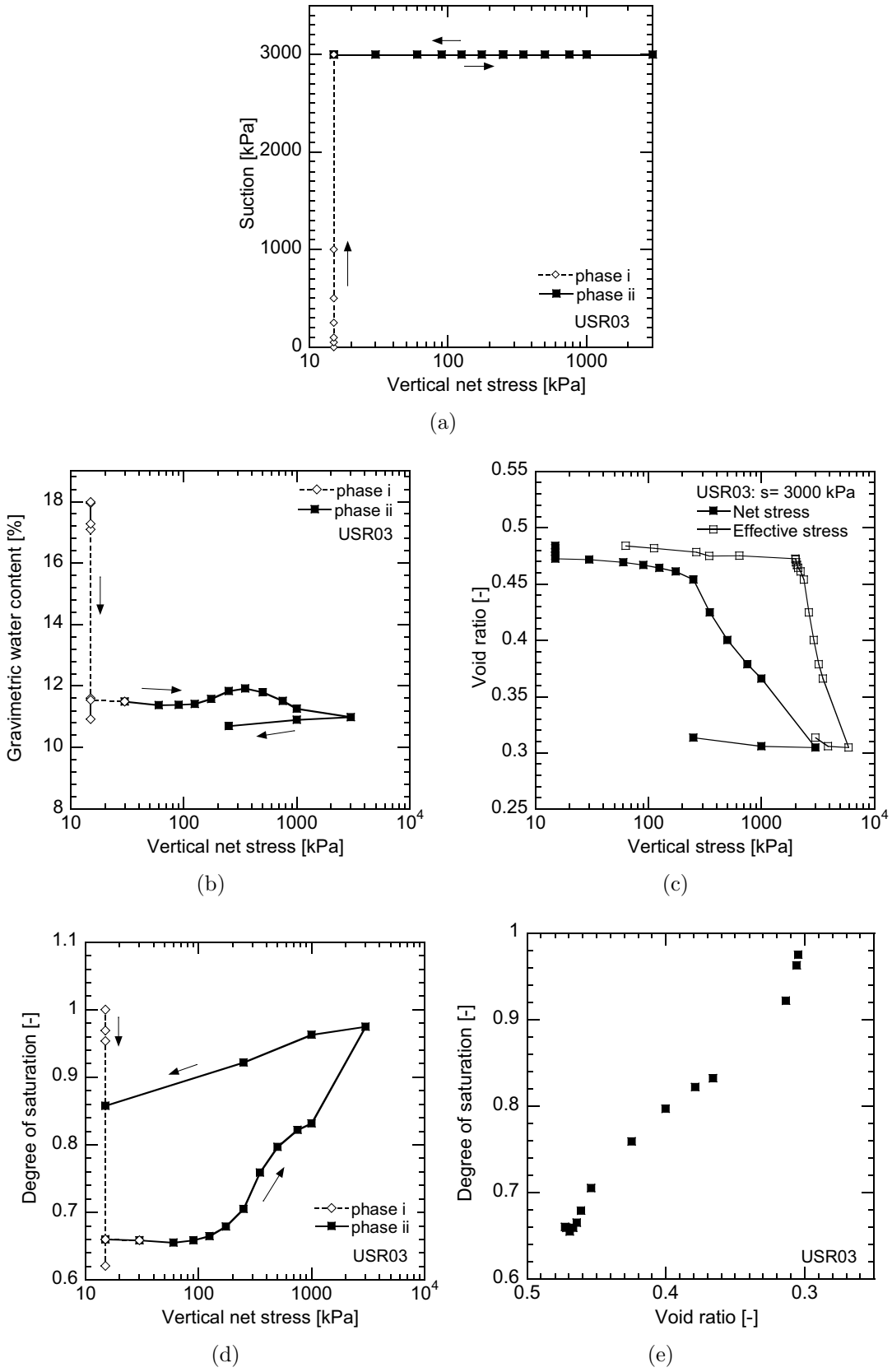


*Figure 4.31:* Results of test USR03: reconstituted Bioley silt, (a) stress path, (b) variation of gravimetric water content, (c) oedometric curve, (d) variation of degree of saturation, (e) variation of degree of saturation at constant suction

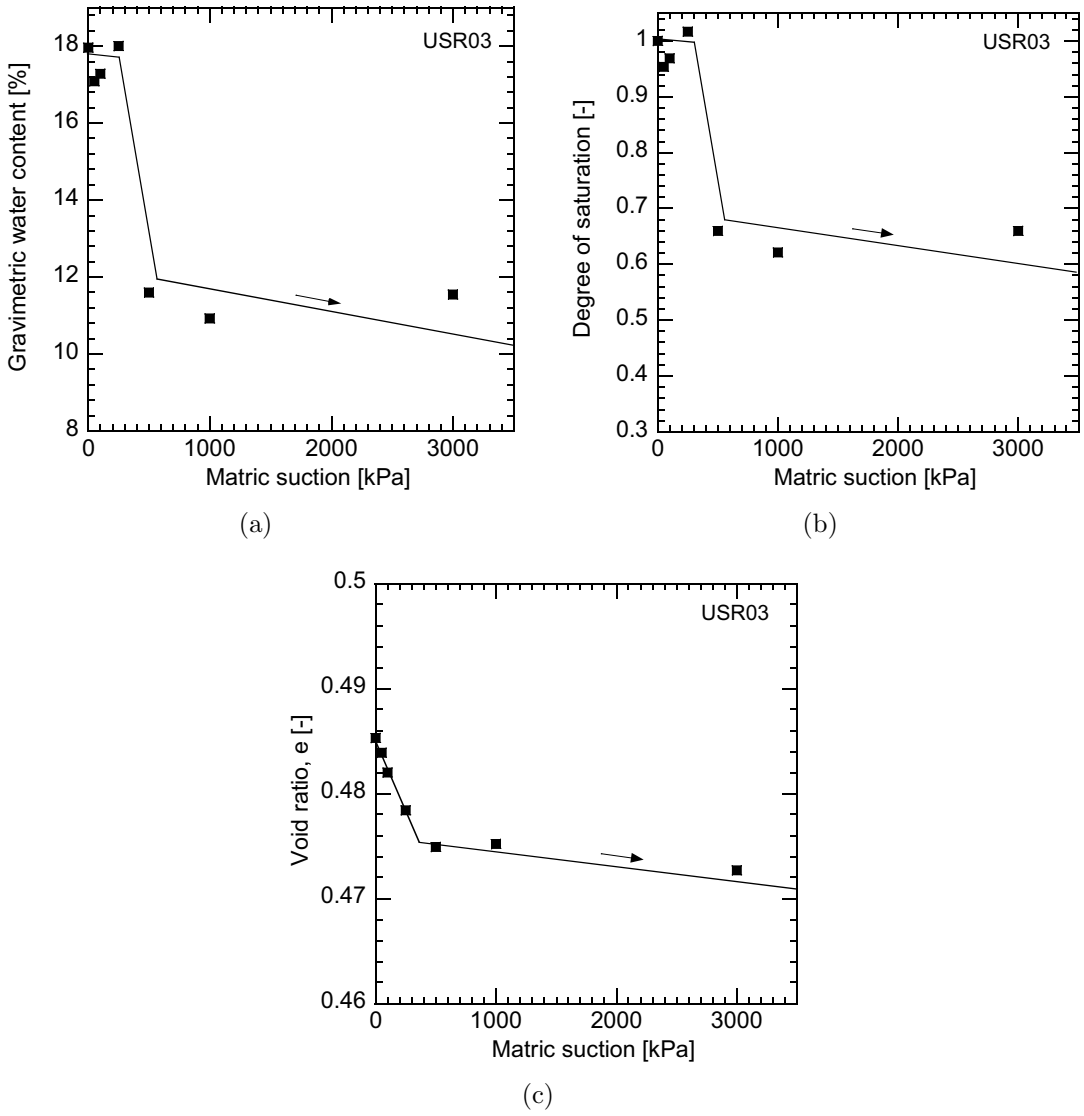


*Figure 4.32:* Water retention curves of reconstituted Bioley silt (test USR03), suction increase under constant vertical net stress, (a) water content-suction, (b) degree of saturation-suction, (c) suction-induced deformation

The evolution of water content and degree of saturation of the sample as a function of applied suction in the first suction increase phase are presented in Figures 4.32(a) and 4.32(b) respectively. It is observed that below the matric suction of 250 $kPa$, the degree of saturation remains almost equal to one, i.e. the sample remains saturated. This suction is referred to as *air entry value suction* and represents the suction at which the water phase becomes discontinued and air enters to the soil. The drop in these curves is followed by low steep part representing insignificant change of water content and degree of saturation with suction increase.

Evolution of void ratio with suction (Fig. 4.32(c)) shows that the major suction-induced shrinkage of the sample occurs at suctions below the air entry value.

The observed phenomenon is of great importance in modeling of both the variation of degree of saturation and the suction induced deformation in soil. These results are in agreement with the interpretation of suction-induced volume change given by Geiser (1999) and presented in Section 2.2.1.

### 4.5.3 Osmotic oedometer tests on aggregated soil

#### (i) Test USS01

Test series of USS are similar to series USR in nature with the exception that tests were carried out on aggregated soils and the initial state of the material was not saturated (see Sec. 4.5.1). Similar to USR tests, these tests have been completed in two phase: *phase i* including the suction increase and *phase ii* corresponding to net vertical stress increase under constant suction.

The first test of this series USS01 corresponds to oedometric compression of aggregated soils under a suction of circa 3000 $kPa$. The followed stress path in this test is shown in Figure 4.33(a).

In the first step, suction has been increased from the initial value to the final suction of about 3000 $kPa$. Simultaneously, the net vertical stress was increased to 15 $kPa$. Figure 4.33(b) shows that the suction increase is associated with a major decrease of water content from 12.7 to 8.3%. However, it is understood from the net stress oedometric curve in Figure 4.33(c) that, unlike the USR series, the shrinkage and change in the void ratio due to suction increase is insignificant for this test.

Following the same methodology as in the preceding test series, degree of saturation is obtained using the water content and the void ratio at each step. This yields determination of the vertical effective stress. Figure 4.33(c) shows the change in void ratio as a function of the effective vertical stress. The effective oedometric preconsolidation stress is estimated to about 500 $kPa$.

Both oedometric compression curves in terms of net stress and effective stress, in Figures 4.33(c), exhibit non-linear part for higher values of stress at their end. This is in line with the observation made in Section 4.4.2 for dry aggregated samples. Accordingly, as mentioned in that section, it is not possible to define a constant compressibility index for the test. The swelling index in this test has been determined as:

$$C_s = 0.03$$

Evolution of degree of saturation with applied net stress and the void ratio is depicted in Figures 4.33(d) and 4.33(e) respectively. As expected, the initial phase of suction application gives a decrease to the degree of saturation. However in the subsequent compression phase under constant suction, there is an initial decrease in degree of saturation which is followed by an increase.

The subsequent increase of degree of saturation should be ascribed to the closure of macropores under almost constant water content; while, this cannot describe the initial increase of degree of saturation observed in these results.

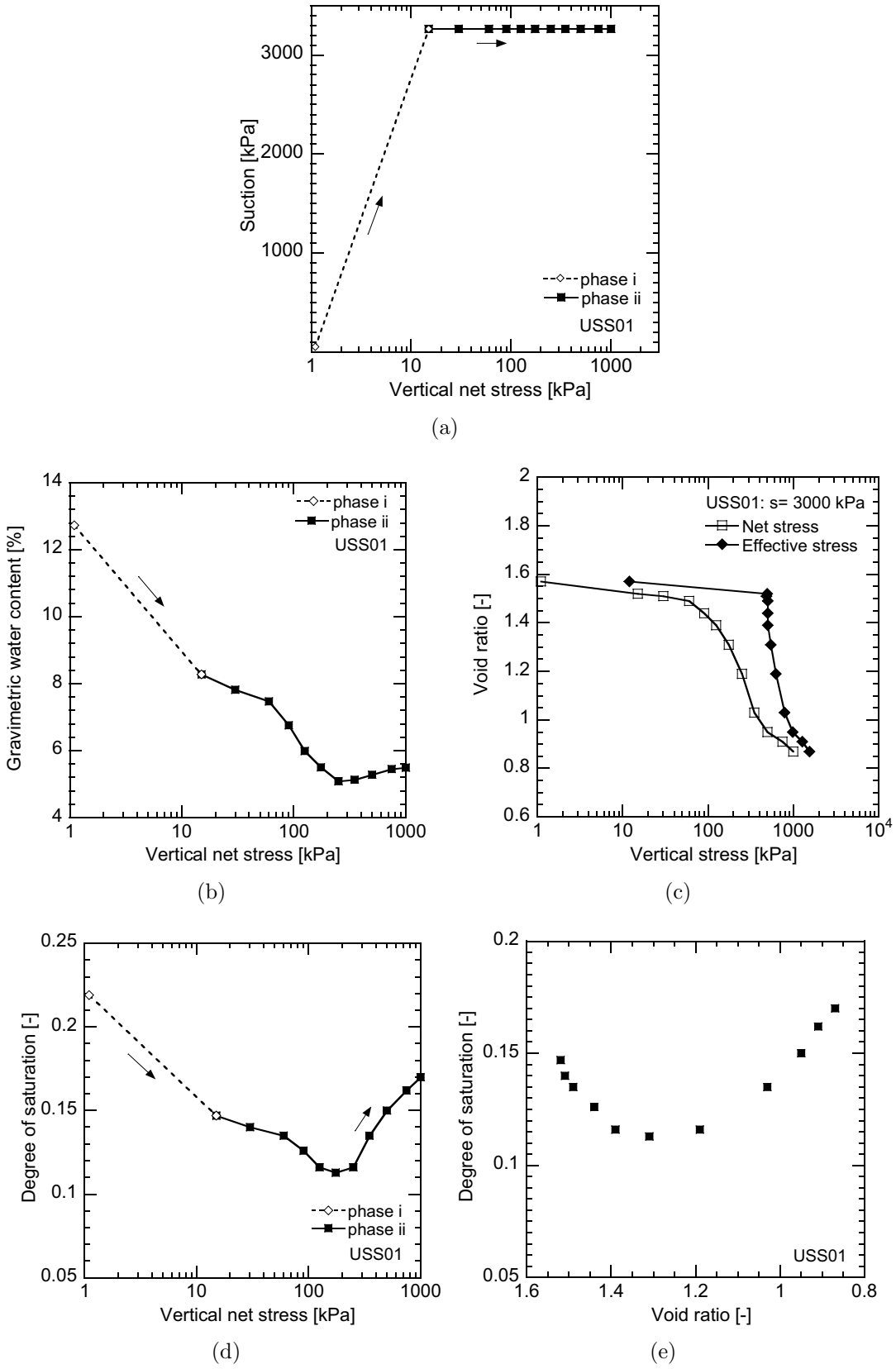


*Figure 4.33:* Results of test USS01: aggregated Bioley silt, (a) stress path, (b) variation of gravimetric water content, (c) oedometric curve, (d) variation of degree of saturation, (e) variation of degree of saturation at constant suction

### (ii) Test USS02

Test USS02 carried out on aggregated sample corresponds to oedometric compression under a suction of circa 1000 $kPa$. Due to operational errors, the test failed at the maximum vertical net stress of 350 $kPa$.

Figure 4.34(a) presentes the followed stress path. Suction was increased in a single step under the constant vertical net stress of 1.1 $kPa$.

As in the preceding test, suction increase caused the main decrease of water content (14.5 to 12% in Figure 4.34(b)) with no significant volume change of the sample (Fig. 4.34(c)).

The oedometric compression curve in terms of effective stress (Fig. 4.34(c)) exhibits an effective oedometric preconsolidation stress of about 200 $kPa$. The compression curve shows no non-linearity neither when expressed in terms of effective stress nor in terms of net stress. This is believed to be due to the low value of the maximum applied stress (maximum effective stress of 720 $kPa$). The swelling index for this test is:

$$C_s = 0.01$$

As depicted in Figure 4.34(d), the degree of saturation decreases during the suction increase phase. During the compression phase, the degree of saturation initially remains almost constant and is then followed by a smooth increase. The plot of the degree of saturation as a function of void ratio in Figure 4.34(e) shows that all the points lie almost on a curve which is increasing reversibly with void ratio.

### (iii) Test USS03

The stress path followed in Test USS03 is shown in Figure 4.35(a). The sample was subjected to matric suction of circa 500 $kPa$ while maintaining the vertical net stress at 1.1 $kPa$.

As a results of suction increase, a decrease of water content from 15 to 12.6 percent has been observed as presented in Figure 4.35(b). This figure shows that the subsequent compression is initially associated with slight decrease of water content. However during the final steps of compression and the unloading step, water content increases.

This phenomenon is believed to be related to the structure of the sample and the evolution of pores between the aggregates. Evaluation of soil strutcure and its evolution will be addressed in the next chapter.

Figure 4.35(c) shows the void ratio as a function of both net and effective vertical stress. It is clear from the net stress curve that the changes in void ratio during phase i is negligible. Both curves show non-linear compression curves at higher values of stress. In this figure, the effective oedometric preconsolidation stress is estimated to be around 110 $kPa$. The swelling index determined from the first part of the curve is:

$$C_s = 0.001$$

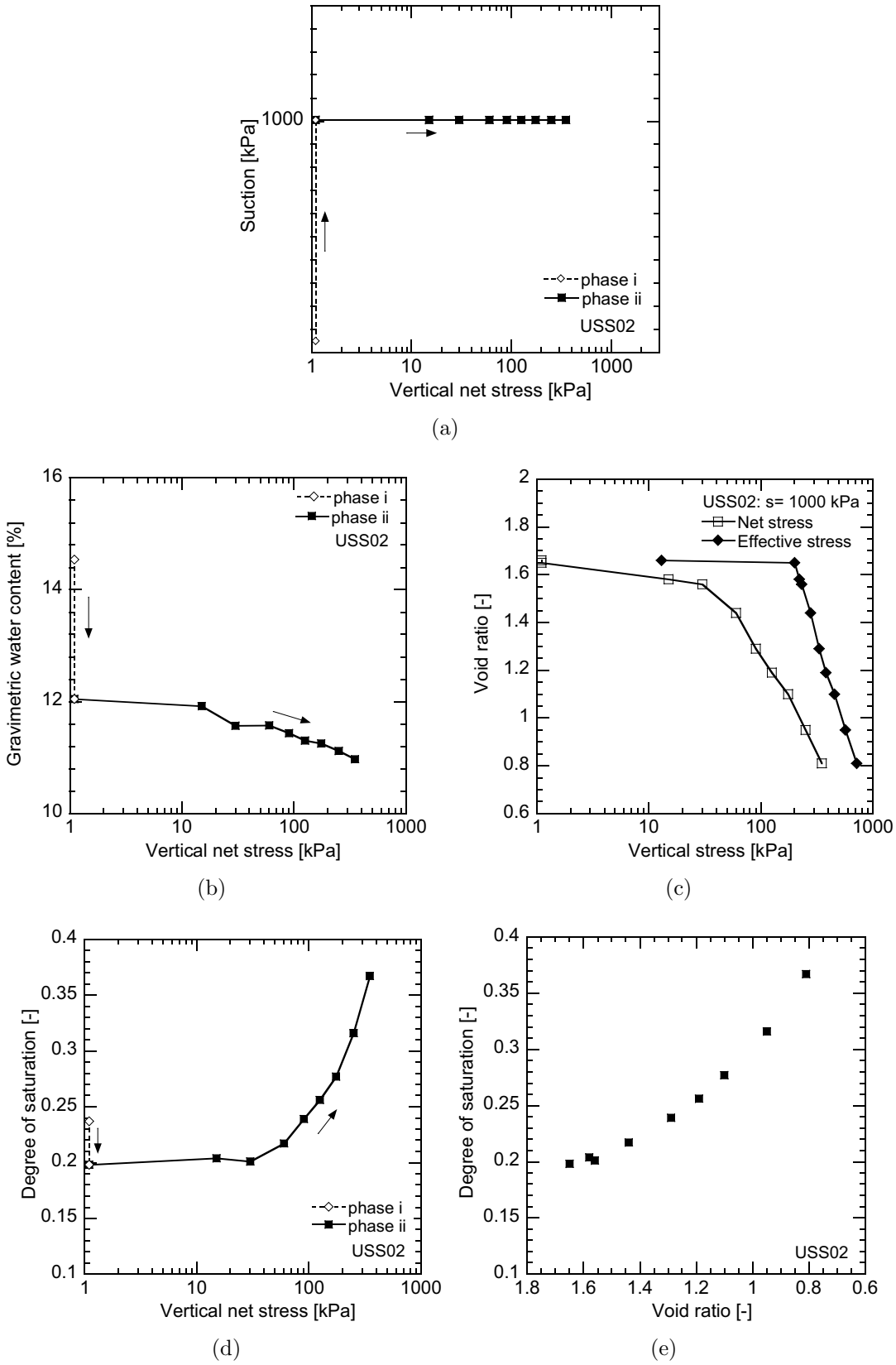


*Figure 4.34:* Results of test USS02: aggregated Bioley silt, (a) stress path, (b) variation of gravimetric water content, (c) oedometric curve, (d) variation of degree of saturation, (e) variation of degree of saturation at constant suction

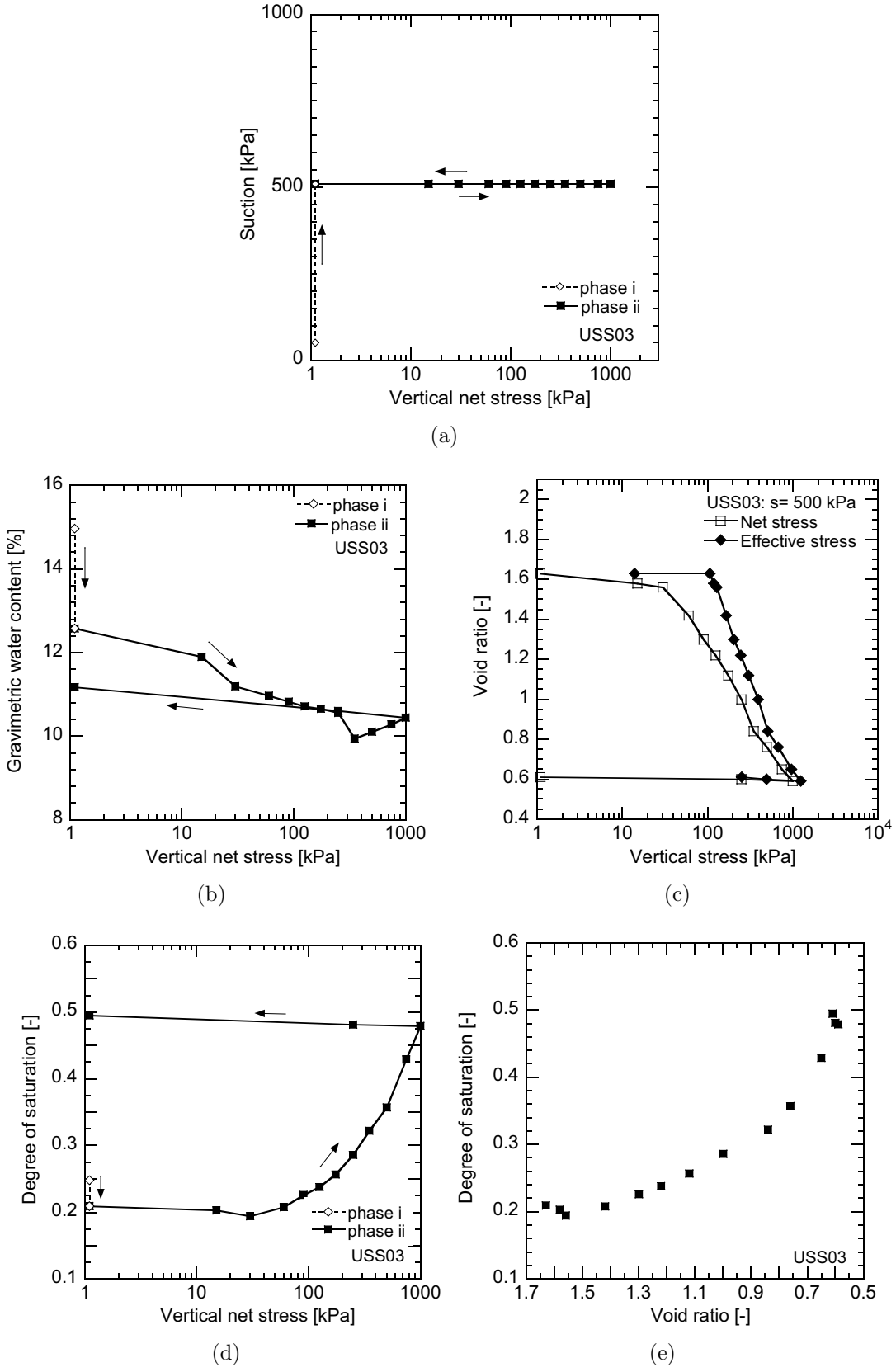


*Figure 4.35:* Results of test USS03: aggregated Bioley silt, (a) stress path, (b) variation of gravimetric water content, (c) oedometric curve, (d) variation of degree of saturation, (e) variation of degree of saturation at constant suction

Figure 4.35(d) shows a slight decrease in the degree of saturation during the suction increase of phase i. Because of the large empty macropores between the aggregates, the degree of saturation at the beginning of compression in phase ii corresponds to the relatively low value of 0.21.

As in the USS02, the degree of saturation in test USS03 remains constant at the early steps of compression and then increases with loading. No important change in degree of saturation is observed during the swelling steps.

Plotted as a function of void ratio, the degree of saturation for both loading and unloadings appears to stay on the same curve (Fig. 4.35(e)). At the higher values of void ratio corresponding to the early steps of compression, the variation of degree of saturation is insignificant and the curve exhibits almost a plateau.

**(iv) Test USS04**

The last experiment of this series is test USS04 which corresponds to oedometric test at suction of circa 1500 $kPa$. Figure 4.36(a) shows the stress path followed in this test. At the second phase of the test, the vertical net stress was increased to the maximum value of 3000 $kPa$.

As shown in Figure 4.36(b), a slight increase of water content has been observed during phase i. This observation disagrees with the expected behavior, i.e., the shrinkage of the sample as a results of suction increase.

The induced change of degree of saturation due to the slight initial increase of water content is insignificant in comparison with the rest of the test (Fig. 4.35(d)). The evolution of water content during the compression phase appeared to be similar to the one in test USS03, i.e. an initial decrease followed by final increase.

Changes in the void ratio as a function of both net and effective vertical stress are presented in Figure 4.36(c). In this figure, a clear non-linearity is observed for the compression curve plotted in both net and effective stress. However, the non-linearity is better observed in the effective stress curve.

The effective oedometric preconsolidation stress in this sample is about 410 $kPa$. The swelling index has been determined as:

$$C_s = 0.015$$

The evolution of the degree of saturation of the sample during compression in terms of vertical net stress and void ratio are illustrated in Figure 4.36(d) and 4.36(e) respectively.

The degree of saturation remains around the low value of 0.26 during the initial steps of compression, while it increases with the successive loading steps until reaching 0.66 at the maximum vertical net stress of 3000 $kPa$. Subsequent unloading brought the degree of saturation to 0.59 at the end of the test.

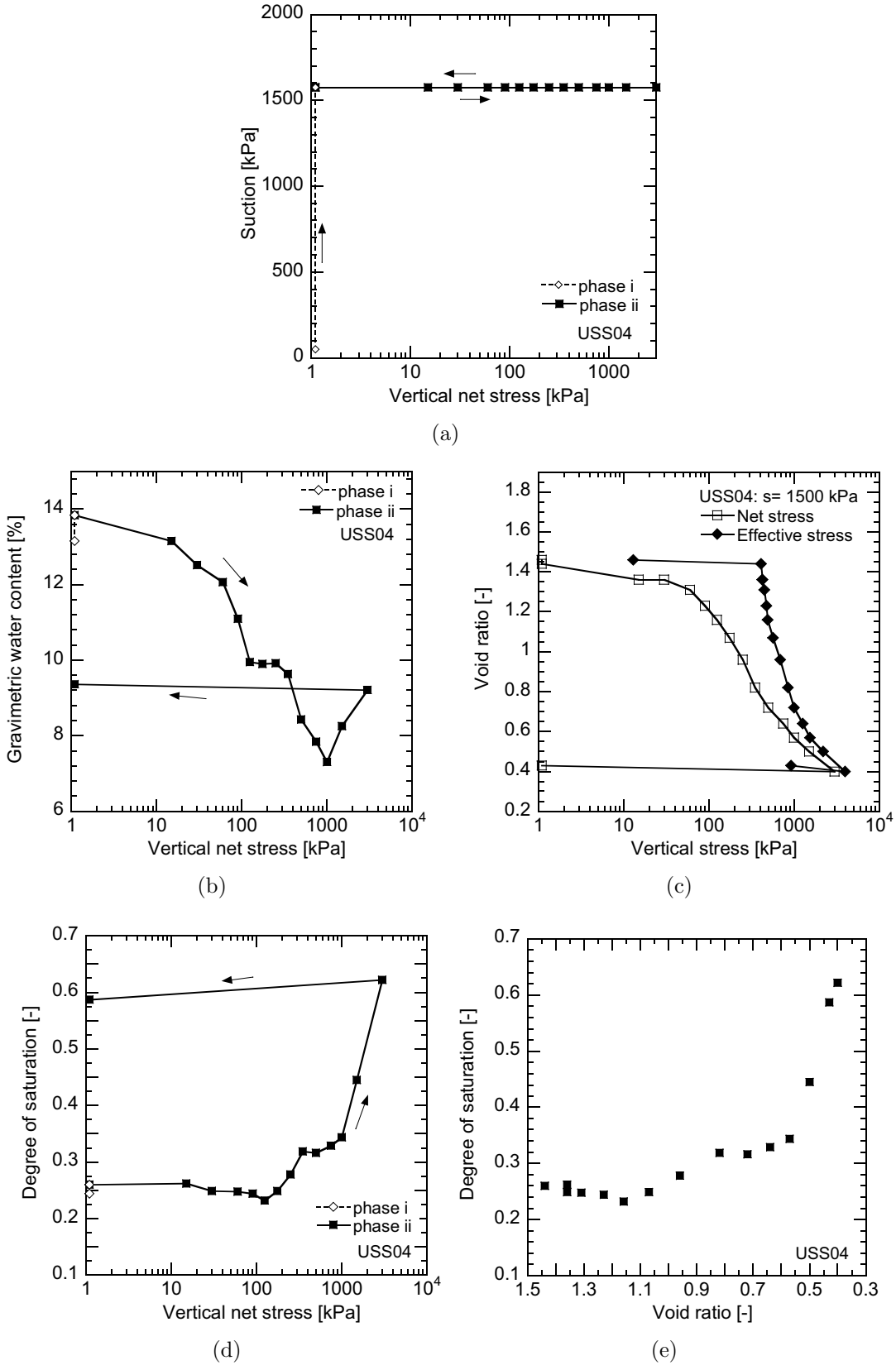


*Figure 4.36:* Results of test USS04: aggregated Bioley silt, (a) stress path, (b) variation of gravimetric water content, (c) oedometric curve, (d) variation of degree of saturation, (e) variation of degree of saturation at constant suction

## 4.6 Comparison and discussion of results

### 4.6.1 Aggregated versus reconstituted samples

The effects of soil structure on the material behavior could be evaluated by comparing the results of tests on aggregated and the corresponding reconstituted soil at the same condition of saturation.

The comparison between the oedometric curves of dry aggregated (series 5) and reconstituted (series 9) samples for Bioley silt is presented in Figure 4.37. Both series of tests were performed on normally consolidated samples. However, it was previously shown that the aggregated samples exhibit an overconsolidated behavior at the initial part of compression. Comparison of results show that aggregated samples exhibit higher initial void ratio than reconstituted soils. The difference in void ratio is due to the initial open structure of the aggregated soils with macropores. This difference decreases at higher values of applied.

The slope of the initial compression, i.e., apparently overconsolidated part, in aggregated sample is almost identical to the slope of unloading line. It is observed that, for the aggregated Abist sample (Fig. 4.38(a)), the slope of unloading line remains unchanged and it is the same for the first unloading-reloading and the final unloading of the sample at the end of compression. In the case of Bioley silt, it is also observed that the slope of the unloading (swelling) line is almost the same in aggregated and reconstituted samples. In this case, however, unloading was performed at the stress level for which the aggregated structure has been already obliterated significantly, as indicated by the convergence of two curves. It is, thus, normal that the two soils have the same behavior on the unloading path at the end of compression. It is difficult to make a firm conclusion about the influence of aggregation on the unloading-reloading slope based only on these results. However, in lack of more experimental results and for sake of simplicity in modeling purposes, any influence of soil structure on the behavior of material during unloading-reloading is assumed to be negligible.

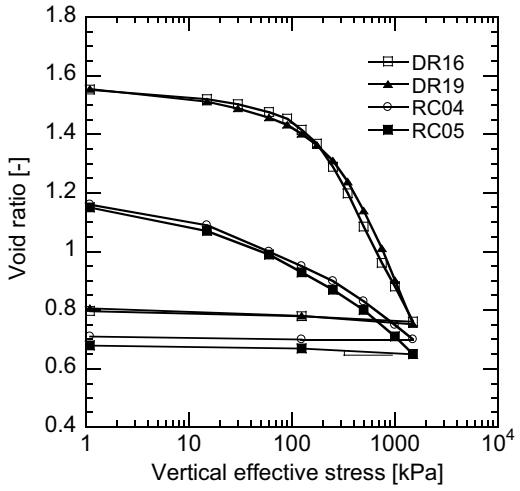


*Figure 4.37:* Comparison of the oedometric curves of dry aggregated aggregated (DR16 & DR19) and reconstituted (RC04 & RC05) Bioley samples

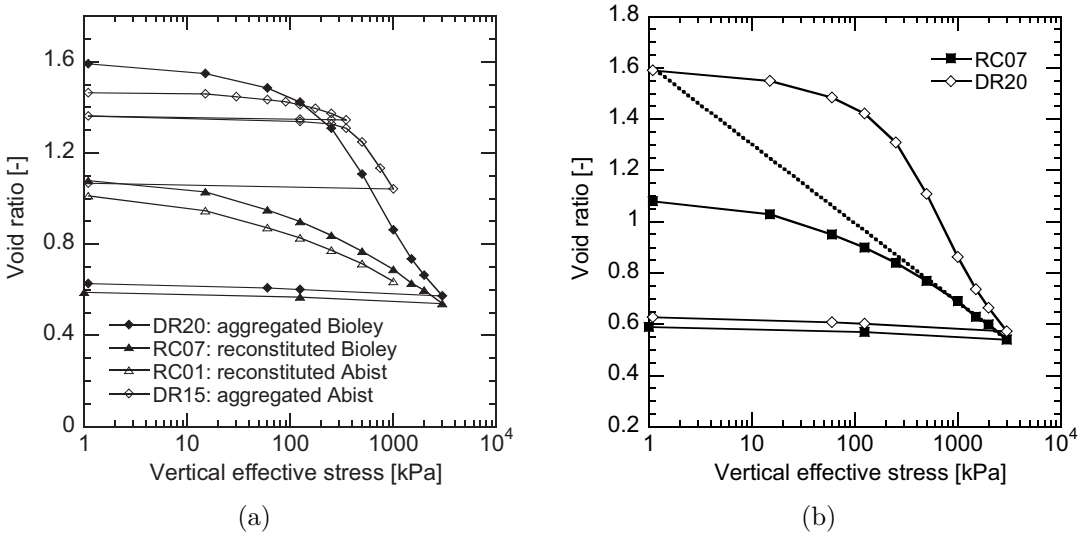


*Figure 4.38:* Comparison of the oedometric curves of dry aggregated and reconstituted samples: (a) aggregated and reconstituted Bioley (DR20 & RC07) and Abist (DR15 & RC01) samples (b) convergence of aggregated (DR20) and reconstituted (RC07) compression curve

Despite the similarity between the swelling index of aggregated and reconstituted samples; slopes of virgin compression in two materials differ strongly.

Figure 4.38(b) illustrates results of tests on aggregated samples of DR20 and reconstituted sample of RC07, where the loading has been continued up to maximum applied stress of 3000 $kPa$. The dotted line in this figure represents the virgin oedometric compression line of reconstituted soil. These results suggest that the compression curves of aggregated and reconstituted samples tend to converge at high values of applied stress. It is observed that the virgin compression line of the reconstituted soil is an asymptote to the compression curve of aggregated soil which is intersecting with the curve at its very beginning.

Similar comparison of results can be made for unsaturated aggregated and reconstituted samples at the same suction. Comparison of these results in terms of effective stress is presented for suction levels of circa 500, 1500 and 3000 $kPa$ in Figure 4.39. As for the dry samples, the unsaturated aggregated samples exhibit higher void ratio in comparison to the reconstituted soil. At the same suction, there is an insignificant difference between the swelling index of aggregated and reconstituted samples. As in dry tests, the virgin compression part of the curves is different for reconstituted and aggregated samples of the same suction. The values of initial tangential compressibility index in aggregated samples is higher that the compressibility index of reconstituted soils.

It is observed that the two curves converge at higher values of effective stress. This evidence is more clear in Figure 4.39(b) where the effective stress has been increased up to about 4000 $kPa$. It is observed that the virgin compression line of the reconstituted soil (dotted line) is an asymptote to the oedometric curve of aggregated sample with an intersection at initial values of effective stress in the very beginning of the curve.

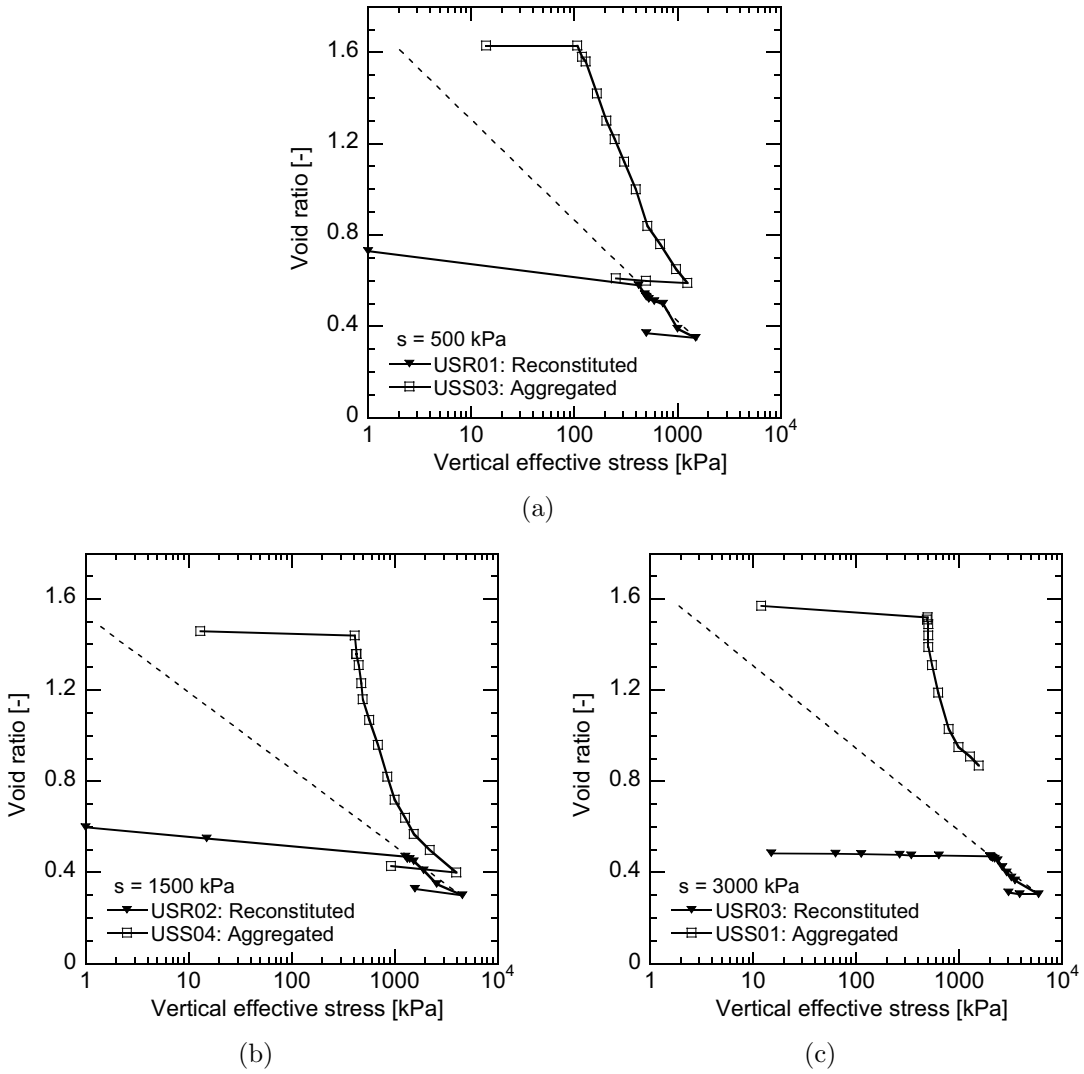


*Figure 4.39:* Comparision of unsaturated oedometer response of aggregated and reconstituted Bioley Silt, (a) $s = 500\ kPa$, (b) $s = 1500\ kPa$, (c) $s = 3000\ kPa$

The virgin oedometric compression curve of aggregated and reconstituted samples at saturated condition could be evaluated using results of soaking tests. Results of oeodmetric soaking of aggregated and reconstituted soils at vertical stress of 1.1 and 125 $kPa$ are respectively depicted in Figures 4.40(a) and 4.40(b). It is observed that, in both cases, the saturation compression curve of samples coincide after soaking.

All the four curves are compared in Figure 4.41. This figure illustrates that the saturated compression curve and the subsequent unloading curve is identical for all the four samples. In other words, the saturated virgin compression curve (and unloading curve) is an intrinsic characteristic of the material which is independent of the initial structure of the soil. When aggregated samples are subjected to consolidation at fully saturated condition, they end up with a state lying on this curve. As previously stated, aggregated structure of the soil is removed at such condition and the soil behaves as a reconstituted soil.

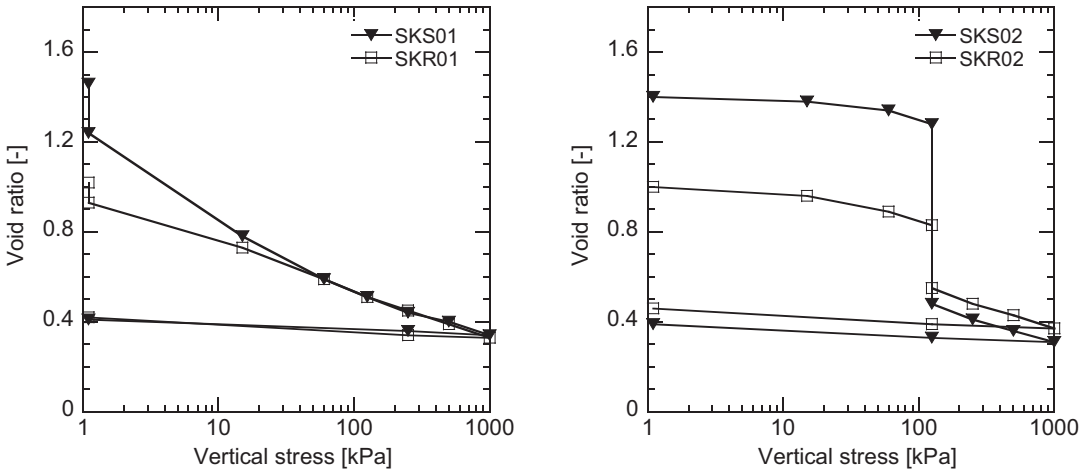


(a) (b)

*Figure 4.40:* comparison between the oedometric soaking of aggregated (SKS) and reconstituted (SKR) Bioley silt under the same vertical stress, (a) Soaking at vertical stress 1.1 $kPa$, (b) Soaking at vertical stress 125 $kPa$

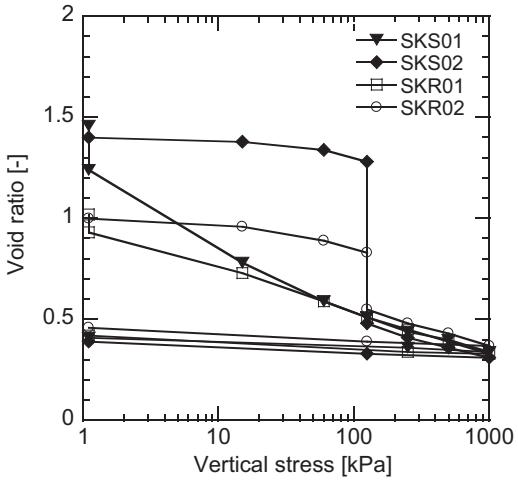


*Figure 4.41:* Comparison between the oedometric soaking of aggregated (SKS) and reconstituted (SKR) Bioley silt

### 4.6.2 Suction effects

Effects of suction variation on the material behavior have been evaluated by comparing the results of tests on samples of same material and soil structure at different suctions.

Results of unsaturated and saturated reconstituted samples are compared in Figure 4.42 in terms of net stresses. It appears that in terms of net stress, the normal consolidation line of unsaturated samples almost coincide with the one of saturated sample.

Depicted in terms of effective stress, the results of reconstituted samples

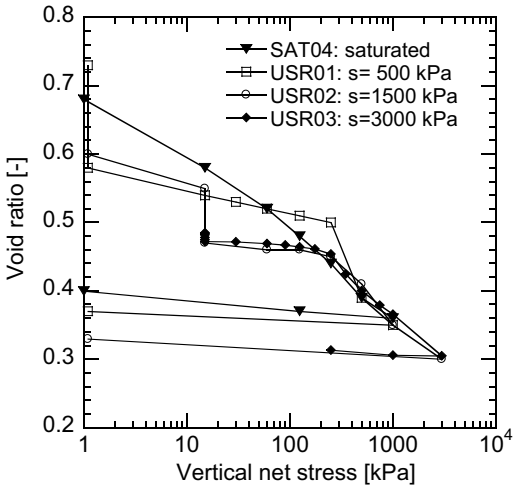


*Figure 4.42:* Comparison of unsaturated oedometer response of reconstituted Bioley Silt in terms of net stress at different suction levels

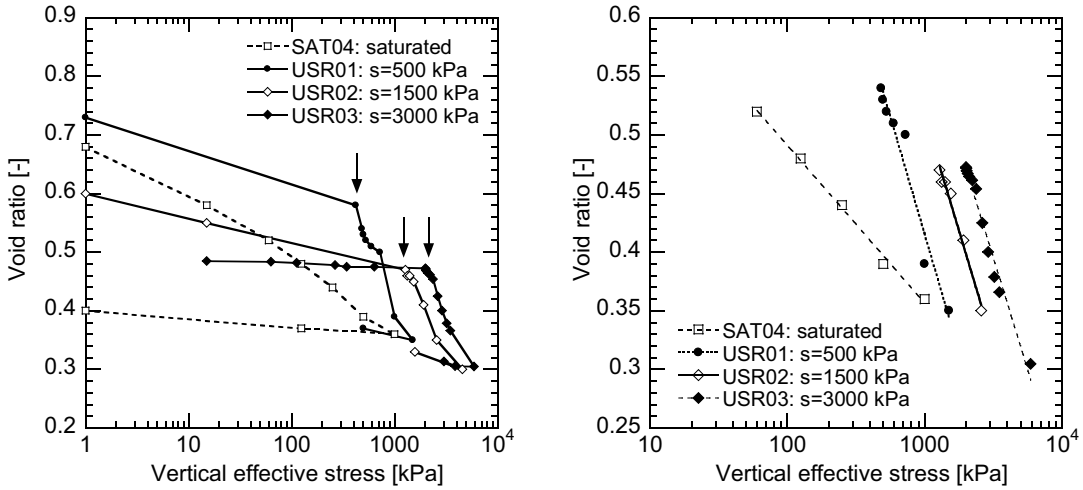


*Figure 4.43:* Comparison of unsaturated oedometer response of reconstituted Bioley Silt in terms of effective stress at different suction levels, (a) apparent preconsolidation stress, (b) tangential compressibility index

can be better compared in Figure 4.43. It is observed that the initial slope of compression curve (due to the suction increase) is higher for samples USR01 and USR02 in comparison with USR03. Due to the lack of intermediate suction steps in the first two tests, it is hard to judge about the slope of the first linear part of these curves. In other word, the total observed deformation at the end of suction increase phase might be a combination of reversible and irreversible deformations which cannot be anymore distinguished in these plots.

Also observed in Figure 4.43(a) is an increase of effective preconsolidation stress with suction for reconstituted samples. As observed in this figure and better illustrated in Figure 4.43(b), the normal consolidation line of reconstituted

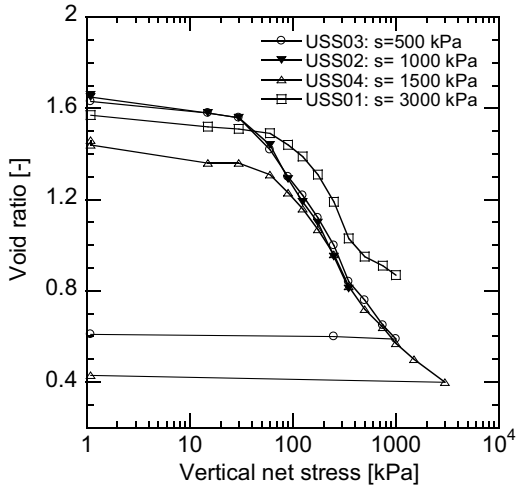


*Figure 4.44:* Comparison of unsaturated oedometer response of aggregated Bioley Silt presented in net stress at different suction levels

soil shifts to the right due to suction increase. This is equivalent to the increase of the effective preconsolidation stress with suction for a soil sample of a given state. Quantitative comparison of the increase in the effective preconsolidation stress of these samples is not directly possible because of the difference in the initial sates of the samples as well as the possible occurrence of irreversible deformations during the loading. Such a comparison needs postulation of yield limits, a key issue which will be addressed in Chapter 6.

Figure 4.43(b) illustrates the normal consolidation compression part of the oedmetric curves for saturated and unsaturated samples. This allows evaluation of suction effects on the slope of the virgin consolidation compression of the samples. A clear increase of this slope is observed when the sate of the sample is changed from saturated to unsaturated. It is, however, difficult to make a distinction between the slope of the curve at two suctions of 500 and 1500 $kPa$.

In order to evaluate the suction effects on the aggregated samples, four unsaturated samples tested at different matric suction of 500 $kPa$ (USS03), 1000 $kPa$ (USS02), 1500 $kPa$ (USS04), and 3000 $kPa$ (USS01) are compared with each other. The oedometeric compression curves of these samples in terms of net stress are plotted in Figure 4.44. It can be observed that the suction-induced deformations at the onset of the tests are small. With the exception of test USR01, the three others appear to coincide in the virgin compression part. The change in net apparent preconsolidation stress is insignificant.

Figure 4.45 presents the oedometric compression curves of aggregated samples in terms of effective stress, depicted for the tangential compressibility (Fig. 4.45(a)) and for the effective apparent preconsolidation stress (Fig. 4.45(b)). These results could be evaluated independent of their initial void ratio when expressed in terms of normalized void ratio with respect to initial void ratio, as plotted in Figure 4.46. It is observed in these figures that the tangential compressibility index of the samples at the onset of yielding increases with suction. In the other word, yielding of the sample is associated with more dramatical deformation at higher values of suction.

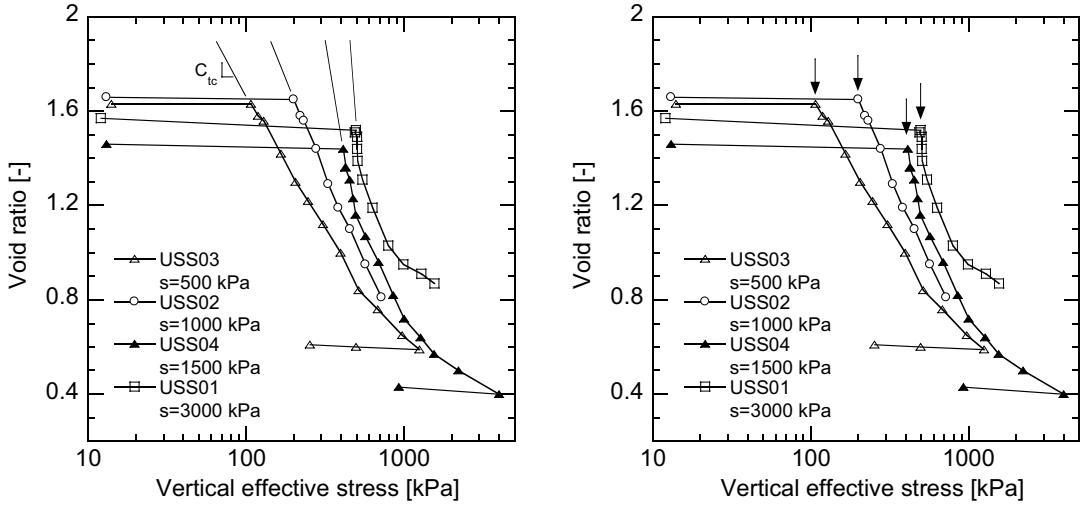


*Figure 4.45:* Comparison of unsaturated oedometer response of aggregated Bioley Silt at different suction levels, (a) tangential compressibility index, (b) apparent preconsolidation stress

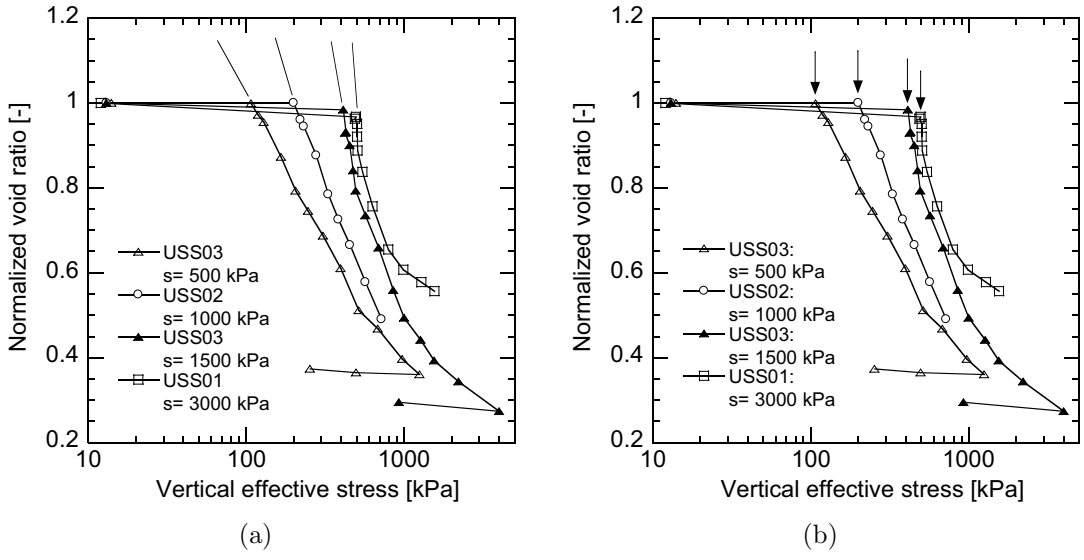


*Figure 4.46:* Comparison of unsaturated oedometer response of aggregated Bioley Silt at different suction levels normalized for the initial void ratio, (a) tangential compressibility index, (b) apparent preconsolidation stress

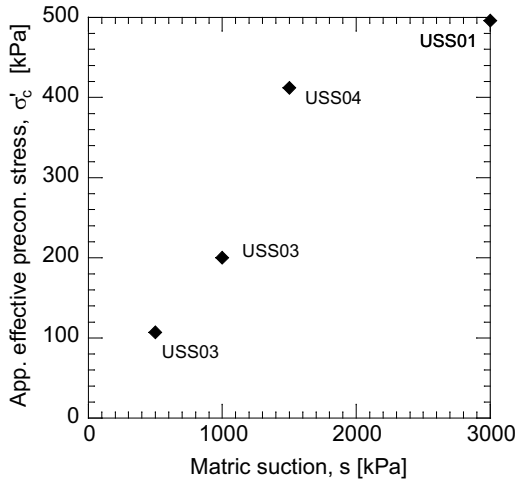


*Figure 4.47:* Increase of apparent effective preconsolidation stress with suction in structured (aggregated) samples

Clear increase in apparent preconsolidation stress can be observed as suction increases. The apparent preconsolidation stress of the aggregated samples could be compared to each other since the initial state of the samples are more or less the same.

Figure 4.47 shows the evolution of the apparent effective preconsolidation stress with suction in these samples. It is seen that this stress increases with suction; starting from 110 $kPa$ in sample USS03 with suction of 500 $kPa$, the apparent effective preconsolidation stress reaches around 500 $kPa$ in test USS01 where the applied suction is 3000 $kPa$.

As previously shown for reconstituted samples, suction has also an increasing effect on the effective preconsolidation stress of these sample. The difference in the increase rate of apparent preconsolidation stress in aggregated and reconstituted samples could be evaluated based on the change in the horizontal separation of the two compression curves with suction (see Fig. 4.39).

For this purpose, consider the schematic representation of compression curve of aggregated (structured) and reconstituted samples of the same suction in Figure 4.48(a). The intersection of the compression curve of aggregated soil with the NCL of reconstituted soil (point I in Fig. 4.48(a)) represents a possible state of the reconstituted soil which shares the initial state with the aggregated soil.

The ratio of the initial apparent preconsolidation of the aggregated soil over the effective stress corresponding to this point ($\sigma'_{vc}/\sigma'^{*}_{vc}$) are plotted versus the suction for the three pairs of aggregated and reconstituted samples in Figure 4.48(b). Increase of this ratio with suction means that the increase rate of effective apparent preconsolidation with suction is higher in aggregated samples than in reconstituted ones.

This observation indicates the additional effects of suction in aggregated (structured) soil, and is of great importance for constitutive modeling.

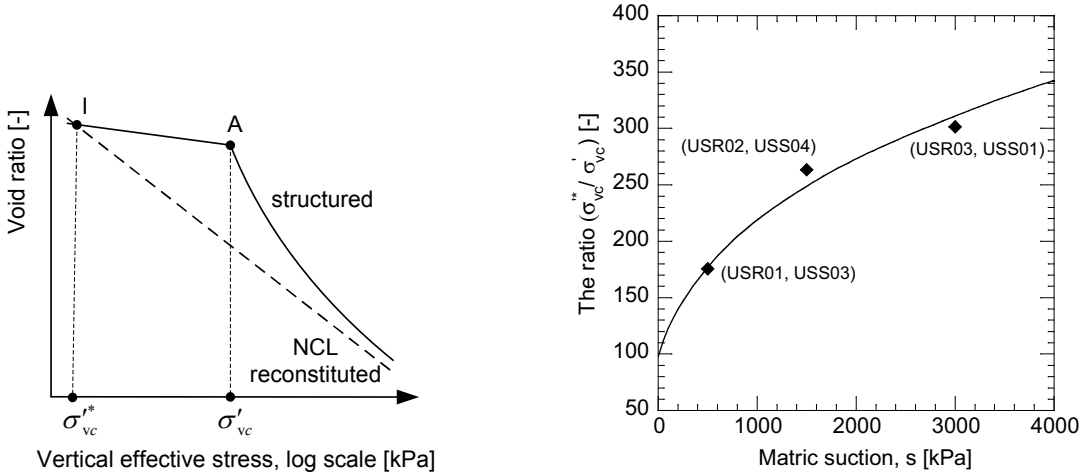


(a) (b)

*Figure 4.48:* Influence of suction on the effective aapparent preconsolidation stress in structured (aggregated) and reconstituted samples: (a) schematric representation of compression curves, (b) evolution of the ratio $\sigma'^{*}_{vc}/\sigma'_{vc}$ with suction

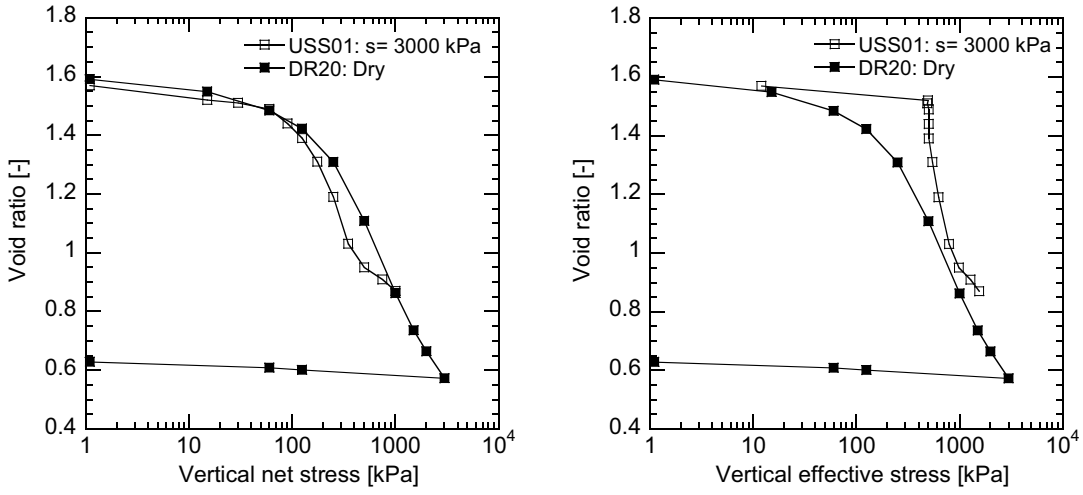


(a) (b)

*Figure 4.49:* Dry and unsaturated ($s$=3000 $kPa$) response of aggregated Bioley Silt, (a) net stress, (b) effective stress

In order to compare the behavior of wet and dry samples, sample USS01 with high suction value of 3000 $kPa$ is compared with dry sample DR20 (Fig. 4.49). It is observed in Figure 4.49(a), where results are plotted in terms of net stress, that unsaturated curve is located to the left side of the dry curve. The apparent preconsolidation stress in terms of net stress is higher for the dry sample. In terms of net stress, this evidence is in agreement with increase of apparent preconsolidation with suction, i.e., dry soil is considered as an extreme state with a high suction. However, different interpretation should be made when the results

are presented in terms of effective stress. It is observed in Figure 4.49(b) that dry oedometric curve is located to the left side of the unsaturated curve. The apparent effective preconsolidation stress as well as the tangential compressibility index of the dry sample is lower that those of the unsaturated sample. With degree of saturation being zero in dry sample, the effective stress should be theoretically the same as in saturated sample. However it was already observed (Sec. 4.4.4.2) that despite the similarity in effective stress, saturated and effective samples behave differently; therefore, direct comparison of behaviors becomes rather complex. Such a difference in the behavior of dry and saturated soils has been already reported by Geiser (1999). The observed differences should be described with respect to the inter-particle forces and the physical interpretation of effective stress in soils.

## 4.7 Summary of results

The experimental results presented in the preceding sections could be classified in three main parts including the evidences (i) merely related to soil structure effects at constant suction, (ii) related to the intrinsic suction effects in reconstituted soil regardless of the soil structure, and (iii) related to the combined effects of soil structure and suction on the material behavior.

On the basis of this classification, the main experimental results of this chapter could be summarized as follows.

**Soil structure effects:** These effects are evaluated using the experimental results of aggregated (structured) samples and their comparison with reconstituted soils at the same suction.

1. There is an initial stiff behavior followed by yielding in oedometric compression of normally consolidated aggregated samples. The yield limit is referred to as *apparent preconsolidation stress*, which is a function of not only stress state and stress history but also soil structure.
2. The initial apparent preconsolidation stress is identical for intact aggregated soil samples of the same structure.
3. In the aggregated samples, slope of the initial apparent preconsolidated compression is the same as that of the unloading at the end of the test. This slope is identical to the swelling index of reconstituted soil. This leads to the idea that slope of unloading-reloading is not affected by soil structure. This conclusion is hypothetical and needs further evaluation by unloading-reloading of the sample not only at the end of the test by also in the intermediate steps.
4. Beyond the initial apparent preconsolidation stress, virgin compression curve of aggregated samples is non-linear with an initial tangential slope called *tangential compressibility index*.
5. The tangential compressibility index of aggregated samples is higher than the compressibility index of reconstituted soil at the same suction.
6. At a given value of applied stress, a sample of aggregated soil has a higher

void ratio than a sample of corresponding reconstituted soil, and the compression curve of aggregated soil is located to the right side of the reconstituted compression curve at the same suction.
7. The compression curves of aggregated and reconstituted soils at the same suction tend to converge at higher values of applied effective stress.
8. For a given matric suction, the virgin compression line of the reconstituted soil is an asymptote to the compression curve of aggregated soil intersecting the curve at the initial virgin state.
9. There is a strong difference between compression behavior of dry and saturated samples of aggregated soil. However, the theoretical effective stress is the same for an applied total stress.
10. Aggregated samples subjected to a combination of wetting and mechanical loading in soaking tests appeared to loose their aggregated structure and to exhibit a behavior analogous to reconstituted soils.

**Intrinsic suction effects:** These effects correspond to the effects of suction variation in reconstituted soils and are evaluated based on the results of unsaturated tests of reconstituted samples.

11. Effective apparent preconsolidation stress in reconstituted samples increase with suction.
12. Slope of normal consolidation line in the effective stress plane, namely compressibility index, increases from saturated to unsaturated samples while it remains almost constant for within the unsaturated samples.
13. Suction effect on the swelling index is insignificant for reconstituted soil.

**Combined effects of suction and soil structure:** These effects are evaluated by comparing the the results of aggregated (structured) and reconstituted samples at different suctions.

14. Tangential compressibility index increases with suction. Higher the matric suction in aggregated samples, more dramatic the yielding.
15. Suction effect on the swelling index is insignificant for aggregated soil.
16. Initial effective apparent preconsolidation stress decreases as a result of wetting. In the other word, samples with higher matric suction exhibit higher values of effective apparent preconsolidation stress.
17. The horizontal separation between the compression curve of aggregated soils and intrinsic normal consolidation line in the oedometric space $e - \log \sigma'_v$ increases with suction. Or, to put in in other way, the increase of effective preconsolidation pressure with suction is higher for aggregated soils rather than reconstituted soil.

The experimental evidences presented in this chapter and summarized above provided a list of features that an appropriate constitutive model of unsaturated aggregated soil should be able to address. The relation between these features and the soil structure at smaller scales will be evaluated in the next chapter. The whole set of experimental evidences, then, will used in Chapter 6 to propose the constitutive model.

# Chapter 5

# Experimental study of soil structure

This chapter presents the description of the experimental study of soil structure, carried out using a combination of different methods. First, the objectives and the choice of experimental approaches are presented. It is followed by a brief description of the methods including the theoretical backgrounds for each method. Then, results of each series of experiments and their interpretation are presented separately. Finally, the results are compared and the main experimental evidence are summarized at the end. Experimental results of this part together with the results presented in the preceding chapter provide a multi-scale experimental base for constitutive modeling of the mechanical behavior of the material.

## 5.1 Objectives and methods

### 5.1.1 Objectives and experimental approaches

The experimental study of soil structure in the present work is aimed to (i) characterize the fabric of aggregated soil and compare it with reconstituted soil, (ii) evaluate the influence of mechanical loading and suction variation on the soil fabric, and (iii) to quantify the evolution of soil structure during the mechanical loading or drying-wetting process, and relate it to the macroscopic state of the material.

An appropriate choice of the method for study of soil structure should be made with respect to the type of material and the kind of desired information about the structure. As proposed by Mitchell and Soga (2005), several methods might be used in order to obtain information of more than one type or level of detail. In the present work, a combination of three different methods has been used to provide the possibility of rigorous evaluation of soil structure at different scales:

1. Mercury intrusion porosimetry (MIP) is used to determine the pores size distribution of soil samples.

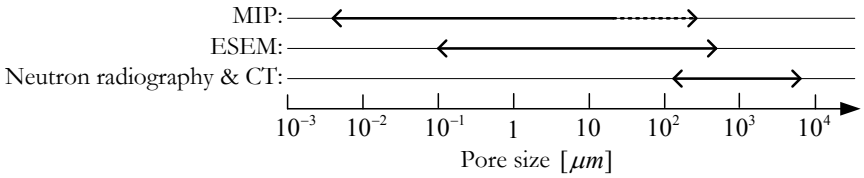


*Figure 5.1:* Pore size range examined by different methods in the present study

2. Environmental scanning electron microscopy (ESEM) is used to make direct observation of the soil fabric.
3. Neutron radiography and computed tomography (CT), with the help of which relation between the macroscopic deformation and evolution of soil structure due to external loading has been evaluated and quantified.

These methods differ in various aspects. Mainly, the level of details and the scale at which the pores and particles could be evaluated are different. The typical ranges of the pores examined by these methods are shown in Figure 5.1 for the present study. There is a small overlap between the scales covered by neutron tomography in one side and, MIP and ESEM in the other side. The MIP and ESEM are used to evaluate the microstructure of soils at the level of pores within and in the vicinity of the aggregates. However, neutron tomography is employed to examine the macropores between the aggregates in large oedometric samples. These methods and their theoretical backgrounds are briefly described in the following sections.

### 5.1.2 Mercury intrusion porosimetry

The Mercury Intrusion Porosimetry technique, abbreviated as MIP, provides a quantitative description of the soil porosity, and, in particular, the distribution of pore sizes within the soil mass. Theoretical background of the method originates in the work of Washburn (1921) who obtained a pore size distribution from pressure-volume data for mercury penetrating into a porous body.

The MIP method is based on the principle that a non-wetting fluid, which is one whose contact angle with a particular solid is greater than 90 degrees, will not intrude the pores of a porous body unless it is forced by an applied pressure. In the MIP technique, air is the wetting fluid and mercury is the non-wetting fluid since it behaves as a non-wetting liquid toward most substances.

In the MIP test, a dry porous sample is placed in a small holder (dilatometer), and under vacuum condition, the holder is filled with mercury. Due to very low residual pressure, mercury surround the sample without entering the pores. During the experiment, mercury is forced to enter into the pores by applying a controlled increasing pressure and the penetrated volume of mercury is detected for each pressure increment. The decreasing volume of mercury in the sample holder represents the pore volume.

In a porous body, the surface tension forces are opposed to the penetration of non-wetting liquids. The pressure applied to mercury compensates the pressure difference over the mercury meniscus in the porous body. This pressure is inversely proportional to the meniscus curvature radius. Assuming that soil pores

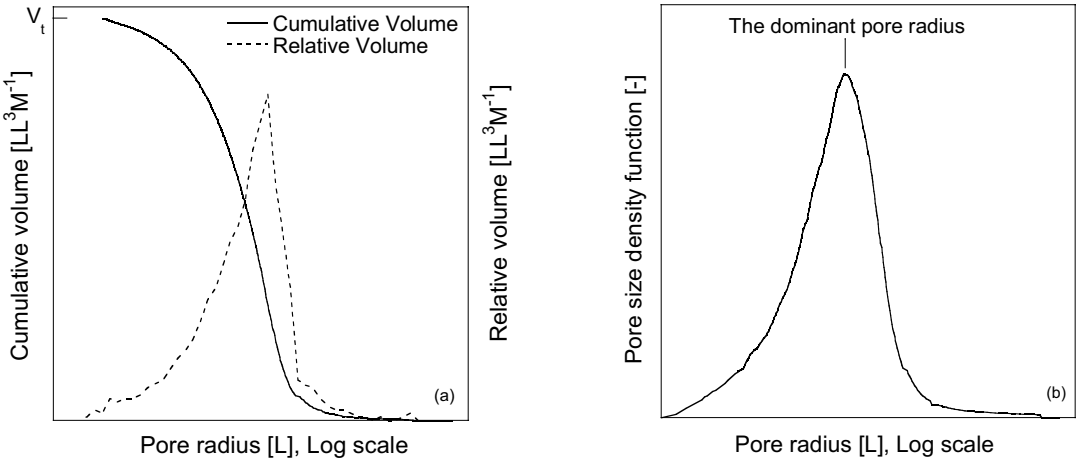


*Figure 5.2:* Schematic representation of MIP results

are cylindrical flow channels, Laplace's equation, known also as Washburn's equation (Washburn, 1921), is used to determine the pore radius associated with each mercury pressure increment (as in Eq. 2.3):

$$r_p = \frac{2T_s \cos\theta}{p} \tag{5.1}$$

where $r_p$ is the entrance pore radius and $\theta$ is the contact angle of fluid interface to solid (140 degrees is an average value for mercury-air interface as suggested by Penumadu and Dean (2000)).

Figure 5.2 depicts the typical form of the curves representing the MIP results in this study. The information obtained from the MIP tests are presented here in three forms: *the cumulative volume*, *the relative volume* and *the pore size density function*.

*The cumulative volume* of mercury injected into the sample is obtained as a function of the equivalent pore radius. The cumulated volume is often expressed per unit mass of the sample (i.e. with a unit of $mm^3g^{-1}$). The maximum cumulated volume, $V_t$, in Figure 5.2 is a measure of the porosity of the sample. Usually, due to the wide range of pore radii, i.e. several orders of magnitude, a logarithmic scale is used for the pore radii.

Results of MIP tests could also be presented in terms of *relative intruded volume* corresponding to the increments of pressure increase (or pore radius). This provides a tool to compare the volume fraction of pores with different sizes within the material.

However, It is customary to interpret the MIP data in terms of *Pore size Density Function* (Juang and Holtz, 1986). The pore size density function is the derivative of the cumulated intruded volume with respect to the logarithm of the entrance pore radius:

$$f(\log r_i) = \frac{\Delta V_i}{\Delta(\log r)} \tag{5.2}$$

where $\Delta V_i$ is the injected mercury volume at a given pressure increment corresponding to pores having a radius of $r_i \pm (\Delta \log r)/2$. Plot of pore size density

function versus the pore radius represents the pore size distribution, abreviated here as PSD. Using the pore size density function, the dominant pore radius within the material can be determined, as depicted in Figure 5.2.

It should be pointed out that determination of PSD with the MIP test is influenced by several experimental side effects, such as pore entrapment, pore neck, etc. As a consequence, the measured PSD might differ from the real PSD of the tested soil and the pore radius associated with each pressure increment is only an entrance pore radius. The volume of entrapped pores could be assessed by release of applied pressure after reaching the maximum pressure. As a simplification, the term *entrance* is omitted when dealing with pore radii calculated from MIP data.

The MIP method has been successfully used to study the evolution of soil fabric due to the mechanical loading and suction variations (Cuisinier and Laloui, 2004; Griffiths and Joshi, 1990; Gens et al., 1995; Al-Mukhtar et al., 1996; Delage et al., 1996).

### 5.1.3 Environmental scanning electron microscopy

Direct observation of the spatial arrangement, size and shape of pores and particles is a useful method to achieve a better understanding of the soil fabric. A common technique is the scanning electron microscopy (SEM). The technique has been extensively employed to study the structure of soil (Collins and McGown, 1974; Delage and Lefebvre, 1984; Al-Mukhtar, 1995; Vulliet, 1986). Since the microscope provides large levels of magnitude, up to 20000 times larger, with a high areal resolution, it is possible with this technique to make observations at the very small scales down to the soil particles (0.1 $\mu$m to 1 $\mu$m). Information provided by this technique are mainly qualitative and therefore some authors used this method as a supplement to mercury intrusion porosimetry (Delage and Lefebvre, 1984; Monroy, 2005)

One drawback of the SEM is that it is normally not possible to examine samples that produce any significant amount of vapor when placed in a vacuum. Because of this limitation, soil samples must be dried, using non-destructive drying methods such as freeze-drying, before observation can be made. The surface of insulator sample needs to be coated with a conductive material, usually gold-palladium. No change in the sample condition is allowed during the observations made by these types of equipments. Therefore, these equipments cannot be used to make a continuous observation of drying or wetting process in soil samples.

The limitation of SEM have been overcome by in the environmental scanning electron microscope (ESEM). In the ESEM, material samples do not need to be desiccated and coated with conductive element, and thus they can be examined at their natural state and their original characteristics may be preserved for further testing or manipulation. Moreover, ESEM provides the possibility of dynamically altering the sample environment and following the deliberate hydration and dehydration of the sample. This is done by changing the relative humidity in the chamber by means of a combined change in temperature and

water vapor pressure. For instance, the combination of low temperature (e.g., 4°C) and high water vapor pressure (e.g., 6.1 Torr, 1 torr ≈ 133 Pa) permits achieving 100% relative humidity ($RH$) at the sample surface.

Due to the flexible testing conditions provided by ESEM, this method could appropriately finds its application in the study of the structure of geomaterials.

### 5.1.4 Neutron radiography and tomography

Neutron radiography is a non-destructive method, which together with image analysis, provides a powerful tool for the experimental study of soil structure (Degueldre et al., 1996). Since, in general, the sample is not permanently changed by the radiation, radiographic techniques are considered as non-destructive testing methods. In the case of geomaterials, the non-destructive aspect is limited by the necessity of non-in-situ testing (Pleinert and Degueldre, 1995; Degueldre et al., 1996).

Radiography is based on the application of the universal law of radiation passing through matter. Neutron radiography is, principally, similar to X-ray radiography and the difference is in the source of radiation. The efficiency of the method is mainly dependent on the power and quality of the source.

In general, neutron radiography and tomography involve three steps: (i) radiographic measurement, (ii) extraction of data from the detector, and (iii) further processing of the information.

In neutron radiography, a collimated neutron beam is transmitted through the sample. Neutrons can be absorbed, scattered, or pass undisturbed through the sample. Since different materials have different attenuation coefficients, the transmitted neutron beam carries the information about the mass and thickness of the neutron-attenuating components. The intensity of the neutron flux behind the sample is detected by a neutron area detector.

The radiography data provides two-dimensional (2D) information about the sample. Neutron Tomography takes this a step further and entails rotating the sample in the beam and recording multiple 2D images through an angular range of 180 degrees. From the data set, a three-dimensional (3D) representation through the object can be reconstructed using the computed tomography (CT) algorithms. It is possible to use image analysis to measure different structural properties of the material such as porosity and the pore size.

In recent years, both X-ray and neutron radiography and tomography had found their applications in soil science and geomaterials (see Sec. 2.5.1). Compared with X-ray, neutron radiography and tomography have been less used for geomaterials. This should be due to the facility limitations and higher experimental costs. The main advantage of neutron radiography to X-ray is its high sensitivity to hydrogen-containing materials. The technique has been successfully applied to various problems requiring information on water content and water transport in soils (Pleinert and Degueldre, 1995). Neutron radiography and tomography has been also used by Carminati (2006) in the joint study of the present research project to evaluate the water exchange between the aggregates and flow through series of aggregates.

## 5.2 Fabric evaluation using MIP and ESEM

### 5.2.1 Sample preparation

The main concern in the MIP and ESEM tests was first, to evaluate the micro-structure of aggregated soils when fully saturated after a soaking test, and secondly to assess the difference between the micro-structure of aggregated and reconstituted samples at the same stress state in the oedometric compression.

Eight specimens were examined for their pore size distribution (PSD) by MIP, of which six have been evaluated by ESEM observations at constant or varying relative humidity ($RH$). The specimens are listed in Table 5.1 and the conditions at which they were prepared are illustrated in Figure 5.3.

The first specimen (AGG) was a single dry aggregate of Bioley silt and it was tested to estimate the porosity of aggregates used in this study. The seven other specimens were trimmed out of the samples of reconstituted (PR) and aggregated (PS) Bioley silt subjected to different conditions of saturation and vertical stress in the oedometer cell. The saturated samples (PR2, PS3, PS4) were obtained by simple soaking of dry samples in conventional oedometer cells and the unsaturated samples (PS1, PS2, PR1, PR3) were conditioned in the osmotic oedometer cell.

Both soaking tests and unsaturated tests were carried out in the same way as described in the previous chapter with the exception that the initial height in unsaturated sample was selected to be about 15 $mm$ instead of 35 $mm$ in order to reduce the required time for suction equilibrium. During the oedometric loading, deformation of the sample has been monitored to obtain the porosity at the end of the loading.

*Table 5.1:* Specimens examined by MIP and ESEM

| **specimen** | AGG | PS1 | PS2 | PS3 | PS4 | PR1 | PR2 | PR3 |
|---|---|---|---|---|---|---|---|---|
| **MIP** | ✓ | ✓ | ✓ | ✓ | ✓ | ✓ | ✓ | ✓ |
| **ESEM** ($RH = cte$) | ✓ | | ✓ | ✓ | ✓ | | ✓ | ✓ |
| **ESEM** ($RH \neq cte$) | ✓ | | | | | | ✓ | |

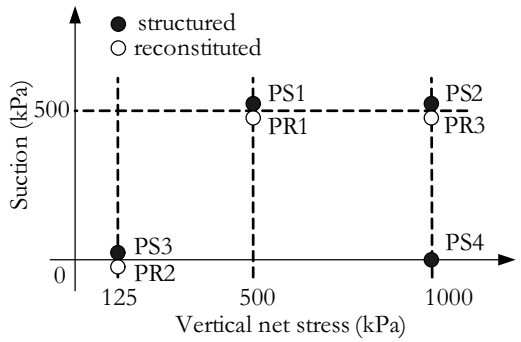


*Figure 5.3:* Samples of Bioley silt tested for PSD determination using MIP technique

At equilibrium, the soil sample was removed from the cell and three identical specimens of about $1 \times 1 \times 1\,cm$ were carefully trimmed out of it (named, e.g. PR1a, PR1b, PR1c), of which one or two (depending on the case) were used for MIP and one for ESEM. The rest of the oedometric soil sample was used for measurement of the water content. Specimens were then placed in a small closed glass containers covered with plastic film to maintain the original water content during the time they were transfered from LMS to the dehydration and MIP facility (less than 2 hours).

### 5.2.2 Description of MIP tests

The MIP tests were carried out in the Laboratory of Construction Materials, LMC, at EPFL. The MIP method implies all the pore water and vapour in the specimen to be removed before the test. Therefore prior to the PSD determination, the samples have been dried using freeze-drying method at LMC.

In this method, the pore space can be dried without the risk of being influenced by the induced surface tension forces at the air-water interface. Compared with air drying and other drying methods, the freeze drying has been reported to better preserve the original soil structure during the dehydration process (Delage and Lefebvre, 1984; Gillott, 1973; Vulliet, 1986).

At LMC, the samples were placed in separate small plastic bags and the bags were directly placed in a container of liquid nitrogen at the temperature of $-196°C$. The bags were kept in the closed container for about 2 hours. Frozen samples were then placed in a freeze-drier for a period of 24 hours. This allowed the vacuum drying of frozen samples by sublimation.

Efficiency of this method in removing the soil humidity was verified by measurement of water content for one of the three identical specimens of PR1. After freeze drying, the samples were placed in an oven at the temperature of $-105°C$ for 4 days. No difference in the mass of the specimen was observed before and after the oven drying indicating that all the water in the specimen had been already removed during the freeze drying.

The MIP measurements at LMC were carried out using two operating units from Thermo Electron Corporations: a low pressure (Pascal 140) and a high pressure (Pascal 440) unit. The low-pressure unit has a dual role, i.e., it prepares the specimen and the dilatometer for the analysis and carries out low-pressure porosimetry measurements.

The small soil specimen is placed in the dilatometer and inserted into the low pressure unit. The air is evacuated and the mercury is allowed to surround the specimen under vacuum condition. Incremental increasing pressure is then applied to the mercury and the intruded volume is recorded automatically by the unit. The pressure range for the low-pressure unit is from 0.1 to 400 $kPa$ with the pressure resolution of 0.1 $kPa$. This corresponds to pore radii between 1.9 and 58 $\mu m$. At the end of measurements on the low-pressure unit, the dilatometer containing the specimen and mercury is transfered onto the high pressure unit where the pressure is increased up to 400 $MPa$ corresponding to a pore radius of 1.8 $nm$.

In the case of materials with large pores, an optional Ultra-macropore kit could be used only in the low pressure unit allowing to detect pores with a radius of up to about 300 $\mu m$. However, a specimen tested with the Ultra-macropore kit could not be used for measurements in the high-pressure unit. This option was used only for two aggregated samples of PS1b and PS2b.

As mentioned in Section 5.1.1, the maximum pore size which could be detected by MIP method is still far from the large macropores in the loose aggregated soil samples of this study (with inter-aggregate pore size of about 1 or 2 $mm$). Therefore, the selected specimens for MIP tests are those in which large inter-aggregate pores are, to some extend, closed due to compaction or saturation. Nevertheless, it should be noted for that, depending on the case, there might be a portion of macropore volume which remains undetected in the analysis of MIP results.

Soil specimens in MIP method are specimens with a definite geometrical boundary. When dealing with such samples, a possible concern could be the effect of applied mercury pressure on the structure of the material. In the other word, the concern would be the compressibility effect of mercury on the soil sample (Penumadu and Dean, 2000). The mercury surrounding the specimen provides a confining pressure on the soil. This pressure, acting as a mechanical load, might change the soil structure. However, these effects might be significant only in the early stages where the pores are mostly empty. As the test goes on, the pores are progressively filled with mercury of the same pressure; hence, the difference between internal and external pressure of the soil specimen reduces. Although these effects are inevitable in the MIP method, they could be neglected knowing that the applied pressures in the early stages are low.

### 5.2.3 MIP Results

#### 5.2.3.1 Porosity of specimens

The total cumulative volume ($mm^3g^{-1}$), when divided by the specific volume of the solid particles (370 $mm^3g^{-1}$ for Bioley silt), gives the porosity of the sample which is called here *MIP-based* porosity.

Results of MIP tests for sample of dry Bioley aggregate, AGG, are presented in Figure 5.4. The dominant pore radius is 0.073 $\mu m$ and the total intruded volume is 105 $mm^3g^{-1}$ corresponding to a MIP-based porosity of 22.2%. These values characterize an aggregate as a dense packing of particles with low values of pores and small pore sizes. However, in most of the tested aggregates, larger surface pores could be observed even with naked eye. It seems that the MIP method was unable of examining those larger pores, either because of their size or because of their connectivity with the aggregate surface boundary.

The MIP-based values of void ratio for the samples of series PR and PS are compared in Figure 5.5 with the corresponding values calculated using direct measurements of deformation in the oedometer cell. With the exception of PR3, all samples are reasonably placed around the 1:1 line, most of them being located below this line.

The difference between the directly measured void ratio and the one derived

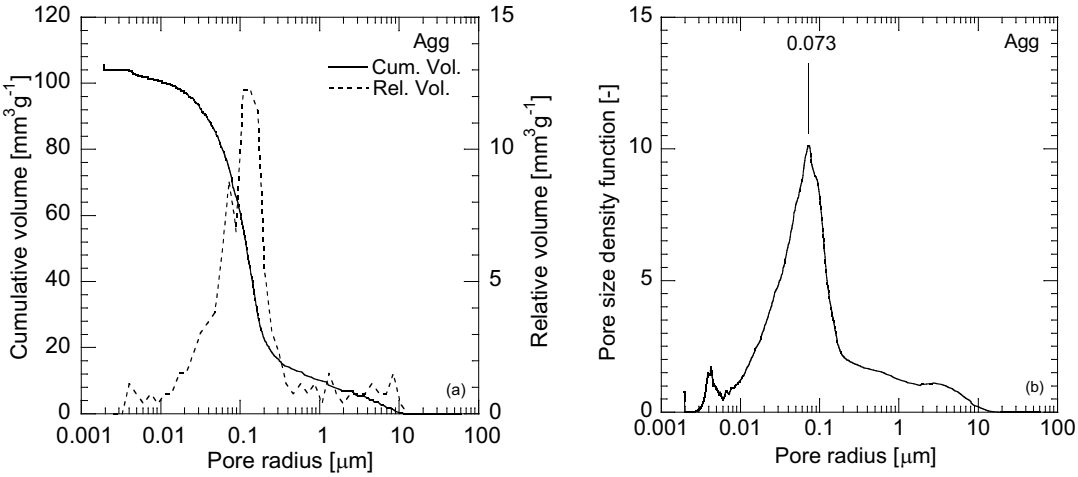


*Figure 5.4:* MIP results for dry aggregate of Bioley silt (AGG)

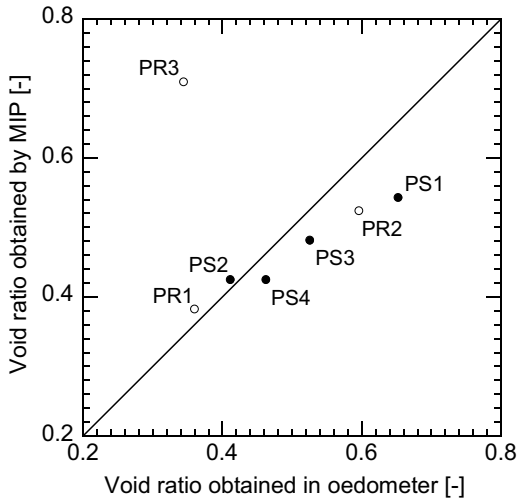


*Figure 5.5:* Comparison of the void ratio obtained by MIP and direct measurements

from MIP measurements should be ascribed to the limitation of MIP in detecting very large, very small and entrapped pores. Therefore, the MIP method is usually expected to give lower values of porosity than the real porosity of the material. The discrepancy in the result of sample PR3 is believed to be due to the technical or operational errors during the measurements which leads to unreliable PSD results.

#### 5.2.3.2 Unsaturated aggregated samples

Results of standard MIP tests for two unsaturated samples PS1 and PS2 are presented in Figures 5.6(a)-(b) and 5.7(a)-(b) respectively.

As expected, the total intruded volume for sample PS2 subjected to vertical stress of 1000 $kPa$ is lower than that for PS1 which has been compressed only to 500 $kPa$. The pore size density function in both cases exhibits a cut-off at its right limit (large pores), while at the left end (smallest pores), it smoothly

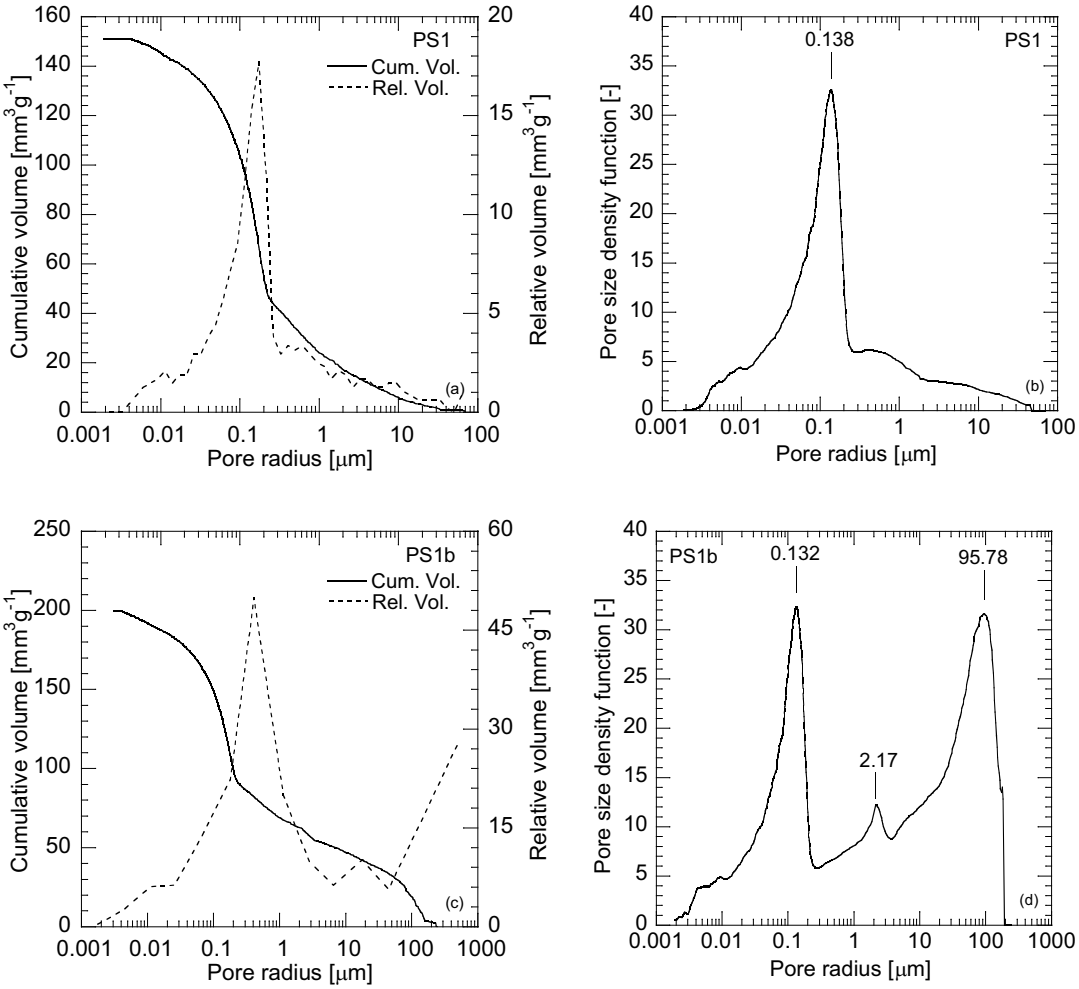


*Figure 5.6:* MIP results for sample PS1: (a)-(b) with standard option, (c)-(d) with Ultra-macropore option

reduces to zero. The cut-off at the right end is imposed by the maximum detectable pore size in the actual configuration of the test.

Accordingly, evidence of a cut-off at the right end of PSD curve is interpreted here as an indication of the possible presence of larger pores in the sample. Instead, a PSD with a smooth decline to zero at the right end represents a sample with pores entirely lying within the range of detected pore size.

For further assessment of larger pores, the Ultra-macropore kit was used in the low-pressure unit. The results were then combined with the high-pressure measurements to obtain the PSD in a continuous range. The results, named as PS1b and PS2b, are presented in Figures 5.6(c)-(d) and 5.7(c)-(d) for PS1 and PS2 respectively.

Using the ultra-macropore option instead of standard option, the total intruded volume for sample PS1 has increased from the value of circa 155 $mm^3g^{-1}$ to about 200 $mm^3g^{-1}$. This increase indicates the presence of a significant volume of large pores that could be detected only with ultra-macropores option. The PSD of sample PS1 in Figure 5.6(d) shows a bi-modal distribution with the dominant pore radius corresponding to 0.132 $\mu m$ and 95.78 $\mu m$.

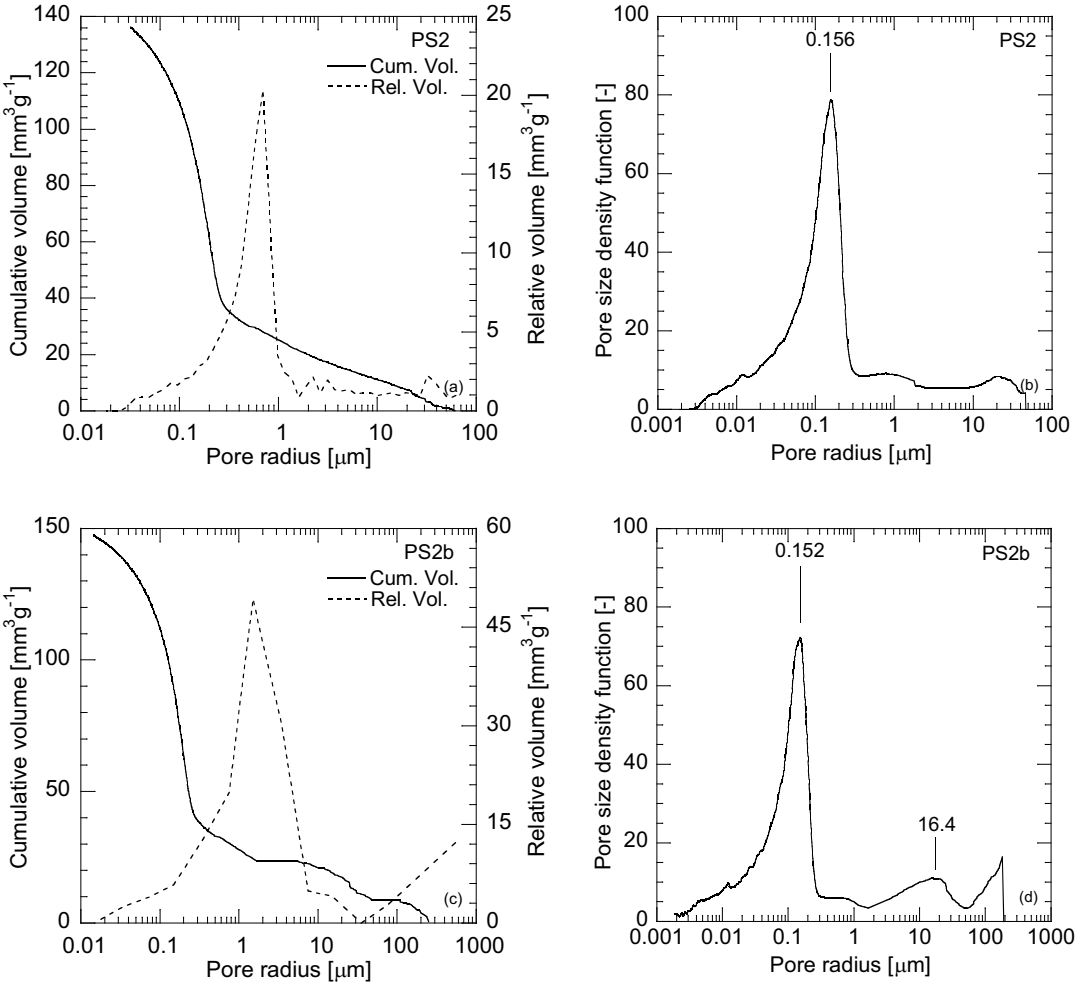


*Figure 5.7:* MIP results for sample PS2: (a)-(b) with standard option, (c)-(d) with Ultra-macropore option

A low intensity peak corresponding to the pore radius of 2.17 $\mu m$ is observed in between the two main peaks. The PSD curve again shows a cut-off at the right end.

The peak on the left (0.132 $\mu m$) corresponds to the most dominant size of micropores. Although the right side peak indicates the presence of larger pores in the specimen, it represents only a subset of the macropores as defined in the present study (inter-aggregate pores).

The cut-off in PSD shows that there are still some undetected larger pores in the specimen. Since the specimen has been compacted to the vertical net stress of 500 $kPa$ at which, normally, an important part of macropores are closed, it is not expected to have a dominant large pore size in the range of undetected pore size.

In the case of PS2 (Fig. 5.7(d)), in addition to the dominant pore radius of 0.156 $\mu m$, a low intensity peak corresponding to pore radius of 16.4 $\mu m$ can be also observed. As in PS1, the PSD of this sample also shows a cut-off at the right end with the difference that the slope of the curve is positive at the point of cut-off.

#### 5.2.3.3 Aggregated samples after soaking

Figure 5.8 depicts the PSD of sample PS3 soaked at the vertical stress of 125 $kPa$. These results show a single mode PSD with the most dominant pore radius of 0.281 $\mu m$. A low intensity peak corresponding to the pore radius of about 3.5 $\mu m$ can be also observed in this figure.

A slight cut-off phenomenon could be observed at the pore radius of about 50 $\mu m$ corresponding to the maximum detectable pore size by the standard MIP test. As mentioned previously, this cut-off might reflect the possible presence of some undetected larger pores, even if no indication of a dominant large pore size peak could be observed.

Figure 5.9 illustrates the results of sample PS4 corresponding to the aggregated sample soaked at the vertical stress of 1000 $kPa$. The sample represents a smooth PSD with a single dominant pore radius corresponding to 0.161 $\mu m$.

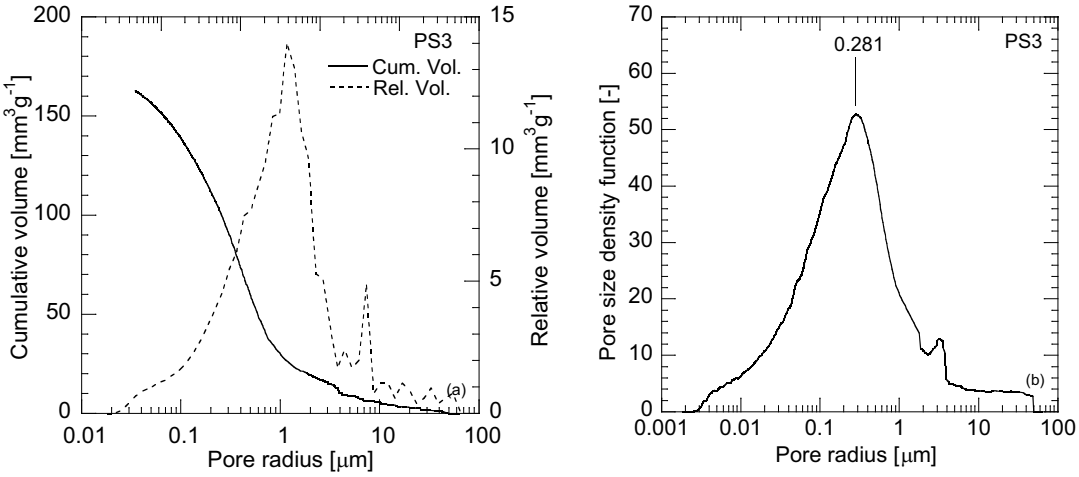


*Figure 5.8:* MIP results for sample PS3

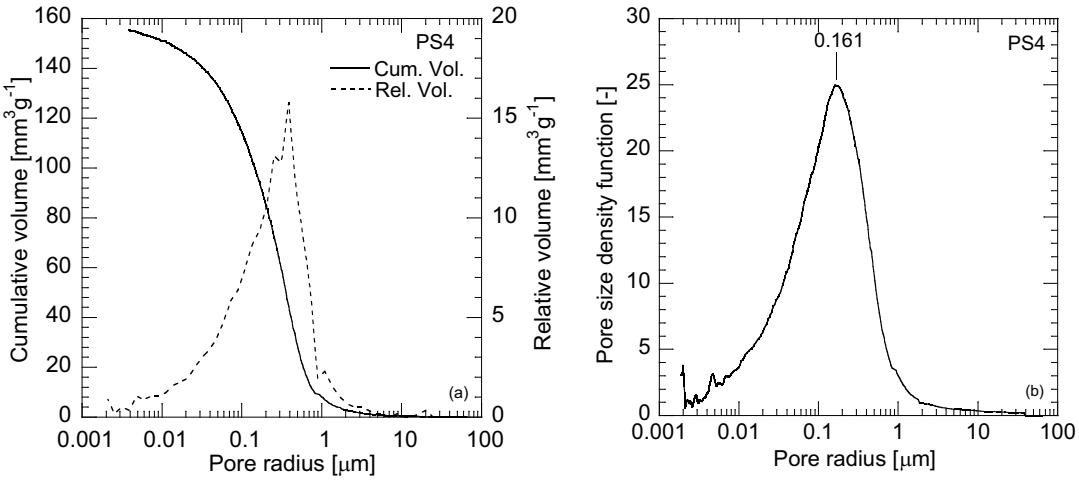


*Figure 5.9:* MIP results for sample PS4

#### 5.2.3.4 Reconstituted samples

The MIP results for three reconstituted samples of PR1, PR3, and PR2 are respectively presented in Figures 5.10, 5.11 and 5.12. The PSD shows to be uni-modal in all the three samples with smooth boundaries in the case of PR1 and PR2.

In the case of PR3, discontinuity of the PSD could be observed in the boundary of larger pores for the PSD. As shown previously, the MIP-based void ratio of this specimen does not agree with the void ratio obtained by direct measurement. Accordingly, the PSD of this sample, at least at the range of large pores, is not reliable.

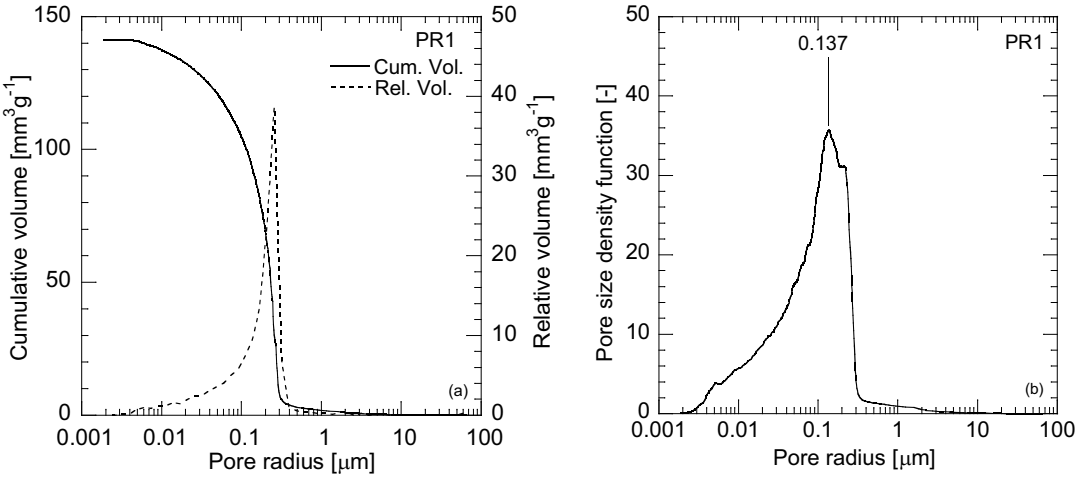


*Figure 5.10:* MIP results for sample PR1

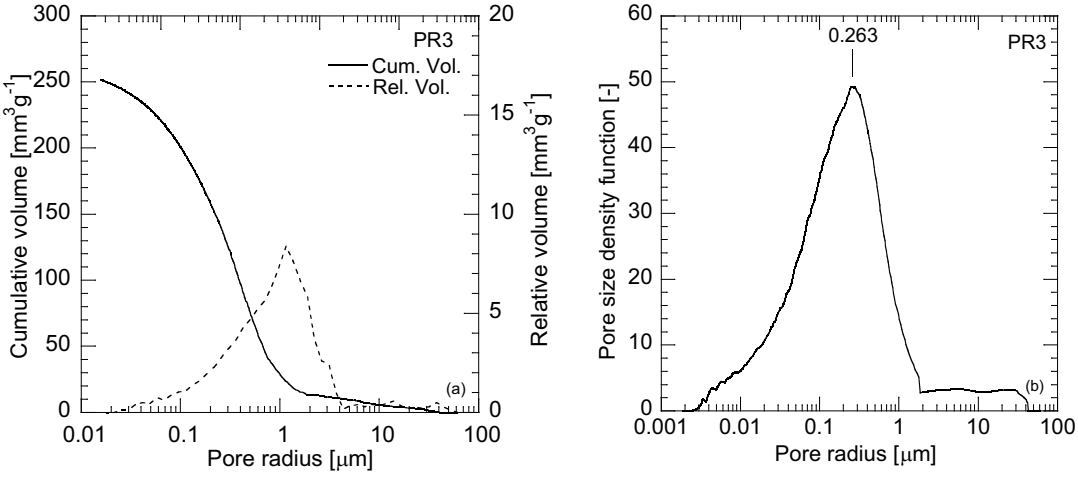


*Figure 5.11:* MIP results for sample PR3

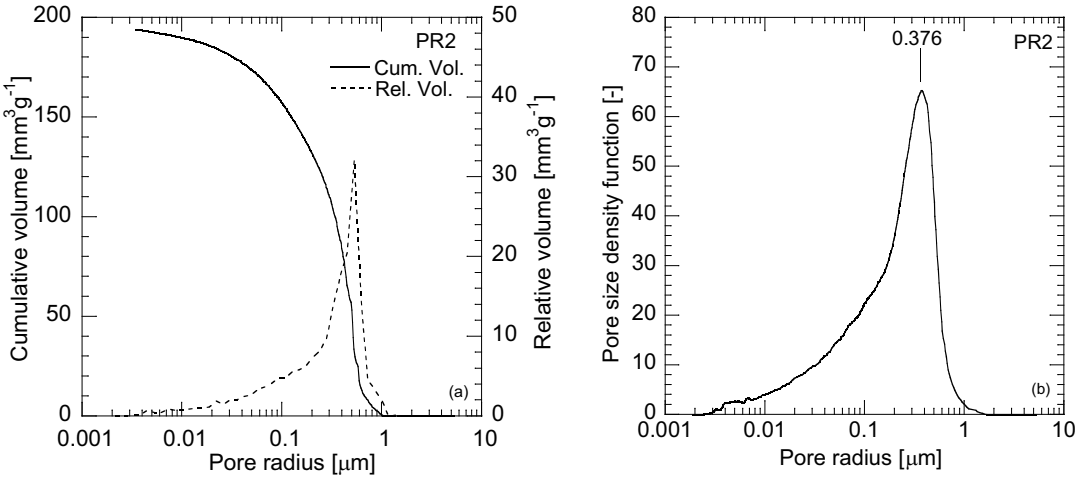


*Figure 5.12:* MIP results for sample PR2

#### 5.2.3.5 Comparison of results

Figure 5.13 presents the comparison of the MIP results with respect to different effects. Effects of compaction on unsaturated aggregated samples are evaluated by comparing the results of PS1 and PS2 in Figure 5.13(a). The peak representing a subset of macropores in PS1 was vanished in PS2 as a results of compaction. However, a firm conclusion on the evolution of whole macropores is difficult due to the limitation of MIP method for larger pores. Although the difference in the dominant pore size is not significant, the peak intensity changes significantly from about 33 in PS1 to 80 in PS2. This shows that the compaction of the sample has strongly increased the portion of smaller pores in the sample, while possibly it would give a decrease to the volume of macropores.

The influence of soaking is evaluated in Figure 5.13(b) by comparing the fabrics of unsaturated sample PS2 and soaked sample PS4, both subjected to the vertical stress of 1000 $kPa$. The dominant pore size is found to remain almost unchanged while its intensity decreases strongly. This is believed to be due to the collapse of aggregated structure and the wetting induced deformation of the sample. The smooth uni-modal distribution of the PSD shows that soaking of the sample at the relatively high stress of 1000 $kPa$ has almost completely removed the macropores in the sample.

Compaction effects on the fabric of aggregated samples after soaking have been evaluated by comparing the results of sample PS3 and PS4 plotted in Figure 5.13(c). As shown previously, both samples exhibit single-mode PSD. With a slight increase in the dominant pore size, the corresponding intensity has been strongly decreased from 52 in PS3 to about 24 in PS4. This shows that in the case of uni-modal PSD, compaction strongly decreases the volume of the dominant pores while slightly shifts the the dominant pore size toward smaller values.

The PSD of aggregated samples PS1, PS2, and PS3 are respectively compared with reconstituted samples PR1, PR3, and PR2 in Figures 5.13(d), 5.13(e), and 5.13(f). Each pair of samples represents the same suction and vertical

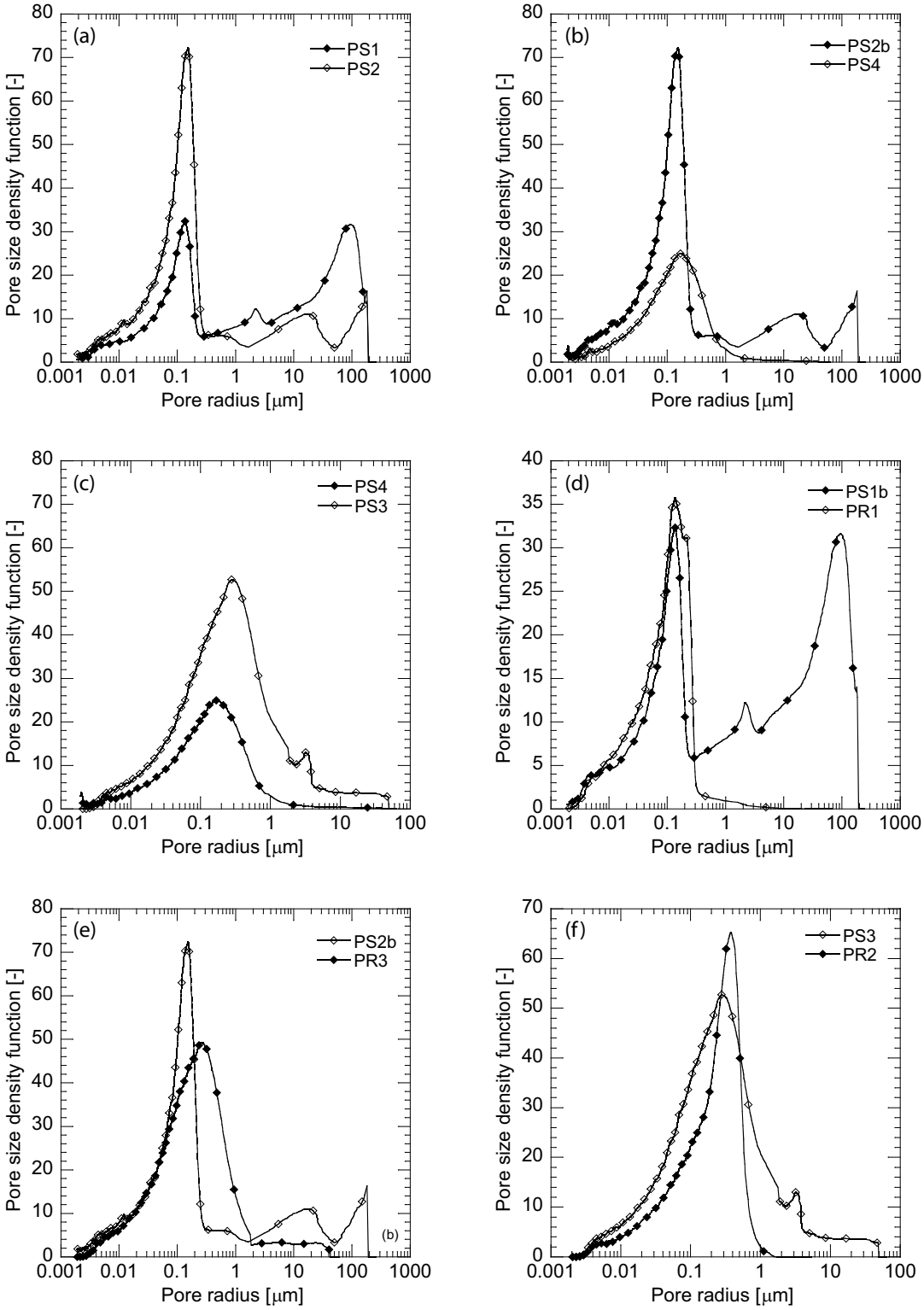


*Figure 5.13:* Comparison of MIP results: (a) unsaturated compaction effects, (b) wetting effects, (c) saturated compaction effects, (d,e,f) structure effects

stress. In sample PS1 where the PSD is bi-modal, the micropore peak almost completely coincide with the peak in the reconstituted sample. It is observed in all three figures that the most dominant pore size is almost identical for aggregated and reconstituted samples. In PS2 and PS3 where the PSD is uni-modal, the peak in aggregated sample occurs over a wider range of pore radii compared with the reconstituted samples. Moreover, the peak intensity of reconstituted soil is higher than the aggregated samples. The significant difference between the peak intensity of reconstituted (PR3) and aggregated (PS2) specimen in Figure 5.13(e) seems to be an experimental failure (see Sec. 5.2.2).

### 5.2.4 Description of ESEM observations

The ESEM observations were made at University of Neuchatel, Faculty of Science, Institute of Microtechnics. The ESEM used in this work was a PHILIPS XL30 ESEM-FEG microscope and it allowed a wide range of magnifications up to 20000× with a high resolution of 2 $nm$.

Two types of observations were made using the ESEM. In the first type, the samples have been observed at constant relative humidity of 25%; while in the second one, relative humidity of the chamber has been changed in a wetting-drying cycle including the $RH$ steps of 25%, 50%, and 85%. Experiments of this latter type were explicitly aimed to evaluate micropores within the soil at dynamic conditions of humidity.

For each specimen, a small fragment of the soil was carefully glued onto the specimen holder in order to guarantee a static condition during observations. The holder containing the sample was then placed into the ESEM chamber. For all samples, the first observations were made at a $RH$ of 25% which corresponds to a temperature of 4 $°C$ and a pressure of 1.5 $Torr$ ($\approx$ 200 $Pa$). In the case of sample PR2 and AGG, the $RH$ was then changed by keeping the temperature constant while increasing-decreasing the pressure. Observations were made at different levels of magnification in the range of 250× to 2000×. A total numer of more than 160 ESEM images were taken for the six samples (see Table 5.1), of which the most representative ones will be discussed here.

### 5.2.5 ESEM results

**Specimen PS2 and PR3:** The observations made on aggregated samples PS2 and reconstituted sample PR3 are shown in Figure 5.14. These sample have been both subjected to the vertical total stress of 1000 $kPa$ under the matric suction of 500 $kPa$.

Comparison of images taken with magnification of 250× shows that the reconstituted sample PR3 exhibits a fabric which is much more homogeneous compared with the aggregated sample PS2. The difference in the texture of two samples is clearly identified at higher magnifications of 500× and 1000×. Particles in PS2 are found to be grouped in connected assemblages. However, no evidence of regular aggregation could be observed in range of examined magnifications.

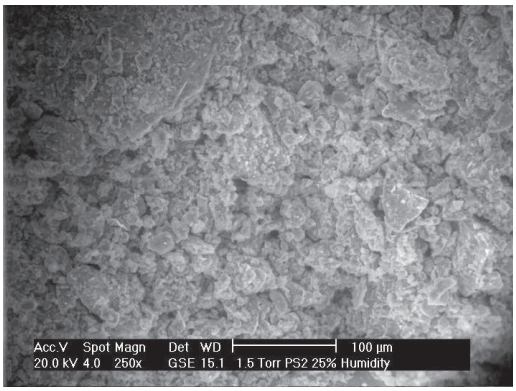


(a) PS2 (250×)

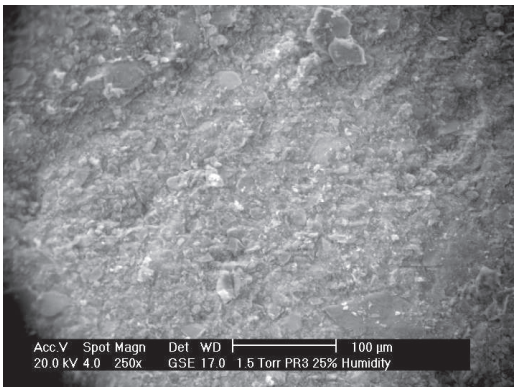


(b) PR3 (250×)

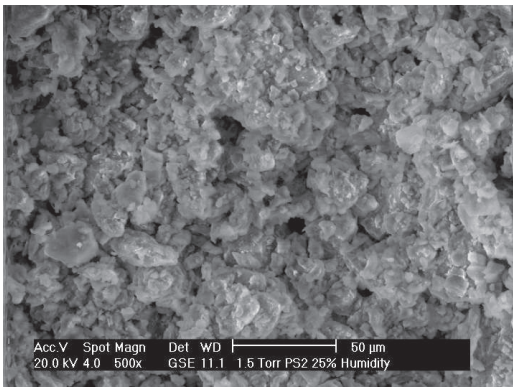


(c) PS2 (500×)

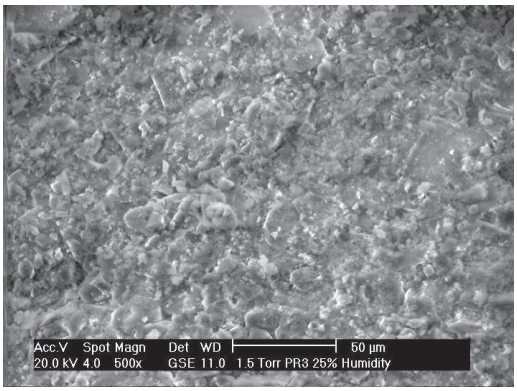


(d) PR3 (500×)

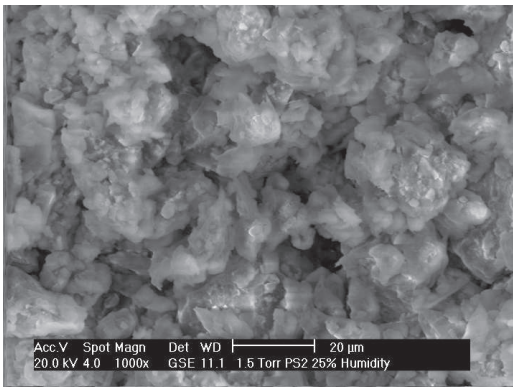


(e) PS2 (1000×)

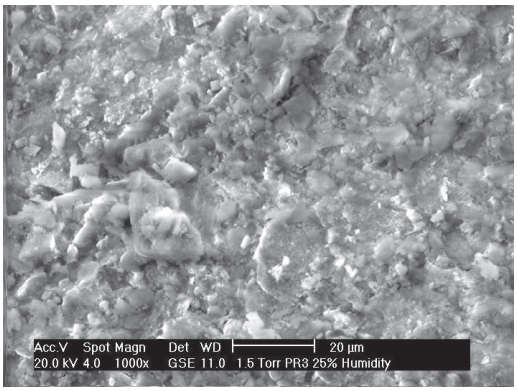


(f) PR3 (1000×)

*Figure 5.14:* ESEM results: aggregates sample PS2 and reconstituted sample PR3

A uniform distribution of pores could be observed within the fabric of PR3. This observation is in agreement with the earlier evidence of uni-modal PSD determined by MIP.

On the contrary, fabric of the aggregated sample PS2 is characterized with larger trans-assemblage pores of between 10 $\mu m$ and 20 $\mu m$. This observation is in good correlation with MIP results of Figure 5.7 where a small peak of around 16 $\mu m$ was identified in addition to the dominant pore size in the PSD of the sample PS2.

**Specimen PS3 and PR2:** Figure 5.15 shows the observations made on reconstituted sample PR2 and soaked aggregated sample PS3. Both samples have been loaded to a vertical total stress of 125 $kPa$ in the oedometer under saturated condition.

In the 250× magnified images, the two samples exhibit more or less similar textures. The fabric in both samples appears to be homogeneous with a uniform distribution of pores. At this scale, the fabric is characterized only with particle matrices with no particular structural feature.

In the images taken at higher magnifications, however, slight difference could be observed between the two fabrics. Matrices of particles in PR2 were shown to have an irregular prominence in the form of particle-assemblages. However, no significant difference in the pore size could be still recognized between two specimens and in general the two fabric¨s resemble each other.

This observation confirms that soaking of aggregated samples under mechanical loading significantly destroys the initial structure of the sample and brings the soil toward a reconstituted state from which all the structural features are removed.

**Specimen PS2 and PS4:** The ESEM results are presented in Figure 5.16 for unsaturated aggregated samples PS2 and saturated aggregated sample PS4. Different in the suction level, both samples have been loaded to the vertical stress of 1000 $kPa$.

The difference between the two specimens is almost insignificant in the images taken at magnification of 250×. Aggregation of particles was found to be a common feature in the fabric of both samples. Accordingly, intra-assemblage pore could be observed in both fabrics.

The size of the intra-assemblage pores could be better assessed in the images taken with higher magnification of 500× and 1000×. At this scale, sample PS2 exhibits a more diversity of pore size in its fabric in comparison with PS4. These pores seem to be larger in the case of PS2. Furthermore, these pores are inter-connected in PS2; while, occurrence of large pores in PS4 was found to be scarce and scattered.

Larger pores in PS2 describes the evidence of small peaks in the range of large pore sizes in the PSD of sample PS2. It appears that these pores are either closed or isolated as a result of compaction and the soil is brought with a uni-modal PSD having lower intensity of the dominant pore size.

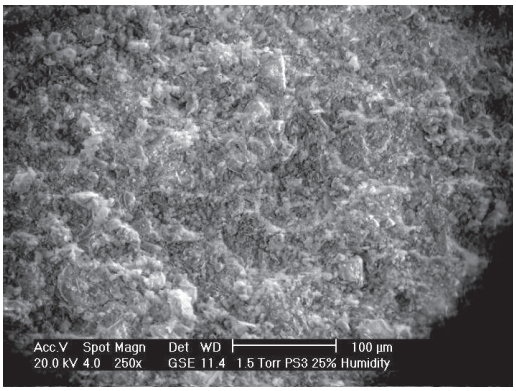


(a) PS3 (250×)

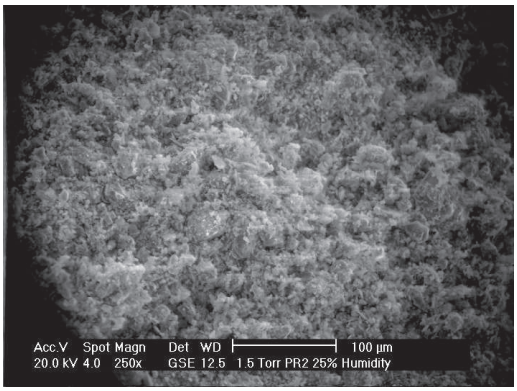


(b) PR2 (250×)

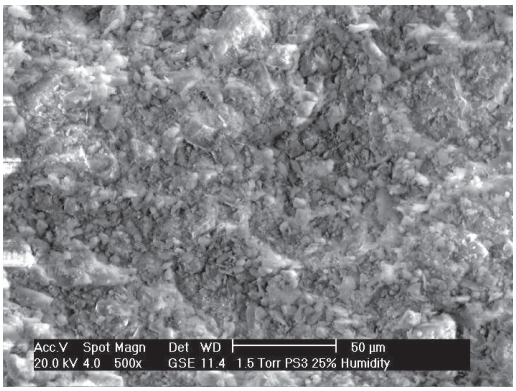


(c) PS3 (500×)

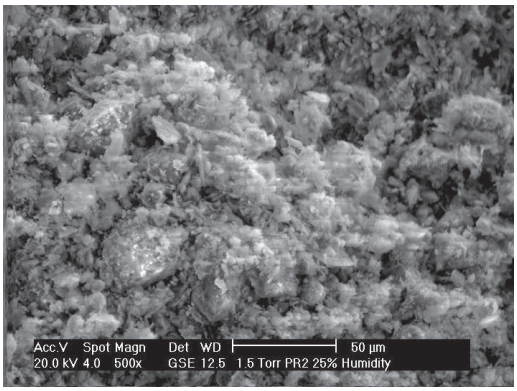


(d) PR2 (500×)

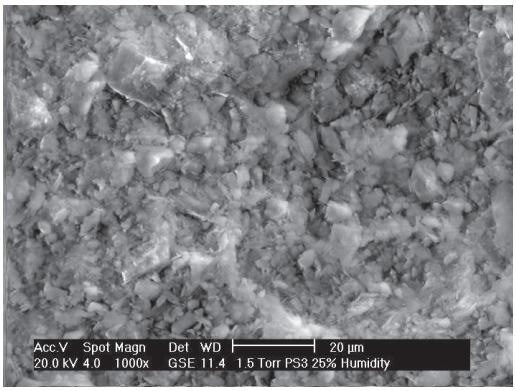


(e) PS3 (1000×)

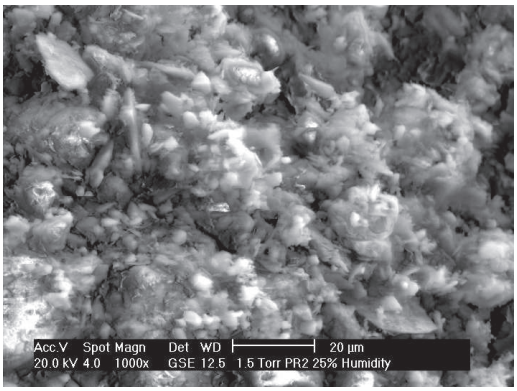


(f) PR2 (1000×)

*Figure 5.15:* ESEM results: aggregated sample PS3 and reconstituted sample PR2

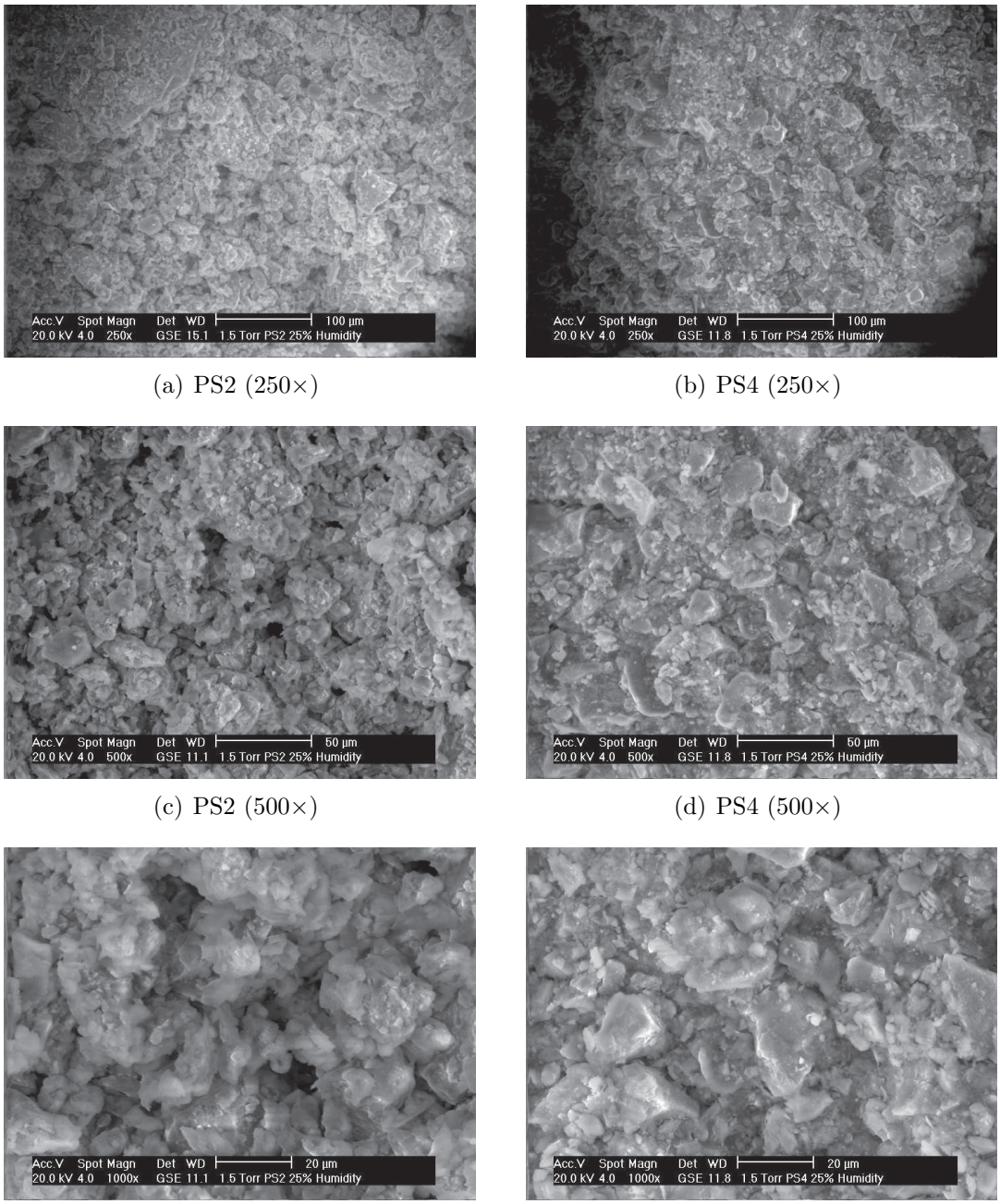


(a) PS2 (250×) (b) PS4 (250×)

(c) PS2 (500×) (d) PS4 (500×)

(e) PS2 (1000×) (f) PS4 (1000×)

*Figure 5.16:* ESEM results: aggregated sample PS2 and reconstituted sample PS4

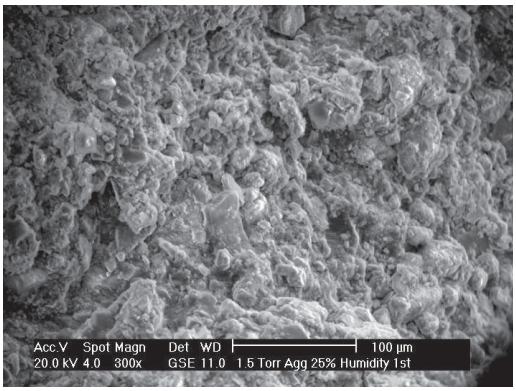


(a) $RH = 25\%$, initial state

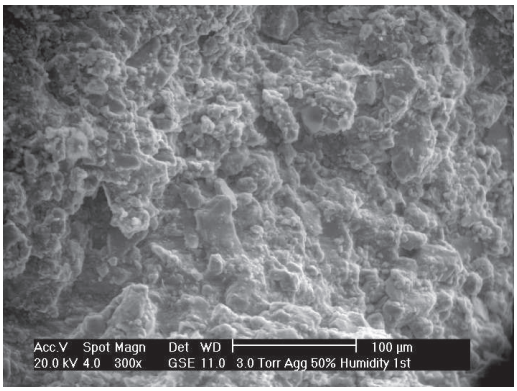


(b) $RH = 50\%$, wetting

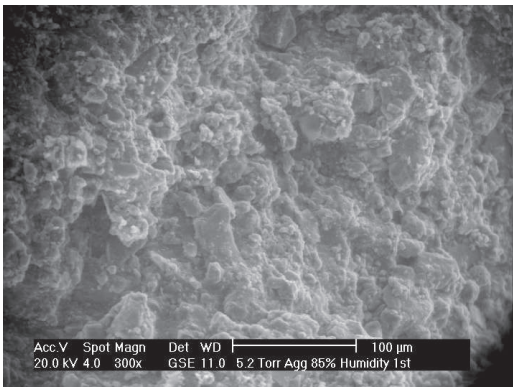


(c) $RH = 85\%$

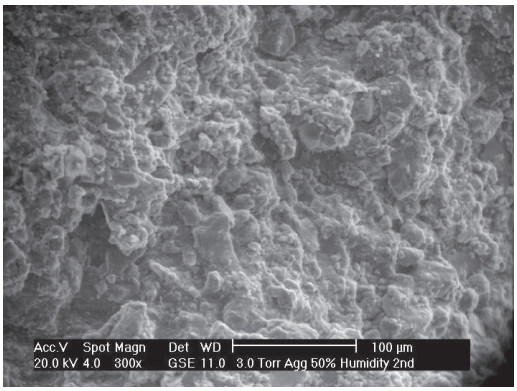


(d) $RH = 50\%$, drying

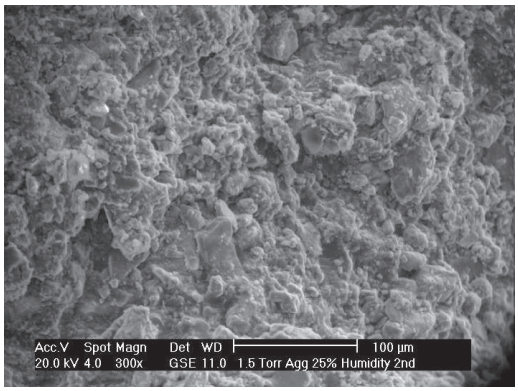


(e) $RH = 25\%$, drying

*Figure 5.17:* ESEM results of dry Bioley aggregate (AGG) at magnification of 300×

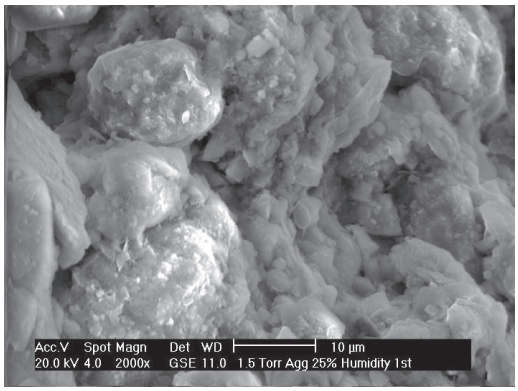


(a) $RH = 25\%$, initial state

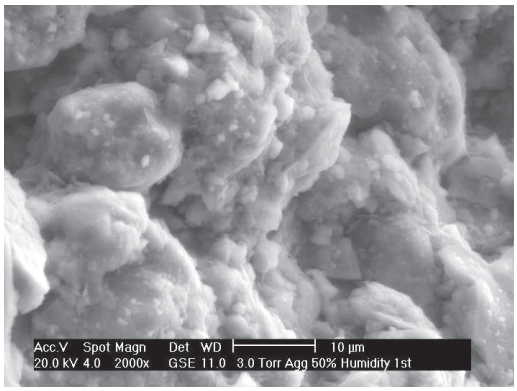


(b) $RH = 50\%$, wetting

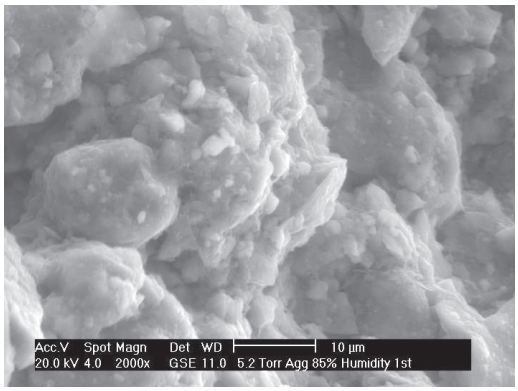


(c) $RH = 85\%$

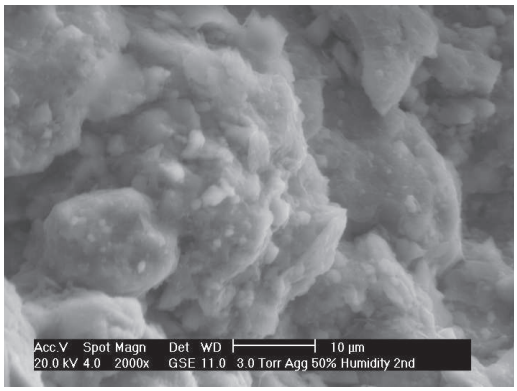


(d) $RH = 50\%$, drying

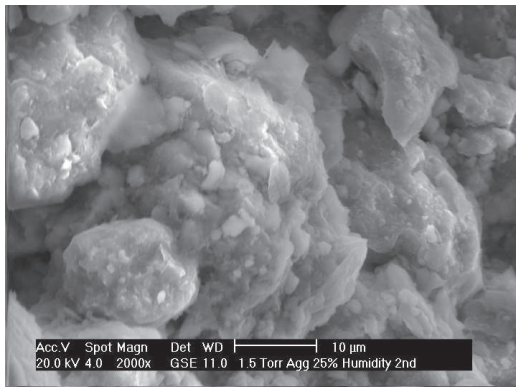


(e) $RH = 25\%$, drying

*Figure 5.18:* ESEM results of dry Bioley aggregate (AGG) at magnification of 2000×

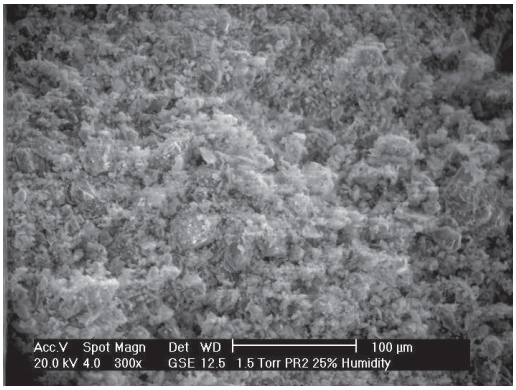


(a) $RH = 25\%$, initial state

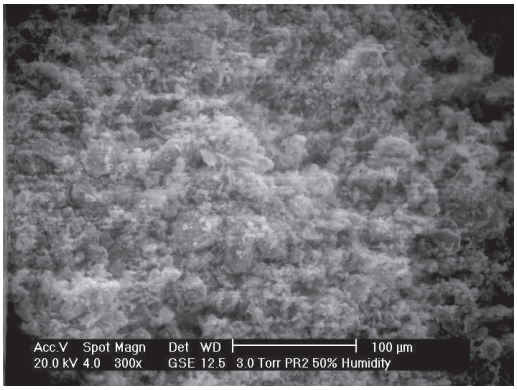


(b) $RH = 50\%$, wetting

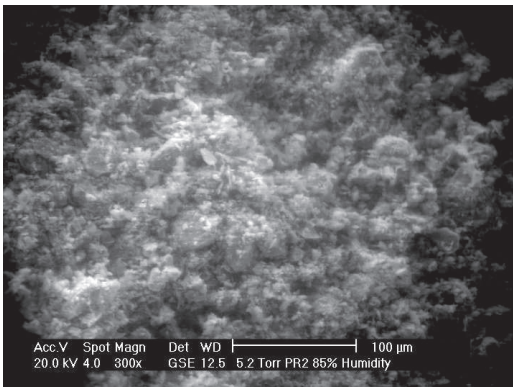


(c) $RH = 85\%$

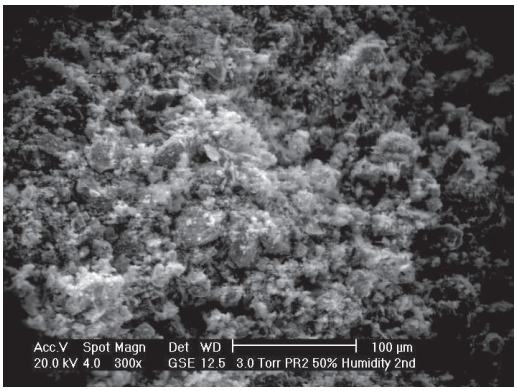


(d) $RH = 50\%$, drying

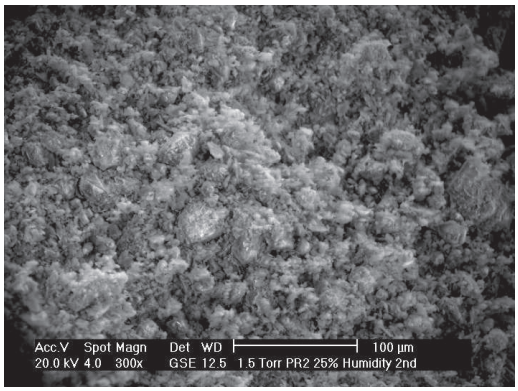


(e) $RH = 25\%$, drying

*Figure 5.19:* ESEM results of reconstituted Bioley specimen PR2 at magnification of 300×

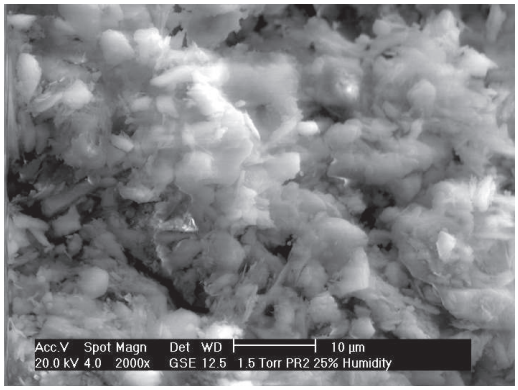


(a) $RH = 25\%$, initial state

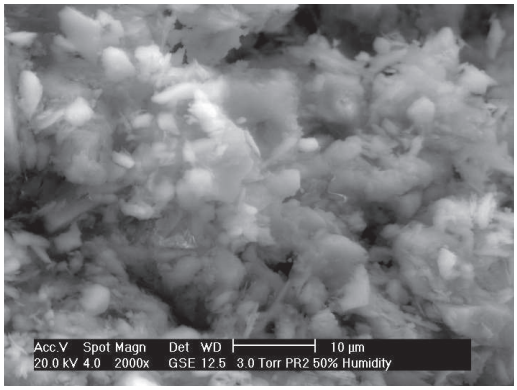


(b) $RH = 50\%$, wetting

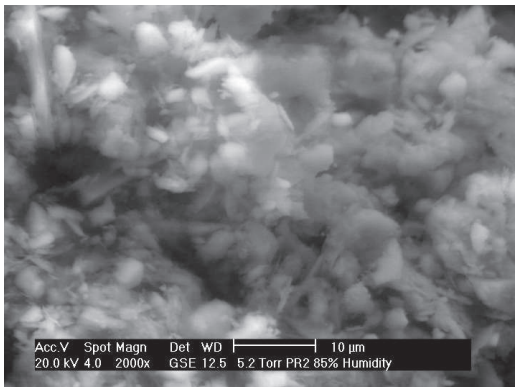


(c) $RH = 85\%$

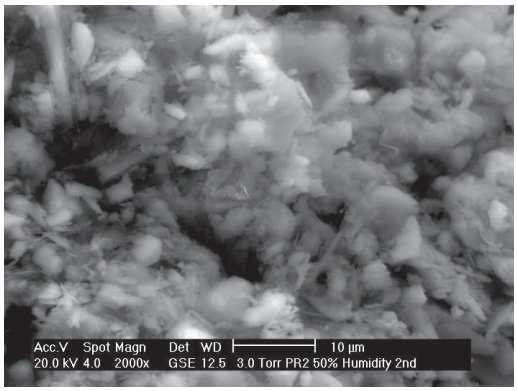


(d) $RH = 25\%$, drying

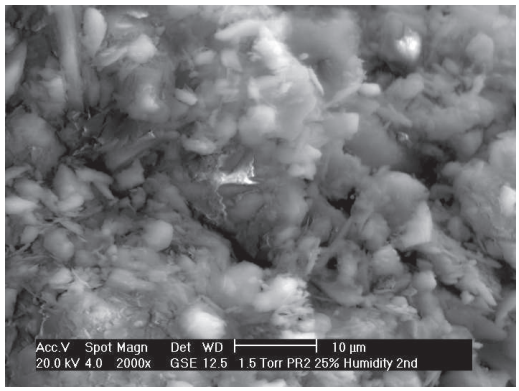


(e) $RH = 50\%$, drying

*Figure 5.20:* ESEM results of reconstituted Bioley specimen PR2 at magnification of 2000×

**Specimen AGG and PR2 in variable *RH*:** Figures 5.17 and 5.18 show images taken during wetting and drying of the specimen of dry aggregate (AGG) with two magnification of 300× and 2000×. Similar results are presented in Figures 5.19 and 5.20 for specimen PR2.

The fabric of dry aggregate specimen AGG in Figure 5.17 appears to be a compacted fabric involving inter-locking particles. However, no evidence of large pores could be observed in these figures. This observations are in agreement with the MIP results revealing that dry aggregates are dense packages of particles with low value of porosity.

Consequent image of this specimen at varing $RH$ in Figure 5.17 show no difference between the fabric at different states during wetting and drying. Even at 2000× magnified images of Figure 5.18, no evolution could be identified in the fabric, considering the fact that local position of element in the field of view might change due to the movement of the specimen during wetting and drying.

The results are slightly different for specimen PR2 in Figures 5.19 and 5.20. Although the initial and final fabrics are quite similar, a slight increase could be observed in the size of the pores from the initial state, $RH = 25\%$, to the wettest state with $RH = 85\%$. However, the difference is not of high significance.

It is noteworthy that the wetting-drying cycles were carried out in a short time of less than 10 minutes. This period of time seems to be too short for the elements of soil to become into the humidity equilibrium through the gas phase. This might, to some extend, justify the insignificant change of soil fabric during the variation of relative humidity.

## 5.3 Tomography evaluation of soil structure under mechanical loading

### 5.3.1 Material and method

In this series of experiments, a dry aggregated sample of Abist soil (average aggregate size of 4 $mm$) was subjected to incremental oedometric loading-unloading, and the structural evolution of the sample during theses steps was evaluated using neutron tomography data which has been acquired at the end of each step (see Sec. 4.3.1 for material properties). The oedometric sample, indicated as sample M, was prepared by free placement of dry aggregates in the cell followed by slight compaction. This is similar to the preparation method used for dry oedometer tests (see Sec. 4.4.1). This method of preparation yielded a sample exhibiting a relatively high initial void ratio of 1.63 due to the large macropores within the sample.

### 5.3.2 Experimental set up and procedure

The experiment was carried out using a custom-designed oedometer specially designed and developed at LMS for this experiment. The new cell is schematically depicted in Figure 5.21. The cell accommodates a cylindrical sample of

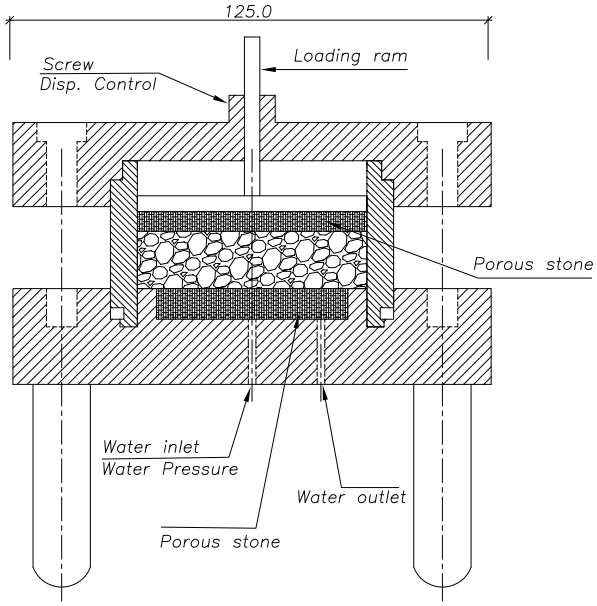


*Figure 5.21:* Schematic representation of the oedometric cell developed for neutron tomography experiments

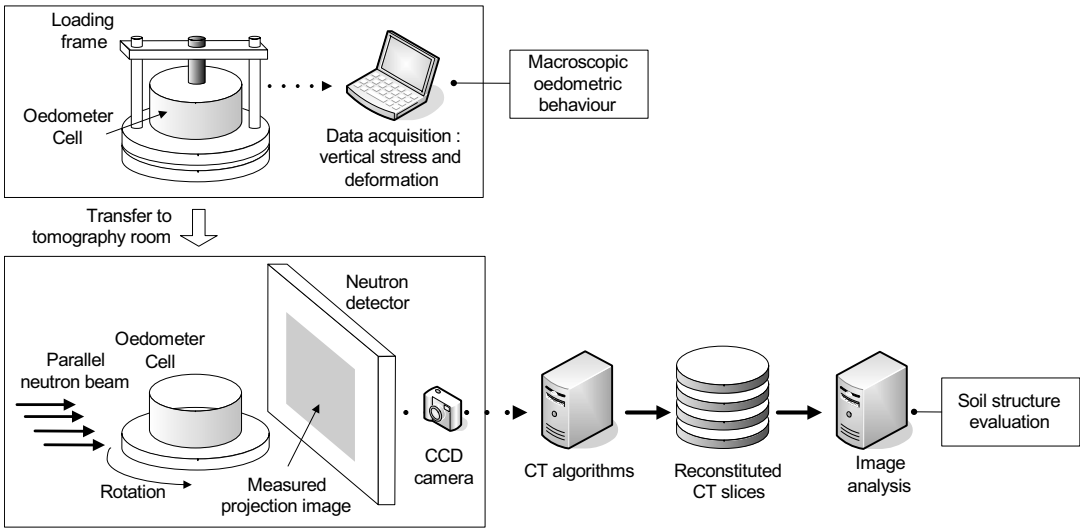


*Figure 5.22:* Schematic representation of experimental steps and data processing

60 *mm* in diameter and 15 *mm* in height. The sample is closed in the cell in order to prevent any humidity exchange during the test. A lateral screw was provided on the top cap which allowed blocking the loading piston and preventing the swelling when required. The new oedometric cell was built with aluminum, a material with a low neutron attenuation coefficient which is almost transparent to neutron beams (while steel is not). This ensures that the cell does not interfere in the images of the soil sample inside the cell.

The experiment was carried out at the thermal neutron radiography beamline NEUTRA of the Paul Scherrer Institute (PSI), Switzerland. Figure 5.22 schematically illustrates the experimental procedure and the data processing

*Table 5.2:* Applied vertical stress at the oedometric loading steps

| Step | **L0** | **L1** | **L2** | **L3** | **L4** | **L5** | **L6** | **L7** |
|---|---|---|---|---|---|---|---|---|
| $\sigma_v[kPa]$ | 1 | 31 | 195 | 1 | 92 | 195 | 283 | 424 |
| Step | **L8** | **L9** | **L10** | **L11** | **L12** | **L13** | **L14** | |
| $\sigma_v[kPa]$ | 1 | 195 | 301 | 424 | 584 | 743 | 1 | |

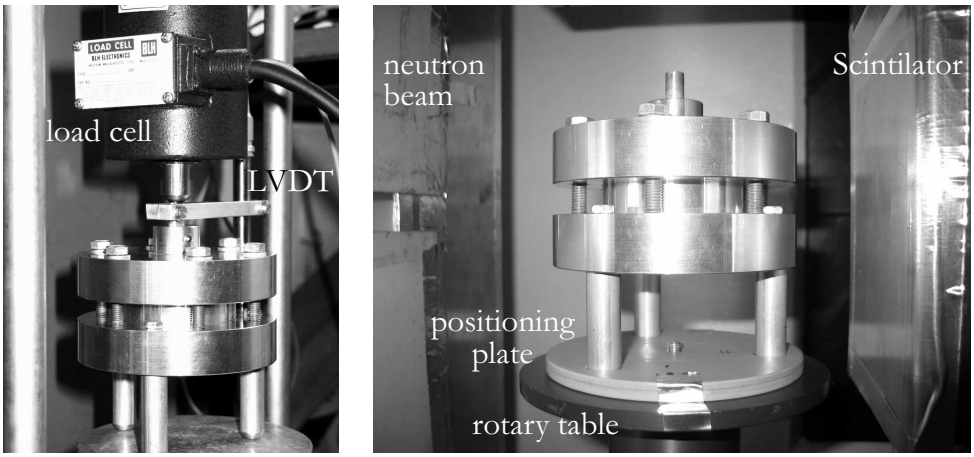


*Figure 5.23:* Experimental setup at PSI, left: cell in the loading frame, right: cell in the neutron beamline

steps followed during the course of this work. The sample was first loaded in a displacement controlled loading frame out of the tomography room. The sample in the new cell was subjected to different vertical stress increments. Values of vertical total stress at different steps are given in Table 5.2. A total of 15 steps including loading and unloading steps were applied, and at each step the vertical deformation of the sample was recorded by direct measurement using a linear variable differential transducer (LVDT). The macroscopic oedometric response of the sample, namely the total vertical displacement of the sample versus the applied total stress, was deduced from the direct measurements of displacement. After reaching equilibrium at each loading step, the cell was moved from the loading cell to the neutron beam and a tomography of the sample was made. During this step, swelling of the sample in the cell was prevented using the lateral blocking system provided on the piston specifically for this purpose. Thanks to a positioning plate placed on the rotary table (see Fig. 5.23), the cell could be placed always at the same initial position in the neutron beam in order to provide comparable images. The field of view has been limited to the sample using some shielding plates (Fig. 5.23).

The beam diameter width could be varied from 15 to 40 $cm$ and the flux from $2.5 \times 10^7$ to $3.5 \times 10^6$ $neutrons\ cm^{-2}s^{-1}$. To acquire tomography data, the neutron flux at the sample position was $9.4 \times 10^6$ $neutrons\ cm^{-2}s^{-1}$. Based on the sample size and detector system, the exposure time for a single radiograph is selected as about 17 $s$. The radiography image has a linear spatial resolution of 0.146 $mm$ pixel. The intensity of the neutron flux behind the sample is detected

by a neutron area detector. The detector is a cooled CCD camera system (DV 434, Andor Technology) looking onto a 6LiF doped ZnS scintillator screen converting neutron flux into light emission. The radiographs are two-dimensional gray-value images with values proportional to the transmitted neutron flux. For neutron tomography a set of radiograms was recorded while rotating the sample stepwise by 180 degrees with a constant small angular increment of 0.9 degree.

Projected image data required pre-processing before they could be used as an input to the tomography reconstruction algorithm. The pre-processing of images and the reconstruction of tomography volumes have been done by the joint partner of the project at PSI-NEUTRA using the computer tools provided for this purpose.

First, the images had to be normalized for equal neutron exposure and corrected for spatial variations in the incident neutron beam and the inhomogeneity of the scintillator screen (flatfield correction). For the flatfield correction, the sample projection images were divided by a radiography image without sample. Moreover, disturbing effects due to neutron scattering were compensated with a correction algorithm given by Hassanein et al. (2005).

After these corrections, slices perpendicular to the rotation axis were reconstructed by filtered back projection (Vontobel et al., 2006). The computed tomography algorithms then yielded the three-dimensional array of the local neutron attenuation coefficient in the sample.

### 5.3.3 Processing of raw image data

The raw tomography results consisted of a three-dimensional sample volume with a voxel (the 3D equivalent of a 2D pixel) size of 146 $\mu m$. The reconstructed volumes were processed by a sequence of spatial filters before being used in the analysis. Processing of the image data was performed using *MATLAB* and the image analysis software *VGStudio Max 1.2.1*[1]. The main principals of image processing remains the same in both methods. *VGStudio MAX* provides powerful tool for image processing and analysis including filter operations, segmentation, spatial and morphological analysis, as well as reasonable possibility of visualization of the volumes, segments and sections.

The image processing is based on the analysis of gray value in the 3D volume. The gray value of each image is best represented by the histogram of gray values which represents number of vowels for each gray value. Processing of image data have been done in three steps: (i) filter operation, (ii) segmentation, (iii) structural analysis.

Figure 5.24(a) shows the histogram of gray values and the visualisation of the raw tomography data only corrected for scattering effects. The histogram exhibits a bi-modal distribution. The first peak corresponds to the voids, the cell and the noises and the second one to the soil matrix within the aggregates. In order to remove the noises and to obtain a better image quality, the reconstructed volumes has been processed by a $5 \times 5 \times 5$ median filter.

[1]Image processing and analysis using *MATLAB* were carried out in collaboration with A. Carminati and A. Kaestner at ITÖ-ETHZ.

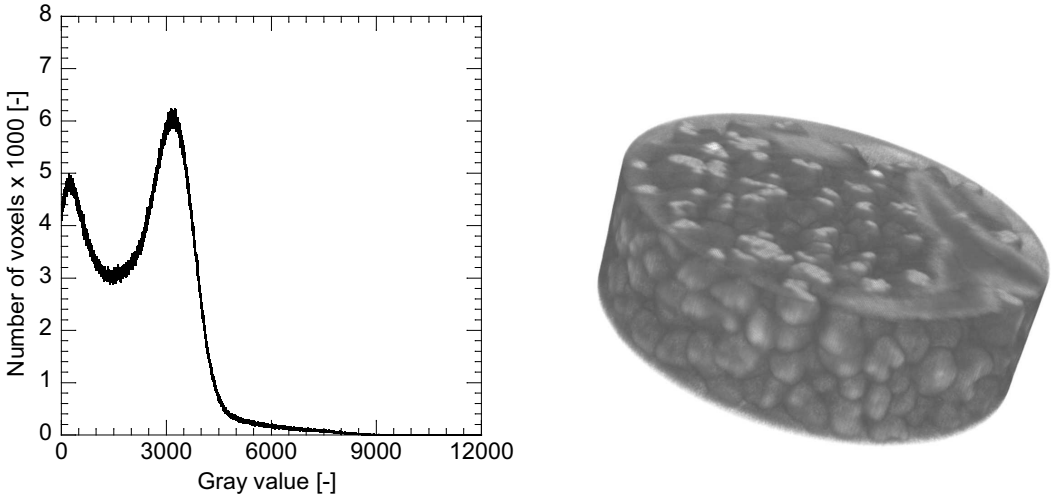


(a) (b)

*Figure 5.24:* Raw tomography data for the initial state of the sample M: (a) histogram, (b) visualized volume

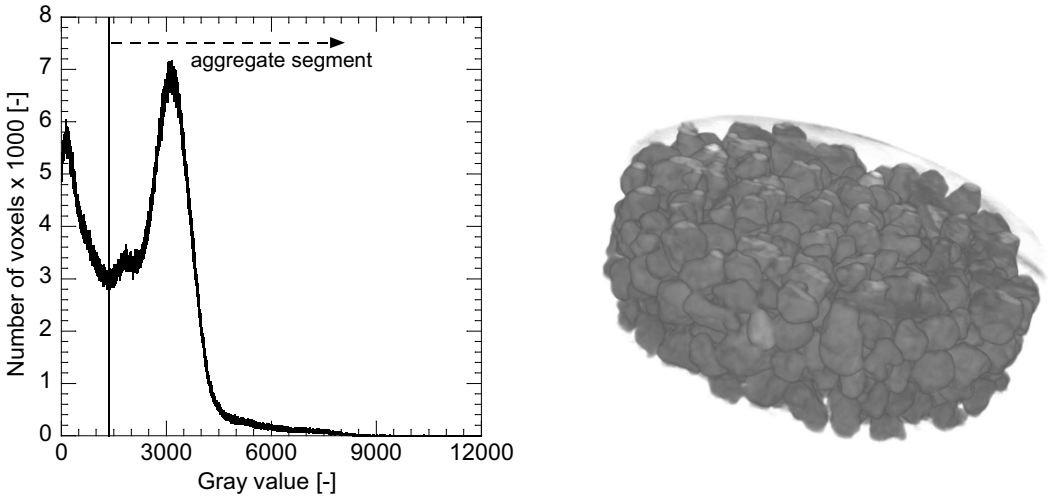


(a) (b)

*Figure 5.25:* Tomography data for the initial state of the sample M after filter operation and segmentation: (a) histogram, (b) visualized volume

In the next step, the volumes have been segmented in order to extract the aggregates volume. This has been done by finding the point of minimum between two peaks in the histogram. This corresponds to the point where the first derivative of the smooth histogram function is zero and its second derivative is positive. This point was selected as the threshold and the voxels to the right side of this limit have been identified as aggregates (Fig. 5.25).

The spatial resolution of the images (146 $\mu m$) does not allow detecting micropores inside the aggregates; therefore, the segmented volume of aggregates contains both solid particles and intra-aggregate pores. Figure 5.26 shows the segmented volumes sample M and its cross-section at different loading steps.

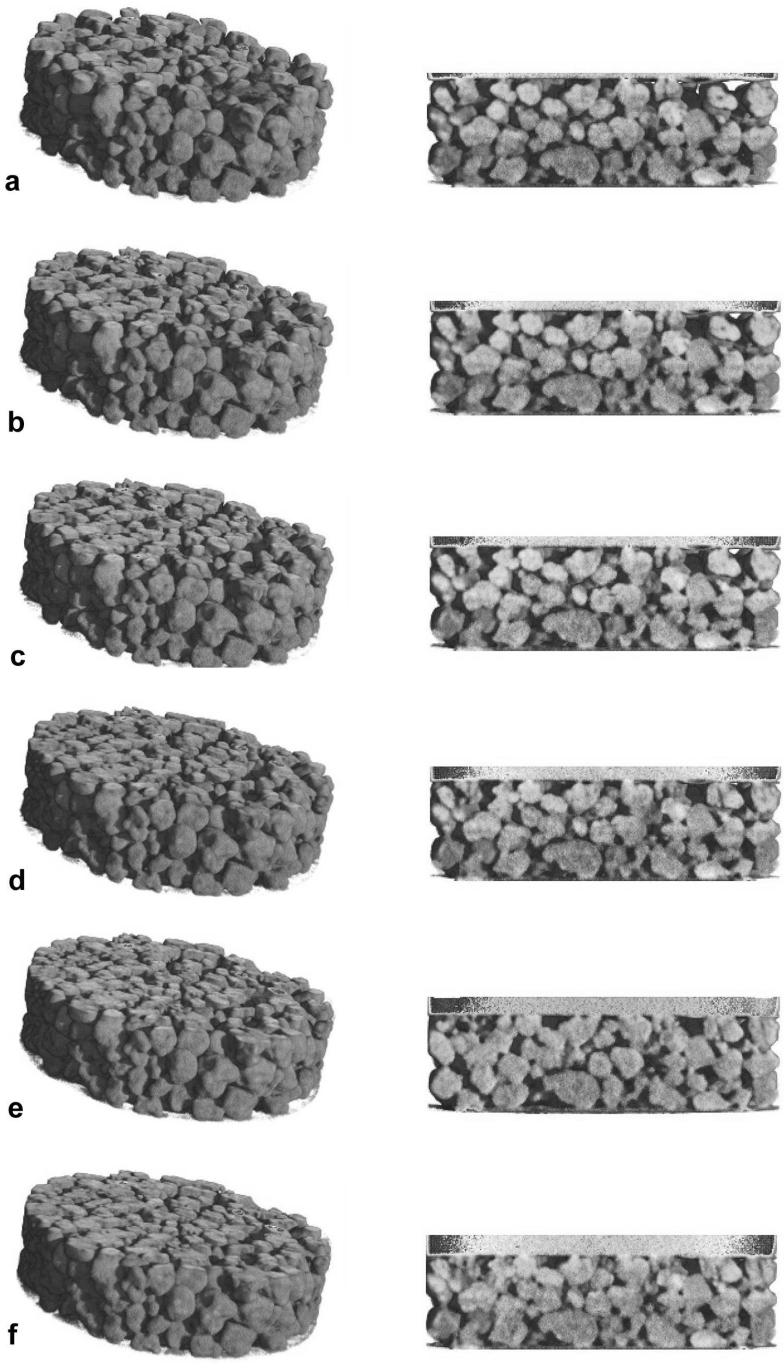


*Figure 5.26:* Reconstructed volume and cross-section of the sample obtained by neutron tomography at vertical stress of (a) 1.1 (b) 194.5 (c) 282.9 (d) 424.4 (e) 583.6 (f) 742.7 $kPa$, (Initial sample size: 60 $mm$ diameter and 15 $mm$ height)

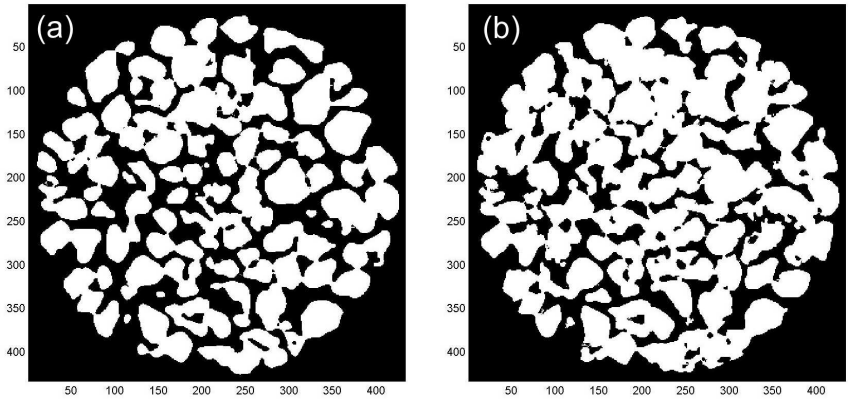


*Figure 5.27:* Horizontal cross-sections of scanned samples. The neutron transmission images were segmented into aggregates (white) and inter-aggregate pores (black), (a) initial state, 1.1 $kPa$, (b) final state, 742.7 $kPa$, the numbers denote the coordinates in pixels with pixel size of 146 microns.

The segmented volumes were then used for structural analysis. Figure 5.27 depicts a binary image of the horizontal slice of the sample at initial and final state of compression.

Volume of macropores and aggregates in these volumes can be determined by counting the corresponding number of voxels. In order to prevent interference from the boundary effects in the analysis, an internal section has been extracted from the volume and used for the analysis

The macroporosity at each load step has been deduced from this binary volume using the following relation:

$$n^2 = 1 - (N^V_{agg}/N^V_{total}) \tag{5.3}$$

where $N^V_{agg}$ and $N^V_{total}$ are, respectively, the number of voxels corresponding to aggregate volume and total volume in a section of tomography volume data.

### 5.3.4 Macroscopic results

The oedometric curve of the sample derived from direct measurements of deformation is plotted in Figure 5.28. The oedometric compression curve of the sample exhibits an initial stiff behavior followed by yielding.

As shown in Chapter 4, the initial stiff part of the compression curve is the characteristic of aggregated soils. This phenomenon could be described in the same way as induced overconsolidation; although, the nature of the phenomenon is different. The yield stress has been therefore called apparent preconsolidation stress, which is a function of not only stress state and stress history but also the particular structure of the soil structure.

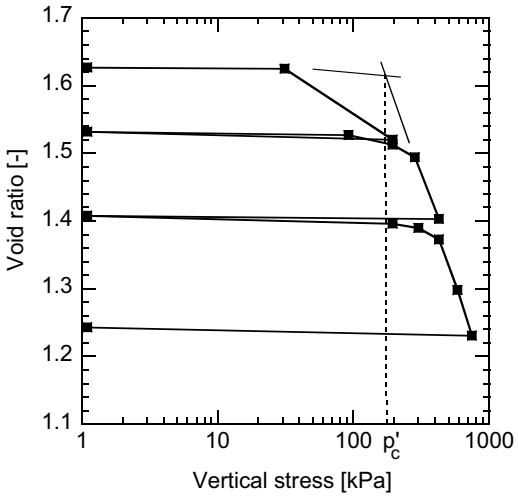


*Figure 5.28:* Oedometric curve of the sample M

### 5.3.5 Characterization of soil structure evolution

The concept of double porosity, presented in Section 2.1.5, is postulated here for the purpose of soil structure evaluation. The relation between total porosity, macro- and microporosity in aggregated soil is given by Equation (3.38):

$$n = n^1 + n^2$$

where $n$ is the total porosity and $n^1$ and $n^2$ respectively denote the microporosity corresponding to the pores within the aggregates (intra-aggregates) and the macroporosity corresponding to the pores between the aggregates (inter-aggregate). In aggregated soils, macropores are retained by aggregated structure and the aggregates themselves are formed as a result of inter-particles. Breakage and de-structuring of aggregates causes the macroporosity to decrease and, therefore, it causes the soil fabric to change. Due to this interaction between the soil fabric and inter-particle bonding (two components of soil structure), the current macroporosity of the sample is considered here as a representative measure of soil structure. Hence, macroporosity of the sample at different loading steps is extracted from the tomography data in order to track soil structure evolution during the test.

Figure 5.29 shows the evolution of macroporosity deduced from image analysis, as well as total porosity from direct measurements. The two curves follow similar evolution patterns and differ mainly in magnitude. However for a given stress increment, macroporosity decreases slightly more than total porosity. It is therefore concluded that in the applied range of stress values, the main deformation is due to a decrease in the volume fraction of macropores. This observation, in a general sense, is in agreement with results of MIP tests of Section 5.2.3 which showed that compaction primarily affects the larger pores. Attention should be given to the fact that the large pores examined in MIP method correspond to a subset of macropores of under study in the neutron tomography analysis.

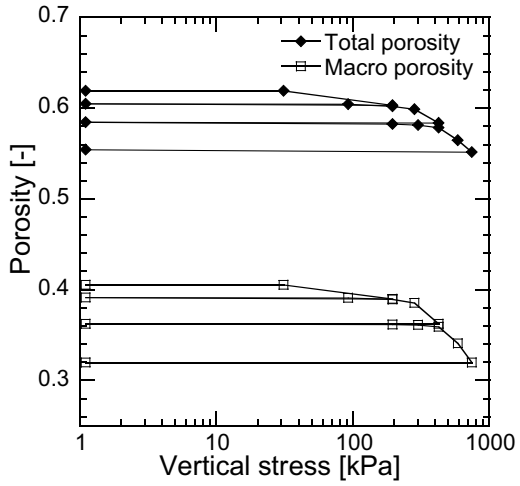


*Figure 5.29:* Evolution of total porosity and macroporosity versus applied stress in sample M

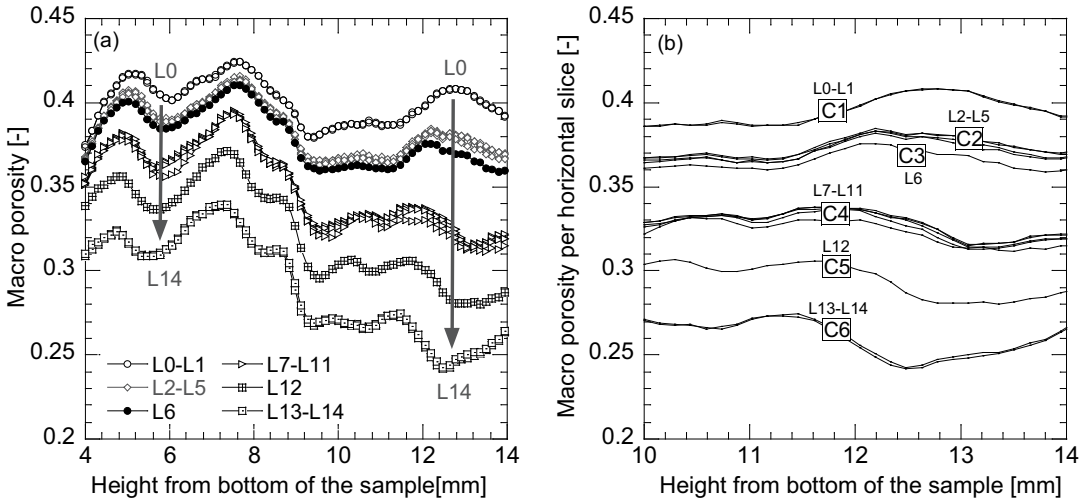


*Figure 5.30:* Distribution of macroporosity along the height of the sample M for different loading

The values of macroporosity plotted in Figure 5.29 are the average values in the whole sample; however, local values of macroporosity during the loading are not necessarily the same in different parts of the sample. In order to evaluate the effects of induced external loading in different parts of the sample, macroporosity was analyzed as a function of space (vertical distribution through the sample) and loading history[2]. The sample was divided into horizontal disks of one unit thickness (1 voxel) along its height, and hence, macroporosity of each single disk represented the value of macroporosity at the given height of the disk in the sample. The results of this analysis are plotted in Figure 5.30(a) for

[2]Image analysis of this section and the next section for the macropore size distribution and the chord length were carried out in collaboration with P. Lehmann at ITÖ-ETHZ.

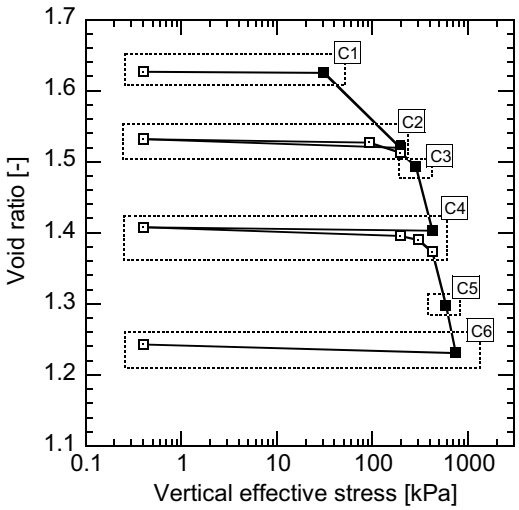


*Figure 5.31:* The six structural classes on the oedometric curve of the sample M

different loading steps L0 to L14 (see Table 5.2). Each curve in this figure represents the distribution of macroporosity along the height of the sample for the given loading step. In order to prevent interference from the boundary effects and height variations in the sample on the analysis, only the middle 10 cm of the sample was considered.

It can be observed in Figure 5.30(a) that changes in macroporosity are not homogeneous in the sample; a more pronounced decrease of macroporosity occurs in the upper part of the sample. A magnified plot of this upper part is shown in Figure 5.30(b). An interesting aspect of this figure is the fact that the fifteen steps of loading and unloading can be reduced into six main classes indicated by C1 to C6. This division classifies the state of the material at different loading steps on the basis of the induced changes in soil structure, such that each class represents a set of loading steps during which no major modification of macroporosity occurs.

Accordingly, the classification of loading steps could be also shown on the oedometric compression curve of the sample as depicted in Figure 5.31. This figure reveals that the initial states, with an applied stress of less than the initial apparent preconsolidation stress, reside in the same class. Moreover, all of the states situated on an unloading-reloading path belong to a single class. Changes in class are observed only during the normal compression (consolidation) of the sample. This shows that states sharing the same apparent preconsolidation stress remain in the same class and therefore they exhibit the same soil structure. Subsequently, changes in the soil structure occur only with changes in preconsolidation stress levels. On the other hand, preconsolidation pressure it self changes only with occurrence of irreversible (plastic) deformation. In other words, changes in macroporosity are associated mainly with plastic strain. This important experimental finding has a major impact on the modeling of this phenomenon.

### 5.3.6 Evaluation of structure degradation mechanisms

In the previous section, the evolution of soil structure was linked to the macroscopic description of soil structure through effective preconsolidation stress. However, modeling of the evolution of soil structure due to applied stress (or induced deformation) requires, as a key issue, knowledge of structural degradation mechanisms. This could be achieved through the geometric information of the macropores that reflect changes in the size and shape of the macropores, and their relative positions and arrangements in the sample during the loading process. These two issues are considered here for different loading steps. For the sake of simplicity, for further macroporosity analysis, each class (C1 to C6) is denoted only by one single representative loading step.

In order to address the first issue, the evolution of macropore size distribution of the sample was evaluated. The three dimensional pore size distribution was analyzed by inserting spherical structural elements in the macropore space (Lehmann et al., 2007). The cumulated macropore size distribution (MPSD) of the sample is plotted for the six identified classes in Figure 5.32. It is observed that the pore diameter corresponding to a given cumulated volume fraction decreases as the applied stress increases. It indicates the decrease in the size of macropores. This evidence is in agreement with the earlier evidence in the MIP results indicating that the major decrease in the volume fraction of large pores with compaction. Quantitative comparison of pore sizes, however, could not be done due to the fact that range of examined pore sizes are different in two methods.

Three dimensional geometrical analysis of the pore space is required to verify if the change in size is as well associated with the change in shape of macropores. A candidate parameter for this purpose is the chord length distribution. Chords are line segments between the intersections of a line with the interface of aggregates and macropores. Changes in the chord length of macropores in

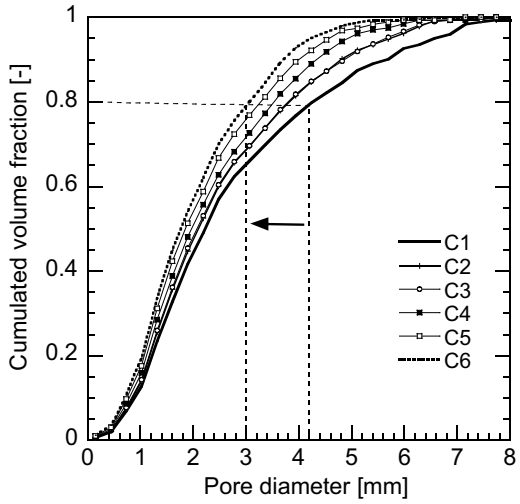


*Figure 5.32:* Cumulated macropore size distribution of sample M

three dimensions could be used to evaluate the change in the pore shape.

The chord length in the vertical (z-axis) as well as two perpendicular horizontal directions (x and y-axis) were calculated for segmented volumes of both macropores and aggregates. The methods of image analysis is described in Lehmann et al. (2007). Chord lengths are plotted in Figure 5.33 versus the corresponding volume fraction of pores (Fig. 5.33(a)-(c)) and aggregates (Fig. 5.33(d)-(f)) for the six classes.

These figures illustrate the increase in the applied stress associated with a decrease in the volume fraction of longer chord lengths and increases in the shorter ones for the macropores. This observation was made for all three dimensions. The relative increase of the volume fraction (with respect to initial value) for the most dominant pore radius in the initial state is 49.8, 47.8, and 45.2% in x, y and z directions, respectively. This indicates that macropore variations in size occur almost isotropically in the three directions; hence, no significant change in the shape of the macropores occurs.

Contrary to the macropores, the shorter chord lengths of aggregates decrease with loading. One interpretation of this observation is that individual aggregates merge together, and therefore, the thickness of the layer of the aggregate space increases.

The second issue to be addressed, in order to understand structural degradation mechanisms, is the relative arrangement and redistribution of macropores in the sample during the loading process. For this purpose, it is important to make a distinction between two modes of de-structuring which cause the soil fabric to change: (i) local closure of macropores and (ii) rearrangement of macropores in the sample.

Figure 5.34(a) schematically illustrates the system of aggregates and macropores in an aggregated soil. Local closure and rearrangement of macropores are depicted in Figures 5.34(b) and 5.34(c) respectively.

In the first phenomenon, a change in fabric is mainly due to local changes in the size of the macropores without significant rearrangements of the pores; it is reasonable to associate this mode of degradation with an isotropic loading condition.

The second phenomenon is linked to distortional deformation which occurs during deviatoric stress paths. The open question is whether the mechanism of structural degradation that results in a aggregated (structured) soil reaching a fully de-structured state (Fig. 5.34(d)) is isotropic, deviatoric or a combined mechanism of the two.

Mechanisms of structure degradation were investigated here by the analysis of gray value images. In this analysis, the gray value represents the aggregate mass; i.e., the higher the gray value in a region, the greater the concentration of aggregate mass. The gray values are averaged as a function of radial distance from the vertical axis. The mean gray value represents the circumferential concentration of the aggregate mass at a given distance from the vertical centre line of the sample. These values are calculated and shown in Figure 5.35 for the six identified classes. Relative minimums represent regions with less aggregate mass and more pores.

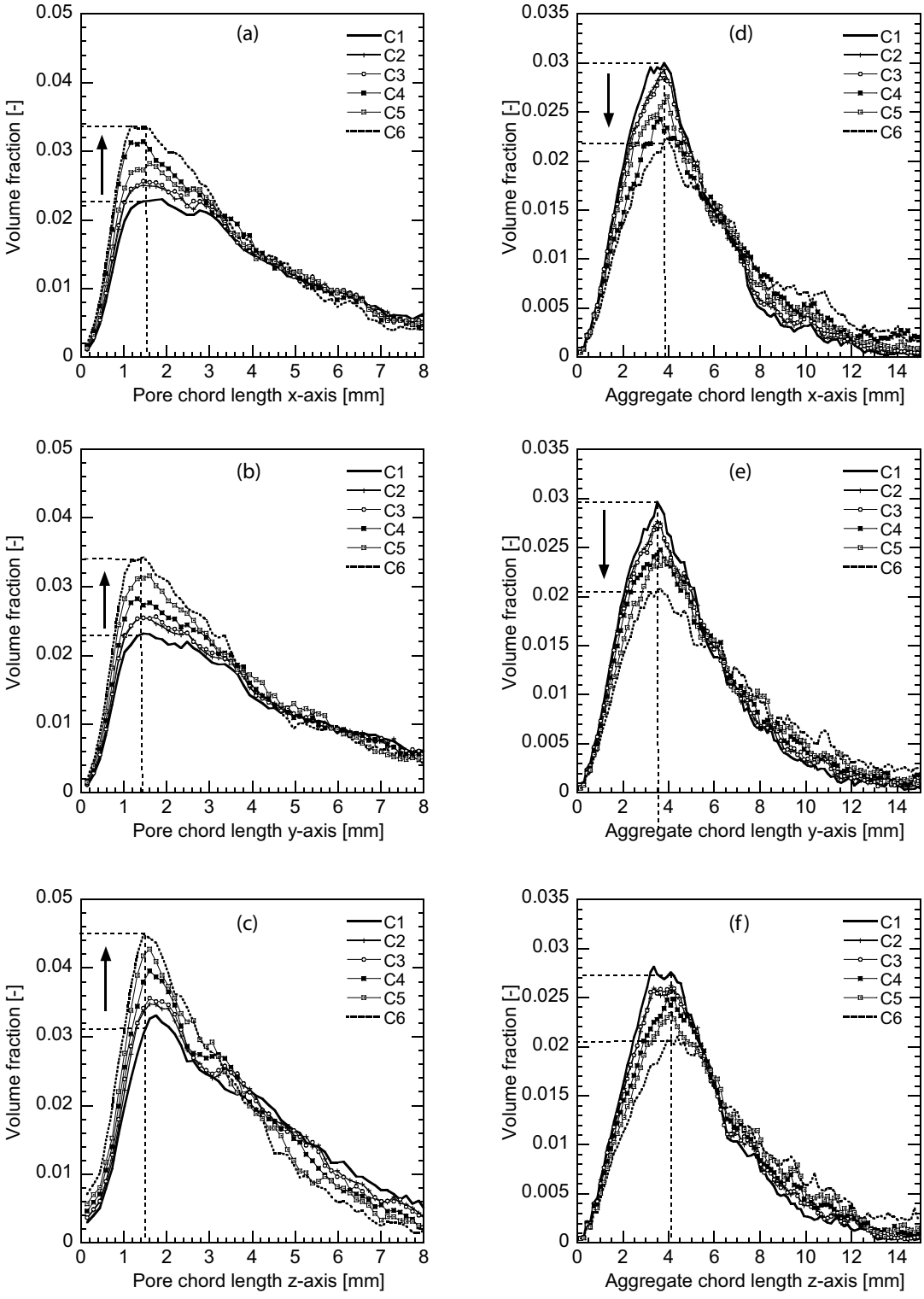


*Figure 5.33:* Chord length distribution of macropore space (a, b, c) and aggregates (d, e, f) in the vertical (z-axis) and two perpendicular horizontal (x and y-axis) directions for sample M

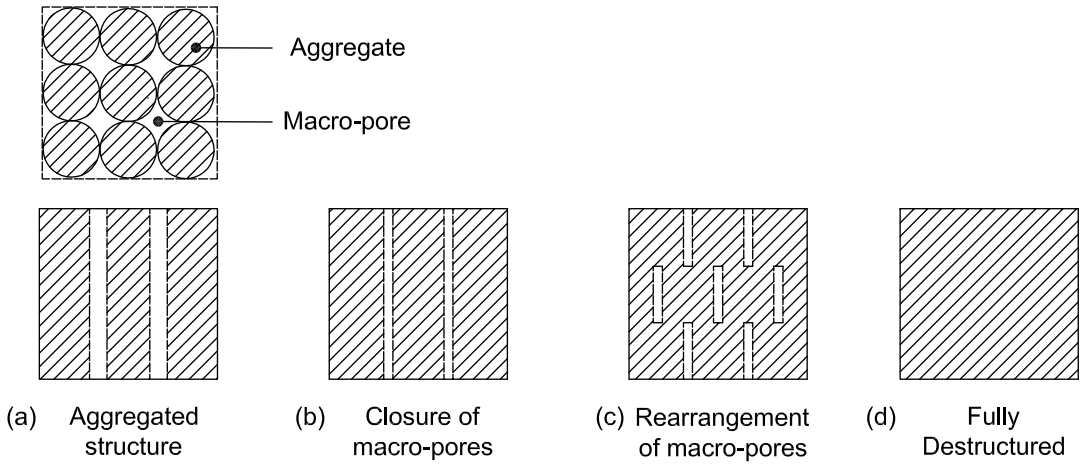


*Figure 5.34:* System of macropores and aggregates during de-structuring of an aggregated soil

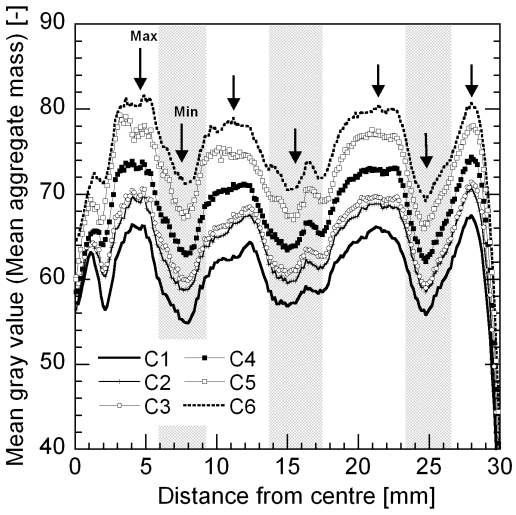


*Figure 5.35:* Mean gray value (mean aggregate mass) as a function of distance from the center of the sample M

Two main observations can be made in Figure 5.35 as the applied load increases: (i) the average gray value in the sample increases while the maintaining the relative extrema, i.e., the gray value curve does not flatten with compression, and, (ii) the relative positions of extrema do not change.

The first observation suggests that at the applied range of stress an important fraction of macropores still exists between the aggregates. This means that state of material is still far from a homogeneous state were all the macropores are closed. The second observation could be interpreted to mean that there is no significant rearrangement of macropores (aggregates) at the current condition of loading, and the relative positions of macropores and aggregates remain almost the same. This evidence indicates that the diminution of macroporosity in the sample is mainly due to the local closure of macropores; therefore, the active

mechanism of degradation in the current loading condition is mainly isotropic.

Considering these two pieces of evidence, it is understood that the active isotropic mechanism for structural degradation by itself is not enough to fully remove the aggregated structure of the material.

It is, therefore, concluded that a fully de-structured state of material could be achieved only through a combination of both isotropic and deviatoric mechanisms of de-struction. More experimental results are required to verify the generality of this observation for different loading conditions and different ranges of applied stress.

## 5.4 Tomography evaluation of soil structure under suction variation

### 5.4.1 Material and method

In this series of experiments, an aggregated sample of Bioley silt was subjected to a cycle of drying and wetting with the variation of matric suction between 20 and 3000 $kPa$ under the constant vertical net stress of 15 $kPa$ and structural evolution of the sample during theses steps was evaluated using neutron tomography data acquired for the sample at the end of each step. The test was carried out using the osmotic oedometer cell.

Due to high sensitivity of neutrons to small amount of hydrogen, two types of water, namely normal and heavy water, were used in the experiment. Heavy water is transparent while normal water exhibits an opaque medium in the neutron beam. Using heavy water, the wet aggregates with an initial water content of 13.7% were prepared following the method described in Section 4.3.2. The sample was prepared in the osmotic cell at LMS in the similar way as in unsaturated oedometer tests (see Sec. 4.5.1). The sample was then transfered to PSI for neutron radiography and tomography experiments.

### 5.4.2 Experimental set up and procedure

The experiment was carried out using the osmotic cell. As mentioned in Section 4.2, the cell had been built with aluminum due to its transparency to neutron beams. Together with the cell, the electronic balance, the pump and tubes as well as the PEG solutions and the reservoir where transfered to PSI for the experiment.

Acquiring radiography and tomography data was made in the same way as in the dry test described in Section 5.3. The oedometer cell was directly positioned and fixed on the rotary table in the beam. The electronic balance, the reservoir and the pump were placed in a closed box next to the beamline. The acquisition of the balance data were made using a computer placed in the tomography room and controlled by a remote desktop from outside. Using a holder built for this purpose, three lead blocks corresponding to a vertical stress of 15.7 $kPa$ were placed on the loading piston.

*Table 5.3:* Suction steps in th eneutron tomography experiments

| **Step** | **1** | **2** | **3** | **4** | **5** |
|---|---|---|---|---|---|
| $\sigma_v$ $[kPa]$ | 15.7 | 15.7 | 15.7 | 15.7 | 15.7 |
| $s$ $[kPa]$ | 50 | 500 | 3000 | 500 | 50 |
| **Water** | heavy | normal | normal | heavy | heavy |

Different suctions were applied by changing the solution in the reservoir. Different steps of applied suction are presented in Table 5.3. Normal water was used to prepare the PEG solution for drying steps in order to observe the difference between water in the soil and the solution. In the wetting steps, heavy water was used in order to keep the transparency of water in the images.

A time interval of about 36 to 48 hours was provided between each suction step. During this time, radiography images of the sample were acquired every 1 minutes for the first 5 minutes, every 5 minutes for 20 minutes and finally every 20 minutes for the remaining time. For tomography data, the pump was stopped at the end of each step and a set of radiograms was recorded while rotating the sample stepwise by 180 degrees with a constant angular increment of 0.9 degree.

Projected image data were normalized for equal neutron exposure and corrected for spatial variations in the incident neutron beam and the inhomogeneity of the scintillator screen in the same manner as in dry test (see Sec. 5.3). These images were then used to reconstruct the three-dimensional array of the sample volume.

### 5.4.3 Processing of raw image data

#### 5.4.3.1 Radiography data

The radiography images of the sample were processed using the image processing software *ImageJ* which allows processing and analysis of two dimensional image data. The radiography image of the initial state of the sample is shown in Figure 5.36(a). This image consists of a gray scale image in which different components such as the soil, the aluminum cell and the liquid PEG solution are identified by different gray values. It can be seen that aluminum with a low neutron attenuation coefficient exhibits a higher transparency compared with the soil particles. The image corresponds to the beginning of step 2 where the PEG solution of normal water for a suction of 500 $kPa$ is in circulation beneath the sample. In this figure, the solution is observed as a dark region in the input and output of the cell.

The sample at each state, during drying or wetting, could be compared with the initial state by dividing the actual radiography image by the initial image:

$$[img] = [img1].[img0]^{-1} \tag{5.4}$$

where $[img1]$ and $[img0]$ are respectively actual and initial gray value matrix of the radiography image.

Figure 5.36(b) and Figure 5.36(c) show the actual image of the sample divided by initial image at the end of the suction step 500 and 3000 $kPa$ during the drying phase respectively. In these images, darker regions correspond to lower gray values and represent regions with higher normal water concentration.

It is observed in Figure 5.36(b) that during application of suction 500 $kPa$ using a PEG solution of normal water, the normal water has been entered into the sample from the circulation system. This shows that in spite of the pressure gradient from the soil toward the solution due to osmotic phenomenon, there is still diffusion of solution water through the sample. This is a clear evidence that in the osmotic method, the semi-permeable membrane does not embed the passage of water by diffusion. Accordingly, small soil salt also can move with this water. This confirms only the matric suction and not the total suction is controlled in the osmotic method. It can be seen that at the end of this step, the diffused water front has reached, uniformly, only to about the half height of the sample.

Figure 5.36(c) shows the similar comparison for the sample at the end of step 3 corresponding to suction of 3000 $kPa$. This image represents slightly darker values at the top, while distribution of gray value is more homogeneous as in Figure 5.36(b). This shows that (i) diffused water has been redistributed in the sample and (ii) an important amount of water has been moved out of the sample into the solution.

The contrary distribution of gray value could be observed during wetting steps shown in Figure 5.37. During the wetting, heavy water has been entered into the sample.

#### 5.4.3.2 Tomography data

As in dry tests, the raw tomography results consisted of a three dimensional sample volume with a voxel (the 3D equivalent of a 2D pixel) size of 146 $\mu m$. Similarly, before being used for structural analysis, the volumes have been subjected to a $5 \times 5$ Median filter using the software *VGStudio MAX 1.2.1*.

Results of radiography images showed that most significant change of humidity at each step occurred at the bottom half of the sample. This is related to the permeability of the soil and the time interval between the steps. Accordingly, in order to have a homogeneous specimen, only an internal section of the volume from the bottom half has been selected for structural analysis. The choice of this section, shown in Figure 5.38(b), ensures the uniform distribution of suction and humidity within the specimen and also prevents the interference of boundary effects into analysis.

This section was then segmented into aggregates and macropores. The segmentation has been done using the calibration and segmentation tool provided in *VGStudio MAX 1.2.1*. The structural analysis of the segmented volume then yields the volume fraction of aggregates (including micropores) at different suction steps.

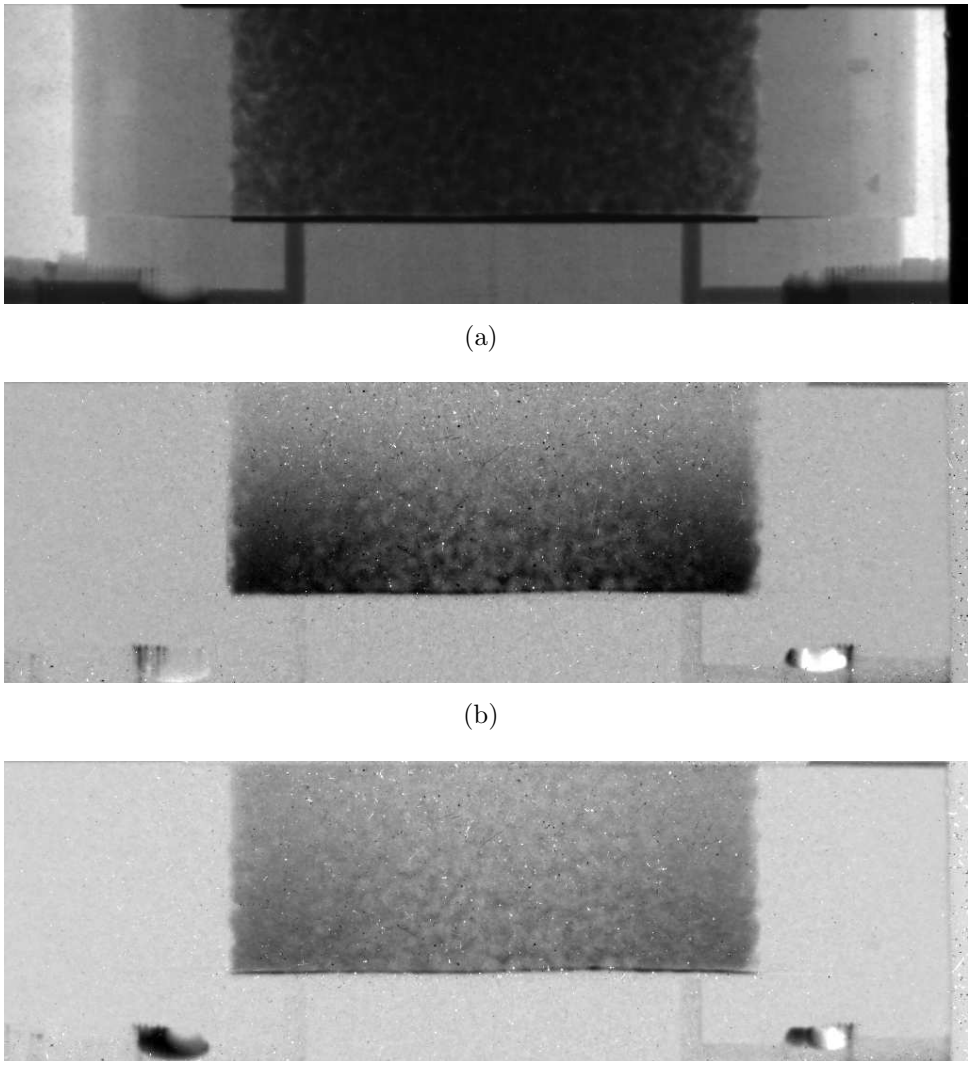

(a)

(b)

(c)

*Figure 5.36:* Radiography image of sample H during drying: (a) initial state image, (b) image at the end of suction step 500 $kPa$ divided by initial image, (c) image at the end of suction step 3000 $kPa$ divided by initial image

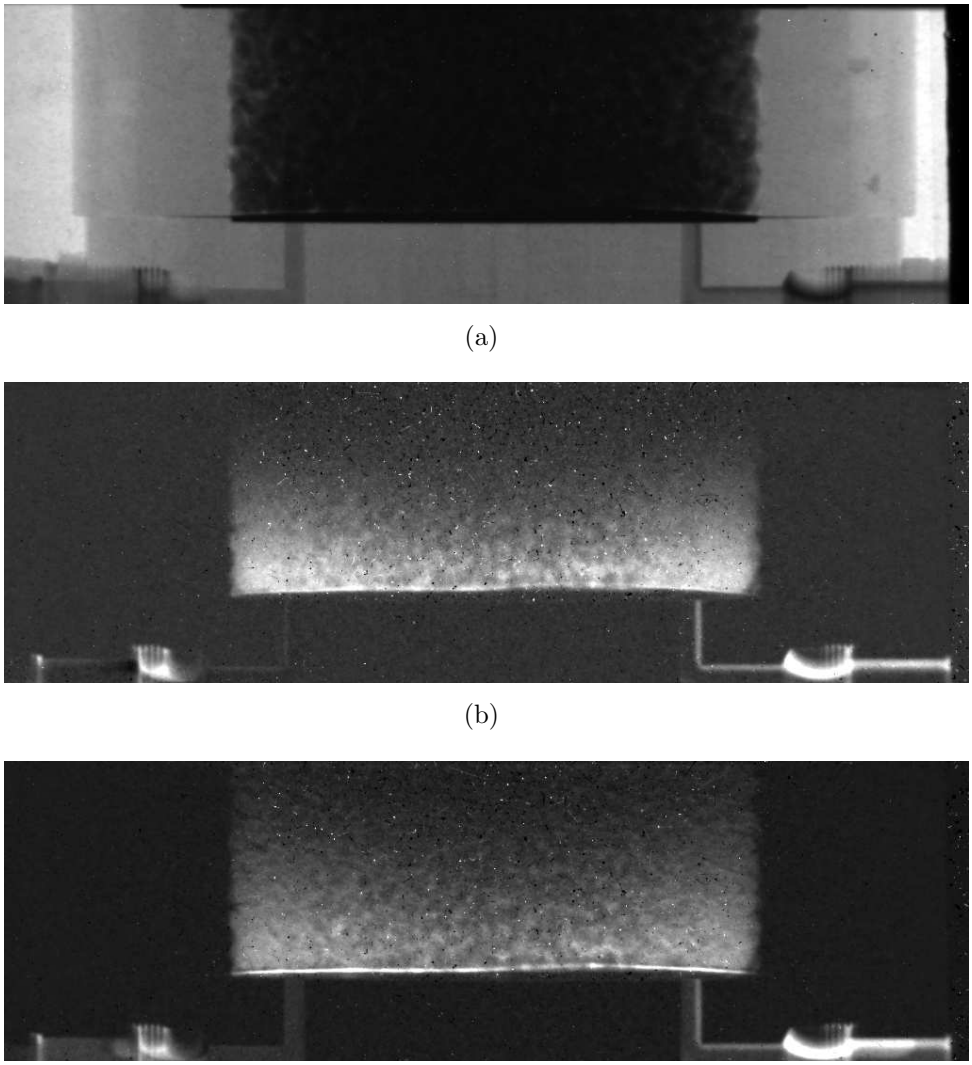

(a)

(b)

(c)

*Figure 5.37:* Radiography image of sample H during wetting: (a) driest state image (end of suction step 3000 $kPa$), (b) image at the end of suction step 500 $kPa$ divided by the direst state image, (c) image at the end of suction step 50 $kPa$ divided by the driest state image

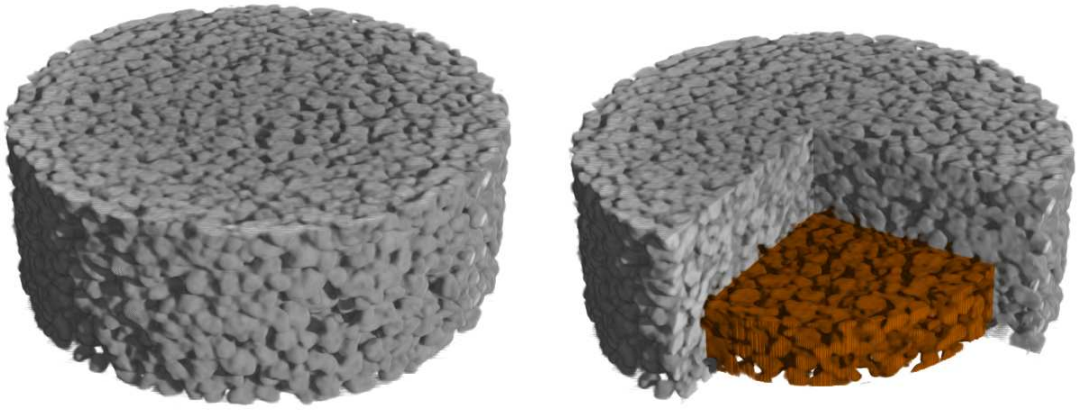

(a) (b)

*Figure 5.38:* Tomography data for sample H after filter operation and segmentation: (a) whole volume, (b) selected segment for structural analysis

### 5.4.4 Suction-induced volume change of aggregates

The total deformation of the sample was derived based on the height of the sample determined in the radiography images for each step. These results shows that the total deformation of the sample during the experiment is insignificant an corresponds to decrease of the initial void ratio of 1.31 to the final values of 1.28. An equivalent observation had already been made for unsaturated aggregated samples of Bioley silt subjected to suction increase (see Sec. 4.5.3).

On the basis of the segmented volumes, volume fraction of aggregates has been derived for each step. The aggregate volume fractions are plotted in Figure 5.39(a). The initial volume fraction of aggregates in the sample is 0.670 which yields a complementary value of macroporosity equal to 0.33. Considering the initial total porosity of the sample 0.567 (void ratio 1.31), the derived value of macroporosity corresponds to a microporosity of 0.237. This value is almost identical to the corresponding values deduced from MIP tests of single aggregate (0.222 in Sec. 5.2.3).

It is observed that suction increase gives a decrease to the volume of aggregates, with the most volume decrease occurring in the first suction step between 50 $kPa$ and 500 $kPa$. The volume change beyond this suction is less significant. The volume change during the wetting phase exhibited a reversible response for the suction decrease from 3000 $kPa$ to 500 $kPa$. During this phase, the volume of aggregates slightly increased with a small rate of variation with suction. Below the suction of 500 $kPa$ until reducing to the initial suction of 50 $kPa$, volume of aggregates kept increasing volume with the same rate of variation as in the first step of wetting.

These results could be compared with the results presented in Section 4.5.2 for the volume variation of reconstituted sample USR03 subjected to a suction increase to 3000 $kPa$. It is observed that the aggregates in sample H followed the same pattern of volume change as in sample USR03 corresponding to a higher volume change at lower suctions and lower volume change at higher

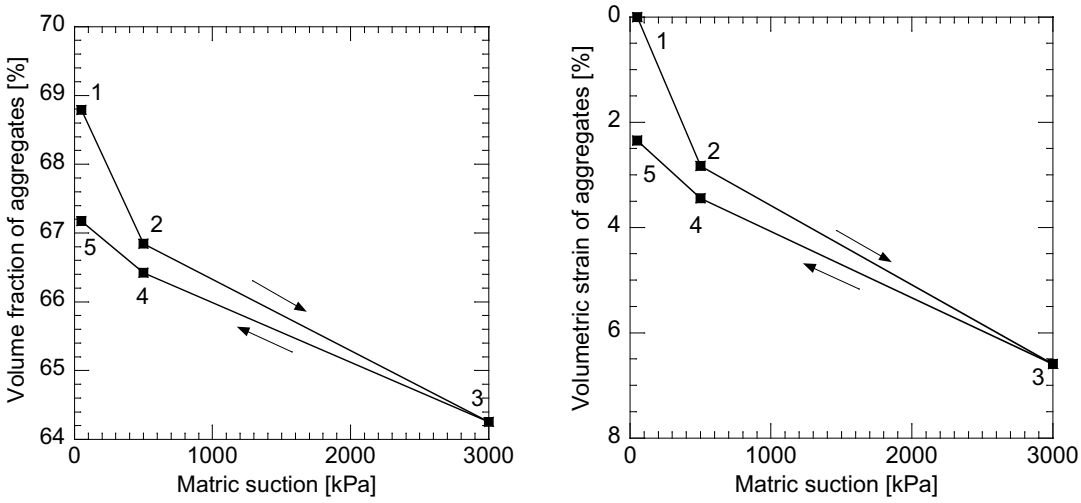


(a) (b)

*Figure 5.39:* Evolution of aggregate volume with suction in sample H: (a) volume fraction, (b) volumetric strain

suction. However, the magnitude of strains are different in two samples. It is therefore concluded that the aggregates exhibit a micro structure with a behaviour comparable with reconstituted soil.

## 5.5 Summary of results

The main experimental observations made for the soil structure in this section are summarized below.

1. MIP results showed that unsaturated aggregated samples initially exhibit a multi-modal PSD with at least two dominant pore radii. The peak of smaller pores correspond to the most dominant size of micropores (intra-aggregate pores); while, the peak of larger pores represents only a subset of the macropores (inter-aggregate pores) with the radius lying in the range of detectable pores in MIP method.
2. At the same condition, a corresponding reconstituted soil exhibits a uni-modal PSD with the dominant pore radius coinciding with the micropores in aggregated samples.
3. When subjected to wetting until saturation, the PSD of aggregated sample tend to a uni-modal distribution with the larger pores vanishing and the dominant pore size being at the range of micropores in the initial fabric. However, the intensity of the dominant pore size decreases strongly as a result of the collapse of aggregated structure. The dominant pore size is almost identical to the dominant pore size of the corresponding reconstituted soil. The peak pore size density function in saturated sample is distributed over a wider range of pore sizes in comparison with reconstituted soil and the micropores of unsaturated aggregated samples.

4. When compacted under unsaturated condition, the macropores in the bi-modal PSD of aggregated samples decrease and the micropores increase with the dominant micropore size being unchanged.
5. In the case of saturated samples where the PSD of aggregated samples are uni-modal, compaction results in a decrease in the intensity of dominant pore size while shifting the dominant pore size slightly toward smaller pores.
6. ESEM observations showed that soaked aggregated samples exhibit an almost homogeneous texture as in reconstituted soil.
7. The fabric and texture of single aggregate resembles the one of reconstituted soil with the exception of having more inter-locking particles within the aggregates fabric.
8. Tomography analysis showed that during mechanical loading, the macropores are essentially affected while the change in the micropores are almost insignificant. Therefore, evolution of macropores represents the evolution of the soil structure during the loading process.
9. Change in the volume fraction of macropores is mainly associated with plastic deformations and variation during elastic deformation is insignificant.
10. Mechanism of structure degradation in mechanical loading appears to have a combined isotropic and distortional nature.
11. A single aggregate can be considered as a packing of soil particles with given physical boundaries, the hydro-mechanical properties of which could be compared with that of the reconstituted soil matrix.

The above multi-scale evidences propose to consider the aggregated soil as a structured soil with double porosity in which (i) micropores are similar to the pores in reconstituted soil and, (ii) macropores are additional pores formed due to structural features (inter-particle bonding). The hydro-mechanical behavior of aggregates, in general sense, is similar to that of the reconstituted soil matrix. Any degradation of structures due to mechanical loading or humidity variation, results in closure of macropores and brings the state of the soil closer to a reconstituted state.

These results together with the macroscopic experimental evidences provide an experimental basis for describing and modeling the behavior of unsaturated aggregated soil.

# Chapter 6

# Mechanical constitutive model

The governing equations of Chapter 3 revealed the need for an appropriate mechanical constitutive model for stress-strain response of structured soils with double porosity. It was also shown that, under unsaturated condition, a water retention model is also needed to describe the relation between the degree of saturation, suction, and porosity. In the onset of this study, these equations were presented in their general form. This chapter treats the explicit form of these models. In this chapter, the coupled mechanical constitutive model and the water retention model, incorporating the degradation of structures, are proposed for unsaturated aggregated soils or structured soils with double porosity. The chapter is organized as follows. The constitutive framework and the fundamental mathematical equations are presented first. Subsequently, the macroscopic and the pore scale experimental observations of the preceding chapters are combined to figure out the general requirements of the new model for aggregated soil and to introduce the soil structure parameters in the development of such constitutive models. Thereafter, this concept is applied to an elasto-plastic constitutive model and the explicit formulation of the new constitutive model is developed. The model parameters and the typical numerical response of the model will be evaluated next. Finally, the model is validated by simulating the experimental results of this study. At the end, the capability of the model in reproducing the behavior of bonded soils is evaluated.

## 6.1 Constitutive framework

### 6.1.1 Stress framework

An essential preliminary step to constitutive modeling of unsaturated soils is determining the stress framework and the effective stress in solid skeleton (Jommi, 2000). The existing stress framework approaches for constitutive modeling of unsaturated soils were reviewed in Section 2.6.2.1. As discussed in that section, using suction together with a constitutive stress containing both suction and degree of saturation provides an appropriate stress framework for development of a consistent constitutive model for soils.

In the present study, the generalized effective stress and matric suction are

selected as stress variables in the development of the constitutive model. The stress tensor for solid and fluid phases in an unsaturated double porous mixture was evaluated in Chapter 3 using the multi-phase mixture theory. On the basis of a thermodynamic analysis, the rigorous expression of total suction and effective stress in unsaturated soils with double porosity were derived and were given by Equations (3.82) and (3.83) respectively. Those equations provide a set of general stress variables for constitutive modeling of unsaturated soils with double porosity.

As discussed in Section 3.3.1, in the absence of macropores or in the case of having the macropores drained (as in the experiments of this work), the expression of effective stress is simplified to the generalized effective stress for unsaturated single porosity soils (Eq. 2.9):

$$\boldsymbol{\sigma'} = (\boldsymbol{\sigma} - p_a\mathbf{I}) + S_r(p_a - p_w)\mathbf{I}$$

In latter case, with the assumption of equal gas pressure within the soil pores, water potential could be represented by a single value of total suction equal to the suction within the soil matrix or micropores.

The above form of generalized effective stress and total matric suction are used here to develop the constitutive model. As discussed in 2.6.2.1, opting for the generalized effective stress and suction as stress variables allows keeping consistency in description of material behavior at different states of saturation. This approach has been selected for the constitutive framework of this study. A discussion of the adoption of this stress framework and its comparison with the two independent stress variables approach, i.e., net stress and suction, is given in Nuth and Laloui (2005) and Nuth and Laloui (2007a).

### 6.1.2 Critical state line for unsaturated aggregated soils

The constitutive model developed in this work is based on the critical state concept (Schofield and Wroth, 1968). Hence, it is necessary to evaluate the critical state line (CSL) in unsaturated aggregated soils. The CSL for saturated soil is formulated in terms of three state variables, $p'$, $q$ and $v$, and was defined by two equations (Roscoe et al., 1958):

$$q = Mp' \tag{6.1a}$$

$$v = \Gamma - \lambda \ln p' \tag{6.1b}$$

in which $v$ is the specific volume, and $p'$ and $q$ are respectively triaxial devitroic and mean effective stress:

$$p' = \frac{1}{3}(\sigma'_1 + 2\sigma'_3) \tag{6.2a}$$

$$q = \sigma'_1 - \sigma'_3 \tag{6.2b}$$

with $\sigma'_1$ and $\sigma'_3$ being vertical and radial triaxial stresses respectively. Parameter $\lambda$ is the slope of normal consolidation line (NCL) and of CSL in $v - \ln p'$ space,

and $\Gamma$ is a material parameter. In these equation, $M$ is the slope of the CSL in the stress space $q - p'$. For triaxial compression, it reads:

$$M = \frac{6 \sin \varphi'}{3 - \sin \varphi'} \tag{6.3}$$

with $\varphi'$ being the critical state friction angle. Description of the critical state concept for saturated soils is well documented in many textbooks of soil mechanics (e.g. Atkinson and Bransby, 1978; Wood, 1990) and will not be repeated here. Instead, the emphasis is placed on the influence of partial saturation and soil structure on the CSL.

Critical state concept in unsaturated soils has been evaluated by different authors (among them, Alonso et al., 1990; Toll and Ong, 2003; Wheeler and Sivakumar, 1995). Khalili et al. (2004) successfully investigated the uniqueness of the CSL in the $q-p'$ space for unsaturated soils with different suctions. They used the Bishop's effective stress with a particular expression for the Bishop's parameter. Uniqueness of the CSL in terms of generalized effective stress as given by Equation (2.9) has been evaluated by Nuth and Laloui (2007a). These authors processed the experimental data reported by Sivakumar (1993) and Geiser et al. (2006) and compared the interpretation of CSL in terms of net stress and generalized effective stress. The results of that work are depicted in Figures 6.1 and 6.2. These results shows the unification of CSL for unsaturated soils regardless of the suction level.

Recently, Tarantino and Tombolato (2005) evaluated the effect of water menisci on ultimate shear strength. Based on the results of this work, Tarantino (2007) presented a possible critical state framework for unsaturated compacted soils with an aggregated structure. He introduced some micro-scale parameters in the equations of CSL. However, due to the associated difficulty with their

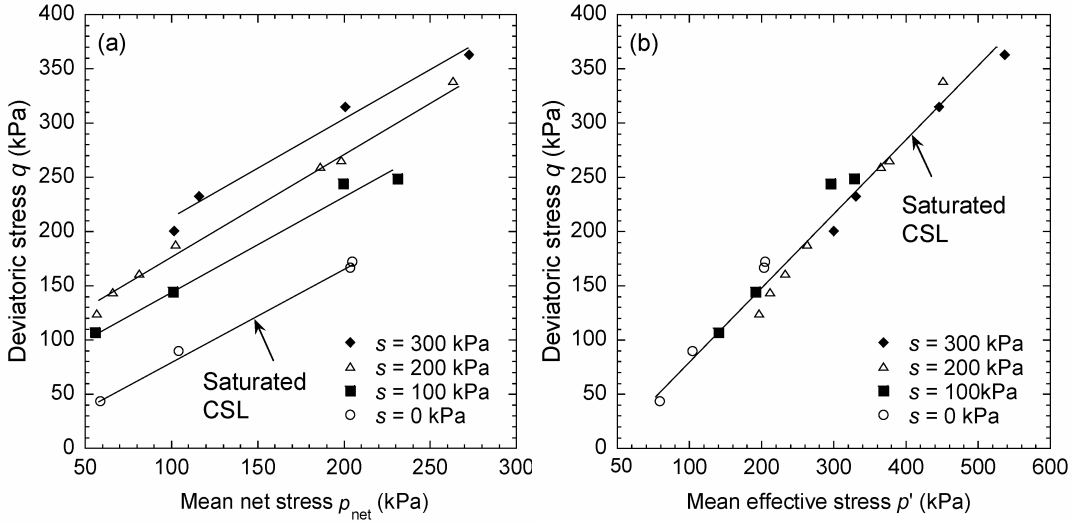


*Figure 6.1:* CSL for Kaolin at different suctions in the stress plane, data after Sivakumar (1993), (Nuth and Laloui, 2007a)

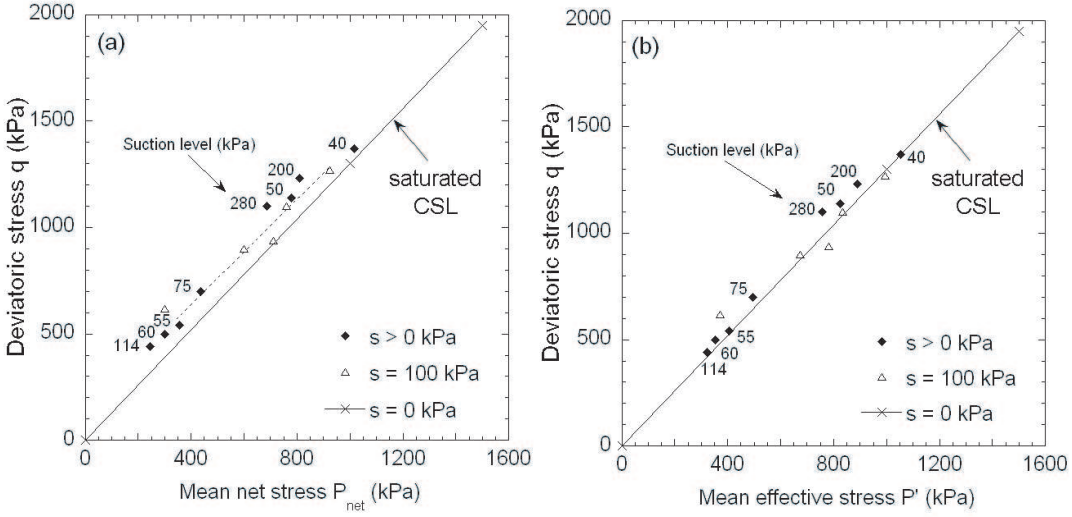


*Figure 6.2:* CSL for Sion silt at different suctions, data after Geiser et al. (2006), (Nuth and Laloui, 2007a)

physical interpretations, later in that work, these parameters were treated as fitting parameters. In the constitutive model developed for natural structured soils, a review of which was presented in Section 2.6.3, slope of CSL ($M$) has been assumed to be independent of soil structure and therefore to be the same in structured and reconstituted soils. This statement is a consequence of the assumption that soil structure and its degradation, whatever its cause may be, affects only internal variables and not other material properties, e.g. friction angle.

Based on the above considerations, it is postulated in this study that the slope of the CSL in the generalized effective stress plane $q - p'$ is an intrinsic material parameter which is independent of the saturation condition and of the soil structure.

### 6.1.3 Fundamental formulation

The mechanical constitutive model is developed in the framework of strain hardening elasto-plasticity. The required fundamental elements of an elasto-plastic model will be presented in this section. The first essential step in deriving a complete stress-strain relation in an elasto-plastic model is decomposition of the total increment of strain tensor, $\mathrm{d}\boldsymbol{\varepsilon}$, into an elastic reversible part, $\mathrm{d}\boldsymbol{\varepsilon}^e$ and a plastic irreversible part, $\mathrm{d}\boldsymbol{\varepsilon}^p$:

$$\mathrm{d}\boldsymbol{\varepsilon} = \mathrm{d}\boldsymbol{\varepsilon}^e + \mathrm{d}\boldsymbol{\varepsilon}^p \tag{6.4}$$

The elastic part of strain is obtained from the models of elasticity:

$$\mathrm{d}\boldsymbol{\varepsilon}^e = \boldsymbol{C}^e : \mathrm{d}\boldsymbol{\sigma'} \tag{6.5}$$

In this relation, $\boldsymbol{C}^e$ is the elastic compliance tensor of rank four. Using the

elastic constitutive tensor $\boldsymbol{D}^e$, the above equation can be written as:

$$\mathrm{d}\boldsymbol{\sigma'} = \boldsymbol{D}^e : \mathrm{d}\boldsymbol{\varepsilon}^e = \boldsymbol{D}^e : (\mathrm{d}\boldsymbol{\varepsilon} - \mathrm{d}\boldsymbol{\varepsilon}^p) \tag{6.6}$$

The plastic stress tensor, $\boldsymbol{\varepsilon}^p$, have to be obtained through the procedure defined in theory of plasticity. A criterion that defines the limit of elasticity and onset of plastic deformations under any possible combination of stresses is known as *yield criterion*. A general mathematical form of the yield criterion can be expressed in terms of the stress tensor (or the three stress invariants) in combination with a set of internal hardening parameters:

$$f(\boldsymbol{\sigma'}, \boldsymbol{\zeta}) = f(I_1, I_2, I_3, \boldsymbol{\zeta}) = 0 \tag{6.7}$$

where $\boldsymbol{\zeta}$ is a vector representing the set of internal variables, and $I_1, I_2$ and $I_3$ are first, second, and third invariants of stress tensor. The vector of internal parameters $\boldsymbol{\zeta}$, also referred to as the vector of hardening parameters, represents the measure of hardening (or softening). In strain hardening models, this is usually a function of plastic strains:

$$\boldsymbol{\zeta} = \boldsymbol{\zeta}(\boldsymbol{\varepsilon}^p) \tag{6.8}$$

The material behavior is considered to be elastic if the stress state remains inside the closed space determined by $f$ in the stress space. The complete conditions for plastic and elastic behavior for a hardening elasto-plastic material reads:

$$\text{Elastic:} \quad f(\boldsymbol{\sigma}, \boldsymbol{\zeta}) < 0 \quad \text{or} \quad \mathrm{d}f = \frac{\partial f}{\partial \boldsymbol{\sigma}} : \mathrm{d}\boldsymbol{\sigma} \leq 0 \tag{6.9a}$$

$$\text{Plastic:} \quad f(\boldsymbol{\sigma}, \boldsymbol{\zeta}) = 0 \quad \text{and} \quad \mathrm{d}f = \frac{\partial f}{\partial \boldsymbol{\sigma}} : \mathrm{d}\boldsymbol{\sigma} > 0 \tag{6.9b}$$

When the stress state is already on the yield surface, three possible conditions exist for a further stress increment:

$$\text{Unloading:} \quad f(\boldsymbol{\sigma}, \boldsymbol{\zeta}) < 0 \quad \text{and} \quad \mathrm{d}f < 0 \tag{6.10a}$$

$$\text{Neutral loading:} \quad f(\boldsymbol{\sigma}, \boldsymbol{\zeta}) = 0 \quad \text{and} \quad \mathrm{d}f = 0 \tag{6.10b}$$

$$\text{Loading:} \quad f(\boldsymbol{\sigma}, \boldsymbol{\zeta}) = 0 \quad \text{and} \quad \mathrm{d}f > 0 \tag{6.10c}$$

Equations (6.9) implies that for both unloading and neutral loading, material behavior is elastic and plastic behavior occurs only when the loading condition is satisfied for a stress state on the yield limit.

According to the theory of plasticity, the increments of plastic strain is expressed as:

$$d\boldsymbol{\varepsilon^p} = \lambda^p \frac{\partial g}{\partial \boldsymbol{\sigma}} \tag{6.11}$$

which is referred to as *flow rule*. In these equation, $\lambda^p$ is a positive scalar called *plastic multiplier* representing the magnitude of plastic strain; and, $g(\boldsymbol{\sigma'}, \boldsymbol{\zeta})$ is known as *plastic potential*, through which direction of plastic strain vectors are defined. If the plastic potential is assumed to be the same as the yield function, the plastic flow rule is called *associated flow rule*. However, for many geological

materials, the yield function and the plastic potential function are often different which represents a *non-associated flow rule*. The plastic multiplier is obtained from the Prager's consistency condition (Prager, 1949) which requires the stress state to remain on the yield limit as plastic strains occur:

$$df = \frac{\partial f}{\partial \boldsymbol{\sigma}} : d\boldsymbol{\sigma} + \frac{\partial f}{\partial \boldsymbol{\zeta}} : \frac{\partial \boldsymbol{\zeta}}{\partial \boldsymbol{\varepsilon}^p} : d\boldsymbol{\varepsilon}^p = 0 \tag{6.12}$$

Substituting Equation (6.11) into Equation (6.12) and solving for the plastic multiplier yields:

$$\lambda^p = \frac{1}{H} \frac{\partial f}{\partial \boldsymbol{\sigma}} d\boldsymbol{\sigma} \tag{6.13}$$

where $H$ is the hardening modulus given by:

$$H = -\left( \frac{\partial f}{\partial \boldsymbol{\zeta}} : \frac{\partial \boldsymbol{\zeta}}{\partial \boldsymbol{\varepsilon}^p} \right) : \frac{\partial g}{\partial \boldsymbol{\sigma}} \tag{6.14}$$

Using Equation (6.6) and the flow rule (Eq. 6.11), plastic multiplier in Equation (6.13) reads:

$$\lambda^p = \left( \frac{\frac{\partial f}{\partial \boldsymbol{\sigma}} : \boldsymbol{D}^e}{H + \frac{\partial f}{\partial \boldsymbol{\sigma}} : \boldsymbol{D}^e : \frac{\partial g}{\partial \boldsymbol{\sigma}}} \right) : d\boldsymbol{\varepsilon} \tag{6.15}$$

The complete incremental stress strain relation is then derived by introducing the plastic multiplier of Equation (6.15) and the flow rule into the stress strain relation of Equation (6.6):

$$d\boldsymbol{\sigma'} = \boldsymbol{D}^{ep} : d\boldsymbol{\varepsilon} \tag{6.16}$$

where $\boldsymbol{D}^{ep}$ is the elasto-plastic constitutive matrix:

$$\boldsymbol{D}^{ep} = \boldsymbol{D}^e - \frac{(\boldsymbol{D}^e : \frac{\partial g}{\partial \boldsymbol{\sigma}}) \otimes (\frac{\partial f}{\partial \boldsymbol{\sigma}} : \boldsymbol{D}^e)}{H + \frac{\partial f}{\partial \boldsymbol{\sigma}} : \boldsymbol{D}^e : \frac{\partial g}{\partial \boldsymbol{\sigma}}} \tag{6.17}$$

The above equation represents the general form of the complete stress-strain relation in an elasto-plastic constitutive model. The constitutive tensors $\boldsymbol{D}^e$ and $\boldsymbol{D}^{ep}$ are tensors of rank four with 81 components in the cartesian coordinate system ($3^4$ components), and could be represented by a $9 \times 9$ matrix (because the stresses and strains have nine components each). Due to symmetry of stress and strain tensors, however, the number of independent components reduces to 21 which are represented by a symmetric $6 \times 6$ matrix shown by $\mathbf{D}^e$ and $\mathbf{D}^{ep}$ (regular instead of italic bold letter).

Depending on special features of the material behavior under consideration, the explicit formulation of models might be different. Regardless of the complexity of the formulation, the ingredients of any constitutive model developed in the framework of elasto-plastic hardening can be summarized as follows (Wood, 1990): (i) elastic properties: to describe the recoverable deformation in elastic domain; (ii) yield surface: to determine the limit when the occurrence plastic deformations starts; (iii) plastic potential: to understand the mechanism of plastic deformation and direction of plastic strains; and, (iv) hardening rule: to determine the magnitude of plastic deformation and evolution of yield surface.

## 6.2 Requirements of the new model

### 6.2.1 Features to be addressed

The extra features of the behavior of aggregated soil are evaluated in reference to the *corresponding reconstituted soil* of the same mineralogy at the same suction. Following Burland (1990), properties of reconstituted soil are here called *intrinsic* properties and shown by an asterisk subscript ($^*$). Furthermore, the subscript ($_0$) is selected to designate the properties of saturated soil. The idea in the model developments is to start from a constitutive model which is already capable of describing the behavior of reconstituted soils and to extend it for aggregated soils by adding extra features.

As the next step after definition of the constitutive framework, the experimental observations of Chapter 4 should be employed to evaluate the features that the new constitutive model of aggregated soil should be able to address. The macroscopic experimental results of this study were obtained through an oedometric testing program. Accordingly, the stress-strain behavior of the samples in Chapter 4 were presented in terms of one-dimensional compression-swelling curves in oedometric plane, namely void ratio, $e$, versus vertical effective stress, $\sigma'_v$. However when description and development of constitutive models are concerned, it is more convenient to interpret the stress-strain response in the isotropic plane $v - p'$. This is because of the fact that this latter space could be more easily linked to the stress space $q - p'$ in which usually the yield surface is defined.

Having the coefficient of earth pressure at rest, $K_0$, the oedometric compression curves can be plotted in the isotropic compression curve. Atkinson and Bransby (1978) showed that, with a good approximation, the one-dimensional compression (swelling) and the isotropic compression (swelling) can be assumed to be parallel (Fig. 6.3a). However, this assumption is valid for soils for which the coefficient of lateral earth pressure at rest, $K_0$,remains constant during virgin compression. Therefore, the parallelism of isotropic and oedometric compression lines in the general case is an assumption which allows interpreting the oedometric results in the isotropic compression plane. In this case, the compressibility and swelling index, $C_c$ and $C_s$, are related to the slope of the NCL and swelling line in the $v - \ln p'$ plane, $\lambda$ and $\kappa$:

$$C_c = 2.3\lambda \tag{6.18a}$$

$$C_s = 2.3\kappa \tag{6.18b}$$

Unlike the isotropic compression, the value of $q/p'$ for oedometric compression is not zero (Fig. 6.3a) and the stress path depends on $K_0$:

$$\frac{q}{p'} = \frac{3(1 - K_0)}{(1 + 2K_0)} \tag{6.19}$$

The location of the oedometric compression with respect to the isotropic compression curve in the isotropic plane depends on the shape of the yield surface. However, for a given yield surface, there is a one and only one isotropic

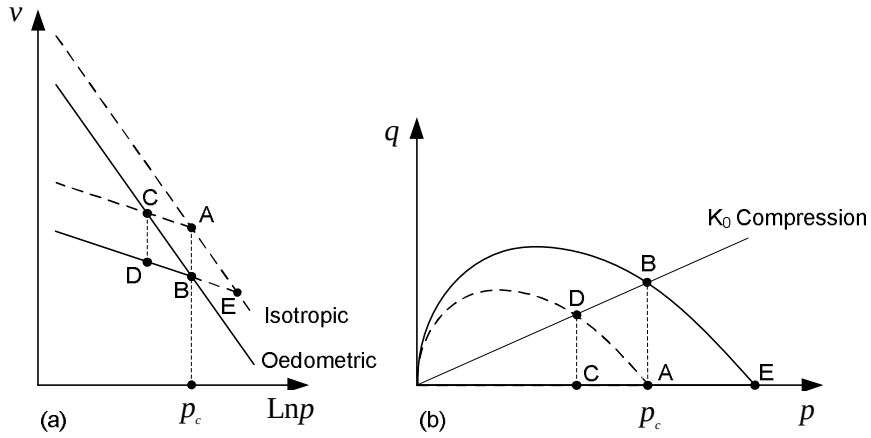


*Figure 6.3:* Oedometric and isotropic compression: (a) isotropic compression space (b) $q - p'$ stress space

compression curve corresponding to the oedmetric compression curve. This correspondence is used here to describe the relation between the experimental results and the special features of the model in the isotropic plane. A general shape of yield surface with its size being controlled by the isotropic preconsolidation pressure, as in Cam-clay, is used here for this purpose (Fig. 6.3a).

In Section 4.7, the observed macroscopic experimental evidences were summarized and classified with respect to three different effects:

**a. Pure effects of structure,** describing the difference in the behavior of reconstituted and aggregated soil at the same saturation condition.
**b. Intrinsic suction effects,** representing the effects of partial saturation on reconstituted soil.
**c. Combined effects of suction with structure,** describing the influence of suction on the the properties of the structural units.

From those results, it was understood that suction can affect the mechanical behavior of aggregated soils through two different mechanisms. Primary effects of suction, the so-called intrinsic suction effects, are similar to the suction effects in reconstituted soil and it is related to the capillary effects in the soil matrix. A major effect is the increase of the apparent preconsolidation pressure with suction. The secondary suction effects in aggregated soils correspond to the influence of suction on the soil structure and its properties. An equivalent division of suction effects was made by Leroueil and Barbosa (2000) and Alonso and Gens (1994) in unsaturated cemented soils. In the case of cemented soils, Alonso and Gens (1994) argued that the capillary effects (intrinsic suction effects) are not probably as strong as the capillary effects for the reconstituted soil. They discussed that the bonding cement tends to occupy the position of particle contacts and the curvature of menisci cannot possibly reach the low values admissible in the ideal point contacts.

Table 6.1 presents the interpretation of experimental evidences of Section 4.7 within the constitutive framework. This table indeed provides a "*To do list*" for development of the new model.

*Table 6.1:* Special features of the compression behavior of aggregated soils; numbers within the parenthesis correspond to the summarized list of Sec. 4.7

| No. | Experimental evidence | Modeling feature |
|---|---|---|
| **a** | **Soil structure effects** | |
| a1 | (1) initial stiff behavior followed by yielding in normal consolidation compression in aggregated samples, (2) uniqueness of initial apparent preconsoidation stress in samples with the same structure, | $f_0 \neq 0$ |
| a2 | (3) identical slope of the initial stiff compression and unloading curves in aggregated samples, identical slope of unloading-reloading line for aggregated and reconstituted samples in effective stress plane | $\mathbf{D}^e = \mathbf{D}^{e*}$ |
| a3 | (4) non-linear virgin compression curve in aggregated samples beyond the initial apparent preconsolidation stress (5) with an initial tangential compressibility index higher than the compressibility index of reconstituted soil at the same suction. | $(\mathbf{D}^{ep}) \neq (\mathbf{D}^{ep})^*$ |
| a4 | (5) the compression curve of aggregated soil situated to the right side of the corresponding reconstituted compression curve | $f > f^*$ |
| a5 | (7-10) convergence tendency of the compression curve of strutcured soil to the one of reconstituted soil at high strains and when subjected to combination of wetting and mechanical loading | $f \rightarrow f^*$ |
| **b** | **Intrinsic suction efects** | $s_2 > s_1$ |
| b1 | (11) increase of effective apparent preconsolidation stress of reconstituted samples with suction | $(f^*)_2 > (f^*)_1$ |
| b2 | (12) change in the slope of normal consolidation line with suction in the effective stress plane. | $(\mathbf{D}^{ep*})_1 \neq (\mathbf{D}^{ep*})_2$ |
| b3 | (13) insignificant change of the expansion index of reconstituted soil with suction in the effective stress plane | $(\mathbf{D}^{e*})_1 = (\mathbf{D}^{e*})_2$ |
| **c** | **Combined effects of suction with structure** | $s_2 > s_1$ |
| c1 | (14)increase of post-yield compressibility index in the effective stress plane with suction increase | $(\mathbf{D}^{ep})_1 \neq (\mathbf{D}^{ep})_2$ |
| c2 | (15) insignificant change of the expansion index of aggregated soil with suction | $(\mathbf{D}^{e})_1 = (\mathbf{D}^{e})_2$ |
| c3 | (16) increase of initial effective apparent preconsolidation stress decreases as a result of suction increase | $(f_0)_2 > (f_0)_1$ |
| c4 | (17) increase in the ratio of initial effective apparent preconsolidation stress in aggregated soil over the corresponding value in reconstituted soil | $\left(\frac{f_0}{f_0^*}\right)_2 > \left(\frac{f_0}{f_0^*}\right)_1$ |

In translating the experimental results evidences into modeling features, the preconsolidatoin stress represents the size of the yield surface, and, the swelling and compressibility index respectively represent the elastic and elasto-plastic properties of the soil.

In the following subsections, the modeling features listed in this table are used to depict the conceptual basis of the constitutive model and to describe the required modifications for the ingredients of an elasto-plastic model. This task is considered as an essential step prior to the development of the model formulation (Koliji et al., 2007). The proposed modifications, in general, are applicable to all plastic hardening constitutive models and can extend them for aggregated soils.

### 6.2.2 Pre-yield and elastic behavior

An idealized isotropic compression curve of reconstituted and aggregated soil is depicted in Figure 6.4(a). The intrinsic normal consolidation line (iNCL) represents the normal consolidation line of reconstituted soil. The virgin consolidation line of aggregated soil is denoted by SCL standing for structural consolidation line, where, the term normal is removed in order to avoid confusions stemming from the existence of an initial stiff behavior.

It is observed that the SCL is characterized with an initial stiff behavior followed by yielding (Point A in Fig. 6.4(a)). Yielding is determined by the apparent preconsolidation pressure which is identical for samples of the same structure at similar stress state and stress history.

Initial elastic domain is taken into account by introducing an initial yield limit (Fig. 6.4(b)), the size of which is controlled by initial apparent preconsolidation pressure, $p'_{ci}$, representing the initial soil structure (Evidence a1). As a hypothesis in the present model (and in the most of the models presented in Sec. 2.6.3) the shape of the yield surface in aggregated (structured) soil is assumed to be identical to the one corresponding to reconstituted material. The behavior of material inside this yield limit is elastic.

Experimental results show that there is no significant difference in the slope of the reversible part of the compression curve in aggregated and reconstituted sample (Evidence a2 in Table 6.1). However, the unloading of the samples was performed at the stress level for which the aggregated structure has been already removed significantly, as indicated by the convergence of two curves. Therefore, as mentioned previously, it is normal that the two soils have the same behavior on the unloading path at the end of compression. In the lack of further experimental evidences, the influence of soil structure on the unloading-reloading curve has been neglected. Accordingly, it is assumed that elastic properties of the soil are not affected by the structure (as in the models presented in Sec.2.6.3).

It was also experimentally shown that change in the slope of the elastic compression-swelling with suction is insignificant for both reconstituted and aggregated soil (Evidence b3 and c2 Table 6.1). This is in line with the experimental results reported by Geiser (1999) and Rifa'i (2002) which revealed that

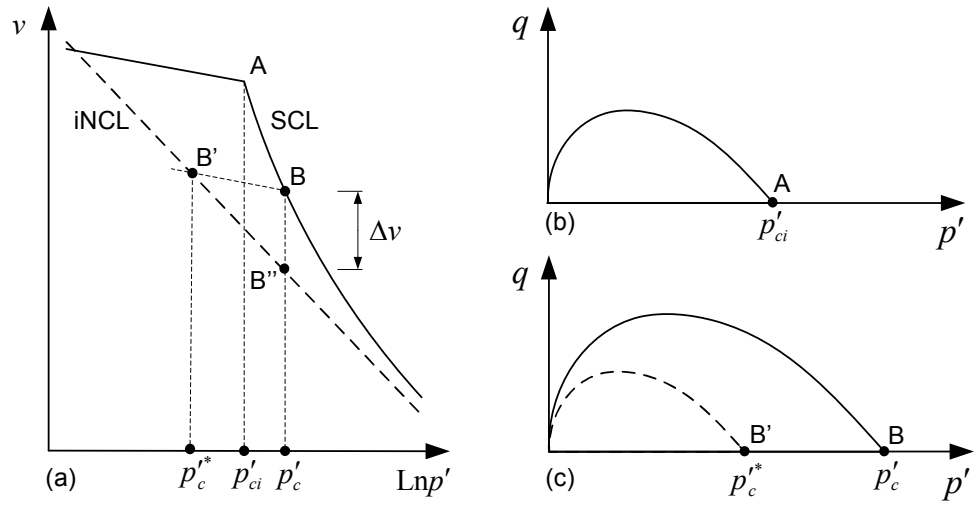


*Figure 6.4:* Soil structure effects: (a) Isotropic compression (b) Initial yield surface (c) Extended yield

variation of elastic rigidity with change in saturation is insignificant.

Accordingly, the elastic part of the model for unsaturated aggregated soil remains unchanged as for saturated reconstituted soils and parameters of elasticity are directly taken from saturated reconstituted soil.

### 6.2.3 Yielding and apparent preconsolidation pressure

It is observed (Evidence a4 in Table 6.1) that the consolidation line of aggregated soil (SCL) is located to the right side of the normal consolidation line of reconstituted soil (or intrinsic normal consolidation line iNCL). According to the classical soil mechanics, only states to the left of iNCL are possible for reconstituted soil. However, SCL situated to the left side of this line shows that higher values of mean stress can be applied to the aggregated soil without causing it to yield. This means that the aggregated material can sustain higher void ratio at the same stress state ($\Delta v$ in Fig. 6.4(a)). With the assumption of identical shape of yield surface for both reconstituted and aggregated soil, this behavior can be described by a change in the size of the yield surface due to an increase in the yield limit (Fig. 6.4(c)).

Considering the isotropic preconsolidation pressure as the parameter controlling the size of the elastic region, the size of yield surface in aggregated soil is therefore determined by the apparent preconsolidation pressure which depends both on stress history and soil structure. As proposed by Gens and Nova (1993), this limit can be considered as an extension of the yield limit of the corresponding reconstituted soil. Accordingly, the apparent preconsolidation pressure of aggregated soil can be written as:

$$p'_c = \psi^{st} p'^{*}_c \tag{6.20}$$

where $p'_c$ is the apparent preconsolidation pressure of aggregated soil, $p'^{*}_c$ is a reference pressure corresponding to the apparent preconsolidation pressure of

reconstituted soil at the same suction which represents the stress history and intrinsic (primary) suction effects. $p_c'^*$ is a function of suction (Evidence b1 in Table 6.1) and the hardening parameters of the reference model. $\psi^{st}$ in the above equation is a function controlling the extension of yield limit with respect to the reconstituted reference state. This function depends on the structure of material and represents the soil structure effects on the apparent preconsolidation pressure. The initial value of this function indicates the initial soil structure and initial apparent preconsolidation pressure. Due to the secondary effects of suction in aggregated soils which affects the soil structure, this function might vary with suction (Evidence c3 in Table 6.1). The explicit form of this function and the soil structure parameters will be discussed in Section 6.3.

### 6.2.4 Post-yield behavior and hardening

When the initial (and subsequent) yield limit is reached, the current yield surface will evolves according to a hardening rule. The isotropic hardening is postulated here, based on which the yield surface changes only in size and not in shape. The yield surface of the reconstituted soil follows a strain hardening rule, i.e., it changes in size with occurrence of plastic strains (change in $p_c'^*$). Moreover, phenomenon of yielding is associated with degradation of structures which rules the evolution of function $\psi^{st}$. Therefore, as the yield limit is reached both the reconstituted and aggregated surfaces change; however, the growth rate is not necessarily the same. The size of the yield locus in aggregated soil is controlled by two phenomena: (i) plastic strain hardening (or softening), and (ii) softening due to structure degradation. The two phenomena are distinguished in the evolution of the apparent preconsolidation pressure. The evolution rule of the apparent preconsolidation pressure for aggregated soil is obtained from the incremental form of Equation (6.20):

$$\frac{\mathrm{d}p_c'}{p_c'} = \frac{\mathrm{d}\psi^{st}}{\psi^{st}} + \frac{\mathrm{d}p_c'^*}{p_c'^*} \tag{6.21}$$

The first term on the r.h.s of this equation represents changes of apparent preconsolidation pressure due to structure effects or softening (or hardening) of the material due to degradation (formation) of structures induced by loading. This term depends on the expression of the structural function $\psi_{st}$. The second term represents the strain and suction hardening (or softening) due to stress state, stress history and intrinsic suction effects. This term denotes the evolution of preconsolidation pressure for reconstituted soil. Therefore, it follows the evolution rule of the reference model with the reconstituted soil properties.

The two phenomena are schematically depicted in Figure 6.5. For point $B$ on the SCL, further isotropic compression brings the soil to point $C$. However, according to the hardening rule of the reconstituted soil, the apparent preconsolidation (yield limit) should follow a path on the iNCL and reach to the point $C'$. Hence, the different between $C$ and $C'$ stems from the softening due to structure degradation. On the stress plane $q - p'$, the current yield surface passes through point $B$. The second term on the r.h.s of Equation (6.21) is

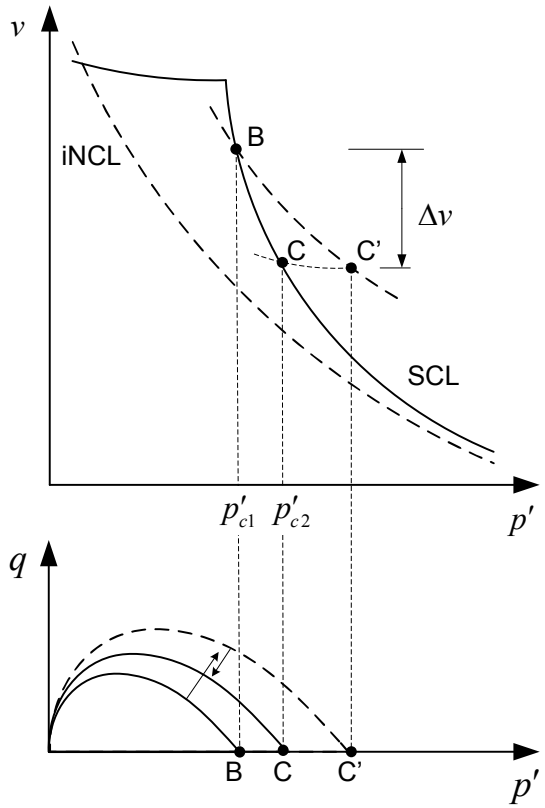


*Figure 6.5:* Evolution of apparent preconsolidation pressure and yield limit in aggregated soil

responsible for enlargement of the yield surface to the one passing through $C'$; while, the first term describes the shrinkage of this latter surface to the new yield surface passing through $C$. At an ultimate state of de-structuring, the two surfaces coincide (Edivence a5 in Table 6.1).

### 6.2.5 Plastic multiplier and plastic potential

The magnitude of plastic strain, given by plastic multipliers, is determined by solving the consistency equation (Eq. 6.12). When Equation (6.20) is introduced in the consistency equation, the plastic modulus and, subsequently, the magnitude of plastic strains changes (Evidence a3 in Table 6.1). Accordingly, the hardening modulus, $H$, in the model of aggregated soil has two components:

$$H = H^* + H^{st} \tag{6.22}$$

where $H^*$ is the hardening modulus of the original model representing the original hardening (softening) and $H^{st}$ is an additional part that takes into account softening (or hardening) due to structure degradation (or formation). With advances in induced structure degradation, the influence of the first term in Equation (6.21) decreases and model predictions for aggregated soil become more analogous to reconstituted soil.

Again, it should be noted that the hardening modulus of reconstituted soil, $H^*$, represents also the instrinsic suction effects in the reconstituted soil and it

might change with suction (Evidence b2 in Table 6.1). $H^{st}$ also might change with suction due to the dependency of soil structure effects on suction (Evidence c1 in Table 6.1).

Flow rule for aggregated soil can be associated or non-associated with a similar or different expression as in reconstituted soil. An appropriate choice of flow rule should be based on experimental results which investigate the effects of structures on the direction of plastic strains. However, in lack of experimental results, it is assumed that the flow rule of reconstituted soil is valid for aggregated soil as well. With this hypothesis, the expression of plastic potential is maintained as in the reconstituted soil and only the reconstituted preconsolidation pressure is replaced by the apparent preconsolidation pressure of aggregated soil.

## 6.3 Soil structure parameters

### 6.3.1 Degree of soil structure

The conceptual model proposed in the preceding section essentially uses the function $\psi^{st}$ to include soil structure effects in the model. Proposing a consistent mathematical expression for this function requires, as a first step, quantification of soil structure as a physical state parameter of the material. This should be done based on the pore scale experimental observations of Chapter 5.

Interpretation of these results in Section 5.5 showed that the main difference in the fabric of aggregated and reconstituted soil stems from the existence of macropores in aggregated soils. It was discussed that the magnitude of macroporosity at each state could represent the actual state of soil structure with respect to its initial state and a fully reconstituted state. Although macroporosity appears to be a useful measure for evaluating soil structure, it may widely vary for different types of soil. Quantification of soil structure and its degradation requires an internal parameter capable of representing the state of the material in relation to its initial intact condition. For this purpose, the *degree of soil structure*, $R$, is introduced here as the ratio of the current macro void ratio, $e^2$, to its initial value at intact state, $e_i^2$:

$$R = \frac{e^2}{e_i^2} \tag{6.23}$$

with the macro void ratio being

$$e^2 = \frac{n^2}{(1-n)} \tag{6.24}$$

where $n$ and $n^2$ are total and macroporosity respectively (see Eq. 3.38 in Chapter 3). Degree of soil structure, $R$, is as an internal scaling parameter that equals 1 for an intact aggregated soil with macropores, and zero for a fully de-structured soil with no macropores. Any degradation of the structures, irrespective of its cause, might alter soil structure and consequently change the degree of soil structure.

Equation (6.23) defines the degree of soil structure, $R$, as a physical parameter at the pore scale. In order to contribute to the macroscopic description of the material, this parameter has to be linked to macroscopic variables of the material. Experimental observation of this study already showed that macroporosity is altered only when the apparent preconsolidation stress of the material changes and irrecoverable (plastic) strains occur (see Sec. 5.3.5). Accordingly, soil structure modifications, previously linked to the evolution of apparent preconsolidation stress, could now be described with respect to the occurrence of plastic deformations. As far as the deformation of the material is elastic, the degree of soil structure does not change, and a change in soil structure is associated only with the occurrence of plastic deformation. Identifying the plastic deformation of the material as a macroscopic variable associated with structural degradation, the general relation for degree of soil structure reads:

$$R = R(\boldsymbol{\varepsilon}^p, \boldsymbol{\omega}) \tag{6.25}$$

where, $\boldsymbol{\varepsilon}^p$ is the plastic strain tensor; and, $\boldsymbol{\omega}$ is a material parameter that controls the rate of structural degradation with plastic deformation.

In order to replace the general from of Equation (6.25) by a mathematical expression, components of the plastic strain tensor need to be appropriately selected. Two commonly used components of strain tensor are volumetric plastic strain, $\varepsilon_v^p$, and deviatoric strain, $\varepsilon_d^p$, which are defined in terms of the invariants of the strain tensor. For a general strain tensor in the cartesian three-dimensional space, the expression of these strains are given as:

$$\varepsilon_v = (\varepsilon_{xx} + \varepsilon_{yy} + \varepsilon_{zz}) \tag{6.26}$$

$$\varepsilon_d = \frac{\sqrt{2}}{3}\left[(\varepsilon_{xx} - \varepsilon_{yy})^2 + (\varepsilon_{yy} - \varepsilon_{zz})^2 + (\varepsilon_{zz} - \varepsilon_{xx})^2 + 6(\varepsilon_{xy}^2 + \varepsilon_{yz}^2 + \varepsilon_{zx}^2)\right]^{\frac{1}{2}} \tag{6.27}$$

in which the subscripts $x$, $y$, and $z$ define the components of the strain tensor with respect to three dimensions. Volumetric strain is, in general, associated with isotropic loading and deviatoric strain with distortional loading. These two loading conditions correspond respectively to isotropic and deviatoric mechanisms of structure degradation. The experimental results of the previous section showed that the fully de-structured state of the material could be achieved only through a combination of both isotropic and deviatoric mechanisms for de-structuring. Accordingly, both volumetric and deviatoric plastic strains should appear in a mathematical expression describing the evolution of degree of soil structure. For this purpose, a de-structuring strain ,$\varepsilon^D$, is introduced here in terms of volumetric and deviatoric strains:

$$\varepsilon^D = A\int |\mathrm{d}\varepsilon_v^p| + (1-A)\int |\mathrm{d}\varepsilon_d^p| \tag{6.28}$$

The parameter $A$ varies between 0 and 1 and it determines the contribution of the two mechanisms in the de-structuring process. The elaboration of a routine experimental method for the determination of this parameter in complicated stress paths requires further study.

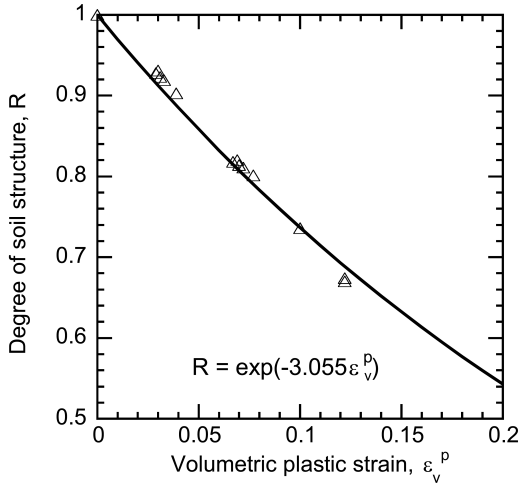


*Figure 6.6:* Degree of soil structure obtained from neutron tomography analysis

Having $\varepsilon^D$ as the plastic strain associated with structure degradation, an evolution rule could be now proposed for the degree of soil structure. Such a relation should imply the degree of soil structure as a decreasing function of combined plastic strain. Moreover, according to the physical definition of the degree of soil structure in Equation (6.23), it should vary between 1 for intact aggregated soil (with intact macropores) and zero for fully de-structured soil (with no macropore). An exponential function is a potential candidate for such a relationship. The efficiency of an exponential function could be verified on the basis of pore scale experimental observations presented in Chapter 5. The evolution of the degree of soil structure was deduced from the tomography results of Section 5.3. The degree of soil structure defined by Equation (6.23) was calculated from the binary segmented volume of the sample for each loading step. Increments of plastic strain were obtained by subtracting from the increments of total strain, the corresponding increments of elastic strain. Figure 6.6 shows the values of the calculated degree of soil structures for the soil sample at different loading steps. Parameter $A$ was selected to be one in Equation (6.28) due to the active isotropic mechanisms of structural degradation.

As illustrated in Figure 6.6, the evolution of the degree of soil structure can be reasonably reproduced by a decreasing exponential function of plastic strain. Accordingly, the following general evolution rule is proposed for the degree of soil structure:

$$R = \exp(-\omega \varepsilon^D) \tag{6.29}$$

or, in incremental from,

$$\mathrm{d}R = -\omega R \, \mathrm{d}\varepsilon^D \tag{6.30}$$

The key point in the proposed equation is its experimental basis and the relation between pore scale and the macroscopic behavior established through this equation. Equation (6.29) quantifies the evolution of soil structure using plastic strains, and therefore, it can be appropriately integrated in constitutive models for soil behavior in a framework of strain hardening elasto-plasticity.

### 6.3.2 Structure degradation

The isotropic compression curves of reconstituted and aggregated soils are depicted in Figure 6.7. According to Equation (6.20), the horizontal distance of the two curves in isotropic compression plane for any specific volume, e.g. $BB'$ in Figure 6.7, is given by $\ln(\psi^{st})$ with function $\psi^{st}$ corresponding to the state of aggregated soil. The initial value of this function, $\psi_i^{st}$ is a material parameter corresponding to $R = 1$. This parameter represents the horizontal separation of the two curves at initial apparent preconsolidation pressure.

When the soil is fully de-structured, there is no extra effect of soil structure, and therefore, the two yield limits are the same, i.e, $\psi^{st} = 1$. This is equivalent to the earlier observation that the two compression curves tend to converge at higher values of applied stress. The function $\psi^{st}$ represents the extra strength of the material due to inter-particle bonding effects; it is expressed in terms of degree of soil structure which itself is defined by the soil fabric. Hence, the key issue here is to relate the bonding and fabric effects, namely the two components of soil structure.

It was previously observed (see Sec. 4.7) that at a given value of applied stress, aggregated soil shows a higher void ratio (or specific volume) than reconstituted soil. This is due to the existence of macropores within the aggregated soil. Therefore, the difference in void ratio between aggregated and reconstituted soil for a given value of $p'$ (e.g. $AA''$ in Figure 6.7 for initial apparent preconsolidation pressure) has to be attributed to macropores. As a result of induced degradation of structures, the macroporosity decreases and the microporosity becomes the dominant porosity, as in reconstituted soils. Hence, the vertical separation of the two curves in isotropic compression space decreases.

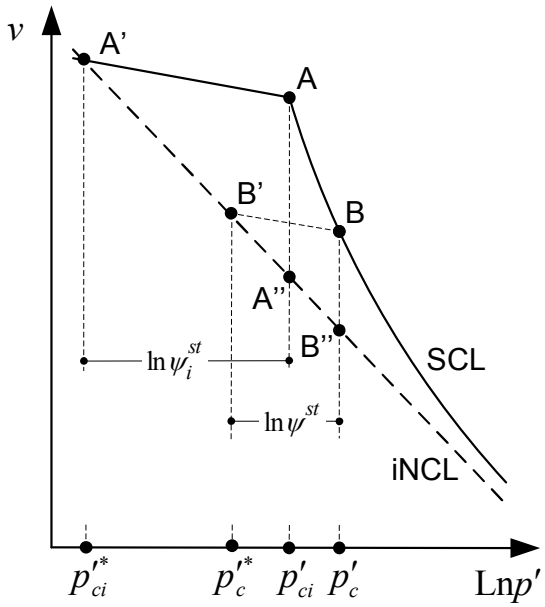


*Figure 6.7:* Normal consolidation curves of aggregated (solid line) and reconstituted (dotted line) soils

At an ultimate state with no macropores, the two curves converge.

Therefore, the relation between the current difference in the void ratio (or specific volume) of aggregated and reconstituted soil in isotropic plane ($BB''$ in Figure 6.7) and its value at initial yielding ($AA''$) can be approximated as:

$$\frac{BB''}{AA''} = \frac{e^2}{e_i^2} = R \tag{6.31}$$

On the other hand, geometrical similarity between triangles $AA'A''$ and $BB'B''$ yields:

$$\frac{BB''}{AA''} = \frac{BB'}{AA'} = \frac{\ln(\psi^{st})}{\ln(\psi_i^{st})} \tag{6.32}$$

Introducing Equation (6.31) into Equation (6.32), and then solving for the function $\psi^{st}$ gives:

$$\psi^{st} = \exp\left[R \ln\left(\psi_i^{st}\right)\right] \tag{6.33}$$

The above equation presents the actual $\psi^{st}$ as a function of its initial value and the corresponding degree of soil structure.

### 6.3.3 Influence of suction on structure parameters

The secondary suction effects in aggregated soils are linked to the influence of suction on soil structure properties, namely on soil fabric and inter-particle bonding. Suction variation might alter the arrangement of pores and particles, and at the same time, it might modify the strength of inter-particle bondings. These two effects and the explicit consideration of their effects on the soil structure parameters are discussed here.

The experimental results of Chapter 4 showed that the initial apparent preconsolidation pressure for both reconstituted and aggregated soils increases with suction (Evidence b1 and c3 in Table 6.1). However, the rate of increase with suction is not the same and it is higher for aggregated soil (Evidence c4). This phenomenon is ascribed to the increase in the strength of inter-particle bonding due to suction increase. In simple words, bonding strength increases with suction and this provides a higher value of apparent preconsolidation pressure. Therefore, suction increase contributes to the increase of apparent preconsolidation pressure in aggregated soil through two mechanisms: intrinsic (capillary) effects and strengthening of inter-particle bonding in soil structure. An equivalent description was given by Leroueil and Barbosa (2000) and Alonso and Gens (1994) for contribution of the suction to the increase of preconsolidation pressure in unsaturated bonded soils.

The observed behavior corresponds to an increase in the horizontal distance between the SCL and iNCL in Figure 6.7 due to suction increases. This implies the function $\psi^{st}$ to increase with suction. Mathematically, this can be taken into account by providing $\psi^{st}$ as a an increasing reversible function of suction

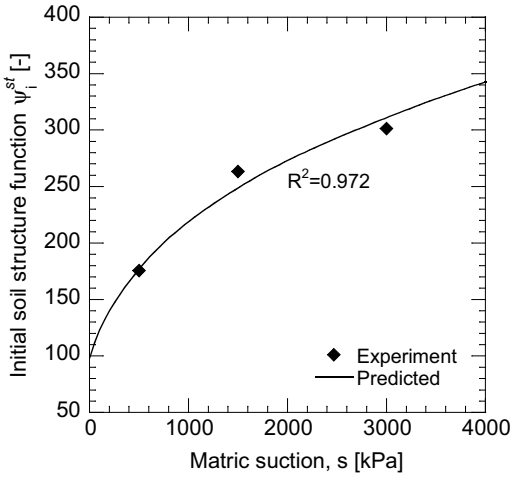


*Figure 6.8:* Influence of suction on the soil structure parameter $\psi^{st}$

with respect to a reference state. Figure 6.8 plots the experimental values of $\psi_i^{st}$ for the three unsaturated aggregated and corresponding reconstituted samples (see Sec. 4.6). The observed evolution was found to be successfully reproduced using the following equation:

$$\psi^{st} = \psi_{\text{ref}}^{st} \left( \frac{s + p_{at}}{s_{\text{ref}} + p_{at}} \right)^{n_{st}} \qquad \psi_i^{st} \neq 1 \tag{6.34}$$

in which $\psi_{\text{ref}}^{st}$ is the reference value of the function at the reference suction $s_{\text{ref}}$, and the exponent $n_{st}$ is a material parameter. For predictions of Figure 6.8, the reference suction is 500 $kPa$ and $n_s = 0.336$. The atmospheric pressure $p_{at}$ in the denominator allows having the saturated state (zero suction) as the reference state; meanwhile, the reference suction could be a non-zero value. The condition $\psi_i^{st} \neq 1$ limits the validity of this equation to the aggregated (structured) soils, in which the initial yield limit is basically influenced by the inter-particle bonding effects.

The second effect of suction on soil structure is related to the soil fabric. Experimental results of Chapter 5 showed that the soil fabric, and specially the macropores are strongly affected by suction variations. Equivalent observations has been reportedly observed by other researchers (Simms and Yanful, 2001, 2002; Cuisinier and Laloui, 2004). Change in fabric, per se, could alter the characteristic behavior of the aggregated (structured) soil.

As a direct approach, a mathematical model has been developed to model the suction-induced changes in the pores size distribution (PSD) of a double porosity soil (Koliji et al., 2006). Using the concept of a suction-influenced domain, the proposed model is able to reproduce the main observed fabric evolution between the saturated and dry states.

The detailed formulation of the proposed model for the evolution of PSD and its predictions are given in Appendix C. The model was found to successfully reproduce the main aspects of suction induced effects on soil structure using direct mathematical relations and physical concepts.

Such a mathematical model could be appropriately used when material deformation or water retention properties are to be linked to the PSD in an independent framework. However, the integration of such models in the elasto-plastic constitutive models of soil behavior is associated with some difficulties. The difficulties arise mainly from the direct mathematical prediction of porosity evolution without passing through elasto-plasticity considerations.

As an alternative approach, it is stipulated that plastic strains and consequently evolution of degree of soil structure, irrespective of its cause, is the only responsible for the major modifications of the soil fabric. In parallel, parameter $\omega$ is allowed to change with suction, i.e., the rate of evolution of soil fabric with plastic strain depends on the suction level.

Experimental results (see Sec. 4.6) showed that the post-yield compressibility of aggregated samples increases with suction and the samples exhibit more brittle yielding at higher suctions (Evidence c1 in Table 6.1). The more brittle the material behavior, the higher the rate of structure degradation with plastic strains. A possible approach to describe this behavior is to propose the parameter $\omega$ as an increasing function of suction. A logarithmic relation could be adopted for this purpose:

$$\omega = \omega_{\text{ref}} + \Omega_{st} \text{Ln} \left( \frac{s + p_{at}}{s_{\text{ref}} + p_{at}} \right) \tag{6.35}$$

where $\omega_{\text{ref}}$ is the reference value of the parameter at the reference suction, $s_{\text{ref}}$, and, $\Omega_{st} > 0$ is a material parameter which controls the rate of increase with suction. As in Equation (6.34), the atmospheric pressure, $p_{at}$, is added to avoid infinite values when the saturated state is considered as reference ($s_{\text{ref}} = 0$).

Although Equation (6.35) could be used for a given range of suction, it predicts an unlimited increase of $\Omega_{st}$ with suction which is not realistic. An alternative expression is an asymptotic relation which might be probably closer to real behavior:

$$\omega = \omega_{\text{ref}} \left[ (1 - \alpha_{st}) \exp(-\Omega_{st} s) + \alpha_{st} \right] \tag{6.36}$$

where $\alpha_{st}$ is a constant related to the maximum value of $\omega$ for an infinite suction, and $\Omega_{st}$ is a parameter which controls the rate of change of $\omega$ with suction.

### 6.3.4 Determination procedure

The soil structure parameters have been introduced on the basis of combined physical experimental observations at macro scale and pore scale. However, it is always preferred for the model parameters to be determined using simple experiments without needing for micro scale experiments.

The first parameter to be determined is the parameter $\omega$ which controls the rate of structure degradation with plastic strain. This parameter can be estimated using the results of isotropic or oedometric normal consolidation of aggregated and corresponding reconstituted soil (Fig. 6.9(a)).

As discussed previously, the mechanism of structure degradation is this loading condition is mainly isotropic ($A = 1$) and the volumetric plastic strain is the main responsible of structure degradation. According to the reasoning given in Section 6.3.2, the value $b/a$ at each point $n$ represents the degree of soil structure, $R$. In the other hand, volumetric plastic strain at each point can be evaluated by subtracting from the total strain the corresponding increments of elastic strain. Hence, for a given point in the compression plane (Fig. 6.9(a)), a corresponding point can be located in Figure 6.9(b).

Considering the isotropic degradation mechanism associated with volumetric plastic strain, $\omega$ in Equation 6.29 can be determined by providing the best fitting to the existing data. Having $\omega$ defined, parameter $A$ in more complicated stress paths where the deviatoric mechanism of structure degradation would be probably involved could be as well evaluated.

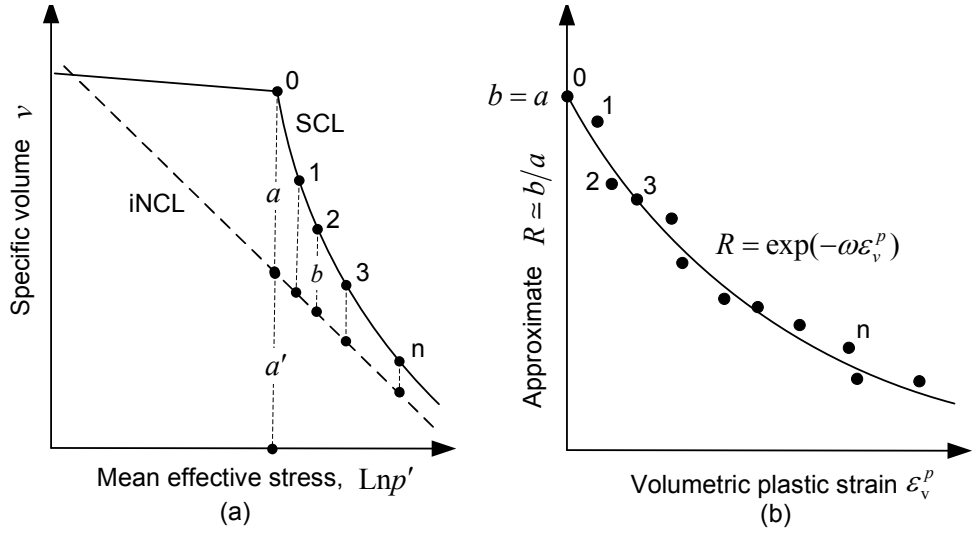


*Figure 6.9:* Determination of the soil structure parameter $\omega$

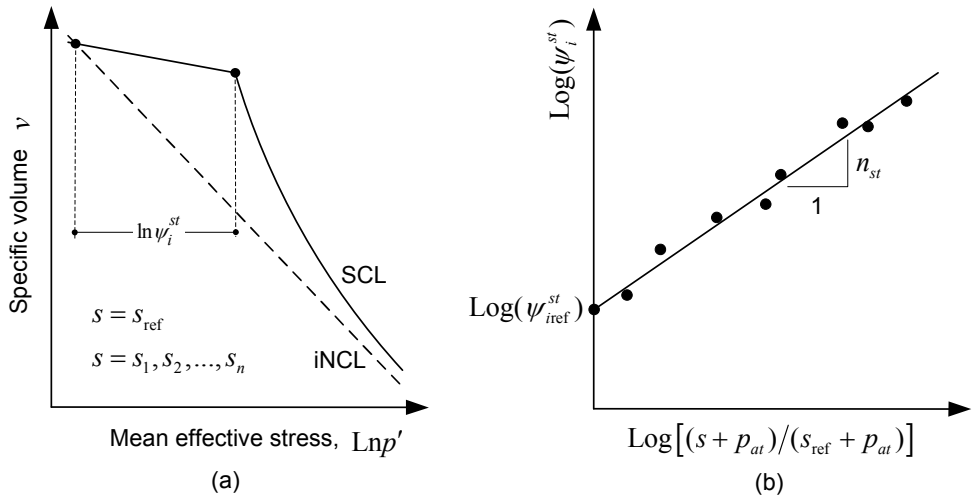


*Figure 6.10:* Determination of the soil structure parameter $n_{st}$

If the procedure described above is repeated at different suctions, the variation of $\omega$ with suction and therefore the parameter $\Omega_{st}$ can be evaluated. Finally, parameter $n_{st}$ which describes the suction-induced hardening of the structure should be evaluated by comparing values of $\psi_i^{st}$ at different suctions including the reference suction, $s_{\text{ref}}$ (Fig. 6.10(a)). As shown in Figure 6.10(b), parameter $n_{st}$ can be determined providing the best fitting to the experimental data.

## 6.4 Model formulation ACMEG-2S

### 6.4.1 Introduction to the model developments

The general requirements for extension of a reference model from reconstituted saturated soil to unsaturated aggregated soils were outlined in Section 6.2. The required soil structure parameters were also presented in Section 6.3. In this section, the explicit mathematical formulation of a new constitutive model for unsaturated aggregated soils will be developed based on the framework presented in the preceding sections.

The simplified isothermal Hujeux model (Aubry et al., 1985; Hujeux, 1985) with two plastic mechanisms has been adopted as the reference model for reconstituted saturated soils. The simplified model has been used in this work and other parallel ongoing researches at LMS-EPFL as a reference model for further extensions to different environmental effects and development of a new family of models called *ACMEG*[1]. The mathematical formulation presented here refers to the extension of the reference model to unsaturated aggregated soil. The model is called ACMEG-2S, indicating the double effects of suction and structure in aggregated soil which is a structured soil with double porosity.

The model adopts the multi-mechanism plasticity concept (Koiter, 1960). In this concept, each dissipation process is described by an evolution law which is activated by a yield limit, a dissipation potential, and a plastic multiplier (Rizzi et al., 1996). The onset of plasticity for each mechanism is determined by the yield limit. The elastic region is, therefore, determined by all the plastic mechanisms. Plastic strains multiplier is the additive sum of the plastic strain multipliers provoked by each mechanism. These multipliers are deduced from the consistency equation which should be satisfied for the active mechanisms. The fundamental equations of multi-mechanism plasticity are similar to what presented in Section 6.1.3 for single dissipation plasticity. Those equations could be used for multi-mechanism plasticity, provided that yield surface, plastic potential, and plastic multipliers are introduced in the equations as vectors. These vectors have equal number of components, which is the number of plastic mechanisms.

The reference model is based on the critical state concept. It uses nonlinear elasticity and two plastic mechanisms, i.e. isotropic and deviatoric. The plastic mechanisms are coupled through the volumetric plastic strain. The model adopts an isotopic plastic strain hardening with the volumetric plas-

[1]Advanced Constitutive Model for Environmental Geomechanics

tic strain being the hardening parameter. The flow rule is associated for the isotropic mechanism and it could be associated or non-associated for the deviatoric mechanism. Compared with the Original Cam-clay model (Roscoe and Schofield, 1963), the simplified Hujeux model provides more flexibility for the shape of the yield surface and better reproducing of the progressive occurrence of plastic deformations. Formulation of the reference model will be presented in line with its extension to unsaturated aggregated soils through the following subsections.

Following the adopted stress framework (Sec. 6.1.1), namely generalized effective stress and suction, the expression of the stress-strain relationships will be maintained as in the saturated model and the Terzaghi's effective stress will be replaced by the generalized effective stress in the expressions of the unsaturated model. New dependency of the apparent preconsolidation on suction and soil structure will be introduced and consequently, hardening moduli and plastic multipliers will be modified.

For simplicity, the formulation of the model will be first developed for the case of triaxial test, that is when two effective principal stresses are equal and the directions of principal stresses are fixed with respect to material element. The two effective stress variables normally used in critical state soil mechanics are mean effective pressure, $p'$, and deviatoric stress, $q$, given in Equation (6.2):

$$p' = \frac{1}{3}(\sigma'_1 + 2\sigma'_3)$$
$$q = \sigma'_1 - \sigma'_3$$

where $\sigma'_1$ and $\sigma'_3$ denote vertical and radial triaxial stresses respectively. Based on the input work analysis, the associated strains are volumetric strain, $\varepsilon_v$, for $p'$ and deviatoric strain, $\varepsilon_d$, for $q$:

$$\varepsilon_v = \varepsilon_1 + 2\varepsilon_3 \tag{6.38a}$$
$$\varepsilon_d = \frac{2}{3}(\varepsilon_1 - \varepsilon_3) \tag{6.38b}$$

with $\varepsilon_1$ and $\varepsilon_3$ representing the vertical and radial triaxial strains respectively. The generalization of the model formulation to the three-dimensional case will follow afterward.

### 6.4.2 Elastic components of the model

The starting point is decomposition of the strain increments into elastic and plastic part:

$$\varepsilon_v = \varepsilon_v^e + \varepsilon_v^p \tag{6.39a}$$
$$\varepsilon_d = \varepsilon_d^e + \varepsilon_d^p \tag{6.39b}$$

Following the postulation of Section 6.2.2, the elastic behavior and the involved properties are not affected neither by unsaturation nor by the soil structure effects. Accordingly, elastic part of the model is identical to the reference

model. It uses an isotropic non-linear relation for the elastic stress-strain relation which yields:

$$\mathrm{d}\varepsilon_v^e = \frac{\mathrm{d}p'}{K} \tag{6.40a}$$

$$\mathrm{d}\varepsilon_d^e = \frac{\mathrm{d}q}{3G} \tag{6.40b}$$

in which $K$ and $G$ are respectively the pressure dependent bulk elastic modulus and shear elastic modulus given by:

$$K = K_{\mathrm{ref}} \left( \frac{p'}{p'_{\mathrm{ref}}} \right)^{n_e} \tag{6.41a}$$

$$G = G_{\mathrm{ref}} \left( \frac{p'}{p'_{\mathrm{ref}}} \right)^{n_e} \tag{6.41b}$$

In these equations $K_{\mathrm{ref}}$ and $G_{\mathrm{ref}}$ are bulk and shear elastic modulus at the reference mean pressure of $p'_{\mathrm{ref}}$; and, the exponent $n_e$ is a material parameter. The two elastic parameters are linked by the Poisson's ratio, $\nu$:

$$G = \frac{3(1-2\nu)}{2(1+\nu)} K \tag{6.42}$$

It is noteworthy that the increments of volumetric elastic strain in general could be also obtained based on the incremental form of the unloading-reloading line in the isotropic plane of $v - \ln p'$:

$$\mathrm{d}\varepsilon_v^e = \kappa \frac{\mathrm{d}p'}{vp'} \tag{6.43}$$

where $\kappa$ is the slope of unloading-reloading line (Fig. 6.12(a)). By comparison with Equation (6.40a), this implies that

$$K = \frac{vp'}{\kappa} \tag{6.44}$$

In the above equation, a constant slope $\kappa$ of the unloading-reloading line in the semi-logarithmic compression plane implies a bulk modulus that increases with mean stress, $p'$. The effect of small decrease in volume $v$ during the unloading is likely to be very smaller than the effect of increase in $p'$ (Wood, 1990). However, consistency of the above relation with Equation (6.41) implies:

$$\frac{\mathrm{d}v}{v} = (n_e - 1) \frac{\mathrm{d}p'}{p'} \tag{6.45}$$

The elastic parameters in the above-mentioned equations are equal to those of the corresponding saturated reconstituted soil:

$$\mathfrak{A} = \mathfrak{A}_0^* \qquad \mathfrak{A} = K_{\mathrm{ref}}, G_{\mathrm{ref}}, n_e, (\kappa, \nu) \tag{6.46}$$

where $\mathfrak{A}$ is generic material parameter and $\mathfrak{A}_0^*$ designates the parameters of reconstituted saturated soil.

### 6.4.3 Yield criteria

The plastic behavior in the reference model is governed by two plastic mechanisms: isotropic and deviatoric plastic mechanism. The limit of elasticity and the onset of plastic deformations in each mechanism is determined by the yield criterion corresponding to that mechanism:

$$\text{isotropic:} \qquad f^*_{iso} = p' - p'^*_{c0} r_{iso} = 0 \tag{6.47}$$

$$\text{deviatoric:} \qquad f^*_{dev} = q - M^* p' \left(1 - b^* \ln \frac{p' d^*}{p'^*_{c0}}\right) r_{dev} = 0 \tag{6.48}$$

in which $p'^*_{c0}$ is the effective preconsolidation pressure in reconstituted saturated soil, $M$ is the slope of the critical state line in the effective stress plane $q - p'$, $b^*$ is a shape parameter, and $d^*$ is the ratio of the effective preconsolidation pressure over the effective critical state pressure belonging to the same yield surface.

The two variables $r_{iso}$ and $r_{dev}$, called isotropic and deviatoric elastic radius respectively, are provided in order to avoid abrupt change in the rate of deformation at the point of preconsolidation pressure and to allow a smooth transition from the elastic to plastic domain which is more realist. They represent the degree of mobilization of the plastic mechanisms through the following equations:

$$r_{iso} = r^e_{iso} + \frac{\varepsilon_v^{p,iso}}{c^* + \varepsilon_{vi}^{p,iso}} \tag{6.49a}$$

$$\mathrm{d}r_{iso} = \frac{(1 - r_{iso})^2}{c^*} \mathrm{d}\varepsilon_v^{p,sio} \tag{6.49b}$$

and

$$r_{dev} = r^e_{dev} + \frac{\varepsilon_d^{p,dev}}{a^* + \varepsilon_d^{p,dev}} \tag{6.50a}$$

$$\mathrm{d}r_{dev} = \frac{(1 - r_{dev})^2}{a^*} \mathrm{d}\varepsilon_d^{p,dev} \tag{6.50b}$$

where $r^e_{iso}$, $r^e_{dev}$ are the initial radii of elastic domain for respectively isotropic and deviatoric mechanism, and, $c^*$ and $a^*$ are material parameters. $\varepsilon_v^{p,iso}$ denotes the volumetric plastic strain induced by isotropic mechanism, and $\varepsilon_d^{p,dev}$ is the deviatoric strain induced by deviatoric mechanism. Hence, the above equations imply evolution of isotropic and deviatoric elastic radii only with the plastic strains arising from the corresponding mechanism. The maximum value of $r_{iso}$ and $r_{dev}$ is equal to one and corresponds to the total mobilization of the relevant mechanism.

As discussed in Section 6.1.2, the slope of the critical state line of a saturated reconstituted soil in the generalized effective stress plane $q - p'$ is not affected neither by partial saturation nor by soil structure effects. Following the postulation of Section 6.2.3, the shape of yield function for unsaturated aggregated soil remains the same as for the saturated reconstituted soil. This requires having the same $b$ and $d$ for two soils. Furthermore, it is plausible to assume that

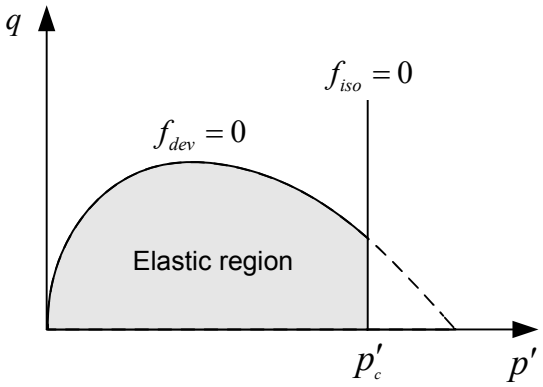


*Figure 6.11:* Yield surfaces and elastic region in ACMEG-2S model

the mobilization of plastic mechanisms with the provoked plastic deformation is independent of the suction and soil structure. Therefore, parameters $a$ and $c$ are assumed to remain at their constant value for reconstituted saturated soils. Hence, the parameters involved in the expression of yield functions are directly inherited from the saturated reconstituted soil:

$$\mathfrak{A} = \mathfrak{A}_0^* \qquad \mathfrak{A} = M, a, c, b, d \tag{6.51}$$

which is in line with the previously made postulation that the soil structure and its degradation would affect only internal variables and not other material properties.

Accordingly, the equations of saturated yield functions could be adopted for unsaturated aggregated soil by using generalized effective stress and the apparent preconsolidation. Maintaining the general expression of the yield criteria in the reference model, the yield functions in the new model reads:

$$\text{Isotropic:} \qquad f_{iso} = p' - p'_c r_{iso} = 0 \tag{6.52}$$

$$\text{Deviatoric:} \qquad f_{dev} = q - Mp' \left(1 - b\ln\frac{p'd}{p'_c}\right) r_{dev} = 0 \tag{6.53}$$

In this equation $p'_c$ is the isotropic yield pressure or the apparent isotropic preconsolidation pressure in which the effects of suction and soil structure are both considered. The expression of isotropic yield function is independent of deviatoric stress, while the deviatoric yield function involves both deviatoric and isotropic mean effective pressure. In the generalized effective stress plane $q - p'$, the above two functions constitute a yield surface similar to the original Cam-Clay type, as given by deviatoric yield function, trimmed by a vertical line parallel to $q$ axis representing the isotropic yield function (Fig. 6.11).

Parameter $d$, occasionally referred to as the spacing ratio (Yu, 2006), is the ratio of the saturated preconsolidation pressure over the saturated effective critical state pressure in the same yield surface for the soil (see Fig. 6.12(a)):

$$d = \frac{p'^*_{c0}}{p'^*_{cr0}} \tag{6.54}$$

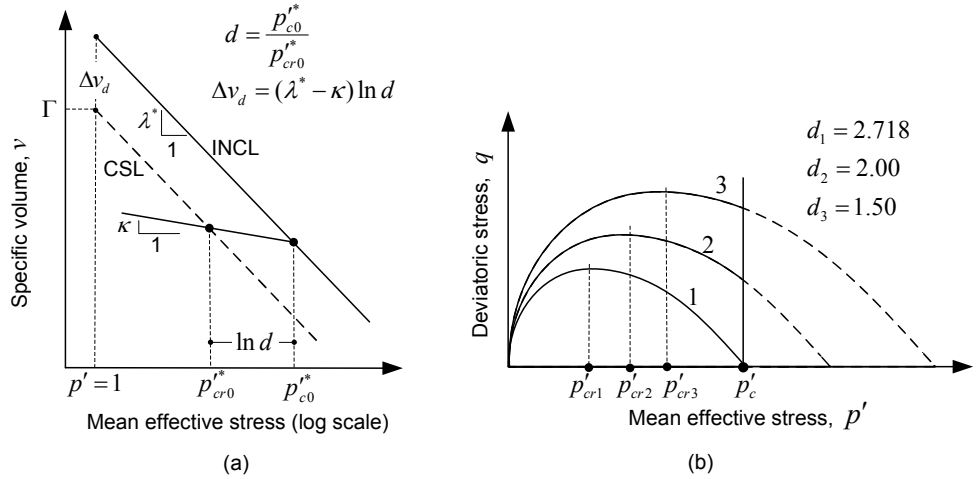


*Figure 6.12:* Spacing ratio parameter, $d$

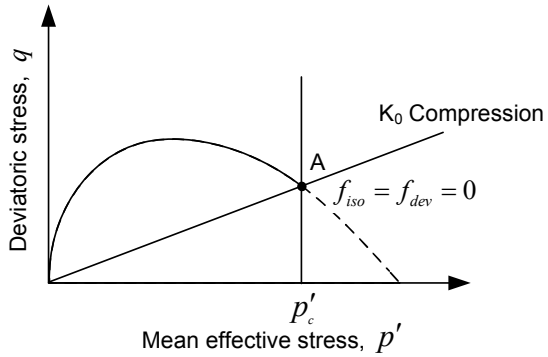


*Figure 6.13:* A plastic state on the oedometric stress path

In the original and modified Cam-clay models, $d$ is fixed at 2.718 and 2.0 respectively. In this model (and in the model of Yu (1998)), this parameter is allowed to vary with material type. Experimental data indicates that for clays $d$ typically lies in the range of 1.5 to 3 (Yu, 1998). Figure 6.12(b) depicts the influence of $d$ on the relative position of two yield limits in the stress plane.

Parameter $b$ affects the shape of the deviatoric yield surface and it is considered as a material parameter which could vary for different types of soils. A possible evaluation of the relation between $b$ and $d$ could be made for a plastic stress state like point A in Figure 6.13 on the oedometric compression stress path. At this condition, both isotropic and deviatoric yield functions might be zero for the same stress state. This implies a pair of parameters $b$ and $d$ which satisfy the following relation:

$$b = \frac{\left(1 - \dfrac{K_0}{M}\right)}{\ln d} \tag{6.55}$$

in which $K_0$ is the coefficient of lateral earth pressure at rest, i.e. a function of Poisson's ratio $\nu$.

Following this discussion, $b$ and $d$ could be considered as dependent parameters. However, this conclusion is preconditioned by accepting the fact that (i) both yield functions should be simultaneously zero, (ii) the $K_0$ coefficient is constant during the loading. Hence, evaluation of the relation between $b$ and $d$ demands more profound investigations.

### 6.4.4 Apparent preconsolidation pressure and hardening

The model uses an isotropic hardening rule. The size of the elastic region could change while maintaining its shape. The size of the elastic domain is governed by the apparent preconsolidation pressure. Hence, the hardening rule describes the evolution of the apparent preconsolidation pressure.

The apparent effective preconsolidation pressure in aggregated soil can evolve because of (i) the intrinsic strain hardening or softening as in reconstituted soils, (ii) intrinsic suction-induced hardening of the soil matrix, (iii) dependency of apparent preconsolidation pressure on soil structure and its degradation , and (iv) suction-induced hardening in the soil structure.

**(i) Intrinsic strain hardening:** The hardening rule of the reference model governs the intrinsic strain hardening (or softening) of the model. It uses a volumetric plastic strain hardening rule similar to the Cam-clay model to describe the evolution of the preconolidation pressure in the corresponding saturated reconstituted soil:

$$p_{c0}^{\prime *} = p_{c0i}^{\prime *} \exp(\beta \varepsilon_v^p) \tag{6.56}$$

in which $p_{c0}^{\prime *}$ and $p_{c0i}^{\prime *}$ are respectively actual and initial values of the saturated preconsolidation pressure, and

$$\beta = \frac{(1+e_i)}{\lambda^* - \kappa} \tag{6.57}$$

where $e_i$ denotes the initial void ratio, and $\lambda^*$ is the slope of intrinsic isotropic normal consolidation line (iNCL) in the $v - \ln p'$ space (Fig. 6.12(a)). The incremental form of Equation (6.56) using the actual void ratio, $e$, reads:

$$\frac{\mathrm{d}p_{c0}^{\prime *}}{p_{c0}^{\prime *}} = \frac{(1+e)}{\lambda^* - \kappa} \mathrm{d}\varepsilon_v^p \tag{6.58}$$

Originally proposed as the hardening rule for saturated condition, the above equations are supposed to describe the strain hardening of the material regardless of the saturation condition. Therefore, it should account for the changes in the compressibility of the soil with suction (Evidence b2 in Table 6.1) which is schematically shown in Figure 6.14. In line with the experimental results, a logarithmic evolution rule is proposed for $\lambda^*$:

$$\lambda^* = \lambda_0^* + \Omega_s \ln\left(\frac{s + p_{at}}{p_{at}}\right) \tag{6.59}$$

where $\lambda_0^*$ corresponds to saturated NCL, $\Omega_s$ is a material parameters, and $p_{at}$ is the atmospheric pressure which has been added in order to avoid zero value in the logarithm.

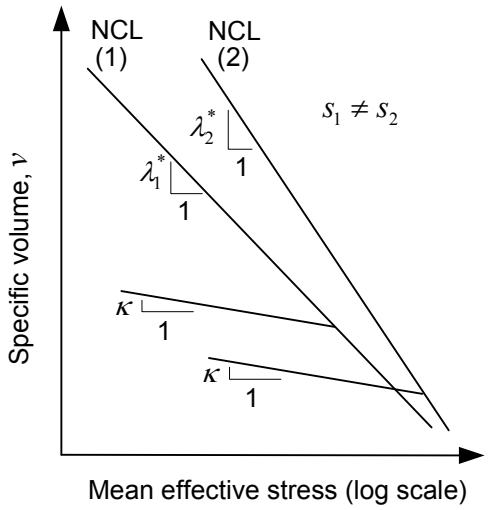


*Figure 6.14:* Change in the compressibility of soil with suction

**(ii) Intrinsic suction-induced hardening:** On the basis of experimental results from compression tests under isotropic stress states and at constant levels of suction, Nuth and Laloui (2007b) proposed a reversible function to quantify the evolution of preconsolidation pressure with suction in unsaturated reconstituted soils:

$$p_c'^* = p_{c0}'^* \qquad ; \text{if } s_e > s > 0 \tag{6.60a}$$

$$p_c'^* = p_{c0}'^* \left[1 + \gamma_s \log\left(\frac{s}{s_e}\right)\right] \qquad ; \text{if } s_e < s \tag{6.60b}$$

with $s_e$ being the air entry value of the soil and $\gamma_s$ a material parameter. This relation was found to successfully represent the effects of suction on the apparent preconsolidation of reconstituted soils (Nuth and Laloui, 2007b). The proposed set of equations, termed as LC Curve after Alonso et al. (1990), are depicted in Figure 6.15(a). Let's consider a sample which has been isotropically loaded to point $A$ in Figure 6.15(b) and then unloaded to point $B$ at saturated condition. For this sample the above equations correspond to the dashed curve. When suction is increased under constant net stress, the effective stress increases as well and the sample follows the stress path $BA'C'D$. Stress state remains in the elastic region until point $A'$. At this point plastic deformation starts occurring until point $C'$ corresponding to the air entry value where the stress state could return back to the elastic region.

In the present work, a similar relation modified for double porous fabric has been adopted to quantify the intrinsic suction effects. In a structured soil with double porosity, two dominant pore sizes and consequently two air entry value suctions exist. It is plausible to assume that intrinsic suction effects are governed by the air entry value of micropores within the soil aggregates where the soil matrix is similar to the reconstituted soil (see Sec. 5.5). Accordingly, Equation (6.60) should be optimized to (i) maintain, as much as possible, the values of $p_c'^*$ predicted for reconstituted soil, and (ii) use $s_e^1$ insteads of the

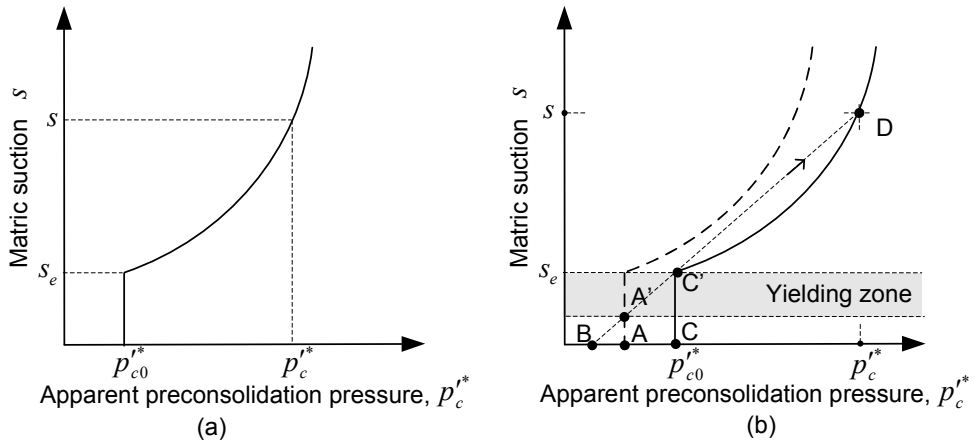


*Figure 6.15:* Suction-induced hardening in reconstituted soils, after Nuth and Laloui (2007b)

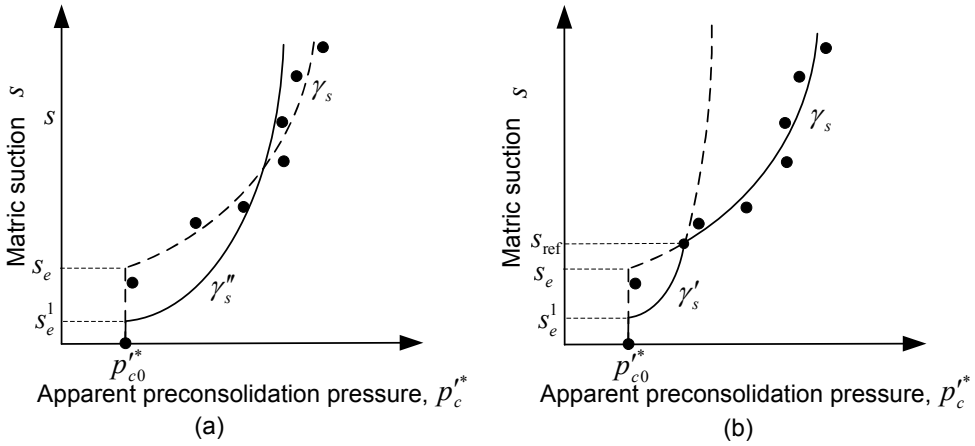


*Figure 6.16:* Intrinsic suction-induced hardening in aggregated soils

air entry value suction of reconstituted soil, $s_e$. This guarantees a realistic prediction for the evolution of $p'^*_c$ in reconstituted soil while forcing the yielding zone to be determined by $s^1_e$ instead of $s_e$, which is physically more reasonable. Mathematically, two solutions could be sought. The first one is to determine a new $\gamma_s$ (e.g. $\gamma''_s$) using $s^1_e$ and the experimental data of the reconstituted soil (Fig. 6.16(a)). The second solution is to select a reference suction $s_{\text{ref}} > s_e$ and to use a relation based on $s^1_e$ and a new $\gamma_s$ (e.g. $\gamma'_s$) only for suctions below this reference suction while keeping the rest of the curve unchanged. This corresponds to the bold continues line in the schematic illustration of Figure 6.16(b). This latter approach is believed to be more realistic for the aggregated soils at high values of suction. Adopting such an approach, the apparent preconsolidation pressure reads:

$$p'^*_c = \psi^s {p'_{c0}}^* \tag{6.61}$$

in which $\psi_s$ is defined as:

$$\psi^s = \begin{cases} 1 & ; \text{if } 0 < s < s_e^1 \\ 1 + \gamma_s' \log\left(\dfrac{s}{s_e^1}\right) & ; \text{if } s_e^1 \leq s < s_{\text{ref}} \\ 1 + \gamma_s \log\left(\dfrac{s}{s_e}\right) & ; \text{if } s \geq s_{\text{ref}} \end{cases} \tag{6.62}$$

Parameter $\gamma_s'$ is a dependent parameter and therefore the above equation does not introduce any additional parameter. Equalizing values of $p_c'^*$ at $s_{\text{ref}}$ given by the second and third expressions in Equation (6.62), parameter $\gamma_s'$ is determined to be:

$$\gamma_s' = \frac{\ln\left(\dfrac{s_{\text{ref}}}{s_e^1}\right)}{\ln\left(\dfrac{s_{\text{ref}}}{s_e}\right)}\gamma_s \tag{6.63}$$

In the absence of macropores, Equation (6.62) will be identical to the model of reconstituted soil. The reference suction $s_{\text{ref}} > s_e$ is an arbitrary suction. For the sake of simplicity, it is selected to be the same reference suction used for soil structure parameters.

**(iii) Dependency on soil structure and its degradation:** Presence of inter-particle bonding within the aggregates increases the apparent preconsolidation pressure in aggregated soil, and, their subsequent degradation results in softening of material.

Effect of soil structure on the apparent preconsolidation pressure was discussed in Sections 6.2.3 and 6.3. The expression of the apparent preconsolidation pressure in aggregated soils was given by Equation (6.20):

$$p_c' = \psi^{st} p_c'^*$$

where $\psi^{st}$ represents the soil structure effects and it is given by Equation (6.33):

$$\psi^{st} = \exp\left[R \ln\left(\psi_i^{st}\right)\right]$$

and $R$ is degree of soil structure given by Equation (6.29):

$$R = \exp\left(\omega \varepsilon_v^p\right)$$

In the above equation, $\omega$ controls the rate of structure degradation with plastic strains which changes with suction according to Equation (6.35):

$$\omega = \omega_{\text{ref}} + \Omega_{st} \text{Ln}\left(\frac{s + p_{at}}{s_{\text{ref}} + p_{at}}\right)$$

and $\psi_i^{st}$ represents the initial structure of the soil.

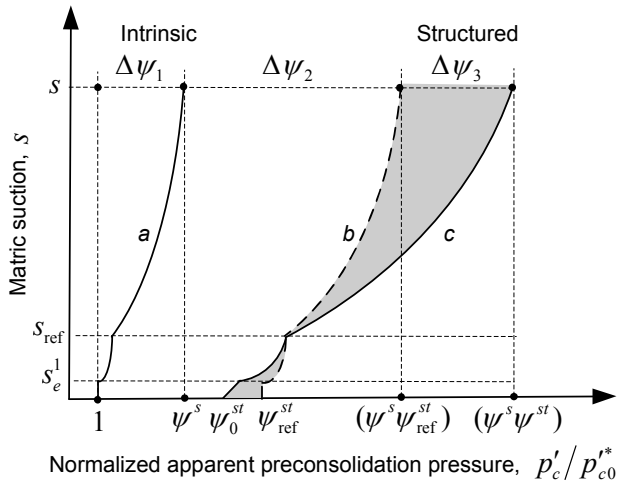


*Figure 6.17:* Combined effects of suction and soil structure on the apparent isotropic preconsolidation pressure of aggregated (structured) soil

**(iv) Suction-induced hardening of soil structure:** As presented in Section 6.3.3, the secondary influence of suction in aggregated soil is linked to the increase in the strength of structural units with suction. This additional influence of suction on soil structure properties is taken into account by Equation (6.34):

$$\psi^{st} = \psi^{st}_{\text{ref}} \left( \frac{s + p_{at}}{s_{\text{ref}} + p_{at}} \right)^{n_{st}} \qquad \psi^{st}_i \neq 1$$

In the above equations, the subscript $(_{\text{ref}})$ denotes the values corresponding to the reference suction.

Combining the above-mentioned effects of suction and soil structure (Eqs. 6.20 and 6.61) yields the following expression for the apparent preconsolidation pressure in unsaturated aggregated soils:

$$p'_c = \psi^{st}\psi^s p'^*_{c0} \tag{6.64}$$

The double effects of suction on the apparent preconsolidation pressure in aggregated (structured) soils are illustrated in Figure 6.17. In this figure, the abscissa is the ratio of apparent preconsolidation pressure over the saturated preconsolidation pressure in reconstituted sate, $p'_c/p'^*_{c0}$. The increase of apparent preconsolidation pressure due to intrinsic suction effect, $\Delta\psi_1$, given by Equation (6.62) is represented by curve *a*. Multiplication of this curve with a reference soil structure function $\psi^{st}_{\text{ref}}$ gives the curve *b* which represents the increase in the apparent preconsolidation pressure due to intrinsic suction, $\Delta\psi_1$, and pure soil structure effects, $\Delta\psi_2$, without considering the suction-hardening of soil structure. Accounting for this latter effect by Equation (6.34), the final evolution of apparent preconsolidation pressure with suction in aggregated soils is represented by curve *c*. The gray area between curve *b* and *c* in Figure 6.17 corresponds to the gain in the apparent effective preconsolidation pressure due to the suction effects on the soil structure, $\Delta\psi_3$, as given by Equations (6.34). This effect is a hardening effect for suctions beyond $s_{\text{ref}}$ and a softening effects for suction below this suction.

### 6.4.5 Plastic potential and plastic multipliers

For each plastic mechanism, there is a potential function corresponding to the yield function. The plastic potential is in general obtained through the integration of the stress-dilatancy relation. The reference model stipulates that the isotropic plastic mechanism provokes only volumetric strain, indicated as $\varepsilon_v^{p,iso}$, and deviatoric strains are always null in the isotropic mechanism ($\varepsilon_d^{p,iso} = 0$). Accordingly, it is assumed that the soil obeys the normality rule in the isotropic mechanism. Hence, the isotropic plastic potential is automatically given by the same expression of the isotropic yield function. In the deviatoric mechanism, both deviatoric and isotropic strains could be provoked, for which the model uses the following stress-dilatancy relation:

$$\frac{\mathrm{d}\varepsilon_v^{p,dev}}{\mathrm{d}\varepsilon_d^{p,dev}} = \alpha \left( M - \frac{q}{p'} \right) \tag{6.65}$$

where $\varepsilon_v^{p,dev}$ and $\varepsilon_d^{p,dev}$ designate, respectively, plastic volumetric and plastic deviatoric strains provoked by the deviatoric mechanisms. The above equation assumes that the plastic work per unit volume of a soil sample provoked by the deviatoric mechanism is dissipated partially, and not entirely, in friction and $\alpha$ determines the partial fraction. This can be compared with stress dilatancy of original Cam-clay in which Schofield and Wroth (1968) assumed that $\alpha = 1$. An $\alpha$ different than one results in a non-associated flow rule for the deviatoric mechanism. The plastic potential can be obtained based on the integration of Equation (6.65).

Similar to the reference model, an associated flow rule for isotropic mechanism and a non-associated flow rule for deviatoric mechanisms is adopted in the new model. Maintaining their expressions in the reference model, the potential functions in the new model are given as:

$$\text{Isotropic:} \qquad g_{iso} = f_{iso} = p' - p'_c r_{iso} = 0 \tag{6.66}$$

$$\text{Deviatoric:} \qquad g_{dev} = \frac{q}{\alpha M p'} + \ln p' + cte = 0 \tag{6.67}$$

The plastic potentials are used in the flow rule (Eq. 6.11) to determine the relative proportionality of the plastic strains:

$$\mathrm{d}\varepsilon_v^{p,iso} = \lambda_{iso}^p \frac{\partial g_{iso}}{\partial p'} = \lambda_{iso}^p \tag{6.68a}$$

$$\mathrm{d}\varepsilon_d^{p,iso} = \lambda_{iso}^p \frac{\partial g_{iso}}{\partial q} = 0 \tag{6.68b}$$

$$\mathrm{d}\varepsilon_v^{p,dev} = \lambda_{dev}^p \frac{\partial g_{dev}}{\partial p'} = \lambda_{dev}^p \frac{1}{Mp'} \alpha \left( M - \frac{q}{p'} \right) \tag{6.68c}$$

$$\mathrm{d}\varepsilon_d^{p,dev} = \lambda_{dev}^p \frac{\partial g_{dev}}{\partial q} = \lambda_{dev}^p \frac{1}{Mp'} \tag{6.68d}$$

where $\lambda_{iso}^p$ and $\lambda_{dev}^p$ are plastic multipliers of isotropic and deviatoric plastic mechanism respectively and they represent the magnitude of plastic strains.

The volumetric or deviatoric plastic strains of the plastic mechanisms should be added to give the total volumetric or deviatoric plastic strain:

$$\mathrm{d}\varepsilon_v^p = \sum_k \lambda_k^p \frac{\partial g_k}{\partial p'} \tag{6.69a}$$

$$\mathrm{d}\varepsilon_d^p = \sum_k \lambda_k^p \frac{\partial g_k}{\partial q} \tag{6.69b}$$

in which $k$ denotes the number of plastic mechanisms. This yields:

$$\mathrm{d}\varepsilon_v^p = \mathrm{d}\varepsilon_v^{p,iso} + \mathrm{d}\varepsilon_v^{p,dev} = \lambda_{iso}^p + \lambda_{dev}^p \frac{1}{Mp'} \alpha \left( M - \frac{q}{p'} \right) \tag{6.70}$$

$$\mathrm{d}\varepsilon_d^p = \mathrm{d}\varepsilon_d^{p,dev} = \lambda_{dev}^p \frac{1}{Mp'} \tag{6.71}$$

The plastic multipliers, $\lambda_{iso}^p$ and $\lambda_{dev}^p$, are determined providing the Prager's consistency condition (Eq. 6.12) being satisfied for both mechanisms. The consistency equation can be rearranged in the following form:

$$\mathrm{d}f_{iso} = \frac{\partial f_{iso}}{\partial p'}\mathrm{d}p' + \frac{\partial f_{iso}}{\partial q}\mathrm{d}q - H_{ii}\lambda_{iso}^p - H_{id}\lambda_{dev}^p = 0 \tag{6.72a}$$

$$\mathrm{d}f_{dev} = \frac{\partial f_{dev}}{\partial p'}\mathrm{d}p' + \frac{\partial f_{dev}}{\partial q}\mathrm{d}q - H_{di}\lambda_{iso}^p - H_{dd}\lambda_{dev}^p = 0 \tag{6.72b}$$

in which the hardening moduli are given by the following expressions:

$$H_{ii} = -\frac{\partial f_{iso}}{\partial r_{iso}}\frac{\partial r_{iso}}{\partial \lambda_{iso}^p} - \frac{\partial f_{iso}}{\partial \varepsilon_v^p}\frac{\partial \varepsilon_v^p}{\partial \lambda_{iso}^p} - \frac{\partial f_{iso}}{\partial \psi_{st}}\frac{\partial \psi_{st}}{\partial \lambda_{iso}^p} \tag{6.73a}$$

$$H_{id} = -\frac{\partial f_{iso}}{\partial r_{dev}}\frac{\partial r_{dev}}{\partial \lambda_{dev}^p} - \frac{\partial f_{iso}}{\partial \varepsilon_v^p}\frac{\partial \varepsilon_v^p}{\partial \lambda_{dev}^p} - \frac{\partial f_{iso}}{\partial \psi_{st}}\frac{\partial \psi_{st}}{\partial \lambda_{dev}^p} \tag{6.73b}$$

$$H_{di} = -\frac{\partial f_{dev}}{\partial r_{iso}}\frac{\partial r_{iso}}{\partial \lambda_{iso}^p} - \frac{\partial f_{dev}}{\partial \varepsilon_v^p}\frac{\partial \varepsilon_v^p}{\partial \lambda_{iso}^p} - \frac{\partial f_{dev}}{\partial \psi_{st}}\frac{\partial \psi_{st}}{\partial \lambda_{iso}^p} \tag{6.73c}$$

$$H_{dd} = -\frac{\partial f_{dev}}{\partial r_{dev}}\frac{\partial r_{dev}}{\partial \lambda_{dev}^p} - \frac{\partial f_{dev}}{\partial \varepsilon_v^p}\frac{\partial \varepsilon_v^p}{\partial \lambda_{dev}^p} - \frac{\partial f_{dev}}{\partial \psi_{st}}\frac{\partial \psi_{st}}{\partial \lambda_{dev}^p} \tag{6.73d}$$

Mathematical manipulation of the derivative of the yield functions together with use of Equations (6.68) yields:

$$H_k = H_k^* + H_k^{st} \qquad k = ii, id, di, dd \tag{6.74}$$

where $H_k^*$ represents represents that part of the hardening modulus correspond-

ing to the reconstituted model:

$$H_{ii}^{*} = p_c' \frac{(1 - r_{iso})^2}{c} + p_c' \beta r_{iso} \tag{6.75a}$$

$$H_{id}^{*} = p_c' \beta r_{iso} \frac{1}{Mp'} \left( M - \frac{q}{p'} \right) \alpha \tag{6.75b}$$

$$H_{di}^{*} = Mp' b \beta r_{dev} \tag{6.75c}$$

$$H_{dd}^{*} = - \left( 1 - b \ln \frac{p' d}{p_c'} \right) \frac{(1 - r_{dev})^2}{a} - b\beta \left( M - \frac{q}{p'} \right) \alpha r_{dev} \tag{6.75d}$$

and $H_k^{st}$ is the hardening modulus arising from soil structure effects:

$$H_{ii}^{st} = p_c' \boldsymbol{\omega} R \ln(\psi_i^{st}) A r_{iso} \tag{6.76a}$$

$$H_{id}^{st} = p_c' \boldsymbol{\omega} R \ln(\psi_i^{st}) (1 - A) r_{iso} \frac{1}{Mp'} \left( 1 + \left| M - \frac{q}{p'} \right| \alpha \right) \tag{6.76b}$$

$$H_{di}^{st} = Mp' b \boldsymbol{\omega} R \ln(\psi_i^{st}) A r_{dev} \tag{6.76c}$$

$$H_{dd}^{st} = Mp' b \boldsymbol{\omega} R \ln(\psi_i^{st}) (1 - A) r_{dev} \frac{1}{Mp'} \left( 1 + \left| M - \frac{q}{p'} \right| \alpha \right) \tag{6.76d}$$

The above formulation of hardening moduli are derived without any explicit derivative with respect to suction. Consequently, the effects of suction variation should be implicitly considered in the above formulation. This means that for any increment of suction, d$s$, the suction dependent variables, namely $p_c'$, $\beta$, $\boldsymbol{\omega}$, and $\psi^{st}$, should be updated with respect to the suction increment prior to be implemented in the above formulation.

Having the four hardening moduli determined, the consistency equation (Eq. 6.72a) could be solved for the plastic multipliers to obtain the plastic strains. This completes the description of the model formulation for the case of triaxial condition. The stress-strain response of the material for triaxial condition could be summarized in the following matrix equations for the elastic response:

$$\begin{bmatrix} \mathrm{d}\varepsilon_v^e \\ \mathrm{d}\varepsilon_d^e \end{bmatrix} = \begin{bmatrix} 1/K & 0 \\ 0 & 1/3G \end{bmatrix} \begin{bmatrix} \mathrm{d}p' \\ \mathrm{d}q \end{bmatrix} \tag{6.77}$$

and the plastic response:

$$\begin{bmatrix} \mathrm{d}\varepsilon_v^p \\ \mathrm{d}\varepsilon_d^p \end{bmatrix} = \frac{1}{Mp'(H_{ii}H_{dd} - H_{di}H_{id})} \begin{bmatrix} H_{dd} - H_{id}L & -H_{id} \\ -H_{di} - H_{ii}L & H_{ii} \end{bmatrix} \begin{bmatrix} \mathrm{d}p' \\ \mathrm{d}q \end{bmatrix} \tag{6.78}$$

in which $L = Mb\ r_{dev} - (q/p')$. The Plastic matrix equation operates only if plastic deformations occur.

### 6.4.6 General stress-strain relationship

The formulation of the model, previously given for triaxial condition, is generalized in this section to the three-dimensional condition. For the general three-dimensional $(x, y, z)$ stress state, the model is formulated in terms of suction and the three stress invariants $(p', J, \theta)$. The mean effective stress, $p'$ reads:

$$p' = \frac{1}{3}\text{tr}(\boldsymbol{\sigma'}) = \frac{1}{3}(\sigma'_{xx} + \sigma'_{yy} + \sigma'_{zz}) \tag{6.79}$$

in which tr designates the trace of the tensor. $J$ is the second invariant of deviatoric stress tensor:

$$J = \frac{1}{2}\text{tr}(\mathbf{S} : \mathbf{S}) \tag{6.80}$$

where the deviatoric stress tensor, $\mathbf{S}$, describes only the distortional components:

$$\mathbf{S} = \boldsymbol{\sigma'} - p'\mathbf{I} \tag{6.81}$$

The alternative expression in terms of stress components is:

$$J = \frac{1}{6}\left[(\sigma'_{xx} - \sigma'_{yy})^2 + (\sigma'_{yy} - \sigma'_{zz})^2 + (\sigma'_{zz} - \sigma'_{xx})^2\right] + \sigma'^2_{xy} + \sigma'^2_{yz} + \sigma'^2_{zx} \tag{6.82}$$

The third invariant is the Lode's angle, $\theta$, defined as:

$$\theta = -\frac{1}{3}\sin^{-1}\left[\frac{3\sqrt{3}}{2}\left(\frac{\frac{1}{3}\text{tr}(\mathbf{S}^3)}{J^{\frac{3}{2}}}\right)\right] \tag{6.83}$$

where $\text{tr}(\mathbf{S}^3) = S_{ij}S_{jm}S_{mi}$ in the indicial notation.

The generalized definition of the deviatoric stress, $q$, (Eq. 6.2) reads:

$$q = \sqrt{3J} \tag{6.84}$$

Physically, $p'$ represents the mean pressure, $J$ represents the magnitude of shear stress and $\theta$ indicates the direction of shear stress. The generalized definition of volumetric and deviatoric strains read (Eq. 6.26):

$$\varepsilon_v = (\varepsilon_{xx} + \varepsilon_{yy} + \varepsilon_{zz})$$

$$\varepsilon_d = \frac{\sqrt{2}}{3}\left[(\varepsilon_{xx} - \varepsilon_{yy})^2 + (\varepsilon_{yy} - \varepsilon_{zz})^2 + (\varepsilon_{zz} - \varepsilon_{xx})^2 + \frac{3}{2}(\gamma^2_{xy} + \gamma^2_{yz} + \gamma^2_{zx})\right]^{\frac{1}{2}}$$

where $\gamma_{xy}$, $\gamma_{yz}$, and $\gamma_{zx}$ are engineering shear strains, and their magnitude are twice those of their counterparts $\varepsilon_{xy}$, $\varepsilon_{yz}$, and $\varepsilon_{zx}$, respectively.

The stress and strain tensors ($3 \times 3$ matrix) are here represented by six element vector of cartesian components and are denoted by $\boldsymbol{\sigma}$ and $\boldsymbol{\epsilon}$ (instead of $\boldsymbol{\sigma}$ and $\boldsymbol{\varepsilon}$ used for tensorial form):

$$\boldsymbol{\sigma'} = \begin{bmatrix} \sigma'_{xx} & \sigma'_{yy} & \sigma'_{zz} & \sigma'_{xy} & \sigma'_{xz} & \sigma'_{yz} \end{bmatrix}^T \tag{6.85a}$$

$$\boldsymbol{\epsilon} = \begin{bmatrix} \varepsilon_{xx} & \varepsilon_{yy} & \varepsilon_{zz} & \gamma_{xy} & \gamma_{xz} & \gamma_{yz} \end{bmatrix}^T \tag{6.85b}$$

In this form, the calculations involve only the straightforward matrix multiplication using the inner product with single contraction (.).

The starting point is decomposition of the total strain increments into elastic and plastic part (Eq. 6.4):

$$\mathrm{d}\boldsymbol{\epsilon} = \mathrm{d}\boldsymbol{\epsilon}^e + \mathrm{d}\boldsymbol{\epsilon}^p \tag{6.86}$$

The elastic strain increment is related to the increment of generalized effective as follows (like Eq. 6.5):

$$\mathrm{d}\boldsymbol{\epsilon}^e = \mathbf{C}^e \cdot \mathrm{d}\boldsymbol{\sigma'} \tag{6.87}$$

where $\mathbf{C}^e$ is the elastic compliance matrix or the inverse of the elastic stiffness matrix, $\mathbf{D}^e$. For the isotropic non-linear elasticity, this matrix reads:

$$\mathbf{C}^e = \mathbf{D}^{e-1} = \begin{bmatrix} \frac{1}{3G}+\frac{1}{9K} & \frac{1}{9K}-\frac{1}{6G} & \frac{1}{9K}-\frac{1}{6G} & 0 & 0 & 0 \\ \frac{1}{9K}-\frac{1}{6G} & \frac{1}{3G}+\frac{1}{9K} & \frac{1}{9K}-\frac{1}{6G} & 0 & 0 & 0 \\ \frac{1}{9K}-\frac{1}{6G} & \frac{1}{9K}-\frac{1}{6G} & \frac{1}{3G}+\frac{1}{9K} & 0 & 0 & 0 \\ 0 & 0 & 0 & \frac{1}{G} & 0 & 0 \\ 0 & 0 & 0 & 0 & \frac{1}{G} & 0 \\ 0 & 0 & 0 & 0 & 0 & \frac{1}{G} \end{bmatrix} \tag{6.88}$$

in which $K$ and $G$ are given in Equation (6.41).

The vector of yield functions becomes:

$$\mathbf{F} = \begin{bmatrix} f_{iso} & f_{dev} \end{bmatrix}^T \tag{6.89}$$

with

$$\text{Isotropic:} \qquad f_{iso} = p' - p'_c r_{iso} = 0 \tag{6.90a}$$

$$\text{Deviatoric:} \qquad f_{dev} = \sqrt{3J} - M_\theta p' \left(1 - b\ln\frac{p'd}{p'_c}\right) r_{dev} = 0 \tag{6.90b}$$

where $M_\theta$ is regarded as a function of Lode's angle $\theta$. The following relationship for $M_\theta$ has been proposed by Sheng et al. (2000):

$$M_\theta = M\left(\frac{2l^4}{1 + l^4 + (1-l^4)\sin(3\theta)}\right)^{\frac{1}{4}} \tag{6.91}$$

in which

$$l = \frac{3 - \sin\varphi}{3 + \sin\varphi} \tag{6.92}$$

with $\varphi$ being the friction angle at critical state. The vector of plastic potential functions takes the following form:

$$\mathbf{G} = \begin{bmatrix} g_{iso} & g_{dev} \end{bmatrix}^T \tag{6.93}$$

with

$$\text{Isotropic:} \quad g_{iso} = f_{iso} = p' - p'_c r_{iso} = 0 \tag{6.94a}$$

$$\text{Deviatoric:} \quad g_{dev} = \frac{\sqrt{3J}}{M_\theta p'} + \ln p' + cte = 0 \tag{6.94b}$$

As in classical theory of plasticity, the plastic strain tensor is obtained from the flow rule:

$$\mathrm{d}\boldsymbol{\epsilon}^p = \boldsymbol{\lambda^p} \cdot \mathbf{n}_G \tag{6.95}$$

where $\boldsymbol{\lambda^p}$ is the matrix of plastic multipliers:

$$\boldsymbol{\lambda^p} = \begin{bmatrix} \lambda^p_{iso} & \lambda^p_{dev} \end{bmatrix} \tag{6.96}$$

and $\mathbf{n}_G$ is the flow rule direction:

$$\mathbf{n}_G = \frac{\partial \mathbf{G}}{\partial \boldsymbol{\sigma'}} = \begin{bmatrix} \frac{\partial g_{iso}}{\partial \sigma_{xx}} & \frac{\partial g_{iso}}{\partial \sigma_{yy}} & \frac{\partial g_{iso}}{\partial \sigma_{zz}} & \frac{\partial g_{iso}}{\partial \sigma_{xy}} & \frac{\partial g_{iso}}{\partial \sigma_{xz}} & \frac{\partial g_{iso}}{\partial \sigma_{yz}} \\ \frac{\partial g_{dev}}{\partial \sigma_{xx}} & \frac{\partial g_{dev}}{\partial \sigma_{yy}} & \frac{\partial g_{dev}}{\partial \sigma_{zz}} & \frac{\partial g_{dev}}{\partial \sigma_{xy}} & \frac{\partial g_{dev}}{\partial \sigma_{xz}} & \frac{\partial g_{dev}}{\partial \sigma_{yz}} \end{bmatrix}^T \tag{6.97}$$

For a given stress state on the yield surface, $M_\theta$ value could be determined using Equation (6.91). Yu (2006) discussed that this value could be used in the stress dilatancy relation to determine directions of plastic strains, and in this way all the necessary differentials of the plastic potential with respect to stresses can be evaluated. In other word, $M_\theta$ is regarded as a constant for a given stress state. Therefore, derivative of plastic potentials with respect to stress reads:

$$\mathbf{n}_G = \frac{\partial \mathbf{G}}{\partial p'} \frac{\partial p'}{\partial \boldsymbol{\sigma'}} + \frac{\partial \mathbf{G}}{\partial J} \frac{\partial J}{\partial \boldsymbol{\sigma'}} \tag{6.98}$$

Using the indicial notation and the explicit forms of Equations (6.66) and (6.67), the derivative of potential functions with respect to stress can be written as:

$$\frac{\partial g_{iso}}{\partial \boldsymbol{\sigma'}} = \frac{\partial g_{iso}}{\partial \sigma'_{ij}} = \begin{cases} \frac{1}{3} & ; \text{if } i \neq j \\ 0 & ; \text{if } i = j \end{cases} \tag{6.99a}$$

$$\frac{\partial g_{dev}}{\partial \boldsymbol{\sigma'}} = \frac{\partial g_{dev}}{\partial \sigma'_{ij}} = \begin{cases} \frac{1}{M_\theta p'} \left[ \frac{1}{2} \sqrt{\frac{3}{J}} (\sigma'_{ij} - p) + \frac{1}{3} \left( M - \frac{\sqrt{3J}}{p'} \right) \right] & ; \text{if } i \neq j \\ \frac{1}{M_\theta p'} \sqrt{\frac{3}{J}} \sigma'_{ij} & ; \text{if } i = j \end{cases} \tag{6.99b}$$

The Prager's consistency condition for multiple dissipation process reads (Rizzi et al., 1996):

$$\mathrm{d}\mathbf{F} = \mathbf{n}_F \cdot \mathrm{d}\boldsymbol{\sigma'} - \mathbf{H} \cdot \boldsymbol{\lambda^p} = 0 \tag{6.100}$$

where

$$\mathbf{n}_F = \frac{\partial \mathbf{F}}{\partial \boldsymbol{\sigma'}} \tag{6.101}$$

and $\mathbf{H}$ is the matrix of hardening moduli:

$$\mathbf{H} = \begin{bmatrix} H_{ii} & H_{id} \\ H_{di} & H_{dd} \end{bmatrix} \tag{6.102}$$

the components of which are determined in Equation (6.73). Similar to the triaxial formulation, the matrix of hardening is decomposed in two parts:

$$\mathbf{H} = \mathbf{H}^{*} + \mathbf{H}^{st} \tag{6.103}$$

where $\mathbf{H}^{*}$ is the matrix hardening moduli corresponding to the reconstituted model and $\mathbf{H}^{st}$ represents the matrix of hardening moduli arising from soil structure effects. Discussion of suction considerations presented in Section 6.4.5 is also valid here.

The incremental relation between stress and strain in the double mechanism model reads:

$$\mathrm{d}\boldsymbol{\sigma'} = \mathbf{D}^{e} \cdot (\mathrm{d}\boldsymbol{\epsilon} - \mathbf{n}_{G} \cdot \boldsymbol{\lambda^{p}}) \tag{6.104}$$

Introducing this equation into Equation (6.100) and solving for the matrix of plastic multipliers yields:

$$\boldsymbol{\lambda^{p}} = (\mathbf{H} + \mathbf{n}_{F} \cdot \mathbf{D}^{e} \cdot \mathbf{n}_{G})^{-1} \cdot (\mathbf{n}_{F} \cdot \mathbf{D}^{e}) \cdot \mathrm{d}\boldsymbol{\epsilon} \tag{6.105}$$

Finally, replacing the plastic multiplier in Equation (6.104) by the above expression yields

$$\mathbf{D}^{ep} = \mathbf{D}^{e} - \mathbf{D}^{e}.\left[\mathbf{n}_{G} \cdot (\mathbf{H} + \mathbf{n}_{F} \cdot \mathbf{D}^{e} \cdot \mathbf{n}_{G})^{-1} \cdot (\mathbf{n}_{F} \cdot \mathbf{D}^{e})\right] \tag{6.106}$$

The above equation represents the elasto-plastic constitutive matrix in the general three-dimensional stress-strain space.

### 6.4.7 Variation of degree of saturation

In addition to the mechanical constitutive model, another constitutive model is needed to describe the variation of degree of saturation in unsaturated states. A general form of the water retention constitutive model was presented in Chapter 3 (as in Eq. 3.94):

$$S_r = S_r(s, e) \tag{6.107}$$

An explicit form of the equation for an undeformable soil was proposed by Van Genuchten (1980). The proposed equation, abbreviated as vG equation, relates the volumetric water content to the suction. However with the assumption of soil incompressibility, this equation can be rewritten in terms of degree of saturation rather than volumetric water content. It is assumed that the degree of saturation tends to zero when suction tends to infinity, i.e., the residual degree of saturation is zero. With this assumption, a simplified version of the vG expression reads:

$$S_r = [1 + (\alpha_w s)^{N}]^{(1/N)-1} \tag{6.108}$$

where $\alpha_w$ $[ML^{-1}T^{-2}]$ and $N$ $[-]$ are the van Genuchten's shape parameters. Qualitatively, $\alpha$ is inversely related to the air entry value, and $N$ is inversely related to the width of the pore-size distribution (Green et al., 1996).

A modified version of the vG equation for homogeneous soils was presented by Vogel et al. (2000), with the air entry value being used as additional parameter. Assuming the residual degree of saturation to be zero, this new relation reads:

$$S_r = \begin{cases} 1 & ; \text{if } s \leq s_e \\ [1 + (\alpha_w s)^N]^{(1/N)-1} & ; \text{if } s > s_e \end{cases} \tag{6.109}$$

The vG type equation assumes a homogeneous soil structure with a continuous pore size distribution. Therefore, it represents a unimodal relationship. In the case of aggregated soils, further modifications are required.

The presence of aggregates and macropores in natural soils usually results in a retention curve having at least two points of inflection (Coppola, 2000). The influence of fabric on the water retention curves was discussed in Section 2.3.1, and examples of bi-modal water retention curves of aggregated soils were given in Figure 2.9. To model the bi-modal retention curves, a double porosity approach should be used. Durner (1992), cited in (Coppola, 2000), proposed the following form for the retention curve of a soil multi-porosity:

$$S_r = \sum \phi^i [1 + \left(\alpha_w^i s\right)^{N^i}]^{(1/N^i)-1} \tag{6.110}$$

where $N_i$ and $\alpha_w^i$ are the shape parameters for the retention properties corresponding to the pores classified in the $i^{\text{th}}$ mode of porosity, for which the volume fraction of pores is represented by $\phi^i$. This latter parameter has been already introduced in Equation (3.69) of Chapter 3 for a double porous medium:

$$\phi^i = \frac{n^i}{n} \qquad ; \; i = 1, 2$$

with $n^1$, $n^2$, and $n$ being respectively the micro, macro, and total porosity.

Coppola (2000), after Ross and Smettem (1993), used a simple one-parameter function for describing the retention properties of macropores and obtained the following retention equation for incompressible aggregated soils:

$$S_r = \phi^1 [1 + \left(\alpha_w^1 s\right)^N]^{(1/N)-1} + \phi^2 (1 + \alpha_w^2 s) \exp(-\alpha_w^2 s) \tag{6.111}$$

where the retention property of the macropores is described only by parameter $\alpha_s^2$.

Comparing Equation (6.110) with the expression of degree of saturation in double porosity given by Equation (3.43) and introducing the air entry value as additional parameter in the same way as in Equation (6.109), yields the following relations for an incompressible double porous media:

$$s_L^1 = \begin{cases} 1 & ; \text{if } s \leq s_e^1 \\ [1 + (\alpha_w^1 s)^N]^{(1/N)-1} & ; \text{if } s > s_e^1 \end{cases} \tag{6.112}$$

and

$$s_L^2 = \begin{cases} 1 & ; \text{if } s \leq s_e^2 \\ (1 + \alpha_w^2 s) \exp(-\alpha_w^2 s) & ; \text{if } s > s_e^2 \end{cases} \tag{6.113}$$

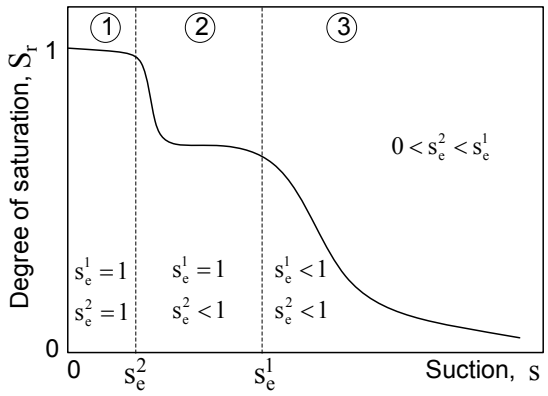


*Figure 6.18:* Schematic water retention curve in soils with double porosity

where $s_L^1$ and $s_L^2$ are local degrees of saturation in micro and macropores defined by Equation (3.40), and $s_e^1$ and $s_e^2$ are the air entry values suction corresponding to micro and macropores respectively.

In the joint research project of this study, presented in the companion dissertation of Carminati (2006), the water retention properties of single aggregates of Abist soil were evaluated using neutron radiography and tomography. Carminati et al. (2007c) showed that Equation (6.112) could successfully represent the water retention curve of the tested soil aggregates. Therefore, Equations (6.111), (6.112) and (6.113) can be combined to obtain the expression of degree of saturation in an incompressible double porous media:

$$S_r = \begin{cases} 1 & ; \text{if } s \leq s_e^2 \\ \phi^1 + \phi^2(1+\alpha_w^2 s)\exp(-\alpha_w^2 s) & ; \text{if } s_e^1 > s > s_e^2 \\ \phi^1[1+(\alpha_w^1 s)^N]^{(1/N)-1} + \phi^2(1+\alpha_w^2 s)\exp(-\alpha_w^2 s) & ; \text{if } s > s_e^1 \end{cases} \tag{6.114}$$

The water retention curve given by these equations is schematically represented in Figure 6.18. Three different zones of saturation are illustrated in the water retention curve of double porous soil in this figure: zone 1 where both macro and micropores saturated, zone 2 where micropores saturated and macropores unsaturated, and zone 3 where both macro and micropores unsaturated.

In aggregated soils with large inter-aggregate pores, the air entry value of macropores is much lower than that of micropores:

$$s_e^2 << s_e^1 \tag{6.115}$$

This is the case for most of natural aggregated soils as well as the aggregated soils tested in the present study. In these materials, the air entry value of macropores can be neglected comparing to that of micropores. Therefore, it is plausible to assume that the macropores become drained at the very early stages of desaturation and local degree of macropore saturation is therefore zero ($s_L^2 = 0$). Accordingly, the total degree of saturation is determined only based on the saturation and desaturation of the micropores:

$$S_r \approx \phi^1 s_L^1 \tag{6.116}$$

In this case, Equation (6.114) for incompressible aggregated soils with macropores can be simplified as follow:

$$S_r = \begin{cases} 1 & ; \text{if } s = 0 \\ \phi^1 & ; \text{if } s_e^1 > s > 0 \\ \phi^1[1 + (\alpha_w^1 s)^N]^{(1/N)-1} & ; \text{if } s > s_e^1 \end{cases} \tag{6.117}$$

The vG type equations presented above are suitable for undeformable soils and cannot be used to predict the variation of the degree of saturation during the mechanical loading at constant suction. Experimental evidence of the increase in the degree of saturation during a mechanical compression under constant suction has been already presented in Chapter 3 both for reconstituted (see Fig. 4.29(d), 4.30(d), and 4.31(d)) and aggregated soils (see Fig. 4.36(d), 4.36(d), and 4.36(d)). Similar results were reported for reconstituted clays by Gallipoli et al. (2003), Wheeler et al. (2003) and Monroy (2005). In order to model this behavior, the water retention relation should be first modified for reconstituted soils, and in further developments it will be extended to aggregated soil. To address this issue in reconstituted soils, Wheeler et al. (2003) expressed the incremental variation of degree of saturation in terms of modified suction defined as the product of matric suction and porosity ($ns$). A more general approach is to replace the suction in Equation (6.109) for homogeneous reconstituted soils by its product with a general function of the void ratio, $e^{\psi}$:

$$S_r = \begin{cases} 1 & ; \text{if } s \leq s_e \\ [1 + \left(\alpha_s e^{\psi} s\right)^N]^{(1/N)-1} & ; \text{if } s > s_e \end{cases} \tag{6.118}$$

where the exponent $\psi$ denotes the contribution of void ratio in the variation of degree of saturation. It should be noted that $\alpha_s$ is not necessarily equal to $\alpha_w$. This equation is equivalent to the earlier modifications proposed by Gallipoli et al. (2003).

In addition to the given relation between suction and degree of saturation, Equation (6.118) can also predict the increase in the degree of saturation of the reconstituted soil during a mechanical compression under constant suction. The appropriate parameters are those providing the best prediction of degree of saturation due to variation of both suction and void ratio.

In a soil with double porosity, the microporosity represents the pores of the soil matrix (intra-aggregate pores). Therefore, Equation (6.118), originally proposed for reconstituted soils, could be used to model the water retention of the micropores, providing that the void ratio, $e$, is replaced by the micro void ratio, $e^1$:

$$s_L^1 = \begin{cases} 1 & ; \text{if } s \leq s_e^1 \\ [1 + \left(\alpha_s (e^1)^{\psi} s\right)^N]^{(1/N)-1} & ; \text{if } s > s_e^1 \end{cases} \tag{6.119}$$

In order to use the above relations in a constitutive model, the parameters $e^1$ and $\phi^1$ in Equations (6.119) and (6.117) have to be expressed in terms of state parameters involved in the model. This is done here using the definition of degree of soil structure (Eq. 6.29), and the phase relations presented in Section 3.2.1.

Combining Equations (6.29), (3.38), and (3.38) yields:

$$e^1 = e - e_i^2 R \tag{6.120a}$$

$$\phi^1 = 1 - (e_i^2 R/e) \tag{6.120b}$$

in which , $e_i^2$ is the initial value of macro void ratio in the material. Introducing the above equations into Equations (6.119) and (6.117) and comparing with Equation (6.112) result the following equation for degree of saturation in a compressible soil with double porosity:

$$S_r = \begin{cases} 1 & ; \text{if } s = 0 \\ 1 - (e_i^2 R/e) & ; \text{if } s_e^1 > s > 0 \\ [1 - (e_i^2 R/e)][1 + \left(\alpha_s (e - e_i^2 R)^{\Psi} s\right)^N]^{(1/N)-1} & ; \text{if } s > s_e^1 \end{cases} \tag{6.121}$$

The initial volume fraction of macropores, $\phi_i^2$, used in the water retention relation should be determined using the porosimetry methods such as MIP. However, following the reasoning given in Section 6.3.4 for determination of soil structure parameters, a rough estimation of this parameter in aggregated (structured) soils might be given by the values $a/a'$ in Figure 6.9(a). Such estimation postulates that the volume fraction of micropores in aggregated and reconstituted soils are identical and the difference arises from the macropores.

## 6.5 Assessment of model parameters

### 6.5.1 Model parameters

The model requires three elastic parameters: $K_{\text{ref}}$, elastic bulk modulus at the reference mean effective stress $p'_{\text{ref}}$; $\nu$, the Poisson's ratio; and $n_e$, the exponent of non-linear elasticity.

The model also requires the following elasto-plastic parameters: $\lambda^*$, slope of the intrinsic normal consolidation line in the compression plane $v - \ln p'$; $M$, slope of critical state line in the $q - p'$ effective stress plane; $d$, the spacing ratio which is the ratio of saturated preconsolidation effective pressure over the saturated critical mean effective pressure belonging to the same yield surface; $b$, a shape parameter for deviatoric yield surface; $a$ and $c$, parameters controlling the growth of initial elastic radii with occurrence of plastic strains in deviatoric and isotropic mechanisms respectively; and $\alpha$, parameter of non-associativity flow rule for deviatoric plastic mechanism.

The extension of the mechanical model to unsaturated soils introduces three parameters: $\gamma_s$, parameter of intrinsic suction-induced hardening; $s_e$, the air entry value suction (replaced by air entry value of micropores $s_e^1$ in aggregated soil); and $\Omega_s$, the parameter controlling the variation of $\lambda^*$ with suction.

Three additional parameters $\alpha_s$, $\Psi$, and $N$ are required to describe the water retention behavior of reconstituted soils.

The aggregated model then introduces four further parameters: $\omega_{\text{ref}}$, controlling rate of de-structuring with occurrence of plastic strains at the reference suction $s_{\text{ref}}$; $A$, relative proportion of deviatoric and volumetric de-structuring;

$\Omega_{st}$, parameter controlling the variation of de-structuring parameter $\omega$ with suction; and $n_{st}$, describing the effect of suction on the strength of inter-particle bonding.

To use the model for simulation of soil response, certain initial conditions need to be specified. These are: $p'^{*}_{c0i}$, initial intrinsic saturated preconsolidation pressure; $r^{e}_{dev}$ and $r^{e}_{iso}$, the initial values of elastic radii; $\psi^{st}_{i\text{ref}}$, parameter describing the initial structure of the soil at the reference suction; and, $\phi^{2}_{i}$ the initial volume fraction of macropores.

Finally, it is necessary, as in all unsaturated elasto-plastic models, to specify the initial suction and stress-state. Of course, this must lie within the initial yield surface.

The model parameters are summarized in Table 6.5.1. In most cases, it is possible to reduce the number of required model parameters and to achieve a simplified set of parameters, as for instance, in OCC or MCC models. In these models, the exponent of non-linear elasticity is equal to one, i.e. $n_e = 1$. Moreover, the spacing ratio, $d$, could be fixed at 2.718 as in OCC or at 2 as in MCC for all types of soils. To recover an expression similar to that of OCC type, the shape parameter, $b$, could be fixed at one. Furthermore, postulating a constant value of $K_0$, it was shown that two parameters $b$ and $d$ could be linked using Equation (6.55).

*Table 6.2:* Parameters of ACMEG-2S constitutive model

| **symbol**. | **Description** |
|---|---|
| | **Elastic properties** |
| $K_{\text{ref}}$ | elastic bulk modulus at the reference mean effective stress, $p'_{\text{ref}}$ |
| $\nu$ | Poisson's ratio |
| $n_e$ | exponenet of non-linear elasticity |
| | **Elasto-plastic parameters** |
| $\lambda^*$ | slope of isotropic normal consolidation line in $v - \ln p'$ space |
| $M$ | slope of critical state line in the $q - p'$ effective stress plane |
| $d$ | spacing ratio |
| $b$ | shape parameter for deviatoric yield surface |
| $a$ | growth rate parameter for deviatoric elastic radius |
| $c$ | growth rate parameter for isotropic elastic radius |
| $\alpha$ | parameter of non-associativity of flow rule for deviatoric plastic mechanism |
| | **Partial saturation parameters** |
| $s^1_e$ | air entry value suction (of micropores) |
| $\gamma_s$ | parameters of the intrinsic suction-induced hardening |
| $\Omega_s$ | parameter controlling the variation of $\lambda^*$ with suction |
| $\alpha_s$ | WRC parameter |
| $N$ | WRC parameter |
| $\psi$ | WRC parameter for influence of void ratio |
| | **Soil structure parameters** |
| $\omega_{\text{ref}}$ | de-structuring rate control parameter at reference suction, $s_{\text{ref}}$ |
| $A$ | relative proportion of deviatoric and volumetric de-structuring |
| $\Omega_{st}$ | parameter controlling the variation of $\omega$ with suction |
| $n_{st}$ | parameter of suction-induced hardening in soil structure |

The two parameters $a$ and $c$ are used to describe the mobilization of two plastic mechanisms. These parameters allow a gradual transition between elastic and elasto-plastic behavior. If this transition is not likely to be addressed, it could be assumed that the two mechanisms are fully mobilized from the onset of plasticity. In this case, the initial values of degree of mobilizations, i.e. $r^e_{dev}$ and $r^e_{iso}$, should be set as one and there would be no more need to assign the parameters $a$ and $c$.

Finally due to low variation of $\lambda^*$ and $\omega$ with suction, it is often reasonable to select an average value for these parameters for unsaturated cases. This choice eleminates the need to determine the parameters $\Omega_s$ and $\Omega_{st}$.

Nevertheless, choice of the main material parameters and further simplifications depends on the nature of the concerned problem as well as the main features which are required to be addressed by the model.

### 6.5.2 Parameter determination for Bioley silt

As a part of the model assessment in next sections, the model will be used to simulate the oedometer tests of the present study carried out on Bioley silt. Accordingly, the required parameters of the model for Bioley silt have been determined and presented in this section.

**Elastic parameters:** Bioley silt has been used as a reference material at EPFL-LMS and its properties has been abundantly characterized for different studies. Among them, the existing results of CD triaxial tests on the saturated reconstituted samples (EPFL-LMS, 2002) have been used here to determine the required elastic parameters of the model.

In these results, the elastic bulk modulus was given for three confining pressures of 100, 200 and 300 $kPa$; while, the reference pressure, $p'_{\text{ref}}$, in this study has been selected to be 1000 $kPa$. Using the three available experimental values and Equation (6.41), the elastic bulk modulus at the confining pressure of 1000 $kPa$ was determined to be 297 $MPa$. This reference bulk modulus together with the experimental values were then used again in Equation (6.41) to determine the exponent of non-linear elasticity for the reference pressure of 1000 $kPa$, yielding $n_e = 0.9$ (Fig. 6.19). The Poisson's ratio is given to be $\nu = 0.4$ which corresponds to a reference elastic shear modulus, $G_{\text{ref}}$, of 63.6 $MPa$.

**Elasto-plastic parameters:** Using Equation (6.18) and the compressibility index obtained in test SAT04, the slope of iNCL in $v - \ln p'$, $\lambda^*$, is determined to be 0.056. According to the laboratory data (EPFL-LMS, 2002), the friction angle of saturated reconstituted Bioley silt is 31.8° which corresponds to $M = 1.278$ (Eq. 6.3). In the absence of experimental results, the choice of values for parameters $b$ and $d$ would be arbitrary. Here, $d$ has been set to 2 as in the MCC and $b$ was selected to be 1 in line with the the expression of OCC. Parameter $\alpha$ is selected to be 1 for the flow rule. In the case of simulations in which the initial elastic radii are not one, value of 0.001 has been used for both parameters $a$ and $c$.

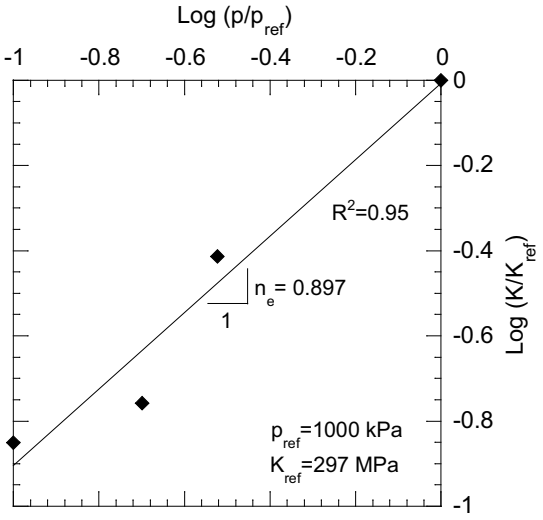


*Figure 6.19:* Determination of the exponent of non-linear elasticity for Bioley silt

**Partial saturation parameters:** Based on the results of test USR03, the air entry value of reconstituted soil has been determined to be 250 $kPa$ (see Sec. 4.5.2). Parallel to this study, Carminati (2006) investigated the water retention properties of similar aggregates using neutron radiography and reported the air entry value of micropores, $s_e^1$, to be 50 $kPa$. The same value is used for aggregates of Bioley silt.

Results of reconstituted samples (USR01, USR02 and USR03) were used to evaluate paramater $\gamma_s$. Figure 6.20(a) schematically shows the stress path followed by this samples. The samples were first consolidated to point $A$ and then unloaded to point $B$. When suction is increased under constant net stress, the sample undergoes plastic deformations between point $A'$ and $C'$ and the saturated preconsolidation stress changes from point $\sigma'_{vc_1}$ to $\sigma'_{vc_2}$. In order to determine parameter $\gamma_s$, the apparent preconsolidation stress $\sigma'_{vc}$ should be compared with this latter saturated preconsolidation stress ($\psi^s = \sigma'_{vc}/\sigma'_{vc_2}$). In the case of USR01 and USR02, suction has been increased in a single step and therefore only points $B$ and $D'$ could be known. Assuming that $BD'$ is linear along all its length ($C'D'$ might be non-linear), point $C$ and correspondingly $\sigma'_{vc_2}$ for these samples are given by the intersection of $BD'$ and the horizontal line of $s = s_e$. In the case of USR03, suction was increased in different steps and the $\sigma'_{vc_2}$ is directly given by the effective stress at $s = s_e$. These values are determined and presented in Table 6.5.2 for the three samples. The normalized values of apparent preconsolidation stress with respect to the saturated preconsolidation stress ($\psi^s = \sigma'_{vc}/\sigma'_{vc_2}$) are presented in Figure 6.20(b). Using the least square method, $\gamma_s = 6.53$ was found to provide the best fit.

Figure 6.21(a) shows the evolution of $\lambda^*$ with suction observed in the experimental results. The best fit of Equation 6.59 to these data corresponds to $\Omega_s = 0.0262$, however it could hardly describe the increase of $\lambda^*$ from saturated to unsaturated samples. Since, variation of $\lambda^*$ in the three unsaturated tests is insignificant, an alternative approach is to use a constant average value of $\lambda^* = 0.151$ for simulation of unsaturated tests.

*Table 6.3:* Required values for determination of $\gamma_s$ for Bioley silt

| Test | $s[kPa]$ | $\sigma'_{vc_1}[kPa]$ | $\sigma'_{vc_2}[kPa]$ | $\sigma'_{vc}[kPa]$ | $\psi^s$ |
|---|---|---|---|---|---|
| USS01 | 500 | 60 | 240 | 480 | 2.00 |
| USS02 | 1500 | 90 | 220 | 1280 | 5.81 |
| USS03 | 3000 | 200 | 265 | 2100 | 7.92 |

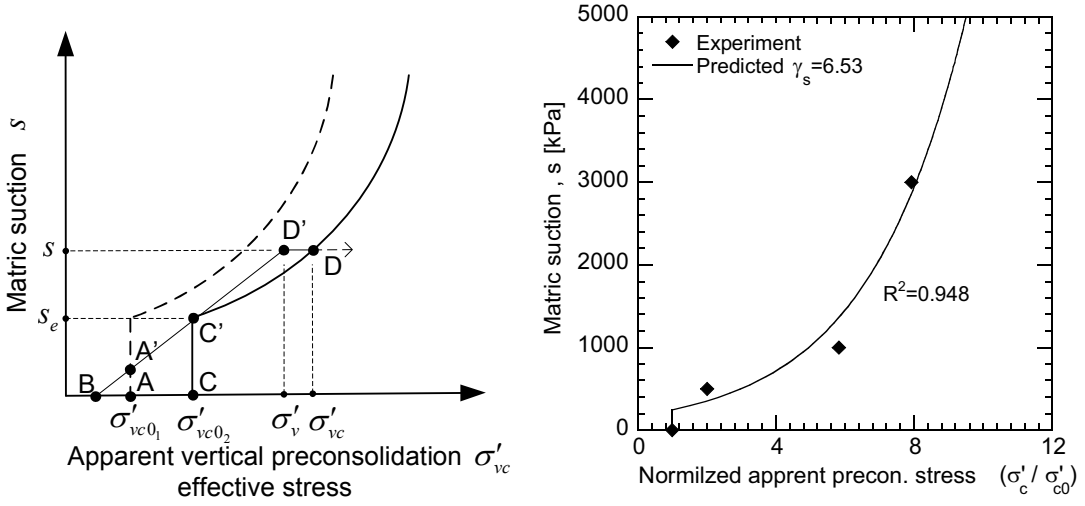


(a) (b)

*Figure 6.20:* Determination of $\gamma_s$ for intrinsic suction hardening effects in Bioley silt

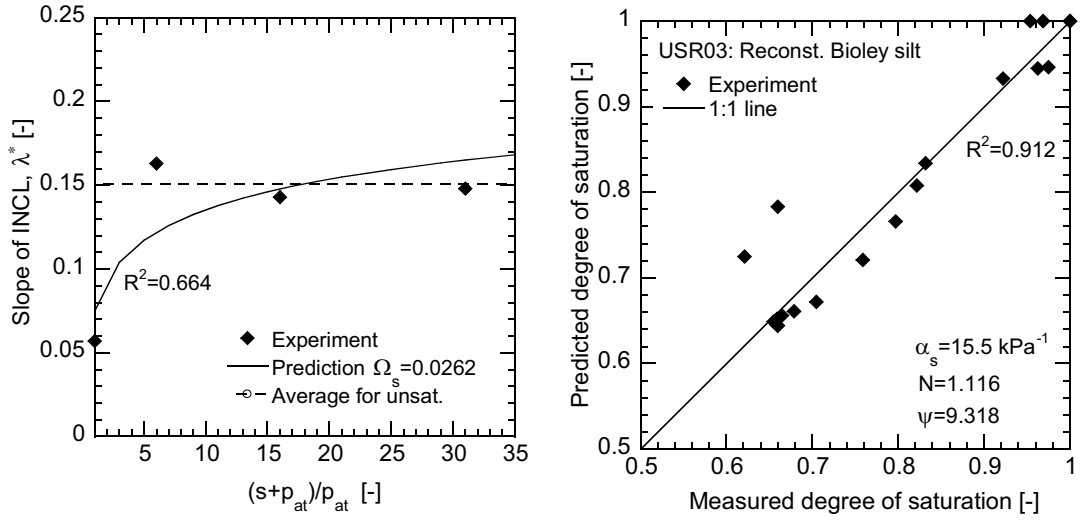


(a) (b)

*Figure 6.21:* Determination of the partial saturation parameters for Bioley silt: (a) parameter $\Omega_s$, (b) water retention parameters $\alpha_s, N, \psi$

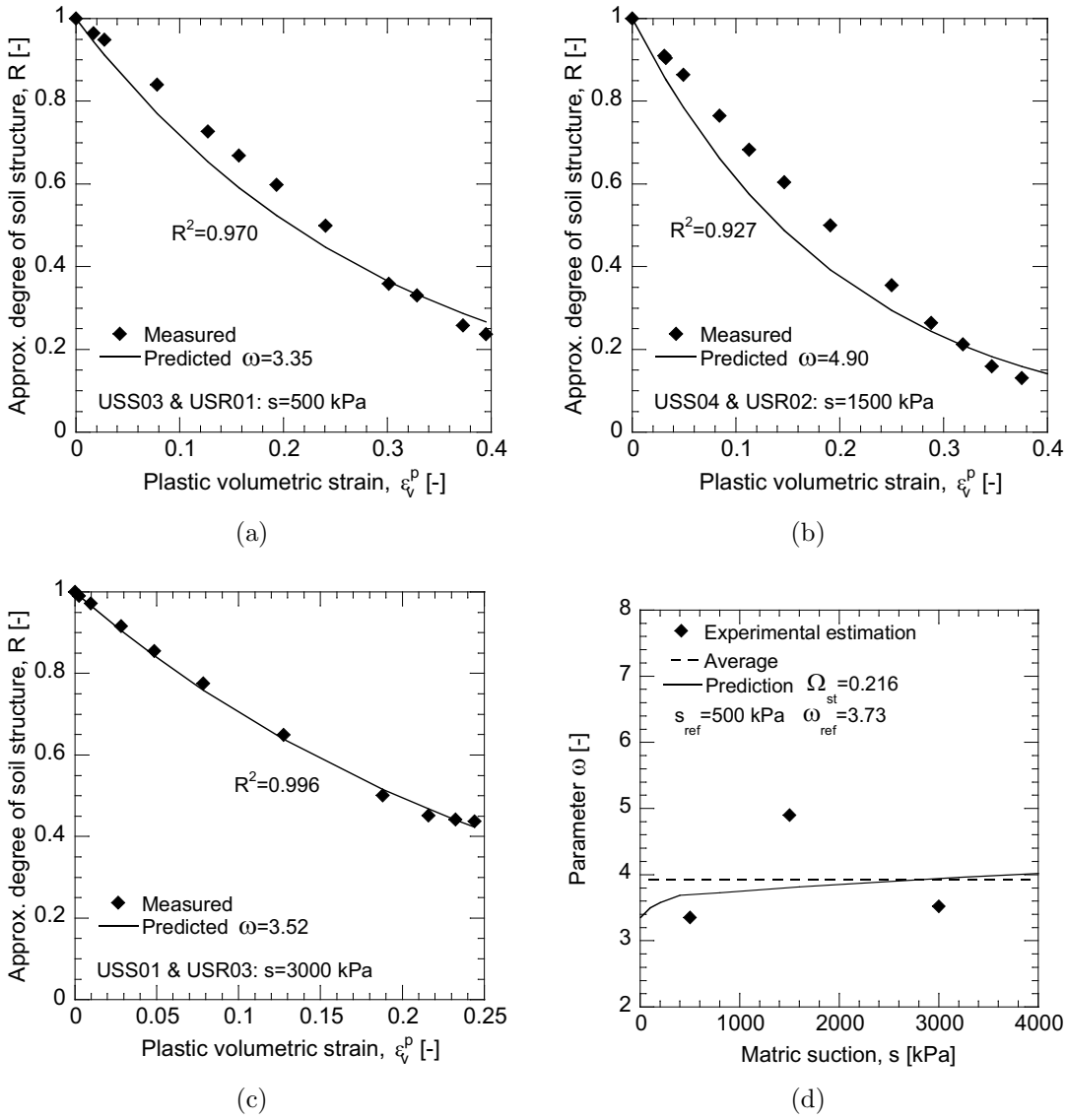


*Figure 6.22:* Determination of soil structure parameters $\omega$ and $\Omega_{st}$: (a) $s = 500\ kPa$, (b) $s = 1500\ kPa$, (c) $s = 3000\ kPa$, (d) evolution of $\omega$ with suction

The water retention parameters were determined for reconstituted Bioley silt by performing a three-dimensional least-squares fit, in $Sr : s : e$ space, of Equation (6.121) to the results of sample USR03. The obtained values are $N = 1.116$, $\psi = 9.318$, and $\alpha_s = 15.5\ kPa^{-1}$. Measured and predicted values of degree of saturation using these parameters are depicted in Figure 6.21(b).

**Soil structure parameters:** Based on the tomography results, it was shown in Section 5.3 that structure degradation of aggregated soil in oedometric stress path is mainly isotropic. Accordingly, parameter $A$ is selected to be 1 for the simulation of the oedometric tests of this study. The determination procedure described in Section 6.3.4 has been used to depict the approximative evolution of degree of saturation with volumetric plastic strains for three suction levels based on the oedometric compression curves of reconstituted and aggregated

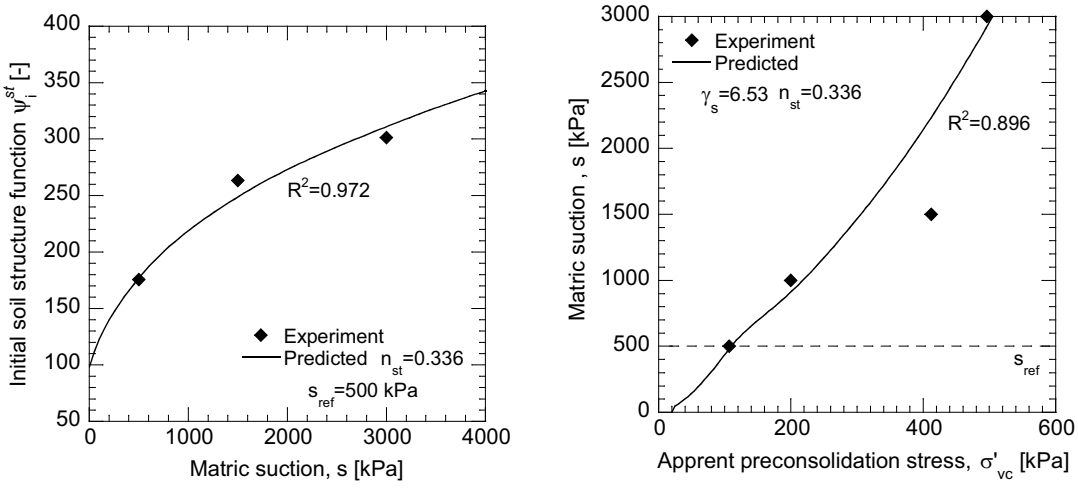


(a) (b)

*Figure 6.23:* Influence of suction on the soil fabric: (a) evolution of $\psi_i^{st}$ with suction, (b) apparent preconsolidation pressure vs suction

*Table 6.4:* Parameters of Bioley silt for simulation of oedometer tests

| **Parameter** | | **value** | **Parameter** | | **value** |
|---|---|---|---|---|---|
| $K_{\text{ref}}$ | $[MPa]$ | 297 | $\gamma_s$ | $[-]$ | 6.53 |
| $G_{\text{ref}}$ | $[MPa]$ | 63.7 | $s_e/s_e^1$ | $[kPa]$ | 250/50 |
| $n_s$ | $[-]$ | 0.897 | $\Omega_s$ | $[-]$ | 0.0262 |
| $\lambda^*$ | $[-]$ | 0.0567 | $\alpha_s$ | $[kPa^{-1}]$ | 15.5 |
| $M$ | $[-]$ | 1.278 | $N$ | $[-]$ | 1.116 |
| $d$ | $[-]$ | 2 | $\psi$ | $[-]$ | 9.32 |
| $b$ | $[-]$ | 1 | $\omega_{\text{ref}}$ | $[-]$ | 3.73 |
| $a$ | $[-]$ | 0.001 | $A$ | $[-]$ | 1 |
| $c$ | $[-]$ | 0.001 | $\Omega_{st}$ | $[-]$ | 0.216 |
| $\alpha$ | $[-]$ | 1 | $n_{st}$ | $[-]$ | 0.336 |

samples. These results and the estimated value of parameter $\omega$ are presented in Figures 6.22(a), 6.22(b), and 6.22(c). Evolution of this parameter with suction is shown in Figure 6.22(d). The bold line in this figure represents the fitting of Equation (6.35) which corresponds to $\Omega_{st}$ equal 0.216 for the reference suction $s_{\text{ref}}$ being 500 $kPa$. However, values predicted by this equation are far from those experimentally estimated. Alternatively, the average value of 3.92 for this parameter could be used with $\Omega_{st}$ being zero.

Finally, parameter $n_{st}$ was determined using the experimental values of the initial soil structure function, $\psi_i^{st}$, at different suctions, as described in Section 6.3.4. This value has been calculated for the pairs of aggregated and corresponding reconstituted samples and is presented in Figure 6.23(a) for the three suction levels. Using Equation (6.34) to reproduce this evolution, the exponent $n_{st}$ was determined to be 0.336 for the reference suction $s_{\text{ref}}$ of 500 $kPa$. Figure 6.23(b) shows the successful prediction of apparent preconsolidation of aggregated samples using Equation (6.64) with the set of parameters determined above. The model parameters for Bioley silt are summarized in Table 6.4

## 6.6 Simulation and validation

### 6.6.1 Numerical integration of the constitutive equations

Numerical integration of the constitutive equations of the model ACMEG-2S has been done using the driver of constitutive equations developed at the Ecole Centrale de Paris LAWYER (Modaressi et al., 1989). The Hujeux type constitutive model in the code has been modified by (Francois, 2005) with respect to the new ACMEG model, the reference model for saturated reconstituted soils.

In the present work, a new version of the code has been developed for the constitutive equations of the model ACMEG-2S. The programming involved introducing new parameters and variables as well as major modification of the relevant sub-routines of the code.

A simplified algorithm of the integration of constitutive equations is presented in Figure 6.24. A brief description of the different steps of the algorithm is given below.

At the first step, the input data including the material properties, material state and imposed loading are read. Loading could be applied through the combination of imposed deformation, net stress or suction.

In the next step, the model parameters are initialized and state of stress is controlled to be within the initial yield limit. If this latter condition is satisfied, the code continues to calculate the increments of loading and it determines the generalized effective stress for the material. It uses a return mapping type algorithm is which stress and strains of a given step ($n$: step counter) are predicted based on elastic analysis and then corrected using plastic iteration ($i$ is the iteration counter).

After this step, the internal parameters are updated and the yield function is tested with new parameters. If the material meets the plasticity condition, the plastic strains are calculated using the hardening moduli with updated internal variable. Then the stress will be corrected with real elastic matrix and calculated plastic strains. If the material remains elastic, this latter step is reached without passing through plastic steps. Finally, an error test is provided to verify the convergence in the solution. If condition of convergence is not met, the iteration is continued; otherwise, it passes to the next step.

### 6.6.2 Typical numerical response

Typical response of the model and the influence of the structure parameters $\omega$ and $\psi_i^{st}$ at isotropic and deviatoric condition have been evaluated by simulating isotropic consolidation and triaxial compression tests. Simulations are made using the unique set of parameters listed in Table 6.4.

#### 6.6.2.1 Isotropic consolidation

Influence of parameter $\omega$ on the isotropic compression response of the model is illustrated in Figure 6.25. The simulations are made with the initial values $p'^{*}_{c0i} = 10\ kPa$ and $\psi_i^{st} = 30$ with the exception of iNCL for which $\psi_i^{st} = 1$. It

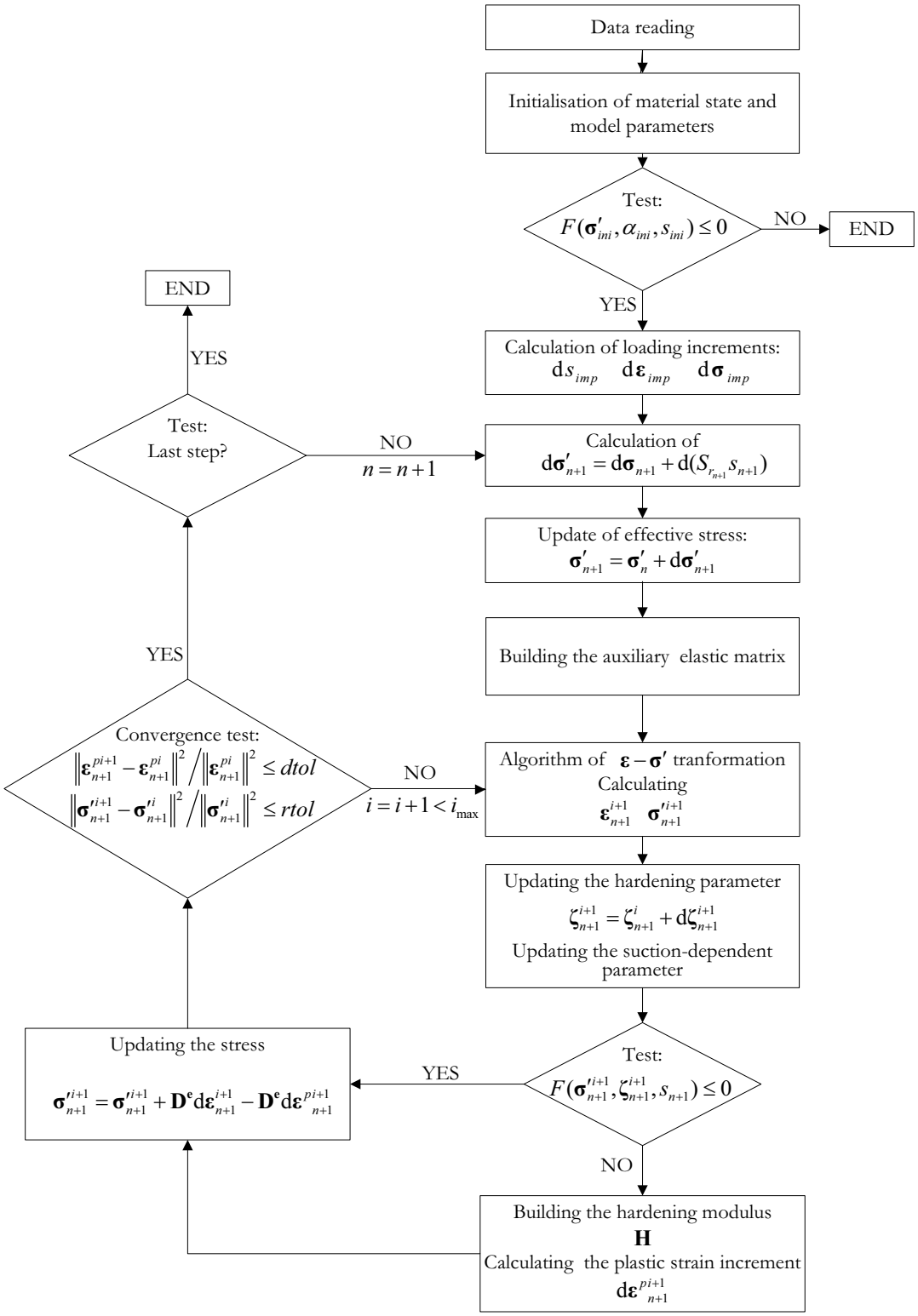


*Figure 6.24:* Algorithm of integration of constitutive equations

can be seen in Figure 6.25(a) that for a value of $\omega = 0$ the compression curve of aggregated (structured) soil is parallel to iNCL. In this case no degradation could be observed in the additional specific volume retained by the soil structure. The rate of reduction in the additional specific volume increases with the magnitude of $\omega$. For the high value of $\omega = 12$, the consolidation curve of aggregated soil almost converges with the iNCL at the end of consolidation.

Figure 6.25(b) depicts the evolution of degree of soil structure, $R$, with the applied load for different simulations. Below the apparent preconsoidation pressure where the response is elastic, $R$ remains equal to one; beyond this

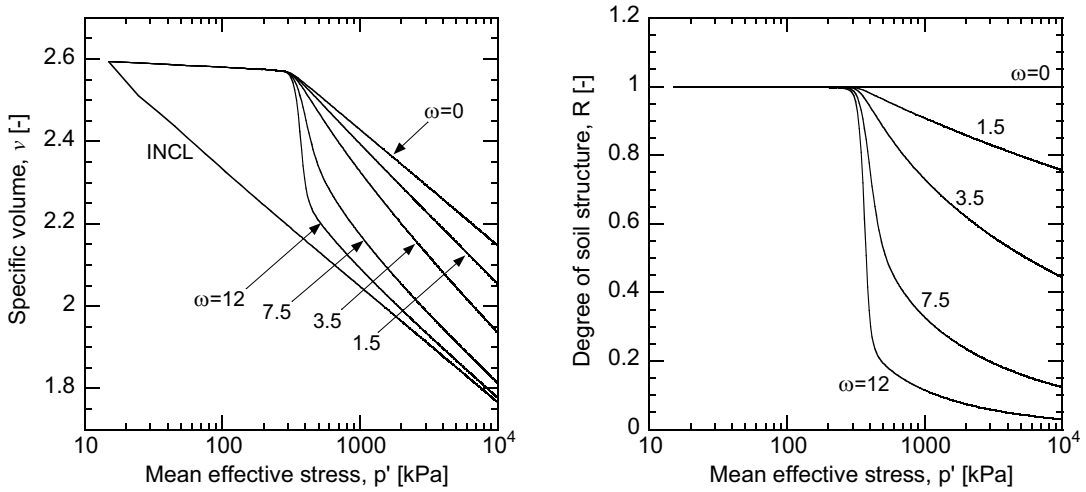


(a) (b)

*Figure 6.25:* Influence of parameter $\omega$ on the isotropic compression behavior: (a) stress-strain response, (b) degree of soil structure

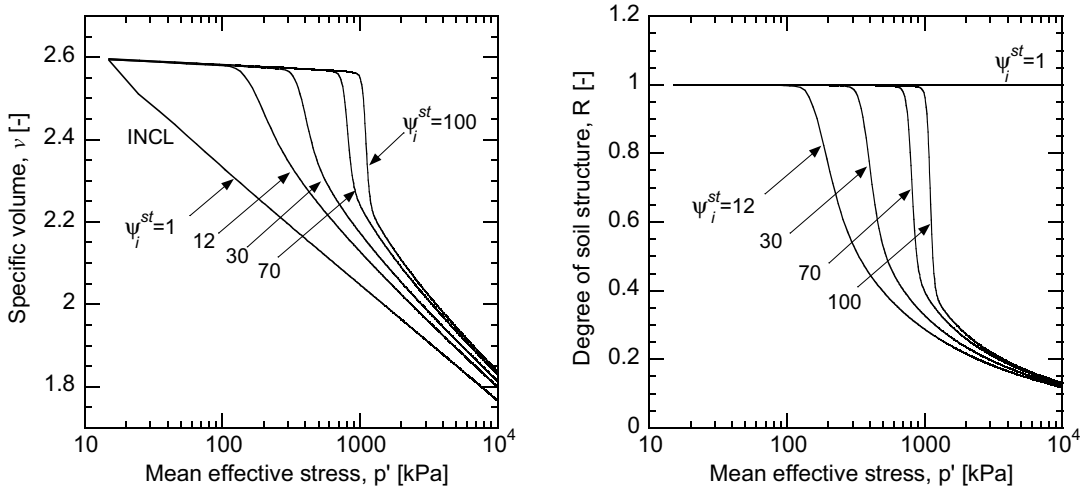


(a) (b)

*Figure 6.26:* Influence of parameter $\psi_i^{st}$ on the isotropic compression behavior: (a) stress-strain response, (b) Degree of soil structure

limits, it tends to zero with occurrence of plastic deformations.

The isotropic compression response has been further evaluated for the influence of the initial structure of the soil represented by $\psi_i^{st}$ (Fig. 6.26(a)). Parameter $\omega$ is fixed at 7.5. When $\psi_i^{st} = 1$, the compression curve corresponds to the iNCL. It is observed in Figure 6.26(a) that the form of yielding depends on the initial soil structure; i.e., the higher the value of $\psi_i^{st}$, the more brittle the yielding. Evolution of $R$ in Figure 6.26(b) shows that the final values of $R$ converge at the end of compression.

#### 6.6.2.2 Conventional triaxial compression (CTC)

Two conventional triaxial compression tests at confining pressure of $\sigma' = 50$ and 200 $kPa$ have been simulated, each one with four different values of $\omega$. The results are plotted in Figures 6.27 and 6.28.

It is observed in Figure 6.27(a) that for a soil with a given initial structure, the peak strength remains the same, even if the post-peak response is different. Moreover, it can be seen that the final state is independent of the soil structure and it corresponds to the critical state. For higher values of $\omega$ the critical state is reached at lower values of axial strain. This corresponds to the flat part of the $\varepsilon_v - \varepsilon_1$ in Figure 6.27(b).

At the confining pressure of $\sigma_3' = 200\ kPa$, the sample appears to be slightly over consolidated. The reconstituted specimen $\omega = 0$ shows no peak behavior (Fig. 6.28(a)). However when $\omega$ is increased, specimen shows to represent a peak response.

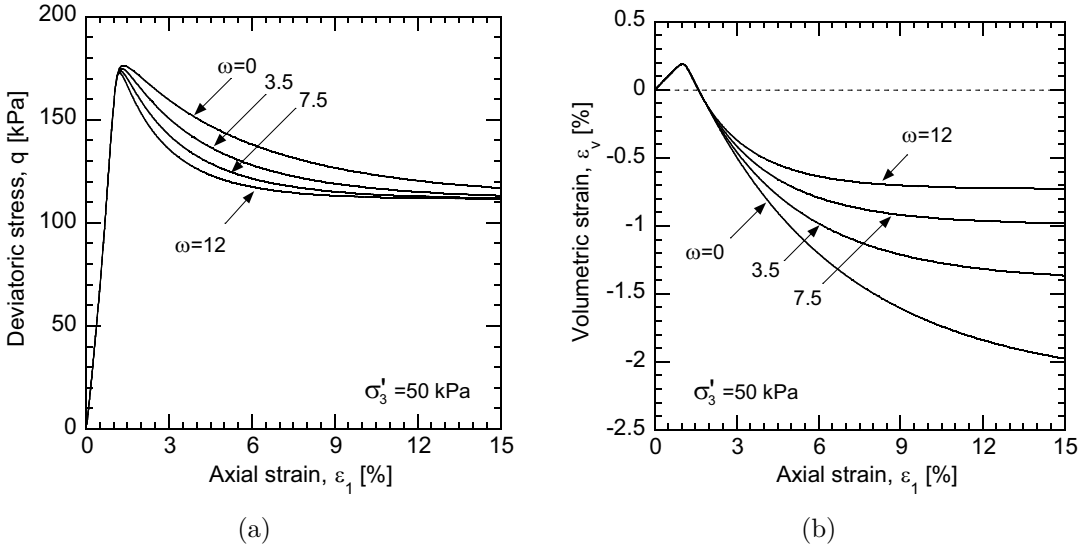


(a) (b)

*Figure 6.27:* Influence of parameter $\omega$ on the conventional triaxial compression response with $\sigma_3 = 50\ kPa$: (a) $q - \varepsilon_1$, (b) $\varepsilon_v - \varepsilon_1$

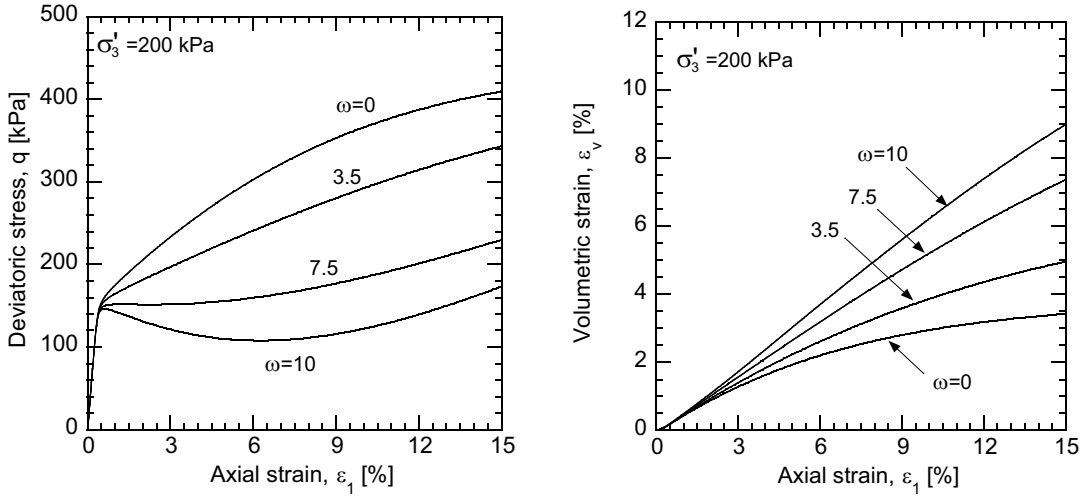


(a) (b)

*Figure 6.28:* Influence of parameter $\omega$ on the triaxial compression behaviour with $\sigma_3 = 200\ kPa$: (a) $q - \varepsilon_1$, (b) $\varepsilon_v - \varepsilon_1$

### 6.6.3 Simulation of the oedometer tests

The model has been tested for its ability to reproduce the oedometric experimental results of Bioley silt tested during the course of this study, the detailed description of which were presented in Chapter 4. The most representative tests on dry, saturated and unsaturated samples of reconstituted and aggregated Bioley silt have been simulated and the simulations are compared with the experimental results. The set of material parameters listed in Table 6.4 were used for the simulations, unless otherwise stated. The specified initial condition will be separately presented for each simulation.

#### 6.6.3.1 Saturated and dry samples

Among the oedometer tests on dry and saturated samples, three have been selected for simulations. These are: SAT04, saturated reconstituted sample; RC07, dry reconstituted sample; and DR20, dry aggregated sample of Bioley silt.

**Test SAT04:** The test corresponds to the saturated reconstituted sample and therefore $\psi_i^{st} = 1$ and $\phi_i^2 = 0$. However when only saturated state is concerned, parameter $\phi_i^2$ does not interfere in the calculations. An initial normally consolidated state at zero suction has been imposed. Figure 6.29(a) compares the numerical simulation with the experimental results for the saturated reconstituted Bioley silt sample SAT04. Quite good agreement could be observed between the simulation and the experimental results. Results of this simulation at the compression phase represents the iNCL for Bioley silt.

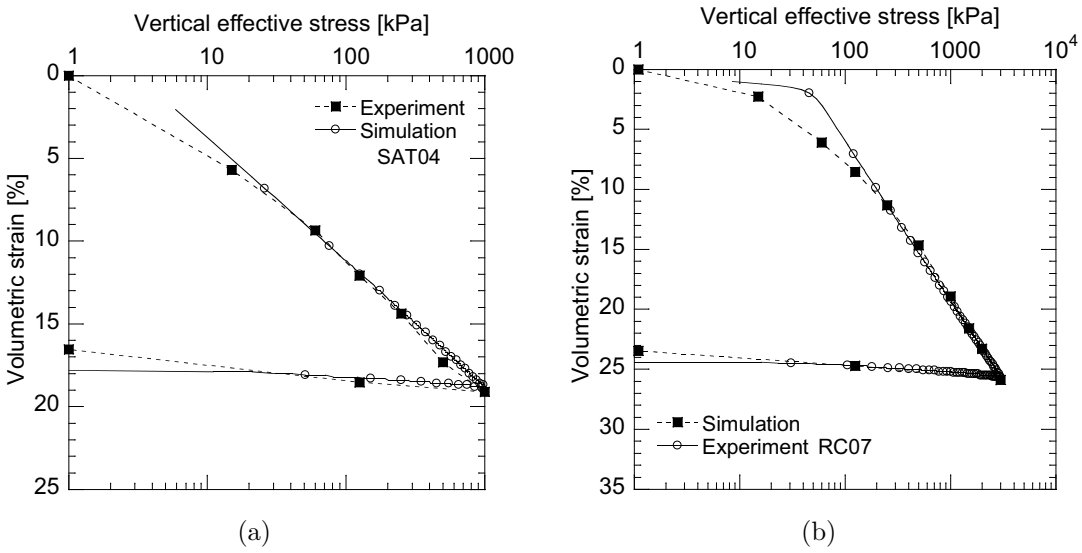


*Figure 6.29:* Simulation of saturated and dry reconstituted Bioley samples: (a) saturated sample, (b) dry sample

**Test RC07:** The test was carried out on reconstituted dry sample of Bioley silt. As presented in Chapter 4, the compressibility index of dry and saturated samples are different; while the difference in their swelling index is insignificant. With the exception of $\lambda^*$ which has been particularly determined for dry samples, saturated material parameters of Table 6.4 were used for this simulation. For simulation, only net vertical stress has been changed and suction has been virtually kept constant at zero. This means that the test is simulated in the same manner as in saturated test. The initial condition of $\psi_i^{st} = 1$ with a vertical preconsolidation stress of 50 $kPa$ has been applied. Comparison between the experimental results and numerical simulations for test RC07 is presented in Figure 6.29(b). As in saturated sample, the model could successfully reproduce the experimental results during both loading and unloading phases.

**Test DR20:** This test corresponds to dry aggregated sample of Bioley silt. Based on the comparison between the oedometric compression of dry aggregated and reconstituted samples, $\psi_i^{st}$ has been determined to be 90 with $p_{c0}'^{*} = 0.5\ kPa$. In the simulation of the test, a value of soil structure paramater $\omega$ equal to 3.055 has been used. This value was deduced from neutron tomography results of dry aggregated Abist soil, and due to similarity of materials, is assumed to be representative also for Bioley silt (see Sec. 6.3.1). All other parameters were maintained as in the input file for dry reconstituted sample RC07. As in RC07, the test was simulated in the same manner as saturated tests. Figure 6.30(a) shows the comparison between the experimental results and the model predictions for the this test. The model was found to successfully reproduce the initial elastic domain followed by yielding beyond the apparent preconsolidation stress. Tangential slope of the virgin compression curve is higher than that of reconstituted soil and it decreases as the applied stress increases. This is because of the

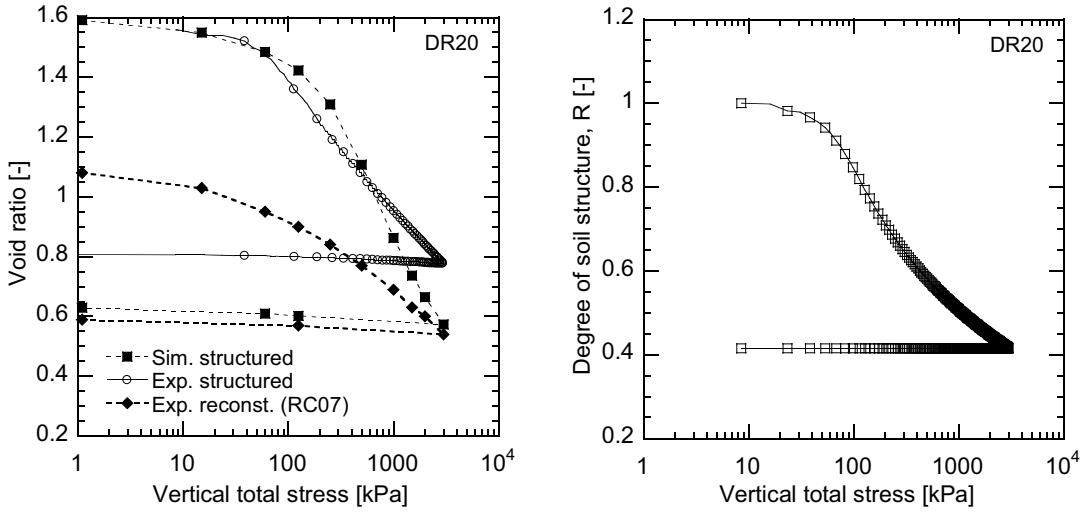


(a) (b)

*Figure 6.30:* Simulation of oedometric response of dry aggregated Bioley sample: (a) oedometric compression, (b) evolution of degree of soil structure

*Table 6.5:* Initial condition for unsaturated reconstituted Bioley samples

| **Test** | $e_i$ | $p^*_{c0i}$ | $\sigma_{vnet}$ | $s_i$ | $r^e_{iso}$ | $r^e_{dev}$ | $\psi^{st}_i$ | $\phi^2_i$ |
|---|---|---|---|---|---|---|---|---|
| USR02 | 0.6 | 60 $kPa$ | 1 $kPa$ | 0 | 0.5 | 0.5 | 1 | 0 |
| USR03 | 0.48 | 90 $kPa$ | 15 $kPa$ | 0 | 0.5 | 0.5 | 1 | 0 |

material softening due to structure degradation. Good agreement of results in the oedometric behavior could be observed; however, some divergence between experimental and simulation results could be observed at higher stresses. Evolution of the degree of soil structure with the applied vertical stress is presented in Figure 6.30(b). Prior to yielding, degree of soil structure maintains its value equal to one and then it tends to zero with occurrence of plastic deformations.

#### 6.6.3.2 Unsaturated reconstituted samples

The model has been used to simulate the oedometric tests on two unsaturated reconstituted samples of Bioley silt USR02 and USR03. The simulations were made using the parameters presented in Table 6.4 and the initial conditions given Table 6.5.

**Tests USR02:** The simulation involves three loading phases: increase of the vertical stress to 15 $kPa$ at saturated condition, suction increase from zero to 500 $kPa$ under constant vertical net stress of 15 $kPa$, and then mechanical loading and unloading by changing the vertical net stress between 15 and 3000 $kPa$, while keeping the suction unchanged.

The simulated stress-strain response is compared with the experimental results in terms of net and effective stress Figures 6.31(a) and 6.31(b) respectively. Quite good agreement between the model prediction and the experimental re-

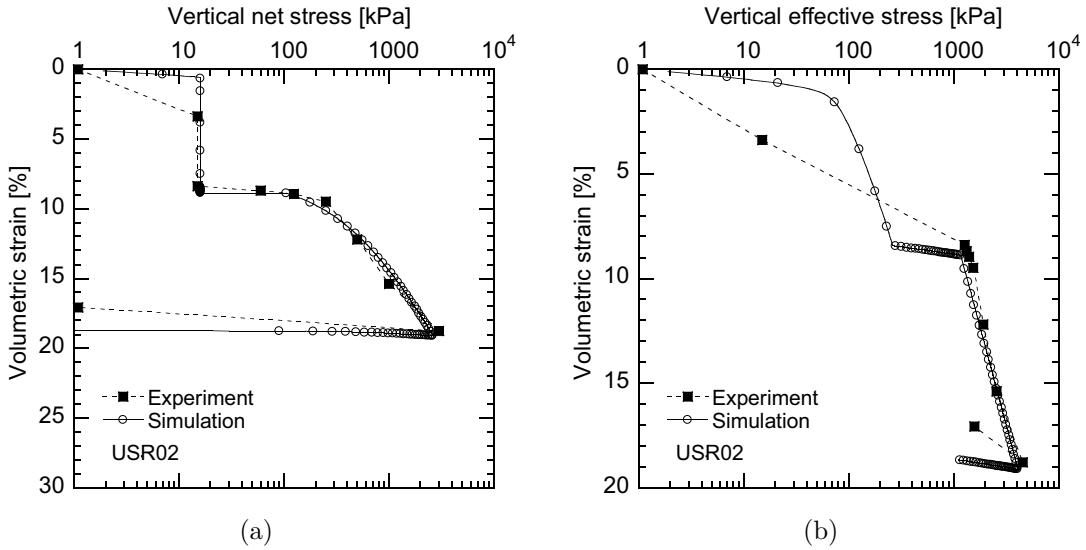


*Figure 6.31:* Comparison of simulation and experimental results for stress-strain response in test USR02: (a) $\varepsilon_v - \sigma_{vnet}$, (b) $\varepsilon_v - \sigma'_v$

sults is observed in terms of net stress. The model provides a satisfactory reproduction of the suction-induced deformation under constant net vertical stress. In terms of effective stress, lack of experimental points for stresses below 1000 $kPa$, does not allow direct comparison of results in this range. This is due to the fact that suction has been increased in a single step during the first phase of the experiment. However when the maximum suction of 500 $kPa$ is reached, a good coincidence between the model simulation and the experimental is observed. The simulated behavior should be described with reference to Figure 6.20(a). The initial stiff behavior corresponds to the saturated over consolidated state. When the effective stress reaches the preconsolidation stress (point $A'$ in Fig. 6.20(a)), sample starts to yield until the point where suction reaches the air entry value and the stress state returns back in the yield limit (point $C'$ in Fig. 6.20(a)). At this point, sample starts to exhibit again an elastic behavior until reaching the suction-induced apparent preconsolidation stress where the sample becomes elasto-plastic (point $D'$ in Fig. 6.20(a)).

Simulation of the soil response to suction variation is compared with the experimental results in Figure 6.32. The suction-induced deformation with respect to total deformation could be better evaluated in Figure 6.32(a). Evolution of degree of saturation during the loading is depicted in Figures 6.32(b), 6.32(c), and 6.32(d) as a function of vertical net stress, suction and void ratio respectively. The initial drop in degree of saturation during suction increase appears to be over predicted in the simulations. Thanks to the modified relation for $S_r$ as a function of both $s$ and $e$, the model could successfully reproduce the increase in degree of saturation during the constant suction compression.

**Tests USR03:** The simulation of unsaturated oedometer tests on reconstituted sample USR03 involves the following steps: the initial suction increase from zero to 3000 $kPa$ under constant vertical net stress of 15 $kPa$, and then

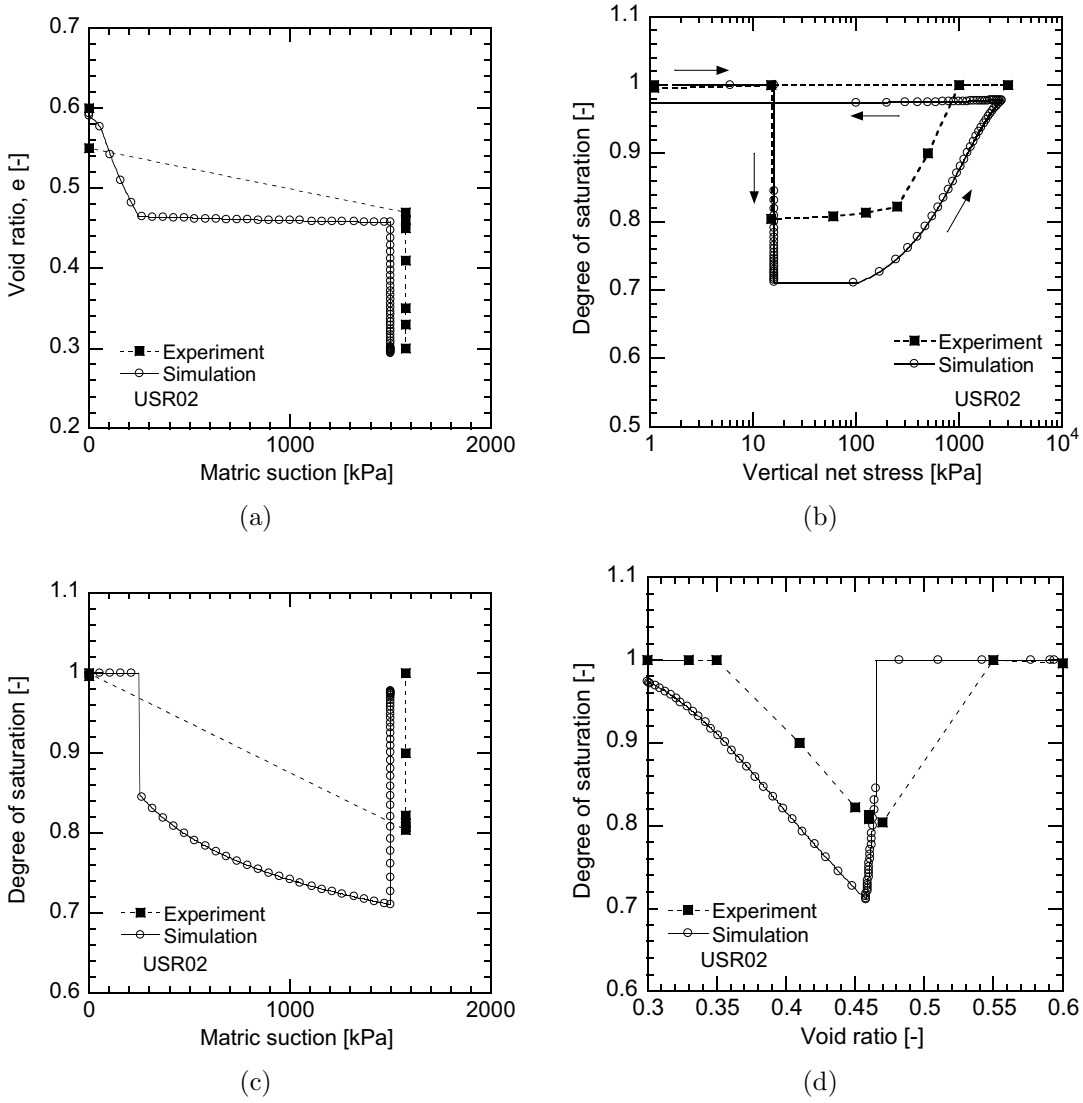


*Figure 6.32:* Comparison of simulation and experimental results for soil response to suction variation in test USR02: (a) $e - s$, (b) $S_r - \sigma_{\mathrm{v}net}$, (c) $S_r - s$, (d) $S_r - e$

mechanical loading and unloading by changing the vertical net stress between 15 and 3000 $kPa$, while keeping the suction unchanged. Unlike sample USR02, in this test the suction was increased in different steps rather than a single step. Therefore, the simulation of suction-induced deformation could be compared with experimental results. Model simulation and the experimental results of the strain-stress responses are presented in Figure 6.33. It is seen that the model could reasonably represent the stress-strain response in terms of both net and effective stress. The slight difference between the simulations and experimental results arises from the over prediction of suction-induced deformations in the model simulation. In Figure 6.33(b), this can be seen as a small drop of void ratio during the initial stiff compression. Comparison between the simulations and the experimental results of the soil response to the suction variation

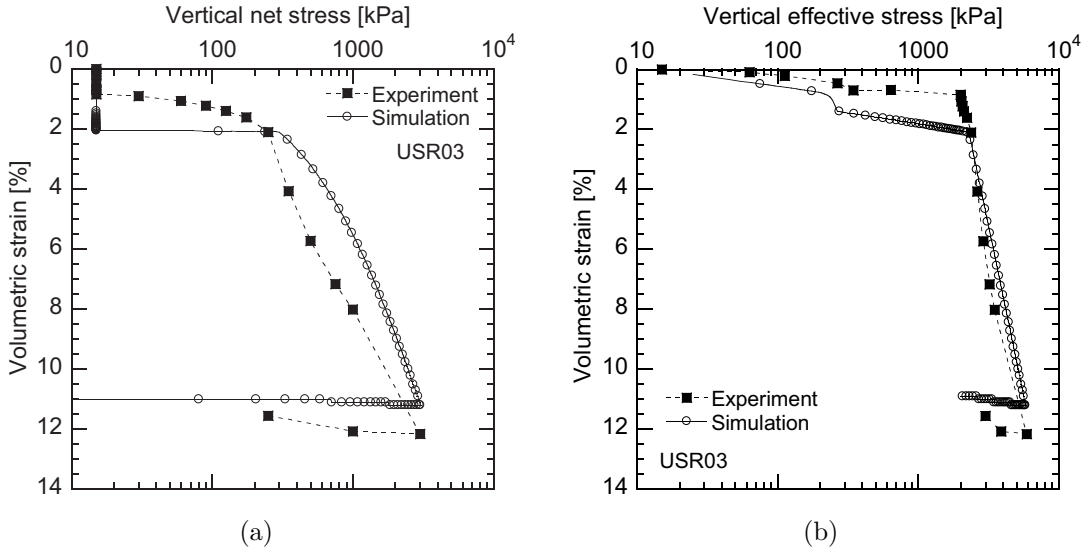


*Figure 6.33:* Comparison of simulation and experimental results for stress-strain response in test USR03: (a) $\varepsilon_v - \sigma_{vnet}$, (b) $\varepsilon_v - \sigma'_v$

are shown in Figure 6.34. The model could successfully predict the degree of saturation at the end of suction increase phase. However, there are discrepancy of simulated and measured degree of saturation for intermediate suction steps. As in the preceding simulation, the model could well represent the increase in degree of saturation due to mechanical compression under constant suction.

#### 6.6.3.3 Unsaturated aggregated samples

In order to validate the capability of the model in reproducing the behavior of unsaturated aggregated soils, three oedometric tests on unsaturated aggregated samples of Bioley silt (series USS) were simulated and simulations have been compared with the experimental results. The three samples USS03, USS04, and USS01 respectively correspond to maximum suction of circa 500, 1500 and 3000 $kPa$. In this simulations, parameters $\lambda^*$ and $\omega$ have been fixed at their average value for the unsaturated reconstituted tests (see Sec. 6.5.2). The rest of parameters are those presented in Table 6.4. The initial conditions for these simulations are given in Table 6.6. Values of $\phi_i^2$ have been deduced from MIP results of single aggregate (sample AGG) in Section 5.2.3, based on which porosity of single aggregate was determined to be 22%. The reference suction $s_{\text{ref}}$ is 500 $kPa$; and the initial soil structure function at this suction is $\psi_{i\text{ref}}^{st} = 175.63$ which corresponds to $p_{c0i}'^{*} = 0.15\ kPa$.

*Table 6.6:* Initial condition for unsaturated aggregated Bioley samples

| **Test** | $e_i$ | $\sigma_{vnet}$ | $s_i$ | $r_{iso}^e$ | $r_{dev}^e$ | $\phi_i^2$ |
|---|---|---|---|---|---|---|
| USS03 | 1.63 | 15 $kPa$ | 50 $kPa$ | 0.5 | 0.5 | 0.63 |
| USS04 | 1.46 | 15 $kPa$ | 50 $kPa$ | 0.5 | 0.5 | 0.61 |
| USS01 | 1.57 | 15 $kPa$ | 50 $kPa$ | 0.5 | 0.5 | 0.62 |

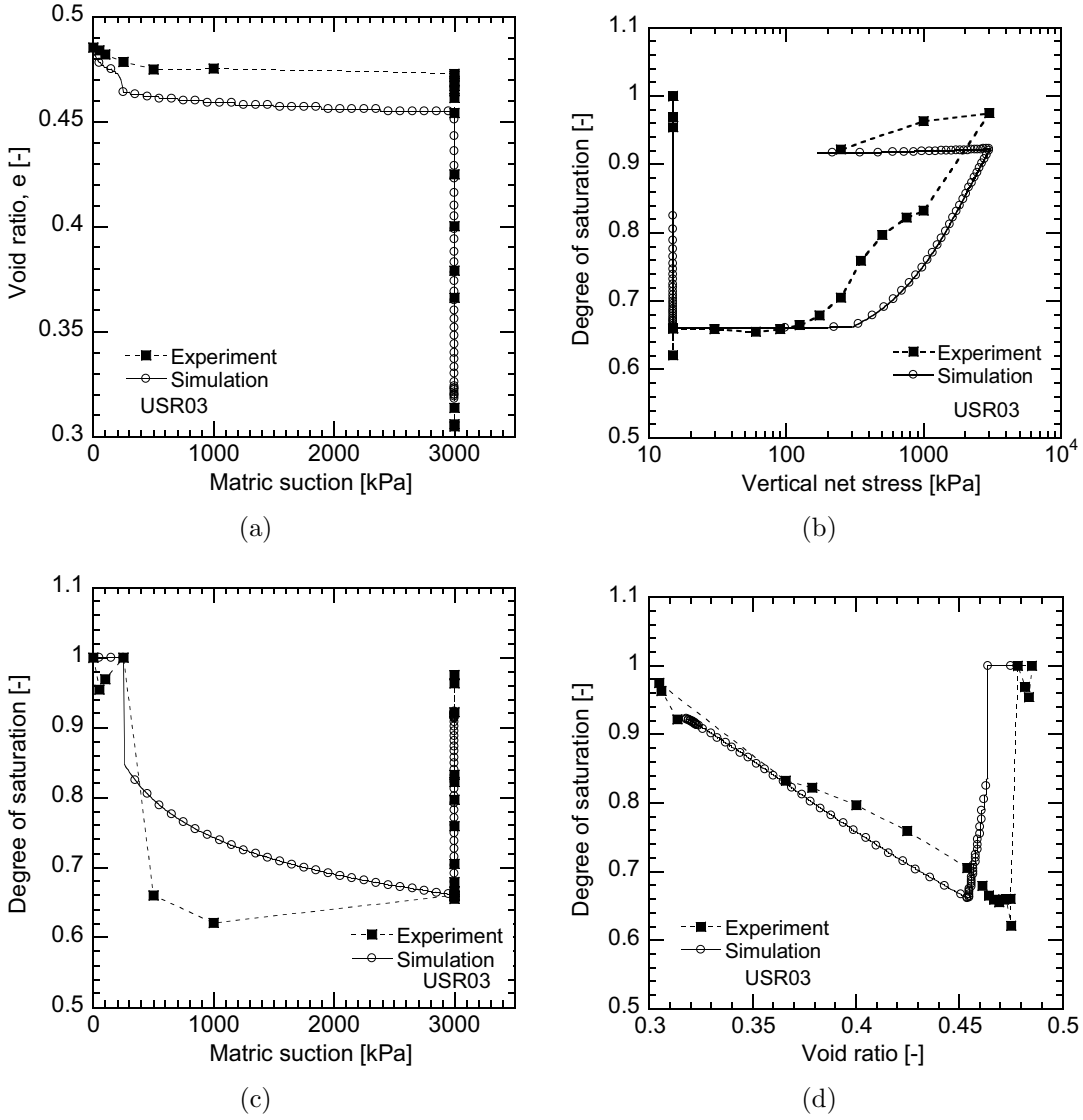


*Figure 6.34:* Comparison of simulation and experimental results for soil response to suction variation in test USR03: (a) $e - s$, (b) $S_r - \sigma_{\mathrm{vnet}}$, (c) $S_r - s$, (d) $S_r - e$

**Test USS03:** Simulation of the oedometric test on the unsaturated aggregated sample USS03 involves the following phases: first, the suction is increased from 50 to 500 $kPa$, then mechanical loading and unloading is applied by changing the vertical net stress between 15 and 3000 $kPa$, while maintaining the constant suction. Results of the simulation are compared with experimental results in Figure 6.35. Since the suction-induced deformations in aggregated samples appeared to be insignificant, interpretation of results in terms of net stress ($e - \sigma_{\mathrm{vnet}}$) and suction-induced deformation ($e - s$) have been excluded for theses tests. Figure 6.35(a) shows the evolution of degree of soil structure, $R$, during the increase in effective stress. Degree of soil structure reduces from 1 at the beginning of the test to 0.26 at the end of the compression. During the unloading it remains constant. As observed in Figure 6.35(b), the model could successfully reproduce the effective stress-strain response of the sample.

It is seen, in the rest of these figures, that the evolution of degree of saturation during the loading process has been quite well modeled. Thanks to the modified water retention relation for soil with double porosity (Eq. 6.121), the model could address the main features in the evolution of degree of saturation during the test. First of all, despite a relatively low value of initial suction ($s_i = 50\ kPa$), a low degree of saturation of about 2.9 has been predicted. This is due to the existence of empty macropores. As in the experimental results, an insignificant decreases of degree of saturation has been simulated due to suction increase. During the subsequent mechanical loading at constant suction, degree of saturation strongly increases because of closure of macropores. This behavior could be better observed in Figures 6.35(d) and 6.35(e) where the evolution of degree of saturation is expressed in terms of suction and void ratio.

**Test USS04:** As in the preceding simulation, the oedometric test on the unsaturated aggregated sample USS04 has been simulated by an initial suction increase phase which is from 50 to 1500 $kPa$ and a mechanical loading and unloading phase which is applied by changing the vertical net stress between 15 and 3000 $kPa$ under constant suction. Comparison between simulation of test USS04 and the experimental results is depicted in Figure 6.36. Figure 6.36(a) shows the evolution of degree of soil structure, $R$, as a function of the effective stress. At the beginning of the test, degree of soil structure is equal to one and it reduces to 0.24 at the end of the test. As shown in Figure 6.36(b), the model predicts appropriately the initial yield and post-yield behavior. However, at higher values of applied stress, the model prediction diverges from the experimental results. Opting for an average value of $\omega$, probably lower than its real value, is believed to be the reason for this divergence.

As it is seen in Figure 6.36(c), the model could reasonably represent the evolution of degree of saturation during the test. Simulated and experimental values of $S_r$ as a function of $s$ and $e$ are shown in Figure 6.36(d) and 6.36(e) respectively. As in the preceding simulation, the model address the main features in the evolution of degree of saturation, among them being the important increase of this parameter due to mechanical compression at constant suction.

**Test USS01:** The last simulated oedometer test is USS01 which corresponds to the unsaturated aggregated sample with a maximum suction of about 3000 $kPa$. Simulations phases are as in the previous tests with the exception that net stress has been increased only to 1000 $kPa$. Model predictions for sample USS01 are compared with experimental results in Figure 6.37.

It is observed that the model successfully reproduces the stress-strain response of the sample in terms of effective stress (Fig. 6.37(a)). However for the soil response to suction variation, the simulated values of degree of saturation were found to be relatively over predicted with respect to the experimental values. This can be observed in Figure 6.37(b) where evolution of $S_r$ is presented in terms of void ratio. Same type of discrepancy of results could be observed for predicted and measured values of $S_r$ when expressed in terms of suction and net stress. Accordingly, those interpretation have been excluded here.

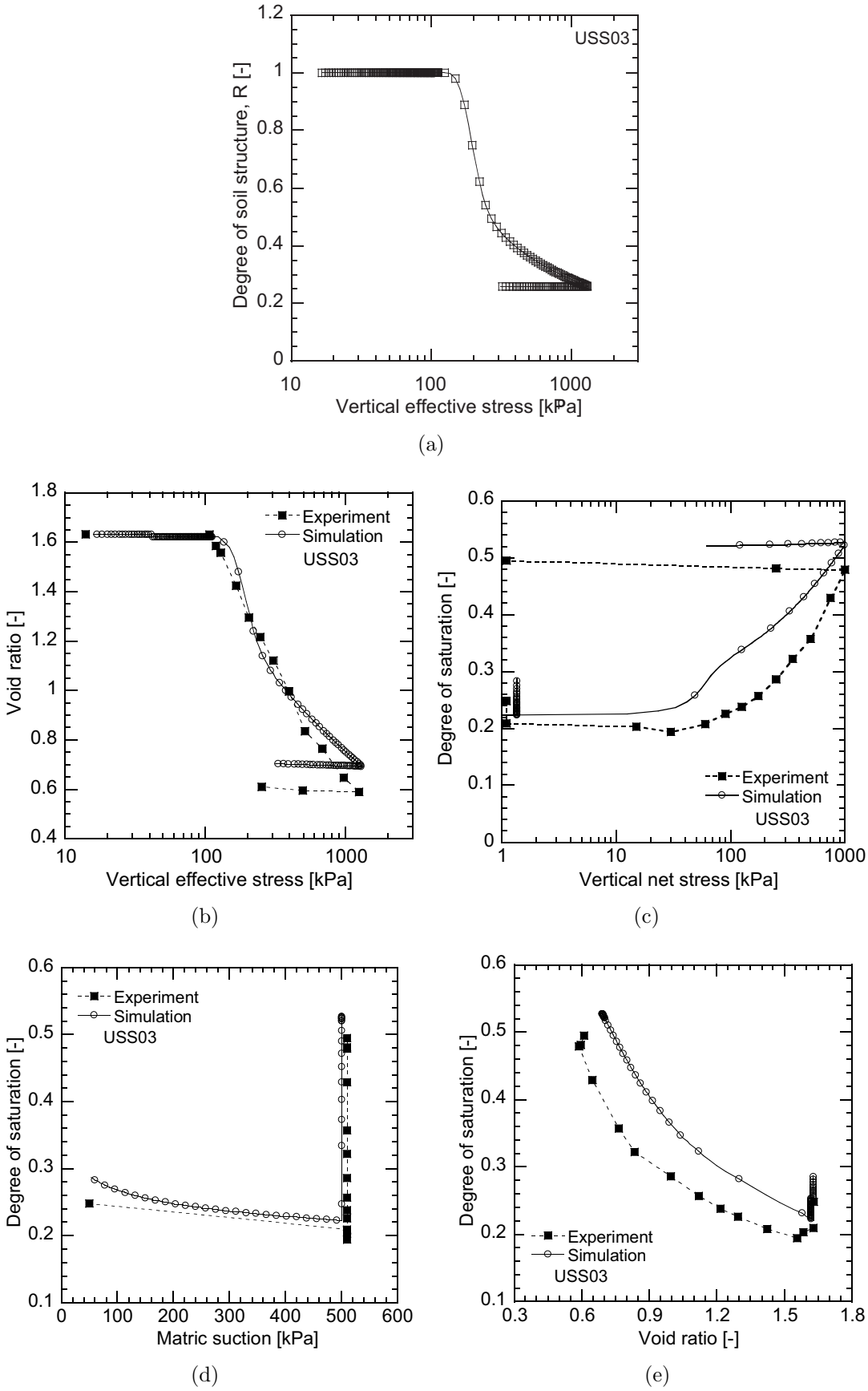


*Figure 6.35:* Comparison of simulation and experimental results for test USS03: (a) $R - \sigma'_{\mathrm{v}}$, (b) $e - \sigma'_{\mathrm{v}}$, (c) $S_r - \sigma_{\mathrm{v}net}$, (d) $S_r - s$, (e) $S_r - e$

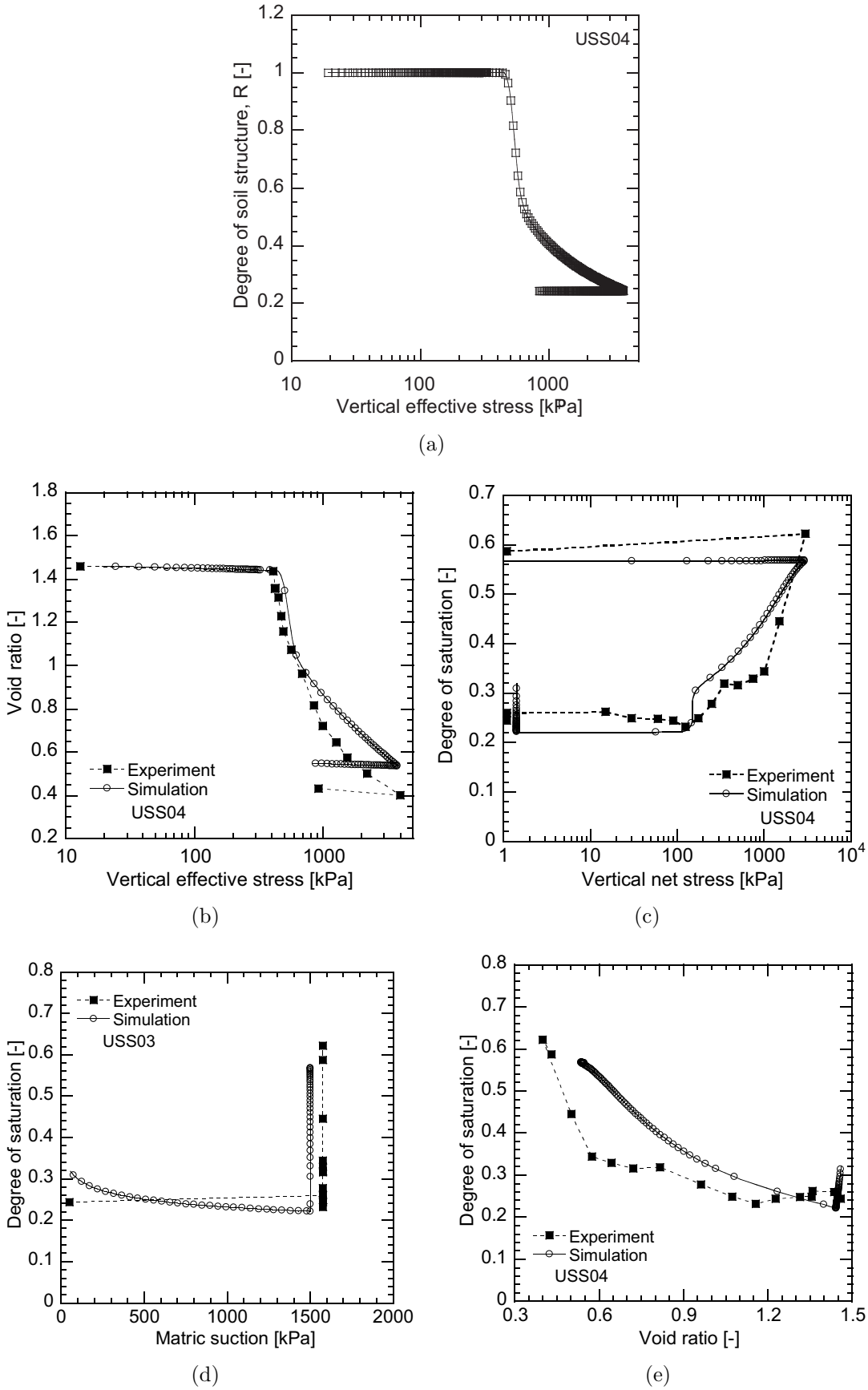


*Figure 6.36:* Comparison of simulation and experimental results for test USS04: (a) $R - \sigma'_{\mathrm{v}}$, (b) $e - \sigma'_{\mathrm{v}}$, (c) $S_r - \sigma_{\mathrm{vnet}}$, (d) $S_r - s$, (e) $S_r - e$

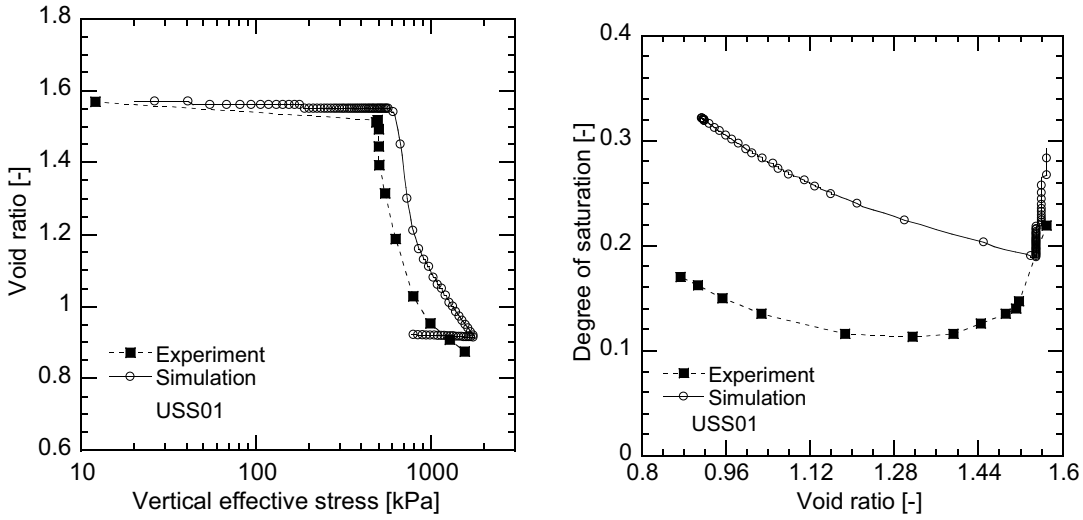


(a) (b)

*Figure 6.37:* Comparison of simulation and experimental results for test USS01: (a) $e - \sigma'_{\mathrm{v}}$, (b) $S_r - e$

### 6.6.4 Assessment of model for saturated bonded soils

The capability of the proposed constitutive model has been tested for modeling the behavior of natural structured and bonded soils. For this purpose, the model has been used to simulate the experimental results of bonded soils available in the literature. The experimental evidence on the behavior of unsaturated structured soils are scarce and the results given here correspond to saturated soils.

The behavior of four different soils has been considered and the results of a total of twelve tests on structured and corresponding reconstituted soils have been simulated. The selected materials are: Pisa clay, Leda clay, Corinth marl and natural carlcarenite. The reference of the experimental study and the main reported parameters for these materials are listed in Table 6.7. The listed values for Leda clay, Corinth marl and natural carlcarenite have been reported by Liu and Carter (2002). Values of $\psi_i^{st}$ for these soils has been determined by comparison of the isotropic or oedometric compression curve of reconstituted

*Table 6.7:* Description of the saturated natural bonded soils

| **soil** | **Reference** | $M$ | $\lambda^*$ | $\kappa$ | $\psi_i^{st}$ |
|---|---|---|---|---|---|
| Pisa Clay | Callisto and Calabresi (1998) | 1.20 | 0.230 | 0.035 | 6.4 |
| Leda clay | Yong and Nagaraj (1977) | 1.20 | 0.223 | 0.030 | 19.9 |
| Corinth marl | Anagnostopoulos et al. (1991) | 1.38 | 0.047 | 0.008 | 16.5 |
| Natural calcarenite | Lagioia and Nova (1995) | 1.45 | 0.208 | 0.016 | 2.1 |

*Table 6.8:* Common model parameters for the simulated bonded soils

| **Parameter** | $n_s$ | $d$ | $b$ | $a$ | $c$ | $\alpha$ | $A$ |
|---|---|---|---|---|---|---|---|
| **value** | 1 | 2 | 1 | 0.001 | 0.001 | 1 | 1 |

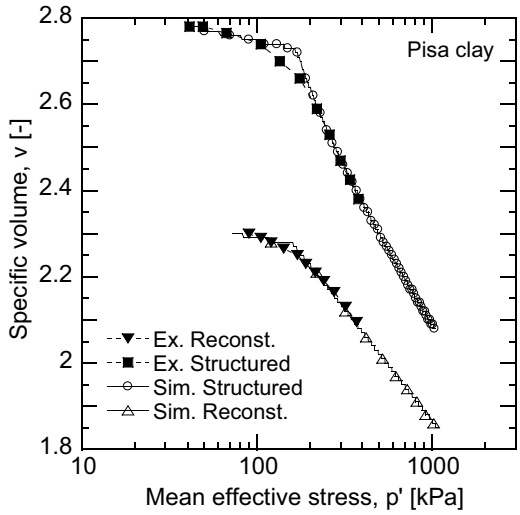


*Figure 6.38:* Comparison between the simulation and experimental results for isotropic compression of Pisa Clay, experimental data after Callisto and Calabresi (1998)

and structured soils. A common set of parameters listed in Table 6.8 has been used for the rest of parameters. Since, the results are all for saturated samples, the partial saturation parameters are excluded in this table. Soil structure parameter $\omega$ is determined in each case based on back prediction of oedometric or isotropic compression results.

**Pisa clay:** Pisa clay is a soft clay formed by deposition in a backwater environment. Experimental study and interpretation of the experimental results for Pisa clay have been reported by Callisto and Calabresi (1998) and Callisto and Rampello (2004). To model the behavior of structured soil, the initial state of the soil is defined by $p_c'^*0 = 25\ kPa$ and $v = 2.78$. The simulation and the experimental results for isotropic compression test of Pisa clay is presented in Figure 6.38. Adjusting the parameter $\omega = 4.2$, the model gives a reasonable representation of the compression behavior of structured soil.

**Leda clay:** Experimental study of reconstituted and structured Leda clay have been carried out by Yong and Nagaraj (1977). The set of parameters listed in Table 6.7 has been used after Liu and Carter (2002) to simulate the experimental results. Figure 6.39(a) compares the model simulations and the experimental results for oedometric tests on reconstituted and structured Leda clay in which parameter $\omega$ was identified to be 8.2. The model can successfully reproduce the behavior of material during its oedometric compression. This obtained values of $\omega$ was used to simulate the compression behavior on the stress path $q/p' = 1$. Results of this simulation, presented in Figure 6.39(b), show that the predicted yielding limit is lower than the experimental value. This might be related to the shape of yield surface. This results in over prediction of induced deformations for a given value of mean effective pressure.

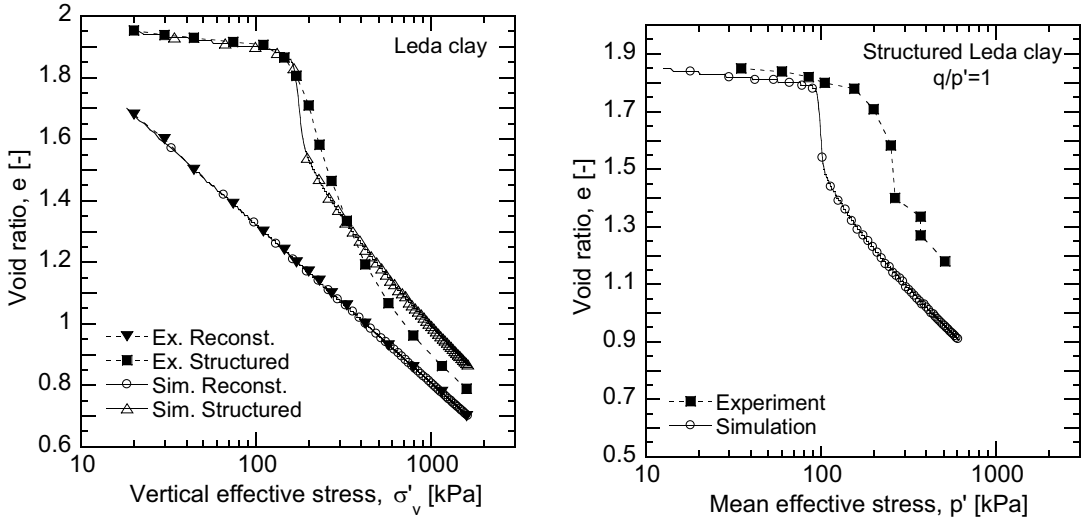


(a) (b)

*Figure 6.39:* Comparison between the simulation and experimental results for Leda Clay, experimental data after Yong and Nagaraj (1977): (a) oedometric compression, (b) $q/p' = 1$ compression

**Corinth marl:** The behaviour of natural Corinth marl has been experimentally evaluated by Anagnostopoulos et al. (1991). Results of that work have been compared with the model predictions. The first set of experimental results correspond to isotropic compression and swelling tests on both structured and reconstituted Corinth marl. These tests were used to determine the soil structure parameters. Figure 6.40(a) compares the model simulation with the experimental results for the isotropic tests in which parameter $\omega$ was identified as to be 25.1. Using this value, the model could successfully simulate the compression experimental results. In the second set of experiments, results of CTC (conventional triaxial compression) shearing tests at two different confining pressure of 1500 and 4000 $kPa$ have been reported. Figure 6.40 compares the model simulation and the experimental results for CTC tests on Corinth marl. It is seen that there is a good agreement between the simulations and experimental results for the evolution of deviatoric stress with deviatoric strain. However, some discrepancies between the model simulation and experimental results could be observed for the evolution of volumetric strain versus deviatoric strain. In general, the model could reasonably reproduce the behavior of the structured Corinth marl.

**Calcarenite soil:** The experimental evaluation of the behavior of natural calcarenite has been carried out by Lagioia and Nova (1995). The natural calcarnite is a highly cemented material formed by marine deposition. Using the material parameters listed in Table 6.7, the isotropic compression behavior of natural carcarenite has been simulated and parameter $\omega$ has been determined to be 25 which represents a high de-structuring tendency with occurrence of plastic strains. Consequently, material exhibits a brittle behaviour at the point

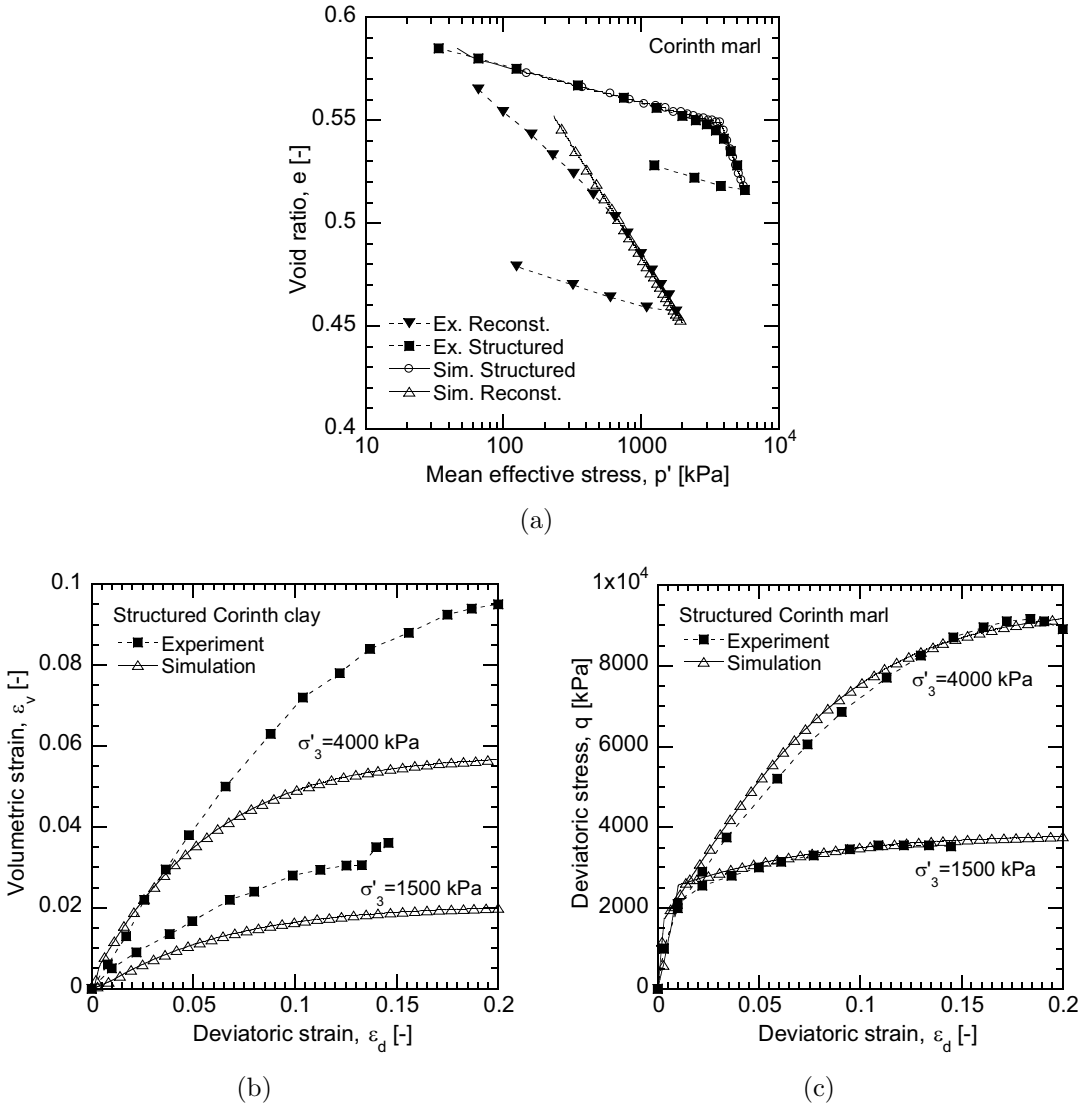


*Figure 6.40:* Comparison between the simulation and experimental results for Corinth marl, experimental data after Anagnostopoulos et al. (1991): (a) isotropic compression, (b) CTC: $\varepsilon_v - \varepsilon_d$, (c) CTC: $q - \varepsilon_d$

of yielding. Model simulations are compared with the experimental data for calcarenite marl in Figure 6.41(a).

The CTC tests on Carcarenite at confining pressure of 900 and 3500 $kPa$ have been simulated and the results are compared with experimental values in Figures 6.41(b), 6.41(c), and 6.41(d). The model appeared to underestimate the volumetric strains during the CTC test at the confining pressure of 900 $kPa$. However, it could reasonably represent the material behaviour dueing the CTC test at the confining pressure of 3500 $kPa$ both in terms of stress and strain.

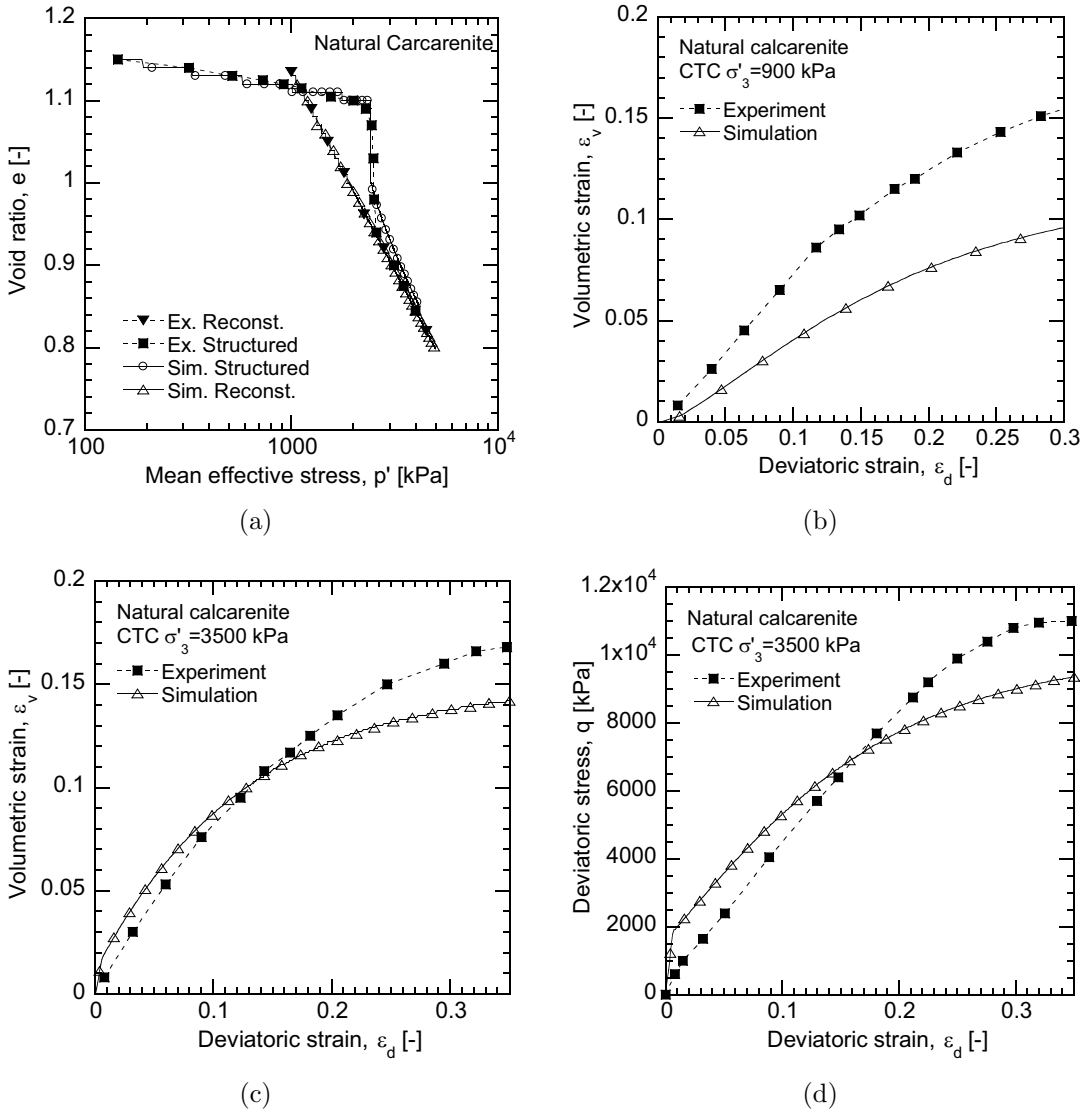


*Figure 6.41:* Comparison between the simulation and experimental results for CTC tests at $\sigma_3' = 3500\ kPa$ on calcarenite marl, experimental data after Lagioia and Nova (1995): (a) isotropic compression, (b) CTC $\sigma_3' = 900\ kPa$ : $\varepsilon_v - \varepsilon_d$, (c) CTC $\sigma_3' = 3500\ kPa$ : $\varepsilon_v - \varepsilon_d$, (d) CTC $\sigma_3' = 3500\ kPa$ : $q - \varepsilon_d$

## 6.7 Conclusion

In this chapter, the focus was placed on the development of a mechanical constitutive model for unsaturated aggregated soil which is a structured soils with double porosity. A generalized effective stress and the critical state concept in unsaturated soils were used to obtain a unified model of soil behavior regardless of the humidity condition. The constitutive framework of elasto-plasticity with strain hardening has been selected for model developments.

As the first approach, the experimental results of this study obtained at macro scale and pore scale were combined to outline the requirements of the new model. On the basis of the experimental evidences, a conceptual framework was proposed for extension of any elasto-plastic model of reconstituted saturated soils to unsaturated aggregated soils. The experimental results, and in particular, pore scale observations were further evaluated to quantify the soil structure and its evolution. A parameter called degree of soil structure was proposed to physically quantify the soil structure in terms of macropore volume fraction. This parameter and its evolution was then linked, as a state parameter, to the plastic strains. This provides, for the first time to our knowledge, an experimentally based relation relating the internal soil structure to its macrosocpic behavior. Partial saturation was evaluated to have a double effect in aggregated soils: primary effects on soil matrix and secondary effects in combination with soil structure. These effects have been formulated by introducing the apparent preconsolidation pressure which depends on stress state and history as well as on soil structure and suction.

The proposed framework was then used to develop the explicit formulation of a constitutive model for unsaturated aggregated soils. The new model, called ACMEG-2S, is a Hujeux type elasto-plastic model with two plastic mechanisms. The model formulation for the simplified case of triaxial condition and the general three-dimensional stress-strain condition were presented. A driver of constitutive laws was used to integrate the constitutive equations and to perform numerical simulations.

The capability of the model was examined for reproducing the experimental results of this study. Results shows that the model could successfully address the main features observed during the experiments. Among them, the non-linear stress-stress relationship during the virgin compression of aggregated soil could be successfully modeled. Thanks to a new water retention equation incorporating both suction and void ratio, the model can reasonably represent the increase of degree of saturation during the compression at constant suction. The model response has been also assessed for saturated bonded soils, for which the experimental results have been reported in the literature. In general, the model could reasonably reproduce the behavior of these materials in different mechanical loadings.

# Chapter 7

# Conclusions and recommendations for future research

## 7.1 Conclusions

The present study has looked to the mechanical behavior of unsaturated aggregated soils. Particle aggregation is a commonly observed phenomenon in different soils such as natural clays and agricultural soils. In the general sense, aggregated soils are structured soils with double porosity due to intra- and inter-aggregate pores. Aggregation may affect the mechanical and the water retention behavior of the soil and makes it different from that of a reconstituted soil of the same mineralogy.

An extensive literature review revealed the need for the experimental study of the mechanical behavior of aggregated soils, and in general structured soils, under unsaturated condition. The experimental and theoretical knowledge was lacking about the relation between the macroscopic behavior and the soil structure, defined as the combination of soil fabric and inter-particle bonding. It was realized that major improvements are still needed in the mechanical constitutive modeling of structured soils with double porosity, specially under unsaturated condition. The required improvements are mainly related to the explicit consideration of soil structure evolution, combined effects of suction and structure, and the pore scale experimental supports.

The present work was aimed to study the mechanical behavior of unsaturated aggregated soil with respect to the soil structure and its evolution. To achieve this goal, it combined theoretical developments, multi-scale experimental study and constitutive modeling. The present research was conducted in four main parts as it follows.

- The coupled governing equations were derived for the hydro-mechanical processes in double porous soil. This step allowed identifying the field variables and the involved constitutive equations.
- The stress-strain response and the water retention properties of aggregated and reconstituted soil at different saturation conditions were evaluated

using the oedometric testing method.
- The soil structure and its evolution due to the mechanical loading and suction variation were investigated using the experimental methods of mercury intrusion porosimetry, environmental scanning electron microscopy, and neutron tomography.
- Based on the combination of the multi-scale experimental evidences, improvement of an elasto-plastic hardening model, coupled with water retention behavior, was proposed for unsaturated aggregated soil.

This last chapter summarizes the main findings from this study, and provides some recommendations for future research. For clarity, the conclusions have been divided into three categories: (i) governing equations; (ii) experimental approach, and (ii) constitutive modeling.

### 7.1.1 Governing equations

The multiphase mixtures theory was used to derive the governing equations of coupled hydro-mechanical phenomena in double porous media. The mixture of soil with double porosity was divided into two distinct but overlapping and interacting mixtures. Mixture 1 was a mixture of solid and fluids representing the aggregates and pores within them. While, mixture 2 was a mixture of only fluid constituents representing the fluids in macropores. The balance equations were written for each mixture with additional terms provided for interaction of the phases and the mixtures.

The stress tensor was evaluated for each phase as well as for the whole system of two mixtures. The non-equilibrium or extra part of stress tensor in solid was identified as the effective stress.

Accordingly, a new expression of effective stress was derived for unsaturated double porous soil in terms of total stress, gas pressure and suction in macro- and micropores. The effective stress parameters were linked to the macro- and microporosity as well as local degree of liquid saturation in two system of pores.

It was shown that if the macropores are closed, the expression of effective stress reduces to the effective stress of Bishop for unsaturated soils with Bishop's coefficient being the degree of saturation. If both volumes of macropores and the gas phase are zero, then the well known effective stress of Terzaghi is recovered.

The total liquid (gas) pressure was expressed as an weighted averaged value of liquid (gas) pressure in macro- and micropores with the weight coefficients representing the liquid (gas) volume fraction which belongs to each system of pores. The total suction comprised of two terms: a weighted averaged value of suction in macro- and micropores, and a second term arising from the difference in the gas pressure of two system of pores.

In the next step, the constitutive equations were evaluated. For this purpose, the principle of phase separation of Passman et al. (1984) was postulated which implies that the dependent variables of any constituent depend only on the independent variables of that constituent; while, the growth dependent variables depend on all of the independent variables.

The following constitutive equations were identified:

- Mechanical constitutive equation
- Equation of state for liquid
- Equation of fluid flow
- Liquid retention equation
- Fluid mass transfer between mixtures

For the equation of state, an equation of barotropic liquid state was adopted. For the sake of simplicity, the fluid flow was assumed to be governed by the generalized Darcy's equation in both system of pores. The fluid mass transfer was assumed to be controlled by a leakage term whose driving variables were the fluid pressure. The remaining two constitutive equations were introduced in their general form: the mechanical constitutive equation for the stress-strain response of the soil, and the water retention equation for the relation between the degree of saturation, suction, and the porosity.

Balance and constitutive equations were then combined and the new coupled hydro-mechanical formulation of a three-phase model for unsaturated double porous media were derived. The derived equation represent a set of five equations for five main unknowns: solid velocity and four fluid pressures (liquid and gas pressures in macro- and micropores). The proposed formulation identified the field variables and the required constitutive models. The set of new coupled formulations provided a conceptual model that is apt to represent the hydro-mechanical processes in double porous media. For instance, it allows modification of field variables with change of macro- or microporosity, even if the total porosity remains constant.

Among the constitutive equations, the equation of fluid flow and fluid mass transfer have been evaluated in the companion PhD thesis of this study (Carminati, 2006). The main constitutive equations concerned in the present study are the mechanical constitutive and the water retention model. The main focus in the remaining parts of the present study was to experimental evaluate these relations, and to propose the explicit form of these relations in terms of identified field variables.

## 7.1.2 Experimental approach

### 7.1.2.1 Methods

A multi-scale experimental program using different methods was carried out to evaluate the macroscopic response of the soil as well as the soil structure and its evolution at the pore scale.

In the first part of the experimental study, oedometric testing method was used to characterize the macroscopic stress-strain response and the water retention behavior of the soil. A new suction-controlled oedometer using the osmotic method was developed for testing of unsaturated samples. The following points should be outlined in relation with the the development and calibration of the new osmotic oedometer:

- The relation between the concentration of the aqueous polyethylene glycol ethylene (PEG) solution and suction was evaluated on the basis of

literature knowledge from soil mechanics as well as other disciplines like chemistry and biology. Two relations, as proposed by Delage et al. (1998) and Money (1989), were used for calibration of osmotic pressure with concentration of PEG independent of its molecular weight.
- Measurement of mass, instead of the volume, of the PEG solution was used to reduce the influence of temperature on the measurements.
- Exchanged water measurements were separately corrected for evaporation from the cell and from the tubing system.
- To overcome the problems associated with damage of the membrane, two overlapping membranes were simultaneously used for each test.
- The direction of flow within the circulating system was adjusted so that the fluid could be pulled from, rather than pushed into, the cell. Doing so, the positive pressure beneath the membrane can be removed and the possible upward deflection of membrane can be avoided. It was also important to keep a constant direction and rate of flow during the experiment.

In the next experimental part, soil structure and its evolution was investigated using a combination of three different methods: (i) mercury intrusion porosimetry (MIP), (ii) environmental scanning electron microscopy (ESEM) and (iii) neutron tomography.

The ESEM and MIP methods were used to evaluate the pore size distribution of the soil at the level of matrix pores and pores within and in the vicinity of the aggregates. Large inter-aggregate pores could not be examined by MIP method. Neutron tomography was used, as an advanced non-destructive method, to examine the macropores and between the aggregates and their evolution in large oedometric samples. This method, together with image analysis, allowed a three-dimensional analysis of the geometry of aggregates and pores between then in the soil sample.

#### 7.1.2.2 Experimental results

Two soils were tested in the experimental program: Abist soil, a silty clay from the central part of Switzerland; and the Bioley silt coming from western Switzerland. Most of the tests, however, were carried out on the Bioley silt.

Both materials were tested in reconstituted and aggregated samples. Abist soil was a natural aggregated soil, hence, the aggregates were selected by direct sieving of the material. In the case of Bioley silt, the aggregates with an average size of about 2 $mm$ were selected by crushing and sieving of compacted soil at the dry side of optimum. The aggregates were then dried in oven.

The dry aggregates were highly sensitive to wetting and showed to be easily disaggregated in direct contact with water. Therefore, the saturated testing of aggregated samples was not possible while preserving the aggregated structure. In the case of unsaturated aggregated samples, water was added to dry aggregates using a vaporizer in different steps in order to allow a slow water equilibrium within the intra-aggregates pores.

In the first part of the experimental study, four types of experiments were carried out: (i) dry oedometer tests, (ii) soaking tests in which dry sample were

subjected to inundation in oedometric cell, (iii) saturated oedometer tests, and (iv) suction-controlled oedometer tests.

Results of experiments were interpreted in terms of void ratio, water content, degree of saturation, suction, and the effective stress. The adopted effective stress was the effective stress of double porous soil, simplified for the case where the macropores are drained. This simplified form reduced to the Bishop's effective stress with the Bishop's coefficient being the degree of saturation.

The experimental findings were classified in three groups: soil structure effects in aggregated soils, suction effects in reconstituted soils (intrinsic suction effects), and combined effects of suction and structure in aggregated soils. The soil structure effects were evaluated by comparing the response of aggregated versus the corresponding reconstituted samples of the same suction. The intrinsic suction effects were evaluated by comparison between the response of saturated reconstituted sample with samples at different suctions. Finally, combined effects of partial saturation and soil structure were evaluated by comparing the response of structured and reconstituted samples at different suctions. The main findings of this part of experimental study are as follows.

- Structured samples showed an initial apparent preconsolidation stress which depends not only on the stress state and stress history but also on the soil structure.
- Slope of unloading-reloading curves appeared to be almost identical for aggregated and reconstituted samples. This conclusion is hypothetical and needs further evaluation through unloading-reloading of the aggregated samples not only at the end of the test by also in the intermediate steps.
- The virgin compression curve of aggregated soil showed to be a non-linear curve situated on the right side of the normal consolidation line (NCL) of reconstituted soil. The initial tangential slope, defined at the yielding point, was higher than the slope of NCL of the corresponding reconstituted soil.
- At a given value of stress, sample of aggregated soil exhibited a higher void ratio in comparison with the corresponding reconstituted soil.
- At higher values of applied effective stress, the compression curves of aggregated and reconstituted soils tend to convergence. The NCL of the reconstituted soil appeared to be an asymptote to the compression curve of aggregated soil which intersects the curve at its lowest stress.
- Despite the theoretical similarity, the oedometric response of dry and saturated samples of aggregated soil were found to be different. Possibly, the effective stress in dry soil is affected by some forces which are removed in wet condition.
- After soaking of dry samples, the state of both aggregated and reconstituted samples fell down on the saturated NCL of reconstituted soil.
- For the unsaturated samples of both reconstituted and structured soil, the degree of saturation showed to change not only with suction but also with the void ratio.
- It was observed that the degree of saturation increased during the mechanical loading, even at constant suction. This phenomenon was more

pronounced for aggregated samples, because of the empty macropores being closed during compression.
- The influence of suction on the swelling index of both reconstituted and aggregated samples was insignificant.
- Slope of NCL in the effective stress plane increased from saturated to unsaturated samples; while, it appeared to remain almost constant for unsaturated samples.
- Tangential compressibility index in the aggregated samples increased with suction.
- The effective apparent preconoslidation stress increased with suction for both reconstituted and aggregated samples. However, the rate of increase was higher for aggregated samples.

In the next experimental part, the soil structure and its evolution were examined using the combination of the three methods of MIP, ESEM, and neutron tomography. Combination of these methods allowed investigating the soil structre at different scales.

The MIP tests and ESEM observations were made for the specimens of reconstituted and aggregated soils subjected to different vertical stresses and suctions. The neutron tomography was used to evaluate the evolution of the aggregated soil structure during the oedometric loading. The main findings of this experimental part of the can be summarized as follows.

- Results of MIP experiments showed that the unsaturated aggregated specimens initially exhibit a multi-modal pore size distribution (PSD) with at least two dominant pore radii. While at the same condition, the PSD of corresponding reconstituted soil is a uni-modal curve with the dominant pore radius coinciding with the micropores in aggregated sample.
- Compared with ESEM and Tomography data, it was understood that the peak of smaller pores in the PSD of aggregated specimen corresponds to the most dominant size of micropores (intra-aggregate pores); while, the peak of larger pores represents only a subset of the macropores (inter-aggregate pores) whose radii lie within the detectable range of pores sizes in MIP method.
- After soaking, the PSD of aggregated samples reduced to a uni-modal distribution with the most dominant pore size being similar to the initial micropores (similar to reconstituted sample) with a lower intensity. These conclusions were confirmed by the ESEM evidence of an almost homogeneous texture for aggregated samples after soaking.
- Compaction of aggregated samples with bi-modal PSD reduced the intensity of macropore peak and slightly increased the micropore peak.
- The ESEM observations revealed that the matrix within a single aggregate is, somehow, similar to that of a reconstituted soil with respect to the texture. The difference appeared to be in the pore size and inter-locking particles within the aggregates fabric.
- Neutron tomograpgy experiments showed that, during the mechanical loading, the macropores evolve significantly and they can represent the

evolution of soil structure.
- An important finding was that the change in the volume fraction of macropores is associated with plastic deformations mainly and variation during elastic deformation is insignificant.
- The three-dimensional image analysis of the chord length and geometry of the pores showed an almost isotropic variation of macropores in the oedometric stress path. Despite the major modification of soil structure, state of soil at the end of the test was still far from being completely destructured.
- According to three-dimensional analysis of the soil structure, it appeared that the fully destructured state could be reached through a combination of isotropic and deviatoric de-structuring mechanisms.
- From the combination of these results, it was understood that aggregated soil, in general, is a structured soil with at least two dominant pore sizes. The micropores are similar to the pores in reconstituted soil matrix; while, the macropores are additional pores whose presence depend on the inter-particle bonding. When the soil is subjected to degradation of structures, the macropores are closed and the soil fabric approaches the fabric of the corresponding reconstituted soil.

### 7.1.3 Constitutive modeling

In the onset of the present study, the mechanical and water retention models were identified as the main constitutive equations. In the last part of the study, an explicit from of a mechanical constitutive model, coupled with improved water retention model was proposed for unsaturated aggregated soils on the basis of the experimental evidences.

A new basis was proposed for extension of the constitutive models of reconstituted soils to aggregated soils within the framework of hardening elasto-plasticity. The proposed constitutive framework, adopts the generalized effective stress and suction as stress variables. The main features of the proposed constitutive modeling framework could be summarized as follows.

- A new parameter called degree of soil structure was introduced to physically quantify the soil structure in terms the macroporosity. This parameter and its evolution was then linked, as a state parameter, to the plastic strains.
- The yield limit in unsaturated aggregated soil was defined as an extension of the yield limit in reconstituted saturated soil. The elastic properties were assumed to be independent of suction and soil structure effects.
- The apparent effective preconsoliodatoin pressure in aggregated soils was introduced as an extension of the effective preconsolidation pressure of reconstituted soil. The extension is controlled by two multiplicative functions in terms of suction and the degree of soil structure.
- For the above-mentioned function of soil structure, a mathematical expression was derived in terms of the initial soil structure and the degree of soil structure.

- Partial saturation was evaluated to have a double effect in aggregated (structured) soils: primary or intrinsic effects on soil matrix and secondary effects in combination with soil structure.
- Primary effects were modeled using an explicit reversible function for suction-induced hardening effects on the apparent preconsolidation pressure. The secondary effects were introduced by establishing the dependency of soil structure function on suction.

Within the proposed framework, a new hardening elasto-plastic model was formulated based on the critical state concept. The new model for unsaturated aggregated soils, called ACMEG-2S, uses non-linear elasticity and two plastic mechanisms: isotropic and deviatoric. The model formulation was presented, first, for the simplified case of triaixal condition, and then, for the general stress-strain condition.

In addition to the mechanical model, an improved water retention model was proposed which incorporates the combined effects of suction, volume change, and the evolving double porous fabric..

The mechanical and the water retention models are coupled through the suction and the degree of saturation appearing in the effective stress, void ratio, and the degree of soil structure. The coupled constitutive model unified the combined effects of partial saturation, inter-particle bonding, and soil fabric.

Using a driver of constitutive laws, the model was examined for its capability in reproducing the experimental oedometric response of the tested samples. Comparison between the simulations and the experimental results revealed that the model was able to successfully address the main features observed during the experiments. For instance, it reproduced the non-linear stress-stress relationship during the virgin compression of aggregated soil as well as the increase of degree of saturation during the compression at constant suction.

The model was also tested for its capability in predicting the behavior of structured bonded soils. The model reasonably reproduced the mechanical response of saturated bonded soils reported in the literature.

## 7.2 Outlook for future works

Improvement of governing equations can be proposed by further elaboration of the constitutive laws of fluid flow and fluid mass transfer between the mixtures. The results of the joint study carried out by Carminati (2006) can be used to incorporate a more rigorous constitutive equation of liquid flow instead of the Darcy's law.

The leakage term, representing the fluid transfer between two system of pores could be also subject of the more deepened study. As evaluated in the companion thesis by Carminati (2006), improvements of these constitutive relations should mainly focus on incorporating the geometrical properties of the fabric, the contact points between aggregates, as well as the saturation state of the soil.

Concerning the experimental approach, there is still room to evaluate the

influence of stress path on the soil fabric and on the macroscopic stress-strain response. Important contributions can be done by running triaxial tests on samples of aggregated and reconstituted soil at different suctions and to evaluate the soil structure evolution during and after the loading.

The mechanisms of soil structure degradation in complex stress paths needs further assessments. Such an assessment may lead in proposing routine experimental procedures for determination of the relative contribution of different mechanisms to the soil structure degradation.

The influence of soil structure on the elastic properties of the soil can be further investigated. To this end, various unloading-reloading paths should be carried out under different stress states in triaxial or oedometric tests.

In order to investigate the direct effect of humidity variation on soil structure, ESEM observation of soil specimens at varying relative humidity (RH) can be performed with longer time intervals between the RH steps.

Improvement of the constitutive model can be done if a better understanding of the soil behavior is achieved through experimental approaches. The stress dilatancy rule and its dependency on combined effects of soil structure and partial saturation can be further evaluated and improved in the model. A new coupling link can be added to the model between the variation of the air entry value suction and the soil straining, a major contribution which demands significant amount of experimental study.

Finally, as a prospective research topic, the proposed constitutive model and the modified form of governing equations can be implemented into a finite element code for solution of boundary value problems. Such developments would be of great interest for a wide range of geotechnical engineering problems involving structured soils with double porosity. Examples of such applications are the engineering study of flow and deformation around the oil reservoirs or in clay barriers of waste disposals.

# References


Aifantis, E. (1977). Introducing a multi-porous medium. *Developments in Mechanics*, 8:209–211.

Al-Mukhtar, M. (1995). Macroscopic behavior and microstructural properties of a kaolinite clay under controlled mechanical and hydraulic state. In *1st International Conference on Unsaturated Soils / UNSAT 95*, volume 1, pages 3–9, Paris.

Al-Mukhtar, M., Belanteur, N., Tessier, D., and Vanapalli, S. (1996). The fabric of a clay soil under controlled mechanical and hydraulic stress states. *Applied Clay Science*, 11:99–115.

Al-Mukhtar, M., Robinet, J. C., and Liu, C. W. (1993). Hydro-mechanical behaviour of partially saturated low porosity clays. In *Engineered fills*, pages 87–98. Thomas Telford.

Alonso, E. (1998). Modelling expansive soil behaviour. In *Proceeding of the 2nd International Conference on Unsaturated Soils*, volume 2, pages 37–70, Beijing, China.

Alonso, E. and Gens, A. (1994). Keynote lecture: on the mechanical behaviour of arid soils. In *Conference on Engineering Characteristics of Arid soils*, pages 173–205, London.

Alonso, E., Gens, A., and Gehling, W. (1994). Elastoplastic model for unsaturated expansive soils. In *Numerical Methods in Geotechnical Engineering*, pages 11–18. Balkema.

Alonso, E., Gens, A., and Hight, D. (1987). Special problem soils. General report. In *Proceedings of the 9th European Conference on Soil Mechanics and Foundation Engineering*, volume 3, pages 1087–1146. Dublin.

Alonso, E., Gens, A., and Josa, A. (1990). A constitutive model for partially saturated soil. *Géotechnique*, 40(3):405–430.

Alonso, E., Gens, A., and Lloret, A. (1991). Double structure model for the prediction of long-term movements in expansive materials. In *Computer Methods and Advances in Geomechanics*, volume 1, pages 541–548. Balkema.

Alonso, E., Lloret, A., and Gens, A. (1995). Experimental behavior of highly expansive double-structure clay. In *1st International Conference on Unsaturated Soils / UNSAT 95*, volume 1, pages 11–16, Paris.

Alonso, E., Vaunat, J., and Gens, A. (1999). Modelling the mechanical behaviour of expansive clays. *Engineering Geology*, 54:173–183.

Alshibli, K. A., Sture, S., Costes, C., Frank, M. L., Lankton, M. R., Batiste, S. N., and Swanson, R. A. (2000). Assessment of localized deformations in sand using X-ray computed tomography. *Geotechnical testing journal*, 23(3):274–299.

Anagnostopoulos, A., Kalteziotis, N., Tsiambaos, G., and Kavvadas, M. (1991). Geotechnical properties of the corinth canal marls. *Geotechnical and Geological Engineering*, 9(1):1–26.

Anderson, S. H. and Hopmans, J. W. (1994). Tomography of soil-water-root processes. *Soil Science Society of America*, 36.

Applegate, H. G. (1960). Freezing+point depressions of hoagland's carbowax system. *Nature*, 186:232–233.

ASTM D2487 (2000). Standard classification of soils for engineering purposes (unified soil classification system). ASTM International.

Atkinson, J. H. and Bransby, P. L. (1978). *The Mechanics of Soils, An Introduction to Critical State Soil Mechanics*. McGraw-Hill, London.

Aubry, D., Kodaissi, E., and Memoin, Y. (1985). A viscoplastic constitutive equation for clays including a damage law. In *5th International Conference on Numerical Methods in Geomechanics*, pages 421–428, Nagoya.

Bachmat, Y. and Bear, J. (1986). Macroscopic modelling of transport phenomena in porous media. 1: The continuum approach. *Transport in Porous Media*, 1(3):213–240.

Barden, L. and Sides, G. (1970). Engineering behavior and structure of compacted clays. *Journal of Soil Mechanics and Foundation Analysis*, 96:1171–1200.

Barrenblatt, G. (1963). On certain boundary value problems for the equation of seepage of liquid in fissured rock. *Journal of Applied Mathematics and Mechanics. Translation of the Soviet journal : Prik-ladnaja Matematika i Mekhanika (PMM)*, 27:513–518.

Barrenblatt, G., Zheltov, I., and Kochina, I. (1960). Basic concepts in the theory of seepage of homogeneous liquids in fissured rocks. *Journal of Applied Mathematics and Mechanics. translation of the Soviet journal : Prik-ladnaja Matematika i Mekhanika (PMM)*, 24(5):852–864.

Baudet, B. and Stallebrass, S. (2004). A constitutive model for structured clays. *Géotechnique*, 54(4):269–278.

Bedford, A. and Drumheller, D. S. (1983). Theories of immiscible and structured mixtures. *International Journal of Engineering Science*, 21(8):863–960.

Bernier, F., Volckaert, G., Alonso, E., and Villar, M. (1997). Suction-controlled experiments on boom clay. *Engineering Geology*, 47(4):325–338.

Biot, M. (1941). General theory of three-dimensional consolidation. *Journal of Applied Phyisics*, 2:155–164.

Biot, M. A. (1956). The theory of propagation of elastic waves in a fluid-saturated porous solid. 1: Low frequency range. *Journal of Acoustical Society of America*, 28:168–178.

Biot, M. A. (1972). Theory of finite deformation of porous solids. *Indiana University Mathematical Journal*, 24:Biot.

Bishop, A. (1959). The principle of effective stress. *Tecknish Ukeblad*, 106:859–863.

Bjerrum, L. (1967). Progressive failure in slopes of overconsolidated plastic clay and clay-shales. *Journal of Soil Mechanics and Foundations Division, ASCE*, 93(SM5):3–49.

Bjerrum, L. (1972). Embankments on soft ground. In *Performance of Earth Supported Structures, Proceedings of the Speciality Conference*, volume 2, pages 1–54, Lafayette, IN. ASCE.

Blight, G. E. (1967). Effective stress evaluation for unsaturated soils. *Journal of Soil Mechanics and Foundations Division, ASCE*, 93:125–148.

Bocking, K. and Fredlund, D. (1980). Limitations of the axis translation technique. In *IV International Conference on Expansive Soils*, volume 1, pages 117–135, Denver.

Bolzon, G., Schrefler, B. A., and Zienkiewicz, O. C. (1996). Elastoplastic soil constitutive laws generalized to partially saturated states. *Géotechnique*, 46(2):279–289.

Bowen, R. M. (1980). Incompressible porous media models by use of the theory of mixtures. *International Journal of Engineering Science*, 18(9):1129–1148.

Bowen, R. M. (1982). Compressible porous media models by use of the theory of mixtures. *International Journal of Engineering Science*, 20(6):697–735.

Bowen, R. M. (1989). *Introduction to continuum mechanics for engineers*. Plenum Press, New York.

Bressani, L. A. and Vaughan, P. R. (1989). Damage to soil structure during triaxial testing. In *Proceedings of the International Conference on Soil Mechanics and Foundation Engineering*, volume 1, pages 17–20.

BS 1377 (1990). Methods of test for soils for civil engineering purposes. British Standards Institution, London.

Burger, C. A. and Shackelford, C. D. (2001). Soil-water characteristic curves and dual porosity of sand-diatomaceous earth mixtures. *Journal of Geotechnical and Geoenvironmental Engineering*, 127(9):790–800.

Burland, J. (1990). On the compressibility and shear strength of natural clays. *Géotechnique*, 40(3):329–378.

Burland, J. B., Rampello, S., Georgiannou, V. N., and Calabresi, G. (1996). A laboratory study of the strength of four stiff clays. *Géotechnique*, 46(3):491–514.

Calabresi, G. and Scarpelli, G. (1985). Effects of swelling caused by unloading in overconsolidated clay. *Proc. 11th international conference on soil mechanics and foundation engineering, San Francisco, August 1985. Vol. 2, (Balkema)*, pages 411–414.

Callari, C. and Federico, F. (2000). FEM validation of a double porosity elastic model for consolidation of structurally complex clayey soil. *International Journal for Numerical and Analytical Methods in Geomechanics*, 24:367–402.

Callisto, L. and Calabresi, G. (1998). Mechanical behaviour of a natural soft clay. *Géotechnique*, 48(4):495–513.

Callisto, L. and Rampello, S. (2004). An interpretation of structural degradation for three natural clays. *Canadian Geotechnical Journal*, 41:392–407.

Carminati, A. (2006). *Unsaturated water flow through aggregates*. PhD thesis, ETHZ.

Carminati, A., Kaestner, A., Flühler, H., Lehmann, P., Or, D., Lehmann, E., and Stampanoni, M. (2007a). Hydraulic contacts controlling water flow across porous grains. *Physical Review E - Statistical, Nonlinear, and Soft Matter Physics*, 76(2).

Carminati, A., Kaestner, A., Hassanein, R., Ippisch, O., Vontobel, P., and Flühler, H. (2007b). Infiltration through series of soil aggregates: Neutron radiography and modeling. *Advances in Water Resources*, 30(5):1168–1178.

Carminati, A., Kaestner, A., Ippisch, O., Koliji, A., Lehmann, P., Hassanein, R., Vontobel, P., Lehmann, E., Laloui, L., Vulliet, L., and Flühler, H. (2007c). Water flow between soil aggregates. *Transport in Porous Media*, 68(2):219–236.

Charlier, R., Li, X., Bolle, A., Geiser, F., Laloui, L., and Vulliet, L. (1997). Mechanical behaviour modelling of an unsaturated sandy silt. In *14th International Conference on Soil Mechanics & Foundation Engineering*, pages 641–644, Hamburg: Balkema.

Cleman, J. D. (1962). Stress/strain relations for partly saturated soil. *Géotechnique*, 12(4):348–350.

Collin, F., Li, X. L., Radu, J. P., and Charlier, R. (2002). Thermo-hydro-mechanical coupling in clay barriers. *Engineering Geology*, 64(2-3):179–193.

Collins, K. and McGown, A. (1974). The form and function of microfabric features in a variety of natural soils. *Géotechnique*, 24(2):223–254.

Coop, M. R. and Atkinson, J. H. (1993). The mechanics of cemented carbonate sands. *Géotechnique*, 43(1):53–67.

Coppola, A. (2000). Unimodal and bimodal descriptions of hydraulic properties for aggregated soils. *Soil Science Society of America Journal*, 64(4):1252–1262.

Cotecchia, F. and Chandler, R. J. (1998). One-dimensional compression of a natural clay: Structural changes and mechanical effects. In *2nd International Symopsium on hard soils-soft rocks*, pages 103–114, Naples.

Cotecchia, F. and Chandler, R. J. (2000). A general framework for the mechanical behaviour of clays. *Géotechnique*, 50(4):431–447.

Coussy, O. (1995). *Mechanics of Porous Continua*. Wiley Ltd., New York.

Coussy, O., Dormieux, L., and Detournay, E. (1998). From mixture theory to biot's approach for porous media. *International Journal of Solids and Structures*, 35(34-35):4619–4635.

Croney, D. (1952). The movement and distribution of water in soils. *Géotechnique*, 3(1):1–16.

Cuccovillo, T. and Coop, M. R. (1999). On the mechanics of structured sands. *Géotechnique*, 49(6):741–760.

Cui, Y. and Delage, P. (1996). Yielding and plastic behaviour of an unsaturated compacted silt. *Géotechnique*, 46(2):291–311.

Cuisinier, O. and Laloui, L. (2004). Fabric evolution during hydromecanical loading of a compacted silt. *International Journal for Numerical and Analytical Methods in Geomechanics*, 28(6):483–499.

Cuisinier, O. and Masrouri, F. (2004). Testing the hydromechanical behavior of a compacted swelling soil. *Geotechnical Testing Journal*, 27(6):598–606.

Cunningham, M. R., Ridley, A. M., Dineen, K., and Burland, J. B. (2003). The mechanical behaviour of a reconstituted unsaturated silty clay. *Géotechnique*, 53(2):183–194.

Dafalias, Y. F. (1986). Bounding surface plasticity. I: Mathematical foundation nad hypoplasticity. *Journal of Engineering Mechanics*, 112(9):966–987.

De Boer, R. (1996). Highlights in the historical development of the porous media theory. *Applied Mechanics Reviews*, 49(4):201–262.

De Boer, R. and Didwania, A. K. (2002). Capillarity in porous bodies: Contributions of the Vienna school and recent findings. *Acta Mechanica*, 159:173–188.

De Boer, R. and Ehlers, W. (1988). A historical review of the formulation of porous media theories. *Acta Mechanica*, 74(1-4):1–8.

Degueldre, C., Pleinert, H., Maguire, P., Lehmann, E., Missimer, J., Hammer, J., Leenders, K., Böck, H., and Townsend, D. (1996). Porosity and pathway determination in crystalline rock by positron emission tomography and neutron radiography. *Earth and Planetary Science Letters*, 140:213–225.

Deinert, M., Parlange, J.-Y., Steenhuis, T. S., Unlü, K., Selker, J., and Cady, K. B. (2002). Real-time measurment of water profiles in a sand using neutron radiography. In *Hydrology Days 2002*, pages 56–63.

Delage, P., Audiguier, M., Cui, Y.-J., and Howat, M. D. (1996). Microstructure of compacted silt. *Canadian Geotechnical Journal*, 33:150–158.

Delage, P., Cui, Y. J., and De Laure, E. (2001). Récents développements de la technique osmotique de contrôle de succion. In *Proceeding of the 15th International Conference on soil mechanics and geotechnical engineering*, pages 575–578. Istanbul.

Delage, P., Howat, M. D., and Cui, Y. J. (1998). The relationship between suction and swelling properties in a heavily compacted unsaturated clay. *Engineering Geology*, 30:31–48.

Delage, P. and Lefebvre, G. (1984). Study of the structure of a sensitive champlain clay and of its evolution during consolidation. *Canadian Geotechnical Journal*, 21(1):21–35.

Delage, P., Vicol, T., and Suraj de Silva, G. (1992). Suction controlled testing of non-saturated soils with an osmotic consolidometer. In *7th International Conference on Expansive Soils*, pages 206–211. Dallas.

Desai, C. (1974). A consistent fnite element technique for work-softening behaviour. In *The International Conference on Computation Methods in Nonlinear Mechanics*, Austin.

Desai, C. (1995). Constitutive modelling using the disturbed state as microstructure self-adjustment concept. In *Continuum Models for Materials with Microstructure*, pages 239–296.

Desai, C. S. (2001). *Mechanics of Materials and Interfaces: The Disturbed State Concept*. CRC Press.

Desrues, J., Chambon, R., Mokni, M., and Mazerolle, F. (1996). Void ratio evolution inside shear band in triaxial sand specimens studies by computed tomography. *Géotechnique*, 46(3):529–546.

Diebels, S. (2000). A macroscopic description of the quasi-static behavior of granular materials based on the theory of porous media. *Granular Matter*, 2(143-152).

Dineen, K. and Burland, J. (1995). A new approach to osmotically controlled oedometer testing. In *1st Internationa Conference on Unsaturated Soils*, volume 2, pages 459–465, Paris.

Durner, W. (1992). Predicting the unsaturated hydraulic conductivity using multiporosity water retention curves. In *M.Th. Indirect methods for estimating the hydraulic properties of unsaturated soils*, pages 185–202, Univ. of California, Riverside.

Ehlers, W. (1993). Constitutive equations for granular materials in geomechanical context. In Hutter, K., editor, *Continuum mechanics in environmental sciences and geophysics*, volume 337 of *CISM-Lecture notes*, pages 313–402, Wien. Springer.

Ehlers, W., Graf, T., and Diebels, S. (2003). On the description of partially saturated soils by the theory of porous media. *PAMM*, 2(1):230–231.

Elsworth, D. and Bai, M. (1990). Continuum representaion of coupled flow-deformation response of dual porosity media. In Rossmanith, H. P., editor, *Mechanics of jointed and faulted rock*, pages 681–688, Vienna. Balkema.

EPFL-LMS (2002). Eassai CD sur limon de Bioley pour test programme Momo, test -1-1. Technical report, LMS-EPFL.

Esteban, F. (1990). *Caracterización de la expansividad de una roca evaporítica. Identificación de los mecanismos de hinchamient*. PhD thesis, Universidad de Cantabria.

Francois, B. (2005). Driver des loi de comportement thermo-mécanique.

Fredlund, D. (1975). A diffused air volume indicator for unsaturated. *Canadian Geotechnical Journal*, 12(4):533–539.

Fredlund, D. and Morgenstern, N. (1977). Stress state variables for unsaturated soils. *Journal of geotechnical engineering division, ASCE*, 103:447–466.

Fredlund, D. and Rahardjo, H. (1993). *Soil mechanics for unsaturated soil*. John Wiley & Sons, Inc.

Gallipoli, D., Gens, A., Sharma, R., and Vaunat, J. (2003). An elasto-plastic model for unsaturated soil incorporating the effects of suction and degree of saturation on mechanical behaviour. *Géotechnique*, 54(4):293–295.

Geiser, F. (1999). *Comportement mécanique d'un limon non saturé. Etude expérimentale et modélisation constitutive*. PhD thesis, No. 1942, Ecole Polytechnique Fédérale de Lausanne.

Geiser, F., Laloui, L., and Vulliet, L. (2006). Elasto-plasticity of unsaturated soils: Laboratory test results on a remoulded silt. *Soils and Foundations*, 46(5):545–556.

Gens, A., Alonso, E., Suriol, J., and Lloret, A. (1995). Effect of structure on the volumetric behavior of a compacted soil. In *1st International Conference on Unsaturated Soils / UNSAT 95*, volume 1, pages 83–88, Paris.

Gens, A. and Alonso, E. E. (1992). A framework for the behaviour of unsaturated expansive clays. *Canadian Geotechnical Journal*, 29:1013–1032.

Gens, A. and Nova, R. (1993). Conceptual bases for a constitutive model for bonded soils and weak rocks. In *Geotechnical Engineering of Hard Soils - Soft Rocks*, pages 485–494. Balkema.

Gens, A., Sanchez, M., and Sheng, D. (2006). On constitutive modelling of unsaturated soils. *Acta Geotechnica*, 1:137–147.

Gerke, H. H. and Van Genuchten, M. T. (1993). A dual-porosity model for simulating the preferential movement of water and solutes in structured porous-media. *Water Resources Research*, 29(2):305–319.

Ghafouri, H. R. and Lewis, R. W. (1996). A Finite Element double porosity model for heterogeneous deformable porous media. *International Journal for Numerical and Analytical Methods in Geomechanics*, 20(11):831–844.

Gillott, J. (1973). Methods of sample preparation for microstructural analysis of soil. soil microscopy. In *4th International Working-Meeting on Soil Micromorphology*, pages 143–164, Kingston, Jamaica.

Graham, J., Crooks, J. H. A., and Lau, S. L. K. (1988). Yield envelopes: identification and geometric properties. *Géotechnique*, 38(1):125–134.

Gray, W. G. and Schrefler, B. A. (2001). Thermodynamic approach to effective stress in partially saturated porous media. *European Journal of Mechanics A/Solids*, 20(4):521–538.

Gray, W. G. and Schrefler, B. A. (2007). Analysis of the solid phase stress tensor in multiphase porous media. *International Journal for Numerical and Analytical Methods in Geomechanics*, 31(4):541–581.

Green, T., Constantz, J., and Freyberg, D. (1996). Upscaled soil-water retention using van genuchten's function. *Journal of Hydrologic Engineering*, 1(3):123–130.

Griffiths, F. j. and Joshi, R. C. (1990). Change in pore size distribution due to consolidation of clays. *Géotechnique*, 40(2):303–309.

Gwo, J. P., Jardine, P. M., Wilson, G. V., and Yeh, G. T. (1995). A multiple-pore-region concept to modeling mass-transfer in subsurface media. *Journal of Hydrology*, 164(1-4):217–237.

Hassanein, R., Lehmann, E., and Vontobel, P. (2005). Methods of scattering corrections for quantitative neutron radiography. *Nuclear Instruments and Methods in Physics Research*, A 37:1093–1106.

Hassanizadeh, M. and Gray, W. G. (1979a). General conservation equations for multi-phase systems: 1. Averaging procedure. *Advances in Water Resources*, 2:131–144.

Hassanizadeh, S. M. and Gray, W. G. (1979b). General conservation equations for multi-phase systems: 2. Mass, momenta, energy, and entropy equations. *Advances in Water Resources*, 2:191–203.

Hassanizadeh, S. M. and Gray, W. G. (1990). Mechanics and thermodynamics of multiphase flow in porous-media including interphase boundaries. *Advances in Water Resources*, 13(4):169–186.

Hilf, J. (1956). *An investigation of pore-water pressure in compacted cohesive soils*. PhD thesis, Technical Memorandum 654, University of Denver, Colorado.

Hoffmann, C., Alonso, E., and Romero, E. (2006). Fabric changes of a pellet-based bentonite buffer material and their effects on mechanical behaviour. In *4th International Conference on Unsaturated Soils, UNSAT06*, volume 2, pages 2523–2534, USA, Arizona.

Horn, R. (2003). Stress - strain effects in structured unsaturated soils on coupled mechanical and hydraulic processes. *Geoderma*, 116(1-2):77–88.

Houlsby, G. (1997). The work input to an unsaturated granular material. *Géotechnique*, 47(1):93–196.

Huang, H., Hassan, A. E., and Hu, B. X. (2003). Monte Carlo study of conservative transport in heterogeneous dual-porosity media. *Journal of Hydrology*, 275(3-4):229–241.

Hujeux, J. (1985). Une loi de comportement pour le chargement cyclique des sols. In *Génie Parasismique*, Les éditions de l'ENPC, pages 287–353. Paris.

Hutter, K., Laloui, L., and Vulliet, L. (1999). Thermodynamically based mixture models of saturated and unsaturated soils. *Mechanics of cohesive-frictional materials*, 4:295–338.

Huyakorn, P. S., Lester, B. H., and Faust, C. R. (1983). Finite Element techniques for modeling groundwater flow in fractured aquifers. *Water Resources Research*, 19(4):1019–1035.

Jennings, J. and Burland, J. (1962). Limitations to the use of effective stresses in partially saturated soils. *Géotechnique*, 12(2):125–144.

Jommi, C. (2000). Remarks on the constitutive modelling of unsaturated soils. In *Experimental Evidence and Theoretical Approaches in Unsaturated Soils*, pages 139–153.

Juang, C. and Holtz, R. (1986). A probabilistic permeability model and the pore size density function. *International Journal For Numerical and Analytical Methods in Geomechanics*, 10:543–553.

Kalaydjian, F. (1987). A macroscopic description of multiphase flow in porous media involving spacetime evolution of fluid/fluid interface. *Transport in Porous Media*, 2(6):537–552.

Kassif, G. and BenShalom, A. (1971). Experimental relationship between swell pressure and suction. *Géotechnique*, 21(3):245–255.

Kavvadas, M. and Amorosi, A. (2000). A constitutive model for structured soils. *Géotechnique*, 50(3):263–273.

Khalili, N., Geiser, F., and Blight, G. E. (2004). Effective stress in unsaturated soils: Review with new evidence. *International Journal of Geomechanics*, 4(2):115–126.

Khalili, N. and Khabbaz, M. (1998). A unique relationship for x for the determination of the shear strength of unsaturated soils. *Géotechnique*, 48(5):681–687.

Khalili, N. and Valliappan, S. (1991). Flow through fissured porous media with deformable matrix: Implicit formulation. *Water Resources Research*, 27(7):1703–1709.

Khalili, N. and Valliappan, S. (1996). Unified theory of flow and deformation in double porous media. *European Journal of Mechanics A/Solids*, 15(2):321–336.

Khalili, N., Valliappan, S., and Wan, C. (1999). Consolidation of fissured clays. *Géotechnique*, 49(1):75–89.

Khalili, N., Witt, R., Laloui, L., Vulliet, L., and Koliji, A. (2005). Effective stress in double porous media with two immiscible fluids. *Geophysical Research Letters*, 32(15):L26309.

Kodikara, J., Barbour, S., and Fredlund, D. (1999). Changes in clay structure and behaviour due to wetting and drying. In *8th Australia New Zeland Conference on Geomechanics*, volume 1, pages 179–185. Hobart.

Koiter, W. T. (1960). General theorems for elastic-plastic solids. In *Progress in solid mechanics*, pages 165–221, Amsterdam: North-Holland.

Koliji, A., Laloui, L., Cusinier, O., and Vulliet, L. (2006). Suction induced effects on the fabric of a structured soil. *Transport in Porous Media*, 64(2):261–278.

Koliji, A., Vulliet, L., and Laloui, L. (2007). Soil structure evolution: Experimental and constitutive consideration. In *Numerical models in geomechanics, NUMOG X*, pages 133–138, Rhodes, Greece.

Kubik, J. (1986). Macroscopic description of geometrical pore structure of porous solids. *International Journal of Engineering Science*, 24(6):971–980.

Lagerwerff, J. V., Ogata, G., and Eagle, H. E. (1961). Control of osmotic pressure of culture solutions by means of polyethylene glycol. *Science*, 133:1486–1487.

Lagioia, R. and Nova, R. (1995). An experimental and theoretical study of the behaviour of a calcarenite in triaxial compression. *Géotechnique*, 45(4):633–648.

Laloui, L., Klubertanz, G., and Vulliet, L. (2003). Solid-liqiud-air coupling in multiphase porous media. *International Journal For Numerical and Analytical Methods in Geomechanics*, 27:183–206.

Lapierre, C., Leroueil, S., and Locat, J. (1990). Mercury intrusion and permeability of louisville clay. *Canadian Geotechnical Journal*, 27:761–773.

Lehmann, P., Berchtold, M., Ahrenholz, B., Tölke, J., Kaestner, A., Krafczyk, M., Flühler, H., and Künsch, H. (2007). Impact of geometrical properties on permeability and fluid phase distribution in porous media. *Submitted*.

Leroueil, S. (2006). The isotache approach. where are we 50 years after its development by professor suklje? In *13th Danube-European Conference on Geotechnical Engineering*, volume 2, pages 55–88, Ljubljana.

Leroueil, S. and Barbosa, A. (2000). Combined effect of fabric, bonding and partial saturation on yielding of soils. In *Asian Conference on Unsaturated Soils*, pages 527–532.

Leroueil, S., Tavenas, F., and Le Bihan, J. P. (1983). Propriétés caractéristiques des argiles de l'est du Canada. *Canadian Geotechnical Journal*, 20(4):681–705.

Leroueil, S. and Vaughan, P. R. (1990). The general and congruent effects of structure in natural soils and weak rocks. *Géotechnique*, 40(3):467–488.

Lewallen, K. and Wang, H. (1998). Consolidation of a double-porosity medium. *International Journal of Solids Structures*, 35(34-35):4845–4867.

Lewandowska, J., Szymkiewicz, A., Burzynski, K., and Vauclin, M. (2004). Modeling of unsaturated water flow in double-porosity soils by the homogenization approach. *Advances in Water Resources*, 27:283–296.

Lewis, R. W. and Ghafouri, H. R. (1997). A novel finite element double porosity model for multiphase flow through deformable fractured porous media. *International Journal for Numerical and Analytical Methods in Geomechanics*, 21:789–816.

Liu, M. D. and Carter, J. P. (1999). Virgin compression of structured soils. *Géotechnique*, 49(1):43–57.

Liu, M. D. and Carter, J. P. (2000a). Modelling the destructuring of soils during virgin compression. *Géotechnique*, 50(4):479–483.

Liu, M. D. and Carter, J. P. (2000b). On the volumetric deformation of reconstituted soils. *International Journal for Numerical and Analytical Methods in Geomechanics*, 24:101–133.

Liu, M. D. and Carter, J. P. (2002). A structured Cam Clay model. *Canadian Geotechnical Journal*, 39(6):1313–1332.

Liu, M. D., Carter, J. P., Desai, C., and Xu, K. (2000). Analysis of the compression of structured soils using the disturbed state concept. *International Journal for Numerical and Analytical Methods in Geomechanics*, 24:723–735.

Lloret, A., Villar, M. V., Sanchez, M., Gens, A., Pintado, X., and Alonso, E. E. (2003). Mechanical behaviour of heavily compacted bentonite under high suction changes. *Géotechnique*, 53(1):27–40.

Loret, B., Hueckel, T., and Gajo, A. (2002). Chemo-mechanical coupling in saturated porous media: elastic- plastic behaviour of homoionic expansive clays. *International Journal of Solids and Structures*, 39(10):2773–2806.

Loret, B. and Khalili, N. (2000). A three-phase model for unsaturated soils. *International Journal for Numerical and Analytical Methods in Geomechanics*, 24:893–927.

Loret, B. and Khalili, N. (2002). An effective stress elastic-plastic model for unsaturated porous media. *Mechanics of Materials*, 34(2):97–116.

Lubliner, J. (1991). A simple model of generalized plasticity. *International Journal of Solids Structures*, 28(6):769–778.

Ma, C. M. and Hueckel, T. (1993). Thermomechanical effects on adsorbed water in clays around a heat-source. *International Journal for Numerical and Analytical Methods in Geomechanics*, 17(3):175–196.

Marcial, D., Delage, P., and Cui, Y. J. (2002). On the high stress compression of bentonites. *Canadian Geotechnical Journal*, 39:812–820.

Marle, C. M. (1982). On macroscopic equations governing multiphase flow with diffusion and chemical reactions in porous media. *International Journal of Engineering Science*, 20(5):643–662.

Matyas, E. and Radhakrishna, H. (1968). Volume change characteristics of partialy saturated soils. *Géotechnique*, 18:432–448.

Mitchell, J. K. (1993). *Fundamentals of soil behavior*. Wiley.

Mitchell, J. K. and Soga, K. (2005). *Fundamentals of soil behavior*. John Wiley & Sons, Inc., New Jersey, third edition.

Mitchell, J. K. and Solymar, Z. V. (1984). Time-dependent strength gain in freshly deposited or densified sand. *Journal of Geotechnical Engineering - ASCE*, 110(11):1559–1576.

Modaressi, A. and Abou-Bekr, N. (1994). A unified approach to model the behaviour of saturated and unsaturated soils. In *8th International Conference on Computer Methods and Advances in Geomechanics*, pages 1507–1513. Balkema, Rotterdam.

Modaressi, A., Modaressi, H., Piccuezzu, E., and Aubry, D. (1989). Driver de la loi de comportement de hujeux.

Money, N. P. (1989). Osmotic pressure of aqueous polyethylene glycols. *Plant Physiology*, 91:766–769.

Monroy, R. (2005). *The influence of load and suction changes on the volumetric behaviour of compacted London Clay*. PhD thesis, Imperial College London.

Mroz, Z. (1967). On the description of anisotropic work hardening. *Journal of the Mechanics and Physics of Solids*, 15:163–175.

Murad, M. A. and Cushman, J. H. (2000). Thermomechanical theories for swelling porous media with microstructure. *International Journal of Engineering Science*, 38:517–564.

Musso, A., Miliziano, S., and Federico, F. (1990). One-dimensional consolidation of structured media. In *Mechanics of jointed and faulted rock*, pages 673–680, Vienna. Balkema.

Nigmatulin, R. I. (1979). Spatial averaging in the mechanics of heterogeneous and dispersed systems. *International Journal of Multiphase Flow*, 5:353–385.

Nova, R., Castellanza, R., and Tamagnini, R. (2003). A constitutive model for bonded geomaterials subject to mechanical and/or chemical degradation. *International Journal for Numerical and Analytical Methods in Geomechanics*, 27(9):705–732.

Nur, A. and Byerlee, J. D. (1971). An exact effective stress law for elastic deformation of rock with fluids. *Journal of geophysical research*, 76(26):6414–6419.

Nuth, M. and Laloui, L. (2005). An introduction to the constitutive modelling of unsaturated soils. *Revue européenne de génie civil*, 9(5-6):651–670.

Nuth, M. and Laloui, L. (2007a). Implications of a generalized effective stress on the constitutive modelling of unsaturated soils. In *Theoretical and Numerical Unsaturated Soil Mechanics*, Springer Proceedings in Physics, pages 75–82, Weimar. Springer.

Nuth, M. and Laloui, L. (2007b). New insight into the unified hydro-mechanical constitutive modelling of unsaturated soils. In *The 3rd Asian Conference on Unsaturated Soils*, pages 109–126, China. Science Press.

Oka, F., Leroueil, S., and Tavenas, F. (1989). Constitutive model for natural soft clay with strain softening. *Soils and Foundations*, 29(3):54–66.

Or, D. (1996). Wetting-induced soil structural changes: The theory of liquid phase sintering. *Water Resources Research*, 32(10):3041–3049.

Otani, J. (2006). X-ray computed tomography for geotechnical engineering. In *Advances in X-ray Tomography for geomaterials, Geox06*, pages 95–115, Aussois, France.

Otani, J., Mukunoke, T., and Obara, Y. (2000). Application of x-ray ct method for characterization of failure in soils. *Soil & Foundations*, 40(2):113–120.

Pao, W. and Lewis, R. (2002). Three-dimensional finite element simulation of three phase flow in a deforming fissured reservoir. *Comp. Meth. Appl. Mech. Eng.*, 191(23-24):2631–2659.

Passman, S. L., Nunziato, J. W., and Walsh, E. K. (1984). A theory of multiphase mixtures. In *Rational thermodynamics*. Springer-Verlag, second edition.

Peck, A. and Rabbidge, R. (1969). Design and performance of an osmotic tensiometer for measuring capillary potential. *Soil Science Society of America*, 33:196–202.

Penumadu, D. and Dean, J. (2000). Compressibility effect in evaluating the pore-size distribution of kaolin clay using mercury intrusion porosimetry. *Canadian Geotechnical Journal*, 37:393–405.

Peyton, R. L., Haeffner, B. A., Anderson, S. H., and Ganzer, C. J. (1992). Applying X-ray CT to measure micropore diameters in undisturbed soil cores. *Geoderma*, 53:329–340.

Pini, G. and Putti, M. (1997). Parallel finite element laplace transform method for the non- equilibrium groundwater transport equation. *International Journal for Numerical Methods in Engineering*, 40(14):2653–2664.

Pleinert, H. and Degueldre, C. (1995). Neutron radiographic measurement of porosity of crystalline rock samples: A feasibility study. *Journal of Contaminant Hydrology*, 19:29–46.

Prager, W. (1949). Recent developments in the mathematical theory of plasticity. *Journal of Applied Physics*, 20(3):235–241.

Qi, Y., Al-Mukhtar, M., Alcover, J. F., and Bergaya, F. (1996). Coupling analysis of macroscopic and microscopic behaviour in highly consolidated nalaponite clays. *Applied Clay Science*, 11:185–197.

Rice, J. and Cleary, M. (1976). Some basic stress diffusion solutions of fluid saturated elastic porous media with compressible constituents. *Reviews of Geophysics and Space Physics*, 14:227–291.

Richards, B. (1965). Measurement of free energy of soil moisture by the psychrometric technique using thermistors. In *Moisture equilibria and moisture changes in soils beneath covered area*, pages 39–46, Australia, butterworths.

Ridley, A. (1993). *The measurement of soil moisture suction*. PhD thesis, University of London (Imperial College), London, UK.

Rifa'i, A. (2002). *Mechanical testing and modelling of an unsaturated silt, with engineering applications*. PhD thesis, No. 2612, Ecole Polytechnique Fédérale de Lausanne.

Rizzi, E., Maier, G., and Willam, K. (1996). On failure indicators in multidissipative materials. *Int. J. Solids Structures*, 33(20-22):3187–3214.

Romero, E. (1999). *Characterisation and thermo-hydro-mechanical behaviour of unsaturated Boom clay: an experimental study*. PhD thesis, Universidad Plitécnica de Cataluña.

Romero, E., Gens, A., and Lloret, A. (1999). Water permeability, water retention and microstructure of unsaturated compacted boom clay. *Engineering Geology*, 54(1-2):117–127.

Romero, E., Gens, A., and Lloret, A. (2001). Temperature effects on the hydraulic behaviour of an unsaturated clay. *Geotechnical and Geological Engineering*, 19(3-4):311–332.

Roscoe, K. and Burland, J. (1968). On the generalized stress-strain behaviour of wet clay. In *Engineering plasticity*, pages 535–609. Cambridge University Press, Cambridge.

Roscoe, K. and Schofield, A. N. (1963). Mechanical behaviour of an idealised wet clay. In *European Conference on Soil Mechanics and Foundation Engineering*, volume 1, pages 47–54, Wiedbaden.

Roscoe, K., Schofield, A. N., and Wroth, C. (1958). On the yielding of soils. *Géotechnique*, 8(1):22–52.

Ross, P. J. and Smettem, K. R. J. (1993). Describing soil hydraulic-properties with sums of simple functions. *Soil Science Society of America Journal*, 57(1):26–29.

Rouainia, M. and Wood, D. M. (2000). A kinematic hardening constitutive model for natural clays with loss of structure. *Géotechnique*, 50(2):153–164.

Russell, A. R. and Khalili, N. (2006). A unified bounding surface plasticity model for unsaturated soils. *International Journal for Numerical and Analytical Methods in Geomechanics*, 30(3):181–212.

Sanchez, M. (2004). *Thermo-hydro-mechanical coupled analysis in low permeability media*. PhD thesis, Technical University of Catalonia.

Sanchez, M., Gens, A., Guimaraes, L. D., and Olivella, S. (2005). A double structure generalized plasticity model for expansive materials. *International Journal for Numerical and Analytical Methods in Geomechanics*, 29(8):751–787.

Schanz, M. and Diebels, S. (2003). A comparative study of biot's theory and the linear theory of porous media for wave propagation problems. *Acta Mechanica*, 161(3-4):213–235.

Schofield, A. N. and Wroth, C. (1968). *Critical state soil mechanics*. McGraw-Hill, London.

Schonfeldt, N. (1969). Surface active ethylene oxide adducts. pages 130–385. Pergamon press, Oxford.

Sharma, R. S. (1998). *Mechanical behaviour of unsaturated highly expansive clays*. PhD thesis, University of Oxford.

Sheng, D., Sloan, S. W., and Yu, H. S. (2000). Aspects of finite element implementation of critical state models. *Computational Mechanics*, 26:185–196.

Simms, P. H. and Yanful, E. K. (2001). Measurement and estimation of pore shrinkage and pore distribution in a clayey till during soil-water characteristic curve tests. *Canadian Geotechnical Journal*, 38(4):741–754.

Simms, P. H. and Yanful, E. K. (2002). Predicting soil-water characteristic curves of compacted plastic soils from measured pore-size distribution. *Géotechnique*, 52(4):269–278.

Simunek, J., Jarvis, N. J., van Genuchten, M. T., and Gardenas, A. (2003). Review and comparison of models for describing non-equilibrium and preferential flow and transport in the vadose zone. *Journal of Hydrology*, 272(1-4):14–35.

Simunek, J., Wendroth, O., Wypler, N., and Van Genuchten, M. T. (2001). Non-equilibrium water flow characterized by means of upward infiltration experiments. *European Journal of Soil Science*, 52(1):13–24.

Sivakumar, V. (1993). *A critical state framework for unsaturated soil*. PhD thesis, University of.

Skempton, A. (1961). Effective stress in soils, concrete and rocks. In *Pore Pressure and Suction in Soil*, volume 4-16, London. Butterworths.

Slatter, E. and Allman, M. (2000). Suction controlled testing of unsaturated soils. In *8th Australia New Zealand Conference on Geomechanics*, pages 893–901. Hobart.

Smith, P. R., Jardine, R. J., and Hight, D. W. (1992). The yielding of bothkennar clay. *Géotechnique*, 42(2):257–274.

Solymar, M., Lehmann, E., Vontobel, P., and Nordlund, A. (2003). Relating variations in water saturation of a sandstone sample to pore geometry by neutron tomography and image analysis of thin sections. *Bulletin of Engineering Geology and the Environment*, 62:85–88.

Sorensen, K. K., Baudet, B. A., and Simpson, B. (2007). Influence of structure on the time-dependent behaviour of a stiff sedimentary clay. *Geotechnique*, 57(1):113–124.

Spectrum Laboratories INC. (2006). Laboratory product catalog. Breda.

Sridharan, A., Altaschaeffl, A., and Diamon, S. (1971). Pore-size distribution studies. *Journal of the Soil Mechanics and Foundation Division ASCE*, 97:771–787.

Steuter, A. A., Mozafar, A., and Goodin, J. R. (1981). Water potential of aqueous polyethylene-glycol. *Plant Physiology*, 67(1):64–67.

Svendsen, B. and Hutter, K. (1995). On the thermodynamics of a mixture of isotropic materials with constraints. *International Journal of Engineering Science*, 33(14):2021–2054.

Taibi, S. (1994). *Comportement mécanique et hydraulique des sols partiellement saturés*. PhD thesis, Ecole Centrale de Paris.

Tang, A.-M. and Cui, Y.-J. (2005). Controlling suction by the vapour equilibrium technique at different temperatures and its application in determining the water retention properties of mx80 clay. *Canadian Geotechnical Journal*, 42:287–296.

Tarantino, A. (2007). A possible critical state framework for unsaturated compacted soils. *Géotechnique*, 57(4):385–389.

Tarantino, A. and Jommi, C. (2005). Hydraulic and mechanical behaviour of unsaturated soils: Experimental evidence and constitutive modelling.

Tarantino, A. and Mongiovi, L. (2000). A study of the efficiency of semi-permeable membranes in controlling soil matrix suction using the osmotic technique. In *The Asian Conference on Unsaturated Soils*, pages 303–308, Singapore.

Tarantino, A. and Tombolato, S. (2005). Coupling of hydraulic and mechanical behaviour in unsaturated compacted clay. *Géotechnique*, 55(4):307–317.

Tavenas, F. and Leroueil, S. (1990). Laboratory and in-situ stress-strain-time behaviour of soft clays: state-of-the-art paper. In *International Symposium of Geotechnical Engineering of Soft Soils*, Mexicocity.

Terzaghi, K. (1936). The shear resistance of unsaturated soil. In *1st International Confonference on Soil Mechanics and Foundation Engineering*, volume 1, pages 54–56.

Terzaghi, K. (1944). Ends and means in soil mechanics. *Engng J. (Canada)*, 27(12):608–612.

Terzaghi, K., Peck, R. B., and Mesri, G. (1996). *Soil mechanics in engineering practice*. John & Wiley Sons, Inc., third edition.

Toll, D. G. and Ong, B. H. (2003). Critical-state parameters for an unsaturated residual sandy clay. *Géotechnique*, 53(1):93–103.

Truesdell, C. (1984). *Rational thermodynamics*. Springer-Verlag, second edition.

Truesdell, C. and Noll, W. (1992). *The non-linear field theories of mechanics*. Springer-Verlag.

Tullis, B., Lindsay, J., and Wright, S. (1992). The imaging of wetting front instabilities in porous media using neutron radiography. In *Neutron Radiography*, pages 363–372. San Francisco.

Tuncay, K. and Corapcioglu, M. Y. (1995). Effective stress principle for saturated fractured porous media. *Water Resources Research*, 31(12):3103–3106.

Van Genuchten, M. T. (1980). A closed-form equation for predicting the hydraulic conductivity of unsaturated soils. *Soil Science Society of America Journal*, 44:892–898.

Vaughan, P. R. and Kwan, C. W. (1984). Weathering, structure and in situ stress in residual soils. *Géotechnique*, 34(1):43–59.

Vaughan, P. R., Maccarini, M., and Mokhtar, S. M. (1988). Indexing the engineering properties of residual soil. *Quarterly Journal of Engineering Geology*, 21(1):69–84.

Vaunat, J., Cante, J. C., Ledesma, A., and Gens, A. (2000). A stress point algorithm for an elastoplastic model in unsaturated soils. *International Journal of Plasticity*, 16(2):121–141.

Villar, M. V. (1999). Investigation of the behaviour of bentonite by means of suction-controlled oedometer tests. *Engineering Geology*, 54(1-2):67–73.

Villar, M. V. and Martin, P. L. (1996). Suction-controlled oedometer tests in montmorillonite clay: preliminary results. In *Engineering geology of Waste Disposals*. London.

Vogel, H. and Roth, K. (1998). A new approach for determining effective soil hydraulic functions. *European Journal of Soil Science*, 49:547–556.

Vogel, T., van Genuchten, M. T., and Cislerova, M. (2000). Effect of the shape of the soil hydraulic functions near saturation on variably-saturated flow predictions. *Advances in Water Resources*, 24(2):133–144.

Vontobel, P., Lehmann, E. H., Hassanein, R., and Frei, G. (2006). Neutron tomography:method and applications. *Physica B: Condensed Matter*, 385-386:475–480.

Vulliet, L. (1986). *Modelisation des pentes naturelles en mouvement*. PhD thesis, No. 635, Ecole Polytechnique Fédérale de Lausanne.

Wang, H. and Berryman, J. (1996). On constitutive equations and effective stress principles for deformable, double-porosity media. *Water Resources Research*, 32(12):3621–3622.

Warren, J. and Root, P. (1963). The bavavior of naturally fractured reservoirs. *Society of Petroleum Engineers*, 3(3):245–255.

Washburn, E. (1921). Note on a method of determining the distribution of pore sizes in a porous material. In *Proceedings of the National Academy of Sciences*, volume 7, pages 115–116.

Wesley, L. D. (1990). Influence of structure and composition on residual soils. *Journal of geotechnical engineering*, 116(4):589–603.

Wheeler, S. J., Sharma, R. S., and Buisson, M. S. R. (2003). Coupling of hydraulic hysteresis and stress-strain behaviour in unsaturated soils. *Géotechnique*, 53(1):41–54.

Wheeler, S. J. and Sivakumar, V. (1995). An elasto-plastic critical state framework for unsaturated soil. *Geotechnique*, 45(1):35–53.

Whitaker, S. (1986). Flow in porous media II: The governing equations for immiscible, two-phase flow. *Transport in Porous Media*, 1(2):105–125.

Williams, J. and Shaykewich, C. F. (1969). An evaluation of polyethylene glycol (p.e.g.) 6000 and p.e.g. 20000 in the osmotic control of soil water matric potential. *Canadian Journal of Soil Science*, 49:397–401.

Wilmanski, K. (1995). Lagrangean model of two-phase porous material. *Journal of non-equilibrium thermodynamics*, 20:50–77.

Wilmanski, K. (1996). Porous media at finite strains: The new model with the balance equation for porosity. *Archives of Mechanics*, 48:591–628.

Wilson, R. and Aifantis, E. (1982). On the theory of consolidation with double porosity. *International Journal of Engineering Science*, 20(9):1009–1035.

Wong, R. C. K. (2000). Shear deformation of locked sand in triaxial compression. *Geotechnical Testing Journal*, 23(2):158–170.

Wood, D. M. (1990). *Soil behaviour and critical state soil mechanics*. Cambridge University Press, Cambridge.

Wood, D. M. (1995). Kinematic hardening model for structured soil. In *Numerical Models in Geomechanics -NUMOG V*, pages 83–88.

Wu, W., Li, X., Charlier, R., and Collin, F. (2004). A thermo-hydro-mechanical constitutive model and its numerical modelling for unsaturated soils. *Computers and Geotechnics*, 31(2):155–167.

Yong, R. and Nagaraj, T. (1977). Investigation of fabric and compressibility of a sensitive clay. In *Proceedings of the International Symposium on Soft Clay*, pages 327–333, Asian Institute of Technology.

Yong, R. and Warkentin, B. (1975). *Introduction to soil behavior*. The MacMillan Co, New York.

Yu, H. S. (1998). CASM: A unified state parameter model for clay and sand. *International Journal for Numerical and Analytical Methods in Geomechanics*, 22(8):621–653.

Yu, H. S. (2006). *Plasticity and Geotechnics*. Advances in Mechanics and Mathematics. Springer, New York.

Zehrouni, M. I. (1991). *Rôle de la pression interstitielle négative dans le comportement des sols-Application aux routes*. PhD thesis, Ecole Centrale de Paris.

Zeng, Y., Ganzer, C. J., Peyton, R. L., and Anderson, S. H. (1996). Fractal dimension and lacunarity of bulk density determined with x-ray computed tomography. *Soil Science America Journal*, 60:178–1724.

Zienkiewicz, O. C. and Mroz, Z. (1984). Generalized plasticity formulation and application to geomechanics. In *Mechanics of Engineering Materials*, pages 655–679. John Wiley & Sons, Inc.

Zur, B. (1966). Osmotic control of matric soil-water potential. I: Soil-water system. *Soil Science*, 102(6):394–398.

# Appendix A

# Control tests for the new osmotic oedometer cell

The new osmotic oedometer has been controlled in series of tests in order to verify the efficiency of different components and to control the oedometer results prior to be used in the experimental testing program. These tests are summarized in Table 4.3 and briefly described below.

**Test C1:** The reservoir was filled with distilled de-aired water and the closed circulation system was set up without the cell. Mass variation of the reservoir was monitored periodically. Provided this condition, (i) the circulation was continued at least for 3 hours to check the stability of balance measurement; and, (ii) velocity of the pump was changed to check whether it could influence the balance measurements.

Results showed stability of mass measurement by the balance. It was also observed that providing a static stable physical condition of the system, balance measurements could not be influenced by pump speed (Check no.1).

**Test C2:** The reservoir was filled with distilled de-aired water and the circulation system was connected to the empty cell with the membrane. During the circulation f liquid, (i) diffusion of water beneath the membrane was checked (direct observation by naked eye); (ii) leakage of fluid out of the cell was controlled (direct observation by naked eye); and, (iii) deformability and stability of the membrane was observed by changing the velocity and direction of pump operation.

No leakage of fluid from the cell was observed and the actual configuration of cell was found to be enough to prevent any fluid leakage (Check no. 2). It was observed that water could diffuse all around the mesh beneath the membrane (Check no. 3). Deformation of the membrane due to the liquid pressure beneath the membrane was monitored at different condition of testing (Check no. 4). It was found that that direction of pump rotation as well as the difference of water head in the cell and reservoir both had important effects on the deformation of the membrane. When water in the reservoir had a overhead to the cell and it is pushed into the cell, the membrane showed an important upturn deformation. In order to avoid this problem, condition of equal heads in reservoir and cell was

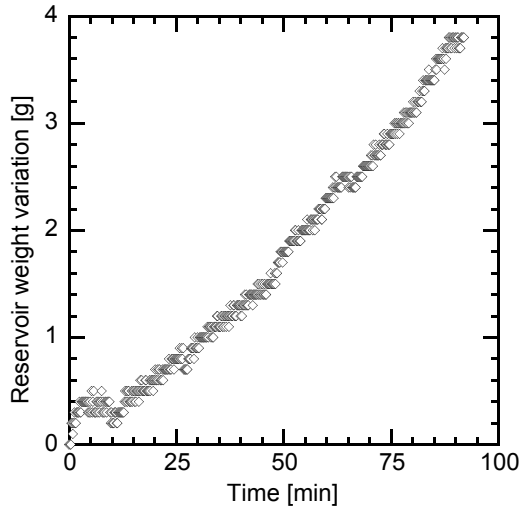


*Figure A.1:* Variation of reservoir weight with time when the cell is filled with water

provided; and, liquid was pulled from instead of pushed into the cell. Results revealed the importance of maintained a uniform operation velocity of pump in order to have a stable condition for the membrane.

**Test C3:** The reservoir was filled with PEG solution of 0.3 concentration and the circulation system was connected to the cell with the membrane. Instead of soil sample, the cell was filled with distilled de-aired water. Circulation of the solution was started and continued for at least 3 hours. In this condition, (i) the measured values of the balance was monitored, and (ii) Brix number of the solution and the water in the cell was measured before and after the test to check the efficiency of the membrane to prevent PEG from entering to the cell.

The mass of exchanged is plotted in Figure A.1. As expected, a clear increase in the weight of reservoir due to water transfer from cell to the reservoir was observed (Check no. 5). Brix number of solution corrected for temperature was 21% and 20.1% at beginning and end of the test respectively. The Brix number of water in the cell was remained zero. These results showed that first, the membrane allowed only pure water to pass (Check no. 6); and also, there was no leakage of solution to the cell from the membrane boundary (Check no. 7).

**Test C4:** Test C3 was repeated with the exception that cell was empty. During the circulation of liquid for 5 hours, (i) it was controlled whether there fluid could pass through the membrane into the cell (ii) the Brix number of the liquid in the cell was measured to check whether the accumulated liquid in the cell was pure water or not. Measurement was made three times during the test.

Slow accumulation of liquid in the cell was observed. Brix number of solution corrected for temperature was 20.5% and 21.1% at beginning and end of the test respectively. While, the Brix number of the liquid in the cell was equal 0 showing that the membrane allowed only the pure water to pass. These results confirmed the efficiency of the membrane in selectively preventing the

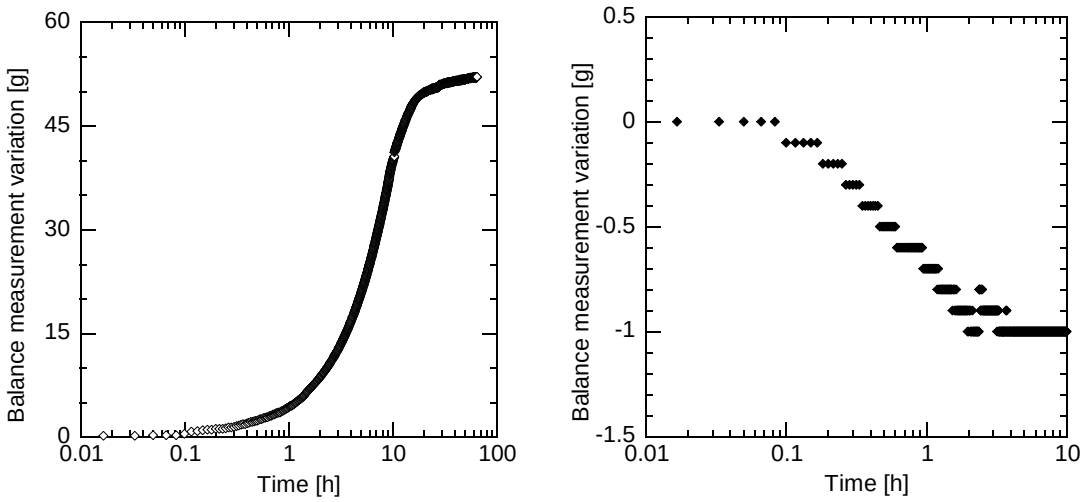


*Figure A.2:* Determination of equilibrium time in a single suction step: (a) Drying path, (b) Wetting path

*Table A.1:* Water content of the sample deduced from balance measurements for drying and wetting path

| **Test** | $w_i$ [%] | $M_s[g]$ | $\Delta M_w[g]$ | $\Delta w$[%] | $w_f$[%] | $\frac{w_i + \Delta w - w_f}{w_f - w_i} \times 100$ |
|---|---|---|---|---|---|---|
| C5 | 42.8 | 210.5 | 52.1 | -24.7 | 16.6 | 5.75 |
| C6 | 15.05 | 186.48 | 0.8 | 0.43 | 15.62 | 24.1 |

passage of only the PEG mocelules (Check no. 8). As well, observation made during this test showed, one again, that no leakage of solution from boundary of the membrane to the cell could occur (Check no. 7).

**Test C5:** Test C3 was repeated with the exception that instead of the water, a sample of saturated slurry of Bioley silt was placed directly in the cell. Circulation was continued until reaching equilibrium in mass measurements by the balance. Water content of the sample was measured before and after the test. The exchanged value of water given by the the balance measurements was compared with the difference in the initial and final water content of the sample.

Figure A.2(a) shows weight of extracted water from the sample versus time in a semi-logarithmic scale. Time of equilibrium can be clearly recognized in this plot. The obtained values of water content are listed in Table A.1. For the whole change of water content, a difference of 5.75 per cent was observed between direct measurement and calculated values from balance measurements; this difference could be decreased by more careful preparation of the sample and sample weighting before and after the test (Check no. 9).

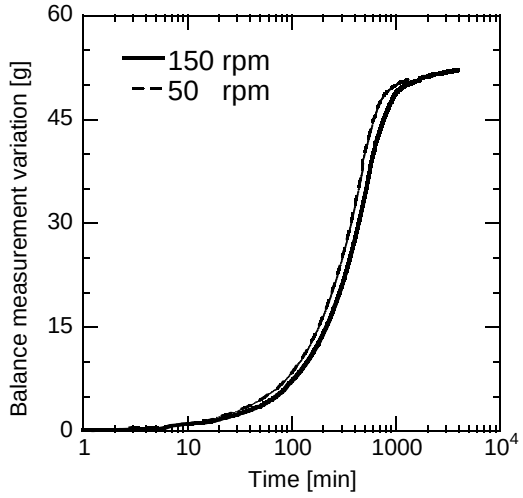


*Figure A.3:* Variation of equilibrium time with pump velocity

**Test C6:** Test C5 was repeated for a wetting path. In this test, the reservoir was filled with pure water instead of PEG solution and the sample was initially an unsaturated sample of Bioley silt.

Figure A.2(b) shows weight of adsorbed water by the sample versus time in a semi-logarithmic scale. Time of equilibrium can be clearly recognized in this plot. Table A.1 compares the water content of soil obtained from direct measurements at the end of the test as well as calculated from balance measurements (Check no. 10). In this case the difference with respect to the total change of water content was 24%, however, this could be due to small values of water change. In general, the difference between obtained variations during wetting and drying path showed that this method is less precise for wetting paths.

**Test C7:** Test C5 was repeated with a different pumping speed to compare the influence of this factor on the equilibrium time.

Results illustrated in Figure A.3 showed a slight decrease of equilibrium time for water exchange when the pump speed increases; however, this change was not significant (Check no. 11).

**Test C8:** A saturated oedometer test was performed on reconstituted Bioley silt. Two similar tests were carried out in the new osmotic cell and conventional oedometer cell inorder to validate the oedometric results of the new cell. In the osmotic cell, the reservoir was filled with de-aired water and instead of the membrane, a filter paper was used to facilitate the drainage. Results obtained by two oedometers were found to be in quite good agreement (see Sec. 4.4.3).

# Appendix B

# Supplementary experimental results

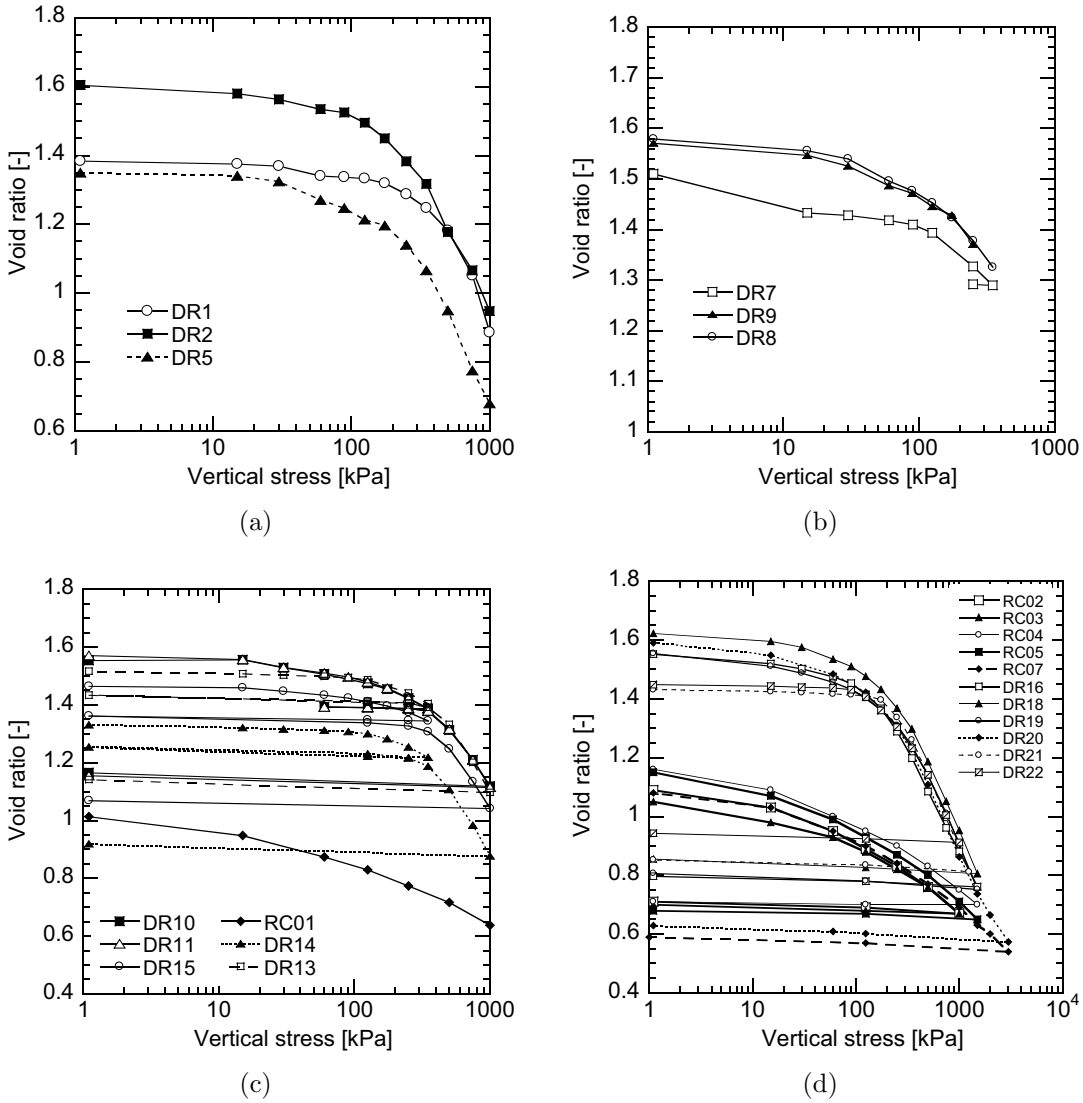


*Figure B.1:* Supplementary results of dry oedometer tests: (a) series 1, (b) series 2, (c) series 3, 4 and 7, (d) series 5, 6, 8 and 9

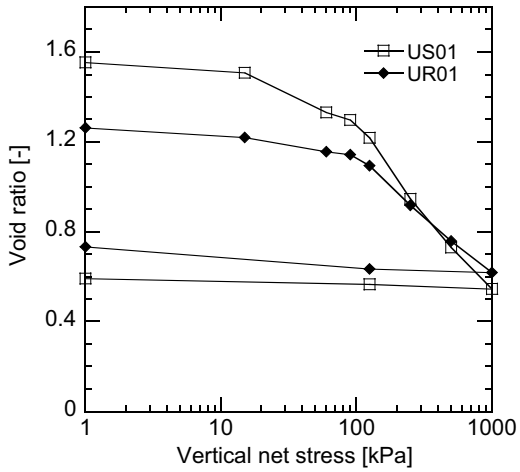


*Figure B.2:* Oedometic curves of aggregated (US01) and reconstituted (UR01) samples of Bioley silt under suction of 40 $kPa$, tested in hydrocon cell

*Table B.1:* Water exchange during the oedometer tests in hydrocon cell

| **Sample** | $M_s$ $(gr)$ | $w_f$ (%) | $w_i$ (%) | $\Delta w$ (%) | $M_w$ $(gr)$ | $V_{wi}$ $(cm^3)$ | $V_{wf}$ $(cm^3)$ | $\Delta V_w$ $(cm^3)$ |
|---|---|---|---|---|---|---|---|---|
| US01 | 53.04 | 10.8 | 11.8 | 1 | 0.53 | -817.85 (-851.912) | -864.648 | (-12.736) |
| UR01 | 58.18 | 10.2 | 11 | 0.8 | 0.47 | -20.39 | -11.678 | 8.712 |

# Appendix C

# Modeling suction effects on the fabric of an aggregated soil

In this section, a mathematical model is presented to simulate the PSD modification during the suction increase based on the PSDs of the saturated and the drier cases. Due to the fact that the concept of volume fraction, defined here as the volume of pores per unit weight of the soil, is more suitable for the physical understanding of behavior, the proposed model was developed on this basis. A validation of the model results with respect to experimental ones then concludes this section.

## C.1 Suction increase effect on PSD

Here, the effect of suction increase on the pore size distribution (PSD) of a double porosity soil has been evaluated based on the experimental work of Cuisinier and Laloui (2004). In that study, the PSD of a sandy loam has been determined at different levels of suction under constant vertical net stress in oedometric condition.

The PSD of the tested material for five suction levels was shown in Figure 2.17 in terms of pore size density function, and here, it is presented in Figure C.1 in terms of volume fraction. Two pore classes can be seen (micro and macropores) in this figure with the he limit between them being about 1 $\mu m$.

Knowing the sample's initial fabric (zero suction), the analysis of the influence of drying on fabric was carried out. It may be seen in Figure 4 that the suction increase induces modifications of the soil fabric, such as a strong reduction of the macroporosity. It is interesting to note that the reduction of the amount of macropores is accompanied by a relative increase in the microporosity, which can be explained by the shrinkage of the macropores. The comparison of all of these PSD curves shows that the drying process did not affect pores smaller than 0.1 $\mu m$.

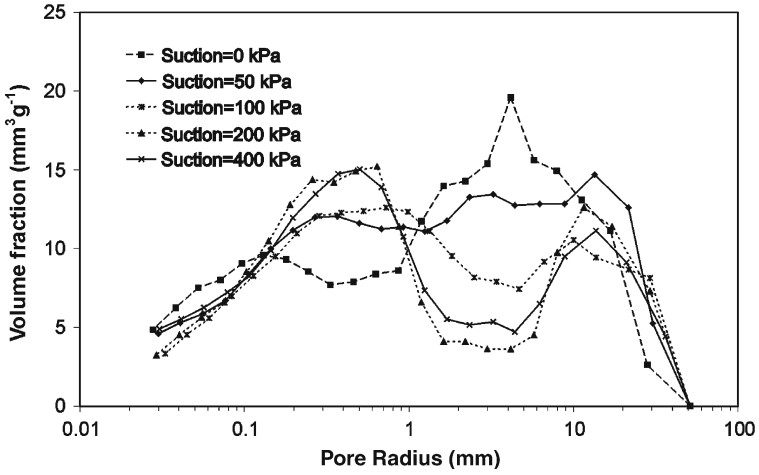


*Figure C.1:* Modification of samples fabric when suction is increased from 0 up to 400 $kPa$ under constant net vertical stress of 10 $kPa$, (after Cuisinier and Laloui, 2004)

## C.2 Characterization of pore classes

The modeling concept is as follows: giving two limit cases, the saturated case (zero suction- initial case) and the driest case (suction of 400 $kPa$ - final case), we determine the modification of the PSD curves for intermediate cases.

From the results in Figure C.2, four different zones of pore classes can be recognized: Zones 1 and 4 are related to the pores which are only slightly affected by suction and on which the influence of suction can be neglected. Zone 2 corresponds to the micropores; the volume fraction of these pores increases as suction increases. The pore volume fraction of the pores that belong to the third zone reduces as suction increases. The behavior of these pore classes are different and they should be distinguished in the model formulation. Three pore radii R1, R2 and R3 determine the limits between pore zones.

## C.3 Suction influence domain

The relationship between any suction, $s$, and the corresponding pore radius, $r_p$, can be determined by Equation (5.1) using the value of contact angle $\theta$ equal to zero (air-water interface):

$$s = \frac{2T_s}{r_s} \tag{C.1}$$

where the surface tension of the water, $T_s$, is equal to 0.07275 $Nm^{-1}$. $r_s$ is the drained pore radius at that value of suction $s$ and it can be considered as the minimum pore radius influenced by suction $s$ (note that in doing so, hysteretic effects are neglected). Using Equation C.1, it is possible to determine the suction influence domain for a given suction value. This domain can be defined as a domain in which the pores have radii greater than $r_s$. Thus, Zone 3 is subdivided into Zones 3a and 3b when $r_2 < r_s < r_3$ (see Figure C.2).

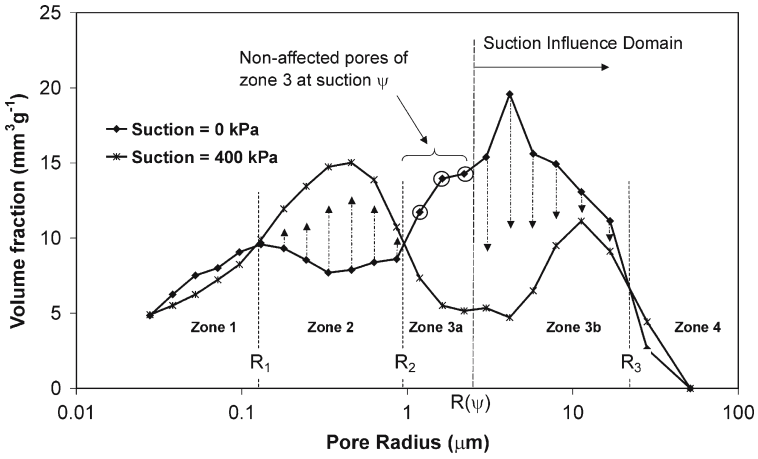


*Figure C.2:* Different zones of pore classes, Suction influence domain and evolution of pore classes

## C.4 Modeling steps

The following general framework to model the PSD modifications is outlined as follows:

- volume fraction of pores of Zone 1 and 4 are not affected by suction increase;
- as suction increases, only the pore volume of Zone 3 (macropores) can decrease;
- a part of the volume fraction decrease of Zone 3 will be added to Zone 2 and consequently the volume fraction of Zone 2 (micropores) will increase;
- it is assumed that, at a given suction, only the volume fraction of pores of Zone 3 located in the suction influence domain is added to the volume fraction of pores of Zone 2. This concept is illustrated in Figure C.1.

Based on this framework, PSD (or volume fraction distribution) modification at a given suction $s$ can be evaluated by considering five intervals of radii.

### C.4.1 Zone 1

As already mentioned, volume fractions of pores located in Zone 1 are only slightly affected by suction. Therefore, in this model, it is assumed that these pores keep their initial value of volume fraction. This implies:

$$\vartheta(r_p, s) = \vartheta(r_p, s_0); \qquad r_p < r_1 \tag{C.2}$$

where $r$ is the pore class radius, $\vartheta(r_p, s)$ is the predicted volume fraction of pores at suction $s$ and $\vartheta(r, s_0)$ is the volume fractions of pore class measured at the initial stage (zero suction, $s = 0$).

### C.4.2 Zone 4

Here again, no changes are expected, and thus:

$$\vartheta(r_p, s) = \vartheta(r_p, s_0); \qquad r_p > r_3 \tag{C.3}$$

### C.4.3 Zone 3a

For the pores located in Zone 3 but not in the suction influence domain (Zone 3a, Fig. C.2, no reduction in their volume fraction is experienced and, thus:

$$\vartheta(r_p, s) = \vartheta(r_p, s_0); \qquad r_2 < r_p < r_s \tag{C.4}$$

### C.4.4 Zone 3b

In this zone, the volume fraction of each pore class can be obtained by subtracting a specific value of volume fraction from the initial PSD. As already assumed for a given suction, only pores of Zone 3 located in the suction influenced domain (Zone 3b) show reduction in their volume fractions. It can be concluded that the total volume fraction that should be subtracted from the initial case (saturated) during the suction increase from the initial to final case is calculated by:

$$\Theta_s = \sum_{r_p > r_s} (\vartheta(r_p, s_0) - \vartheta(r_p, s_f)); \qquad r_2 < r_p < r_3 \qquad (zone\ 3b) \tag{C.5}$$

where $\Theta_s$ is the total influenced volume fraction, $\vartheta(r_p, s_0)$ is the initial volume fraction of pore class with radius $r$ at suction $s$, and $\vartheta(r_p, s_f)$ is the final volume fraction at suction $s_f$ of the final case.

It should be noted that in a soil with different pore sizes, the large pores might be entrapped by the smaller ones. It means that some parts of the larger pores are not accessible to be influenced by suction until the smaller pores that trap them are influenced and drained.

As a result of pore trapping, only a portion of $\Theta_s$ should be subtracted from the initial PSD, called the effective volume fraction, $\Theta_{se}$. As a first approximation, the relationship between $\Theta_s$ and $\Theta_{se}$ can be assumed as:

$$\Theta_{se} = C_3 \Theta_s \tag{C.6}$$

where $C_3$ is a function of $s$ (to be defined). Knowing $\Theta_{se}$, the new location of the PSD for a specific suction $s$ can be found by linear interpolation between the initial and the final cases:

$$\vartheta(r_p, s) = \vartheta(r_p, s_0) - C_3(\vartheta(r_p, s_0) - \vartheta(r_p, s_f)); \qquad r_s < r_p < r_3 \tag{C.7}$$

In the lack of experimental evidence on pore trapping, an approximation should be made for the value of $C_3$. A possible expression for $C_3$ can be constructed by considering that:

- for $r_s < r_2$, $C_3 = 1$ because the PSD curve obtained by MIP is assumed to be the real curve without air trapping.
- for $r_s < r_3$, $\Theta_s = 0$ and $C_3$ can take any value, $\Theta_{se}$ being always zero.
- for intermediate cases, the trapped air is expected to be a function of the ratio $\Theta_s/\Theta_3$, where $\Theta_3$ is the total volume fraction difference between the initial and final cases in Zone 3:

$$\Theta_3 = \sum_{r_2<r_p<r_3} (\vartheta(r_p, s_0) - \vartheta(r_p, s_f)) \tag{C.8}$$

Back-calculations from the experimental results provided by Cuisinier and Laloui (2004) showed that a possible candidate for $C_3$ is:

$$C_3 = \left(\frac{\Theta_s}{\Theta_3}\right)^2 \tag{C.9}$$

### C.4.5 Zone 2

In order to model the volume fraction variation of pores in Zone 2, some information about the amount of affected macropore volume fraction which is going to be added to the micropores is required. Volume variation of a soil during the application of suction can be divided in two parts. The first one is the external volume variation which can result in a total porosity reduction, and the second one is the internal volume variation which is related to the shrinkage of macropores and subsequent change into micropores. Therefore, for each macropore class located in Zone 3, there is only a portion of the total experienced volume fraction reduction which is added to the micropore classes. It is assumed that, at each suction step, this portion is determined by a constant coefficient which is equal to the ratio of total micropore increase to the total macropore decrease from the initial to the final case. Therefore, this coefficient can be determined as follows:

$$C_2 = \frac{\Theta_2}{\Theta_3} \tag{C.10}$$

where

$$\Theta_2 = \sum_{r_1<r_p<r_2} (\vartheta(r_p, s_0) - \vartheta(r_p, s_f)) \tag{C.11}$$

The total moving volume fraction from macropores to micropores, $\Theta_{2e}$ which is a portion of the total influenced volume fraction $\Theta_s$ is determined by this coefficient:

$$\Theta_{2e} = C_2\Theta_s \tag{C.12}$$

This volume fraction should be distributed among the micropores and added to the initial volume fractions. The new location of the PSD for a specific suction can be found (as in Eq. C.7) by linear interpolation. As a result, the modeled volume fraction of pores located in Zone 2 can be estimated by:

$$\vartheta(r_p, s) = \vartheta(r_p, s_0) - \frac{\Theta_{2e}}{\Theta_2}(\vartheta(r_p, s_0) - \vartheta(r_p, s_f)); \qquad r_1 < r_p < r_2 \tag{C.13}$$

## C.5 Model assessment

The model presented is conceived for the simulation of the modification of the pore space geometry of double porosity structured soils subjected to a suction increase. It is mainly based on the concept of the suction influence domain and includes experimental evidence of the effect of suction on micropores and macropores. In order to validate this model, it was used to simulate the PSD modification for the experiments presented in Section 2 of this paper.

The initial data needed for the model are the PSD curves for the saturated state (zero suction) and drier state (suction of 400 $kPa$). The model predictions made for the PSD curves at suction levels of 50, 100 and 200 $kPa$ will be analyzed. The comparison between the simulated curves with the experimental results is given in the following paragraphs.

Table C.1 illustrates the introduced and the obtained data for the intermediate case of suction equal to 50 $kPa$.

The required initial data for modeling are given in the columns 1 to 3. They consist in radii of the pores that represent different pore classes (column 1), the values of volume fractions at the initial suction ($s = 0$, column 2) and the final suction ($s = 400$ $kPa$, column 3).

Comparing the initial and the final PSD curves together and considering their intersection at different points, the limits between the zones is determined (Fig. C.2). Therefore, four different zones are recognized and attributed to the pore classes as it is done in column 4.

In column 5 the pores of zone 3 are divided into zone 3a and zone 3b. Zone 3a represents the pores that have pore radius less than the pore radius corresponding to the current suction ($s = 50$ $kPa$). According to equation 1 the corresponding pore radius is equal to 2.91 $\mu m$.

Equations (C.2), (C.3) and (C.4) give the volume fraction of pores at zones 1, 4 and 3a equal to their initial values. This is shown in columns 6, 7 and 8 respectively. To determine the volume fraction of pores in zone 3b, it is first required to calculate the values of $\Theta_s$ and $\Theta_3$. According to Equations (C.5) and eq:uptheta3, the values of $\Theta_s$ and $\Theta_3$ are respectively equal to the summation of the values of column 9 and 10. In this example, these values are $\Theta_s = 43.40$ and $\Theta_3 = 65.35$ and using these values in Equation (C.9), one can have $C_3 = 0.441$. Having the value of $C_3$ and using Equation (C.7), the values of volume fraction for zone 3b may be calculated. These values are given in column 11.

The three parameters $\Theta_2$, $C_2$ and $\Theta_{2e}$ are required to calculate the volume fraction of pores in zone 2. $\Theta_2$ is calculated using Equation (C.11), i.e. equal to the summation of column 12. The value of $\theta_2$ here is 29.66. Substituting this value in Equation (C.10), the value of $C_2$ is obtained equal to 0.454. Therefore, according to Equation (C.12), it is obtained $\Theta_{2e} = 19.70$. Finally, using Equation (C.13), the values of volume fraction for zone 2 are determined as it is shown in column 13. The model prediction data are then summarized in column 14.

*Table C.1:* Initial and calculated PSD data for the intermediate case of suction equal to 50 $kPa$

| 1 | 2 | 3 | 4 | 5 | 6 | 7 | 8 | 9 | 10 | 11 | 12 | 13 | 14 |
|---|---|---|---|---|---|---|---|---|---|---|---|---|---|
| $r$ ($\mu m$) | $\vartheta(r_p, s_0)$ | $\vartheta(r_p, s_f)$ | Zone | Zone 3a,b | Zone 1 | Zone 4 $\vartheta(r_p, s)$ | Zone 3a | $\vartheta(r_p, s_0) - \vartheta(r_p, s_f)$ for zone 3b | $\vartheta(r_p, s_0) - \vartheta(r_p, s_f)$ for zone 3 | Zone 3b $\vartheta(r_p, s)$ | $\vartheta(r_p, s_0) - \vartheta(r_p, s_f)$ for zone 2 | Zone 2 $\vartheta(r_p, s)$ | Model $\vartheta(r_p, s)$ |
| 51.32 | 0.00 | 0.00 | 4 | - | - | 0.00 | - | - | - | - | - | - | 0.00 |
| 28.17 | 2.63 | 4.43 | 4 | - | - | 2.63 | - | - | - | - | - | - | 2.63 |
| 16.80 | 11.14 | 9.13 | 3 | 3b | - | - | - | 2.01 | 2.01 | 10.25 | - | - | 10.25 |
| 11.25 | 13.07 | 11.13 | 3 | 3b | - | - | - | 1.94 | 1.94 | 12.22 | - | - | 12.22 |
| 7.92 | 14.93 | 9.50 | 3 | 3b | - | - | - | 5.43 | 5.43 | 12.54 | - | - | 12.54 |
| 5.76 | 15.61 | 6.49 | 3 | 3b | - | - | - | 9.12 | 9.12 | 11.59 | - | - | 11.59 |
| 4.16 | 19.58 | 4.72 | 3 | 3b | - | - | - | 14.86 | 14.86 | 13.02 | - | - | 13.02 |
| 3.00 | 15.39 | 5.35 | 3 | 3b | - | - | - | 10.04 | 10.04 | 10.96 | - | - | 10.96 |
| 2.20 | 14.27 | 5.15 | 3 | 3a | - | - | 14.27 | - | 9.12 | - | - | - | 14.27 |
| 1.63 | 13.96 | 5.52 | 3 | 3a | - | - | 13.96 | - | 8.45 | - | - | - | 13.96 |
| 1.19 | 11.72 | 7.35 | 3 | 3a | - | - | 11.72 | - | 4.38 | - | - | - | 11.72 |
| 0.86 | 8.61 | 10.74 | 2 | - | - | - | - | - | - | - | 2.14 | 10.025 | 10.03 |
| 0.63 | 8.39 | 13.89 | 2 | - | - | - | - | - | - | - | 5.50 | 12.042 | 12.04 |
| 0.46 | 7.89 | 15.03 | 2 | - | - | - | - | - | - | - | 7.14 | 12.628 | 12.63 |
| 0.33 | 7.71 | 14.74 | 2 | - | - | - | - | - | - | - | 7.04 | 12.381 | 12.38 |
| 0.24 | 8.55 | 13.46 | 2 | - | - | - | - | - | - | - | 4.91 | 11.809 | 11.81 |
| 0.18 | 9.32 | 11.95 | 2 | - | - | - | - | - | - | - | 2.63 | 11.066 | 11.07 |
| 0.13 | 9.58 | 9.89 | 2 | - | - | - | - | - | - | - | 0.31 | 9.7883 | 9.79 |
| 0.10 | 9.06 | 8.25 | 1 | - | 9.06 | - | - | - | - | - | - | - | 9.06 |
| 0.07 | 8.01 | 7.23 | 1 | - | 8.01 | - | - | - | - | - | - | - | 8.01 |
| 0.05 | 7.52 | 6.25 | 1 | - | 7.52 | - | - | - | - | - | - | - | 7.52 |
| 0.04 | 6.25 | 5.52 | 1 | - | 6.25 | - | - | - | - | - | - | - | 6.25 |
| 0.03 | 4.85 | 4.90 | 1 | - | 4.85 | - | - | - | - | - | - | - | 4.85 |

volume fractions in $mm^3 g^{-1}$

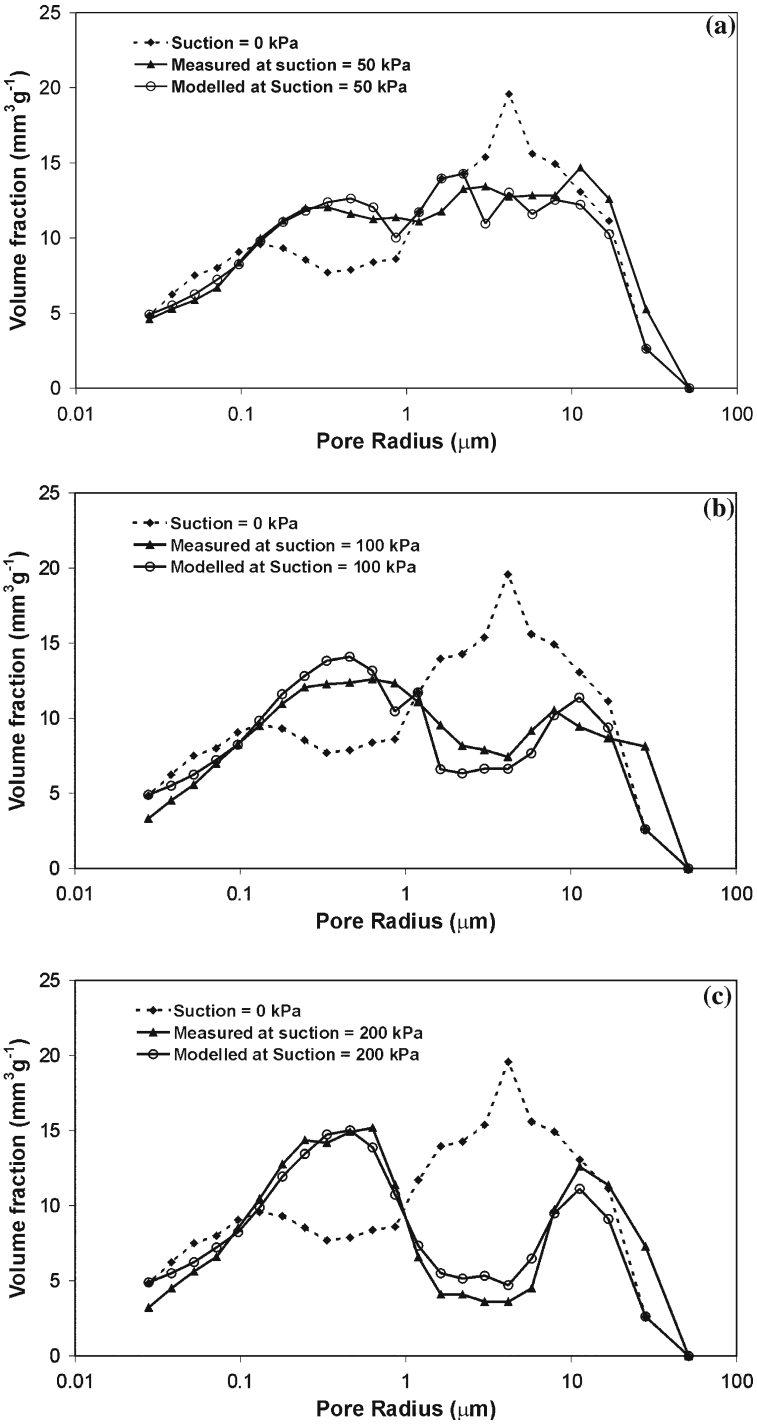


*Figure C.3:* Variation of reservoir weight with time when the cell is filled with water

The same calculation are made for the other intermediate suction values ($s = 100$, 200 $kPa$) and the results are shown in Figure C.3. As may be seen in Figure C.3(a), the model correctly reproduces the decrease of macropores as well as the increase of micropores. The lower limit domain of the suction influence is situated at a radius of about 3 $\mu m$. The modeled macropores under this limit have the same values of volume fraction as those for the saturated case. This aspect was also observed for the experimental points. The same satisfactory prediction applies to the behavior at a suction of 100 $kPa$ (Fig. C.3(b)), even if the experimental and the simulated results are not perfectly superposed. Almost all macropores are affected by the suction increase. The numerical simulation at a suction of 200 $kPa$ is shown in Figure C.3(c). The model reproduces the behavior of the three zones remarkably well. In Zones 1 and 4 (pore radius less then $r_1$ and greater than $r_3$) the effect of suction is very limited. In Zone 3 (macropores), the important decrease in the volume fraction is well reproduced. This is also the case for Zone 2 (micropores), where the significant increase in micropores is well predicted. The modelled volume fractions at 200 $kPa$ are the same as those at 400 $kPa$ are due to the fact that this latter one is the final limit of the model.